



BRNO UNIVERSITY OF TECHNOLOGY

VYSOKÉ UČENÍ TECHNICKÉ V BRNĚ

FACULTY OF ELECTRICAL ENGINEERING AND COMMUNICATION

FAKULTA ELEKTROTECHNIKY A KOMUNIKAČNÍCH TECHNOLOGIÍ

DEPARTMENT OF ELECTRICAL POWER ENGINEERING

ÚSTAV ELEKTROENERGETIKY

ACCELERATOR DRIVEN SUBCRITICAL NUCLEAR REACTORS: HISTORY, CHALLENGES, AND PERSPECTIVES OF THESE ADVANCED NUCLEAR SYSTEMS

PODKRITICKÉ URYCHLOVAČEM ŘÍZENÉ JADERNÉ REAKTORY: HISTORIE, AKTUÁLNÍ VÝZVY A
PERSPEKTIVY TĚCHTO POKROČILÝCH JADERNÝCH ZAŘÍZENÍ

ASSOCIATE PROFESSORSHIP THESIS

HABILITAČNÍ PRÁCE

AUTHOR

AUTOR PRÁCE

ING. KAREL KATOVSKÝ, PH.D.

BRNO 2019

ABSTRAKT

Urychlovačem řízené podkritické jaderné reaktory jsou pokročilé reaktorové systémy, které jsou provozovány v podkritickém ustáleném stavu s externím zdrojem neutronů ve formě urychlovače částic s vhodným terčem. Jedná se o systémy, které jsou ve stádiu výzkumu a vývoje a které mohou v budoucnu pomoci s řešením problematiky vyhořelého jaderného paliva či dlouhodobě udržitelné jaderné energetiky obecně – s využitím thoria či ochuzeného uranu jako paliva. Ve výzkumu ADS (Accelerator Driven Systems – urychlovačem řízených systémů) hrají zásadní roli jaderná data – účinné průřezy, výtěžky jaderných reakcí, výtěžky reakcí produkujících neutrony, energetická spektra emitovaných částic. Předkládaná práce obsahuje jak výsledky výpočtů, tak zejména experimentální data získaná autorem a jeho kolegy díky unikátním zařízením provozovaným ve Spojeném ústavu jaderných výzkumů v Dubně. Habilitační práce má formu komentovaného souboru 12 článků, které postupně procházejí odbornou kariérou autora práce; hlavní částí práce je monografie společně publikovaná autorem a profesorem Vinodem Verma Kumarem, hostujícím profesorem na Rajiv Gandhi University, Itanagar, Arunáčalpradéš, Indie.

KLÍČOVÁ SLOVA

ADS; urychlovačem řízený systém; urychlovačem řízený podkritický reaktor; vyhořelé jaderné palivo; transmutace; účinný průřez; reakční rychlost; spektrum neutronů; jaderná data; JINR; SUJV; Dubna

ABSTRACT

Accelerator driven subcritical nuclear reactors are advanced nuclear systems being operated in subcritical steady-state with external neutron source in the form of particle accelerator with proper target. These systems are under research and development now, they might help with spent nuclear fuel question in the future or they may make nuclear power sustainable using thorium or depleted uranium as a fuel. Investigation of ADS (Accelerator Driven Systems) is particularly focused on nuclear data – cross sections, nuclear reaction yields, neutron yields, energy spectra of emitted particles. Thesis presented consists of calculation results, as well as of experimental data obtained by the author and his colleagues on unique facilities being operated in Joint Institute for Nuclear Research at Dubna. Associated professorship thesis contains 12 articles and papers, which are systematically describing professional career of the author; the main part is a monography jointly published by the author and Dr. Vinod Verma Kumar, visiting professor at Rajiv Gandhi University, Itanagar, Arunachal Pradesh, India.

KEYWORDS

ADS; accelerator driven system; accelerator driven subcritical reactor; spent fuel; transmutation; cross section; reaction rate; neutron spectrum; nuclear data; JINR; Dubna

PACS NUMBERS

28.90.+i Other topics in nuclear engineering and nuclear power studies

25.40.Sc Spallation reactions

25.60.Dz Interaction and reaction cross sections

28.65.+a Accelerator-driven transmutation of nuclear waste

KATOVSKÝ, K. *Podkritické urychlovačem řízené jaderné reaktory: Historie, aktuální výzvy a perspektivy těchto pokročilých jaderných zařízení*, Brno: Vysoké učení technické v Brně, Fakulta elektrotechniky a komunikačních technologií, habilitační práce, 2019.

PROHLÁŠENÍ

Prohlašuji, že svou habilitační práci na téma *Podkritické urychlovačem řízené jaderné reaktory: historie, aktuální výzvy a perspektivy těchto pokročilých jaderných zařízení* jsem vypracoval samostatně s použitím odborné literatury a dalších informačních zdrojů, které jsou citovány v práci a uvedeny v seznamu literatury. Jelikož je habilitační práce podávána jako komentovaný soubor publikací autora, je samostatná s ohledem na podíl spoluautorů uvedených v daných publikacích; stejně tak použitá literatura, kterou bylo nutno nastudovat a použít, není uvedena v práci, ale v referencích daných publikací.

Jako autor předkládané habilitační práce dále prohlašuji, že v souvislosti s vytvořením této práce jsem neporušil autorská práva třetích osob, zejména jsem nezasáhl nedovoleným způsobem do cizích autorských práv osobnostních a/nebo majetkových a jsem si plně vědom následků porušení ustanovení §11 a následujícího autorského zákona č. 121/2000 Sb., o právu autorském, o právech souvisejících s právem autorským a o změně některých zákonů (autorský zákon), ve znění pozdějších předpisů, včetně možných trestněprávních důsledků vyplývajících z ustanovení části druhé, hlavy VI. díl 4 Trestního zákoníku č. 40/2009 Sb.

Věnováno mému otci.

Chtěl bych na tomto místě poděkovat svým odborným mentorům, panu Dr. Jindřichu Adamovi, panu profesoru Vinodu Verma Kumarovi, docentu Ivanu Haysakovi a paní profesorce Anahit Balabekyan. Bez jejich idejí, nadšení, konzultací a podpory bych nikdy nedokázal práci dokončit. Zásadní poděkování ale nepatří jen mým mentorům, ale i mým studentům. Jsou to jejich články, konference, granty a konzultace, které mě v posledních 10 letech udržovaly v odborné formě a pomáhaly mi dále růst. Víím, že zde není možné jmenovat všechny ty více než dvě desítky studentů, se kterými jsem se problematikou ADS zabýval, ale neodolám zmínit Milana Štefánika, Ondřeje Šťastného a Lukáše Závorku z FJFI ČVUT v Praze a Jana Varmužu, Miroslava Zemana, Josefa Svobodu a Dušana Krále z FEKT VUT v Brně. V nich jsem našel nejen pilné studenty a kolegy, ale i přátele na celý život.

Předmluva

Jako svoji habilitační práci předkládám knihu Spent Nuclear Fuel and Accelerator-Driven Subcritical Systems [1], kterou jsme napsali společně s prof. Vinodem Kumarem a která vyšla v nakladatelství Springer Nature Singapore v lednu 2019. Knihu doplňuji několika články, které postupně procházejí celou mojí akademickou kariérou spojenou s tématem habilitační práce – urychlovačem řízenými podkritickými systémy. První z nich [2] vychází ještě z mé diplomové práce [3] a byla prezentována spolužákem, Dr. Křepelem na konferenci AccApp'01 v Renu. Následně se jedná o publikace, které jsme připravili s mým školitelem [4,5,6] a jež vyvrcholily článkem publikovaným v impaktovaném časopise European Physical Journal [7] tři roky po obhajobě mé disertační práce [8]. Ikdž jsem v letech 2008 až 2012 strávil v SUJV Dubna pouhý týden, nadále jsem zůstal v kontaktu se svým bývalým školitelem a začala se prohlubovat moje spolupráce se skupinou prof. Balabekyan a prof. Kumara. Z tohoto období pocházejí publikace [9,10,11]. Po roce 2012 se počet mým publikací dále zvyšuje, nicméně je to tím, že jsem se začal intenzivněji věnovat práci s doktorandy, motivoval jsem je k psaní článků a k zodpovědnosti za jejich vydání. Ač množství článků v tomto období narůstá, nemám z této doby prakticky žádné články jako hlavní autor – vždy jsem raději volil cestu toho, aby hlavním zodpovědným autorem byl někdo z mých doktorandů. Z počátku se jednalo hlavně o práce mých prvních dvou doktorandů – Milana Štefánika [12] a Lukáše Závorky, kteří nakonec své disertace obhájili v roce 2015¹. Následně přibýly práce mých doktorandů z FEKT: Jana Varmuži, Miroslava Zemana [13] a Josefa Svobody. V poslední době, poté, co se podařilo sestavit na UEEN FEKT VUT tzv. „Jadernou skupinu“ a podařilo se navázat spolupráci s několika prestižními univerzitami činnými v oblasti ADS, se daří rozvíjet společné zahraniční projekty, experimenty v zahraničí, organizovat stáže i psát společné publikace. Zatím nejvíce těžíme ze spolupráce s indickými univerzitami², a s Arménií a Ukrajinou; pro potřeby habilitační práce jsem vybral náš společný článek se skupinou profesora Nand Lal Singha z MSU Baroda, sepsaný jeho doktorandem Rajnikant Makwanou³ [14] a náš společný článek se skupinou docenta Ivana Ivanoviče Haysaka z univerzity v Užhorodu, sepsaný doktorandem Robertem Holombem⁴ [15].

¹ Dr. Štefánik je nyní zodpovědnou osobou za neutronové generátory v UJF AV ČR a právě dokončuje svoji habilitační práci, kterou chce podat na JFI ČVUT. Dr. Závorka získal místo postdoka v PTB Braunschweig a následně druhé postdoktorácké místo v Los Alamos National Laboratory, kde působí dodnes.

² MoU s The Maharaja Sayajirao University of Baroda in Vadodara, Gujarat; Guru Gobind Singh Indraprastha University of New Delhi; University of Rajasthan in Jaipur; Banaras Hindu University Varanasi, Uttarpradesh; Rajiv Gandhi University, Itanagar, Arunachal Pradesh

³ Rajikant Makwana odevzdal svoji disertační práci a uchází se o místo postdoka v naší skupině

⁴ Robert Holomb po obhájení své diplomové práce na Užhorod National University nastoupil jako doktorand do naší skupiny a je společně veden mnou a docentem Ivanem I. Haysakem z UzhNU.

Obsah

Předmluva	- 5 -
Úvod	- 7 -
Obecný úvod do problematiky urychlovačem řízených systémů.....	- 8 -
Transmutace vyhořelého jaderného paliva, thoriová energetika, využití ochuzeného uranu	- 8 -
Podkritické reaktory řízené vnějším neutronovým zdrojem.....	- 9 -
Jaderná data a neutronová spektra	- 10 -
Účinné průřezy a rychlosti interakcí.....	- 10 -
Energetické rozložení – spektrum neutronů	- 11 -
Experimentální zařízení	- 11 -
Výpočetní nástroje pro studium urychlovačem řízených systémů	- 12 -
Vybrané výsledky.....	- 13 -
Experimenty a výzkum v oblasti ADS.....	- 13 -
Knihovny jaderných dat.....	- 13 -
Integrální experimenty	- 14 -
Implementace výsledků do modelů jaderných reakcí.....	- 15 -
Určování neutronových spekter a účinných průřezů	- 16 -
Spektrum neutronů	- 16 -
Účinné průřezy	- 17 -
Závěr	- 19 -
Reference	- 21 -

Úvod

Jaderná energetika – průmysl přinášející novou dimenzi do výroby energie, využívající mnohem intenzivnějších a efektivnějších energetických přeměn a bezprecedentní hustoty energie než klasická energetika; průmysl umožňující osvobodit se od lokálních fosilních zdrojů či importu a získat větší energetickou nezávislost; odvětví spojené se svobodou západu⁵ i současným rozmachem východu; stigmatizované a spojované s jadernými zbraněmi, mnohými odepsaná část energetického mixu, zavrhnutá, zastaralá a nyní znovu nalezená, moderní a nepostradatelná v boji proti změnám klimatu!

Ve chvílích, kdy píšu tyto řádky, začíná v New Yorkském sídle OSN klimatický summit svolaný generálním tajemníkem OSN Antonio Guterresem. Státníci ze všech zemí světa diskutují nad změnami klimatu a předhánějí se v závazcích týkajících se snížení emisí skleníkových plynů. Světové společenství národů by mělo snížit emise skleníkových plynů do roku 2030 o 45% a do roku 2050 by mělo prý být uhlíkově neutrální. Na druhém konci světa ale ve stejnou chvíli hoří tropické pralesy takovým způsobem, že lidé v brazilských, indonéských nebo malajských městech už měsíc neviděli nejen hvězdy na nočním nebi, ale ani na druhou stranu silnice. Pralesy však nehoří kvůli suchu nebo po úderu blesku, hoří, protože je zapálili místní lidé (s podporou svých politických představitelů!), aby zvýšili svoji životní úroveň (a případně dodali dostatek palmového oleje pro naše margaríny nebo biopaliva). Mimo emotivní Greta Thunbergové je možné slyšet i odbornější ale stejně naléhavé hlasy, že je třeba již konečně začít konat – zakázat biopaliva, přestat s pálením uhlí a ropy, změnit kompletně dopravu a začít se chovat zodpovědně. O tom, že součástí této zodpovědnosti musí v současnosti být i jaderná energetika nelze pochybovat. Některé ekologické iniciativy (včetně Greenpeace) již zařadili jadernou energetiku do portfolia bezemisních zdrojů (jádro dokáže být méně emisní než mnohé obnovitelné zdroje, díky technologii P2G – Power to Gas může produkovat i „záporné“ emise CO₂ a umožnit tak „bezemisní“ provoz některým průmyslovým odvětvím, které zatím bez produkce CO₂ nejsou uskutečnitelné) a počítají s „přechodných“ využitím jaderné energetiky do doby, než lidstvo zvládne ve velkém provozovat fúzní reaktory nebo dokáže provozovat elektroenergetickou soustavu pouze s obnovitelnými zdroji. Jaderná energetika, mimo své bezemisní uhlíkové stopy, nabízí stabilní a dlouhodobě bezpečný zdroj elektrické energie a tepla, zajištění průmyslu s vysokou přidanou hodnotou a vyučení vysoce vzdělaných lidí v zemích, které se pro jadernou energetiku rozhodly. Mezi tyto země patří i Česká republika a je tedy naší povinností do detailů toto odvětví studovat a zabývat se veškerými jeho zákonitostmi.

Jaderná energetika má dvě Achillovy paty – možnost úniku radionuklidů do životního prostředí během celého životního cyklu (těžba, výroba paliva, provoz, likvidace) a radioaktivní odpady, které během provozu jaderného zdroje nebo po jeho skončení vznikají. Mezi vysoce aktivní odpady bude v nějaké podobě patřit i jaderné palivo – již spotřebované a nadále neschopné udržet štěpnou řetězovou reakci v daném typu reaktoru. Ať je již prohlásíme za odpad celé nebo pouze jeho část, budeme se v každém případě muset vypořádat s vysoce toxickým odpadem, který zůstává nebezpečný po nepředstavitelně dlouhou dobu. Pomoci se zodpovědným nakládáním s vyhořelým jaderným palivem mohou pokročilé jaderné reaktory, zdá se, že nejefektivněji by mohly pomoci

⁵ Stať „Jaderná energetika a svoboda západu“ je světoznámý článek vzniklý z korespondence českého fyzika Františka Janoucha s Andrejem Sacharoven v letech 1976-1977. Článek vyjadřuje podporu pana Sacharova názoru profesora Janoucha, že citují: „*jaderná energie je conditio sine qua non pro politickou svobodu a nezávislost Západu a pro vytváření příznivějšího mezinárodního politického klimatu*“

reaktory řízené urychlovačem. S jejich pomocí by bylo možné zkrátit dobu potřebnou pro bezpečné ukládání radioaktivních odpadů z vyhořelého jaderného paliva z desítek tisíc let na pouhé stovky let.

Podkritickým jaderným reaktorům určeným pro transmutaci vyhořelého jaderného paliva se věnuje předkládaná habilitační práce. Problematika leží na pomezí jaderné energetiky a jaderné fyziky, umožňuje tedy být velmi atraktivní pro studenty, doktorandy i postdoky – vždy je dostatek nové zajímavé práce, základního výzkumu, snů, vizí a idejí; nicméně stále je nadosah průmyslová aplikace a pomoc společnosti v efektivním a nízkoodpadovém boji se změnami klimatu.

Obecný úvod do problematiky urychlovačem řízených systémů

Transmutace vyhořelého jaderného paliva, thoriová energetika, využití ochuzeného uranu

Jaderné reaktory provozované od padesátých let 20. století až do současnosti jsou založené na štěpení pomocí tzv. tepelných neutronů⁶. Jedná se o neutrony, které jsou zpomalené v moderátoru až na energii odpovídající tepelné rovnováze s prostředím moderátoru. Nespornou výhodou těchto reaktorů je míra pravděpodobnosti pro štěpení jader uranu či plutonia; nevýhodou ale zůstává napjatá neutronová bilance a velké množství vznikajících minoritních aktinoidů (Np, Am, Cm, Cf). Výměna paliva v těchto reaktorech je buď kontinuální (těžkovodní, grafitové) nebo kampaňovitá (vždy po jednom až dvou letech). Část paliva, kterou je nutno vyměnit za palivo čerstvé, se nazývá použité jaderné palivo, často se setkáváme se zaužívaným termínem vyhořelé jaderné palivo. Tento termín, ač široce používaný⁷, je technicky nesprávný, protože palivo obsahuje ještě velké množství uranu, plutonia, minoritních aktinoidů a pouze cca 3% štěpných produktů, které již nelze využít k produkci tepla štěpením.

Technicky a fyzikálně lze však oněch 97% vyhořelého jaderného paliva znovu použít, část je použitelná i v tepelných reaktorech po přepracování na palivo typu RepU⁸ nebo MOX⁹; větší část však vyžaduje štěpení rychlými neutrony a/nebo transmutaci na štěpný materiál. K tomu lze využít pouze reaktorové systémy, které mají velmi dobrou neutronovou bilanci:

- těžkovodní jaderné reaktory s obohaceným palivem,
- reaktory s palivem ve formě tekutých solí a s kontinuální separací neutronových jedů,
- rychlé množivé reaktory,
- reaktory s vnějším zdrojem neutronů.

Přesně pro tyto typy lze využít jako potenciální palivo také thorium, jehož přírodní zásoby jsou pravděpodobně větší než zásoby uranu, nebo ochuzený uran, který je na světě skladován v obrovských množstvích jako pozůstatek po obohacování – ať již pro mírové či vojenské účely. Každý z uvedených systémů má však i své nevýhody, ať je to technologická složitost, finanční náročnost či jisté nedostatky v inherentní jaderné bezpečnosti. Fyzikálně velmi nadějným se jeví reaktorový

⁶ Reaktorů založených na rychlých neutronech bylo a je v provozu pouze několik jednotek

⁷ I autor této práce je zvyklý jej používat

⁸ Reprocessed Uranium

⁹ Mixed Oxide Fuel (UO₂+PuO₂)

systém, který je provozován v podkritickém stavu a který je udržován na ustáleném výkonu vnějším neutronovým zdrojem. Inherentní bezpečnost tohoto reaktoru je bezprecedentní, rozvoj nekontrolovatelné štěpné řetězové reakce není možný. Problémem je však potřebná vysoká vydatnost neutronového zdroje – požadovanou hodnotou dosud nedisponuje žádný neutronový zdroj současnosti. Nejintenzivnějšími zdroji neutronů jsou jaderné reaktory samy; vyšších hodnot vydatností mohou dosáhnout pouze neutronové zdroje založené na urychlovačích částic.

Jak jsem již uvedl, vyhořelé palivo, které je vyvezeno z aktivní zóny reaktoru do externích skladovacích prostor (bazénu skladování, meziskladu) se skládá ze štěpných produktů, které se většinou rozpadají beta rozpadem, a jejichž poločasy rozpadu jsou od jednotek dnů po stovky tisíc let, přičemž nejpravděpodobnější hodnoty poločasu přeměny jsou v nižších desítkách let¹⁰. Pokud předpokládáme, že bude nutné uchovávat tyto odpady přibližně 10 poločasů rozpadu, docházíme k číslům okolo 300 let – to je doba potřebná k tomu, abychom odpad složený pouze ze štěpných produktů skladovali tak, aby měrná radiotoxicita tohoto odpadu byla obdobná jako u vytěžené uranové rudy. Vyhořelé jaderné palivo však obsahuje i transurany – izotopy plutonia a tzv. minoritní aktinoidy, které když zahrneme do výše uvedené úvahy, dostaneme dobu potřebnou k uchování vyhořelého paliva jakožto odpadu v desítkách až stovkách tisíc let, než dosáhne měrné radiotoxicity jako původní uranová ruda. Všechny aktinoidy však lze štěpit za pomoci neutronů – některé za pomoci tepelných neutronů, všechny za pomoci rychlých neutronů. Máme-li k dispozici dostatečně silný zdroj rychlých neutronů, můžeme v hypotetickém jaderném reaktoru „spálit“ všechny transurany (včetně uranu samotného) na štěpné produkty za zisku tepelné energie. Část této energie by byla využita pro provoz externího neutronového zdroje.

Toto je myšlenka transmutoru, reaktoru, který by využíval vyhořelé palivo z tepelných jaderných reaktorů. Jaderný palivový cyklus by se tak podařilo úspěšně uzavřít. Podaří-li se uvést v budoucnu transmutační jaderné reaktory do provozu, výrazně se tak omezí potřeba ukládat vyhořelé jaderné palivo v hlubinných úložištích. Ukládání budou požadovat pouze štěpné produkty, u nichž je doba nutná ke skladování řádově nižší, v pouhých stovkách let.

Podkritické reaktory řízené vnějším neutronovým zdrojem

Jaderný reaktor se může fyzikálně nacházet ve třech různých stavech – nadkritickém, podkritickém a kritickém. Kritický stav značí časově vyrovnanou neutronovou bilanci a ustálený stav, nadkritický stav vede k exponenciálnímu růstu výkonu, podkritický stav k exponenciálnímu poklesu výkonu až k zastavení štěpné řetězové reakce. Mimo těchto tří stavů však můžeme ještě rozlišovat dva stavy – jaderný reaktor s vnějším zdrojem neutronů nebo bez vnějšího zdroje. Chování kritického jaderného reaktoru ovlivní vnější zdroj neutronů tak, že způsobí lineární nárůst výkonu; u nadkritického reaktoru dojde k superpozici nárůstů výkonu; nicméně u podkritického reaktoru dojde k ustálení výkonu jaderného reaktoru na hodnotě, která je úměrná koeficientu násobení soustavy a vydatnosti vnějšího zdroje¹¹. Pokud by byl vnějším neutronovým zdrojem urychlovač částic s příslušným terčem produkujícím neutrony, který by mohl na základě požadavku operátora měnit vydatnost zdroje a kdykoliv pouhým stisknutím tlačítka vypnout produkci neutronů, dostali bychom inherentně bezpečný jaderný reaktor s velmi dobrou neutronovou bilancí. U takového systému by nás

¹⁰ ¹³⁷Cs a ⁹⁰Sr mají poločasy rozpadu přibližně 30 let a jejich kumulativní výtěžek ze štěpení je v jednotkách %

¹¹ Obecně také závisí na spektru neutronů z vnějšího zdroje

neomezovaly požadavky na použití materiálů s nízkým účinným průřezem pro absorpci neutronů, neutronové jedy, strusky a podobně.

Fyzikální chování takového reaktoru je poněkud specifické a odlišuje se od chování kritického systému, klade požadavky zejména na přesné kontinuální měření reaktivity a zpětnou vazbu tohoto měření na vydatnost zdroje [16]. U urychlovačem řízených systémů je také velmi odlišné spektrum neutronů ze zdroje, obsahující i neutrony s vysokou energií [1 kap.4]. Tyto neutrony mohou způsobovat množení neutronů nejen štěpením, ale i skrze interakce (n,xn) ; výpočet koeficientu násobení vyžaduje tedy zahrnutí i těchto efektů. Mluvíme poté nejen o koeficientu násobení soustavy k_{ef} , ale i o tzv. významnosti zdroje a upraveném koeficientu násobení se zahrnutím významnosti zdroje, tzv. K_S [16,1 kap. 3.2].

Odborných studií zaměřených na podkritické reaktorové systémy řízené vnějším zdrojem je k dispozici více [1,17,18,19,20]. Obecně nemusí být intenzivním zdrojem neutronů pouze urychlovač s terčem, ale např. i fúzní reaktor [1 kap. 2.1] nebo laserem řízený zdroj [21,22] neutronů¹². Aktivní zóny mohou být také rozděleny na několik téměř nezávislých částí (tzv. dvojreaktorové systémy [23]), kde jedna z nich může být rychlá a druhá tepelná nebo jedna kritická a druhá podkritická řízená vnějším zdrojem (tvořeným kritickým reaktorem nebo kombinací s dalším zdrojem, třeba urychlovačem řízeným). Mluvíme obecně o hybridních reaktorových systémech [24].

Jaderná data a neutronová spektra

Účinné průřezy a rychlosti interakcí

Hlavní náplní vědecko-výzkumné práce autora textu¹³ je problematika jaderných dat pro urychlovačem řízené systémy. Jde zejména o míry pravděpodobností jednotlivých interakcí (tzv. účinné průřezy), o výtěžky jaderných reakcí¹⁴, o reakční rychlosti či nasycené aktivity generovaných nuklidů.

Ke studiu jaderných dat využíváme experimentální aktivační metodu, kterou lze také používat ke zjišťování vlastností neutronového pole. Metoda má pro systémy ADS mnoho výhod. Urychlovače pracují v pulsním režimu, i neutronové pole má tedy charakter časově proměnného pole. Perioda změn je však většinou velmi krátká a může způsobovat problémy některým elektronickým detektorům neutronů. Aktivační detektory však sbírají informaci integrálně, bez ohledu na frekvenci změn pole neutronů, ve kterém jsou umístěny. Druhým problémem je často stínění. Urychlovačem řízené experimentální soustavy generují ve svém okolí během provozu značné pole ionizujícího záření, záření X, gama a neutronů, přičemž ve spektru jsou neutrony i gama kvanta s velmi vysokými energiemi v desítkách či stovkách MeV. Takové záření je velmi obtížné stínit, proto je třeba veškeré manipulace omezit na minimum. Aktivační detektory jsou dostatečně malé a mohou

¹² Laserem řízené zdroje neutronů jsou v současnosti ve stavu základního výzkumu; projektu zaměřeného na takový zdroj se ve spolupráci s ELI Beamlines účastní i naše skupina

¹³ A týmů, ve kterých v dané problematice působil (RKHL LJaP SUJV Dubna, KJR FJFI ČVUT) a působil (UEEN FEKT VUT)

¹⁴ spalace, multifragmentace, štěpení

být umístěny na mnoho míst v soustavě, umožňují tedy komplexní proměření bez nutnosti pohybovat detektory.

Aktivační metoda pro detekci rychlých neutronů úspěšně využívá faktu, že mnoho reakcí probíhá až od určité energie interagující částice. Mluvíme o tzv. prahových detektorech [25]. Pokud dobře zvolíme dostatečné množství prahových detektorů, které nám pokryje co nejširší energetické spektrum, můžeme s přijatelnou nejistotou určit i energetické rozložení neutronů v daném místě soustavy.

Energetické rozložení – spektrum neutronů

Určení spektra neutronů je naprosto zásadní pro provoz jaderného zařízení řízeného urychlovačem částic. Urychlovačem řízená reakce produkující neutrony (nejčastěji spalační) vede ke vzniku jisté složky spektra s neutrony velmi vysokých energií [1, kap.3, kap.4]. Tyto neutrony mají velkou pravděpodobnost, že způsobí vznik dalších neutronů za pomoci reakcí¹⁵ (n, xn). Vliv těchto reakcí na neutronovou bilanci ale i provoz jaderného zařízení řízeného urychlovačem se často velmi podceňuje. Výzkumy v Indii, Číně, ale i v Dubně ukazují, že menší absolutní množství neutronů s vysokými energiemi (nad 100 – 200 MeV) může mít v důsledku stejný nebo vyšší vliv na rychlosti transmutačních reakcí v systému a samozřejmě i na únik neutronů ze soustavy [26,27].

Experimentální zařízení

V dané problematice zatím neproběhlo mnoho experimentů. Popisuje-li se historie urychlovačem řízených systémů, začíná se často v padesátých letech, kdy však motivací fyziků bylo množení štěpného materiálu pro vojenské využití. Skupina fyziků okolo Ernesta O. Lawrence však tehdy uvažovala o jakémsi hybridním jaderném reaktoru, který by dokázal množit ²³⁹Pu či ²³³U a následně je spalovat za vzniku tepla. Tento reaktor si dokonce nechali patentovat jako Electronuclear reactor [28]. O nakládání s vyhořelým jaderným palivem měli odborníci té doby však jiné představy¹⁶. Další vlna zájmu směřuje do 70. let, kdy Vasilkov a Goldanskij [29,30,31] prováděli svoje experimenty s velkou trojúhelníkovou uranovou sestavou. Motivace jejich práce však také nemířila k průmyslové transmutaci radionuklidů, ale za odhalení fyziky mezijaderné kaskády¹⁷ a obecně vzniku neutronů v těžkých terčích ozařovaných lehkými ionty. Až v devadesátých letech 20. století, dvojice známých fyziků – Charles Bowman [32,33] z Los Alamos National Laboratory a laureát Nobelovy ceny Carlo Rubbia [34] z CERN navrhli využití ADS v jaderné energetice¹⁸. Oba měli úplně jinou představu a ubírali se různým směrem¹⁹, nicméně oba vzedmuli vlnu zájmu o ADS²⁰, která gradovala na přelomu 20. a 21. tisíciletí a vydržela i v prvních letech nového tisíciletí. Příliš mnoho experimentální práce se

¹⁵ ale i reakcí multifragmentace nebo vysoko-energetického štěpení

¹⁶ Reálně se uvažovalo (i provádělo) o shazování do hlubin moře nebo vynesení do vesmíru

¹⁷ Jedná se o jednu z fází spalační reakce, která následuje po vnitrojaderné kaskádě a vypařování jader

¹⁸ Velice podobný koncept jako projekt Los Alamos navrhl již v roce 1982 Dr. Furukawa [35]

¹⁹ Carlo Rubbia vidět v ADS možnost orientace na thoriovou energetiku a zajištění energie pro lidstvo na stovky a tisíce let, navrhl tzv. Energy Amplifier, reaktor s pevným thoriovým palivem; Charles Bowman pomocí svého systému ATW – Accelerator Transmutation of Waste viděl v ADS možnost transmutovat dlouho žijící radionuklidy z vyhořelého jaderného paliva z klasických reaktorů současnosti. Navrhl ADS s tekutým palivem ve formě fluoridových solí a s online separací.

²⁰ V devadesátých letech označované ADTT – Accelerator Driven Transmutation Technologies

nepodařilo uskutečnit – zájem o ADS pomalu vyprchal, jistě pomohla i velká finanční náročnost výzkumu. V tomto ohledu jsou unikátní experimentální práce vykonané v SUJV Dubna, které byly započaty v 90. letech minulého století a bez velkých přestávek jsou prováděny dodnes. Je však s podivem, že jejich publicita je poměrně malá; zejména ve srovnání s některými významem srovnatelnými experimenty, kterým se podařilo v rámci komunity získat značnou publicitu (např. MUSE [36], YALINA [37], GUINEVERE [38]). Výzkumné experimentální práce by bylo možné rozdělit do dvou základních skupin [1 kap.6]: 1) zaměřené na časové chování podkritické soustavy s pulsním neutronovým zdrojem ve formě urychlovače částic a příslušného terče a 2) zaměřené na prostorově-energetické rozdělení neutronů v soustavě s urychlovačem řízeným zdrojem neutronů. Většina prací zaměřených na 1. problém využila jako urychlovačem řízený zdroj neutronů „obyčejný“ d-T neutronový generátor, některé soustavy využily neutronový generátor na bázi p+Li či p+Be reakce s energiemi dopadajících protonů v nižších desítkách MeV [39]. Objevily se i experimenty s elektronovým urychlovačem a terčem produkujícím neutrony přes konverzní terč a brzdné záření [40]. Výzkumů s opravdu vysokými energiemi dopadajících částic, které by v případě urychlených hadronů mohly způsobit spalační reakce, proběhlo jen velmi málo²¹.

Výpočetní nástroje pro studium urychlovačem řízených systémů

Jelikož aktuálně není možné v oblasti ADS provádět velké množství experimentů, je nutná znalost nástrojů, které dokáží predikovat chování ADS systémů. Jako každý jaderný reaktor, tak i ADS lze popsat Boltzmanovou integro-diferenciální transportní rovnicí. Problematice se poměrně důkladně věnovali italští fyzikové [41,42,43], obecným postupem od transportní rovnice k reálnému systému lze dosáhnout velmi zajímavých, matematicky krásných (a velmi komplikovaných) výsledků [44,45,46]. Většina fyziků se tedy vydává cestou modelování ADS pomocí metody Monte Carlo, nejčastěji programem MCNP [47] nebo MCNPX [48], což je program, který se před 20 lety vyčlenil z vývoje kódu MCNP a který představoval spojení transportu a reakcí částic při nižších a vyšších energiích²². Vývoj programu byl před dvěma lety ukončen a kód byl zakomponován nazpět do nejnovější verze MCNP-6.2.0. Stále více používaným nástrojem je program [49] FLUKA²³. V současné době lze použít i program [50] GEANT4²⁴, který byl doplněn o transport neutronů v oblasti nízkých energií nebo kód [51] MARS²⁵. Pro různé speciální aplikace vzniká v poslední době mnoho výpočetních programů, které je možné využít i v problematice ADS (programy pro simulaci protonové terapie, pro výpočty radiačního poškození, pro výpočty v astrofyzice či fyzice vrchních vrstev atmosféry, apod.).

²¹ Pouze v CERNU, v SUJV Dubna a v Japonsku [1 kap.6] na zařízení FFAG-KUCA (dopadající protony 100 MeV však nedokáží plně rozvinout vnitrojadernou kaskádu; jedná se tedy pouze o jakýsi limitní případ spalační reakce)

²² První verze MCNPX byla spojením MCNP-4B a výpočetního programu LCS (LAHET Code System), vytvořená v roce 1994 a otevřená pro odbornou veřejnost v roce 1999. S tehdejší kolegou Ing. Janem Ratajem z KJR FJFI ČVUT v Praze se nám podařilo být členy „beta tester komunity“ tohoto programu prakticky od zahájení jeho používání.

²³ Vyvíjený komunitou jaderných fyziků okolo Alberta Fasso ze Stanford Linear Accelerator Center, Kalifornie, USA (většinou fyzikou z CERN – Conseil Européen pour la Recherche Nucleaire, Ženeva a Istituto Nazionale di Fissica Nucleare, Milán)

²⁴ Vyvíjený komunitou napojenou na Evropskou organizaci pro jaderný výzkum – CERN

²⁵ Vyvíjený v laboratoři FermiLab – FNAL – Fermi National Accelerator Laboratory, Batavia, Chicago

Vybrané výsledky

Experimenty a výzkum v oblasti ADS

Problematice urychlovačem řízených systémů se věnuji²⁶ od doby své rešeršní práce²⁷. Zúčastnil jsem se mnoha různých experimentů v SUJV Dubna, následně po roce 2008 se jich začali účastnit i moji studenti, zejména doktorandi. Během let se s pomocí prahových a aktivačních detektorů podařilo proměřit prostorová i energetická rozložení neutronového pole v různých ADS sestavách či spalačnicích²⁸ zdrojích neutronů. Velký důraz se také kladl na měření transmutačních výtěžků jaderných reakcí v ADS s různými izotopy separovanými z vyhořelého jaderného paliva²⁹ ²⁴¹Am, ²³⁷Np, ²³⁹Pu, ²³⁸Pu, ¹²⁹I. Velkou výzvou byly paradoxně jednoduché úlohy – např. měření úniku neutronů a celkový počet štěpení v soustavě. Nejasnosti ve shodě experimentálních měření se simulacemi si vynutily provedení dalších experimentů – měření účinných průřezů na zařízeních poskytujících kvazi-monoenergetická spektra neutronů s energiemi nad 20 MeV. Měření z poslední doby (rok 2018) ukazují také na velmi zajímavý potenciál směsných terčů – směsi lehkých a těžkých jader. Této problematice se začíná naše skupina věnovat na základě nově otevřené spolupráce s Institutem moderní fyziky Čínské akademie věd v Lan-čou ve Vnitřním Mongolsku. Jejich koncepce granulovaného terče³⁰ v kombinaci s naším návrhem směsného lehkotěžkého³¹ terče bude jednou z dalších výzev pro experimenty v SUJV Dubna. Jelikož se jedná o první experimenty tohoto druhu, lze očekávat velký publikační potenciál.

Knihovny jaderných dat

Jaderná data (účinné průřezy, výtěžky reakcí, data o rezonancích, úhlová a energetická rozdělení výtěžků reakcí apod.) se pro účely výpočetních analýz uchovávají v tzv. knihovnách zhodnocených jaderných dat³². Proces „zhodnocení – evaluace“ jaderných dat je založen na použití některého výpočetního programu obsahujícího modely chování částic a atomových jader. Zhodnocená data jsou konfrontována s experimentálními daty³³. Pokud jsou rozdíly v definovaných mezích, evaluovaná data jsou publikována v knihovně a používána. Pokud jsou nalezeny rozdíly, které překračují definované meze, měla by být iniciována změna modelu, případně doplňující experiment. Mnohdy však ani jedno, ani druhé není možné a v knihovnách evaluovaných jaderných dat jsou hodnoty zdaleka neodpovídající skutečnosti. Pokud se jedná o chybu u často používaných nuklidů, jako například uran nebo železo, komunita používající knihovnu (reaktorová fyzika, stínění) dokáže vyvinout dostatečný tlak na evaluátory knihoven a ti provedou revizi knihovny, kam zařadí re-evaluovaná data. Pokud se však jedná o nuklidy exotické – některé minoritní aktinoidy nebo štěpné produkty, je velmi obtížné prosadit nový výpočet, o provedení experimentu nelze často vůbec hovořit. První z článků zařazených

²⁶ s různou intenzitou – např. mezi lety 2008 a 2012 byla intenzita výzkumu ovlivněna mojí postdoktorskou praxí v průmyslu (na Elektrárně Dukovany)

²⁷ ekvivalent bakalářské práce, akademický rok 1997/1998

²⁸ či jiných – generovaných reakcí protonů s lehkými jádry nebo reakcemi elektronů

²⁹ Měření výtěžků na plutoniu bylo předmětem mojí disertační práce

³⁰ Jedná se o jakýsi kompromis mezi pevným a tekutým terčem – terč se skládá z malých (jednotky mm v průměru) kuliček, které jsou v pohybu („tečou“) s pomocí elektromagnetických čerpadel

³¹ Studujeme kombinaci klasických těžkých materiálů – spalačnicích terčů (W, Ta, Pb, Bi, Th, U) a lehkých materiálů produkujících neutrony vysokých energií break-up reakcemi (Li, Be, B, C)

³² Evaluated nuclear data files/libraries – ENDF

³³ Experimentální data jsou uchovávána v knihovně EXFOR

do habilitační práce [2] se zabýval právě citlivostní analýzou podkritického jaderného reaktoru pro ADS³⁴ v programu MCNP-4C. Byla studována citlivost koeficientu násobení soustavy na změnu knihovny jaderných dat ve vstupním souboru. Aktivní zóna obsahovala různé štěpné produkty a minoritní aktinoidy. Studie ukázala, že použití různých knihoven může vést k velmi odlišným výsledkům, problémy byly zejména u exotického aktinoidu, kalifornia; nicméně i změna knihovny u ²⁴¹Am dokázala změnit reaktivitu aktivní zóny o sedm desetin beta efektivního. Studovaný reaktorový systém byl tepelným (mírně epitermálním) jaderným reaktorem, při zvyšování energií neutronů dochází mezi jednotlivými knihovnami k větším rozdílům nebo data chybí úplně. Při spojení reaktoru a spalačního neutronového zdroje je nutné mít k dispozici jaderná data pro energie až do několika stovek MeV.

Po roce 2000, zejména v souvislosti s evropským projektem HINDAS³⁵, vznikem programu TALYS [52] a rozšíření kódu MCNX v ADS komunitě dochází k značnému zvýšení aktivit týkajících se měření a evaluace účinných průřezů a jiných jaderných dat v oblasti energií neutronů nad 20 MeV a také v oblasti reakcí jiných částic než neutronů. Díky unikátním možnostem³⁶ byl v SUJV Dubna zahájen program určování účinných průřezů a výtěžků spalačních reakcí s různými materiály spojenými s ADS (uran přírodní ²³⁸U, plutonium ²³⁸Pu a ²³⁹Pu, americium ²⁴¹Am, neptunium ²³⁷Np, radiojód ¹²⁹I; později i thorium ²³²Th). Experimenty byly prováděny na přímém svazku urychlovače Fázotron v Dželepovově Laboratoři jaderných problémů, nejprve na vyvedeném svazku o energii 660 MeV, později i na vnitřním svazku (energie 100 – 600 MeV). Společně se školitelem³⁷ jsme se věnovali určování výtěžků spalační reakce protonů o energii 660 MeV a tenkého terče z přírodního uranu³⁸. Experiment proběhl v roce 2001 a následná měření na HPGe detektorech trvala více než 2 roky. V naměřených gama spektrech se podařilo identifikovat více než 400 různých izotopů, výsledky byly prezentovány na mezinárodních fórech [4,5] a úspěšně konfrontovány s výpočty. Srovnání výpočtů s experimenty však ukazuje na velké rozdíly mezi jednotlivými modely [5, graf.2]. Již tehdy dosahoval nejlepší shody model INCL-ABLA³⁹, který je určitým standardem kvality výpočtů v oblasti 200 – 800 MeV doposud.

Integrální experimenty

Srovnání výpočetních modelů a experimentálních výpočtů se s příchodem programu MCNPX ukázalo jako naprosto stěžejní otázka v dalším vývoji ADS⁴⁰. V SUJV Dubna byly v té době dvě zařízení, které mohly poskytovat integrální data pro validaci modelů ve výpočetních programech, zejména v MCNPX. Jednalo se o olověný terč s parafínovým moderátorem zvaný „GAMMA-2“ a uranovou sestavu „Energie plus Transmutace“. Spolu se školitelem jsme se v té době účastnili měření na těchto sestavách, naším úkolem bylo určování výtěžků transmutačních reakcí na ²³⁸Pu, ²³⁹Pu, ²³⁷Np, ²⁴¹Am, ¹²⁹I, ¹²⁷I a měření a zpracování dat z prahových aktivačních detektorů. Experimenty neprobíhaly na urychlovači Fázotron, ale na urychlovači se supravodivými magnety s názvem Nuklotron. Tento

³⁴ Model vychází z tehdy velmi populárního ATW/ADTT dr. Bowmana (grafitová zóna s tekutým palivem)

³⁵ High- and Intermediate-energy Nuclear Data for Accelerator-driven Systems

³⁶ Přístup k urychlovačovému času (beam time) a přístup k jaderným materiálům

³⁷ V rámci týmu, který s SUJV Dubna Dr. Adam vedl a ve spolupráci s prof. Michelelem z Univerzity v Hannoveru (metodika měření účinných průřezů spalačních reakcí) a skupinou výpočtářů z Los Alamos National Laboratory

³⁸ V roce 2004 jsme na přímém svazku ozařovali také ²³⁸Pu a ²³⁹Pu

³⁹ Liege IntraNuclear-Cascade model (INCL) coupled with the ABLA evaporation/fission model

⁴⁰ Po roce 2000

urychlovač má na rozdíl od Fázotronu možnost urychlovat různé ionty, teoreticky až do iontů uranu a má možnost vyvádět svazky částic různých energií. Jeho nevýhodou je však nízký střední proud částic, který se pohybuje v desítkách pA oproti jednotkám μA v případě Fázotronu⁴¹. Komplexně zpracované experimenty byly spolu s výsledky z ozařování na přímém svazku součástí mojí disertační práce [7]. Výsledky [6] ukázaly, že v některých případech dochází k obtížně vysvětlitelným odchylkám vypočtených hodnot od hodnot naměřených. Práce se také důkladně věnuje problematice korekcí⁴². S jejich zavedením se podařilo v některých případech snížit nejistotu experimentálních dat nebo dokonce opravit chybu, vnesenou do výsledků nepoužitím příslušných korekcí. Práce se souhrnně věnuje 4 protonovým experimentům s energiemi 700 MeV, 1 GeV, 1,5 GeV a 2 GeV. Detailně je studována problematika celkového počtu štěpení a vlivu jednotlivých částí energetického spektra. Výsledky poukázaly na velký vliv tepelných neutronů na produkční rychlosti reakcí (n,γ) . Simulace následně potvrdily domněnku, že tepelné neutrony v soustavě se nacházející vznikly v polyethylenovém stínění, ze kterého dokázaly „natéci“ zpátky do soustavy „Energie plus Transmutace“. Pro další krok v rozvoji experimentálních ADS výzkumů bylo proto zařízení QUINTA⁴³ opatřeno pouze olověným stíněním.

Ještě před modernizací zařízení „Energie plus Transmutace“ na zařízení QUINTA došlo ke třem ozařovacím experimentům s deuterony o celkových energiích 1,6 GeV [8], 2,52 GeV a 4 GeV. Bylo také sestaveno grafitové zařízení s olověným terčem GAMMA-3, které bylo taktéž ozařováno deuterony na urychlovači Nuklotron [10]. Na obou publikacích se autor habilitační práce podílel již jako externista (vůči SUJV Dubna)⁴⁴; články jsou poměrně rozsáhlé a byly oba přijaty do prestižního European Journal of Physics. Obě práce se zaměřují na srovnání experimentálních a nasimulovaných dat, je zde kladen důraz na výpočet celkového počtu štěpení v thoriových a uranových detektorech. První článek vyvíjí metodiku pro srovnání výsledků s pracemi skupiny okolo Carla Rubii z CERN; některé výsledky v obou článcích je tedy možno srovnat s výsledky experimentu TARC [1 kap.6.1]. Ukazuje se, že podíl reakční rychlosti pro reakci $(n,2n)$ a štěpení na thoriu může překračovat i desítky procent a že významnost reakce (n,xn) v ADS systémech na thoriu je mnohem vyšší než na uranu. Z obou článků vyplývá nutnost zaměřit se jak na výpočty v oblasti neutronových polí s energiemi nad 2 a více MeV a jejich verifikaci & validaci, tak na jaderná data pro tyto oblasti, zejména na data pro oblast nad⁴⁵ 20 MeV.

Implementace výsledků do modelů jaderných reakcí

Výsledky naší experimentální práce se ukázaly být přímo přínosnými pro úpravu modelů jaderných interakcí, konkrétně štěpení [9,11]. Spolupráce se skupinou kolem paní profesorky A. Balabekyan⁴⁶ je

⁴¹ Za stokrát delší ozařovací čas dostáváme stokrát nižší celkový počet částic dopadnuvších na terč

⁴² korekce na nebodovost vzorku oproti bodovému kalibračnímu zářiči, korekce na samopohlčení, korekce na proměnnost protonového toku při ozařování, korekce na koincidenční sumace atd.

⁴³ Následovník experimentální sestavy „Energie plus Transmutace“

⁴⁴ Na první publikaci [8] jsem pracoval ještě jako rovnocenný hlavní autor vůči korespondenčnímu autorovi článku, Dr. Adamovi, na druhém [10] jsem pomáhal hlavnímu autorce Chitře Bhatia, která působila jako doktorand společně pod vedením Dr. Adama a prof. Kumara. Ten již v té době působil jako děkan na Faculty of Basic and Applied Science, Guru Gobind Singh Indraprastha University, New Delhi

⁴⁵ V oblasti pod 20 MeV je nutné věnovat pozornost energiím odlišným od 14 MeV a 2,5 MeV; ikdyž ani zde nejsou vždy data dostatečně kvalitně proměřena

⁴⁶ A její bývalé doktorandky G. Karapetyan, která nyní působí na Univerzitě v Sao Paulu

a byla založena na tom, že jsme společně s Dr. Adamem pracovali na experimentálních datech, na jejichž základě byl její skupinou upraven model vysokoenergetického štěpení. Práce [11] byla publikována ve Physical Review v roce 2013. Brazilští výzkumníci spolu se svými arménskými kolegy navrhli na základě našich experimentálních dat superasymetrický model štěpení uranu protony⁴⁷ o energii 660 MeV, který velmi dobře popisuje vznik produktů reakce 660 MeV protonů a uranu a který v oblasti nukleonových čísel $180 < A < 200$ působí jakožto konkurenční kanál k reakci hluboké spalace (hlubokého tříštění). Svůj předpoklad zavádějí do výpočetního programu CRISP [53] s použitím metodiky MM-NMR. Po zobecnění modelu štěpení a vypařování ze tří módů na čtyři – na jeden symetrický, dva asymetrické a jeden superasymetrický, dostávají výbornou shodu výpočtu s experimentem.

Určování neutronových spekter a účinných průřezů

Závěrečné 4 články [12,13,14,15], které jsem vybral pro svoji habilitační práci, se týkají problematiky, kterou si další výzkum ADS vynutil – pokud jsme chtěli⁴⁸ zodpovědně ve výzkumu ADS pokračovat a nechtěli pořád pouze jen produkovat výpočetní simulace s nejistou mírou neurčitosti⁴⁹, museli jsme se zaměřit na tyto dvě věci:

- na určování neutronového spektra v urychlovačem řízených systémech
- a na určování chybějících účinných průřezů.

Spektrum neutronů

První dva články [12,13] jsou zaměřeny na určování neutronového spektra v systémech řízených urychlovačem a s vysokým podílem neutronů s energiemi nad 10 MeV. V posledních dvou, třech letech se začínají objevovat spektrometrické metody, založené na nových detektorech neutronů, např. ve formě SiC, diamantových krystalů či nových scintilačních koktejlích (nebo i speciálních systémech jako MicroMegas [55], pixelových detektorů [56] či detektor PTB Braunschweig ve formě upravených Bonnerových sfér [57])⁵⁰. V práci [12] se využívá pro stanovení neutronového spektra řežského neutronového generátoru NG-2 umístěného na cyklotronu U-120M sada aktivačních prahových fólií a iterační postup s pomocí metody nejmenších čtverců upraveným⁵¹ programem SAND-II. [58]. Článek, ač je krátký, byl přijat do Nuclear Data Sheets a je jistým standardem pro další měření. V disertační práci [59], do které výzkum v článku publikovaný patří, jsou určována spektra i pro další dva neutronové zdroje na U-120M, s těžkovodním terčem a s lithiovým terčem. Spektra se

⁴⁷ Štěpení a další jaderné reakce se při energiích vyšších než 200 MeV začínají chovat podobně (nikoliv úplně stejně) jak pro reakce iniciované protony, tak neutrony

⁴⁸ Zde myslím zejména „Jadernou skupinu“ na VUT v Brně, ale i práci mých doktorandů Ing. Milana Štefánika a Ing. Lukáše Závorky, které jsem vedl jako externí školitel ještě 3 roky po odchodu z ČVUT a příchodu na VUT

⁴⁹ Dle českého přísloví, že „papír snese všechno“

⁵⁰ Pro všechny tyto typy zůstává velkým problémem možnost vzniku více než 2 reakčních produktů při reakcích nad 17 – 20 MeV

⁵¹ Program je již dlouhá desetiletí určen pro reaktorové aplikace, musel být tedy upraven pro počítání s neutrony nad 20 MeV a musela být vytvořena nová knihovna účinných průřezů

podářilo významně zpřesnit i díky tomu, že bylo použito téměř 30 různých reakcí pro následnou rekonstrukci spektra⁵².

Druhý článek [13] je zaměřen na určování neutronových spekter na spalačních zdrojích neutronů nebo na zdrojích na bázi urychlovače elektronů a konverzního terče. Metoda navržená Dr. Adamem je také založená na využití prahových aktivačních detektorů. Nedochozí ale k fitování spektra, ale k jeho absolutnímu určení – postupuje se od nejvyššího energetického prahu, kde je možná pouze jedna reakce a na základě ní se určí hustota toku neutronů v daném energetickém intervalu (od nejvyššího prahu do energie dopadající částice). Následně se postupuje k nižším prahům, kdy se vždy postupně určuje hodnota hustoty toku neutronů v intervalu od posledního vyššího prahu k prahu nižšímu. Metoda (stejně jako dříve zmíněná metoda) potřebuje jako vstup účinný průřez a simulaci MCNP. Metoda vždy poskytne výsledek včetně nejistoty, nicméně při malém množství prahových reakcí v některé části spektra vede často k poměrně nevzhledným spektrům ve formě širokých „schodů“; na rozdíl od dříve zmíněné metody, které je schopna dát spektrum ve velmi jemné struktuře, nicméně s velmi malou hodnověrností dat v jednotlivých skupinách. Obě metody tedy vyžadují práci poměrně zkušeného fyzika, který musí výsledek vždy zpětně validovat.

Účinné průřezy

Závislost hodnot hustoty toku neutronů ve vysokoenergetických grupách na účinném průřezu vede často k nutnosti použít modelované účinné průřezy – většinou se použijí programy TALYS [52] či EMPIRE [54]. Ačkoliv jsou to programy hojně používané a dostatečně validované, stále v mnoha případech dokáží simulované účinné průřezy být i řádově odlišné od experimentálních dat. U mnoha izotopů a konkrétních energetických intervalů experimentální data chybí úplně. Měřit účinné průřezy interagujících neutronů v oblasti⁵³ nad 20 MeV je velmi obtížné. Naše skupina se rozhodla zapojit do těchto aktivit s pomocí mezinárodní spolupráce. Principiálně naše skupina využívá dvě různé metody (a chystá se osvojit třetí):

- a) využití kvazi-monoenergetického spektra neutronů (lithiový terč ozařovaný protony),
- b) využití podobnosti neutronu a protonu při vysokých energiích,
- c) integrální experiment s využitím přesně charakterizovaného neutronového spektra.

V případě a) je energie protonů od cca 7 MeV do cca 200 MeV; v případě b) musí být energie protonů ve stovkách MeV, od minimálně 100 MeV do cca⁵⁴ 800 MeV; v případě c) se může jednat o urychlovačem generované spektrum, spektrum radionuklidového zdroje nebo též reaktorové spektrum. Pracoviště s lithiovým terčem jsou v celosvětovém měřítku pouze jednotky, přístup na urychlovač protonů s energiemi ve stovkách MeV je jednodušší, nicméně také velmi obtížný. Naše skupina se v současné době zaměřila na měření reakcí na lithiovém terči:

- v oblasti energií menších než 20 MeV společně s indickými kolegy [14]
- v oblasti mezi 20 a 40 MeV společně se skupinou Dr. Štefánika v UJF Řež, v.v.i.

⁵² Procedura se nazývá „neutron spectra unfolding“, matematicky se jedná o dekonvoluci integrálu reakční rychlosti, který se rovná konvoluci funkce neutronového spektra (energeticky závislá hustota toku neutronů) s funkcí účinného průřezu

⁵³ Často je nutno měřit chybějící data už od jednotek MeV

⁵⁴ Horní hranice není fyzikálně omezena, uvedených 800 MeV je spojeno s aktuální potřebou jaderných dat

- v oblasti nad 40 (a do 200 MeV) ve spolupráci s iThembaLabs, kde se naší skupině podařilo vysoutěžit urychlovačový čas na místním cyklotronu a lithiovém generátoru. Ozařování by mělo proběhnout na začátku roku 2020.
- v oblasti nad 200 MeV (a do 400 MeV) existuje jediné zařízení na světě RCNP Osaka⁵⁵.

Na druhé straně se pokoušíme o maximální využití možností daných nám účastí České republiky v SUJV Dubna, zejména přístupem naší skupiny k urychlovači Fázotron. Na tomto urychlovači proběhla také ozařování thoriových fólií na přímém svazku protonů. První výsledky účinných průřezů byly publikovány ve spolupráci s Užhorodskou národní univerzitou naším společným doktorandem Robertem Holombem [15]. Bylo naměřeno velké množství dat, se kterými si musíme detailně poradit a připravit komplexní publikaci, která bude obsahovat opravdu cenná, systematická a komplexní data. V případě integrálních experimentů začínáme spolupracovat se skupinou Dr. M. Košťála z Centra výzkumu Řež [60].

V současné době se „Jaderné skupině“ na UEEN FEKT VUT v Brně daří provádět experimenty na různých místech světa včetně České republiky, máme kvalitní výpočetní programy a další analytické nástroje naprogramované k analýze a zpracování naměřených či vypočtených dat. Jsme schopni provádět validace výpočetních modelů, predikce experimentů i verifikace různých programů vůči sobě. Spolupracujeme s výzkumnými pracovišti v Čechách, na západě, východě i dálném východě; připravujeme se znovu rozvinout spolupráci s jiho- a východo-evropskými partnery⁵⁶. Naší snahou je užší spolupráce s projektem MYRRHA⁵⁷ a s kolegy⁵⁸ z Belgie, ale i s kolegy z Francie⁵⁹ a Velké Británie⁶⁰. Chceme využít šance, kterou nám dává kontakt s našimi bývalými studenty nebo kolegy, ať již v Los Alamos National Laboratory⁶¹ či ve Fermi National Accelerator Laboratory⁶².

Před systémy ADS, stejně jako před naší brněnskou „Jadernou skupinou“ stojí ještě velké výzvy, ponechávající potenciál pro pokračující vědecké bádání na UEEN FEKT VUT v Brně. Je potřeba pokračovat v doplňování databází jaderných dat, provádět experimenty na jiných než jen spalačních neutronových zdrojích, věnovat se teorii a dále zdokonalovat detekční metody a simulační modely.

⁵⁵ Kde naše skupina v roce 2018 neúspěšně žádala o urychlovačový čas. Po skončení měření v iThemba se opět pokusíme soutěže zúčastnit a tentokrát uspět.

⁵⁶ Bulharsko, Rumunsko, Srbsko, Řecko, Ukrajina, Bělorusko, Moldávie, částečně i Polsko, Slovensko i Maďarsko

⁵⁷ Evropský projekt MYRRHA čelí velkému zdržení, se spuštěním reaktoru se počítá v roce 2033

⁵⁸ Působí zde bývalý kolega, Dr. Antonín Krása, se kterým máme některé společné publikace

⁵⁹ Započaty kontakty s IMT Atlantique a LPSC IN2P3 Grenoble

⁶⁰ Se skupinou prof. Rogera Barlowa z University of Huddersfield

⁶¹ Na pozici postdoka zde působí můj bývalý doktorand Dr. Lukáš Závorka

⁶² Na pozici výzkumného pracovníka zde působí bývalý kolega z SUJV Dubna, Dr. Vitalij Pronskikh, se kterým máme mnoho společných publikací

Závěr

Výzkum urychlovačem řízených podkritických jaderných reaktorů v Evropě i Spojených státech Amerických, po roce 2007 poněkud stagnuje, v Ruské federaci stagnace nastává o několik let později. ADS se však nadále rozvíjí v Indii a zejména v Číně. Ta se chystá postavit zařízení CiADS do roku 2024 – výzkumný 10 MW_t reaktor spojený s $2,5 \text{ MW}$ spalačným neutronovým zdrojem, lineárním urychlovačem protonů o energii 500 MeV a proudu 5 mA . Projekt koordinuje Institute of Modern Physics, Chinese Academy of Sciences, Lanzhou, se kterým navázala v roce 2018 spolupráci také naše skupina. Není to však pouze tento projekt, který drží ADS komunitu nad vodou; v ukrajinském Charkově byla letos dokončena podkritická aktivní zóna řízená elektronovým urychlovačem. Zařízení bude sloužit jako zdroj neutronů pro výzkum a aplikace, bude na něm však možné také studovat fyziku ADS, testovat měřicí a detekční zařízení a validovat výpočetní modely. Stále pokračuje projekt MYRRHA, který přes mnoho potíží s financováním, belgickým veřejným míněním po Fukušimě, posunutím termínů dokončení, i tak stále kolem sebe shromažďuje vědeckou komunitu díky workshopům, seminářům a konferencím, které se daří v rámci projektu v Belgii organizovat. V rámci projektu MYRRHA byl také provozován nulový rychlý reaktor VENUS-F, díky kterému se podařilo naměřit cenná data pro validace výpočetních modelů a pro studium kinetiky ADS. Objevila se nová iniciativa kolem Carlo Rubbii – iTheC. Plány na milionové investice do urychlovače v Ruském Troicku nevypadají příliš reálně, nicméně aktivity vedoucí k podání evropských projektů H2020 byly úspěšné. V Texasu paběrkuje projekt ADAM, před přibližně 10 lety s velkým nadšením navržený skupinou okolo významného urychlovačového vědce (údajně jednoho z možných texaských adeptů na Nobelovu cenu za fyziku) profesora Petera McIntyre. V neposlední řadě je, díky dubněnské skupině Dr. Adama (člena také naší, brněnské skupiny), k ozařování připraven spalační terč BURAN (Bolsnoi Uran) v SUJV Dubna.

V oblasti jaderných dat, potřebných pro studium ADS, je stále velmi mnoho bílých míst, velmi mnoho otazníků a nejasností. Důležité je řešit multiplicitu neutronů s pomocí (n, xn) reakcí, výtěžky vysokoenergetického štěpení a vypařování jader, otázku zpožděných neutronů; v energetickém spektru otázku neutronů vyšších energií, kvazistatického pionového píku či píku kvazielastické výměny náboje v jádrech těžkých prvků v průběhu kaskádní části spalační reakce. Zásadní otázkou je validace nové knihovny TENDL, založené na evaluaci jaderných dat s pomocí kódu TALYS. Tyto otázky si žádají nejen nové simulace, ale zejména nové experimenty s nízkou mírou nejistoty. Ačkoliv se to zdá nereálné, naše skupina může svojí iniciativou uspět při sestavení širokého týmu zabývajícího se rozvojem ADS ve střední, jižní a východní Evropě; který z naší iniciativy vzniká na bázi dřívější dubněnské spolupráce; koordinovat tuto spolupráci s vybranými indickými univerzitami, čínským projektem CiADS; být mostem mezi Dubnou, MYRRHA, CERN, Huddersfield, Los Alamos, Fermilab a Texas A&M Univerzity.

Výzkum ADS má na VUT v Brně velký potenciál, aktuálně se problematikou zabývá 6 doktorandů, každý z nich má k dispozici unikátní experimentální data a moderní výpočetní prostředky; každý rok máme zájemce z řad bakalářů i diplomantů. Problematiku v České republice dříve koordinoval Ústav jaderné fyziky AV ČR, v.v.i. společně s Katedrou jaderných reaktorů FJFI ČVUT v Praze⁶³. V současnosti se na UJF a FJFI problematikou aktuálně zabývá jeden doktorand, který navíc

⁶³ Dříve byla zapojena i MFF UK (do a z počátku výzkumu (v letech 1998-2006) také ŠKODA JS, a.s. a FSI VUT v Brně (díky tomu, že ADS bylo v ČR uvažováno v podobě reaktoru s tekutými solemi; ŠKODA JS, a.s. vyvíjela

působí společně s našimi doktorandy v SUJV Dubna. Nesmí se stát, aby se díky tomu problematika ADS v České republice přestala řešit; je třeba, aby se VUT chopilo příležitosti a aby byl výzkum v ČR v oblasti ADS z VUT v Brně koordinován a dále rozvíjen.

Nicméně na VUT je nutné rozvíjet jaderné vzdělávání a výzkum obecně, nejen pouze v problematice ADS. Naše fakulta je vzdušnou čarou vzdálena pouhých 50 km od brány jaderné elektrárny Dukovany. V této lokalitě budou současné jaderné bloky v provozu dalších minimálně 15 let a nové bloky se budou stavět. Je přirozené, aby se provozu i výstavby účastnili zejména absolventi nejbližší technické vysoké školy – Vysokého učení technického v Brně. Jaderné vzdělávání je nutné rozvíjet komplexně, na základě mezifakultní spolupráce a s podporou vedení univerzity a na základě dohody s jadernými firmami v regionu. Vybudování takového systému jaderného vzdělávání je hlavním cílem naší jaderné skupiny, k jehož naplnění bych rád i nadále přispíval výukou, školením doktorandů, vedením diplomových a bakalářských prací, řešením projektů a kontaktem s českými i zahraničními vědeckými i průmyslovými institucemi.

Reference

1. KUMAR, V., KATOVSKÝ, K.: Spent Nuclear Fuel and Accelerator-Driven Subcritical Systems. Green Energy and Technology. Green Energy and Technology. Singapur: Springer Nature Singapore Pte Ltd., 2019. 144 p. ISBN: 978-981-10-7502-5. ISSN: 1865-3529
2. KATOVSKÝ, K., KOBYLKA, D., KŘEPEL, J.: Neutronic, Kinetic, and Thermal-Hydraulic Calculation of Accelerator Driven Target-Blanket, In: Proceedings of ADDTA and AccApp Conference, Reno, NV, USA, 2001. American Nuclear Society. 2002
3. KATOVSKÝ, K.: Modelový výpočet blanketu transmutačních systémů s důrazem na jaderná data a knihovny účinných průřezů, diplomová práce, KJR FJFI ČVUT v Praze, vedoucí Ing. Ľubomír Sklenka, Praha, 2001
4. ADAM, J., KATOVSKÝ, K., MICHEL, R., BALABEKYAN, A., TSOUPOKO-SITNIKOVA, V.M., ET AL.: Investigation of Cross-Sections for the Formation of Residual Nuclei in Reactions Induced by 660 MeV Protons Interacting with Natural Uranium Targets, In: Proceedings of the International Workshop on Nuclear Data for the Transmutation of Nuclear Waste TRAMU. Darmstadt: GSI Darmstadt, 2004
5. KATOVSKÝ, K., ADAM, J., MICHEL, R., BALABEKYAN, A., TSOUPOKO-SITNIKOVA, V.M., ET AL. Investigation of Formation of Residual Nuclei from ^{nat}U by Reactions with 660 MeV Protons, In: Proceedings of International Conference on Nuclear Data for Science and Technology ND'2004. Santa Fe: American Institute of Physics AIP, 2005, vol. 1, 2, pp. 1043-1046
6. ADAM, J., KATOVSKÝ, K., MAJERLE, M., BALABEKYAN, A., KRIVOPUSTOV, M.I., ET AL.: Transmutation studies of radioactive nuclei, Bulgarian Journal of Physics. 2007, vol. 34, no. s1 "Nuclear Methods for Non-Nuclear Applications", pp. 127-152. ISSN 1310-0157
7. KATOVSKÝ, K.: Studium sekundárních neutronů a jader vznikajících při reakcích protonů a neutronů v terčích z uranu a plutonia, disertační práce, KJR FJFI ČVUT v Praze, školitel Dr. Jindřich Adam, Praha, 2008
8. ADAM, J., KATOVSKÝ, K., MAJERLE, M., KRIVOPUSTOV, M.I., KUMAR, V., ET AL.: A study of nuclear transmutation of Th and U-nat with neutrons produced in a Pb target and U blanket irradiated by 1.6 GeV deuterons, European Physical Journal A, Hadrons and Nuclei. 2010, vol. 43, no. 2, pp. 159-173. ISSN 1434-6001
9. BALABEKYAN, A.R., KARAPETYAN, G.S., DEMEKHINA, N.A., ADAM, J., KATOVSKÝ, K.: Symmetric and asymmetric fission modes in proton-induced fission at 660 MeV of ^{238}U , Physics of Atomic Nuclei. 2010, vol. 73, no. 11, pp. 1814-1819. ISSN 1063-7788
10. ADAM, J.; BHATIA, C.; KATOVSKÝ, K.; KUMAR, V.; MAJERLE, M.; PRONSKIKH, V.; TSOUPOKO-SITNIKOVA, V.; KHILMANOVICH, A.; MARTSYNKEVICH, B.; ZHUK, I.; GOLOVATIIOUK, V.; WESTMEIER, W.; POTAPENKO, A.; SOLNYSHKIN, A.: A study of reaction rates of (n,f), (n,g) and (n,2n) reactions in U-nat and Th-232 by the neutron fluence produced in the graphite set-up (GAMMA-3) irradiated by 2.33 GeV deuteron beam. EUROPEAN PHYSICAL JOURNAL A, 2011, roč. 47, č. 7, s. 85-102. ISSN: 1434-6001.
11. DEPPMAN, A.; GUIMARAES, V.; BALABEKYAN, A.; DEMEKHINA, N.; ADAM, J.; KATOVSKÝ, K.: Supersymmetric fission of heavy nuclei induced by intermediate-energy protons, PHYSICAL REVIEW C, 2013, roč. 88, č. 6, s. 1-7. ISSN: 2469-9985.
12. ŠTEFÁNIK, M.; BÉM, P.; GOTZ, M.; KATOVSKÝ, K.; MAJERLE, M.; NOVÁK, J.; ŠIMEČKOVÁ, E. Neutron Spectrum Determination of the p(35 MeV)-Be Source Reaction by the Dosimetry Foils Method. NUCLEAR DATA SHEETS, 2014, vol. 119, no. 5, pp. 422-424. ISSN: 0090- 3752
13. ZEMAN, M.; ADAM, J.; KATOVSKÝ, K.; VRZALOVÁ, J.; ZÁVORKA, L.; NOVOTNÝ, F. et al. Determination of the Secondary Neutron Flux at the Massive Natural Uranium Spallation Target. Conference on the Application of Accelerators in Research and Industry, CAARI 2016; The Worthington Renaissance Fort Worth HotelFort Worth; United States; 30 October 2016 through 4 November 2016; In *Physics Procedia*. 2017. s. 69-78. ISSN: 1875-3892.

14. MAKWANA, R., MUKHERJEE, S., SINGH, N.L., KATOVSKY, K. ET AL.: Measurements of the cross sections of the W-186(n,gamma)W-187, W-182(n,p)Ta-182, Gd-154(n,2n)Gd-153, and Gd-160(n,2n)Gd-159 reactions at neutron energies of 5 to 17 MeV, PHYSICAL REVIEW C, 2017, vol. 96, no. 2, ISSN: 2469-9985
15. HOLOMB, R., TARI, S., KATOVSKÝ, K., HAYSAK, I., ADAM, J., VESPALEC, R., VRZALOVÁ, J., ZÁVORKA, L., ZEMAN, M. et al.: Cross sections of nuclear isomers from the interaction of protons with the thin thorium target, In *EPJ Web of Conferences Volume 204 (2019) XXIV International Baldin Seminar on High Energy Physics Problems "Relativistic Nuclear Physics and Quantum Chromodynamics" (Baldin ISHEPP XXIV)*. EPJ Web of Conferences. Les Ulis: EDP Sciences, 2019. s. 04006-04011. ISSN: 2100-014X
16. GANDINI, A., SALVATORES, M.: The Physics of Subcritical Multiplying Systems, Journal of NUCLEAR SCIENCE and TECHNOLOGY, Vol. 39, No. 6, p. 673–686 (June 2002)
17. NIFENECKER, H., MEPLAN, O., DAVID, S.: ACCELERATOR DRIVEN SUBCRITICAL REACTORS, IoP Publishing Ltd 2003, ISBN 0 7503 0743 9
18. IAEA ADS status reports – TE985 (updates TE1365, TE1504, TE1626, TE1766), Vienna, Austria
19. NEA comparative study: Accelerator-driven Systems (ADS) and Fast Reactors (FR) in Advanced Nuclear Fuel Cycles, OECD Paris, France, 2002
20. KEN NAKAJIMA, ET AL.: Nuclear Back-end and Transmutation Technology for Waste Disposal, Springer Open Tokyo, 2015, ISBN 978-4-431-55110-2
21. . ALVAREZ, J., FERNANDEZ-TOBIAS, J., MIMA, K., ET AL.: Laser Driven Neutron Sources: Characteristics, Applications and Prospects, Physics Procedia 60 (2014), pp. 29 – 38
22. KLEINSCHMIDT, A., BAGNOUD, V., DEPPERT, O., ET AL.: Intense, directed neutron beams from a laser-driven neutron source at PHELIX, PHYSICS OF PLASMAS 25, 053101 (2018)
23. BZUNUNI, S., ET AL.: Characteristics of Two-Reactor Electronuclear Systems, Atomic Energy, May 2002, Volume 92, Issue 5, pp 373–380
24. NIFENECKER, H., DAVID, S., ET AL.: Hybrid Nuclear Reactors, Progress in Particle and Nuclear Physics 43 (1999), pp. 683 – 827
25. AMBARDANISHVILI, T., ET AL.: ACTIVATION NEUTRON DETECTOR, US PATENT US3931523, Jan. 6, 1976
26. DROSG, M.: MONOENERGETIC NEUTRON PRODUCTION BY TWO-BODY REACTIONS IN THE ENERGY RANGE FROM 0.0001 TO 500 MEV, International Workshop on Fast Neutron Physics, September 5 - 7, 2002, Dresden, Germany
27. PROPERTIES OF NEUTRON RESOURCES, IAEA, TE410, 1987
28. LAWRENCE, E.O., McMILLAN, E.M., ALVAREZ, L.W.: ELECTRONUCLEAR REACTOR, US PATENT US2933442, Apr. 19, 1960
29. VASILKOV, V.G., GOLDANSKY, V.I, DZHELEPOV, V.P., DMITRIEVSKY, V.P, Electronuclear method of neutron generation and fissile materials production, Atomic Energy 29 N3 (1970) 151
30. VASILKOV, R. G., GOLDANSKY, V. I., ORLOV, V. V.: Sov. Phys. – Usp. 1983. V. 139, Iss. 3.
31. VASILKOV R. ET AL.: Atom. Energy. 1978. V.44, Iss. 4. P. 329
32. BOWMAN, C.D., ARTHUR, E.D., LISOWSKI, P.W., ET AL.: Nuclear energy generation and waste transmutation using an accelerator-driven intense thermal neutron source, NIM A, vol. 320, 1992, pp. 336-367
33. R.A . Jameson, G.P . Lawrence and C.D . Bowman: Accelerator-driven transmutation technology for incinerating radioactive waste and for advanced application to power production, NIM B, vol. 68, 1992, pp. 474 – 480

34. RUBBIA, C., CARMINATI, F., ET AL.: An Energy Amplifier for Cleaner and Inexhaustible Nuclear Energy Production, Report CERN-AT-93-47(ET), 1993.
35. K. Furukawa et al., The combined system of accelerator molten salt breeder (AMSB) and molten salt converter reactor (MSCR), Japan-US Seminar on Thorium Fuel Reactors, Naora, Japan, October 1982.
36. SOULE, R.: Neutronic Studies in Support to ADS: The MUSE Experiments in the MASURCA Facility, PHYSOR 2002, Seoul, Korea, October 7-10, 2002
37. Gohar, Y., Smith, D. L.: YALINA Facility A Sub-Critical Accelerator-Driven System (ADS) for Nuclear-Energy Research Facility Description and an Overview of the Research Program (1997-2008), ANL-10/05, Argonne National Laboratory, Nuclear Engineering Division, 2010
38. BAETEN, P., ABDERRAHIM, H.A., AOUST, T., ET AL.: The GUINEVERE project at the VENUS facility, Proceedings of PHYSOR, International Conference on the Physics of Reactors – Nuclear Power: Sustainable Resource, Interlaken, Switzerland, Sept. 14-19, 2008
39. HRON, M.: PROJECT SPHINX SPENT HOT FUEL INCINERATOR BY NEUTRON FLUX (THE DEVELOPMENT OF A NEW REACTOR CONCEPT WITH LIQUID FUEL BASED ON MOLTEN FLUORIDES), Progress in Nuclear Energy; Vol. 47, No. 1-4, pp. 347-353, 2005
40. BELLER, D.: Reactor Physics Studies for the AFCI Reactor-Accelerator Coupling Experiments (RACE) Project, University of Nevada, Las Vegas, Transmutation Research Program Projects, status report 2006
41. DULLA, S., RAVETTO, P., PICCA, P., ET AL.: ANALYTICAL BENCHMARKS FOR THE KINETICS OF ACCELERATOR-DRIVEN SYSTEMS, Joint International Topical Meeting on Mathematics & Computation and Supercomputing in Nuclear Applications (M&C + SNA 2007), Monterey, California, April 15-19, 2007, on CD-ROM, American Nuclear Society, LaGrange Park, IL (2007)
42. RAVETTO, P., ROSTAGNO, M.M., BIANCHINI, G., CARTA M., D'ANGELO A.: Application of the Multipoint Method to the Kinetics of Accelerator-Driven Systems, NUCLEAR SCIENCE AND ENGINEERING, vol. 148, pp. 79–88, 2004
43. Talamo, A., Ravetto, P., Gudowski, W.: Advanced Computational Models for Accelerator-Driven Systems, Science and Technology of Nuclear Installations, Volume 2012, Article ID 376164
44. NIFENECKER, H., DAVID, S., ET AL.: Basics of accelerator driven subcritical reactors, NIM A, vol. 463, 2001, 428-467
45. Saracco, P., Dulla, S., Ravetto P.: The adjoint neutron transport equation and the statistical approach for its solution, P. Eur. Phys. J. Plus (2016) 131: 412
46. VAZ, P.: Neutron transport simulation (selected topics), Radiation Physics and Chemistry, Vol. 78, Issue 10, 2009, pp. 829-842
47. WERNER, C.J., BULL, J.S., SOLOMON, C.J., ET AL.: MCNP6.2 Release Notes, LA-UR-18-20808, Los Alamos (2018)
48. WATERS, L.S., MCKINNEY G.W., ET AL.: The MCNPX Monte Carlo Radiation Transport Code, AIP Conference Proceedings 896, 81 (2007)
49. BATTISTONI, G., CERUTTI, F., ET AL.: The FLUKA code: description and benchmarking, AIP Conference Proceedings 896, 31 (2007)
50. ALLISON, J., ET AL.: Recent developments in GEANT4, NIM A, vol. 835, 2016, pp. 186-225
51. MOKHOV, N.V., JAMES, C.C.: The MARS Code System User's Guide Version 15(2016), Fermi National Accelerator Laboratory, P.O. Box 500, Batavia, Illinois 60510, February 02, 2017
52. KONING, A.J., ROCHMAN, D.: Modern Nuclear Data Evaluation With The TALYS Code System, Nuclear Data Sheets 113 (2012) 2841

53. ANÉFALOS, S., DEPPMAN, A. ARRUDA-NETO, J.D.T., ET AL.: The CRISP Code for Nuclear Reactions, AIP Conference Proceedings 769, 1299 (2005)
54. HERMAN, M., CAPOTE, R. ET AL.: EMPIRE: Nuclear Reaction Model Code System for Data Evaluation, Nuclear Data Sheets 108 (2007) 2655–2715
55. TSILEDAKIS, G., DELBART, A. ET AL.: A large high-efficiency multi-layered Micromegas thermal neutron detector, Journal of Instrumentation, 12 P09006, 2017
56. KREJCI, F., ZEMLICKA, J., JAKUBEK J., ET AL.: Development and characterization of high-resolution neutron pixel detectors based on Timepix read-out chips, 18th International Workshop on Radiation Imaging Detectors, 3–7 July 2016, Barcelona, Spain, Journal of Instrumentation, vol. 11 C12026, 2016
57. HOWELL, R.M., BURGETT, E.A., WIEGEL, B., HERTEL, N.E.: Calibration of a Bonner sphere extension (BSE) for high-energy neutron spectrometry, Radiation Measurements vol. 45 (2010) 1233-1237
58. GRIFFIN, P.J., KELLY, J.J.G., VANDENBURG, J.W: User's Manual for SNL-SAND-11 Code, Sandia National Laboratories, SAND93-3957, 1994
59. ŠTEFÁNIK, M.: Experimentálne stanovenie spektier urýchľovačom riadených neutrónových generátorov, disertační práce, KJR FJFI ČVUT v Praze, školitel K. Katovský, 2015
60. Košťál, M., Švadlenková, M., Baroň P., Milčák J., Mareček M., Uhlíř J.: Measurement of $(^{23}\text{Na}(n,2n))$ cross section in well-defined reactor spectra, Applied Radiation and Isotopes, vol. 111, 1-7, 2016

Publikace, jež tvoří habilitační práci:

1. KUMAR, V., KATOVSKÝ, K.: Spent Nuclear Fuel and Accelerator-Driven Subcritical Systems. Green Energy and Technology. Green Energy and Technology. Singapur: Springer Nature Singapore Pte Ltd., 2019. 144 p. ISBN: 978-981-10-7502-5. ISSN: 1865-3529
2. KATOVSKÝ, K., KOBYLKA, D., KŘEPEL, J.: Neutronic, Kinetic, and Thermal-Hydraulic Calculation of Accelerator Driven Target-Blanket, In: Proceedings of ADDTA and AccApp Conference, Reno, NV, USA, 2001. American Nuclear Society. 2002
3. ADAM, J., KATOVSKÝ, K., MICHEL, R., BALABEKYAN, A., TSOUPKO-SITNIKOV, V.M., ET AL.: Investigation of Cross-Sections for the Formation of Residual Nuclei in Reactions Induced by 660 MeV Protons Interacting with Natural Uranium Targets, In: Proceedings of the International Workshop on Nuclear Data for the Transmutation of Nuclear Waste TRAMU. Darmstadt: GSI Darmstadt, 2004
4. KATOVSKÝ, K., ADAM, J., MICHEL, R., BALABEKYAN, A., TSOUPKO-SITNIKOV, V.M., ET AL. Investigation of Formation of Residual Nuclei from ^{nat}U by Reactions with 660 MeV Protons, In: Proceedings of International Conference on Nuclear Data for Science and Technology ND'2004. Santa Fe: American Institute of Physics AIP, 2005, vol. 1, 2, pp. 1043-1046
5. ADAM, J., KATOVSKÝ, K., MAJERLE, M., BALABEKYAN, A., KRIVOPUSTOV, M.I., ET AL.: Transmutation studies of radioactive nuclei, Bulgarian Journal of Physics. 2007, vol. 34, no. s1 "Nuclear Methods for Non-Nuclear Applications", pp. 127-152. ISSN 1310-0157
6. ADAM, J., KATOVSKÝ, K., MAJERLE, M., KRIVOPUSTOV, M.I., KUMAR, V., ET AL.: A study of nuclear transmutation of Th and U-nat with neutrons produced in a Pb target and U blanket irradiated by 1.6 GeV deuterons, European Physical Journal A, Hadrons and Nuclei. 2010, vol. 43, no. 2, pp. 159-173. ISSN 1434-6001
7. BALABEKYAN, A.R., KARAPETYAN, G.S., DEMEKHINA, N.A., ADAM, J., KATOVSKÝ, K.: Symmetric and asymmetric fission modes in proton-induced fission at 660 MeV of ^{238}U , Physics of Atomic Nuclei. 2010, vol. 73, no. 11, pp. 1814-1819. ISSN 1063-7788
8. ADAM, J.; BHATIA, C.; KATOVSKÝ, K.; KUMAR, V.; MAJERLE, M.; PRONSKIKH, V.; TSOUPKO-SITNIKOV, V.; KHILMANOVICH, A.; MARTSYNKEVICH, B.; ZHUK, I.; GOLOVATIIOUK, V.; WESTMEIER, W.; POTAPENKO, A.; SOLNYSHKIN, A.: A study of reaction rates of (n,f), (n,g) and (n,2n) reactions in U-nat and Th-232 by the neutron fluence produced in the graphite set-up (GAMMA-3) irradiated by 2.33 GeV deuteron beam. EUROPEAN PHYSICAL JOURNAL A, 2011, vol. 47, no. 7, pp. 85-102. ISSN: 1434-6001.
9. DEPPMAN, A.; GUIMARAES, V.; BALABEKYAN, A.; DEMEKHINA, N.; ADAM, J.; KATOVSKÝ, K.: Supersymmetric fission of heavy nuclei induced by intermediate-energy protons, PHYSICAL REVIEW C, 2013, vol. 88, no. 6, pp. 1-7. ISSN: 2469-9985.
10. ŠTEFÁNIK, M.; BÉM, P.; GOTZ, M.; KATOVSKÝ, K.; MAJERLE, M.; NOVÁK, J.; ŠIMEČKOVÁ, E. Neutron Spectrum Determination of the p(35 MeV)-Be Source Reaction by the Dosimetry Foils Method. NUCLEAR DATA SHEETS, 2014, vol. 119, no. 5, pp. 422-424. ISSN: 0090-3752
11. ZEMAN, M.; ADAM, J.; KATOVSKÝ, K.; VRZALOVÁ, J.; ZÁVORKA, L.; NOVOTNÝ, F. et al. Determination of the Secondary Neutron Flux at the Massive Natural Uranium Spallation Target. Conference on the Application of Accelerators in Research and Industry, CAARI 2016; The Worthington Renaissance Fort Worth HotelFort Worth; United States; 30 October 2016 through 4 November 2016; In Physics Procedia. 2017. pp. 69-78. ISSN: 1875-3892.
12. MAKWANA, R., MUKHERJEE, S., SINGH, N.L., KATOVSKY, K. ET AL.: Measurements of the cross sections of the W-186(n,gamma)W-187,W-182(n,p)Ta-182,Gd-154(n,2n)Gd-153, and Gd-160(n,2n)Gd-159 reactions at neutron energies of 5 to 17 MeV, PHYSICAL REVIEW C, 2017, vol. 96, no. 2, ISSN: 2469-9985
13. HOLOMB, R., TARI, S., KATOVSKÝ, K., HAYSAK, I., ADAM, J., VESPALEC, R., VRZALOVÁ, J., ZÁVORKA, L., ZEMAN, M. et al.: Cross sections of nuclear isomers from the interaction of protons with the thin thorium target, In EPJ Web of Conferences Volume 204 (2019) XXIV International Baldin Seminar on High Energy Physics Problems "Relativistic Nuclear Physics and Quantum Chromodynamics" (Baldin ISHEPP XXIV). EPJ Web of Conferences. Les Ulis: EDP Sciences, 2019. p. 04006-040011. ISSN: 2100-014X

Green Energy and Technology



Vinod Kumar Verma
Karel Katovsky

Spent Nuclear Fuel and Accelerator-Driven Subcritical Systems

EXTRAS ONLINE

 Springer

Green Energy and Technology

POUZE PRO ÚČELY HABILITAČNÍHO ŘÍZENÍ

Climate change, environmental impact and the limited natural resources urge scientific research and novel technical solutions. The monograph series Green Energy and Technology serves as a publishing platform for scientific and technological approaches to “green”—i.e. environmentally friendly and sustainable—technologies. While a focus lies on energy and power supply, it also covers “green” solutions in industrial engineering and engineering design. Green Energy and Technology addresses researchers, advanced students, technical consultants as well as decision makers in industries and politics. Hence, the level of presentation spans from instructional to highly technical.

More information about this series at <http://www.springer.com/series/8059>

POUZE PRO ÚČELY HABILITAČNÍHO ŘÍZENÍ

Vinod Kumar Verma · Karel Katovsky

Spent Nuclear Fuel and Accelerator-Driven Subcritical Systems

POUZE PRO ÚČELY HABILITAČNÍHO ŘÍZENÍ

 Springer

Vinod Kumar Verma
University of Rajasthan
Jaipur, Rajasthan, India

and

GGSSIP University
New Delhi, India

Karel Katovsky
Department of Electrical Power
Engineering, Faculty of Electrical
Engineering and Communication
Brno University of Technology
Brno, Czech Republic

ISSN 1865-3529

Green Energy and Technology

ISBN 978-981-10-7502-5

<https://doi.org/10.1007/978-981-10-7503-2>

ISSN 1865-3537 (electronic)

ISBN 978-981-10-7503-2 (eBook)

Library of Congress Control Number: 2018950201

© Springer Nature Singapore Pte Ltd. 2019

This work is subject to copyright. All rights are reserved by the Publisher, whether the whole or part of the material is concerned, specifically the rights of translation, reprinting, reuse of illustrations, recitation, broadcasting, reproduction on microfilms or in any other physical way, and transmission or information storage and retrieval, electronic adaptation, computer software, or by similar or dissimilar methodology now known or hereafter developed.

The use of general descriptive names, registered names, trademarks, service marks, etc. in this publication does not imply, even in the absence of a specific statement, that such names are exempt from the relevant protective laws and regulations and therefore free for general use.

The publisher, the authors and the editors are safe to assume that the advice and information in this book are believed to be true and accurate at the date of publication. Neither the publisher nor the authors or the editors give a warranty, express or implied, with respect to the material contained herein or for any errors or omissions that may have been made. The publisher remains neutral with regard to jurisdictional claims in published maps and institutional affiliations.

This Springer imprint is published by the registered company Springer Nature Singapore Pte Ltd.

The registered company address is: 152 Beach Road, #21-01/04 Gateway East, Singapore 189721, Singapore

Preface

Spent nuclear fuel (SNF) is a fallout of nuclear energy programs of the present-day society. In fact, disposal of the radioactive waste (RAW) is a challenge and every human is threatened by it.

It reminds us that thousands of years back the human race was frightened of volcanoes and electric thunders but they provided the concept of the source of fire and hot material. The human race took it as a challenge and spent thousands of years in developing different ways of producing fire and finding thousands of applications too. On the social front, the development of fire even gave birth to cultural and racial problem in different parts of the globe. But, after all, it provided the means of positive developments and showed a definite path of advancement to the entire human race of the time. It may be assumed that in the modern time, the human race is attempting to handle the new, compact, and wonderful source of heat and energy in the form of nuclear energy.

Every energy issue has raised eyebrows of the strong believers of humanity because for the infinite time the sun has been the source of energy and life with which the human race has its strongest relationship. The sun being at far long distance does not raise any intimate threat to the mankind. On the other hand, SNF has a relatively intimate relationship. Its heaped amount on earth and having a feature of its reutilization cannot allow it to be avoided from the developmental process. The book is written for all these concerns so that it can help our education system and future developments.

The nuclear science community is well aware of both threats and applications of the nuclear energy and it is highly concerned with finding solutions. RAW contains a fatal radio-toxic radiation and at the same time a bigger proportion of RAW can be reutilized as a fuel also. It is the result of serious concerns only that despite of the fact that hundreds of nuclear energy reactors are operational world over and there have been only a few accidents. Small accidents can be avoided by generating awareness through education and developing stronger control systems regarding proliferation and sources of threats. This is also deeply related to education that nuclear energy has been grown for peaceful utilization.

While producing the text of the first chapter of the book, we thought several times that how the issue of SNF is a state-of-the-art issue. Ultimately, we kept the subtitle on having a keen look at the national ways of handling the international issues, treaties and standards in their own references, national

interests and sometimes agreeing on an issue and other times disagreeing. These details are presented at the end of the chapter. Still, it can be emphasized that proper education can solve these petty issues in future.

The writing of the book started with the fact that over the last twenty years or more the authors have participated in several experiments and developmental works, organization of several meetings and conferences and producing the manpower for both research and education, and a book is considered to be the best carrier of compilation of such knowledge. Several books have been written on the issues of proliferation and nuclear waste but only a few articles or the periodicals are able to inspire the young minds to begin with a 'start up' and career in research. The book will arouse that kind of keenness for both. The book will support the graduate students and innovators to grow new ideas of research and entrepreneurship also, in the field of new setup of energy utilization and to save from the energy losses.

Efforts have been made that the book comprises existing knowledge till last few years for education purpose. The readers may provide help to the authors in pointing out more details that may be added in the future version of the book. It may, however, be pointed out that the chapter related to data is kept short as one of the authors had presented many recent data in his earlier book entitled *Role of (n, xn) reactions in ADSS* published in the year 2011.

The authors have a deep sense of gratitude to their co-workers who had participated in different experiments with them because they had helped in developing the concept without even known to us about writing of the book. The authors are grateful to the international community who is involved in various related research and development activities and they helped us in providing some of the results of their hard work in response to our personal contacts. The authors are grateful to JINR, Dubna where they used its facilities and entire research framework for their career.

Our sincere thanks are due to Dr. N. S. Raghaw for his help in providing the data of radiation damage, handling various data files and data sites and running the JA-IPU code even at a call at an odd hour. His enormous help at the time of final compilation of the manuscript was commendable.

The authors are thankful to Springer for having the patience for the completion of the manuscript and their prompt responses all throughout its preparation for over a year.

Jaipur/New Delhi, India

Brno, Czech Republic
February 2018

Dr. Vinod Kumar Verma
(Superannuated Professor)

Prof. Karel Katovsky

Contents

1 Spent Nuclear Fuel and Alternative Methods of Transmutation	1
1.1 Spent and Unspent Nuclear Fuel and the Nuclear Waste	1
1.1.1 State-of-the-Art: Spent Nuclear Fuel Issue	1
1.1.2 Radio-Toxicity	2
1.1.3 Extraction or Reprocessing	3
1.1.4 Status of the Unspent Fuel	7
1.1.5 Economy of Reprocessing	8
1.2 Methods of Reduction of the Radioactive Material	9
1.2.1 Disposals, Reposition and Transmutation	9
1.2.2 Other Applications	10
1.3 Issues Related to Nuclear Waste	12
1.3.1 Proliferation and Security	12
1.3.2 Reutilization	14
1.3.3 Radiation Damage and Gas Production	15
1.3.4 Protection of Society and Environment	15
References	18
2 Special Hybrid Systems and Molten-Salt Reactors	21
2.1 Concept of Hybridization of Nuclear Energy	21
2.1.1 Hybrid Nuclear Energy Systems	21
2.1.2 Fusion–Fission Hybrids	24
2.2 Reactor with Liquid Fuel	26
2.2.1 Single-Fluid Reactor	26
2.2.2 Double-Fluid Reactor	26
2.3 Other Hybrid Energy Systems	27
2.3.1 West Texas Model of NHES	27
2.3.2 Northeastern Arizona Model of NHES	27
2.3.3 Wind and PV Hybrid Energy System	29
References	29
3 Spallation Neutron Source, Multiplication and Possibility of Incineration	31
3.1 Neutron Sources and Applications	31
3.1.1 Neutron Sources	31
3.1.2 Spallation Neutron Sources	33

3.2	Neutron Multiplicative Processes	36
3.2.1	Role of (n, xn) and Similar Reactions	37
3.2.2	Multiplication Coefficient and Source Importance.	39
3.3	Utilization of Spallation Neutrons by a Fuel.	43
3.3.1	IAEA Benchmark Design	45
3.3.2	Neutron Flux in Different Regions.	47
3.3.3	Accelerator Current and Radial Heat Distribution	49
	References.	50
4	Requirement of Nuclear Data	53
4.1	Requirement of Nuclear Data Beyond the Existing Power Reactors.	53
4.2	Nuclear Data.	55
4.2.1	Data Requirement of a Target System.	58
	References.	64
5	Transmutation of Spent Nuclear Fuel and Extension of a Fuel Cycle	67
5.1	ADSS for Transmutation of LLNW	67
5.1.1	Long-Lived Actinides (LLA) and the Fission Products (FP).	68
5.1.2	Reduction of Half-Life.	68
5.1.3	Reduction by the Thermal, Fast, and Spallation Neutron Spectra.	70
5.2	Conversion of Fertile into Fissile and the Breeding Process	75
5.3	Extension of the Fuel Cycles	76
	References.	80
6	Major Experimental Facilities for Development of Accelerator-Driven Subcritical System	81
6.1	FEAT and TARC Experiment.	81
6.2	n -ToF Experiments for Measurement of Cross Section	83
6.3	IREN—Facility at Dubna	86
6.4	TRIGA	88
6.5	KEK Setup	90
6.6	BFS Setups.	91
6.7	MUSE and YALINA Setups.	92
6.8	GUINEVERE and VENUS-F Setup	95
6.9	PURNIMA and KAMINI Experimental Reactors	95
6.10	BRAHMA Subcritical Facility at BARC.	97
6.11	GAMMA Series of Experiments at JINR, Dubna	97
6.11.1	GAMMA-2	99
6.11.2	GAMMA-3	101
6.12	Energy + Transmutation Experimental Setup	107
6.13	QUINTA—An Experimental Setup.	109

6.14	MYRRHA and EFIT—A Road Map of ADSS.....	110
6.15	Subcritical Assembly at Dubna (SAD).....	112
6.16	BURAN Setup.....	112
6.17	GEM * STAR Setup.....	115
6.18	Some More ADS Programs of Asian Countries.....	116
	References.....	118
7	Radiation Damage and Development of a MC Software	
	Tool	123
7.1	Radiation Damage—An Important Issue.....	123
7.1.1	Radiation Effects in Materials.....	124
7.1.2	Early Approaches of Assessment of Radiation Damage.....	126
7.1.3	Monte Carlo Simulation Approach of JA-IPU Code.....	130
7.1.4	A Phenomenological Approach of Radiation Damage.....	136
7.1.5	Dynamic Model Approach and JA-IPU.....	139
7.1.6	Radiation Resistant Materials.....	141
	References.....	142

POUZE PRO ÚČELY VĚDECKÉHO ŘÍZENÍ

About the Authors



Dr. Vinod Kumar Verma was Professor of physics at the University of Rajasthan, Jaipur, India, until April 2010 and Professor of engineering physics/nanoscience at the GGSIP University, New Delhi, until January 2016. In his research career spanning more than 40 years, he participated in international collaborations like EMU01, L3, WA93, WA98, GAMMA-2 and 3, E+T, and QUINTA at the Joint Institute for Nuclear Research (JINR), Dubna. He has authored and co-authored over 180 research papers and edited the proceedings of the Workshop on Physics of Accelerator Driven Sub-critical Systems (ADSS). In India, he is best known for his pioneering research on ‘spallation neutrons’ in the course of several S&T projects completed for DST and DAE (Government of India). He has also successfully completed developmental work on two Monte Carlo codes for the ADSS technology, i.e. the CASCADE 2004 version in collaboration with JINR, Dubna and the JA-IPU code for radiation damage with a team of Indian researchers. Over the past 20 years, he has initiated scientific collaborations with teams in the Czech Republic, S. Korea, and Russia on the activities related to ADSS technique. Present book is his second contribution for education and research activity on the ADSS.



Dr. Karel Katovsky graduated with a degree in nuclear engineering. His Ph.D. thesis at the Faculty of Nuclear Sciences and Physical Engineering of the Czech Technical University in Prague (2008) was on the experimental research and the nuclear data problems of ADSS. He subsequently spent several years at JINR, Dubna. He worked at the Computation Reactor Physics Department of SKODA JS, where he dealt with nuclear fuel loading patterns and their optimization. Since 2012, he has been working as Assistant Professor of nuclear engineering at the Brno University of Technology, where he serves as Leader of the Nuclear Power Group to teach nuclear energy. He is the author or co-author of 37 SCOPUS-indexed papers, more than 50 conference papers, and about 30 research reports. He is a member of the Board of the Czech Nuclear Society and of the expert committee for nuclear energy of regional NGO associations in the NPP Dukovany area.

POUZE PRO ÚČELY VĚDECKÉHO ŘÍZENÍ

Spent Nuclear Fuel and Alternative Methods of Transmutation

1

The chapter deals with the status of the spent nuclear fuel and accumulation of unspent nuclear fuel world over. Its fertile, fissile and fission product components are also discussed along with their applications and various methods of reprocessing the SNF. International situation related to reprocessing, security aspects arising from the SNF, and the fissile components along with its handling at individual national level are also summarized.

1.1 Spent and Unspent Nuclear Fuel and the Nuclear Waste

Spent nuclear fuel (SNF) is the nuclear fuel that is irradiated in a power reactor. A few percent of this is utilized in power generation, and a very large part is left behind as a radiotoxic material at the time of discharge of a reactor. In the SNF major actinides, U and Pu are 95–96 and 1%, respectively. Minor actinides (Np, Am, and Cm) are 0.1%, short-lived fission products (FP) are 3–4%, and long-lived FPs are 0.1%. Different composition elements pose different challenges for disposition of SNF. In fact, unspent nuclear fuel (UNF) is of high concern because its components can be utilized for nuclear energy or other atomic devices with least efforts.

1.1.1 State-of-the-Art: Spent Nuclear Fuel Issue

1.1.1.1 Definition of the Problem

By definition, UNF is the fuel that is left after reprocessing of the radiotoxic nuclear material which is discharged from a reactor and that can qualify for re-application in another reactor. Reprocessing is a combined physical and chemical process that acts on the basis of the kind of radioactive material discharged from a reactor, for example, actinides and fission products. Actinides may further be classified as isotopes of uranium or plutonium, fertile or fissile, etc. A nuclear power reactor that produces 1 gigawatt electric power (1 GWe) burns annually ~ 1 ton of fissile fuel which is equivalent to 2 million ton of oil equivalent (toe). According to an inventory [1], a reactor loaded with 26,328 kg of ^{238}U and 954 kg of ^{235}U gives out 280 kg of ^{235}U , 111 kg of ^{236}U , 266 kg of Plutonium (total), 946 kg of total fission products (FP), and 25,655 kg of ^{238}U at the time of discharge of the reactor. As a matter of fact, a nuclear reactor produces enormous amount of energy which is a clean energy compared to that from any fossil fuels like oil and coal used in energy production and they have threatened the environment seriously in last 50 years. Production of radiotoxic materials in

the form of FP and minor and higher actinides in a nuclear power reactor are otherwise manageable, and because of strong security acts, it takes several years to convert it to the unspent nuclear fuel. It is dumped in a repository most of the time.

1.1.1.2 Amounts in Different Reactor Types

Unspent nuclear fuel inventory at time of discharge depends on the loaded fuel inventory, design of a reactor from the point of neutron spectrum, burning of the fuel, production of actinides, hence the fuel cycle and the conditions of shut down or discharge of the reactor. From the point of design, a normal power reactor is different to a breeder reactor. Also, there can be differences from the point of a light water or a heavy water cooled reactor. In most of the reactors, UO_2 fuel cycle is a popularly used fuel cycle. But, there are possibilities of enrichment of UO_2 or even mixing of Plutonium or another fissile fuel such as PuO_2-UO_2 fuel and that has impact on discharge inventory [2]. There can be several possible inventories of loading of a reactor and one of the PFBR [3] with mixed uranium-plutonium MOX fuel, a mixture of PuO_2 and UO_2 in the form of several isotopes that are organized in the two-core reactor is shown by the data in Table 1.1. They are generally categorized as the fast reactors. In fact, fuel mixture and design of loading for a reactor is state-of-the-art technique.

From the highly radioactive discharged material of a reactor which has more than 95% unspent original fuel, newly formed fissile fuel and a large number of elements that find applications in medical science, industry and other applications, extraction of useful material is done several times, albeit, a highly costly affair. So long as extraction is done or the discharged material is planned to be dumped as such it is treated as a nuclear waste.

1.1.1.3 Issue of Radioactive Waste Management

Nuclear waste comprises of liquids and chemicals of a processing plant, scrapes from milling and leftover nuclides after medical applications including the files and containers or the canisters used in transportation as well as the sand and concrete of the ground of processing units. Nuclear waste is classified as (i) low-level waste (LLW), (ii) intermediate level waste (ILW), (iii) high-level waste (HLW), and (iv) transuranic-level nuclear waste (TRUW) according to the radio-toxicity which is discussed in next Sect. 1.1.2 and is subjected to dump, reposition, or other means of dissemination. In some quarters of the technology, unprocessed disposal of a reactor is also named as the 'used nuclear fuel' because of existence of a possibility of application of a part of this as a fuel after extraction. According to one report [4] in US alone nearly 60,000 MT (metric ton) of UNF existed up to the year 2009, and it will be discussed in detail in later part of the chapter.

1.1.2 Radio-Toxicity

Radio-toxicity is always measured by the quantity of radioactive material or the radioactivity alone and in case of biological hazard it has nothing to do with chemical toxicity of the hazard [4]. Ingested or inhaled radio-toxicity is commonly expressed in 'Sieverts (Sv)*'. The radio-toxicity of a given radioactive isotope is equal to the product of multiplication of its activity (Bq) and effective dose coefficient $e(\tau)$ for ingestion or similarly, for inhalation for a period τ expressed in years. The effective dose coefficient $e(\tau)$ (units Sv/Bq) is defined as the committed effective dose per unit acute intake for a period, τ . Equation (1.1) shows the relationship

Table 1.1 Minor actinide (%) in core 1 and core 2 subassembly of a PFBR reactor

Core	Minor actinide (%)					
Core 1/core 2	13.78/18.48	13.94/18.64	14.4/19.6	15/20.3	15.6/21	16/22. 2

between radio-toxicity (Sv/kg) and the effective dose coefficient $e(\tau)$ [4].

$$\text{Radio - toxicity (Sv)} = \text{Activity (Bq)} \times e(\tau) \text{ (Sv/Bq)} \quad (1.1)$$

Radio-toxicity is also expressed as volume of water or air in units of m^3 required to dilute the radioactive material potential below the threshold limit for the general public. In case of ingestion, it is the volume of 'water in m^3 ' and in case of inhalation, it is the volume of 'air in m^3 '. The threshold limit for general public is 50 mrem/year or equivalently 0.5 mSv/year based on average intake of 2 L/day of water or 22 m^3 /day of air. Radio-toxicity, expressed in Sv/kg of some of the elements of UNF, is given in Table 1.2 for calculation of total radio-toxicity for a given amount of radionuclide in kg. For details of effective dose coefficient, $e(\tau)$ of radionuclides refer to updated ICRP 119 [5] in place of ICRP 72.

Different radiations like gamma, electron, muon, neutron, proton, and heavier charged particle give different doses to different tissues and organs. A body has several tissues and organs. If H_T is defined as the equivalent dose in a tissue or an organ T , then the sum of weighted equivalent doses in all tissues or organs of the body can be written as $E = \text{Sum}(W_T H_T)$. Here, W_T is the weight factor for a tissue. For the radiation dependence of equivalent dose, $H_{T,R} = W_R D_{T,R}$. Here, $D_{T,R}$ expressed in (J/kg) is the average absorbed dose for a radiation R in a tissue T . Thus, $H_T = \text{Sum} H_{T,R}$. Weighting factor W_R signifies quality of a radiation being smallest for gamma and higher for different energy neutrons. For proton and heavier charged particles, W_R is even higher. Values of W_R as per ICRP 119 for different radiation are given in Table 1.3. It can be understood from the data that alpha-emitting radionuclides have higher values of $e(\tau)$ than β -emitters. Different energy neutrons have different values of W_R^{**} due to different possibilities of activations. All alpha and heavier mass charged particles are kept in one category.

1.1.3 Extraction or Reprocessing

Extraction of actinides or fission product (FP) from the discharged spent fuel is being processed since 1940 using precipitation process. Adopting a route for reprocessing is based on the kind of a reactor. Following three technologies are developed by various countries,

- a. Hydrometallurgy
- b. Pyrometallurgy
- c. Fluoride volatility

Hydrometallurgy process is rather one of the oldest and a matured technology used for separation of major actinides like plutonium and uranium as well as for the conditioning of the ultimate waste for long-term storage. As the name suggests, it is aqueous and in this category following methods are popular.

- (i) Standard PUREX (**P**lutonium **U**ranium **R**edox **E**xtraction) and extended PUREX
- (ii) UREX
- (iii) COEX
- (iv) NUEX

First PUREX plant using the PUREX process was opened up at Savannah River in 1954. Several reprocessing plants started operation in Belgium, France, Germany, India, Japan, Russia, and UK during 1960–1970. Methods UREX, COEX, and NUEX are the derivations of basic PUREX method [6] and differ in producing not the pure Plutonium.

According to the PUREX process, after nearly 5 years of cooling period of a discharge, in order to dissolve the spent fuel it is exposed to nitric acid solution to give nitrates of plutonium, uranium, minor actinides (Np, Am, and Cm), and the fission products. Volatile elements like iodine, krypton and xenon are removed for the off-gas treatment. More noble fission products are not dissolved and they are treated with care along with the fuel assemblies. The solution with dissolved species is forwarded to the extraction process that depends on affinities with the

Table 1.2 Data of radio-toxicity [1] of some of the long-lived actinides and fission products

Element	Half-life (year)	Decay mode	Radioactivity (Bq/kg)	$e(\tau)$ (Radio-toxicity)
$^{236}\text{Np}_{93}$	1.54×10^5	ϵ (87.3), β (12.5), α (0.16)%	–	–
$^{237}\text{Np}_{93}$	2.14×10^6	α	2.6×10^{10}	110 (0.3×10^4)
$^{238}\text{Pu}_{94}$	87.7	α	6.3×10^{14}	230 (1.4×10^8)
$^{239}\text{Pu}_{94}$	2.41×10^4	α	2.3×10^{12}	250 (0.6×10^6)
$^{240}\text{Pu}_{94}$	6.564×10^3	α	–	250
$^{241}\text{Am}_{95}$	4.33×10^2	α	1.3×10^{14}	200 (0.3×10^8)
$^{242\text{m}}\text{Am}_{95}$	141	α (0.46%)	–	–
$^{243}\text{Am}_{95}$	7.37×10^3	α	–	200
$^{244}\text{Cm}_{96}$	18.1	α	–	120
$^{245}\text{Cm}_{96}$	8.5×10^3	α	–	210
^{79}Se	3.27×10^5	β	–	–
^{93}Zr	1.53×10^6	$\beta\gamma$	–	–
^{97}Tc	4.21×10^6	ϵ	–	–
^{98}Tc	4.20×10^6	β	–	–
^{99}Tc	2.11×10^5	β	6.3×10^{11}	(4.9×10^2)
^{107}Pd	6.5×10^6	β	–	–
^{126}Sn	1.0×10^5	β	–	–
^{129}I	1.57×10^7	β	6.5×10^9	(0.7×10^3)
^{135}Cs	2.3×10^6	β	–	–

*Named after Rolf Maximilian Sievert, 1 Sv = 100 rem = 1 J/kg for absorbed dose. Also, expressed in $\text{m}^2 \text{s}^{-2}$ in MKS. Sievert is used in connection of a biological component and Gray (J/kg) for any non-biological physical object.

**Tissue weighting factor is used as radiation weighting factor, W_R to represent relative biological effectiveness according to ICRP 119. This depends on the kind of a radiation. See Table 1.3 for W_R for different radiation. For an individual organs W_T are used

Table 1.3 Radiation weighting factor W_R as per ICRP 119 publication [6]

Radiation weighting factor		
S. No.	Type of radiation and energy range	W_R
1	Photons of all energies	1
2	Electrons and muons all energies	1
3	Neutrons, energy	5
	(i) <10 keV	10
	(ii) 10–100 keV	20
	(iii) >100 keV–2 MeV	10
	(iv) >2 MeV–20 MeV	5
	(v) >20 MeV	5
4	Protons, other than recoil, energy >2 MeV	5
5	Alpha particles, fission fragments, heavy nuclei	20

aqueous or organic phases. As a result of this, FP and minor actinides are cooperatively on one side and uranium and plutonium on other side. On a more specific electron state manipulation, plutonium remains with the organic phase and

uranium is separated on making aqueous phase which is less acidic. After separation, they are solidified through the de-nitration in case of uranium and oxalate precipitation and calcinations in case of plutonium for the purpose of

storage. The solidified uranium and plutonium are stored in separate tanks, and the leftover solvent still has fission products and the actinides which may further be extracted. In PUREX extraction, nearly 99.87% of uranium and 99.36–99.51% of plutonium are extracted. Plutonium is obtained as an oxide in the form of a powder. The PUREX is subject to several risks of proliferation and transportation. Uranium and plutonium so extracted can be converted to MOX fuel by mixing them.

UREX is a solvent extraction process for extracting uranium and technetium (Tc) from the SNF leaving the plutonium and FP behind in the solution. In UREX method because plutonium is not extracted, it is treated as proliferation resistant. In the process, 99% U and 95% Tc are recovered and rejecting of 99% of trans-uranic isotopes.

In COEX, nuclear fuel is extracted in three streams (i) uranium–plutonium, (ii) uranium, and (iii) fission products and minor actinides, but never plutonium alone for avoiding the proliferation risk. From the first stream, extracted U-Pu is converted into MOX (mixed oxide) fuel for the light water reactors (LWR). The uranium extracted in second stream is sent for several subsidiary processes such as purification, conversion, enrichment, and building as a fuel for a reactor. The fission products and minor actinides are sent for vitrification into the glass logs. Vitrification is a process of capsuling small amount of radioactive material in small glass bids for reposition.

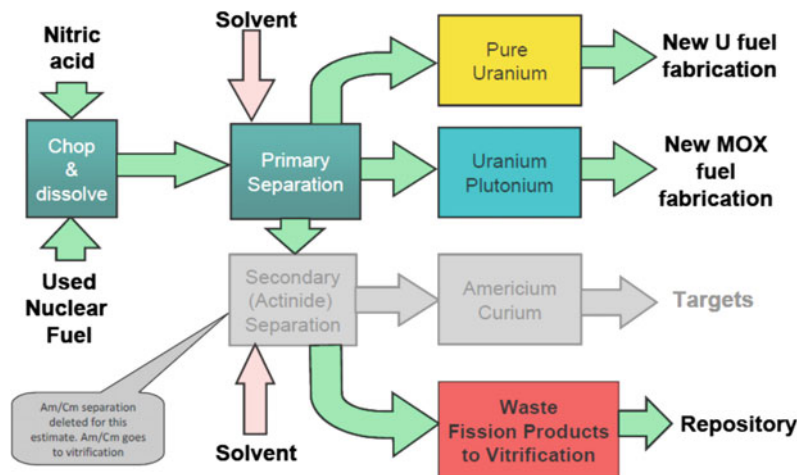
NUEX is a fourth-generation aqueous-based reprocessing system. The process works as first shearing and then dissolution of SNF in nitric acid. Uranium, plutonium, and neptunium are then extracted into a solvent tr-butyl phosphate made by dissolving in odorless kerosene. In primary separation, uranium stream and mixed uranium–plutonium and then neptunium streams are produced. Later, bulk uranium is separated from technetium. Mixed stream is purified from ruthenium. The technique is well established and promoted in France. The conceptual layout of NUEX can be shown as follows Fig. 1.1.

Commissioning of a reprocessing plant is a task involving high risk because of a large number of issues. Some of them can be briefly mentioned as follows,

- (i) high cost
- (ii) long design, construction commissioning period
- (iii) international reprocessing services become even more difficult by way of rules related to safe transport of nuclear fuel, return of all products and the waste with proper packing and certification holding the radiological safety protocols.

Russia, France, and UK have offered reprocessing services internationally and the contracts are offered with full international safe guards. In last two decades, interest has been shown in

Fig. 1.1 Conceptual design of NUEX processing [7]



more innovative technologies of spent fuel treatment having chance to emerge as 'alternative method' to the conventional PUREX processes. These technologies may deserve attention for developing advanced systems by dry technologies, among others,

- integral fast reactor concept for metallic fuel recycle
- vibropac method for oxide fuel recycle
- DUPIC concept for recycle of spent fuel of LWR and HWR.

Metallic fuel of a fast reactor is processed by electrolytic processes. LiCl-KCl with added CdCl₂ is used as the electrolyte which is filled in the steel basket and uranium from the cut pieces of fuel pins is transported to the cathode at a rate of 3 g per ampere-hour in the electrolysis process. The CdCl₂ helps in converting some of the fuel elements into their chlorides. Trans-uranic metals are separated using a setup of different electrodes. 'Pyro-processing,' uses electrical current to sift out the useful elements and does not separate pure plutonium. Uranium is transported to the solid cathode containing small amount of electrolyte salts. In fact, at the cadmium cathode which is suspended in the electrolyte salt, mixture of Pu, Am, Np, Cm, U, and the rare earth FPs are collected [6, 8]. Other FPs are left behind for another processing.

France produces more than 75% of its electricity requirement from nuclear energy, and it also reprocesses the spent fuel for itself as well as for foreign countries in its three reprocessing plants UP1, UP2 (based on PUREX route), and UP3. According to reports [9–12], it has processed 18,000 tHM (tHM = ton of heavy metal) of graphite gas-cooled reactor (GCR) and 22,700 tHM of LWR for itself and other countries. Their capacity of reprocessing is ~1,700 t/year including processing of heavy metals. As a matter of safety, at one of the reprocessing plant at La Hague average occupational exposure has been reported to be 0.073 mSv/year/employee, below the natural background despite of the fact that La Hague plant fabricates the MOX fuel assemblies. This is far less

than many other plants working in Europe. Also, at La Hague the surrounding population has added a dose of 0.01 mSv/yr/person only over a long period of 20 years. As the overall averages are very small, it may be assumed that chance of accumulation of high dose on a group of employees is far away to reach to the critical limit.

Presently, 16 power reactors are operating in India with total power capacity 3.9 GW. Out of them, 2 are BWRs and remaining 14 are PHWR. India has an integral three-stage energy program [13] of reprocessing and recycling of the fuel components for an appropriate reactor. In its second stage, fast breeder reactors (FBRs) are to be backed by the reprocessing plants and plutonium-based fuel fabrication plants. India had its first PUREX reprocessing plant at Trombay for its research reactor and later in 1975, another plant was raised at Tarapur for reprocessing spent fuel of its PHWRs. Its third reprocessing plant was commissioned at Kalpakkam in the year 1998 for meeting the requirements of its nuclear energy program after including the fast breeder reactors. The extracted fissile fuel will be utilized to meet its energy need from second phase onward. For utilization of thorium, Advanced Heavy Water Reactors (AHWR) will employ both (Th–Pu)O₂ and (Th-²³³U)O₂ fuels as one cluster in third stage of its nuclear energy program. This will introduce a challenging task of reprocessing of three components U, Pu, and Th. Most of the experience in THOREX domain has come from the recovery of low amounts of ²³³U bred in irradiated ThO₂ in CIRUS research reactor. An engineering scale facility is in operation at Trombay for the processing and recovery of ²³³U from CIRUS and Dhruva irradiated thorium fuel rods. Studies are being carried out to extract from the ThO₂ fuel bundles of PHWRs.

For some specific details, one can refer to [14, 15] for reprocessing in India.

Tokai processing plant was commissioned in 1981. This can process even MOX spent fuel. Japan through its PUREX reprocessing method has a capacity of processing 800 t U/year and has developed a SNF storage capacity of 3,000 t.

Table 1.4 Status of SNF, reprocessing capacity, direct disposal, and leftover spent fuel in the nuclear energy countries

Country	SNF in year 2005 including MOX (projected with year)	Reprocessing capacity and projected for year 2020 or in future	SNF in year 2007 (tHM)	Pu-in stock
USA	194 tHM (civil). More than 70,000 t is in storage [16]	Reprocessed so far 194 t [11]. 2000 t/yr subject to future permissions	61,000	250–500 t
France	40,700 tHM	~ 1700 t/yr [11]; 18,000 GCR + 18,000 tHM of LWR is reprocessed [11]	13,500	
Canada		Direct disposal	38,400	
Finland		Direct disposal	1,600	
Germany		Direct disposal now	5,850	
Sweden		Direct disposal	5,400	
UK		2400 t/yr, 3 facilities [11]	5,850	
Belgium	105 tHM	No Data		
Russia	67,000 tHM (Ref. Fig. 1 [12])	400 t/year [11]; (2500 t/year, in year 2020 [11])	13,000	
South Korea		Storage or disposal	10,900	
Japan	1018 tHM of max. 3000 tHM capacity	890 t/yr [11]	19,000	
India	No data	260 t/yr (being upgraded to 560 t/yr) [11]	No data	Civil, 2.9 t
China	No data	(825 t/yr) [11]	60–80 tHM/yr projected [11]	
SNF as data	1,79,017 tHM	6669 t/year capacity	~1,74,500 tHM + China	
Gross SNF available in either form from different projections	2,68,000 tHM (2004) [10]. 3,40,000 tHM (2010) [10]. 4,55,000 tHM (2020) [8]	Total reprocessed 90,000 tHM [10]		

A blank column means no data is available. In the last row, projected figures are given which corresponds to commercial and military sources of SNF. In case of countries like Russia and USA, it may be assumed that big amount of SNF is sent to repositories

In Russia, rate of accumulation of SNF from its own VVER-1000 and RBMK-1000 reactors and from the imported fuel was 600 tHM/year in the year 2006, and it will rise to 1,000 tHM/year in the year 2020. Although Russia has big dry storage capacity, yet believes in reprocessing. Reprocessing capacity of one of its RT-1 plant which works on ‘modified PUREX’ route is 400 t/year. So far, it has reprocessed ~4,000 t uranium at its Mayak plant. Looking at the accumulation of thermal SNF and plutonium load requirement of new fast reactors, Russia is constructing a new reprocessing plant of capacity ~1,000 t/year [10].

For detailed discussion of chemistry related to PUREX method, readers are advised to refer to [11].

1.1.4 Status of the Unspent Fuel

Unspent fuel can be defined as the fuel component of reprocessed spent fuel. Naturally, this depends on the reprocessing capacity. In estimation of amount of UNF, new fuel accumulated from the mining is not included for the time being. In Table 1.4, an account of the spent nuclear fuel, processing capacity, and amount of

the unspent nuclear fuel is given from the resources, some of them are already explained in the previous section.

Reprocessing has been an alternative for managing the spent fuel of a reactor or reactors and other nuclear installations. According to an IAEA report [11], by utilizing the PUREX route about one-third of the SNF has been reprocessed and remaining is stored as inventory either in conventional pools or in the more recently developed dry storage systems. After the year 2005, the gap between amount of spent fuel and reprocessed fuel has increased. In the year 2015, the amount of unspent nuclear fuel was $\sim 25\%$ only, i.e., out of 400,000 metric ton of spent fuel only $\sim 100,000$ tons is processed. In Fig. 1.1 of Ref. [11], detailed statistics of the two data of spent and reprocessed fuels from the year 1990 to future projection up to the year 2020 is given. This shows a regular enhancement of gap between amount of SNF and the reprocessed one. In the year 2005, alone in commercial reactors of USA, nearly 2,000 t/year spent fuel is processed and about 50,000 t out of total 70,000 t was in surface storage. As a matter of policy, since 1977 they prohibited reprocessing and preferred to bury it. This is still continued despite of the fact that France, UK and Japan decided to reprocess and to use the unspent mixed oxide fuel for the reactors. It is also true that none of the reactors have so far used the so obtained mixed oxide fuel. It is a hard fact that the unspent nuclear fuel from reprocessing is much costly and chances of proliferations are also not nil. This may also be worth to note that public opinion is that 'why a valuable chunk of wealth is dumped?' and as soon as reprocessing in USA is accepted then the nuclear industry will have large number of employment and energy crises will no more be there. Almost similar situation is in Russia where reprocessing is not promoted probably because there is no crises of fresh nuclear fuel. According to second view of union concerned scientists (UCS) that reprocessing will further enhance already stored piles of plutonium in USA from 250 to 500 t. One reprocessing facility under construction in USA has the objective of converting the surplus plutonium of military stockpiles into mixed oxide fuel for utilization

to produce electricity is a welcome step. According to one report of IPFM prepared in the year 2013 [17], total 495 ± 10 tons separated plutonium is in existence globally up to the year 2012.

We know that from a LWR, nearly 2% fissile fuel is retrieved. Nearly half of it is the plutonium. Assuming total spent fuel which is left unprocessed as 175,000 t, there should be 3,500 t of fissile in the year 2007. Of this, there should be 1,705 t of plutonium.

It may also be pointed out that according to IAEA report [11], several of the reprocessing facilities having capacity >1 t/yr have been decommissioned up to the year 2000 in the countries like France (1993) and India (1977) and work on several others was continued. In India, the Trombay facility is made re-operational in the year 1983.

1.1.5 Economy of Reprocessing

In USA, one of the important issues regarding cost comparison of direct dump and reprocessing is dependent on the kind of reactor producing the SNF. Also, there is a concern whether the reprocessing is done first time for second reactor and then to put the disposal of second reactor in a repository. Thermal reactor uses enriched uranium and fast reactors use plutonium enrichment as source of energy. As a result, fast reactors produce more Pu from ^{238}U . Obviously, reprocessing becomes different. The issue becomes more complex from the point of reposition of minor actinides and the FP. According to Congressional Budget Office (USA) [18] cost estimate would incorporate the following,

- (i) Cost of handling spent fuel after its discharge from a reactor: Service cost of recovering uranium and plutonium from SNF and to fabricate this into usable fuel assemblies, transport, long-term disposal of the waste are not small and need serious considerations. This needs to be compared with the cost of equivalent new fuel to be purchased for the reactor in absence of reprocessed one.

(ii) In case of direct disposal, cost of interim storage, cooling for 3–5 years, transportation, and cost of long-term reposition is normally counted. In case that the SNF is to be retrieved back and processed after few years, then extra cost of transport and hiked rates will add to the cost of disposal.

Dump of a wealth without its use at least one time will always remain a big question.

According to an estimate by Boston Consulting Group, cost of reprocessing is 585 USD per kg and cost of direct disposal is 555 USD per kg. The Kennedy studies [19] include the issues related to cost of trees equivalent to the volume of the disposal and submit the cost of reprocessing to be 700 USD more than the direct disposal. None of the two included the cost difference for the situation if dumped SNF is to be reprocessed after several years of the dump. After several other considerations explained in Ref. [18], BCO on taking cost data developed by DOE calculated that the repository cost is 1036 USD per kg and it is much higher than the cost estimates submitted by BCG and Kennedy School of Government.

It may be pointed out that in these estimates, PUREX has been under consideration; however, pyro-processing is more costly than PUREX and details can be referred in Ref. [6].

1.2 Methods of Reduction of the Radioactive Material

1.2.1 Disposals, Reposition and Transmutation

Reposition means a long-term disposal. Discussion about ways of reposition is of general interest, although a brief discussion related to economy of direct disposal has already been made in previous section. Very-long half-life and highly radiotoxic elements in the spent fuel are listed in Table 1.2 and among the fission products ^{99}Tc and ^{129}I are dominant in radio-toxicity and they exist even after thousands of years. Actinides ^{237}Np and ^{239}Pu need special attention

to isolate them from interacting with the biosphere and proliferation. The issue has received high attention at both levels, i.e., academic and government administrations of several countries. Several ways of discrimination of LLNW have been proposed and those in use are presented in the following,

- (i) **Ocean disposal:** It is continued from the year 1954 to 1993 by several countries like USSR, UK, Switzerland, USA, Belgium, France, Netherlands, Japan, Sweden, Russia, Germany, Italy, and South Korea. Presently, it is banned internationally. Regarding ocean disposal, a serious concern is reported about intensions of sinking of ships that carried radioactive waste [20].
- (ii) **Direct injection:** It is continued by Russia and the USA and after the Blue Ribbon Commission, USA [21], only deep geological repositories are likely to be permitted. The basic requirement is to locate a geological stable formation and to excavate tunnels or a borehole mechanically 500–1,000 m below the bed where a vault or a strong room can be developed to isolate from human environment. Cases of illegal reposition are also recorded during 1980–1990 in African countries.
- (iii) **Transmutation:** Large amount of plutonium produced from the uranium-fed reactors and the military projects is a matter of serious concern. In order to reduce its amount heavily, it can be used as a part of a reactor fuel in specially designed reactors or it can be incinerated or degraded to short half-life. As the cost of uranium is much smaller than any other alternative say Pu, makes Pu difficult to be used as a fuel. Another important concern is heavy accumulation of SNF, and inadequate number of available reprocessing plants makes the rate of reprocessing smaller than the requirement. It may be economical if SNF can be utilized in a reactor for energy production and to reduce the average half-life of SNF. The

technology that can produce energy from the SNF, incinerate plutonium, or utilize it as a fuel needs to be developed, and it has been shown in several calculations as well as innovations that reutilization of SNF can be possible by the new technology of energy amplifiers in next few decades [22–27]. Energy amplifiers or accelerator-driven subcritical systems will be discussed in detail in later chapters.

- (iv) **Space disposal:** Disposing off SNF into space may save planet earth although it is a costly affair. Lagrangian points have been discussed as safer place of disposal. In this process, many flights will be required for the disposal of entire SNF. In the space disposal, most serious problem may arise on failure of even a single flight and then secondary follow-up problems will further complicate it due to non-availability of single international regulation in the event of spill of the waste in several countries.

1.2.2 Other Applications

Radionuclides, both actinides and FP, have found several applications in medical science, radiology, industry, and education. Some of the application areas have reached to a status of a professional subject. Being within the scope of the book, some of the applications are summarized as follows.

1.2.2.1 Nuclear Medicines and Diagnostic Applications

It is a branch of medical imaging where a small amount of radionuclides are used to diagnose and or to treat several diseases. Many of the radioisotopes received from reprocessing of a SNF and some produced by the accelerator beams directly are used in several medical treatments, curing, relief in pain and diagnosing a disease like cancer or to get status in curing a

disease. All such applications are identified under the title of nuclear medicines. Nearly 80% of such isotopes are extracted from the SNF during separation of FP, and 19% are produced using beams from cyclotrons and linear accelerators. Remaining 1% is produced by activation reactions. ^{99m}Tc is highly used in diagnosis and obtained from fission product, ^{99}Mo [28]. One is advised to refer [29, 30] for more details of extraction of ^{99m}Tc . In Table 1.5, some of the details of a few nuclear medicines are given along with their source of production.

1.2.2.2 Industrial Applications

Neutron-, gamma-, X-ray-, beta-, and alpha-emitting radioisotopes are frequently used in industries for sterilization, germination, monitoring defects, voids and moisture content, explorations of ores and minerals and calibration, etc. Portable neutron sources such as Am + Be, Po + Be, and Pu + Be are produced where the α + Be nuclear reactions become the cause of neutron generation and the thermalized neutron sources are generated on scattering with hydrogenous compounds. Such sources are used in investigations related to geological survey of minerals, oil and petroleum for petrochemical industry. Radioactive materials are being used also in security searches of precious metals and toxic nitrogenous materials on ports and other places of high security. Also, processes of transmission of gamma rays are used to determine the elemental content of ash of coal by measuring absorption coefficient, μ on line of coal carried on a conveyor belt. It may be mentioned that the ash has higher concentration of elements of higher atomic number than the natural coal. Mineral concentration is also determined by gamma scattering. Similarly, for measurement of plastic film thickness, beta-emitting isotopes are used.

In modern scientific industrial researches, polymerization has made a very important place. Polymer industry has even replaced successfully metal applications in a large number of products like guns. Hard and lightweight polymer sheets are developed from catalytic action of radiation,

Table 1.5 Some of the commonly used nuclear medicine isotopes, their special usage, and production resource [31]

S. No.	Isotope	Usage	Resource	S. No.	Isotope	Usage	Resource
1	^{11}C , ^{13}N , ^{15}O , ^{18}F	P.E.T; localizing epileptic focus, dementia, psychiatry, and neuropharmacology	Accelerator	11	^{131}I	Treating thyroid cancer, diagnosis of abnormal liver function, renal blood flow	Reactor
2	^{18}F (FDG)	Detection, monitoring progress of cancers during treatment	Accelerator	12	^{201}Tl	Diagnosis of heart muscle death and low-grade lymphomas	Cyclotron
3	^{57}Co	Marker to estimate organ size and in vitro diagnostic kits	Cyclotron	13	^{165}Dy	Synovectomy treatment of arthritis	Reactor
4	^{64}Cu	Wilson's and Menke's diseases, PET imaging, and therapy of tumors	Cyclotron	14	^{169}Er	Relieving arthritis pain in synovial joints	Reactor
5	^{67}Cu	Therapy	Cyclotron	15	^{166}Ho	Treatment of liver tumors	–
6	^{67}Ga	Tumor imaging, localization of inflammatory lesions (infections).	Cyclotron	16	^{192}Ir	Wire form for use as internal radio-therapy source for cancer treatment	Reactor
7	^{68}Ga	PET and PET-CT imaging	Produced from ^{68}Ge	17	^{137}Cs	Sterilization of blood	Reactor
8	^{111}In	Brain studies, colon transit	Cyclotron	18	^{51}Cr	To label red blood cells and quantify gastrointestinal protein	Reactor
9	^{123}I	Diagnosis of thyroid function	Cyclotron	19	^{188}Re	β -irradiation of coronary arteries from an angioplasty balloon	Reactor
10	^{125}I	Cancer brachytherapy (prostate and brain)	Reactor	20	$^{99\text{m}}\text{Tc}$	Used for imaging of the skeleton and heart muscles in particular	^{99}Mo from Reactor

e.g., gamma and neutron. Thus, modifying materials to obtain required resistivity or conductivity, tensile, porosity, hardness, and even to magnetic behavior radioisotopes are in use.

Long life of a power supply or a battery has importance for a satellite and several other technologies. Tritium and nickel-63 can be used for beta-voltaic cells which will have low power but long life. Russia is implementing a project for the development of ^{63}Ni power sources [32, 33]. ^{238}Pu has high decay heat ~ 0.56 W/gm, and it is being used as the radioisotope thermoelectric generators (RTGs) for the last several decades in USA. The heat is produced by stopping of intense alpha and the gamma rays in small thickness layer [32].

1.2.2.3 Laboratory Sources for Education

For laboratory education and other research problems related to nuclear science and technology, several radioactive sources retrieved from the nuclear waste of a reactor are used world over. From reactors following gamma, beta, and alpha sources are synthesized [33, 34]. In gamma, beta, and alpha spectrometry which are part of the nuclear industry following sources are used. They have small activity $\sim \mu\text{Ci}$.

- (i) Gamma radionuclides: ^{60}Co , ^{133}Ba , $^{152,154,155}\text{Eu}$, ^{137}Cs , ^{134}Cs , ^{106}Ru
- (ii) Beta emitters: ^3H , ^{14}C , ^{63}Ni , ^{55}Fe , ^{36}Cl , ^{41}Ca , ^{90}Sr , ^{99}Tc , ^{129}I , ^{135}Cs , ^{94}Nb

- (iii) Alpha emitters (trans-uranic): $^{238-241}\text{Pu}$, ^{241}Am , $^{234,244}\text{Cm}$, ^{237}Np

1.3 Issues Related to Nuclear Waste

1.3.1 Proliferation and Security

The objective of IAEA is to ‘accelerate and enlarge the contribution of atomic energy to peace, health and prosperity throughout the world’ and for this purpose, it may regularly check inventories, take samples and analyze materials related to civil nuclear facilities. IAEA provides safeguard regulations to deter diversion of nuclear material by early detection. The process is complemented by controlling the export of sensitive technologies from the countries like UK and USA by way of voluntary organizations such as ‘Nuclear Supplier Group (NSG).’ The NSG has 46 countries with it presently. The main focus concern of IAEA is not to allow enrichment of uranium beyond the necessity of commercial civil plants. Similarly, it controls production of plutonium by means of either the nuclear weapons or the civil nuclear energy programs. China, France, UK, Russia, and USA are the five countries declared having nuclear weapons. For the issue of proliferation and security following is frequently notified by the IAEA,

Since the foundation of the United Nations in 1957, the International Atomic Energy Agency (IAEA) has promoted two, sometimes contradictory, missions; on the one hand, the agency seeks to promote and spread the use of civilian nuclear energy internationally; on the other hand, it seeks to prevent, or at least detect, the diversion of civilian nuclear energy to nuclear weapons, nuclear explosive devices or purposes unknown. The IAEA as operates a safeguard system as specified under Article III of the Nuclear Non-Proliferation Treaty (NPT) of 1968, which aims to ensure that civil stocks of uranium, plutonium, as well as facilities and technologies associated with these nuclear materials, are used only for peaceful purposes and do not contribute in any way for proliferation or nuclear weapon programs. It is often argued [35] that proliferation of

nuclear weapons to many other states has been prevented by the extension of assurances and mutual defense treaties to these states by nuclear powers, but other factors, such as national prestige, or specific historical experiences, also play a part in hastening or stopping nuclear proliferation. Total 189 countries have already signed Non Proliferation Treaty (NPT) including the five nuclear weapon countries [35].

Besides, the four nations India, Pakistan, North Korea, and Israel have either acquired or presumed to have acquired nuclear weapons and as on today they have not signed the NPT. North Korea had signed NPT but withdrew in 2003 [35].

About the NPT, some of the nations who have acquired nuclear capabilities have put forward [35] the following views,

1. Gandhi Plan of 1988 regards NPT as inherently discriminatory in favor of the nuclear weapon states. It speaks about a timetable for complete nuclear weapons disarmament. It endorsed early proposals of a Comprehensive Test Ban Treaty and for an international convention to ban the production of highly enriched uranium and plutonium for the purpose of weapons. This is also known as the ‘cut-off’ convention.
2. For some years, especially under the Clinton administration of USA pursued a variety of initiatives to persuade India and Pakistan to abandon their nuclear weapon programs and to accept comprehensive international safeguards for all their nuclear activities. In this regard, the Clinton administration had proposed a conference of the five nuclear weapon states and Japan, Germany, India, and Pakistan. India refused this including similar previous proposals. Also, India countered it with a demand that other potential weapon states such as Iran and North Korea should be invited to the conference and that regional limitations would only be acceptable if they were accepted equally by China.
3. Another approach of ‘capping’ the production of fissile material for weapon purposes. This

will hopefully be followed by ‘roll back.’ India and the USA jointly sponsored a UN General Assembly resolution of 1993 which calls for the negotiations for a ‘cut-off’ convention. In case India and Pakistan join such a convention, then they would have to agree to halt the production of fissile materials for weapons and to accept international verification on their relevant nuclear facilities (enrichment and reprocessing plants). India became prepared to join negotiations regarding such a cut-off treaty under the UN Conference on Disarmament.

4. Looking at the limited scope of confidence building between India and Pakistan in the year 1990, each side ratified a treaty of not attacking another’s nuclear installations and in 1991, they exchanged the list of locations of nuclear plants although the lists were not regarded fully accurate.
5. Looking at the security reasons, India dropped its support to CTBT in the year 1995 and in the year 1996, India attempted to block the Treaty itself. After its nuclear test in 1998, India proposed that its ratification may be conditional as the five weapon states have to agree for reduction in their nuclear arsenals. The UN Conference on Disarmament has also called upon both India and Pakistan immediately to accede to the Non-Proliferation Treaty, presumably as non-weapon states.
6. Iran who is a signatory of NPT in regards with civilian use of nuclear energy was not allowed to perform uranium enrichment in secret manner which is a violation of the safeguard obligations of United Nations Security Council.

India has also been discussed in the context of nuclear apartheid. India’s stand is that nuclear issues were directly related to national security and nuclear weapons should be a necessary right for all nations so long as certain states are in possession of nuclear weapons.

As an honest approach following views needs to be considered for all future deliberations,

- (i) No nation has right to threaten other in order to keep up sovereignty.
- (ii) All nations have right to safeguard security of its people and boundaries with safety of earth being more important.
- (iii) Civilian use of nuclear capability is permissible and there can be all checks and tests of enrichment programs of all nations equally.
- (iv) SNF is a wealth pertaining to the earth and all efforts need to be made to reprocess for the energy programs only.
- (v) ‘Saving the earth from nuclear fear’ program need to be initiated with de-activation of nuclear weapons.

Security issues

An independent group of experts on arms-control and non-proliferation was founded in January 2006 in the name of International Panel on Fissile Materials (IPFM) [36]. This comprises experts from 18 countries including both nuclear weapon and non-nuclear weapon states. Following panel members of the IPFM attended the meeting in the year 2013:

Harold Feiveson, Alexander Glaser, Zia Mian, Frank von Hippel (Princeton University, US), Pavel Podvig, Anatoli Diakov (Russia), M. V. Ramana, R. Rajaraman (India), Jean du Preez (South Africa), José Goldemberg (Brazil), Pervez Hoodbhoy, A. H. Nayyar (Pakistan), Rebecca Johnson, Patricia Lewis, Gordon McKerron (UK), Martin Kalinowski, Annette Schaper (Germany), Jungmin Kang (South Korea), Li Bin (China), Miguel Marín Bosch (Mexico), Arend J. Meerburg (Netherlands), Paul Meyer (Canada), Seyed Hossein Mousavian (Iran), Ole Reistad (Norway), Henrik Salander, Johan Swahn (Sweden), Mycle Schneider (France), Masafumi Takubo, Fumihiko Yoshida (Japan) and produced the following findings,

1. In 2013, the global stockpile of nuclear weapons was estimated to be over 17,000 weapons. The USA and Russia together holding over 16,000 of these weapons, and

the other seven nuclear weapon states holding a combined total of about 1,000 weapons.

2. The global stockpile of highly enriched uranium (HEU) at the end of year 2012 is estimated to be about $1,380 \pm 125$ tons. This is sufficient for more than 55,000 simple, first-generation implosion fission weapons.
3. The global HEU stockpile has been reducing. Over the past two decades, about 630 tons of HEU has been blended down, mostly by Russia. The USA, which has eliminated about 141 tons of mostly non-weapon-grade HEU, has chosen to set aside 152 tons of excess weapons HEU for a naval fuel reserve. The USA, UK, Russia, France, and China have all stopped producing HEU for weapons as well as any other purpose, in some cases decades ago. The first four of these states have made official declarations to this effect, China has done so informally. In 2012, Russia announced that it was resuming limited production of HEU for naval and fast reactor fuel. India is also producing HEU for naval fuel. Pakistan is producing HEU for weapons. It is possible that North Korea also may be producing HEU for weapons.
4. The global civilian stockpile now exceeds the military stockpile. There are civilian plutonium separation (reprocessing) programs in the UK, Russia, Japan, India, France, and China. In July 2012, the UK announced plans to close its THORP reprocessing plant, at Sellafield by 2018. This would end reprocessing in the UK. The future of Japan's reprocessing program is unclear in the wake of the March 2011 disaster at the Fukushima nuclear plant.
5. Under the terms of the 2010 of the 'Action Plan on Nuclear Disarmament,' the NPT nuclear weapon states have agreed to cooperate on steps to increase transparency and develop verification capabilities related to nuclear disarmament and in particular to report information that can further the openness and verification. According to the action plan, the nuclear weapon states were expected to report to the NPT Preparatory Committee in 2014 on progress toward meeting these obligations.

The IPFM recommended that the nuclear weapon states could make baseline declarations of the total number of nuclear warheads in their possession as of a specific recent date with a commitment to subsequent annual updates well in advance to the next NPT Review Conference. Also, as part of their baseline declarations by the end of 2015, NPT nuclear weapon states could make the following as public.

- Total national holdings of plutonium and of HEU as of a specific recent date.
- Amounts of HEU and plutonium in other countries and any foreign-owned material in a country.
- The portions of their HEU and plutonium stockpiles available for IAEA safeguards.

Earlier in the 2010 final document of NPT Review Conference emphasizes for the nuclear weapon states 'to declare, as appropriate, to the International Atomic Energy Agency (IAEA) all fissile material designated by each of them as not required for military purposes and to place such material as soon as practicable under IAEA or other relevant international verification and arrangements for the disposition of such material for peaceful purposes.'

Finally, the NPT weapon states need to declare and place under IAEA safeguards the following,

- All plutonium and HEU in civilian use
- All plutonium and HEU recovered from excess weapons or its nuclear weapons' complex and declared excess for weapon purposes and
- All plutonium and HEU going to waste disposal sites.

1.3.2 Reutilization

Is there a possibility to utilize SNF as such in a conventional reactor or any other system and the radio-toxicity of the long life isotopes is reduced to

very short life and the process stands economical? Certainly, the question indicates toward the high amount of the leftover fuel elements to be burnt and LLA and LLFP to be incinerated drastically. Obviously, the problem focuses on the issue of LLFP to be incinerated as well as to reduce or incinerate amount of the reproduced LLFP from the burning of fuel component of SNF. In principle, this will certainly need a system to have very high excess of neutrons beyond the energy economy of the system. In this regard, Jansen [25] reaches to a conclusion that in doing both, energy output can be maintained corresponding up to certain value of neutron multiplication factor, k and excess neutrons for transmutation can be possible in near to $k \sim 1$ system only.

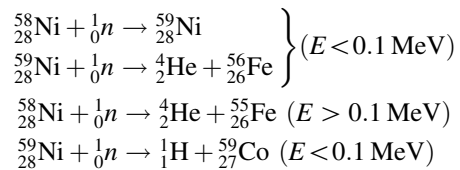
It is known that the LWR produces nearly 95% of the uranium fuel, 1% actinides, and remaining 4% FP. According to Lerner [37], alternatively, using the pyro-processing route of reprocessing all the trans-uranic elements of the spent fuel can be separated from FP for reutilization in a fast reactor without loading of FP of the SNF in the fast reactor. To expedite reutilization, a pyro-processing plant can be installed in between a LWR and the fast reactor. This can be promoted because pyro-processing-based technology [38] has following advantages,

- (i) Several times more utilization of nuclear fuel than just 5%.
- (ii) Uranium supply to continue to the second down the line reactor.
- (iii) Minimization of risk of proliferation because of the integrity of uranium and higher actinide fuel elements.
- (iv) This saves time and cost of transport and reposition. Also, risk period is reduced from thousands of years to hundreds of years.

Another approach being worked out for the last 15–16 years is IV generation reactors [39] with a feature that fuel will be recycled without separation of ^{239}Pu . Similarly, there are proposals of molten salt reactors (MSR) for utilization of thorium.

1.3.3 Radiation Damage and Gas Production

Reposition or even storage of SNF not only spreads radioactivity but produces gases as the decay products along with that are produced by activation or other nuclear reactions. For example fission products may emerge as the gases directly. Neutrons may also activate certain constituent like Ni and Al to produce alpha particles, which on emergence may accept electrons from the surrounding to act as helium gas. Thus, Ni of the steel canisters is reduced to iron and corrosion is promoted. Through the following corrosion reactions on one hand, depletion of nickel of steel takes place and this reduces the strength of the steel and on the other hand, iron gets oxidized. This leads to corrosion and production of hydrogen and helium gases.



Production of helium leads to grain boundary embrittlement and enhancement of swelling rate due to bubble formation. Thus, the high nickel steels become brittle for low doses too. In fact, trapping of rare gas atoms on the vacancy defects retards the annealing [40] and radiation defects become stable. This may induce brittleness. Issue of radiation damage and radiation resistant materials will be discussed in a dedicated Chap. 7 later in the book.

1.3.4 Protection of Society and Environment

The nuclear fuel before loading and after discharge from a reactor influences the environment. Also, small amount of radioactivity goes out of the reactor along with the rejected water and the steam that leak out of the reactor and

ultimately it is absorbed by the soil or the crop in vicinity. Right from the mining of yellow cake by in-situ leaching process and the uranium ore grinding processes which is followed by the leaching the leftover tailings either to go to the soil or in water. In the whole process of leaching, thousands of m³ of water is used and after extraction, water carries small trace of radioactivity which ultimately goes to far distant places during rains and in the dwellings. Effect of accidental release of excess radiation beyond dose limit in case of accident has shown enhanced cases of cancer patients in the surrounding of the plants.

According to IAEA safety standards [41],

Regulating safety is a national responsibility. However, radiation risks may transcend national borders, and international cooperation serves to promote and enhance safety globally by exchanging experience and by improving capabilities to control hazards, to prevent accidents, to respond to emergencies and to mitigate any harmful consequences. States have an obligation of diligence and duty of care, and are expected to fulfill their national and international undertakings and obligations.

The IAEA declared the following 4 Safety Standard Committees (SSC) for the preparation and review of safety standards,

- i. for nuclear safety (NUSSC)
- ii. radiation safety (RASSC)
- iii. the safety of radioactive waste (WASSC), and
- iv. the safe transport of radioactive material (TRANSSC).

The Commission on Safety Standards (CSS) oversees the programs of IAEA safety standards. For safety and protection from radiation, ten principles are envisaged. Under its 7th principle highlighted as 'Protection of present and future generations' means that people and the environment, present and future, must be protected against radiation risks. In the following various important safety majors that are adopted in different nations having nuclear energy have been summarized.

United States of America

Nuclear Regulatory Commission (NRC) [42] of USA has ensured safeguards and security by regulating licensees by way of

- (a) accounting systems for special nuclear and source materials, and
- (b) security programs and contingency plans.

Their responsibilities include the following,

- Domestic safeguards
- Information security
- Radioactive material security.

Office of Nuclear Material Safety and Safeguards (NMSS) develops and implements NRC policy for the regulation and safe management and disposal of spent fuel and HLW. In the USA, Uranium Mill Tailings Radiation Control Act (UMTRCA) is also invoked in the year 1978 as the US Environmental Law. This authorizes the Environmental Protection Agency authority to establish health and environmental standards for the stabilization, restoration and disposal of uranium mill waste.

India

Atomic Energy Act, 1962, controls all nuclear activities in the country. In 1983, Atomic Energy Regulatory Board (AERB) came in existence to carryout regulatory and safety activities under the act. The regulatory authority of AERB is derived from the rules and notifications promulgated under the Atomic Energy Act, 1962. Environmental (Protection) Act, 1986, is added later on.

Also, Government of India invoked 'Atomic Energy (Radiation Protection) Rules, 2004' replacing the Radiation Protection Rules 1971. For more details of safety disposal of nuclear waste (SDNW), weapons of mass destruction (WMD), radiological dispersal devices (RDD), Foreign Trade Development and Regulation Act, 1992 (FDRA) and Nuclear Controls & Planning Wing (NC&PW) are existing. For several other outfits, reader is advised to refer to Nuclear Security in India [43].

France

In France, Transparency and Security in the Nuclear Field Act No. 2006-686 was invoked in June 2006 [44] under the Nuclear Safety Authority which is an independent administrative authority. In signing the act Ministry of Ecology is involved. The authority participates in the surveillance of nuclear safety and radiation protection and for informing the public in these fields. Also, separately, in 2006 Program Act on the Sustainable Management of Radioactive Materials and Wastes was passed to focus largely on environment in connection with the waste management [45].

United Kingdom

In UK, Office for Nuclear Regulation (ONR) is in charge of regulating nuclear sites but the legal responsibility of ensuing nuclear safety lies on the licensee. Government of UK is responsible for nuclear policy through its legislative regulatory framework. ONR sets the regulatory standards. According to statement of ONR Chief Executive Officer [46], 'ONR is not responsible for delivering a safe and secure nuclear industry; this is the responsibility of the nuclear industry itself.'

Also, Environment Agency [47] is an executive non-department public body which is sponsored collectively by the departments of environment, food, rural affairs, and it works to create better places for people and wildlife and support sustainable development of nuclear sites. Similarly, there is Scottish Environment Protection Agency.

China

In China, National Nuclear Safety Administration (NNSA) is a central government agency responsible for regulating nuclear safety, supervision on all civilian nuclear infrastructures in China and has authority of inspecting nuclear safety activities and to regulate the approval mechanism. It was established in the year 1984 under the State Science and Technology Commission, and since then, it has seen several controls. In the year 1998, it was transferred to State Environmental Protection Administration

(SEPA). In the year 2008, SEPA was upgraded to the full-fledged Ministry of Environmental Protection and the NNSA has been working under the ministry. The Ministry is the nation's environmental protection department charged with the task of protecting China's air, water, and land from pollution and contamination [48]. It also serves as China's nuclear safety agency.

Russia

Nuclear Safety Institute (IBRAE) under the Russian Academy of Sciences [49] was established in the year 1988 with the aim of advancing basic research to address the problems of increasing safety of nuclear power plants. It is responsible for the (i) safety of nuclear power and industry, (ii) emergency response and radiation monitoring, (iii) strategic planning of back end of nuclear and radiation hazardous objects, (iv) to provide technological platform for industry and energy integrity, safety and security. Federal Environmental, Industrial and Nuclear Supervision Service (Russian Federation) is also started.

Japan

In Japan under its Atomic Energy, Basic Law Atomic Energy Commission was established in the year 1956. After the Fukushima Nuclear Disaster in 2012, Nuclear Regulatory Authority (NRA) was established [50] replacing 'Nuclear and Industrial Safety Agency,' to provide Nuclear Regulation for People and the Environment. The NRA is an external organization of the Ministry of the Environment with a high degree of independence. After its constitution, NRA has been enhancing nuclear regulations in the following areas,

- (i) Development of counter measures against severe accidents.
- (ii) Introduction of back-fit systems that all nuclear reactor facilities shall meet all new regulatory requirements.
- (iii) Introduction of a 40-year operational time limit for nuclear reactor facilities from the time of start of a facility.

Pakistan

Pakistan has established Pakistan's Nuclear Security Regime, and it covers nuclear materials including radioactive materials, several associated activities, and facilities for their life cycle through following three pillars (i) legislative and regulatory framework (ii) institutions and organizations and (iii) nuclear regulatory systems and measures [51]. Pakistan's Atomic Energy Commission and its Nuclear Regulatory Authority are under its Legislative and regularity framework. Strategic Plan's Division (SPD) works as secretariat of National Command Authority (NCA) and develops technical solutions, Personnel Reliability Programme (PRP), and elaborate intelligence and security setups to deal with issues related to nuclear security, non-proliferation and Weapons of Mass Destruction (WMD) terrorism.

References

1. Nifenecker, H., Meplan, O., David, S.: Accelerator Driven Subcritical Reactors. IOP Publishing Ltd. (2003)
2. Yasin, Z., Iqbal, J., Shahzad, M.I.: Comparison of radionuclide's inventories and activities with slightly enriched uranium and plutonium fuel in CANDU reactors. *J. Nucl. Sci. Technol.* **1**, 31–36 (2011)
3. Raghupati, S., et al.: http://www.efn-uk.org/nuclear/nuc-lib/reactor-reports/index_files/India-PFBR-design.pdf and Puthiyavinayagam, P.: 48th Annual Meeting of TWGFR, IAEA IPPE, Obninsk, Russian Federation. https://www.iaea.org/NuclearPower/Downloadable/Meetings/2015/2015-05-25-05-29NP-TDS/Country/11_TWGFR2015_India_IGCAR.pdf. Accessed 25–29 May 2015
4. Arafat, Y., et al.: Radiotoxicity characterization of HLW from reprocessing of uranium-based and thorium-based fuel-11390. WM2011 Conference, Phoenix, AZ (2011). Accessed 27 February–3 March 2011
5. Clement, C.H.: Editor, authors on behalf of ICRP, Eckerman, K., Harrison, J., Menzel, H.-G., Clement, C.H.: Compendium of dose coefficients based on ICRP publication 60. ICRP publication 119. *Ann. ICRP* **41**(Suppl) (2012)
6. Abdallah, M., Chang, H.M., Hampton, D., Mahmood, A., Mahmood, F.: Calvin Wong: Energy and Energy Policy Closing the Nuclear Fuel Cycle: Reprocessing. <http://franke.uchicago.edu/bigproblems/2012-berry-papers/team3.pdf>. Accessed 2 Apr 2018
7. Phillips, C., et al.: Improving the estimates of wastes from the recycling of used nuclear fuel. WM2013 Conference, Phoenix, Arizona, USA, 24–28 Feb 2013
8. Choi, E.-Y., Jeon, S.M.: Electrochemical processing of spent nuclear fuels: an overview of oxide reduction in pyroprocessing technology. *Prog. Nat. Sci. Mater. Int.* **25**(6), 572 (2015)
9. Spent Nuclear Fuel Reprocessing: NEA/NSC/WPFC/DOC 15. OECD (2012)
10. McCombie, C.: International Perspective: Reprocessing, Storage, and Disposal. NAE National Meeting, Irvine (2003). Accessed 6 Feb 2003
11. <http://www.world-nuclear.org/information-library/nuclear-fuel-cycle/fuel-recycling/processing-of-used-nuclear-fuel.aspx> and Status and Trends in Spent Fuel Reprocessing. IAEA-TECDOC-1467. http://www.pub.iaea.org/MTCD/publications/PDF/te_1467_web.pdf. Accessed Sept 2005
12. Spent Fuel Reprocessing Options. IAEA-TECDOC-1587 (2008). http://www-pub.iaea.org/MTCD/publications/PDF/te_1587_web.pdf. Accessed Aug 2008
13. Banerji, S.: Physics of ADS for energy and transmutation. Inaugural Talk Delivered at Workshop on ADSS for Energy and Transmutation Held at Jaipur (2006). Accessed 23–25 Jan 2006
14. Dey, P.K., Bansal, N.K.: Spent fuel reprocessing: a vital link in Indian nuclear power program. *Nucl. Eng. Des.* **236**(7–8), 723 (2006)
15. Natarajan, R., Raj, B.: Fast Reactor Fuel Reprocessing—An Indian Perspective. In: Proceedings of GLOBAL 2005, Paper No. IL012, Tsukuba, Japan (2005). Accessed 9–13 Oct 2005
16. Shughart II, William F.: Why does not US Recycle Nuclear Fuel. <http://www.forbes.com/sites/realspin/2014/10/01/why-doesnt-u-s-recycle-nuclear-fuel/#5b0e0e1c7db4>. Accessed Oct 2014
17. Global Fissile Material Report 2013: Increasing Transparency of Nuclear Warhead and Fissile Material Stocks as a Step Toward Disarmament. Seventh Annual Report of the International Panel on Fissile Materials. www.fissilematerials.org
18. Orszag, P.R.: Costs of Reprocessing Versus Directly Disposing of Spent Nuclear Fuel. CBO Report (2007). <https://www.cbo.gov/sites/default/files/cbofiles/ftpdocs/88xx/doc8808/11-14-nuclearfuel.pdf>. Accessed Nov 2007 and UCS: Nuclear Reprocessing: Dangerous, Dirty, and Expensive. <http://www.ucsusa.org/nuclear-power/nuclear-plant-security/nuclear-reprocessing/#.V3X5ZNKgE0F>
19. The Economics of Reprocessing vs. Direct Disposal of Spent Nuclear Fuel (Cambridge, Mass: Belfer Center for Science and International Affairs, John F. Kennedy School of Government, Harvard University, December 2003)
20. Mafia sank boat with radioactive waste: Official, AFP. Accessed 14 Sept 2009 and From cocaine to plutonium: Mafia clan accused of trafficking nuclear waste. The Guardian. Accessed 9 Oct 2007

21. Blue Ribbon Commission on America's Nuclear Future: Executive Summary. Accessed Jan 2012
22. Rubbia, C., et al.: Conceptual design of a fast neutron operated high power energy amplifier, CERN/AT/95-44 (ET) (1995). See also Rubbia, C.: A high gain energy amplifier operated with fast neutrons. AIP Conference Proceedings 346, International Conference on Accelerator-Driven Transmutation Technologies and Applications, Las Vegas (NV), US (1994)
23. Carminati, F. et al.: An Energy Amplifier for Cleaner and Inexhaustible Nuclear Energy Production Driven by a Particle Beam Accelerator. CERN/AT/93-47 (ET) (1993)
24. Bowman, C.D. et al.: Nuclear energy generation and waste transmutation using an accelerator-driven intense thermal neutron source. Nucl. Instr. Methods Phys. Res A320, 336 (1992)
25. Janssen, A.J.: Transmutation of Fission Products in Reactors and Accelerator-Driven Systems. ECN-R-94-001 (1994)
26. Salvatores, M., et al.: MUSE-1: A first experiment at MASURCA to validate the physics of sub-critical multiplying systems relevant to ADS. In: Proceeding of the Second International Conference on Accelerator Driven Transmutation Technologies and Applications, Kalmar, Sweden, ADTTA (1996). Accessed 3-7 June 1996
27. Kumar, V., et al.: Role of (n, xn) Reactions in ADS, IAEA-Benchmark and the Dubna CASCADE Code. Pramana-J. Phys. **68**(2), 315-324 (2007) (Also, the volume of Pramana-Journal of Physics is dedicated to studies related to ADSS)
28. Feasibility of Producing Molybdenum-99 on a Small Scale Using Fission of Low Enriched Uranium or Neutron Activation of Natural Molybdenum. Technical Reports Series No. 478. <http://www-pub.iaea.org/MTCD/Publications/PDF/trs478web-32777845.pdf>
29. OECD/NEA: A Supply and Demand Update of the Mo-99 Market (2012)
30. IAEA 2015: Feasibility of Producing Molybdenum-99 on a Small Scale Using Fission of Low Enriched Uranium or Neutron Activation of Natural Molybdenum. Technical Reports Series #478
31. Rao, D.V., Chandra, R., Graham, M.C. (eds.): Physics of Nuclear Medicines-Recent Advances. American Institute of Physics Inc., New York (1984)
32. Radioisotopes in Industry. <http://www.world-nuclear.org/information-library/non-power-nuclear-applications/radioisotopes-research/radioisotopes-in-industry.aspx>
33. Olsen, L.C., Cabauy, P., Elkind, B.J.: Betavoltaic power sources. Phys. Today (2012), 35-38 (2012). www.physicstoday.org
34. Hou, X.: Radiochemical Analysis of ^3H , ^{14}C , ^{55}Fe , ^{63}Ni in Waste and Environmental Samples. Risø National Laboratory for Sustainable Energy, Technical University of Denmark
35. Nuclear Proliferation. https://en.wikipedia.org/wiki/Nuclear_proliferation#Non-proliferation_efforts
36. International Panel on Fissile Materials: Global fissile material report 2013 increasing transparency of nuclear warhead and fissile material stocks as a step toward disarmament. www.fissilematerials.org
37. Lerner, L.: Nuclear fuel recycling could offer plentiful energy. <http://www.anl.gov/articles/nuclear-fuel-recycling-could-offer-plentiful-energy>
38. Williamson, M.: Pyro-processing technologies. http://www.cse.anl.gov/pdfs/pyroprocessing_brochure.pdf
39. Generation IV Nuclear Reactors. <http://www.world-nuclear.org/information-library/nuclear-fuel-cycle/nuclear-power-reactors/generation-iv-nuclear-reactors.aspx>
40. Matzke, H.J.: On the stabilization of radiation damage by the rare earth gases. J. Nucl. Mat. 30, 107 (1969)
41. IAEA Safety Standards Series No. GSR Part 3 (Interim). http://www.pub.iaea.org/MTCD/publications/PDF/p1531interim_web.pdf
42. United States Nuclear Regulatory Commission. <http://www.nrc.gov/security.html>
43. Nuclear Security in India. http://www.indianhighcommission.com.my/Pdf/NUCLEAR_SECURITY_IN_INDIA.pdf
44. Nuclear Safety Authority, Act 206, France. file:///C:/Users/lenovo/Downloads/loiTSN-uk.pdf
45. Program Act on the Sustainable Management of Radio-Active Materials and Wastes, France, 2006. file:///C:/Users/lenovo/Downloads/radioactive-waste-management-act-280606.pdf
46. Office for Nuclear Regulation. ONR. <http://www.onr.org.uk/documents/a-guide-to-nuclear-regulation-in-the-uk.pdf>
47. Environment Agency. <https://www.gov.uk/government/organisations/environment-agency>
48. Ministry of Environmental Protection of the People's Republic of China. https://en.wikipedia.org/wiki/Ministry_of_Environmental_Protection_of_the_People%27s_Republic_of_China
49. The Nuclear Safety Institute (IBRAE). <http://en.ibrae.ac.ru/>
50. Nuclear Regulation Authority. Japan. https://www.nsr.go.jp/english/e_nra/nsr_leaflet_English.pdf
51. Pakistan's Nuclear Security Regimes: <http://www.mofa.gov.pk/documents/PNSR.pdf>. Accessed 7 Apr 2018

Special Hybrid Systems and Molten-Salt Reactors

Complete utilization of heat and escape out neutron flux generated new concept of hybridization of two or more nuclear energy systems which is highly perspective in case of gen. IV reactors. It has high utility in fusion reactors where stopping of high-energy neutrons is almost impossible. Concept is being worked out at the international collaborations. Hybridization of nuclear and non-nuclear systems of producing electricity and utilization of heat resources are also discussed. Such concepts need lot of innovative procedures for integration.

2.1 Concept of Hybridization of Nuclear Energy

So far, two kinds of nuclear energy systems are known; one is for atomic fission energy, and other one is for nuclear fusion energy. An atomic energy reactor, having ^{235}U fuel a single fuel, and it is ignited by a small energy system, a neutron source. This energy input is negligible compared to fission energy. These reactors are also called as neutron poor and energy-rich systems. On the other hand, fusion reactors are neutron rich but energy poor systems. Energy released in one fission reaction is more than 10 times of one fusion reaction. Extra neutrons of a fusion reactor can better be utilized in another system based on fission process by providing blanket of a fissionable fuel outside the fusion reactor dimensions.

In principle in a fission reactor, there is no hybridization as there is an input of neutron energy and there is a single fuel system. Hybridization may be said to take place when there is a combination of fuels, e.g., uranium and plutonium mix or thorium and uranium mix fuels, or there is a mechanism of generating a big neutron source such as spallation neutron source for running a fission reactor for both energy and transmutation purposes. In the latter case, a high-energy spallation neutron generates a large number of neutrons which produce fission reactions as well as transmute the specially organized HLW also.

Another possibility is to combine fusion and fission reactors for utilization of excess neutrons of fusion reactor to enhance energy production by providing a fission material blanket around the fusion reactor [1]. The blanket can have uranium or thorium as a fuel. There can be several other ways of enhancing overall efficiency of the energy system or making a cluster of utilization of any extra availability of resource economically.

2.1.1 Hybrid Nuclear Energy Systems

Fusion reactors are operated on two basic mechanisms. One related to magnetic confinement and other on laser. In case of magnetic confinement of plasma, say, deuterium and tritium plasma, the process of fusion is accelerated

by introduction of accelerated deuterium ion of energy, $E_h \sim 100$ keV. The deuterium ion energy is much above ~ 10 keV temperature of the desired plasma. To get the accelerated ions, one needs small energy accelerators to produce deuterium ion. Efficiency, v_d , of the accelerators, i.e., ratio of KE of accelerated ion, E_h , to the electric energy supplied to the accelerator is $\sim 60\text{--}70\%$.

A figure of merit of the fusion energy system can be defined as the ratio of fusion energy, E_{Fu} , to the given heat energy, E_h ,

$$Q = E_{Fu}/E_h \quad (2.1)$$

Here, E_h is required to heat the plasma. Initially, E_{Fu} is in the form of KE of produced alpha and neutron in a (d, t) plasma system, and it is required to be converted to the heat energy. In case of toroidal Tokamak, large value of Q is expected to be available.

More of the E_{Fu} energy is converted to the heat; factor Q will be higher. Thus, there is a need of a mechanism to be developed for the utilization of kinetic energy of charged particle introduced in the plasma to initiate fusion reaction. In turn, it produces heat on one hand and number of neutrons on the other hand which will be multiplied further by way of a fission reaction in a fusion–fission hybrid system.

Initially, for an elementary process, Q is expected to be $\ll 1$ so long as reaction energy in the form of kinetic energy of product nuclei is not utilized in internal collisions.

$$\begin{aligned} \text{Thus, heat of the system at a time} &= E_h + E_{Fu} \\ &= (1 + Q)E_h \end{aligned} \quad (2.2)$$

The fusion energy, E_{Fu} , ultimately has to be converted into the electric energy. If the conversion efficiency is v_e , then the electric energy output can be written as,

$$\begin{aligned} Q' &= (1 + Q)v_d \times v_e \\ &\sim \frac{1}{4}(1 + Q) \end{aligned} \quad (2.3)$$

A fusion energy system will be called efficient if $Q' \geq 1$. This is possible when $Q \geq 3$. This can be achieved by thermalizing the available kinetic energies of the nuclei produced in the fusion reaction (see Eq. 2.4). Among the existing fusion energy sources working with the magnetic confinement are called as Tokamak [2]. One Tokamak is shown to have plasma performance with $Q = 1$.

Deuterium and tritium are the main ingredients of most of the fusion reactors because of availability of the two reactants. Deuterium is a stable isotope of hydrogen found in water. Tritium is produced in a reactor. Also, it can be produced by reaction of a neutron with Li^6 . Isotope Li^6 is abundantly available in mineral ores. At the same time, (d, t) fusion reaction is favored from the point of lower temperature requirement as can be deduced from the data shown in Fig. 2.1. As a matter of mechanism, when the two nuclei deuterium and tritium are brought close enough to fuse it gives rise to production of an alpha and a high-energy neutron as shown in Eq. (2.4). Barrier penetration energy for the (d, t) reaction is ~ 280 keV [3], and similarly penetration energy is ~ 210 keV for (d, d) and ~ 580 keV for $(d, {}^3\text{He})$ fusion reactions. The (d, t) fusion reaction is as follows:

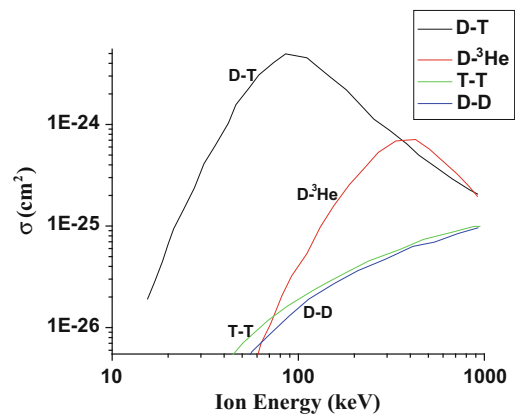
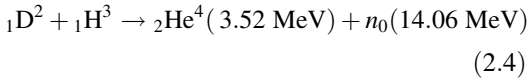
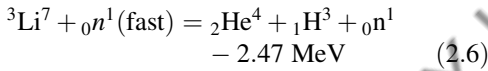
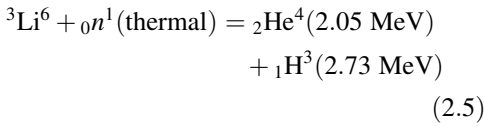


Fig. 2.1 Ion energy versus cross-sectional plot of different fusion reactions [2]



According to Eq. (2.4), available total fusion energy, $E_{\text{FU}} = 17.58 \text{ MeV}$, of which neutron energy share is $\sim 80\%$ and 20% is shared by alpha charged particle. The fusion energy E_{FU} needs to be converted into heat energy. The energy component of charged particle alpha is converted differently to the neutral neutron.

The reactions that may lead to the production of tritium are as follows:



There are several advantages of fusion reactors over the fission reactors, and they are taught in elementary classes, but, a fusion reaction is hard to be achieved in the first place because a small perturbation in reactor condition would probably terminate the reaction [4]. Thus, the basic challenges of a fusion reactor can be summarized as follows,

- (i) Heating of a reacting mixture to a very high temperature is hard because energy goes in overcoming the repulsive force of positively charged nuclei. This is equivalent to a barrier penetration process. For example, as mentioned earlier also, this can be achieved by introducing deuterium ion of kinetic energy $\sim 300 \text{ keV}$ in case of (d, t) reaction. Introduction of high amount of such ions into the fusion system also enhances density of the plasma.
- (ii) On compression of the mixture to a high-density, probability of collision, hence a reaction is enhanced.
- (iii) To keep the reacting mixture together for long enough time for the fusion reaction and to produce energy at a rate that is greater than the rate of input energy provides both heat and compression.

Obviously, attaining a ‘breakeven’ is a technological challenge for sustaining the plasma condition of high temperature and density for longer time. The condition of sustainment can be derived from the ‘Lawson criterion’ that the product of number density of medium and confinement time $n \times \tau$ needs to be greater than 10^{14} . In the year 1991, European scientists have successfully sustained (d, t) plasma bursts for 2 s producing energy equivalent of 2 MW. Experimental Fusion reactor at Princeton sets a record of 1 s of 10.7 MW bursts in the year 1994. Following such successes, USA, Japan, Russia, and the European Union started designing and construction of the International Thermonuclear Experimental Reactor (ITER) facility of 500 MW to sustain for 400 s with $Q > 10$ or sustaining for 3000 s with $Q > 5$. Later on, China, India, and South Korea have also joined the program. Besides, working on hot plasma, several research groups are also working on ‘cold fusion’ of hydrogen at room temperature [4].

Nuclei produced as a result of several kinds of fusion reactions can be thermalized in dense medium, and as a result, very high temperatures are produced. Plasma in the given medium can be confined technologically by way of magnetic confinement or inertial confinement by lasers. Inertial confinement fusion (ICF) is a process to initiate nuclear fusion reactions by heating and compression of a fuel target which is typically kept in the form of a pellet containing a mixture of deuterium and tritium. In Fig. 2.2, a comparison of achievements of fusion energy over three decades by using either of the magnetic confinement or the ICF technology is shown in relation with progress of attaining computer power in the same time span.

In case of the ICF technique, impact of laser light starts compression by shock wave propagation which heats the outer layer of (d, t) fuel. Subsequently, compression of the inner target material [5, 6] starts the desired fusion reaction.

After the fusion energy is thermalized in a fusion system and plasma exceeds the losses, the condition, $Q > 1$ is achieved. Fusion reaction will sustain if fuel is continuously supplied. The plasma is confined by keeping the ions and the

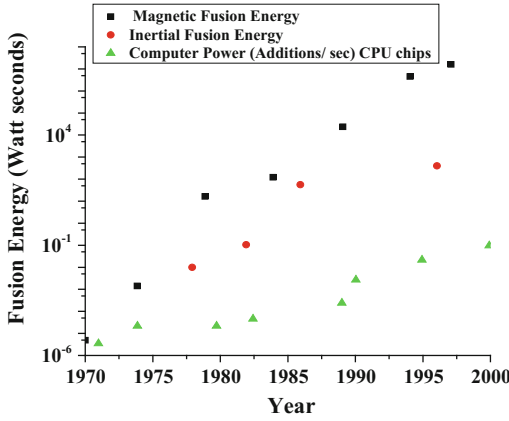


Fig. 2.2 A comparative study of development of magnetic and inertial confinement fusion [2]

neutral has high chance to escape out from the fusion system, and it can be captured in the blanket material of high density of fission fuel and that leads to conversion of its energy into fission. In case of a 14.06 MeV, neutron escaping to the fission blanket may produce a fission and releases energy ~ 190 MeV/ fission. This energy is 13.5 times of energy of the neutron. In a (d, t) plasma system, energy, E_{Fu} , is shared with a fraction, $f_n \sim 80\%$ by neutron and remaining fraction, $(1 - f_n) \sim 20\%$ by a charged particle (cp), alpha in the final state of (d, t) reaction, for example. Thus,

$$\begin{aligned} E_n &= f_n \times E_{Fu} \quad \text{and} \\ E_{cp} &= (1 - f_n) \times E_{Fu} \end{aligned} \quad (2.7)$$

electrons inside the system which is technically difficult.

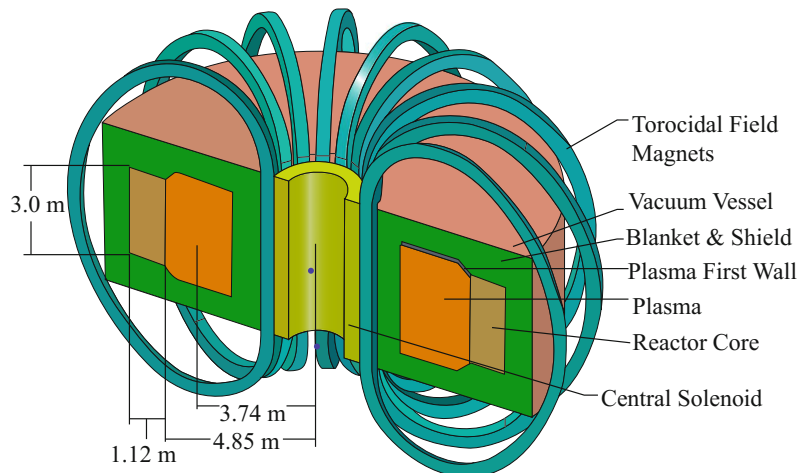
2.1.2 Fusion–Fission Hybrids

A highly common design of fusion–fission hybrid system is shown in Fig. 2.3, where a fusion plasma core is surrounded by the fission blanket of U or Th [7, 8]. In the figure, a design proposal of ITER is projected for a 500 MW fusion power and neutron fluence $\sim 1.8 \times 10^{20}$ n/ s.

As mentioned earlier, a fusion–fission hybrid system necessarily has a fission fuel blanket outside the fusion system. A neutron being

To realize the mechanism of total fusion energy utilization, it is necessary to understand the following schematic diagram as shown in Fig. 2.4 [9]. In the (d, t) fusion chamber, the alpha on colliding with the first wall of the fusion chamber, may be the vanadium metal, will transfer its KE to atoms of the wall causing both heat generation and radiation damage. Thus, the converted KE into the heat and the fission-heat of the blanket will be converted into steam; hence, the electricity or heat may directly be converted to the electricity by another mechanism. A part of the so produced electric energy, E_{rec} , may be fed back to the ion accelerator. Efficiency of the accelerator, η_1 , for converting electric energy,

Fig. 2.3 A most commonly discussed fusion–fission hybrid system under the magnetic confinement [2, 7]



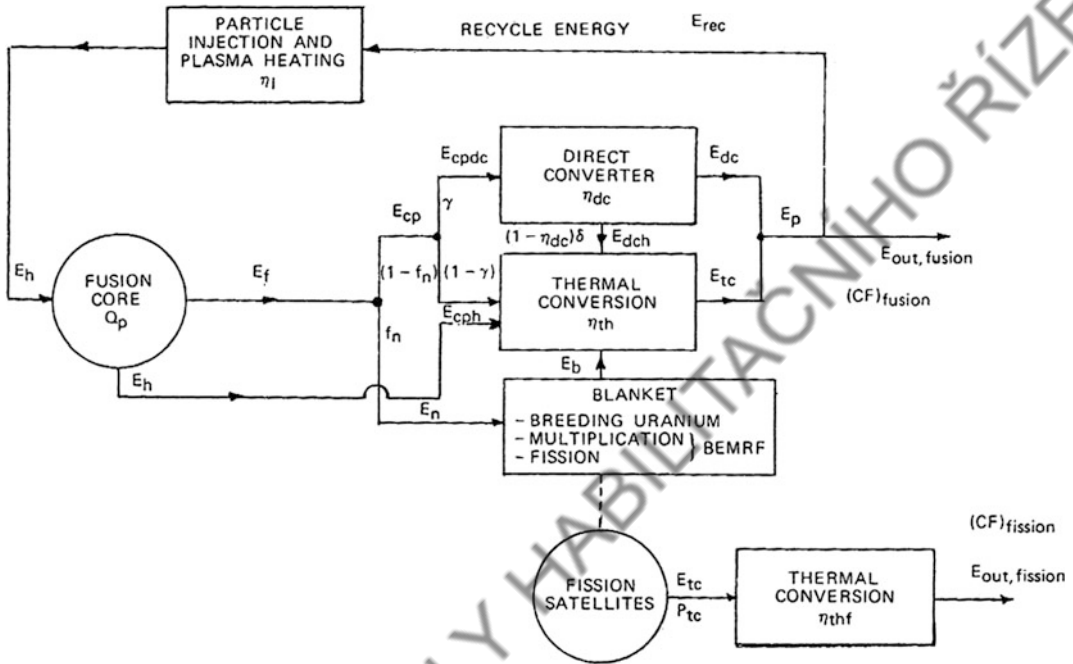


Fig. 2.4 A schematic diagram of fusion energy conversion into electric energy and its internal utilization [9]

E_{rec} , into KE of an ion, E_h , can be written as follows:

$$\eta_I = \frac{E_h}{E_{rec}} \quad (2.8)$$

Similarly, fraction of fusion energy, $(1 - f_n)$, carried by the charged particle like alpha will be converted into heat by a factor, γ ; thus,

$$E_{cpdc} = \gamma E_{cp} \quad (2.9)$$

Further, the E_{cpdc} , heat energy, can be converted directly to electricity by say thermoelectric generator, or it can be converted first to steam and then to electricity by using a turbine as mentioned earlier. The two routes of conversion into electricity are shown as outgoing channels of E_{out} through ‘direct converter’ and the ‘thermal conversion.’ In future works, advance systems of such conversions may be investigated to have better efficiency.

Neutron energy, E_n , is further multiplied by way of the fission energy of fuel through ^{233}U . A part of E_n is also utilized in neutron

multiplication. If BEMRF is the ‘blanket energy multiplication factor,’ i.e., ratio of energy multiplied in blanket to the source neutron energy [9], then the energy in the blanket system may be written as follows:

$$\begin{aligned} E_b &= \text{BEMRF} \times E_n \\ &= \text{BEMRF} \times f_n \times E_{Fu} \end{aligned} \quad (2.10)$$

Besides, as mentioned earlier, there is a chance that neutrons are multiplied in the blanket by way of non-fission reactions or energy deposited in the blanket by other non-fission reactions. In turn, they produce extra energy on interaction with the fission fuel material. This leads to

$$\text{BEMRF} = \text{BEMR} + \frac{\text{no. Th}(n,f) \times 184.2}{\text{Source } n - \text{energy (MeV)}} \quad (2.11)$$

For a detailed discussion of contributions of different conversion systems and parameters of the hybrid system, reader is advised to refer to Ragheb and Singh [9].

2.2 Reactor with Liquid Fuel

^{232}Th isotope is commonly known as ‘thor,’ and it is found as a 100% isotopic composition in the form of thorite (ThSiO_4) and thorianite ($\text{ThO}_2 + \text{UO}_2$). It is 3 times more abundant than uranium in nature. Thorium is also found in ash of coal. Thorium fuel-based fusion–fission hybrid reactor is expected to be a sustainable source of energy for future. The use of the molten-salt reactor (MSR) was pioneered at Oak Ridge National Laboratory first time. At ORNL, two prototypes of molten-salt reactors, namely Aircraft Reactor Experiment (ARE) and Molten-Salt Reactor Experiment (MSRE), were successfully designed, constructed, and operated from the year 1965–69. Later on, the two experimental reactors were suspended from operation for a long period of time in USA.

Two possibilities of using molten salts, one comprising Na–Th–F–Be (as $\text{NaF} \cdot \text{BeF}_2 \cdot \text{ThF}_4$) with the (d, d) neutron source and second Li–Th–F–Be (as $\text{LiF} \cdot \text{BeF}_2 \cdot \text{ThF}_4$) salt with (d, t) source, have been studied. In such hybrid system having thorium as the target blanket and graphite as the neutron reflector, the (d, t) reaction provides $0.74\text{Th}(n, \gamma)$ breeding to ^{233}U compared to $0.76\text{Th}(n, \gamma)$ by the (d, d) neutron source [10, 11]. As shown with the help of Eq. (2.6), tritium is also produced in neutron interaction with ^6Li of a molten salt. Subsequently, this affects breeding of ^{233}U in a (d, t)—fusion reactor because of further generation of a part of neutron flux. The heat advantages in the two cases of plasmas are comparable and enormous. Such reactors can also be named as Molten-Salt Breeder Reactor (MSBR) [12]. Shortly, a MSR has advantages mainly of safety, economy, and efficiency and disadvantages of design difficulties which need separate discussions with details.

2.2.1 Single-Fluid Reactor

Single-fluid prototype reactor was designed at ORNL [13] wherein fluoride salt containing thorium and uranium was filled in a large reactor vessel with graphite rods for the purpose of moderation as

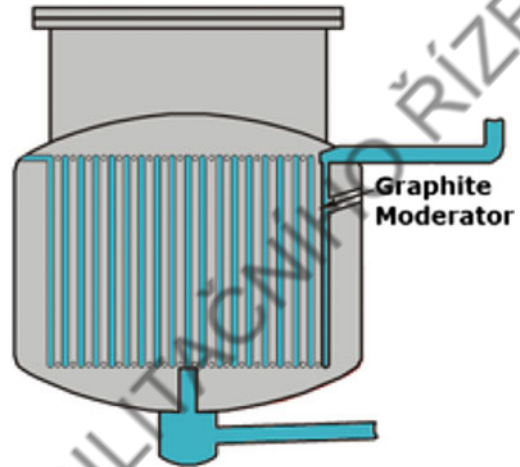


Fig. 2.5 A schematic diagram of single-fluid reactor as one of the liquid fluoride thorium reactors (LFTRs) [13]

shown in Fig. 2.5. In the ORNL MSBR reactor, graphite is reduced near the outer wall of the vessel hence allowing better chance of capture of thermal neutrons by the thorium fuel in the area. This also allowed lesser neutron leakage. Being a liquid fuel, one such reactor has also provisions of removal of fission products and that reduces cost of reprocessing. This will, however, require periodic filling of uranium fuel.

2.2.2 Double-Fluid Reactor

A double-fluid reactor employs two separate liquid fuels. One is the core fuel, and another fuel is in the blanket of the core. The core contains high neutron density to burn ^{233}U . The thorium fuel salt in the blanket absorbs even fast neutrons to convert into ^{233}Pa which slowly decays to ^{233}U . There is lesser chance of ^{233}U to capture slow neutrons to convert into ^{234}U because of the lower amount of slow neutron flux. ^{233}U is recovered by way of fluorination process then allowed for the vacuum distillation, and in this process, fission products are left in the bottom of the blanket as the waste. The ^{233}U fuel so recovered can be filled in the core for burning as a fissile fuel. Recently, Holcomb [14] has discussed various MSR variants with different fuels, coolant possibilities, challenges and advantages.

The design has advantage in the simplified fuel processing because of low fissile inventory being located in a small core. Also, it provides more efficient breeding opportunity as the Th-blanket captures neutrons leaked out from the core. This results in more breeding from a small reactor. The design, however, has weakness in the form of barrier wall between the two fluids as it needs frequent replacement because of its fast radiation damage.

Further, Shimazu [15] has discussed three core concept of FUJI-U3 design having fuel salt $\text{LiF-BeF}_2\text{-ThF}_4\text{-}^{233}\text{UF}_4$ where the fuel to graphite ratio is kept as 0.39, 0.27, and 0.45 in core 1, core 2 and core 3 respectively, for a 200 MWe reactor. The reactor is to be driven by 1 GeV and 200–300 mA proton accelerator. The reactor system will have possibility of multi-beam funnelling to achieve the designed beam current. Life of the FUJI-U3 system with graphite moderator is estimated to be 20–30 years.

2.3 Other Hybrid Energy Systems

Concept of hybridization when extended to other energy systems then it opened up several different possible options of integration of energy inputs like nuclear and other renewable systems or the energy outputs like electricity, gasoline, water and heat etc. using proper complimentary energy conversing processes [16]. For example, different input energy systems like nuclear and solar energy systems may feed to a master grid system after having required input parameter of frequency. By enabling more than one energy conversion units, Nuclear Hybrid Energy Systems (NHES) may provide additional opportunities of flexible energy management, delivering various types of ancillary services such as operating reserves, regulating, ramping, load following and supplemental reserves and for enabling operational flexibility for value, technical, and/or economic optimization. Chen et al. [17] have considered the issues of variability in depth in accordance with the two models that are summarized in the following.

2.3.1 West Texas Model of NHES

West Texas model assumes inputs like nuclear, wind, natural gas, and water resources and to have outputs as electricity and gasoline, etc. In practice, it combines a small nuclear system with wind turbine park to produce electricity and to convert carbon resources to the gasoline using excess thermal capacity as steam. This has a flexible generation resource and a flexible thermal load. From the West Texas model, shown in Fig. 2.6, it can be understood that not only the electricity from the small modular nuclear reactor (SMR, 180 MW) plant and the wind energy turbine (45 MW) electricity can be sent to the electric grid after proper matching of parameters but extra steam of the nuclear plant (conversion capacity ~ 45 MW) can be utilized to generate LPG through a gasoline production plant (GPP). SMR and wind power have maximum capacities as 180 and 45 MW, respectively, and the heat deducted in the form of steam for utilization for the LPG production is also variable with maximum demand of 45 MW. Ultimately, supply ~ 180 MW can be sent to the grid with a little management of wind power and GPP.

2.3.2 Northeastern Arizona Model of NHES

Northeastern Arizona model assumes inputs like nuclear and solar photovoltaic (PV) systems to supply electricity to the grid, and at the same time, it produces fresh drinkable water from the saline water. The Arizona NHES has a flexible electrical load and can be operated as a flexible generation resource and flexible load resource. In Fig. 2.7, schematic diagram of the Arizona NHES model is shown. In the figure, power sharing is shown, and it may be seen that ultimately a lesser power $\sim 135\text{--}165$ MW electricity is fed to the grid compared to the West Texas Model of NHES. The loss of electricity to the grid has been evaluated considering total economics with respect to the region.

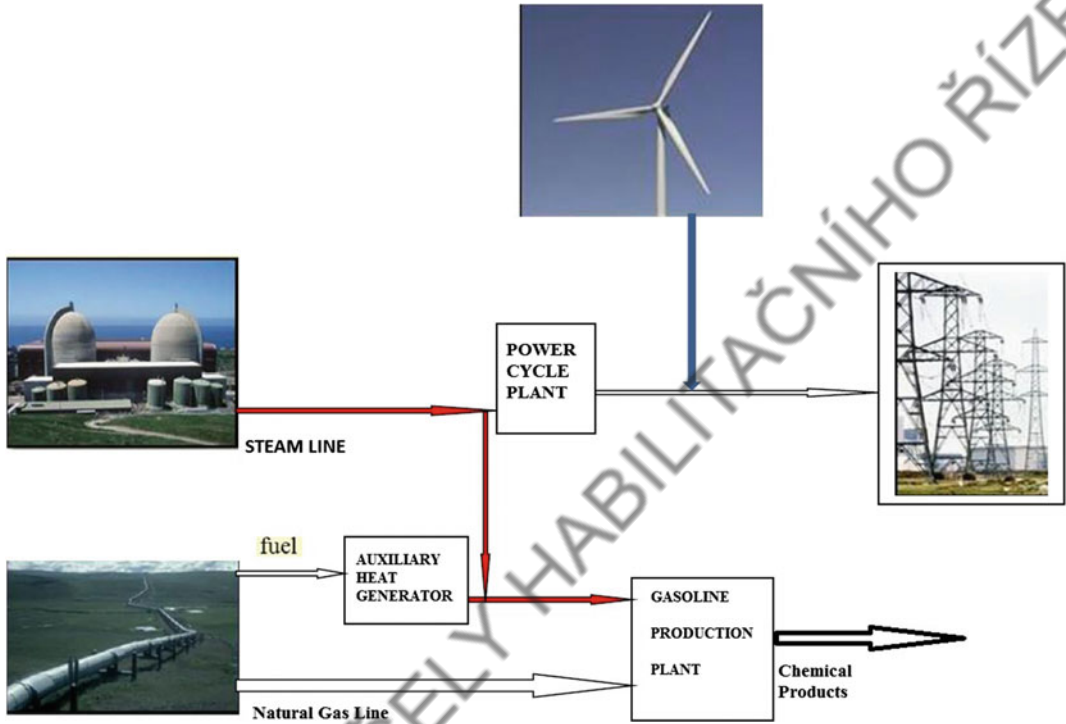


Fig. 2.6 A schematic diagram of West Texas model of NHES

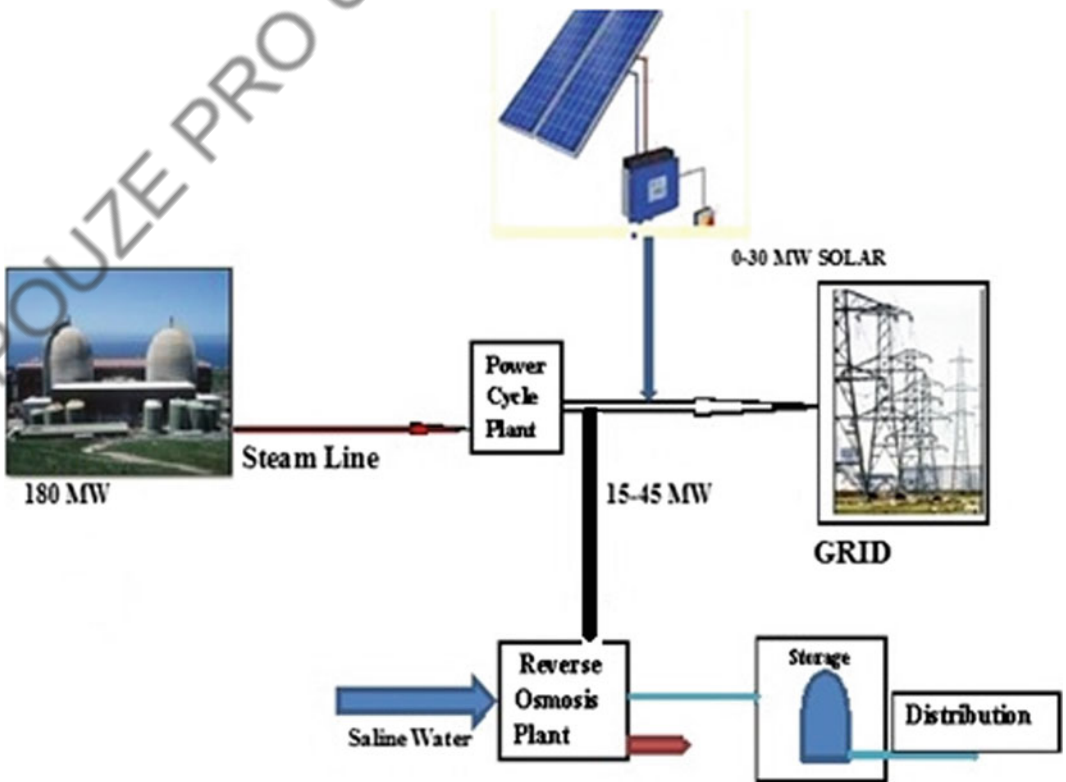


Fig. 2.7 A schematic diagram of the Arizona NHES model

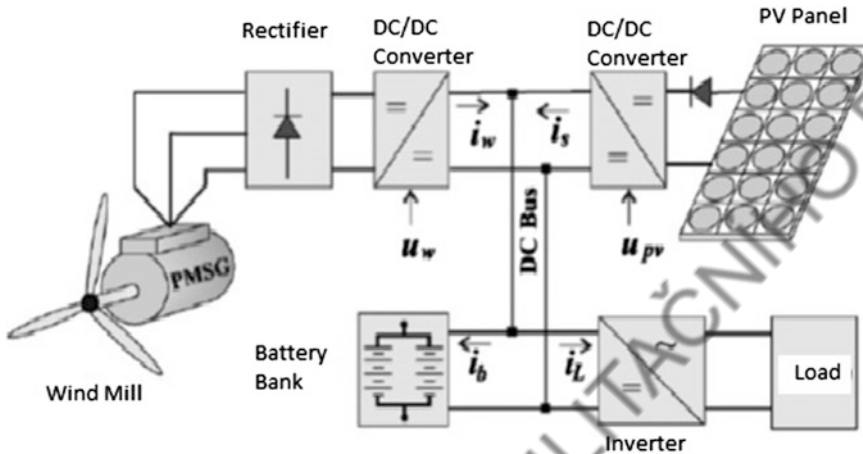


Fig. 2.8 A wind mill and photovoltaic hybrid energy system

Economic functions and operation optimization conditions are worked out and discussed in detail by Chen et al. [17].

2.3.3 Wind and PV Hybrid Energy System

Valenciaga and Puleston [18] have explored possibility of hybrid system of wind and photovoltaic (PV) system and a stand-alone supervision control system. A ‘wind energy conversion systems (WECS)’ comprises a windmill, multipolar synchronous generator (PMSG), a rectifier, and a dc/dc converter for interfacing. PMSG and control is discussed in details by Melicio et al. [19]. The solar module comprises of several solar panels connected to the dc bus as shown in Fig. 2.8. The battery bank and its cost play a fundamental role in the overall system cost [20].

Apparently with the growth of hybrid energy systems and efficient utilization of resources, energy parks will be appearing on the world map. This may also initiate the process of clustering of industries related to energy resources. This may, however, present a different scenario where nuclear energy and other energy resources as well as resource utilization will stand erect in the same area. This may raise several issues related to security, proliferation, and activating new regulations.

References

1. Bethe, H.A.: The fusion hybrid. *Phys. Today* **32**(4), 44 (1979)
2. A Report of the Conference on Hybrid Fusion-Fission Systems. Washington DC (2009). web.mit.edu/fusionission/HybridsPubli/Hybrid_Fusion_Fission_Conference_A.pdf. Accessed 19–20 May 2009
3. Bosch, H.-S., Hale, G.M.: Improved Formulas for Fusion Cross-Sections and Thermal Reactivities. <http://iopscience.iop.org/0029-5515/32/4/I07> and <http://kfe.fjfi.cvut.cz/~valenpe7/files/12FVHE/BoschHale.pdf>
4. Fusion Energy.: National Energy Strategy, Executive Summary, p. 258. <https://www.ems.psu.edu/~radovic/Chapter14.pdf>. Accessed 1991/1992
5. Nakatsutsumi, M., et al.: Investigations of High-Energy-Density State at European XFEL. ICHED 2015 abstract book (2015), San Diego, California. https://www.researchgate.net/profile/Gerd_Priebe/publication/302596511_ICHEd_2015/links/57c5824108ae7642019b0709.pdf?origin=publication_list. Accessed 23–27 Aug 2015
6. Kodama, R., et al.: Fast heating of ultrahigh-density plasma as a step towards laser fusion ignition. *Nature* **412**, 798 (2001)
7. Stacey, W.M., et al.: A TRU-Zr metal-fuel sodium-cooled fast subcritical advanced burner reactor. *Nucl. Technol.* **162**(1), 53 (2008)
8. Freidberg, J.P., Kadak, A.C.: Fusion-fission hybrids revisited. *Nat. Phys.* **5**, 370 (2009)
9. Singh, M.: Fail-Safe Source-Driven Fission and Fusion-Fission Hybrid Reactor Configurations. Master’s thesis, University of Illinois, Urbana, Champaign (2013). <https://www.ideals.illinois.edu/handle/2142/45583> and Ragheb, M., Singh, M.: Electrodynamic inertial fusion generators and fission satellites.

- Thorium Energy Alliance 4th Annual Future of Energy Conference, Loyalla University, Water Tower Campus, Chicago, Illinois, USA (2012). Accessed 31 May–1 June 2012
10. Ragheb, M.M.H.: Fusio-fission thorium hybrid (2017). mragheb.com/.../Fission%20Fusion%20Thorium%20Hybrid.pdf
 11. Ragheb, M.M.H., et al.: Nuclear performance of molten salt fusion-fission symbiotic systems for catalyzed deuterium-deuterium and deuterium-tritium reactors. *Nucl. Tech.* **48**, 217 (1980)
 12. Rosenthal, M.W., et al.: The Development Status of Molten-Salt Breeder Reactors, ORNL-4812. Oak Ridge National Laboratory (1972). <http://www.energyfromthorium.com/pdf/ORNL-4812.pdf>
 13. Briggs, R.B.: Molten-Salt Reactor Program Semi-Annual Progress Report For Period Ending 31 July, 1964. ORNL-3708, Oak Ridge National Laboratory (November 1964). <http://www.energyfromthorium.com/pdf/ORNL-3708.pdf>
 14. Holcomb, D.E.: Molten Salt Reactors Today Status & Challenges, Workshop on MSR Technologies—Commemorating the 50th Anniversary of the Startup of the MSRE, ORNL, 15 Oct 2015
 15. Shimazu, Y.: Current situation of MSR Development in Japan. Graduate School of Engineering, Hokkaido University, Japan (2007). <http://www.uxc.com/smr/Library%5CDesign%20Specific/Fuji%20MSR/Presentations/2007%20-%20Current%20Situation%20of%20MSR%20Development%20in%20Japan.pdf>
 16. Garcia, H.E., et al.: Nuclear Hybrid Energy Systems—Regional Studies: West Texas & Northeastern Arizona: INUEXT-1 5-34503 (2015). <http://www.inl.gov>
 17. Chen, J., et al.: Operations optimizations of nuclear hybrid energy systems. *Nucl. Tech.* **195**, 143 (2016)
 18. Valenciaga, F., Puleston, P.F.: Supervisor control for a stand-alone hybrid generation system using wind and photovoltaic energy. *IEEE Trans. on Energy Convers.* **20**(2), 398 (2005)
 19. Melicio, R., et al.: Wind Turbines with Permanent Magnet Synchronous Generator and Full-Power Converters: Modelling, Control and Simulation: Dr. Ibrahim Al-Bahadly (Ed.). ISBN: 978-953-307-221-0. InTech. <http://www.intechopen.com/books/wind-turbines/wind-turbines-with-permanent-magnet-synchronous-generator-and-full-power-converters-modelling-control>
 20. Borowy, B.S., Salameh, Z.M.: Methodology for optimally sizing the combination of a battery bank and pv array in a wind/PV hybrid system: *IEEE Trans. Energy Convers.* **11**(2), 367–375 (1996)

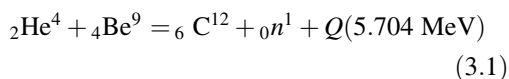
Spallation Neutron Source, Multiplication and Possibility of Incineration

Spallation neutron source is new and has fastly attracted the attention of both nuclear and reactor scientists from the point of its application in incineration of the radioactive waste and nuclear energy production from the fertile fuels. This is a basic lesson of accelerator-driven subcritical system and future copious source of neutron for a variety of applications useful for the material science. Being higher energy than a fast reactor, secondary neutron built up in a reactor provides extra neutron flux required for double utilization in energy and nuclear transmutation. Simple kinetics of multiplication is discussed at large in the chapter. Following it CASCADE code ver. 04 calculation of neutron flux inside the IAEA benchmark design are performed for their application for the incineration of LLNW. The calculations have been compared with calculations of the MCNP code for the heat distribution.

fuel which has hardly been burnt in a critical power reactor having neutron energy up to ~ 10.5 MeV. It may be mentioned that details of spallation neutron spectrum are the central theme of technology of energy amplifier for both energy and incineration of LLNW.

3.1.1 Neutron Sources

In 1930, Bothe and Becker [1] discovered a new radiation in bombardment of alpha radiation of polonium (Po) onto the beryllium target. They called new radiation to be γ radiation. In 1932, Chadwick identified it as neutron [2]. The following nuclear reaction (3.1) was found to be the cause of neutron production. Kinetic energy of alpha particle will contribute toward total kinetic energy of neutron which will escape out of the beryllium target.



3.1 Neutron Sources and Applications

Several kinds of neutron sources have been in existence, and they have a large number of applications including the sector of atomic energy. Production of a newer spallation neutron source is an application of accelerator technology. In case of nuclear energy, high-energy accelerator beam of charged particle with energy >30 MeV can produce a much harder neutron spectrum which can initiate fission in a fertile

Thus, it cannot be a unique value, and each neutron source will have its characteristic neutron energy spectrum. In Table 3.1, details of several neutron sources are given with data of neutron yield in each case. For example, if the strength of ${}^{241}\text{Am}/\text{Be}$ source is assigned to be 5Ci, this means, its rate of alpha emission is $5 \times 3.7 \times 10^{10}/\text{s}$ and the corresponding neutron emission rate is $70 \times 5 \times 3.7 \times 10^{10}/$

Table 3.1 Details of the (α, n) sources. Alpha source, half-life, kinetic energy of alpha, neutron yield per 10^6 alpha particles, and percentage of neutrons with energy $E_n < 1.5$ MeV

Source	Half-life	E_α (MeV)	Neutron yield per 10^6 primary alpha particles		Percent yield with $E_n < 1.5$ MeV	
			Calculated	Experimental	Calculated	Experimental
$^{239}\text{Pu}/\text{Be}$	24,000 years	5.14	65	57	11	9–13
$^{210}\text{Po}/\text{Be}$	138 days	5.30	73	69	13	12
$^{238}\text{Pu}/\text{Be}$	87.4 years	5.48	79	–	–	–
$^{241}\text{Am}/\text{Be}$	433 years	5.48	82	70	14	–
$^{244}\text{Cm}/\text{Be}$	18 years	5.79	100	–	18	15–23
$^{239}\text{Cm}/\text{Be}$	162 days	6.10	118	106	22	29
$^{239}\text{Ra}/\text{Be}$	1,602 years	Multiple	502	–	26	26
$^{227}\text{Ac}/\text{Be}$	21.6 years	Multiple	502	–	28	33–38

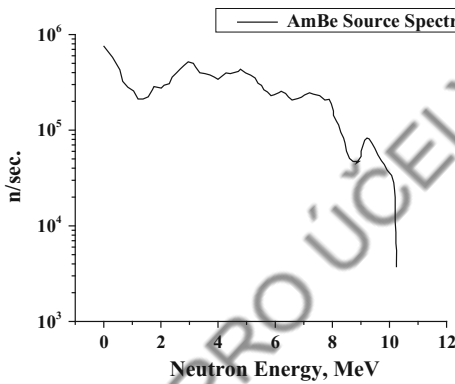
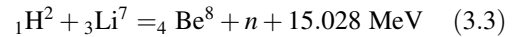
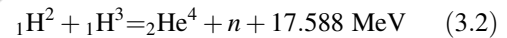


Fig. 3.1 Neutron energy spectrum of Am/Be source by Lorch [2]

$10^6 = 1.295 \times 10^7$ neutrons/s. In Fig. 3.1, neutron energy spectrum of Am/Be source by Lorch [2] is shown. This is one of the neutron source used for conduction of laboratory experiments. Also, the neutron sources given in Table 3.1 are frequently used in several deep underground geological searches of minerals, oil, and petroleum products as they are small in size and have long half-life in years. Similarly, $^{11}\text{Be}(\alpha, n)^{14}\text{N}$ nuclear reaction occur with another isotope of Beryllium and in that case $Q = 0.158$ MeV.

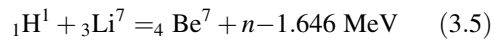
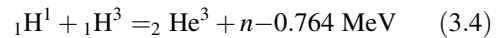
Some of the nuclear reactions of neutron production useful in various research and developments can be briefly summarized as follows:

(d, n) reactions:



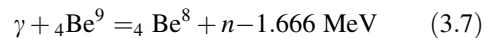
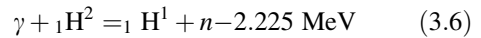
Again, these reactions can be performed in minimum laboratory conditions, and no acceleration of particles is required.

(p, n) reactions:



These reactions can be performed with the help of accelerated proton beams of kinetic energy greater than or equal to Q value.

(γ , n) reactions:



Reactions (3.6) and (3.7) are also called as ‘nuclear photo-electric effect,’ and they can be performed with the help of radioactive sources emitting gammas with energy, $E_\gamma > 1.666$ MeV. Also, neutrons can be produced in (γ, f) reactions with fissionable nuclei. Similarly, at high energies, $(\gamma, 2n)$ reactions are also possible.

In a fission reaction with any fuel element on an average, $\nu > 1$ neutrons are produced, and in a chain reaction in an infinitely large nuclear fuel, neutrons are multiplied. This results in large flux, $\sim 8.9 \times 10^{13}$ n/cm²/s in a thermal reactor and $\sim 1.69 \times 10^{16}$ n/cm²/s in a fast reactor.

3.1.2 Spallation Neutron Sources

Spallation as such is no word in English language, and it is derived from the verb spill of liquid from a container when some material is dropped in the liquid. This was the first time used in cosmic ray studies. After the early introduction of word spallation, nuclear reactions were reported at Berkeley in 1947 and the mechanism of spallation reactions was also discussed by Serber [3] in the same year. In collision of energetic particle like proton and deuteron having energy greater than several tens of MeV/n with a heavy nucleus, several neutrons are spilled out in early cascade along with pions and a part of other constituent nuclear matter of the nucleus. Subsequently, compound nucleus also decays emitting several nucleons and fragments. Fission process in case of actinides enhances the neutron production. The whole lot of neutrons produced in a high-energy collision are commonly identified as spallation neutrons, and they have high technological applications being energetic much beyond the energy of reactor neutrons other neutron sources as described in earlier Sect. 3.1.1. One of the applications of spallation neutrons has emerged in the form of ‘energy amplifiers’ [4, 5] for utilization of fertile uranium and thorium like fuels for nuclear energy and transmutation of the LLNW. The other application of spallation neutron source can be identified in the form of ‘beam of cooled down neutrons’ and separated in different energy ranges, hence different wavelengths as per their utilization in different applications. SINQ in Switzerland [6], ISIS in UK [7], SNS in USA [8], and JSNS in Japan [9] projects are already completed. The SNS project was one of the initiatives taken after the concept of EA [4] was proposed and its initial objective was to develop 1 GeV, 1 μ s

pulsed proton beam with 1 MW power. Its design details are discussed by Henderson et al. [10]. Similarly, JSNS with proton power of 1 MW, energy 3 GeV, current 333 mA, proton pulse time width 1 μ s, frequency, 25 Hz is planned and their details will be discussed in Sect. 7.5. It is expected to produce $\sim 10^{17}$ n/s and a reactor of 15 MW power. For more details of the project, reader is advised to refer to [11].

Accelerated protons or heavier particles with energy >100 MeV/n on colliding with neutron-rich heavy targets like Hg, W, Pb, Bi, U, and Th produce large number of neutrons by different physical processes. Multiplicity of neutrons increases with kinetic energy of the projectile and length of the bulk of the target compared to the width of the target. An early review can be found in the article by Kumar et al. [12] wherein both experimental data of multiplicity has been compared with the model calculations. In Fig. 3.2(a), neutron multiplicity per incident proton (n/p) has been plotted to vary with length (cm) of the cylindrical lead target and compared with the calculated multiplicity from the CASCADE code version 2004 summarized in Ref. [12] itself. The two data show the following logarithmic growth of n/p with the length of the target.

Experimental data follows,

$$n/p = -8.76 + 8.44 \ln L \quad (3.8)$$

CASCADE code data follows,

$$n/p = -9.45 + 8.49 \ln L \quad (3.9)$$

In Fig. 3.2(b), the growth of neutron multiplicity with the diameter of the Pb target is plotted for proton projectile at 1.22 MeV where there are only two data points from the experiments [13]. Calculated data of the CASCADE code differs $\sim 9\%$ with the experiment data. From $d = 8$ –30 cm, n/p growth is only 37% and it can be represented by the following exponential growth,

$$n/p = (25.64 \pm 3.43) - (13.53 \pm 1.85) \exp(-d/20.31) \quad (3.10)$$

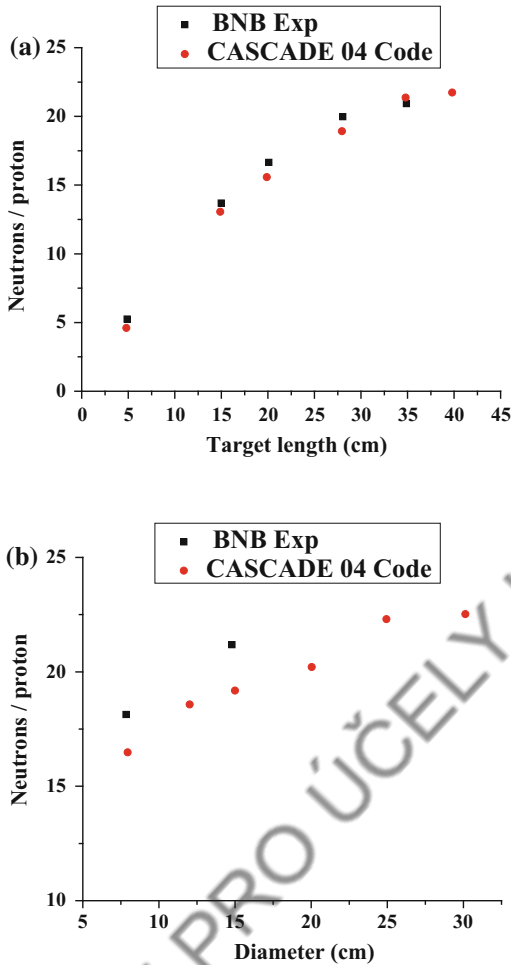


Fig. 3.2 Data of n/p from the BNB experiment [13] plotted as function of (a) length and (b) diameter of the lead (Pb) cylindrical target at 1.2 GeV energy of projectile proton and compared with results of calculations from the CASCADE 04 code [12]

Also, at BNL, neutron multiplicity is measured in reactions of proton colliding with W and Pb targets at energies ranging from 0.8 to 1.4 GeV [14], and the data is compared with calculated values obtained from the Monte Carlo CASCADE 04 code where better satisfactory results are found in case of Pb target [12].

In a Monte Carlo simulation study using the MCNPX code, Polański and Słowiński [15] have compared the neutron multiplicity and neutron spectra in proton and electron colliding with Pb target. In Fig. 3.3, neutron yield is plotted in case

of electron beam energy colliding with the Pb target of size $d \times L = 3.4 \times 3.4 \text{ cm}^2$. Neutron spectra of electron and proton beams colliding with Pb target of size $d \times L = 60 \times 60 \text{ cm}^2$ are also plotted in Fig. 3.3. It may be pointed out that neutron spectra up to 1 MeV is similarly rising in both the cases but neutron multiplicity is about 50–100 times more in case of proton than the electron beam. At higher than 1 MeV neutron energy, it grows ~ 2 to ~ 4 orders of magnitude higher in case of protons than electron beam. On an average ratio, $n/e^- = 0.32$ and $n/p = 34$. On the contrary, activity induced by electron beam is found [15] to be 25 times higher than proton for the same target.

In another attempt, MC Simulation using MCNP-4C2 code shows that 5 MeV electron beam colliding with Be and BeD₂ targets [16] one can get moderated neutrons up to a flux of $1.23 \times 10^8 \text{ n/cm}^2/\text{s}/\text{mA}$ in the presence of graphite moderator. In case of electron, it is easier and economical to enhance beam current compared to proton acceleration. In Table 3.2, summary data of already existing spallation neutron sources is given.

Besides the aforesaid neutron sources [6–9], dedicated spallation neutron sources with several experimental facilities such as GAMMA [26, 27], energy and transmutation ($E + T$) [28–30], QUINTA [31], Subcritical Assembly at Dubna (SAD) [32], TARC [33], n -TOF [34] have used spallation neutron sources in basic experiments related to the ADS technology. Most of them are described in Chap. 6.

Using a Monte Carlo simulation code, such as CASCADE [35] and MCNP [36], neutron spectrum for a combination of the projectile, beam energy and target size can be calculated.

Spallation is the only process, known so far, of production of high flux of highly energetic neutrons from a small size target system. On the other hand, we know that from a thermal power reactor one can produce a neutron flux which is nearly two orders of magnitude smaller and energy is also limited to $\sim 10.5 \text{ MeV}$ compared to a spallation source that produces neutrons up to the projectile energy. The spallation targets are conveniently manageable for other applications; e.g., measurements of reaction cross sections

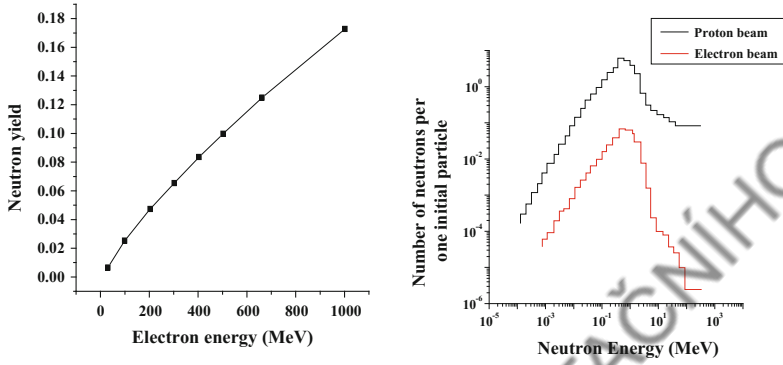


Fig. 3.3 (Left) Neutron yield plotted with electron energy from 30 to 1,000 MeV. (Right) neutron spectra in case of 1 GeV electron (lower histogram) and proton (upper histogram) beams colliding with Pb target calculated from the MCNP-4C2 code [15]

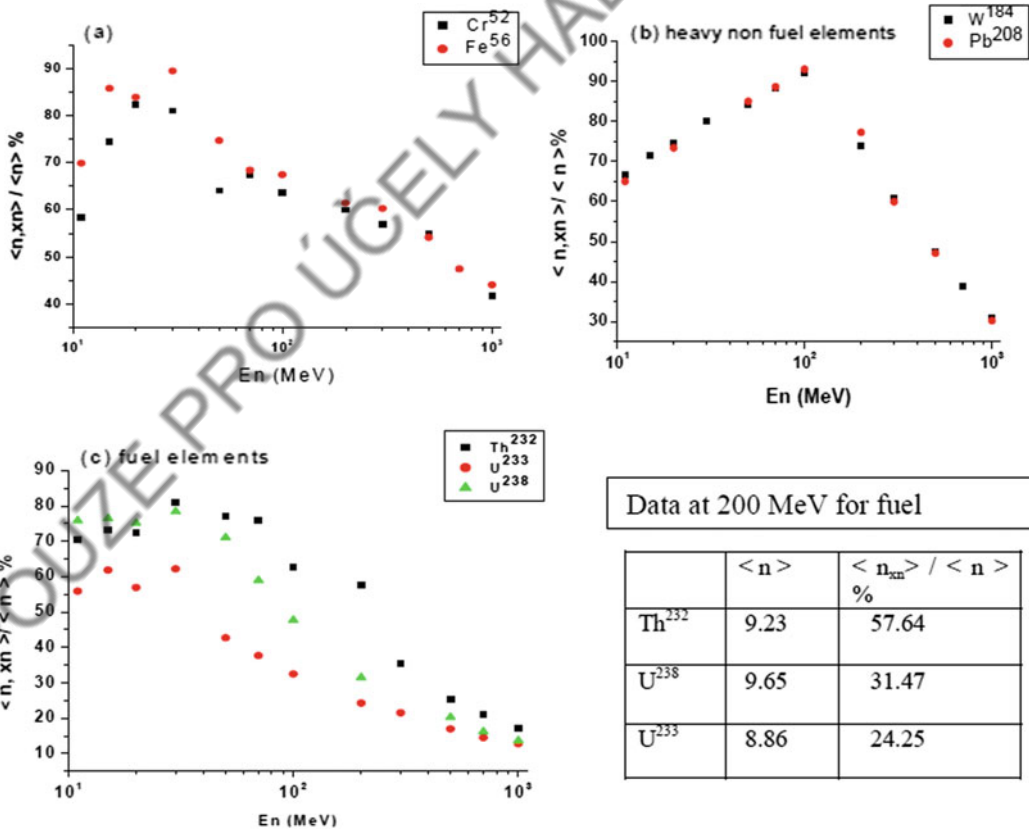


Fig. 3.4 Percentage contribution of (n, xn) nuclear process in neutron multiplication compared to total multiplicity plotted as a function of neutron energy E_n [50] for light mass materials, Cr and Fe, heavy elements, W and Pb, and fissionable fuel elements Th, U, and Pu. Data in the table corresponds to $E_n = 200$ MeV

[37–39] can be done at a fast rate using pulsed neutron source and production of beams of cold and ultra-cold neutrons [40] for a new area of

neutron spectroscopy. Using high-energy neutrons for the measurement of cross section, n -ToF is the state-of-the-art technique because of

Table 3.2 Operation summary of high-energy spallation neutron sources

Name of the facility and location	Proton energy (MeV)/ Current (μA)	Beam power (kW)	Repetition rate (Hz)	Target material	Moderator	Year of facility operating or planned
LANSCE, Los Alamos National Laboratory (USA) [17]	800/70	56	20	Tungsten	L-H ₂ /H ₂ O	1983
SNS, Oak Ridge National Laboratory (USA) [18, 19]	1,000/1,400	1,400	60	Mercury	L-H ₂ /H ₂ O	2006
ISIS, Rutherford Appleton Laboratory (U.K.) [20, 21]	800/200	160	50	Tantalum	L-H ₂ /H ₂ O	1985
IPNS, Argonne National Laboratory (USA) [22]	450/15	7	30	Depleted Uranium	S-CH ₄ /L-CH ₄	1981 (closed 2008)
SINQ, Paul Scherrer Institute, Switzerland [22, 23]	590/1,500	1,000	Continuous	Zircaloy	L-D ₂ /D ₂ O	1996
JSNS, Japan Atomic Energy Agency, Japan [[24, 25]	3,000/333	1,000	25	Mercury	L-H ₂	2008

its high resolution. On a big scale, the *n*-ToF facilities are working at CERN [34, 37–39], GEANIE facility and LANCE [41]. Other facilities using neutrons with nearly reactor energy for cross-section measurements are cyclotron CYCLONE at Louvain-la-Neuve [42, 43], Pohang facility using (γ , *n*) source [44], and GELINA at Geel [45]. Intense resonance neutron source (IREN) [46] has also started working at JINR, Dubna.

For designing of an ADSS as energy and transmutation system, basic data of neutron microscopic cross sections at energies higher than 20 MeV is rarely available and this will take several years to get such data for a large number of elements and several reactions. Using the low-intensity spallation sources [26–31] at JINR Dubna, several attempts have been made to measure spectrum average cross sections (sp. av. cs.) of both fissionable materials and other structural materials of ADS [27, 28, 30, 31, 47, 48]. The sp. av. cs. are derived from the

measurements of reaction rates measured in an experiment.

3.2 Neutron Multiplicative Processes

In case of high-energy neutron interaction with a nucleus, there can be scattering, catastrophic inelastic reaction or a complete absorption and formation of a compound nucleus. Different to complete absorption, a slow neutron on absorption by a fissionable nucleus, there is good chance that net neutron balance is positive. In case of an ADSS, there is copious supply of high-energy spallation neutrons, and multiplication of neutrons will not only be from the fuel elements but also from other reactor materials. This makes ADSS a quite different reactor. Also, in presence of enormous yield of neutrons, there will be much higher radiation damage of the ADSS reactor material compared to normal

critical power reactor. Whether it is a fissionable material or other structure material, the following neutron multiplicative processes are identified for considerations:

- (i) Single-neutron type— (n, n') , (n, np) , (n, nd) , (n, nt) , $(n, n\alpha)$, $(n, n\text{He}^3)$ and $(n, n2p)$, etc.
- (ii) Multiple-neutron type— (n, xn) where $x = 2, 3, \dots$, (n, f) , $(n, 2n\text{He}^3)$, $(n, 2nd)$, $(n, 2nt)$, $(n, 2npd)$, $(n, 2n2p)$, $(n, 3np)$, $(n, 3nd)$, $(n, 3n\text{He}^3)$, $(n, 3nt)$ and $(n, 3n\alpha)$, etc.
- (iii) Neutron removal type— (n, γ) , (n, f) , (n, p) , (n, d) , (n, t) and (n, α) , etc.

As mentioned earlier, neutron multiplication by (a) structure material used in the reactor, i.e., spallation target, moderator, fuel carrying tubes or fuel cartridges and the shielding material and (b) fuel elements are different processes and they need separate analysis. In fact, it adds a dimension to the neutronics of a reactor.

3.2.1 Role of (n, xn) and Similar Reactions

In case of any of the Pb, Bi, Pb–Bi eutectic, or any other material of high atomic number, the (n, xn) and $(n, xnyp)$ -type reactions are important due to multiplication of neutrons by the produced high-energy neutrons. Secondly, even in case of fuel elements like U, Th, or Pu, neutrons are added by way of (n, xn) , higher than $x = 2$ order and $(n, xnyp)$ -type reactions to the fission neutrons. This makes ADSS different than critical reactors [12] because its fuel cycles are extended enormously. Thirdly, due to higher energy radiation, heavy radiation damage takes place, and this stresses upon need of development of radiation resistant materials and to extract highly radiotoxic materials frequently during the operation. In this way, having availability of additional neutrons beyond the energy requirement, incineration of long-lived isotopes like iodine (I), technetium (Tc), and plutonium (Pu) can be possible. Lastly, contribution of (n, γ) reactions

in the process of transmutation will rather be reduced because of smaller cross section of the reaction compared to a critical reactor where the neutron energy spectrum is relatively smaller. For details, reader may refer [49–51].

As the list of materials used in construction of a hybrid ADSS reactor is expected to be large and different to the existing critical reactors, therefore, there is need of additional new experimental data with higher accuracy. Presently, for the development of a design of a prototype after developing understanding of (n, xn) -type reactions, new data libraries are being prepared using the simulated data. Using codes like TALYS-1.0 to calculate cross sections up to 250 MeV energy [52] and CASCADE.04 code in the range from 11 to 1,000 MeV energy [53], for a large number of materials data tables are prepared and presented in reference [49]. In case of several reactions, experimental data [54–56] have been compared with the calculated data from the codes. In case of some of the ADSS materials, percentage contributions of (n, xn) and (n, f) reactions are assessed based on the calculated data and presented in Table 3.3.

The detailed calculated data of neutron multiplicity ratio, $\langle n(n, xn) \rangle / \langle n \rangle$, is plotted in Fig. 3.4 as a function of spallation neutron energy, E_n (MeV), [49] up to 1,000 MeV. The following inferences can be drawn from the data,

- (i) Light structure materials of different masses, e.g., Cr⁵² and Fe⁵⁶, follow a trend different to heavy structure materials like ¹⁸⁴W and ²⁰⁸Pb. Heavy materials show a unique rise of the ratio, $\langle n(n, xn) \rangle / \langle n \rangle$ up to 100 MeV and at higher energies it declines.
- (ii) The ratio, $\langle n(n, xn) \rangle / \langle n \rangle$, when plotted in case of ²³²Th, ²³⁸U, and ²³³U shows no unique feature like heavy structure materials discussed above. Rather the ratio follows, ²³²Th > ²³⁸U > ²³³U. It can be inferred that the contribution of (n, xn) process in neutron multiplication is more in case of more fertile nuclei and least in case of fissile nucleus.

Table 3.3 Total sum of cross sections of (n, xn) reactions, $\Sigma\sigma(n, xn)$ for all x values at the 200 MeV neutron energy for several ADSS materials, fission cross section $\Sigma\sigma(n, f)$ for ^{238}U , ^{235}U , ^{233}U , and ^{232}Th in barns (b) and their percentage contribution w.r.t. total non-elastic cross sections calculated using TALYS-1.0

Element	$\Sigma\sigma(n, xn)$ (mb)	$\Sigma\sigma(n, f)$ (mb)	$\Sigma\sigma_{\text{non-elastic}}$ (b)	$\frac{\Sigma\sigma(n, xn)}{\Sigma\sigma_{\text{non-elastic}}}$ %	$\frac{\Sigma\sigma(n, f)}{\Sigma\sigma_{\text{non-elastic}}}$ %	$\frac{\Sigma\sigma(n, xn)}{\Sigma\sigma(n, f)}$
^{238}U	273.32 *1,846.54	811.02 *262.46	2.11 *2.98	12.96 *62.04	38.46 *8.82	0.34 *7.03
^{235}U	249.28 *1,886.83	587.57 *677.97	1.93 *3.20	12.90 *59.01	30.42 *21.20	0.42 *2.78
^{233}U	272.85 *581.20	538.80 *1,989.7	1.92 *3.21	14.22 *18.12	28.07 *62.02	0.51 *0.29
^{232}Th	357.53 *1,880.13	320.55 *86.71	2.08 *2.93	17.17 *64.12	15.38 *2.96	1.12 *21.66
^{209}Bi	535.81	–	1.78	30.18	–	–
^{208}Pb	495.71	–	1.77	28.04	–	–
^{184}W	406.72	–	1.64	24.88	–	–
^{181}Ta	410.08	–	1.60	25.65	–	–
^{96}Mo	90.06	–	0.97	9.25	–	–
^{93}Nb	71.77	–	0.94	7.66	–	–
^{90}Zr	65.53	–	0.92	7.10	–	–
^{65}Cu	93.80	–	0.72	13.08	–	–
^{63}Cu	37.80	–	0.70	5.37	–	–
^{59}Co	23.77	–	0.62	3.82	–	–
^{58}Ni	4.66	–	0.62	0.75	–	–
^{56}Fe	17.83	–	0.59	3.04	–	–
^{55}Mn	27.29	–	0.58	4.68	–	–
^{52}Cr	22.95	–	0.57	4.06	–	–
^{51}V	28.77	–	0.54	5.37	–	–
^{48}Ti	22.42	–	0.53	4.23	–	–
^{31}P	1.46	–	0.38	0.38	–	–
^{28}Si	1.44	–	0.36	0.40	–	–
^{27}Al	3.27	–	0.33	0.99	–	–

In the last column ratio, $\Sigma\sigma(n, xn)/\Sigma\sigma(n, f)$ is given. All the data corresponds to $E_n = 200$ MeV. Data with (*) corresponds to 10 MeV energy for comparing with data of 200 MeV

Among the considered elements and energy, $E_n = 200$ MeV, the ratio $\frac{\Sigma\sigma(n, xn)}{\Sigma\sigma_{\text{nonelas}}}$ % is highest 30.18% for ^{209}Bi nuclide followed by ^{208}Pb , ^{181}Ta , and ^{184}W , where the ratio is 28.04, 25.55, and 24.84, respectively. Likewise, the ratio for fuel elements ^{238}U , ^{235}U , ^{233}U , and ^{232}Th is 12.96, 12.90, 14.21, and 17.17, respectively. From the neutron multiplication point of view, ^{209}Bi is very good. The ratio $\frac{\Sigma\sigma(n, xn)}{\Sigma\sigma(n, f)}$ % is an

indication of a competition between (n, xn) and (n, f) reactions, and its calculated values for ^{238}U , ^{235}U , ^{233}U , and ^{232}Th at 200 MeV are 0.337, 0.424, 0.506, and 1.12, respectively. This clearly indicates that although the (n, xn) reactions are not so important compared to (n, f) reactions in case of uranium, they play a vital role in the case of ^{232}Th fuel. For lower values of energy, e.g., at 10 MeV, the values of ratio $\frac{\Sigma\sigma(n, xn)}{\Sigma\sigma(n, f)}$ % for ^{238}U , ^{235}U , ^{233}U , and ^{232}Th are 7.03, 2.78, 0.29, and

21.66%, respectively. Thus, at 10 MeV energy, the $(n, 2n)$ reactions are dominant in case of ^{232}Th compared to ^{238}U and ^{235}U also. The ratio can be implemented to define fissional character of a fuel. Thus, the fissional order of four elements can be written as $^{233}\text{U} > ^{235}\text{U} > ^{238}\text{U} > ^{232}\text{Th}$.

3.2.2 Multiplication Coefficient and Source Importance

Let us assume that a cylindrical spallation neutron source of size $d \times L = 20 \times 50 \text{ cm}^2$ is enclosed inside another cylindrical of $x \text{ cm}$ thickness and filled with a fuel. In Fig. 3.5, two analogous cylindrical structures (a) and (b) are shown. In the inner cylinder of Fig. 3.5(a), a static neutron source is assumed, and in case of Fig. 3.5(b), a spallation source irradiated by 1 GeV proton beam of 1 A current is shown.

Spallation neutron energy spectrum produced in 1,000 MeV proton collision with massive lead (Pb) target of size $d \times L = 20 \times 50 \text{ cm}^2$ is calculated from the CASCADE 04 code [51], and it has been plotted in Fig. 3.6. The spectrum lies between 20 eV to $\sim 940 \text{ MeV}$ compared to a thermal and a fast reactor spectrum which shows maximum neutron energy to be $\sim 10.5 \text{ MeV}$

[57]. Spectrum average cross section (sp. av. cs.) defined [58] over the range of a neutron spectrum can be calculated from the flat or group cross sections from the raw cross section data at individual energy. In Table 3.4, calculated values of sp. av. cs. of various reactions occurring in ^{232}Th , ^{233}U , ^{235}U , and ^{238}U fuel elements by the three neutron spectra of thermal, fast reactors and the spallation spectrum are given.

According to a simple derivation for the neutron multiplication by Cullen [59], when I_0 intensity of incident neutrons is allowed to fall on a material in a given direction, then the intensity of surviving neutrons after passing through distance 'x' may be given by,

$$I_x = I_0 \exp(-x\Sigma_t) \quad (3.11)$$

where Σ_t is the total macroscopic cross section of a neutron in the given material. The formulation is applicable as the neutron is non-ionizing, and it changes direction on interaction only. Intensity of the neutron that interacts in a traversal of distance x may be written as follows:

$$(I_0 - I_x) = I_{\text{int}} = I_0(1 - \exp(-x\Sigma_t)) \quad (3.12)$$

The probability of interaction, $P_1 = I_{\text{int}}/I_0$ and the interaction can be of any of the elastic, capture, or fission, etc. Thus, probability of a type of

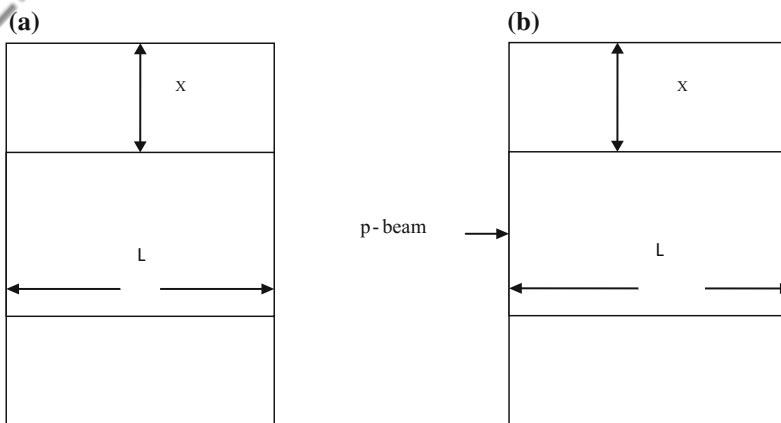


Fig. 3.5 A double cylindrical structure is used in calculations: (a) Inner cylinder is assumed as the source of neutrons, and the outer cylinder is filling with fuel element, (b) inner cylinder of lead is a spallation target

irradiated with 1 GeV proton. Thickness of outer cylinder is assumed to vary as per requirement of neutron multiplication

Fig. 3.6 Spallation neutron spectrum of 1 GeV proton colliding with massive Pb target calculated from the CASCADE 04 code [51]. There are 0.3% neutrons with $E_n > 250$ MeV

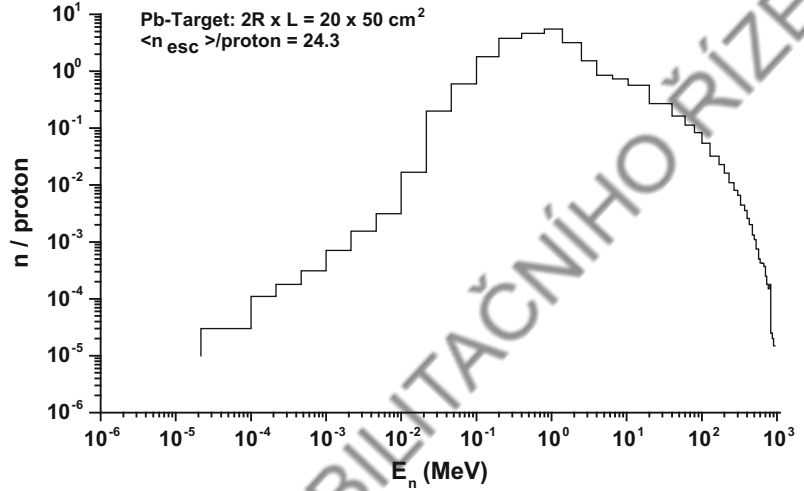


Table 3.4 Spectrum average cross sections, σ (mb) for different reaction channels of the fertile ^{232}Th and ^{238}U and fissile ^{233}U and ^{235}U fuel elements for the spallation, fast, and thermal neutron fluxes. Here, symbols correspond to standard reaction channels of TALYS-1.0 code [52]

$\langle \sigma \text{ (reactions)} \rangle$	^{232}Th	^{233}U	^{235}U	^{238}U
	Spallation Fast Thermal	Spallation Fast Thermal	Spallation Fast Thermal	Spallation Fast Thermal
$\langle \sigma (n, \gamma) \rangle$	146.1 391 5,350	41.8 74.2 431	106.4 270 1,730	116.8 317 5,490
$\langle \sigma (n, n') \rangle$	2,022.7 856 707	1,102.4 470 405	1,684.7 835 642	2,632.2 1,510 995
$\langle \sigma (n, 2n) \rangle$	74.8 7.85 8.97	27.7 3.17 3.97	89.2 15.3 21.6	70.8 13.7 17.4
$\langle \sigma (n, f) \rangle$	35.1 7.29 8.46	2,209.7 2,250 12,600	1,184.2 2,080 12,900	72.4 11.4 14.6
$\langle \sigma (n, 3n) \rangle$	41.38	12.97	32.19	41.20
$\langle \sigma (n, 4n) \rangle$	8.98	6.58	3.53	6.86
$\langle \sigma (n, 5n) \rangle$	12.11	11.51	6.89	7.74
$\langle \sigma (n, 6n) \rangle$	6.98	3.42	4.35	8.13
$\langle \sigma (n, 7n) \rangle$	6.97	1.43	1.35	1.71
$\langle \sigma (n, 8n) \rangle$	0.86	0.83	1.46	0.81
$\langle \sigma (n, 9n) \rangle$	0.56	0.67	0.89	0.82
$\langle \sigma (n, 0n) \rangle$	0.54	0.47	0.62	0.81
$\langle \sigma (n, 11n) \rangle$	0.63	0.20	0.09	0.79
$\langle \sigma (n, 12n) \rangle$	0.06	0.03	0.20	0.07
$\langle \sigma (n, 13n) \rangle$	0.11	0.12	0.13	0.07
$\langle \sigma (n, 14n) \rangle$	0.06	0.0523	0.0667	0.0209
$\langle \sigma (n, 15n) \rangle$	0.034	0.026	0.0332	0.0107

(continued)

Table 3.4 (continued)

$\langle \sigma \text{ (reactions)} \rangle$	²³² Th	²³³ U	²³⁵ U	²³⁸ U
	Spallation Fast Thermal	Spallation Fast Thermal	Spallation Fast Thermal	Spallation Fast Thermal
$\langle \sigma (n, p) \rangle$	0.371	0.51	0.42	0.35
$\langle \sigma (n, d) \rangle$	0.19	0.27	0.23	0.18
$\langle \sigma (n, t) \rangle$	0.05	0.11	0.09	0.06
$\langle \sigma (n, \text{He}^3) \rangle$	1.17×10^{-4}	1.25×10^{-4}	9.93×10^{-5}	8.30×10^{-5}
$\langle \sigma (n, \alpha) \rangle$	0.05	0.24	0.17	0.05
$\langle \sigma (n, np) \rangle$	1.15	1.51	1.33	1.07
$\langle \sigma (n, nd) \rangle$	0.17	0.18	0.16	0.16
$\langle \sigma (n, nt) \rangle$	0.06	0.09	0.08	0.05
$\langle \sigma (n, n\alpha) \rangle$	0.04	0.14	0.03	0.04
$\langle \sigma (n, n\text{He}^3) \rangle$	2.88×10^{-3}	5.64×10^{-3}	0.00487	3.35×10^{-3}
$\langle \sigma (n, pd) \rangle$	1.26×10^{-4}	2.54×10^{-4}	1.99×10^{-4}	1.84×10^{-4}
$\langle \sigma (n, npd) \rangle$	1.68×10^{-4}	7.23×10^{-4}	6.68×10^{-4}	2.74×10^{-4}
$\langle \sigma (n, 2p) \rangle$	4.93×10^{-4}	3.09×10^{-4}	3.33×10^{-4}	4.73×10^{-5}
$\langle \sigma (n, 2n\text{He}^3) \rangle$	4.98×10^{-3}	8.49×10^{-3}	5.25×10^{-3}	3.92×10^{-3}
$\langle \sigma (n, 2nd) \rangle$	0.18	0.25	0.23	0.14
$\langle \sigma (n, 2nt) \rangle$	0.11	0.14	0.12	0.10
$\langle \sigma (n, 2n\alpha) \rangle$	1.46×10^{-3}	3.86×10^{-3}	1.72×10^{-3}	6.91×10^{-4}
$\langle \sigma (n, 2npd) \rangle$	8.40×10^{-4}	1.57×10^{-3}	2.56×10^{-3}	7.64×10^{-4}
$\langle \sigma (n, n2p) \rangle$	4.31×10^{-3}	$5.62 \cdot 10^{-3}$	3.48×10^{-3}	3.31×10^{-3}
$\langle \sigma (n, 2np) \rangle$	0.44	0.39	0.39	0.40
$\langle \sigma (n, 2n2p) \rangle$	4.15×10^{-3}	0.0115	9.27×10^{-3}	4.86×10^{-3}
$\langle \sigma (n, 3np) \rangle$	1.39	1.56	1.56	0.99
$\langle \sigma (n, 3nd) \rangle$	0.34	0.40	0.34	0.25
$\langle \sigma (n, 3n\text{He}^3) \rangle$	3.11×10^{-3}	6.60×10^{-3}	4.85×10^{-3}	2.14×10^{-3}
$\langle \sigma (n, 3nt) \rangle$	0.35	0.38	0.16	0.18
$\langle \sigma (n, 3n\alpha) \rangle$	0.15	0.43	0.30	0.11

interaction can be written as $P_2 = \Sigma/\Sigma_t$ where Σ is the macroscopic cross section of a type of interaction. Thus, for $I_0 = 1$, neutron intensity, fraction probability of a particular type of interaction may be written as:

$$P_1 \cdot P_2 = (1 - \exp(-x\Sigma_t))(\Sigma/\Sigma_t) \quad (3.13)$$

Thus, the production of neutrons in the material filled in x thickness of the outer cylinder of Fig. 3.5 can be written as:

$$P = (1 - \exp(-x\Sigma_t)) \cdot [2\Sigma(n, 2n) + 3\Sigma(n, 3n) + 4\Sigma(n, 4n) \cdots + 9\Sigma(n, 9n) \cdots + \langle \nu \rangle \Sigma(n, f) + 2\Sigma(n, 2np) \cdots + 3\Sigma(n, 3n\alpha) + \cdots] / \Sigma_t \quad (3.14)$$

Here, $\langle \nu \rangle$ is the average number of fission neutrons, and this depends on the fuel element.

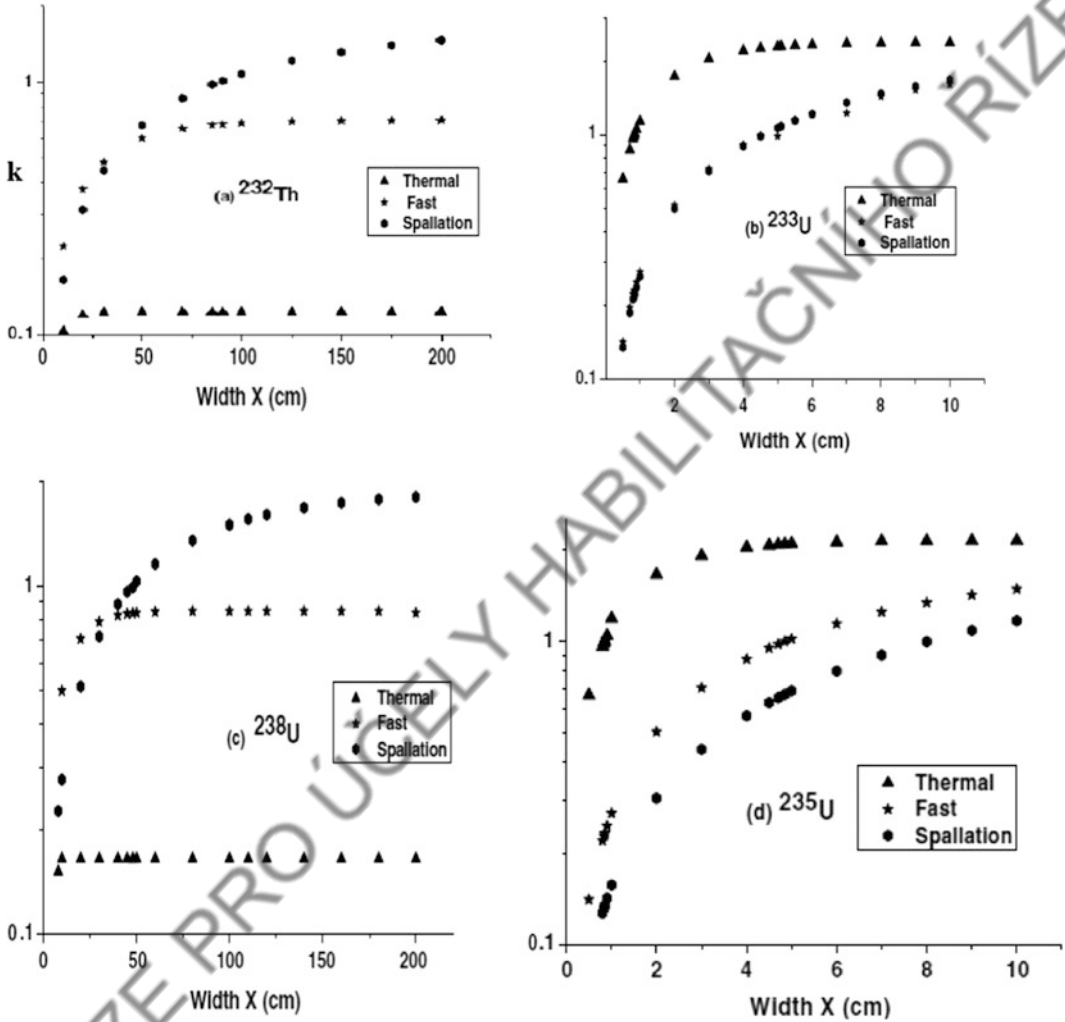


Fig. 3.7 Variation of neutron multiplication coefficient k with the thickness X (cm) for the thermal, fast, and the spallation neutron spectra for (a) ^{232}Th , (b) ^{233}U , (c) ^{238}U ,

and (d) ^{235}U fuel elements when irradiated by the thermal, fast, or spallation neutron spectra [60]

Similarly, removal term, R , for the process of removal, absorption, or utilization of neutrons in the reaction taking place in x thickness can be written as,

$$\begin{aligned}
 R = & (1 - \exp(-x\Sigma_t)) \cdot [(\Sigma(n, \gamma) + \Sigma(n, p) \\
 & + \Sigma(n, d) + \dots + \Sigma(n, np) \\
 & + \Sigma(n, 2n) \dots + \Sigma(n, 9n) + \dots + \Sigma(n, f) \\
 & + \Sigma(n, 2np) \dots + \Sigma(n, 3n\alpha) \dots] / \Sigma_t
 \end{aligned}
 \quad (3.15)$$

In this analysis, only those reactions are accounted that are initiated by neutrons. Other reactions that can contribute substantially are (γ, n) and (γ, f) -type reactions are avoided. Thus, the neutron multiplication coefficient k can be written as:

$$k = P / (R + L) \quad (3.16)$$

Here, L is the neutron loss in leakage. For incident neutron intensity to be unity, i.e., $R + L = 1$, the multiplication coefficient k can be

Table 3.5 Spectrum average cross sections for the neutron poisons in the given thermal, fast, and spallation neutron fluxes

Neutron poison	Spectrum average cross section		
	Thermal spectrum (b)	Fast spectrum (mb)	Spallation spectrum (mb)
$^{83}\text{Kr} (n, \gamma)$	48.46	205	29.29
$^{95}\text{Mo} (n, \gamma)$	5.80	247	47.27
$^{99}\text{Tc} (n, \gamma)$	15.25	514	78.29
$^{101}\text{Ru} (n, \gamma)$	3.12	567	68.26
$^{103}\text{Rh} (n, \gamma)$	51.35	479	72.68
$^{105}\text{Pd} (n, \gamma)$	6.33	719	104.62
$^{107}\text{Pd} (n, \gamma)$	2.93	762	119.11
$^{133}\text{Cs} (n, \gamma)$	19.15	381	56.34
$^{135}\text{Xe} (n, \gamma)$	8.19×10^5	52.5	10.09
$^{143}\text{Nd} (n, \gamma)$	76.32	214	45.55
$^{147}\text{Pm} (n, \gamma)$	103.12	936	153.69
$^{149}\text{Sm} (n, \gamma)$	25,070.44	1,600	199.86

calculated [60] from the value of P . For the three isotopes of uranium and ^{232}Th on filling in the outer cylinder of design of Fig. 3.5(b) one by one in different thicknesses, x results are presented in Fig. 3.7(a)–(d) for ^{232}Th , ^{233}U , ^{238}U , and ^{235}U , respectively. From this, the following inferences can be drawn,

- (i) Both the fertile fuels ^{232}Th and ^{238}U reach a critical limit, $k = 1$, in case of spallation neutrons, and the required fuel thickness comes out to be ~ 100 cm. In a fast reactor, ^{232}Th fuel attains a maximum value, $k = 0.5$, while ^{238}U attains $k = 0.8$.
- (ii) In case of fissile fuels ^{233}U and ^{235}U , both fast and spallation neutron spectra work similarly for attaining a value $k = 1$ at ~ 6 cm. Thermal flux is better for early attainment of $k > 1$ value than fast and spallation spectra.
- (iii) In case of ^{235}U , multiplication coefficient k attains a value differently to ^{233}U in the three neutron spectra. At a given thickness, X value of k follows:
 $k_{\text{Therm}} > k_{\text{Fast}} > k_{\text{Spall}}$.

In critical reactors, nuclides ^{133}Cs , ^{101}Ru , ^{103}Rh , ^{99}Tc , ^{105}Pd , ^{107}Pd , and ^{149}Sm are treated as the neutron poisons in the lead-bismuth cooled fast breeder reactor [61] and ^{83}Kr , ^{95}Mo , ^{143}Nd ,

^{147}Pm , ^{135}Xe , and ^{149}Sm in the thermal flux environment [62]. For the spectrum of spallation neutrons given in Fig. 3.6, the sp. av. cs. are calculated [60] neutron poisons and presented in the last column of Table 3.5 along with the thermal and fast spectra. From the data, it may be inferred that the given neutron poisons of thermal and fast reactors are least effective in case of spallation neutrons and their neutron absorption cross sections can be put in the following order:

$$\sigma^{\text{sp.av.cs.}}(\text{thermal}) > \sigma^{\text{sp.av.cs.}}(\text{fast}) > \sigma^{\text{sp.av.cs.}}(\text{spallation})$$

3.3 Utilization of Spallation Neutrons by a Fuel

Utilization of spallation neutrons is better visualized [60] by imparting neutron on a big block of ^{232}Th , say, with $X = 81.7$ cm and similarly on a block of fissile ^{233}U , say, with $X = 4.5$ cm. Calculated results of contributions of various reactions to the P and R terms using Eqs. (3.14) and (3.15) are presented in Table 3.6.

Neutron multiplication by way of (n, f) reaction in ^{232}Th corresponding to $X = 81.7$ cm thickness of the outer fuel cylinder of Fig. 3.6 is $0.150/0.982 = 15.27\%$ per incident spallation neutron. This also means that spallation neutrons

Table 3.6 Details of removal (R) and production (P) per incident neutron for ^{232}Th and ^{233}U fuel elements filled in the two different thicknesses 'X' of cylinder independent to each other

Channel	Removal, R	Production, P	Removal, R	Production, P
	^{232}Th ($X = 81.7$ cm)		^{233}U ($X = 4.5$ cm)	
(n, γ)	0.251	–	7.14×10^{-3}	–
($n, 2n$)	0.128	0.257	4.73×10^{-3}	9.46×10^{-3}
($n, 3n$)	7.10×10^{-2}	0.2129	2.21×10^{-3}	6.64×10^{-3}
($n, 4n$)	1.54×10^{-2}	6.16×10^{-2}	1.12×10^{-3}	4.49×10^{-3}
($n, 5n$)	2.08×10^{-2}	0.104	1.96×10^{-3}	9.82×10^{-3}
($n, 6n$)	1.20×10^{-2}	7.18×10^{-2}	5.84×10^{-4}	3.50×10^{-3}
($n, 7n$)	1.20×10^{-2}	8.37×10^{-2}	2.44×10^{-4}	1.71×10^{-3}
($n, 8n$)	1.47×10^{-3}	1.17×10^{-2}	1.42×10^{-4}	1.13×10^{-3}
($n, 9n$)	9.50×10^{-4}	8.60×10^{-3}	1.14×10^{-4}	1.02×10^{-3}
($n, 10n$)	9.02×10^{-4}	9.02×10^{-3}	7.99×10^{-5}	7.99×10^{-4}
($n, 11n$)	1.05×10^{-3}	1.15×10^{-2}	3.43×10^{-5}	3.77×10^{-4}
($n, 12n$)	1.07×10^{-4}	1.28×10^{-3}	4.56×10^{-6}	5.47×10^{-5}
($n, 13n$)	1.84×10^{-4}	2.38×10^{-3}	1.92×10^{-5}	2.49×10^{-4}
($n, 14n$)	9.85×10^{-5}	1.38×10^{-3}	8.93×10^{-6}	1.25×10^{-4}
($n, 15n$)	5.74×10^{-5}	8.60×10^{-4}	4.35×10^{-6}	6.53×10^{-5}
(n, p)	6.40×10^{-4}	–	8.70×10^{-5}	–
(n, d)	3.26×10^{-4}	–	4.58×10^{-5}	–
(n, t)	8.47×10^{-5}	–	1.72×10^{-5}	–
(n, He^3)	1.95×10^{-7}	–	2.13×10^{-8}	–
(n, α)	8.14×10^{-5}	–	4.01×10^{-5}	–
(n, f)	6.01×10^{-2}	0.150	0.377	0.940
(n, np)	2.59×10^{-3}	2.60×10^{-3}	2.58×10^{-4}	$2.60 \cdot 10^{-4}$
(n, nd)	2.95×10^{-4}	2.95×10^{-4}	3.01×10^{-5}	3.01×10^{-5}
(n, nt)	1.01×10^{-4}	1.01×10^{-4}	1.58×10^{-5}	1.58×10^{-5}
($n, n\text{He}^3$)	4.95×10^{-6}	4.94×10^{-6}	9.63×10^{-7}	9.63×10^{-7}
(n, na)	7.60×10^{-5}	7.60×10^{-5}	2.34×10^{-5}	2.33×10^{-5}
($n, 2p$)	8.23×10^{-7}	–	5.27×10^{-8}	–
(n, pd)	2.10×10^{-7}	–	4.33×10^{-8}	–
($n, n2p$)	7.39×10^{-6}	7.39×10^{-6}	9.59×10^{-7}	9.59×10^{-7}
($n, 2np$)	2.48×10^{-3}	4.97×10^{-3}	2.27×10^{-4}	4.53×10^{-4}
($n, 2na$)	8.08×10^{-5}	1.62×10^{-4}	2.08×10^{-5}	4.16×10^{-5}
($n, 2nd$)	3.09×10^{-4}	6.18×10^{-4}	4.26×10^{-5}	8.53×10^{-5}
($n, 2nt$)	1.78×10^{-4}	3.55×10^{-4}	2.41×10^{-5}	4.81×10^{-5}
($n, 2nz$)	8.55×10^{-6}	1.71×10^{-5}	1.45×10^{-6}	2.90×10^{-6}
($n, 2npd$)	1.44×10^{-6}	2.88×10^{-6}	2.69×10^{-7}	5.37×10^{-7}
($n, 2n2p$)	7.12×10^{-6}	1.42×10^{-5}	1.97×10^{-6}	3.94×10^{-6}
($n, 3np$)	2.38×10^{-3}	7.13×10^{-3}	2.66×10^{-4}	7.98×10^{-4}
($n, 3nd$)	5.81×10^{-4}	1.74×10^{-3}	6.85×10^{-5}	2.06×10^{-4}
($n, 3nt$)	6.05×10^{-4}	1.82×10^{-3}	6.39×10^{-5}	1.92×10^{-4}

(continued)

Table 3.6 (continued)

Channel	Removal, R		Production, P	
	^{232}Th ($X = 81.7$ cm)		^{233}U ($X = 4.5$ cm)	
$(n, 3n\text{He}^3)$	5.33×10^{-6}	1.60×10^{-5}	1.13×10^{-6}	3.38×10^{-6}
$(n, 3na)$	2.57×10^{-4}	7.71×10^{-4}	7.32×10^{-5}	2.19×10^{-4}
Sum	0.684	0.981	0.397	0.981
k_{eff}	0.982		0.981	
No. of atoms (mass)	4.26×10^{28} (16.39 ton)		8.33×10^{26} (0.32 ton)	

generate nearly 84.73% more neutrons by the reactions other than fission processes, and these processes are not so important in case of fissile materials. In case of ^{233}U for thickness, $X = 4.5$ cm, contribution of (n, f) process is 95.82% per incident spallation neutron and other nuclear processes contribute only 4.18% toward neutron multiplication. In the following, a simple way of calculation of fission energy by the spallation neutrons is presented.

Energy Production in 81.7 cm Thick ^{232}Th

According to CASCADE code ver. 2004, in case of 1,000 MeV proton colliding with Pb target of size $d \times L = 20 \times 50$ cm², on an average 24.3 spallation neutrons/p are expected to be produced. Thus, in passing through 81.7 cm thickness of ^{232}Th , there are:

- (i) Applied neutrons/p = $0.982 \times 24.3 = 23.86$ n/p
- (ii) Neutrons used for fission = $23.86 \times 0.15 = 3.58$ n/p
- (iii) Neutrons, not involved in fission = $23.86 - 3.58 = 20.28$ /p
- (iv) Fission energy production, $H_{0,232} = 3.58 \times 186.7 = 669.3$ MeV/p

Energy Production in 4.5 cm thick ^{233}U

- (i) Neutrons used for fission = $23.86 \times 0.94 = 22.43$ n/p
- (ii) Neutrons, not involved in fission = 1.43/p
- (iii) Fission energy produced, $H_{0,233} = 22.43 \times 197.9 = 4,438.6$ MeV/p

This is ~ 4.4 times higher than input energy 1,000 MeV/p incident energy.

Let us assume that all of the P -neutrons involved in fission is multiplied in each subsequent cascade process over an infinite volume of the subsequent fuel as does in a reactor; then, energy production may be expressed as,

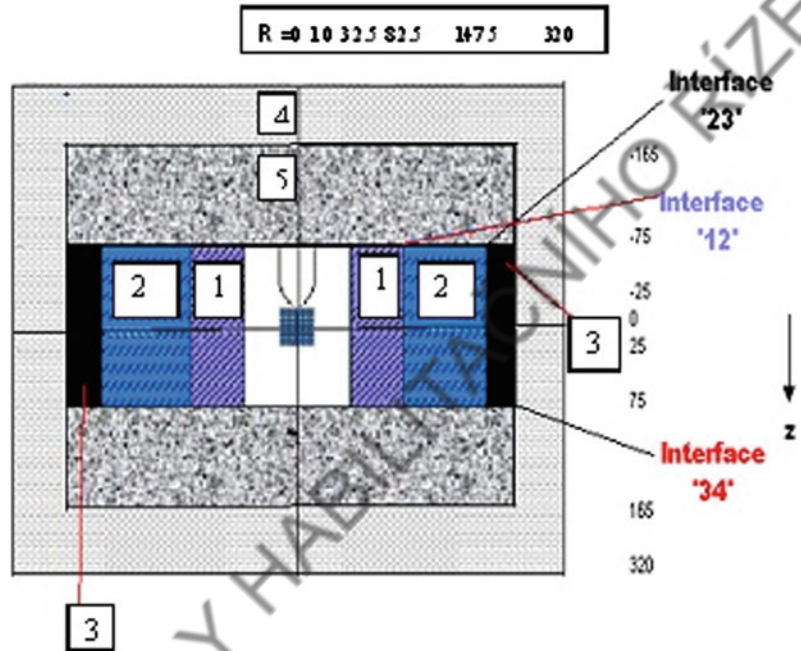
$$H = H_0 \left(\frac{k_{\text{eff}}}{1 - k_{\text{eff}}} \right) \quad (3.17)$$

Thus, the ^{232}Th alone produces heat $\sim 669.3 \times 54.555 = 36,514$ MeV/p, and in case of ^{233}U , heat is $\sim 242,150$ MeV/p for the assumption that $k_{\text{eff}} = k = 0.982$. The weighted average of energy due to the mass-mixture of ^{232}Th and ^{233}U corresponding to the given thickness is expected to yield 40,444 MeV/p which is equivalent to energy gain, $G \sim 40.44$.

3.3.1 IAEA Benchmark Design

In order to access the basic requirements of an ADSS system, i.e., beam, target system, neutron fluence, and strategy of energy and transmutation of the SNF, IAEA floated [63, 64] a hypothetical design of 1,500 MW_{th} ADS reactor (see Fig. 3.8) based on the Th-U fuel cycle. This is termed as IAEA benchmark. The IAEA-ADS benchmark provides an opportunity of mathematical modeling of a future ADS that may help in conducting various experiments and to settle down various questions which normally arise for the design and modeling of the device. The questions can be what will be the (i) neutron flux distribution in different parts/regions of the benchmark assembly (ii) neutron multiplication factor, (iii) transmutation potential (iv) criticality and (v) produced energy distribution. In this direction, a large number of simulation calculations

Fig. 3.8 XZ-cross-sectional view of the ADS benchmark design. The whole structure is in cylindrical shape of dimensions $2R \times L = 640 \times 640 \text{ cm}^2$ [63, 64]



have been performed in different laboratories all over the world.

At first stage of the benchmark, verification of reactivity, burn-up swing as well as some reactivity effects for a fast neutron spectrum from an external spallation-type neutron source at different subcriticality levels like $k_{\text{eff}} = 0.94, 0.96,$ and 0.98 are proposed [63] for the development of a $1,500 \text{ MW}_{\text{th}}$ ADS. In this direction, an important work for determination of concentration of ^{233}U with respect to $^{233}\text{U} + ^{232}\text{Th}$ fuel mixture is done by Carminati and Kady [63]. They estimated percentage of concentration of ^{233}U in $^{233}\text{U} + ^{232}\text{Th}$ mixture using JENDL-3.2 and JEFF-2.2 nuclear data libraries for the criticality $k_{\text{eff}} = 0.982, 0.962,$ and 0.941 . Similarly, an important simulation using MCNP code [36] for neutron multiplication and flux distributions is done by Tueck et al. [64]. They also estimated the concentration of ^{233}U in the core region as function of k_{eff} using MCNP code. It is pointed out when the proportion of ^{233}U increases with respect to ^{232}Th , then k_{eff} improves and it moves toward the criticality level. They have also plotted ratio of spectrum averaged fission cross sections $\langle \sigma_f(^{232}\text{Th}) / \sigma_f(^{233}\text{U}) \rangle$ as function of radial position and established that for lower k_{eff} , the ratio is

high at origin of the core and the ratio decreases toward outer region. Also, for simulation of transmutation and burn-up, an advance code Monte Carlo continuous energy burn-up code (MCB) developed by Cetnar [65] is used. The code is a combination of MCNP-4B code [36] for burn-up calculation and transmutation trajectory analysis (TTA) code [66] for the transmutation calculations. They have studied transmutation of ^{99}Tc and compared with the results of simulation from the MCNP-origin [36] computation system, and it is shown that the results are in good agreement. In another MC simulation approach using the Dubna CASCADE code [29, 35] alone, spallation n -distribution and power density as a function of radial distance and criticality [51] are calculated and results are found to be in good qualitative agreement with results presented by Tueck et al. [64] using the MCNP code. Some of the features of characteristic ADS benchmark reactor and results of calculations by Kumar [51] using the CASCADE code ver. 2004 are discussed in the following.

A cross-sectional view of hypothetical design of ADS benchmark reactor is shown in Fig. 3.8 with fuel and shielding features. At its center, a spallation lead target of dimensions $d \times L = 20$

Table 3.7 Nuclei densities (BOL at 20 °C) of elements in the five regions of the benchmark

Nuclei	Region 1	Region 2	Region 3	Region 4	Region 5
^{232}Th	–	–	7.45E–3	–	–
$^{233}\text{U} + ^{232}\text{Th}$	6.35E–3	7.45E–3	–	–	–
O	1.27E–2	1.49E–2	1.49E–2	–	–
Fe	8.10E–3	8.87E–3	8.87E–3	–	6.63E–3
Cr	1.12E–3	1.06E–3	1.06E–3	–	8.00E–4
Mn	4.60E–5	5.10E–5	5.10E–5	–	3.80E–5
W	4.60E–5	5.10E–5	5.10E–5	–	3.80E–5
Pb	1.77E–2	1.56E–2	1.56E–2	3.05E–2	2.41E–2

50 cm² is placed in vacuum spread over 32.5 cm radial distance. A beam pipe is shown just above the target. Regions marked as ‘1’ and ‘2’ are filled with different mixtures of ^{232}Th and ^{233}U fuels. Region ‘3’ is filled with ^{232}Th alone as a fuel. The compositional details of the five regions are given in Table 3.7.

In Table 3.7, elements other than the nuclear fuel ^{232}Th and ^{233}U correspond to the RCC structure, plenum and other structural materials. Using the spallation neutron spectrum of Fig. 3.6 and the Dubna CASCADE code ver. 2004 MC simulation of the transport of n -spectrum through the regions ‘1’ to ‘3’ have been performed [51] for different proportions of ^{232}Th and ^{233}U in regions ‘1’ and ‘2’ and ^{232}Th alone filled in region ‘3’ to obtain a desired value of k_{eff} . In Table 3.8, data of fuel composition corresponding to the three values of k_{eff} is given from which it is evident that with the fissile enrichment, k_{eff} increases.

3.3.2 Neutron Flux in Different Regions

In order to investigate the possibility of an appropriate region for the transmutation of a kind

of a LLNW, what kind of neutron fluence is required. In a MC simulation by the CASCADE ver. 2004 code, a narrow detector is assumed at the interfaces of regions ‘1’, ‘2’, and ‘3’ while building the input file of the code. An example of building such file is described in appendix of reference [47].

- (i) **Target region:** In the target region, accelerated proton beam of energy 1 GeV collides with the lead target to produce spallation neutrons. Energy spectrum of neutrons is presented in Fig. 3.6. Axial distribution of produced neutrons is not uniform all along the Z-axis but skewed showing maxima at axial distance $Z = 15\text{--}20$ cm [47].
- (ii) **Neutron distribution at interfaces of 1, 2, 3, and 4 regions:** Neutron distributions at the boundaries between the two regions are calculated assuming presence of a neutron detector of 1 cm width placed in between the two adjoining regions. In Fig. 3.9, neutron flux ($n/\text{cm}^2/\text{p}$) has been plotted for the ‘12’, ‘23’, and ‘34’ boundaries for the three k_{eff} values by changing the fuel composition as given in Table 3.8. In the insets

Table 3.8 Different enrichment of ^{232}Th by ^{233}U and effective neutron multiplication, k_{eff}

k_{eff}	Region 1			Region 2		
	^{233}U	^{232}Th	$^{233}\text{U}/[^{233}\text{U} + ^{232}\text{Th}]$ (%)	^{233}U	^{232}Th	$^{233}\text{U}/[^{233}\text{U} + ^{232}\text{Th}]$ (%)
0.923	0.0113	0.1266	8.19	0.0127	0.1426	8.18
0.964	0.0121	0.1257	8.78	0.0137	0.1416	8.82
0.979	0.0125	0.1253	9.07	0.0141	0.1412	9.08

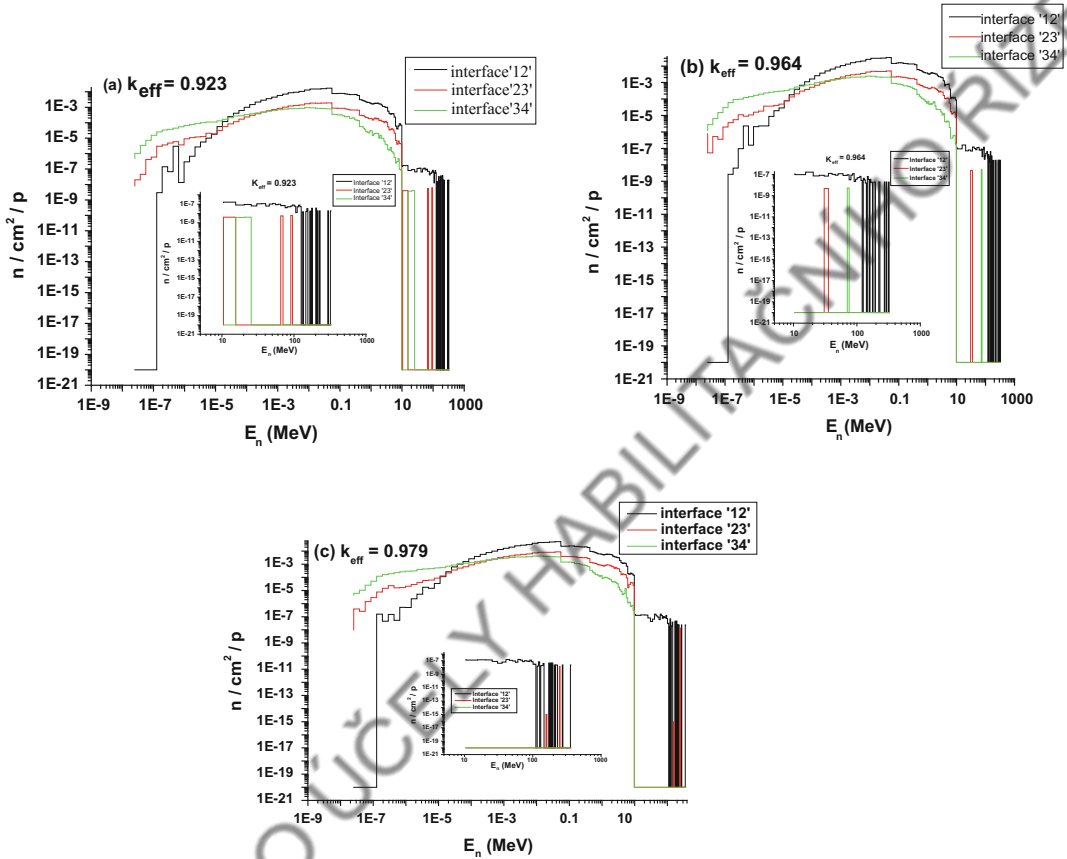


Fig. 3.9 Neutron fluxes ($n/\text{cm}^2/\text{p}$) at the three interfaces of the IAEA benchmark with $k_{\text{eff}} = 0.923, 0.964,$ and 0.979 calculated from the CASCADE ver. 2004 are displayed [47]

of the three (a), (b) and (c), plots elaborated distributions of high-energy neutrons from 10 MeV to highest energy are given.

For summarizing the neutron growth at boundaries, '12', '23', and '34', the flux is categorized in the following three ranges and listed in Table 3.9. The flux corresponds to multiplication of spallation neutrons of 1 GeV $p + \text{Pb}$ collision after transport through the fuel and structure materials assumed in the IAEA benchmark design as given above.

- (i) Range I: $E_n = 0.25 \text{ eV} < E_n \leq 1 \text{ eV}$ (thermal + epithermal range)
- (ii) Range II: $1 \text{ eV} < E_n \leq 0.1 \text{ MeV}$ (resonance range) and

- (iii) Range III: $0.1 \text{ MeV} < E_n \leq \text{maximum energy}$

From the flux data displayed in Table 3.9, the following observations can be made:

- (a) For the three k_{eff} values, flux of thermal + epithermal neutrons of range I increases from inner region to the outer region, while neutron fluxes at other two higher energies decrease.
- (b) Total neutron flux reaching boundary '34' from the boundary '12' increases as 6.3, 8.5, and 9.4% for the three cases of $k_{\text{eff}} = 0.923, 0.964,$ and 0.979 , respectively. Naturally, always more than 6% neutrons are reaching to the shielding wall, i.e., region 4 of the proposed benchmark design.

Table 3.9 Number of neutrons per unit area per incident proton ($n/\text{cm}^2/\text{p}$) and absolute flux ($n/\text{cm}^2/\text{s}$) at interfaces '12', '23', and '34' for $k_{\text{eff}} = 0.923, 0.964, \text{ and } 0.979$ in the three neutron energy ranges

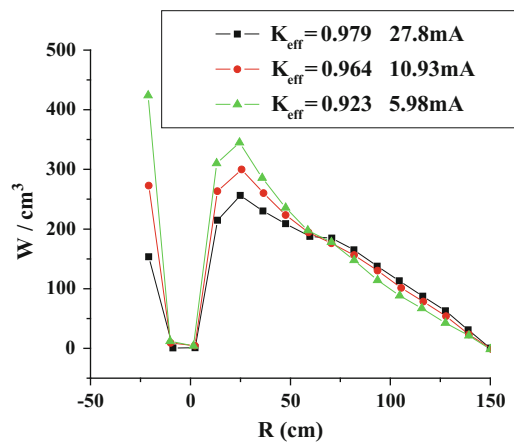
k_{eff} , beam current		n/cm ² /p in neutron energy range			Total (n/cm ² /p)	Flux (n/cm ² /s)
		0.025 < E_n ≤ 1 eV	1 eV < E_n ≤ 0.1 MeV	0.1 < E_n ≤ 326 MeV		
0.923 , 27.8 mA	'12'	3.20E-06	1.51E-01	0.97E-01	0.248	4.3152E+16
	'23'	2.21E-05	1.99E-02	9.92E-03	0.0298	5.1852E+15
	'34'	2.22E-04	1.33E-02	2.27E-03	0.0158	2.7492E+15
0.964 , 10.93 mA	'12'	2.55E-06	2.89E-01	1.95E-01	0.484	3.3057E+16
	'23'	4.37E-05	5.07E-02	26.0E-03	0.0767	5.2386E+15
	'34'	5.70E-04	3.42E-02	6.15E-03	0.0409	2.7934E+15
0.979 , 5.98 mA	'12'	9.26E-07	4.51E-01	3.08E-01	0.759	2.8386E+16
	'23'	8.41E-05	8.75E-02	45.90E-03	0.134	5.0116E+15
	'34'	1.07E-03	5.85E-02	11.0E-03	0.071	2.6554E+15

- (c) In case of $k_{\text{eff}} = 0.979$ criticality, among the total neutron spectrum reaching at the boundary '34', there are $\sim 15.5\%$ neutrons with high energy $0.1 < E_n \leq 326$ MeV. They can be highly useful for transmutation of elements of the nuclear waste. Already, in the structure, thorium is filled in region '3' to be burnt by the hard spectrum. At the same time, it helps in stopping the outgoing flux.
- (d) At $k_{\text{eff}} = 0.979$, neutron flux escaping to the shielding through the boundary '34' is unique and nearly flatly distributed from the thermal to the fast reactor energies. Also, it is ~ 30 times more than the flux of a thermal reactor. In fact, this enhances possibility that a strong thermal reactor can be allowed to operate on the basis of this neutron strength.

in case of $k = 0.979$ respectively for the same power of the reactor. Corresponding to the three current values, the proton beam intensities are 1.74×10^{17} (p/s), 6.83×10^{16} (p/s), and 3.74×10^{16} (p/s), respectively. Neutron flux calculated for the 27.8, 10.93, and 5.98 mA currents for the three criticalities k_{eff} of the reactor are also given in the last column of Table 3.9 separately for the three boundaries between four regions of the reactor shown in Fig. 3.8. Radial heat distribution is also calculated using the CASCADE code ver. 2004 code [51] and given in Fig. 3.10 showing a peak in the

3.3.3 Accelerator Current and Radial Heat Distribution

One ampere current is equivalent to 6.25×10^{18} p/s and for the assumed heat production of 54,000 MeV/p, there will be heat rate 3.375×10^{23} MeV/s which is equivalent to 5.4×10^4 MW. For a hypothetical reactor of 1,500 MW_{th}, one needs 27.8 mA current and this corresponds to $k = 0.923$. It will be much less current ~ 10.93 mA for $k = 0.964$ and 5.98 mA

**Fig. 3.10** Heat density (W/cm^3) as a function of radial distance R of the IAEA benchmark design for the three criticalities k_{eff} [51]

target region and another peak at $R \sim 50$ cm in the fuel region as the fuel ranges from $R = 32$ to 150 cm. Heat distribution corresponding to $k_{\text{eff}} \sim 0.979$ is flatter than at smaller k_{eff} and varies from 0 to 350 W/cm³.

In the end, it may be concluded that the calculated neutron flux in different positions of a reactor can be exploited for the investigations of transmutation of the LLNW and utilization of fertile fuels like ²³²Th and ²³⁸U.

References

- Bothe, W., Becker, H.: Künstliche erregung von kern- γ -strahlen. *Z. Physik.* **66**, 289 (1930)
- Chadwick, J.: *Proc. Royal Soc. (London). Ser. A* **136**, 692 (1932). Lorch, E.A.: Original Am-Be neutron source spectrum. *Int. Jpn. Appl. Radiat. Isot.* **24**, 585 (1973)
- Serber, R.: Nuclear reactions at high energies. *Phys. Rev.* **72**, 1114 (1947)
- Rubbia, C., et al.: Conceptual design of a fast neutron operated high power energy amplifier. CERN Report CERN/AT/95-44 (ET)
- Rubbia, C.: A high gain energy amplifier operated with fast neutrons. In: AIP Conference Proceedings 346, International Conference on Accelerator-Driven Transmutation Technologies and Applications, Las Vegas (NV), US (1994)
- SINQ: The Swiss Spallation Neutron Source. <http://www.psi.ch/sinq/>
- ISIS: ISIS Neutron and Muon Source. <http://www.isis.stfc.ac.uk>
- SNS: Neutrons for New Discoveries and Solutions. <http://neutrons.ornl.gov>
- Futakawa, M., et al.: 1-MW Pulsed Spallation Neutron Source (JSNS) at J-PARC. *Neutron News* **22**, 15–19. JSNS. <http://j-parc.jp/MatLife/en/index.html> (2011)
- Henderson, S., et al.: The Spallation Neutron Source accelerator system design. *Nucl. Inst. Methods Phys. Res. A* **763**, 610 (2014)
- David, J.-C.: Spallation Reactions. A Successful Interplay between Modeling and Applications. [arXiv: 1505.03282v1](https://arxiv.org/abs/1505.03282v1) [nucl-ex], 13 May 2015
- Kumar, V., et al.: Neutron spallation source and the Dubna Cascade Code. *Pramana-Jpn. Phys.* **60**, 469 (2003)
- Hilsher, D., et al.: Neutron multiplicity distribution for GeV proton induced spallation reactions on thin and thick targets of Pb and U. In: Proceedings of the International Workshop on Nuclear Methods for Transmutation of Nuclear Waste, edited by Khan-khasayev, M.Kh., Plendl, H.S., Kurmanov, Z.B., p. 176 (1996)
- Lee, Y.Y., et al.: *Proc. ICANS-XIII PSI-Proc.* **95** (02), 802 (1995)
- Polański A., Słowiński, B.: Neutron fields produced in heavy spallation targets by electron beams. In: International Conference on Recent Developments and Applications of Nuclear Technologies, 15–17 September 2008. Also see, Polański, A., Słowiński, B., Jackowski, T., Pacan, A.: Neutrons production in heavy extended targets by electrons of energy from 15 to 1000 MeV. *Prog. Nucl. Energy* **78**, 1 (2015). Also see <http://dx.doi.org/10.1016/j.pnucene.2014.07.009>
- Auditore, L., et al.: Study of a 5 MeV electron linac based neutron source. *Nucl. Instr. Methods Phys. Res. B* **229**, 137 (2005)
- Roberts, J.A.: The Los Alamos Neutron Science Center (LANSCE). *Neutron News* **10**(4), 11 (1999)
- Mason, T.E., et al.: Spallation Neutron Source in Oak Ridge: a powerful tool for materials research. *Phys. B* **385**, 955 (2006). Also see, <http://neutrons.ornl.gov/>
- Gabriel, T., et al.: Overview of the Spallation Neutron Source (SNS) with emphasis on target systems. *J. Nucl. Mater.* **318**, 1 (2003)
- Eccleston, R., Wilson, C.: Correspondent's reports: a guided tour of ISIS: 2004 update. *Neutron News* **15** (1), 15 (2004)
- Penfold, J.: Scientific review: ISIS second target station: overview and progress. *Neutron News* **15**(2), 9 (2004)
- Wagner, W., et al.: The Swiss spallation neutron source SINQ—developments and upgrades for optimized user service. *Phys. B* **385**, 968 (2006)
- Wagner, W.: The Swiss Spallation Neutron Source SINQ-Layout, Operation, Utilization and R&D for Optimized Neutron Yield. *Proc. ICANS-XVI* **53** (2003). ISSN 1433-559X
- Arai, M., Maekawa, F.: Japan Spallation Neutron Source (JSNS) of J-PARC. *Nucl. Phys. News* **19**(4) (2009)
- Maekawa, F., et al.: First neutron production utilizing J-PARC pulsed spallation neutron source JSNS and neutronic performance demonstrated. *Nucl. Inst. Methods Phys. Res. A* **620**, 159 (2010)
- Westmeier, W., et al.: Transmutation experiments on ¹²⁹I, ¹³⁹La and ²³⁷Np using the Nuclotron accelerator. *Radiochim. Acta* **93**, 65 (2005)
- Adam, J., Barashenkov, V.S., et al.: Measurement of the neutron fluence on the spallation source at Dubna. *Kerntechnik* **70**, 127 (2005)
- Krivopustov, M.I., et al.: First experiments on transmutation studies of ¹²⁹I and ²³⁷Np using relativistic protons of 3.7 GeV. *J. Radioanalytical Nucl. Chem.* **222**, 267 (1997). JINR Dubna preprint E1-97-59. Krivopustov, M.I., et al.: First experiments with a large uranium blanket within the installation energy plus transmutation exposed to 1.5 GeV protons. *Kerntechnik* **68**, 48 (2003)
- Barashenkov, V.S., et al.: Mathematical model of the electronuclear set-up on the beam of JINR synchrotron. *Nucl. Inst. Methods B* **217**, 352 (2004)

30. Adam, J., et al.: A study of nuclear transmutation in Pb-target and U-blanket irradiated by 1.6 GeV deuteron. *Eur. Phys. J. A* **43**, 159 (2010). Adam, J. et al.: A study of reaction rates of (n, f), (n, g) and (n, 2n) reactions in U^{nat} and Th^{232} by the neutron fluence produced in the graphite set up (GAMMA 3) irradiated by 2.33 GeV deuteron beam. *Eur. Phys. J. A* **47**, 85 (2011)
31. Adam, J., et al.: Measurement of the high energy neutron flux on the surface of the natural uranium target assembly QUINTA irradiated by deuterons of 4 and 8 GeV energy. *Phys. Proc.* **80**, 94 (2015)
32. Shvetsov, V., et al.: The Subcritical Assembly in Dubna (SAD)-Part I: coupling all major components of an Accelerator Driven System (ADS). *Nucl. Instr. Methods Phys. Res. A* **562**, 883 (2006). Gudowski, W., et al.: The Subcritical Assembly in Dubna (SAD)-Part II: research program for ADS-demo experiment. *Nucl. Instr. Methods Phys. Res. A* **562**, 887 (2006)
33. Abanades, A., et al.: Results from the TARC experiment: spallation neutron phenomenology in lead and neutron-driven nuclear transmutation by adiabatic resonance crossing. *Nucl. Instr. Methods Phys. Res. A* **478**, 577 (2002)
34. Borcea, C., et al.: Results from the commissioning of the n_TOF spallation neutron source at CERN. *Nucl. Instr. Methods Phys. Res. A* **513**, 524 (2003)
35. Barashenkov, V.S.: Monte Carlo simulation of ionization and nuclear processes initiated by hadron and ion beams in media. *Comp. Phys. Commun.* **126**, 28 (2000)
36. Breisemeister, J.F. (ed.): LA-12625-M, MCNP (A General Monte Carlo N-Particle Transport Code, Version 4A). Los Alamos National Laboratory, Los Alamos, New Mexico, issued (November, 1993)
37. Tagliente, G.: n_TOF collaboration: the n_TOF facility at CERN. *Brazilian J. Phys.* **34**(3A) (September, 2004)
38. Maglioni, C.: CERN EN-STI-TCD, Pb/Bi loop target for EURISOL kick-off meeting, 5/10/2012. <http://pceet075.cern.ch/> and http://www.efnudat.org/FZD_workshop/Wednesday/1302-1000_Vlachoudis.pdf
39. Neutron Cross Section Measurements at n-TOF for ADS Related Studies. <http://iopscience.iop.org/article/10.1088/1742-6596/41/1/038/pdf;jsessionid=4A1B8122075DBA37D070F7B8C2B513DE.c5.iopscience.cld.iop.org>
40. Snow, W.M.: Neutron Physics. <https://www.bnl.gov/nps/files/pdf/SnowNPSS1.pdf>
41. Nelson, R.O., et al.: Stockpile stewardship and nuclear science with GEANIE at LANSCE/WNR, LLNL. Physics Division, Progress Report, Chapter 2, 64. <http://wnr.lanl.gov/>; <http://www.geanie.lanl.gov/> (1996)
42. Bol, A., et al.: A novel design for a fast intense neutron beam. *Nucl. Instr. Meth.* **214**, 169 (1983)
43. Kerveno, M., et al.: Measurement of ^{232}Th (n, 5n γ) cross sections from 29 to 42 MeV. In: International Conference on Nuclear Data for Science and Technology (2007). <https://doi.org/10.1051/ndata:07415>
44. Kim, G.N.: Proceedings of LINAC, p. 383, Gyeongju, Korea. <http://accelconf.web.cern.ch/AccelConf/I02/PAPERS/TU432.PDF> (2002)
45. Salomé, J.M., et al.: Neutron producing targets at GELINA. *Nucl. Instr. Methods* **179**, 13 (1981). Mihailescu, L.C., et al.: A new HPGe setup at Gelina for measurement of gamma-ray production cross-sections from inelastic neutron scattering. *Nucl. Instr. Methods Phys. Res. A* **531**, 375 (2004)
46. Antropov, V., et al.: IREN Test Facility at JINR. <http://linac96.web.cern.ch/Linac96/Proceedings/Tuesday/TUP68/Paper.html>
47. Sharma, M.: Transmutation of long-lived isotopes of conventional reactors using A.D.S. Concept. Ph.D. thesis, University of Rajasthan, Jaipur (2010)
48. Katovsky, K.: Investigation of secondary neutrons and nuclei generated in reactions of high-energy protons and neutrons in uranium and plutonium targets. Ph.D. thesis, CTU, Prague (2008)
49. Bhatia, C., Kumar, V.: Role of (n, xn) reactions in Accelerator Driven Sub critical Systems. Published by LAP LAMBERT Academic Publishing GmbH & Co. KG (2011)
50. Kumar, V., et al.: CASCADE data for the A.D.S. materials for it benchmarking. In: Proceedings ARIA 2008, 1st Workshop on Accelerator Radiation Induced Activation, 13–17 October 2008, Paul Scherrer Institute, Switzerland. PSI Proceedings 09–01. ISSN 1019–0643, 30 (2009)
51. Kumar, V.: Role of (n, xn) reactions in ADS, IAEA-Benchmark and the Dubna CASCADE Code Pramana. *J. Phys.* **68**, 315 (2007)
52. Koning, A.J., et al.: Proceedings of the International Conference on Nuclear Data for Science and Technology, Santa Fe, USA, 26 September–1 October 2004 and www.talys.eu/
53. Barashenkov, V.S., et al.: CASCADE program complex for Monte-Carlo simulation of nuclear processes initiated by high energy particles and nuclei in gaseous and condensed matter. JINR preprint R2-85-173 (1985). Barashenkov, V.S.: A cascade-evaporation model for photonuclear reactions. *Nucl. Phys. A* **231**, 462 (1974)
54. Kim, E., et al.: Measurements of neutron spallation cross sections of ^{12}C and ^{209}Bi in the 20- to 150-MeV energy range. *J. Nucl. Sci. Eng.* **129**, 209 (1998)
55. Kim, E., et al.: Measurements of Neutron Spallation Cross Sections of ^{12}C and ^{209}Bi in the 20- to 150-MeV Energy Range. *J. Nucl. Sci. Eng.* **129**, 209 (1998)
56. Uddin, M.S., et al.: Measurements of neutron induced activation of concrete at 64.5 MeV. *Ann. Nucl. Energy* **36**, 1133 (2009)
57. Accelerator Driven Systems (ADS) and Fast Reactors (FR) in Advanced Nuclear Fuel Cycles.

- A Comparative Study. www.nea.fr/html/ndd/reports/2002/nea3109.html
58. See Exfore entry 33004001 on site <http://www-nds.indcentre.org.in/EXFOR/33005.003>
 59. Cullen, D.E., et al.: ENDF/B-VII.0 Data testing for three fast critical assemblies. Report UCRL-TR-233310 (2007). Cullen, D.E.: PREPRO 2000:2000 ENDF/B pre-processing codes. Report IAEA-NDS-39, Rev. 10, 1 April 2000
 60. Bhatia, C., Kumar, V.: Determination of neutron multiplication coefficient of the fuel elements irradiated by the spallation neutrons. *Phys. Rev. C* **81**, 024614 (2010)
 61. Dudnikov, A., Sedov, A.A.: RBEC-M lead-bismuth cooled fast reactor benchmarking calculations. International Atomic Energy Agency. http://www.iaea.org/OurWork/ST/NE/NENP/NPTDS/Downloads/SMR_CRPI_SRWOSR/2006/RBEC-M%20Kurchatov%20Final.pdf
 62. Thermal Neutron Capture Cross sections and resonance integrals—Fission product nuclear data. <http://www-nds.ipen.br/sgnucdat/b3.pdf>
 63. Carminati, F., Kadi, Y.: ADS Neutronic Benchmark (stage 1): a new approach to the design of accelerator driven systems. In: Proceedings of the International Atomic Energy Agency Technical Committee Meeting, Madrid, Spain, 17–19 September 1997
 64. Tucek, K., et al.: IAEA Accelerator Driven System Neutronic Benchmark. In: Proceedings of the International Atomic Energy Agency Technical Committee Meeting, Madrid, Spain, 17–19 September 1997
 65. Cetnar, J.: A method of transmutation trajectories analysis in accelerator driven system. In: Proceedings of IAEA Technical Committee meeting on Feasibility and Motivation for Hybrid Concepts for Nuclear Energy Generation and Transmutation, Madrid, 17–19 September 1997
 66. Cox, L.J.: LA-UR-11-01654: LNK3DNT Geometry Support: User Guidance for Creating and Embedding and <https://rsicc.ornl.gov/>

POUZE PRO ÚČELY HABITUS

Requirement of Nuclear Data

4

In this chapter, we discuss requirement of nuclear data from the point of accuracy and sectorial demand of different kinds of data for the development of the ADSS technology. While writing the chapter, we realized that compilation of all kinds of data including evaluated data and parameterization of data is a matter of another book. Therefore, advancement of new data built up and related developments have been discussed in the chapter. A few data of simulated displacement cross sections of radiation damage and gas production in the target section of the ADSS are presented in Sect. 4.2.2 of the chapter. These data need their experimental validation.

4.1 Requirement of Nuclear Data Beyond the Existing Power Reactors

As an initial step, electronuclear systems had been extensively discussed first at Lawrence Livermore Laboratory in the year 1976 [1] under the material test accelerator (MTA) project for producing fissile fuels like ^{239}Pu and ^{233}U from the corresponding fertile fuels by making use of spallation neutrons from the deuteron beams of energy 500–600 MeV. Similarly, Canadian, intense neutron generator (ING) [2] project aimed at breeding of fissile fuel from the fertile fuel using the accelerated particle beam was initiated. Depending on the initial calculations and a few experiments conducted on

accelerators, a long list of research and development programs has been made at the national and international levels. A technologist can realize the amount and the kind of data requirement seeing at the schematic diagram of accelerator-driven accelerator system shown in Fig. 4.1 [3].

These programs have been discussed in different chapters of the book. The programs direct more or less on the feasibility studies of measurement of neutron flux and have shown concern of the spent fuel world over. The new technology of ADSS is many times more complicated than designing of a power reactor in the last century. Ikeda [4] has identified that the nuclear data related to hundreds of elements pertaining to target material, fuel elements, fission products, fuel cells, structural materials, and shielding, etc., need to be made available at much higher neutron energies and with much better precision of cross section measurements for many physics aspects of the design. Chemical and metallurgical aspects have other dimensions of the technology.

According to Plompen [5], ‘while discussing about the need of nuclear data again raises several issues of quantitative precision of the data and clever high-quality calculation/simulation.’ Among the nuclear challenges, the following are counted:

- (i) fissile nuclide capture cross section needs to be measured with <5% accuracy

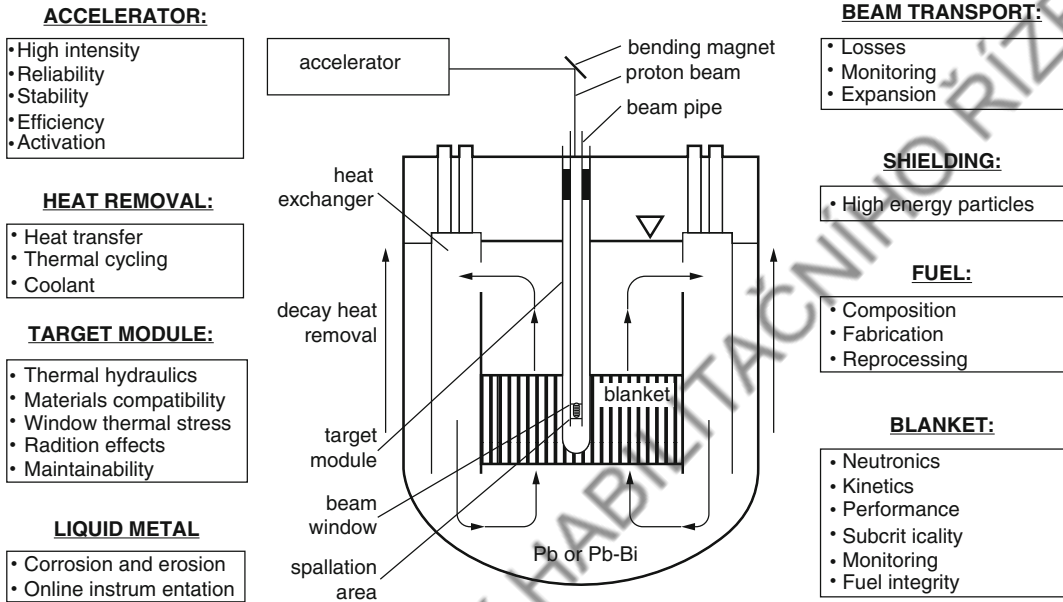


Fig. 4.1 A schematic diagram of ADSS with special components [3]

- (ii) scattering cross sections to be measured with 2–5% and fission cross sections with ~2% accuracy in case of minor actinides (MA)
- (iii) number of fission neutrons to be measured with accuracy and
- (iv) overall neutron spectrum to be measured and estimated.

Effect of accuracy of the data can be understood effectively after an elaborate discussion of new reaction channels opened up by the high-energy neutrons because accuracy of energy efficiency, ΔG of the ADSS depends strongly on the accuracy of cross section measurements as can be seen from the following discussion. Energy efficiency of the ADSS is related to the energy gain, G , and this is a function of neutron multiplication factor, k_s .

$$G = G_0 \left(\frac{k_s}{1 - k_s} \right) \text{ with } G_0 = \left(\frac{\langle E_f \rangle \times n_s}{E_p \times \nu} \right) \quad (4.1)$$

where $\langle E_f \rangle$ = fission energy, E_p = proton beam energy, n_s = number of spallation neutrons, ν = fission neutrons. Neutron multiplication

factor k_s is defined by Eq. (3.16) is equal to production term, P . In case, there is a leak-free system where all neutrons are utilized, then $R + L = 1$ and $k_s = P$. Thus, the accuracy of production term, P , defined as Eq. (3.14) is responsible for the accuracy of gain, G . Equation (3.16) can be rewritten as follows:

$$P = [1 - C] \frac{A}{B} \quad (4.2)$$

where

$$A = [2\Sigma_{n,2n} + 3\Sigma_{n,3n} + \dots + \langle \nu \rangle \Sigma_{n,f} + 3\Sigma_{n,3nx} + \dots]$$

$$B = \Sigma_t \quad \text{and} \quad C = e^{-x\Sigma_t}$$

Symbol Σ corresponds to the macroscopic cross section of a reaction shown as the suffix of the symbol, and $\langle \nu \rangle$ is the average number of fission neutrons.

This leads to

$$\Delta P^2 = \frac{A^2}{B^2} \Delta C^2 + (1 - C)^2 \left\{ \frac{\Delta A^2}{B^2} + \frac{A^2}{B^4} \Delta B^2 \right\} \quad (4.3)$$

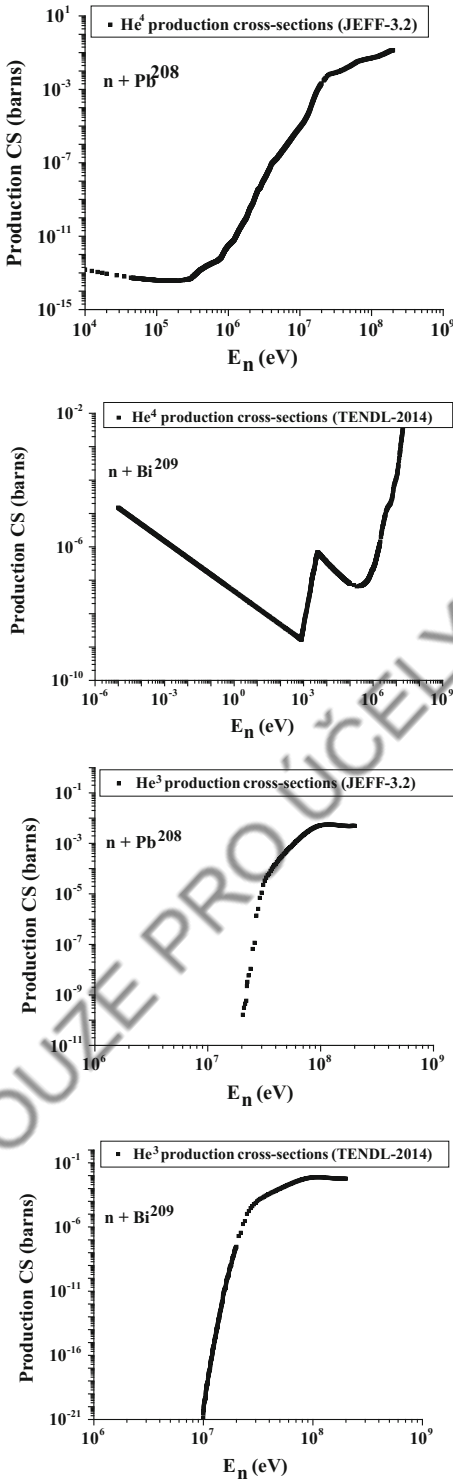


Fig. 4.2 He⁴ and He³ gas production cross sections in $n + \text{Pb}$ and $n + \text{Bi}$ collision plotted as function of neutron energy [34–36]

$$\Delta C = \pm \sum_i e^{-x \Sigma_i} \Delta x \quad (4.4)$$

Thus, the accuracy of determination of production term, P , shows the following behavior:

- (i) Increase of term B or increase of the total cross section, Σ_t is helpful in increasing accuracy of the term, P .
- (ii) Increase of the term B corresponds to decrease of ΔC due to exponential part of the term will be helpful automatically.
- (iii) Decrease of the terms A , ΔA , ΔB , and ΔC will be helpful in increasing accuracy.

Better accuracy means, ΔP is smaller; hence, the energy gain, ΔG , can be estimated precisely. This automatically emphasizes need of better experiments by using fast techniques of measurements, new analytical methods along with need of regular check of data for individual need and to transfer to the IAEA, IAEA-NDS and similar other Web sites.

4.2 Nuclear Data

Fast reactors and ADSS are different in many ways, and the major difference arises due to neutron energy and the target system which is a source of neutrons. Some technical part of the target system is discussed elsewhere in the book. Both fast neutrons and spallation neutron spectra have peaks around 2–4 MeV, but the spallation neutron spectrum is extended up to the projectile beam energy compared to fast reactor neutron energy which exists at ~ 10.5 MeV. Also, according to the CASCADE code calculations, projected in Fig. 3.6 of the last chapter, spallation neutrons produced by 1 GeV proton colliding with the lead target are $\sim 8.68\%$ having energy ≥ 10.5 MeV. They multiply in the fuel ahead to them by way of (n, xn) kind of reactions besides the fission process. In Table 4.1, an attempt is made to identify and summarize large amount of the data required for the ADSS technology.

Table 4.1 Requirement of data of different kinds of target, container, n -poisons, fuel cycles, shielding, and radiation-resistant materials with required precision level as discussed in the text. CS stands for cross section. New requirement of measurements is shown in boldface

System sector	Material elements	Elements (at. mass)	Specific data requirement and references
Target system			
Solid	Pb, Bi, W, Ta, Hg, ^{nat} U, Th	Pb (202, 204, 206, 207, 208); Bi (209); W (182, 183, 184, 186); Ta (181), Th, ^{nat} U	CS $\{(p, \text{reac}), (n, n'), (n, xn), (n, xp), (p, xp), (p, f), (n, f)\}$ with required accuracy [6]
Eutectic	Pb + Bi (ppm level of Ag, Fe, Ni, Sn, Cd, Al, Cu, and Zn)		Heat conduction, neutron poison, study of corrosion and erosion etc.
Container	Al, Sn, Fe, Cr, Ni, Mo, Zr, V, Ta, W, Cl, Na etc.	Al (27); Sn (112, 114–120, 122, 124); Fe (54, 56, 57, 58); Zr (90, 91, 92, 94, 96); Cl (35, 37); Na (23)	1. More CS data on (n, α) and (n, p) and other gas production by HE n's and protons and 2. Threshold displacement energy, E_d
n -poison and toxic gases like Hg and He ⁴ , He ³ and H ¹	Po and other n -poisons	Po (207–209) in Bi (p, xn) Po (210) in Bi (n, γ)	1. CS $\{(p, xn), (n, \gamma), (p, xp)\}$ [6] 2. Po is not a poison for HE neutrons of ADSS 3. Search of new n -poisons for HE spallation neutron spectrum 4. Release of gases, He ⁴ , He ³ , and H ¹ in target system and 5. Presence of Po and Hg in cover gas
Structural material			
Fuel cells	Al, Mg, Si, Fe, Cu, Ti, Zn, Cr, Zr, Si, Py, C, O		1. Gas production data at fast to spallation neutron energies 2. Radiation damage cross sections. and 3. Threshold displacement energy, E_d
Shielding	B, Be, Si, P, Cr, Fe, V, Mn, Ni, Zr, Mo, Nb, Sn, Zn, Cu, C, O, Ti, Ca, Ar, Mg, Na, O, Pb		1. Corrosion, erosion, swelling, brittleness, gas production data, heat conduction 2. Damage cross sections by both gamma and fast neutron spectra. Radiation resistance character of material / elements and 3. Threshold displacement energy, E_d of several elements
Gases	H, He, O		Gas production, swelling, reduction and oxidation rates are required
Beam window	T91/F91, HT9, EP82, 9Cr-1Mo steels	For example, T91/F91 steel has composition: Ni, Cr, Mn, Mo, Si, Ti, V, C, P, S, Nb, N, Al, Cu, As, Sn and Fe	Window materials have been discussed in Sect. 4.1.3.4 including graphene as recent one

(continued)

Table 4.1 (continued)

System sector	Material elements	Elements (at. mass)	Specific data requirement and references
Fuel and produced material			
Fuels	U-Pu, Th-U, N, O, F, Cl	U (234–237, 238), Pu (238–42), Am (241); ^{14,15} N, O, Cl and F	1. (n, f), (n, xnyp), (n, γ) for HE spallation neutron spectrum in case of actinides Complete fuel cycle as discussed in Chap. 5 and 2. Data of He, H and other gas production in (n, α) and (n, p) reactions by HE neutrons including the container material
Produced actinides	Np, Am, Cm, Pu, U	^{237,238} Np, ^{241–243} Am, ^{242–48} Cm, ^{238–40} Pu and ²³³ U	Production cross sections with required accuracy of spallation neutron spectrum are required
Long-lived fission products	Se, Zr, Tc, Pd, Sn, I, Cs	⁷⁹ Se, ⁹³ Zr, ⁹⁹ Tc, ¹⁰⁷ Pd, ¹²⁶ Sn, ¹²⁹ I, ¹³⁵ Cs	1. Fission yield 2. Production CS of fission products 3. CS {(n, γ) and (n, xnyp)} of LLFP

In the time of design of fast power reactors, emphasis on the measurement of interaction cross sections or reaction rates of high-energy neutrons was stressed and the issue of multiplication of neutrons beyond the ($n, 2n$) reactions was not emphasized. Also, issues related to shielding were not so different to the thermal reactors. In case of ADSS, extension of fuel cycles, design of shielding, design of beam window, overall radio-toxicity and radiation damage are dimensionally different let alone the issue of design of the target system.

In this direction, there is spurt in development of Monte Carlo codes for computation of cross sections of high-energy neutrons using theoretical models, multiplication of neutrons, energy applications, and questions related to the damage of materials. In Chap. 6, development of experimental facilities world over has been discussed in this book where kind of data production has been main issue along with validation of the data by the experiments.

Requirement of data is divided in different sections in Table 4.1 as per material requirement of ADSS. Accuracy of data can be

stressed upon in case of the utilization of existing old data and for the purpose of performing new experiments.

Several kinds of fast reactors have been designed, and they are running successfully. Development of generation IV reactors is also on the way, and both categories are utilizing fast reactor spectra. Both energy amplifier and a device of incineration of long-lived highly toxic reactor products, there is need of high energy neutron source. Understandably, in this environment, the fuel cycles of the subcritical reactors are going to be very much different to a normal critical reactor. At the same time, there will be need of much high shielding of the left-over or escaping out neutron flux. Enhancing energy efficiency of the subcritical system means increasing P or complete utilization of a neutron available in a system. This can be done when a neutron loses very small amount of energy by way of radiation damage and development of radiation-resistant materials will become a necessity. Requirement of data for all the major sectors of an ADSS design is discussed as follows.

4.2.1 Data Requirement of a Target System

The target system comprises of a solid or liquid target metal of high Z and high N which can generate high flux of neutrons and transmit them to the fuel blanket. Coupling of the beam through the beam window is also a part of the target system. In case a target is in liquid form like a eutectic, then it may be preferred that it can work as a coolant also. The entire target system is discussed from the data point of view with little focus on the other technical details such as kinetics of eutectic, architecture of the eutectic container, and similar other issues.

4.2.1.1 Target Cum Coolant

The target system is preferably a high Z , high N heavy metal like Pb, Bi, Hg, and even a fertile fuel in the metal phase. The target itself is enclosed in a metallic container. If the target is an eutectic flowing within a specific steel container and the whole target unit is irradiated by a high current (10–30 mA) of high-energy particle beam such as proton or deuteron or even electron. Its initial face toward the beam pipe will be irradiated heavily by the charged particle beam and exposed to heat, produced neutrons and other heavier particles. The nuclear processes responsible for neutron production in particle + A collision are pre-equilibrium, compound evaporation, direct as well as cascade emissions followed by the de-excitation of target nucleus. Irradiation by little proportion of nuclear fragments as well as fission fragments compared to earlier two cannot be denied. Many models and even big codes of particle production involving various cascade processes have been developed, and they have been extensively discussed in Refs. [7–9]. One of the commonly used MC codes, LAHET [10] has been used in several codes of particle transport and production of particles. According to the code, in case of 1 GeV proton colliding with Pb block of dimension say, $d \times L = 8 \times 50 \text{ cm}^2$, total 22.3 neutrons are produced. Out of them, there are 16 neutrons due to evaporation and fission processes, and on an average, 6.3 neutrons are due to

cascade process. Neutrons so produced from the target will multiply in the medium, and various nuclear processes are mentioned in Sect. 3.2. It may be mentioned that all these nuclear processes need updated data of cross section measurements for an accurate design of the ADSS system.

According to Glasbrenner et al. [11], LBE (44.8 wt% Pb + 55.2 wt% Bi) contains impurities of few ppm of elements like Ag, Fe, Ni, Sn, Cd, Al, Cu, and Zn. Along with a big list of data of various reactions with the elements of the eutectic, there is requirement of data of these impurity elements also. In irradiation of Pb–Bi by HE protons, production CS of many isotopes like ^{177}Lu , ^{183}Re , ^{183}Ta , ^{185}Os , ^{188}Ir , ^{188}Pt , ^{189}Ir , ^{191}Pt , ^{195}Hg , ^{195}Pt , ^{196}Au , ^{198}Au , ^{199}Au , ^{201}Tl , ^{202}Tl , ^{203}Hg , ^{203}Pb , ^{205}Bi , ^{206}Bi , ^{206}Po , ^{207}Bi are required [12]. Besides hydrogen and helium, other gases like xenon and krypton and volatile elements like mercury, cesium, iodine, bromine, and rubidium find their way to the cover gas system (CGS) of the reactor. The radio-toxicity increase several thousand times in LBE target system compared to a normal power reactor [13]. Toxic elements like Po and Hg have to be safely removed from the surface of LBE coolant before exhaling gases in atmosphere. This exerts need of production cross section data of the products along with their rate of absorption on surface before exhaling out. Selenium and tellurium produced along with polonium carry special attention to be handled very carefully for removal of polonium [14].

4.2.1.2 Polonium Problem

Production of polonium (Po) is the major problem in case of either Pb or Pb–Bi eutectic [11] to be used as the spallation target. Isotope $^{84}\text{Po}^{210}$ is produced from beta decay of $^{83}\text{Bi}^{210}$ in the one-step process of $^{83}\text{Bi}^{209} (n, \gamma) ^{83}\text{Bi}^{210}$ reaction. Also, $^{84}\text{Po}^{208}$ is produced in beta decay of the product of $^{83}\text{Bi}^{209} (n, 2n) ^{83}\text{Bi}^{208}$ nuclear reaction. Isotope $^{84}\text{Po}^{209}$ is produced in two-step beta decay of the product of $^{82}\text{Pb}^{208} (n, \gamma) ^{82}\text{Pb}^{209}$. In fact, $^{84}\text{Po}^{210}$ is an alpha emitter and causes high radio-toxicity for a long time ($T_{1/2}$ being 138.38 days) particularly when LBE is used as the target + coolant system in an ADSS

design. LBE as a coolant also induces radio-toxicity in large parts of ADSS. Gromov et al. [15] have calculated accumulation of radio-toxicity of three isotopes of polonium, i.e., $^{208-10}\text{Po}$ after operation of LBE irradiated by 20 MW beam, and found that radio-toxicity is 1.11 PBq by ^{210}Po , 1.85 TBq by ^{209}Po and 0.13 TBq by ^{208}Po for a coolant mass of ~ 10 tons.

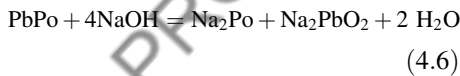
Polonium rapidly combines with lead and forms a stable PbPo, and it becomes basis of removal by the following five processes [15, 16],

- (i) Polonium hydride stripping using the following reaction after flowing hydrogen over the irradiated LBE,



H_2Po being a volatile helps in fast removal and Pb being constituent of LBE remains behind.

- (ii) Direct distillation of PbPo at high temperature.
- (iii) In alkaline extraction, irradiated LBE is reacted with NaOH to form Na_2Po which is separated,



- (iv) By the electrolysis, PbPo is deposited to separate it from LBE.
- (v) Separation of polonium by the formation of solid polonide.

In fact, removal of Po from the irradiated ‘target cum coolant’ is a matter of mass scale extraction of Po, and all the aforesaid methods are under research and development. It is important to note that LBE has been used as coolant by Russian submarines however with no publication on its usage industrially.

LBE-cooled ADS systems have been proposed at Los Alamos National Laboratory for burning actinides and LLFP of spent fuel from light water reactor and another similar system [16].

4.2.1.3 Beam Window

Beam window is another part of the target system, and it works in between vacuum on one side and high-density and high-temperature material on the other side. According to Sugawara et al. [17], material of the beam window should possess the following characteristics of tolerance to severe conditions like (i) pressure of the LBE, (ii) heat generation by the proton beam, (iii) creep deformation at high temperature, (iv) corrosion in the LBE, and (v) radiation damage by neutrons from target and protons of the beam. Using the computational fluid dynamics, STAR-CD code, temperature difference between inside and outside the window has been calculated to vary in between 25 and 60 °C and it is a function of the beam shapes, Gaussian, parabolic, or flat. It is inferred that in case of T91 ferritic/martensitic steel (Mod. 9Cr-1Mo, with Nb, V, Ni, Mn, P, Ti, Al, Cu, S, Si, Co and N and C), parabolic beam profile is more suitable for the given ADSS design conditions [17]. Nuclear data of most of the aforesaid elements/material for incident proton or neutron up to 200 MeV energy is available in standard data libraries and beyond 200 MeV data can be available from the theoretical models or in some cases from the cosmic ray experiments.

Wang et al. [18] have studied graphene-beam-window design considering graphene (carbon dominant) which has high thermal conductivity, high strength, and high transparency to ions. According to a simulation study for a 10 MW proton beam, power spatial distribution of temperature of the window varies from 33 to 55 °C in case of Gaussian and 36.2–78.6 °C in case of square beam profile. The DPA distribution for the 251 $\mu\text{A}/\text{cm}^2$ peak current varies from 8 at the center to 3 on periphery in case of 2D Gaussian beam.

In this way, for the beam window, the following data is required,

- (i) For the $p + \text{C}$, $p + \text{Fe}$, $p + \text{Cr}$, $p + \text{Mo}$, $p + \text{Nb}$, $p + \text{V}$ and $p + \text{N}$ and other similar reactions as given above, interaction data (elastic and inelastic cross sections,

product yield, kinetic energy, and emission angle of the products, etc.) at beam energies varying from 1 to 1.5 GeV with the required accuracy is required. In the present situation of databases such as ENDF VII.0 [19], JENDL 4.0 [20], JEFF 3.1 [21], ROSFOND 2010 [22], TENDL-2009 [23], MENDL-2 [24], etc., data of all required proton energies is not available. One can make use of either the model calculations using TALYS [25], ALICE [26] or utilize the older database developed by Barashenkov et al. [27]. All the data of the database of Ref. [27] cannot be displayed here, and reader is advised to go through a part of the data displayed in Chap. 2 of Ref. [28].

- (ii) Data related to creep rate and strength of the steel or any other perspective material of the beam window, as a function of (i) temperature and (ii) LBE flow speed in between 300 and 600 °C for the ADSS reactor is required. Creep resistance at high temperatures of steels has been studied extensively. For example, creep resistance can be increased by adding evenly distributed nanoparticles as traces in the volume or oxide layer [29, 30] on the surface. Creep rate as function of time at ~ 923 °K in case of boron dispersed in the 9% Cr ferritic steel has been studied [31]. According to Jianu et al. [32], T91 steel has been found to have better strain rate, lesser rupture rate, and rapid transition into the third creep stage at high stress (above 180 MPa) in the LBE environment than air. In Ref. [29], detailed study of the LBE technology is presented.
- (iii) Several groups are engaged in calculating cooling of the beam window with the help of circulating LBE as spallation target and the coolant [33].
- (iv) Radiation damage cross sections and other basic data such as threshold displacement energy, E_d , of the window materials for Fe, Cr, Mo, V, C, N, O is required. Some of the already available data of alpha and ^3He gas production by Pb and Bi targets,

available in standard data files is shown in Fig. 4.2.

4.2.1.4 Lead, Bismuth, and LBE as Spallation Target

High-energy proton beam after emerging from the beam window collides with bulk of a high Z and high N material which can be a solid, e.g., Pb, Bi, W, Ta, Hg, $^{\text{nat}}\text{U}$, or Th, or a liquid in the form of an eutectic. Lead-bismuth eutectic (LBE) is widely accepted as a neutron source and coolant. LBE getting popularity over other solid targets particularly in case of application of hard neutron energy spectrum in systems like ADSS for transmutation of actinides. LBE has melting point 398 ± 1 °K with melting heat (latent heat capacity) 38.6 ± 0.3 kJ/kg and boiling point $1,927 \pm 16$ °K. This shows that LBE has high possibility of heat capacity and can be used as coolant for a system. High boiling temperature shows its high safety feature of elimination of high pressurization and other boiling concerns related to the core of the system. They have been the issues in case of coolants like Na, H_2O , D_2O , and He which have very low boiling points. This also prevents high reactivity effects from boiling. Additionally, both Pb and LBE are inert compared to Na as a coolant. In Table 4.2, physical parameters of Pb, Bi, and LBE recommended [29] for developing spallation target technology are presented.

In place of a solid, an eutectic is being considered because of its multiutility (i) possibility to utilize LBE as a coolant of the reactor as discussed earlier along with being used as a spallation target, (ii) having high thermal conductivity, (iii) lesser problems of changing the target shape, size, and physical behavior after long irradiation by HE beam, and (iv) high thermal capacity for carrying target heat and heat of the reactor. Its main snag is production of polonium (Po) on irradiation which is a neutron poison of thermal and fast reactors and a producer of high radio-toxicity. Other inherent impurities of Pb or LBE like Ag, Cd, Cr, Cu, and Fe, etc. affect thermal and hydraulic characteristics of the reactor. According to a data source [29], recommended data is largely satisfactory

Table 4.2 Recommended values and correlations of thermo-physical quantities, melting point, latent heat (L) of melting, boiling point, latent heat (L) of boiling, critical points, surface tension, density, sound velocity, thermal conductivity and dynamical viscosity of lead (Pb), bismuth (Bi) and molten lead-bismuth eutectic (LBE). Temperature, T , is expressed in Kelvin [29, 30]

Quantity (unit)	Pb		Bi		LBE	
	Data from a correlation	Temp. range (K)	Data from a correlation	Temp. range (K)	Data from a correlation	Temp. range (K)
Melting temp. (K)	600.6	-	544.6	-	398	-
L_Q melting (kJ kg ⁻¹)	23.07	-	53.3	-	38.6	-
Boiling temp. (K)	2,021	-	1,831	-	1,927	-
L_Q boiling (kJ kg ⁻¹)	858.6	-	856.2	-	856	-
T_c (K)	5,000	-	4,500	-	4,800	-
ρ_c (kg m ⁻³)	3,250	-	2,800	-	2,200	-
P_C (MPa)	180	-	135	-	160	-
Surface tension (Nm ⁻¹)	(525.9-0.113 T) × 10 ⁻³	601-1,300	(420.8-0.081 T) × 10 ⁻³	545-1,400	(448.5-0.08 T) × 10 ⁻³	420-1,400
Density (kg m ⁻³)	11,441-1.2795 T	601-1,900	10,725-1.22 T	545-1,300	11,065-1.293 T	400-1,300
Sound velocity (ms ⁻¹)	1,953-0.246 T	601-2,000	1,616 + 0.187 T-2.2 × 10 ⁻⁴ T ²	545-1,800	1,855-0.212 T	400-1,100
Thermal conductivity (Wm ⁻¹ K ⁻¹)	9.2 + 0.011 T	601-1,400	7.34 + 9.5 × 10 ⁻³ T	545-1,000	3,284 + 1.617 × 10 ⁻² T-2.305 × 10 ⁻⁶ T ²	403-1,100
Dynamical viscosity (Pa s)	4.55 × 10 ⁻⁴ exp (1,069/T)	601-1,500	4.456 × 10 ⁻⁴ exp (780/T)	545-1,300	4.94 × 10 ⁻⁴ exp (754.1/T)	400-1,200

with respect to the experiments. Further, studies related to effects of impurities and dissolved additives on surface tension, sound velocity, viscosity, electrical resistivity, and thermal conductivity in case of Pb, Bi, and LBE need to be done to use as coolants.

Spallation process, neutron spectrum, and other characteristics of the neutron multiplication have been discussed in Chap. 3 extensively. As mentioned above, He^4 and He^3 gas production cross sections in spallation neutron colliding with Pb and Bi spallation targets have been shown in Fig. 4.2 [34–36]. In Refs. [34–36], data of other gas production is also given. Radiation damage cross sections of certain materials are given in next section.

4.2.1.5 Data Requirement for the Structure Material

Structure material like steel which is composed of several elements is used for containing LBE, circulation of coolant, and several other shielding structures. Similarly, for encapsulating and cladding of fuels as tube, covering of pallet or for a fuel-cell materials like aluminum, various carbides like ZrC, and SiC are used. They are expected to be irradiated by the beam protons or any such charged particle, produced neutrons, gamma, and heavy fission products in different positions in the reactor. They are strongly affected by the heat fluctuations and other hydraulic conditions. In case of irradiation by the high-energy neutrons of an ADSS, structure materials become source of gas production; i.e., gases like $^4\text{He}^2$ and $^2\text{H}^1$ affect the structure by way of swelling and embrittlement. Neutrons as well as other particles enhance the radiation damage of the structure materials. Radiation damage has been discussed in details in Chap. 7. Both fusion reactors and ADSS reactor are expected to experience a common conditions of high neutron fluence and temperature conditions. Additionally, the ADSS will experience effects of fluctuations of hydrodynamic flow along with jerks arising due to various conditions of solid fuels. The thermal and hydraulic stresses escalate corrosion and erosion of materials. All together, there is demand of data in this direction and in

case of specific materials for the characterization, performance and efficiency calculations. It may be pointed out that even a middle energy reactor neutron (~ 1 MeV) produces helium gas on colliding with the Al-cladding or the Al-tubes of the fuel rods. Helium being inert gas, escapes out and produces bubbles to affect the dynamics of the coolants. Fusion reactors, having inner wall of vanadium alloy, are damaged by hard neutron spectrum as well as helium gas. Produced Helium if escaped toward the fusion core then it helps in enhancing the density in fusion chamber but on escaping in the alloy bulk of the inner wall it grows swelling like effects. In Fig. 4.3, displacement cross sections [37–40] of light materials, Al, V, Cr, and Ti are plotted while in Fig. 4.4 and He^4 and He^3 —production cross sections of V and Zr [34–36] are plotted. These data are simulated data and need validation from experiments for which scientific community needs to evolve methods of measurement of displacement cross sections.

In Table 4.3, basic data of threshold damage energy, E_d , of various target and structure materials [41] is given for a large number of Monte Carlo simulation works and experimental researches related to radiation damage. It may be recalled [42–44] that the thermal effects can influence the displacement energy because change of momentum reduces the recombination of correlated Frenkel pairs and lattice softening. Crystallographic direction plays a significant role [44, 45] in displacement energy and the calculation of the damage.

The requirement of data presented in this chapter needs a large amount of experiments and evaluation of the experimental data obtained from different sources for establishing compatibility and accuracy measures. The issue is discussed in Chaps. 2 and 4 by Chitra and Kumar [28] and in a large number of EXFORE workshops being held world over at the initiative of IAEA and the countries producing nuclear data. While discussing generic issues of a critical analysis of different data libraries, Ganesan has pointed out [46, 47] that in place of expected difference of $\sim 1\%$ in ENDFB6GX and JENDL3GX of neutron absorption cross sections of ^{232}Th shows

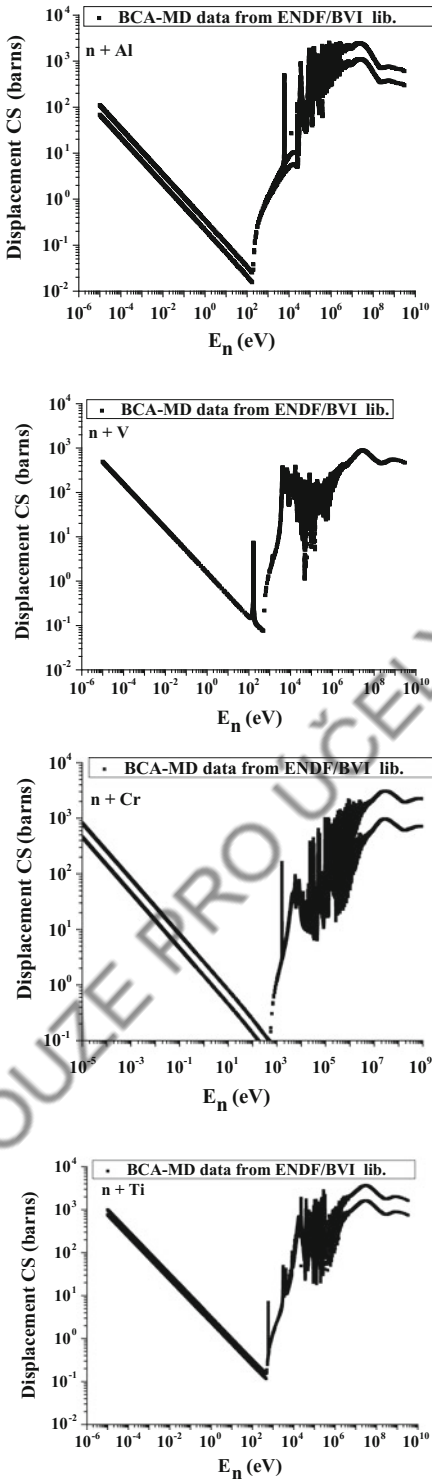


Fig. 4.3 Neutron displacement cross sections Al²⁷, V⁵¹, Cr²⁴, and Ti²² targets plotted as function of neutron energy [34–36]

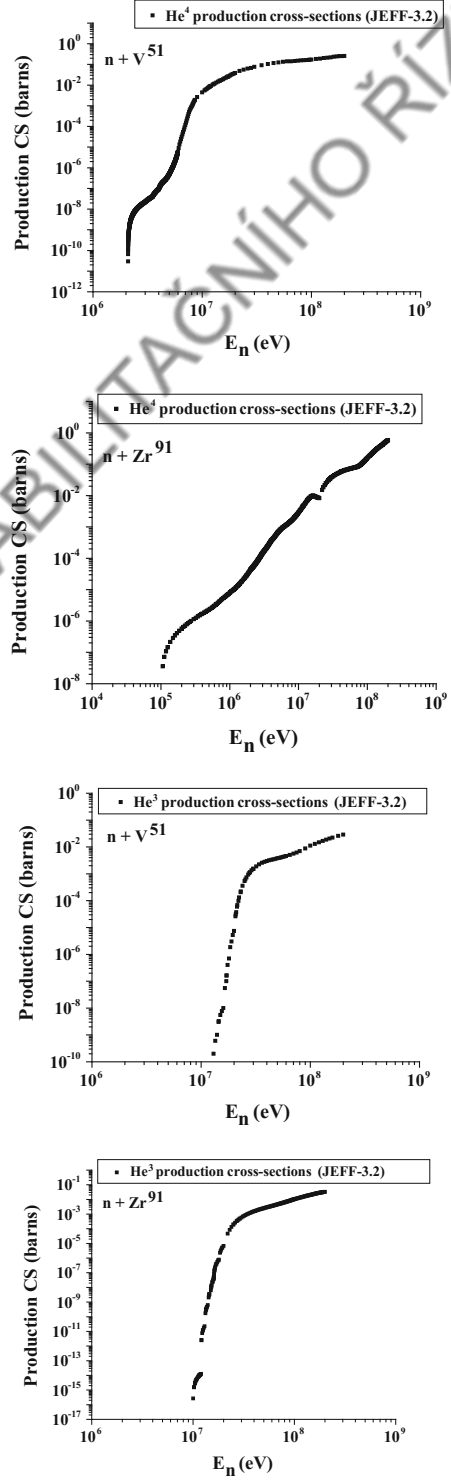


Fig. 4.4 He⁴ and He³ gas production cross sections in $n + \text{V}^{51}$ and $n + \text{Zr}^{91}$ collision of the specific structure materials plotted as function of neutron energy [37–40]

Table 4.3 Displacement threshold energy, E_d (eV) of target and structure materials [41]

Element	Al	Cu	Ni	Ag	Au	Pb	Pt	Pd	Th	Ge	Si	C 1	C 2	V
Lattice	FCC	FCC	FCC	FCC	FCC	FCC	FCC	FCC	FCC	Cubic	Cubic	Cubic	HCP	BCC
E_d (eV)	25, 27	29, 30	33, 40	39	40, 43	19–25	44	41	44	18–30	–	40	30	40
Element	Cr	Mn	α -Fe	Nb	Mo	Ta	W	Ti	Mg	Co	Zn	Zr	Cd	Re
Lattice	BCC	BCC	BCC	BCC	BCC	BCC	BCC	HCP	HCP	HCP	HCP	HCP	HCP	HCP
E_d (eV)	40	40	40–44	60, 78	60, 65	85, 90	90, 100	30	20	36, 40	29	40	30	60

C 1 (diamond C), C 2 (graphite C); lattice Ge, Si, C 1 = diamond cubic

difference ranging from 0 to 600% at 293 °K. Similarly, comparison of fission cross sections of ^{233}U derived from JENDL-3.2 and ENDF/B-VI (Rev.5) files shows different magnitudes of difference at different temperatures. At 0 and 296 °K, discrepancies between the two data are shown to vary between -89.60 to $1,495\%$ and -88.44 to 597.9% respectively. Differences are observed in case of grouping of the data also. The differences have effect on calculations of k_{∞} and critical masses.

References

1. Van Atta, C.M., Lee, J.D., Heckrotte, W: The electronuclear conversion of fertile to fissile material UCRL 52144, Oct 1976 and Van Atta, C.M.: A brief history of the MTA project. In: Proceedings of Information Meeting on Accelerator-Breeding, BNL Upton, New York, pp. 7–29, 18–19 Jan 1997. CONF-770107
2. Bartholomew, G.A., Tunnicliffe, P.R.: The AECL Study for an Intense Neutron Generator AECL-2600 (1966)
3. Knebel, J.U., Heusener, G.: Research on transmutation and accelerator-driven systems at the Forschungszentrum Karlsruhe. Internationale Zeitschrift für Kernenergie Atw Jg. (2000) Heft 6 (2000) 350
4. Ikeda, Y.: Nuclear Data Relevant to accelerator driven system. Nucl. Sci. Technol. **39**(Supplement 2), 13–18 (2002)
5. Plompen, A.: Why do We Still Need Nuclear Data. <https://www.oecd-nea.org/science/meetings/pnd22/presentations/1-PLOMPEN.pdf>
6. Koning, A.J., et al.: Nuclear data for accelerator driven systems. Nuclear models, experiments and data libraries. Nucl. Instrum. Meth. **A414**, 49 (1998)
7. Leray, S.: Nuclear reactions at high energy. Lectures Delivered at the Workshop on Nuclear Data for Science and Technology, Accelerator Driven Waste Incineration, Trieste (2001). http://users.ictp.it/~pub_off/lectures/Ins012/Leray.pdf
8. MONC: Monte Carlo Nucleon Transport Code. http://bts.barc.gov.in/AuthStatic/auth_static.php/npd/monc/index.html
9. Serber, R.: Nuclear reactions at high energies. Phys. Rev. **72**(11), 1114 (1947) and Domengetroy, V.B.: Investigations Related to the Generation of Reaction Products in the Target of Accelerator Driven Systems for Nuclear Waste Incineration, FZKA 6908 (2003)
10. Parel, R.E., Lichtenstein, H.: User Guide to LCS: The LAHET Code System, Report LA-UR-89-3014 (1989)
11. Glasbrenner, H., et al.: Polonium formation in Pb–55.5Bi under proton irradiation, J. Nucl. Mat. **335**, 270 (2004)
12. Artisyuk, V., Saito, M., Sawada, T.: Current status of spallation product data: Nuclear engineering viewpoint. In: JAERI-Conference, p. 27 (2004–05). <http://www.iaea.org/inis/collection/NCLCollectionStore/Public/36/116/36116662.pdf>
13. Accelerator-Driven Systems (ADS) and Fast Reactors (FR) in Advanced Nuclear Fuel Cycles. OECD NEA Report (2002). ISBN 92-64-18482-1
14. Amaya, L.O., Braet, J.: Purification of lead-bismuth eutectic used in accelerator driven systems—9411. In: WM2009 Conference, Phoenix, AZ, 1–5 Mar 2009
15. Gromov, B.F., et al.: Liquid-metal lead-bismuth target for high-energy protons as an intense source of neutrons in accelerator-controlled systems. At. Energ. **80**(5), 378 (1996)
16. Buongiorno, J., Larson, C.L., Czerwinski, K.R.: Discussion on Polonium Extraction System for Pb-Bi cooled Reactors. Report FR0202114. <http://www.iaea.org/inis/collection/NCLCollectionStore/Public/33/031/33031171.pdf>
17. Sugawara, T., et al.: Conceptual design study of beam window for accelerator-driven system, J. Nucl. Sci. Technol. **47**, 953 (2010)
18. Wang, H.: Design of high power graphene beam window. In: MOOCA 03, Proceedings of IPAC 2014, Dresden, Germany, p. 45. ISBN 978-3-95450-132-8 <http://www.nndc.bnl.gov>, <http://www-nds.iaea.org/>, <http://www.nea.fr/dbdata/data/manual-endf/BNL-90365-2009.pdf>
20. Shibata, K., et al.: JENDL -4.0: A new library for innovative nuclear energy systems. In: Proceedings

- of the International Conference on Nuclear Data for Science and Technology, Jeju Island, Korea (ND-2010). <http://www.ndc.jaea.go.jp/jendl/j40/j40.html>. Accessed 26–30 Apr 2010
21. Jacqmin, R., et al.: Status of the JEFF-3 project. In: Proceedings of the International Conference on Nuclear Data for Science and Technology, vol. 1, p. 54 (2002). https://www.nea.fr/dbforms/data/eva/evatapes/jeff_31/
 22. <http://www.ippe.ru/podr/abbn/libr/rosfond.php>
 23. <http://www.talys.eu/tendl-2009/>. ftp://nrg.eu/pub/www/talys/tendl-2009beta/Document/wonder09_rochman.pdf
 24. Shubin, Y.N., et al.: Cross Section Data Library MENDL-2 to Study Activation as Transmutation of Materials Irradiated by Nucleons of Intermediate Energies. Report INDC (CCP)-385, International Atomic Energy Agency, May 1995
 25. Koning, A.J., et al.: Proceedings of the International Conference on Nuclear Data for Science and Technology, Santa Fe, USA, 26 Sept–1 Oct 2004 and www.talys.eu/
 26. Yamano, N.: Tables of isotope production cross-sections (ACSELAM Library). (Sumitomo Atomic Energy). <http://www.ndc.jaea.go.jp/ftpnd/sae/acl.html>. Also see Fukahori, T.: ALICE-F calculation of nuclear data up to 1 GeV. In: Proceedings of the Specialists Meeting on High Energy Nuclear Data, Tokai, p. 114, 3–4 Oct 1991, JAERI-M 92-039 (1992)
 27. Barashenkov, V.S., Toneev, V.D.: Interaction of High Energy particles and Nuclei with Nuclei. Atomizdat, Moscow (1972)
 28. Bhatia, C., Kumar, V.: Role of (n, xn) Reactions in ADSS. Lambert Academic Publishing (2011)
 29. Taneike, M., et al.: Creep-Strengthening of Steel at High Temperatures using Nano-Sized Carbonitride Dispersions. *Nature* **424**, 294 (2003)
 30. Handbook on Lead-Bismuth Eutectic Alloy and Lead Properties, Materials Compatibility, Thermal-hydraulics and Technologies, NEA. <https://www.oecd-nea.org/science/pubs/2015/7268-lead-bismuth-2015.pdf>
 31. Abe, F., et al.: Stabilization of martensitic microstructure in advanced 9Cr steel during creep at high temperature. *Mater. Sci. Eng., A* **378**, 299 (2004)
 32. Jianu, A., et al.: Creep-to-rupture tests of T91 steel in flowing Pb–Bi eutectic melt at 550 °C, *J. Nucl. Mat.* **394**, 102 (2009)
 33. Mantha, V., Mohanty, A.K., Satyamurthy, P.: Thermal hydraulic studies of spallation target for one-way coupled indian accelerator driven systems with low energy proton beam. *Pramana J. Phys.* **68**, 355 (2007)
 34. https://www.nds.iaea.org/public/download-endf/DXS/Gas_Production_XS/DXS. (2015)/Files/
 35. Konobeyev, A.Y., et al.: Evaluated displacement and gas production cross-sections for materials irradiated with intermediate energy nucleons. In: EPJ Web of Conferences, vol. 146, p. 02018 (2017). Accessed <https://doi.org/10.1051/epjconf/201714602018>
 36. Konobeyev, A.Y., Fischer, U.: Complete gas production data library for nuclides from Mg to Bi at neutron incident energies up to 200 MeV. *KIT Scientific Working Papers* 36 (2015). ISSN: 2194-1629
 37. https://www.nds.iaea.org/public/downloadendf/DXS/Displacement_XS/DXS3000. (2011)/Files/
 38. Konobeyev, A.Y., Fischer, U.: Advanced evaluations of displacement and gas production cross sections for chromium, iron, and nickel up to 3 GeV incident particle energy. https://www.nds.iaea.org/public/downloadendf/DXS/Displacement_XS/DXS3000 (2011)/Description_of_methods/DXS_AccApp11.pdf
 39. Konobeyev, A.Y., et al.: Improved displacement cross sections for structural materials irradiated with intermediate and high energy protons. https://www.nds.iaea.org/public/downloadendf/DXS/Displacement_XS/DXS3000.(2011)/Description_of_methods/DXS_AccApp07.pdf
 40. Konobeyev, A.Y., et al.: Evaluated displacement and gas production cross-sections for materials irradiated with intermediate energy nucleons. In: EPJ Web of Conferences, vol. 146, p. 02018 (2017). Accessed <https://doi.org/10.1051/epjconf/201714602018>
 41. OECD/NEA, Working Party on Multiscale Modelling of Fuels and Structural Materials for Nuclear Systems, Expert Group on Primary Radiation Damage. Primary radiation Damage in Materials. www.oecd-nea.org. NEA/NSC/DOC, 9 (2015)
 42. Sosin, A., Bauer, W.: Atomic displacement mechanisms in metals and semiconductors. In: Dienes, G. J. (ed.) *Studies in Radiation Effects in Solids*, vol. 3, pp. 153–357. Gordon and Breach, New York (1969)
 43. Drosd, R., Kosel, T., Washburn, J.: Temperature dependence of the threshold energy for Frenkel pair production in copper. *J. Nucl. Mater.* **69–70**, 804 (1978)
 44. Roth, G., et al.: Energy dependence of the defect production at 78 °K and 400 °K in electron irradiated copper. *Radiat. Effects* **26**, 141 (1975)
 45. Lucasson, P.: The production of Frenkel defects in metals. In: Robinson, M.T., Young Jr., F.N. (eds.) *Fundamental Aspects of Radiation Damage in Metals*. Oak Ridge National Laboratory, United States, pp. 42–65
 46. Ganesan, S.: Nuclear data requirements for accelerator driven sub-critical systems—a roadmap in Indian context. *Pramana J. Phys.* **68**, 257 (2007)
 47. Ganesan, S.: Nuclear data needed to develop new nuclear systems, role of n_TOF facilities to measure resonance cross-sections and nuclear data needs of thorium fuel cycle. In: *Nuclear Physics and Astrophysics at CERN-NuPAC*, Invited Oral Contribution, 10–12 Oct 2005

Transmutation of Spent Nuclear Fuel and Extension of a Fuel Cycle

5

To get rid of the danger of radio-toxicity of the radioactive nuclear waste, there can be several methods including reposition underground or in the space. For sending to the space, even the concept of Lagrangian points is under serious consideration. But all such reposition possibilities are not energy effective solutions because the waste contains a big amount of fissionable material also along with the fertile material that can be used for energy production. As a solution and from the point of reutilization of a bigger part of the unspent nuclear fuel (UNF), its reprocessing and transmutation are the most attractive solutions. However, there will always be a requirement of a solution where reprocessing is not necessary. As already discussed in Chap. 2 that hybrid fusion–fission systems may be consuming big lot of fertile fuels but the problem of long-lived nuclear waste (LLNW) will grow even by the hybrid systems. Thus, the world is looking forward for a better solution of the highly involved problem from the point of both reutilization and reduction of the LLNW by way of development of the accelerator-driven subcritical systems (ADSS).

5.1 ADSS for Transmutation of LLNW

Natural transmutations by way of (i) radioactive decay and (ii) on collision of cosmic rays up to a deep inside the earth are well known. These observations have provided a way of transmutation by the artificial methods. In a power reactor, both transmutations by natural radioactive decay and by way of produced radiation like neutrons, gamma, and fission products take place. The two kinds of natural methods of transmutation are not sufficient because reactors produce much larger amount of UNF and HLW than they are reduced by natural methods. Transmutation by particles with sufficiently high energy fall under the category of artificially or the machine-induced transmutation. Historically, Alchemy has been used to convert lighter metals into a heavier metal hence a transmutation, but it has hardly reached to a respectable acceptance. After the advent of particle accelerators, artificial transmutation attained a scientific way of externally controlled method of activation.

In the spent nuclear fuel, there are actinides and fission products. Both have useful contents for applications as well as they pose danger of high radio-toxicity and risks of proliferation. Thus, the long-lived elements of the nuclear waste (termed as LLNW) are of serious concern from the point of their long survival time in reposition and otherwise they pose threats to the society during the reprocessing and transportation. A technology

Electronic Supplementary Material The online version of this chapter (https://doi.org/10.1007/978-981-10-7503-2_5) contains supplementary material, which is available to authorized users.

© Springer Nature Singapore Pte Ltd. 2019

V. K. Verma and K. Katovsky, *Spent Nuclear Fuel and Accelerator-Driven*

Subcritical Systems, Green Energy and Technology, https://doi.org/10.1007/978-981-10-7503-2_5

for reduction of the LLNW can be appreciated when both energy is produced and it is degraded with respect to radio-toxicity and lifetime. This can be plausible in a system of very high neutron flux which can support both the energy production and the incineration.

5.1.1 Long-Lived Actinides (LLA) and the Fission Products (FP)

In a power reactor using uranium as fuel, isotopes of plutonium (Pu), neptunium (Np), and americium (Am) are among the main long lived actinides (LLA) produced in a reactor besides several isotopes of uranium. Radio-toxicity of several LLAs and FPs has been discussed in Chap. 1, and it has been observed that radioactive elements like Np, Pu, Am, and Cm as the TRU and Technetium (^{99}Tc) and Iodine (^{129}I) are among the FPs having long half-life and they are highly radiotoxic also. In Table 5.1, half-life and decay mode of long-lived TRU and FPs are given. According to Wallenius [1], alpha-emitters MAs and TRUs are most radiotoxic and several of them are long-lived too. Several FPs are long-lived and their dose coefficient is equally high but they are relatively less radiotoxic as evident from the data given in Table 1.2 of Chap. 1. For the complete incineration of the long-lived nuclear waste (LLNW), a strategic planning is required to achieve the goal of degradation on one hand and gain of energy on the other hand.

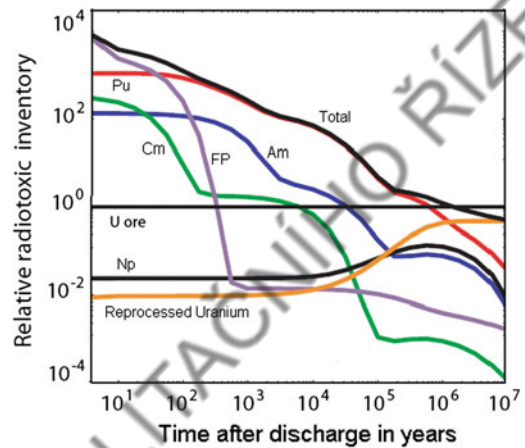


Fig. 5.1 Relative radio-toxicity of LLA and FP with respect to uranium ore in case of light water reactor (LWR) [2]

In Fig. 5.1, relative radio-toxicity (RRT) is plotted as a function of time after the discharge. From the figure, it can be inferred that radio-toxicity of FPs dominate other actinides up to 100 years and later on radio-toxicity of actinides dominates.

5.1.2 Reduction of Half-Life

Long-lived isotopes are a burden for several next generations, and this has been a matter of concern of the society and the nuclear science community in particular. Reposition is an alternative solution till an adequate system of

Table 5.1 Transuranium actinides (TRU) and fission products of a reactor having long life [1]

Element	Half-life (year)	Decay mode	Element	Half-life (year)	Decay mode
$^{236}\text{Np}_{93}$	1.54×10^5	$\epsilon(87.3), \beta(12.5), \alpha(0.2)\%$	^{79}Se	3.27×10^5	β
$^{237}\text{Np}_{93}$	2.14×10^6	α	^{93}Zr	1.53×10^6	$\beta\gamma$
$^{238}\text{Pu}_{94}$	87.7	α	^{97}Tc	4.21×10^6	ϵ
$^{239}\text{Pu}_{94}$	2.41×10^4	α	^{98}Tc	4.20×10^6	β
$^{240}\text{Pu}_{94}$	6.564×10^3	α	^{99}Tc	2.11×10^5	β
$^{241}\text{Am}_{95}$	4.33×10^2	α	^{107}Pd	6.5×10^6	β
$^{242\text{m}}\text{Am}_{95}$	141	$\alpha(0.46\%)$	^{126}Sn	1.0×10^5	β
$^{243}\text{Am}_{95}$	7.37×10^3	α	^{129}I	1.57×10^7	β
$^{244}\text{Cm}_{96}$	18.1	α	^{135}Cs	2.3×10^6	β
$^{245}\text{Cm}_{96}$	8.5×10^3	α	^{79}Se	3.27×10^5	β

*Pu (Minor Actinide), Am (major or higher Actinide), and Cm (major or higher Actinide) are introduced in the fuel of the light water reactor (LWR)

Table 5.2 Typical nuclear reactions, half-life, $T_{1/2}$ (year) and spectrum average cross section (sp. av. cs.) of a product for the spallation neutron spectrum of 1 GeV p + Pb collision with preference of an incineration reaction shown in the last column

Reaction	Half-life of product ($T_{1/2}$)	Spectrum average cross section (mb)	Preferred reaction for incineration
Plutonium ^{239}Pu ($T_{1/2} = 2.41 \times 10^4$ year)			
$^{239}\text{Pu} (n, \gamma) ^{240}\text{Pu}$	6.56×10^3 y	40.78	
$^{239}\text{Pu} (n, f)$		1840	
$^{239}\text{Pu} (n, 2n) ^{238}\text{Pu}$	87.75 y	~ 130 mb	(n, xn)
$^{239}\text{Pu} (n, 3n) ^{237}\text{Pu}$	45.66 d		
$^{239}\text{Pu} (n, 4n) ^{236}\text{Pu}$	2.86 y		
$^{239}\text{Pu} (n, 5n) ^{235}\text{Pu}$	25.3 min		
$^{239}\text{Pu} (n, 6n) ^{234}\text{Pu}$	8.8 h		
$^{239}\text{Pu} (n, 7n) ^{233}\text{Pu}$	20.9 min		
$^{239}\text{Pu} (n, 8n) ^{232}\text{Pu}$	33.1 min		
$^{239}\text{Pu} (n, 9n) ^{231}\text{Pu}$	8.6 min		
$^{239}\text{Pu} (n, 10n) ^{230}\text{Pu}$	1.7 min		
Neptunium ^{237}Np ($T_{1/2} = 2.14 \times 10^6$ year)			
$^{237}\text{Np} (n, \gamma) ^{238}\text{Np}$	2.117 d	189.35	(n, γ)
$^{237}\text{Np} (n, f)$	–	1372	
$^{237}\text{Np} (n, 2n) ^{236}\text{Np}$	1.54×10^5 y	~ 120 mb	
$^{237}\text{Np} (n, 2n) ^{236m}\text{Np}$	22.5 h		
$^{237}\text{Np} (n, 3n) ^{235}\text{Np}$	396.1 d		
$^{237}\text{Np} (n, 4n) ^{234}\text{Np}$	4.4 d		
$^{237}\text{Np} (n, 5n) ^{233}\text{Np}$	36.2 min		
$^{237}\text{Np} (n, 6n) ^{232}\text{Np}$	14.7 min		
$^{237}\text{Np} (n, 7n) ^{231}\text{Np}$	48.8 min		
$^{237}\text{Np} (n, 8n) ^{230}\text{Np}$	4.6 min		
$^{237}\text{Np} (n, 9n) ^{229}\text{Np}$	4.0 min		
$^{237}\text{Np} (n, 10n) ^{228}\text{Np}$	61.4 s		
Iodine ^{129}I ($T_{1/2} = 1.57 \times 10^7$ year)			
$^{129}\text{I} (n, \gamma) ^{130}\text{I}$	12.36 h	61.0	
$^{129}\text{I} (n, 2n) ^{128}\text{I}$	24.99 min	125.49	Both (n, γ) and (n, xn)
$^{129}\text{I} (n, 3n) ^{127}\text{I}$	stable		
$^{129}\text{I} (n, 4n) ^{126}\text{I}$	13.11 d		
$^{129}\text{I} (n, 5n) ^{125}\text{I}$	59.41 d		
$^{129}\text{I} (n, 6n) ^{124}\text{I}$	4.18 d		
Technetium ^{99}Tc ($T_{1/2} = 2.11 \times 10^5$ year)			
$^{99}\text{Tc} (n, \gamma) ^{100}\text{Tc}$	15.8 s		(n, γ)
$^{99}\text{Tc} (n, 2n) ^{98}\text{Tc}$	4.2×10^6 y		
$^{99}\text{Tc} (n, 3n) ^{97m}\text{Tc}$	90.6 d		
$^{99}\text{Tc} (n, 4n) ^{96}\text{Tc}$	4.28 d		
$^{99}\text{Tc} (n, 4n) ^{96m}\text{Tc}$	51.5 min		
$^{99}\text{Tc} (n, 5n) ^{95}\text{Tc}$	20.0 h		

incineration is developed. In case of incineration of actinides, possibility of energy gain by way of fission is a big point of attraction. Only a few of the minor products are long-lived which can be managed if less radiotoxic but difficulty arises in case of long-lived with high toxicity.

In an ADSS, maximum energy of the spectrum of spallation neutrons is very high and different compared to the neutron spectrum of a critical power reactor. Normally, it is called as a hard spectrum. In transport through the fuel, the spectrum is partly degraded in various nuclear elastic, inelastic, absorption reactions and fission. In Sect. 3.3.2, it has been shown that neutron spectra at different positions of an IAEA benchmark design are different when a neutron moves away from the spallation target toward the region 4 of the design. After emergence from region 3, spectrum is nearly a mixture of a thermal and a fast reactor. This provides opportunity to investigate possibility of degradation of long-lived nuclides by way of different kinds of nuclear reactions in the wide neutron energy range [3]. In Table 5.2, spectrum average cross sections of some of the nuclear products of a reactor are summarized with their half-life compared with the half-life of the parent nucleus (to be incinerated) in the environment of spallation neutrons. In turn, this suggests possible choices of degradation as mentioned above.

Besides the fission which is required for energy, ^{239}Pu when subjected to the spallation neutron spectrum, capture reaction cannot be a preferred reaction for incineration because its sp. av. cs. is much smaller than (n, xn) reactions and product of $^{239}\text{Pu}(n, \gamma)^{240}\text{Pu}$ reaction also has half-life much longer than half-life of any product of (n, xn) reactions. In case of ^{237}Np , capture reaction is of choice due to high sp. av. cs. as well as much smaller half-life of its product than the products of (n, xn) reactions. On the other hand, ^{129}I can be degraded by both (n, γ) and (n, xn) reactions. In case of FP ^{99}Tc , capture reaction can be preferred due to lowest half-life of product ^{100}Tc .

In summary, from the point of reduction of half-life, one may have a choice of fuel like ^{238}U or ^{232}Th for the energy in an ADSS being designed having options of accelerating current,

spallation target, and installing LLW in a specified area of fuel blanket for incineration looking at the availability of extra neutrons and their energy.

5.1.3 Reduction by the Thermal, Fast, and Spallation Neutron Spectra

^{239}Pu , ^{237}Np , and ^{129}I : For exploring possibilities of transmutation of ^{239}Pu , ^{237}Np , and ^{129}I by the thermal and fast components, and spallation neutron spectra itself of an ADSS reactor, calculated sp. av. cs. are compared in case of e.g., ^{239}Pu and ^{237}Np [3]. Data of sp. av. cs. for the fission and neutron capture reactions is given in Table 5.3 for the three neutron spectra. In case of ^{239}Pu , spectrum-averaged fission cross section σ_f is ~ 257.0 b for thermal, 1.793 b for fast and 1.84 b for spallation neutron spectrum of ADSS. Apparently, a part of ^{239}Pu can be reduced to the FPs in a thermal reactor for the energy production. How the remaining amount of ^{239}Pu can be degraded by other nuclear reactions and it will depend on availability of extra neutrons. In case of a thermal reactor, the sp. av. cs. of $^{239}\text{Pu}(n, \gamma)^{240}\text{Pu}$ reaction is ~ 128.495 b and the product, ^{240}Pu itself has long half-life 6.56×10^3 year. Its neutron capture cross section ~ 193.0 b is treated in the category of neutron poison of a thermal reactor. Another disadvantage of a thermal reactor is the high production rate of minor actinides by neutron activation, and most of the MAs are poorly fissionable. For example, the trans-plutonic nuclei such as ^{241}Am ($T_{1/2} = 432.0$ years) and ^{243}Am ($T_{1/2} = 7370.0$ years) are produced in the reactor on neutron capture and decay processes and they have relatively poor fission cross section ~ 1.583 and 0.3436 b, respectively, in comparison of neutron capture cross sections, 220.47 and 43.96 b, respectively. Thus, they produce more amount of LLW like $^{242\text{m}}\text{Am}$ ($T_{1/2} = 142.0$ years) and reduce the amount of neutron flux. Therefore, a thermal reactor can be said to be a neutron poorer and no extra neutrons will be available for further transmutation of other LLNW or FP such as ^{99}Tc and ^{129}I beyond the requirement of neutrons for energy production.

Table 5.3 Neutron economy factor (NEF) calculated for ^{239}Pu , ^{237}Np , and ^{129}I and the reaction rates, R in case of thermal, fast, and ADS reactors

Reactor and flux	Fuel/element	sp.av.cs., σ_f (b)	sp.av.cs., σ_c (b)	NEF, $(\sigma_f + \sigma_c)/\sigma_f$	Fission rate, R_f (s^{-1})	Capture rate, R_c (s^{-1})
Thermal, 8.9×10^{13} n/cm ² /s	^{239}Pu	257.6	128.5	1.5	2.29×10^{-8}	1.14×10^{-8}
	^{237}Np	0.447	59.54	134.2	3.98×10^{-11}	0.53×10^{-8}
	^{129}I	–	7.53	–	–	0.57×10^{-9}
Fast, 1.69×10^{16} n/cm ² /s	^{239}Pu	1.793	0.396	1.21	3.03×10^{-8}	0.67×10^{-8}
	^{237}Np	0.521	1.344	3.57	0.88×10^{-8}	2.27×10^{-8}
	^{129}I	–	0.14	–	–	0.24×10^{-8}
ADSS, 2.83×10^{16} n/cm ² /s	^{239}Pu	1.84	0.041	1.02	5.21×10^{-8}	0.12×10^{-8}
	^{237}Np	1.372	0.19	1.14	3.88×10^{-8}	0.54×10^{-8}
	^{129}I	–	0.591[5]	–	–	1.67×10^{-8}

In a fast reactor, sp. av. cs. of capture reactions $^{239}\text{Pu}(n, \gamma)^{240}\text{Pu}$ and $^{240}\text{Pu}(n, \gamma)^{241}\text{Pu}$ are 0.396 and 0.445 b, respectively, and they are much smaller compared to a thermal reactor as discussed above. In case of spallation neutron spectrum, capture cross sections of the two reactions are even smaller, 40.87 and 76.08 mb, respectively.

5.1.3.1 Neutron Economy Factor (NEF)

Comprehensively, neutron economy factor (NEF) of a reactor can be defined by considering utilization of a neutron by fission alone or by the fission + capture reaction. It can be estimated by the ratio $(\sigma_f + \sigma_c)/\sigma_f$ as fission and capture reactions are different in cases of three neutron spectra. The ratio is $(257 + 128.5)/257 = 1.5$ for ^{239}Pu in a thermal reactor, $(1.793 + 0.396)/1.793 = 1.21$, for a fast reactor and $(1.84 + 0.041)/1.84 = 1.02$ for an ADS spallation neutron spectrum. Thus, ADSS requires least number of capture neutrons and can be considered as best for incineration of ^{239}Pu . Similarly, NEF in case of ^{237}Np for the three neutron spectra are given in Table 5.3 and compared with ^{239}Pu . It can be inferred that neutron economy is better in case of ADSS compared to both fast and thermal reactors for both ^{239}Pu and ^{237}Np individually. In case of ^{237}Np , NEF of a thermal reactor is about 120 times worse than ADSS and 40 times worse compared to a fast reactor due to capture cross sections being high.

5.1.3.2 Reaction Rate

A reaction rate $R = \sigma\Phi$ is directly proportional to the elementary interaction cross section for a given flux irradiating the fuel in a given volume. Reaction rate $R(A_r, Z_r)$ can also be defined in terms of production rate, $Q(A_r, Z_r)$ of a reaction product (A_r, Z_r) per target nucleus per incident projectile as $R(A_r, Z_r) = Q(A_r, Z_r)/\{N_t, N_{\text{inc}}\}$. Neutron flux of thermal and fast reactors are $\sim 8.917 \times 10^{13}$ n/cm²/s and $\sim 1.69 \times 10^{16}$ n/cm²/s, respectively, and in case of an ADSS, spallation neutron flux depends on the spallation target material, beam current and the beam particle. As discussed in Sect. 3.2.2, in case of 1 GeV p + Pb target system CASCADE code calculations show that on an average 24.3 spallation neutrons per beam proton are produced [4]. Thus, for 10 mA beam current or equivalently 6.25×10^{16} protons/s there are 1.51×10^{18} spallation neutrons/sec. Considering surface area of spallation target of dimensions $R \times L = 10 \times 60$ cm² (total surface area = 22,608 cm²), the spallation neutron flux $\sim 0.67 \times 10^{14}$ n/cm²/s. If we assume an ADSS reactor as shown in Fig. 3.6 corresponding to the situation that outer fuel cylinder of width 4 cm is filled with ^{239}Pu and $\langle\sigma_f\rangle$ of spallation neutrons is ~ 1840 mb, then the mean free path (m. f. p.) would be 10.86 cm. Thus, in the passage of 4 cm thickness of the fuel (Ref. Fig. 3.6), a spallation neutron makes ~ 0.3 fissions. If in a fission, $\nu \sim 1.9$ neutrons are produced then for every spallation neutron there

are 0.57 neutrons produced in fission. Source neutron multiplication factor $\{k_s/(1 - k_s)\} = 0.57/(1-0.57) \sim 1.3$ inside the so assumed Pu-reactor. Thus, the multiplied source neutron flux would be $0.67 \times 1.3 \times 10^{14} \sim 10^{14}$ n/cm²/s. It is pertinent to point out that multiplication of spallation neutrons by the (n, xn) like channels and multiplication by the fission neutrons in an infinite volume of the fuel will further add to the neutron flux and total flux will be $\sim 10^{16}$ n/cm²/s. Neutron multiplication in case of a fertile fuel by the non-fission reactions is several times stronger than a fissile fuel particularly in case of high-energy spallation neutrons, and it has been discussed in detail in Sect. 3.2.2. In Sect. 3.3.1, neutron flux is estimated for an IAEA hypothetical reactor using the CASCADE code. For the calculations of neutron flux of an ADSS, we have considered IAEA benchmark design as a model and calculated neutron flux at different interfaces of fuel regions of the benchmark. This data has been projected in Table 3.9. Corresponding to criticality, $k = 0.979$ neutron flux at interface '12' is 2.83×10^{16} n/cm²/s in case of Th-U fuel and it has been used for all ADSS calculations given in Table 5.3. However, in case of pure ²³⁹Pu fuel, neutron flux will be somewhat different. It is important to point out that fission rates, R_f of ²³⁹Pu for the thermal, fast, and ADSS reactors are different only within one order of magnitude, i.e., 1.14×10^{-8} , 0.67×10^{-8} and 0.12×10^{-8} , respectively. In case of ²³⁷Np filled in a hypothetical thermal reactor, it is three orders of magnitude weaker compared to a fast reactor. Contrary to this, neutron capture rate R_c differs within one order of magnitude for both ²³⁹Pu and ²³⁷Np. Capture rate of ²³⁷Np is within an order of magnitude in the thermal, fast reactor, and the ADSS reactors. However, it holds valid that the fission dominates in a fast reactor [5] over the thermal reactor. In case of ²³⁷Np, the capture reaction ²³⁷Np (n, γ) ²³⁸Np followed by β^- decay and then the (n, γ) reaction converts ²³⁷Np into a neutron poison, ²⁴⁰Pu [6]. Thus, the chances of production of neutron poison in case of ²³⁷Np fuel are more in

a fast reactor than the two reactors. Capture rate of ²³⁹Pu for the production of ²⁴⁰Pu is lowest in case of ADSS; hence, it reduces risk of production of ²⁴⁰Pu as a neutron poison in ADSS compared to fast and thermal reactors. On the other hand, fission rates of both ²³⁹Pu and ²³⁷Np are very high in ADSS than both fast and thermal reactors.

In a thermal and a fast reactor, the capture and fission reactions play a dominant role over other reactions. However, this understanding changes drastically in case of ADSS because of the presence of very high-energy neutrons. It may be pointed out emphatically that the actinides like ²³⁹Pu when irradiated directly to the spallation neutron spectra then the NEF needs to be redefined by adding contributions of (n, xn) like reactions. Thus, the NEF can be redefined as, $(\sigma_f + \sigma_c + \sigma_{n,xn})/\sigma_f$. If we consider contributions of only $(n, 2n)$ and $(n, 3n)$ reactions in case of ²³⁹Pu, then $\sigma_{n,2n} + \sigma_{n,3n} = 0.04 + 0.06 \sim 0.10$ b and NEF would be 1.07 in place of 1.02. In fact, contribution of all the (n, xn) type reactions further worsens calculation of NEF. Also, when a spallation neutron passes through the thick reactor fuel pile [7], it is slowed down and enhancement of capture cross section σ_c takes place which worsens the NEF value at moderated energies.

5.1.3.3 Transmutation Power of a Reactor, $P(A_r, Z_r)$

Transmutation by capture, fission, and other nuclear reactions has been discussed in detail in the preceding chapters. Choice of one such reaction depends on the nuclide that need to be transmuted. The transmutation power, $P(A_r, Z_r)$ is defined as the quantity of produced masses, $m(A_r, Z_r)$ per unit mass of the target, $m(A_t, Z_t)$ [8, 9]. In Ref. [3], $P(A_r, Z_r)$ is identified as the transmutation power and expressed in terms of the normalized activity, $a(A_r, Z_r)$ without accounting for the decay of a product, (A_r, Z_r) during irradiation.

$$P(A_r, Z_r) = \frac{A_r \cdot a(A_r, Z_r)}{\lambda(A_r, Z_r) m(A_t, Z_t) N_{avo}} \quad (5.1)$$

Alternatively,

$$P(A_r, Z_r) = R(A_r, Z_r) \cdot N_{\text{INC}} \frac{A_r}{A_t} \cdot t_{\text{irr}} \quad (5.2)$$

where

N_{INC}	intensity of beam (s^{-1})
A_r	mass of residual product nucleus
Z_r	atomic number of residual product nucleus
A_t	mass of target nucleus
t_{irr}	irradiation time (s)
$R(A_r, Z_r)$	reaction rate of product (A_r, Z_r)

Normalizing over 10^9 beam particles, transmutation power can be written as,

$$P_{\text{norm}}(A_r, Z_r) = \frac{10^9 P(A_r, Z_r)}{N_{\text{INC}}} \quad (5.3)$$

For comparison of any two reactors, one can select one or a few product residual nuclei for detection experimentally. Based on various experiments, using different proton and deuteron beams reaction rates of transmutation of ^{237}Np and ^{239}Pu are estimated and displayed in Table 5.4. From the Energy + Transmutation setup which is discussed in detail in Chap. 6, it is clear that the neutron spectrum irradiating the fuel elements is the spallation neutrons only in

the beginning and it is moderated and multiplied after passing through the bulk of the fuel or the spallation target.

Integral number of beam protons, imparted on the spallation target is 0.88×10^{13} , 2.93×10^{13} , 1.10×10^{13} and 1.18×10^{13} for the 0.7, 1.0, 1.5 and 2.0 GeV beams, respectively [9]. Transmutation power of the four fission products ^{97}Zr , ^{132}Te , ^{133}I , and ^{135}I are estimated and presented in Fig. 5.2a–d for the ^{237}Np and ^{239}Pu fuel samples as a function of the proton beam energy, E_p .

From the results given in Fig. 5.2, it is clear that at all proton energies $P(A_r, Z_r)$ is always higher in case of ^{239}Pu than ^{237}Np and in case of ^{237}Np alone transmutation power is highest at 1 GeV proton energy. In case of individual FP, transmutation power of ^{239}Pu stays constant at proton energy > 1 GeV but higher than ^{237}Np . This shows that technologically transmutation power of plutonium is nearly independent of the proton beam energy > 1 GeV.

Considering results of ^{237}Np irradiated by neutron fluence from the two deuteron beams of the same setup given in Table 5.4, it can be inferred that they are similar to the results of proton beams at $E > 1$ GeV. This can be considered as an important result for designing an ADSS with p or d beam.

In another setup, GAMMA-3 [10] which is irradiated by the 2.33 GeV deuteron beam colliding with the Pb spallation target, transmutation power

Table 5.4 Comparison of measured sp. av. reaction rates, $\langle R(A_r, Z_r) \rangle$ in case of four proton beams of energies, $E_p = 0.7, 1.0, 1.5,$ and 2.0 GeV and two 1.6 and 2.52 GeV deuteron beams imparted on ^{238}U of $E + T$ setup in case of ^{237}Np . Reaction rates of FP from ^{239}Pu fuel are given in brackets [...] [9]. Measurement uncertainties are shown in brackets () along with the data of reaction rates

Product	Reaction rates $\times 10^{-27}/\text{s}$					
	0.7 GeV p	1 GeV p	1.5 GeV p	2 GeV p	1.6 GeV d	2.52 GeV d
^{238}Np	56.1(24)	151(5)	140(3)	133(3)	182(06)	162(06)
^{97}Zr	0.80(24) [5.52(51)]	2.10(09) [3.24(30)]	2.12(07) [8.82 (80)]	1.59(08) [11.35(10)]	1.98(12)	1.88(29)
^{132}Te	0.56(12) [4.18(17)]	1.79(18) [3.45(14)]	1.77(28) [4.59 (19)]	1.47(11) [13.81(40)]	1.61(12)	2.17(32)
^{133}I	0.83(40) [6.23(21)]	2.14(21) [6.08(21)]	2.01(24) [11.04(38)]	1.82(28) [16.94(15)]	2.00(22)	2.65(75)
^{135}I	1.52(22) [3.90(10)]	1.35(26) [4.86(12)]	2.36(28) [8.78 (22)]	1.96(18) [12.2 (4)]	2.21(22)	–

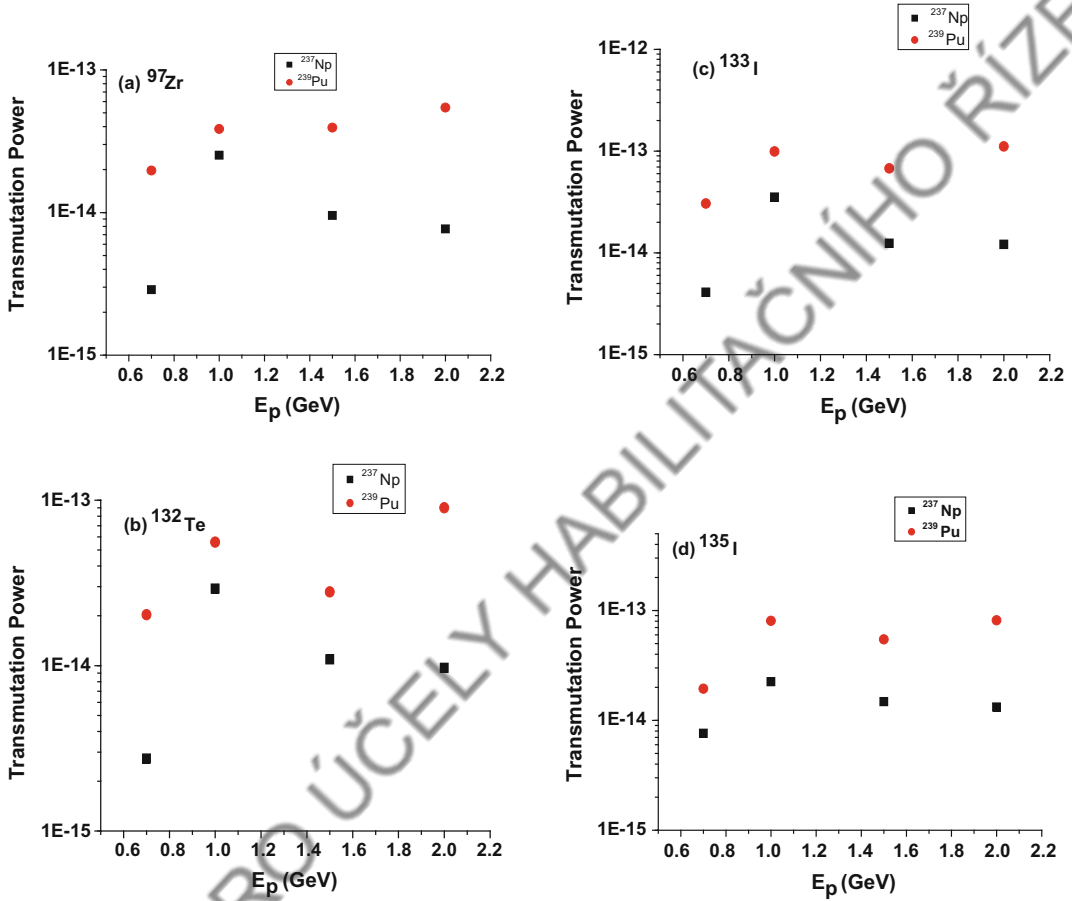


Fig. 5.2 Transmutation power, $P(A_r, Z_r)$ measured in the $E + T$ setup [9] for the four FPs, ^{97}Zr , ^{132}Te , ^{133}I , and ^{135}I of the ^{237}Np and ^{239}Pu fuel samples plotted as a function of proton beam energy, E_p

Table 5.5 Transmutation power of ^{232}Th and $^{\text{nat}}\text{U}$ measured at hole 'a' of the Gamma-3 setup [10] when the setup is irradiated with 2.33 GeV deuteron beam with integral intensity $N_{\text{INT}} = 1.7(1) \times 10^{13}$

Produced Isotope	$\langle R(A_r, Z_r) \rangle$	$P(A_r, Z_r)$	Product	$\langle R(A_r, Z_r) \rangle$	$P(A_r, Z_r)$
^{232}Th :			$^{\text{nat}}\text{U}$		
^{233}Th	3.20(8)E -25	5.50E -12	^{239}Np	3.11(10)E -25	5.34E -12
$^{85\text{m}}\text{Kr}$	3.15(4)E -29	1.97E -16	$^{85\text{m}}\text{Kr}$	1.58(6)E -27	9.65E -15
^{99}Mo	1.99(19)E -28	1.45E -15	^{99}Mo	6.76(18)E -27	4.81E -14
^{131}I	1.69(59)E -28	1.63E -15	^{131}I	3.02(6)E -27	2.84E -14
^{133}Xe	3.00(20)E -28	2.94E -15	^{133}Xe	1.25(18)E -26	1.19E -13
^{135}Xe	1.06(14)E -28	1.05E -15	^{135}Xe	4.1(12)E -27	3.98E -14

in case of ^{232}Th and $^{\text{nat}}\text{U}$ samples are estimated using both the capture and fission products. Results of the analysis are presented in Table 5.5. From the data, it may be inferred that the GAMMA-3 setup can transmute ^{232}Th and $^{\text{nat}}\text{U}$ by the capture reactions almost equally. Transmutation power of fission process is about one order of magnitude higher in case of $^{\text{nat}}\text{U}$ than ^{232}Th . This is because of the fact that $^{\text{nat}}\text{U}$ has a component of fissile ^{235}U . Adam et al. [10] on comparing transmutation powers of ^{232}Th and ^{238}U by way of capture reaction in the $E + T$, GAMMA-3, and TARC setup [11] observed that transmutation power of GAMMA-3 setup is about an order of magnitude higher than the remaining two while the transmutation power of both $E + T$ and TARC are at par equal. This is discussed in greater detail in Chap. 6.

5.2 Conversion of Fertile into Fissile and the Breeding Process

One of the earliest setups for conversion of fertile into fissile fuels like ^{239}Pu and ^{233}U by way of the spallation neutron spectrum produced by the deuteron beam was investigated in the year 1976 under the MTA program [12] of USA. We know that a power reactor works for the sustenance of a chain reaction, and it requires a specific amount of neutron flux. By neutron capture and beta decay, a definite amount of fissile fuel can be produced from a fertile fuel element. Natural fertile elements like ^{232}Th , ^{234}U , and ^{238}U can be converted to ^{233}U , ^{235}U , and ^{239}Pu , respectively, by neutron capture reaction (n, γ) . On a neutron capture, artificially produced fertile elements of a reactor such as ^{240}U and ^{238}Pu can also produce ^{241}Pu and ^{239}Pu fissile elements. Similarly, capture of more than one neutrons in succession can convert a fertile element into fissile element. In this kind of conversion processes, transuranium fissile elements such as ^{245}Cm from ^{242}Pu , ^{239}Pu from ^{236}U , and ^{243}Cm from ^{241}Am are produced. The conversion of fertile into fissile fuel is a strong function of kind of neutron spectrum, e.g., thermal, fast, or spallation neutrons and the structure of the reactor from the point of availability of excess neutrons.

Absorbance of a neutron by a fissionable nucleus can give rise to (n, f) , (n, γ) , and $(n, xnyp)$ types of inelastic reactions, thus

$$\sigma_a = \sigma_f(n, f) + \sigma_c(n, \gamma) + \sigma_{np}(n, xnyp) \quad (5.4)$$

Spectrum average cross sections calculated using TALYS code for both the fast and spallation spectra are given in Ref. [14]. For a breeder reactor, ‘neutron production factor’ η is defined as,

$$\eta = (\sigma_f / \sigma_a) \nu \quad (5.5)$$

ν is the number of fission neutrons. In case of thermal and fast reactors, roughly speaking, mainly fission and marginally $(n, 2n)$ reactions are responsible for the production of extra secondary neutrons and $\nu = 2.50, 2.49$ and 2.97 for the ^{235}U , ^{233}U and ^{239}Pu fissile elements, respectively. Thus, in case of thermal and fast reactors only first two terms of the relation (5.4) are meaningful. In case of spallation neutron spectrum, there is a significant contribution of the third term, σ_{np} particularly in case of fertile fuel targets. Thus, factor ν needs an up-gradation accordingly. In Table 5.6, reproduction factor, η has been calculated for the fast and spallation neutron spectra for the three fissile elements, ^{235}U , ^{233}U , and ^{239}Pu assuming ν corresponding to only fission process of neutron multiplication. In fact, calculation of η is meaningful in case of a fast breeder reactor which produces more amount of fissile material on burning lesser amount of fissile material. In such breeders, conversion ratio (CR), breeding potential ($\text{BR}_{\text{max}} = \eta - 1$), and breeding gain (BG) are defined and they depend on the reproduction factor, η .

In case of spallation neutron spectrum, reproduction of neutrons depends on fission and other $n_{np}(n, xnyp)$ type reactions and η can be redefined as

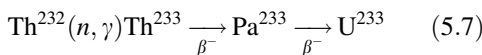
$$\eta^* = \{(\sigma_f + \sigma_{np}) / \sigma_a\} (\nu + \langle n_{np} \rangle) \quad (5.6)$$

In case of spallation, neutron spectrum contribution of $\langle n_{np} \rangle$ is meaningful in case of fertile elements and insignificant in case of fissile

Table 5.6 Reproduction factor, η for the fissile fuels, ^{235}U , ^{233}U , and ^{239}Pu fertile fuels, ^{232}Th and ^{238}U for the fast and spallation neutron spectra. All sp. av. cs. are in (mb) units

Fuel	Fast n -spectrum				Spallation n -spectrum			
	σ_f	$\sigma_c + \sigma_{n,2n}$	ν [13, 14]	η	σ_f	$\sigma_c + \sigma_{np}$ etc.	$\langle n_{np} \rangle$	η^*
^{235}U	2080	270 + 15.3	2.50	2.20	1184	106.4 + 141	–	2.31
^{233}U	2250	74.2 + 3.17	2.49	2.41	2209.7	41.8 + 66.01	0.11	2.45
^{239}Pu	1793	396 + 2.54	2.97	2.43	1840	40.78 + 129.4		~2.9
^{232}Th	7.29	391 + 7.85	2.60	0.05	35.1	146.1 + 154.01	13.82	9.26
^{238}U	11.4	317 + 25.1	2.07	0.07	72.4	116.8 + 139.8	~13	~9.71

elements because in case of thermal and fast reactors sp. av. cs. and average neutron multiplication σ_{np} and $\langle n_{np} \rangle$, respectively, are not significant. In Chap. 3, production term P has been computed by all kinds of reactions including fission reactions and projected in Table 3.6. In case of fertile, ^{232}Th total $P = 0.981$, $P_f = 0.15$ and on taking $\nu = 2.60$ and proportionate value $\langle n_{np} \rangle = 13.82$. For the given data in Table 5.6, $\sigma_f = 35.1$ mb, $\sigma_c = 146.1$ mb, and $\sigma_{np} = 154.01$ mb then the reproduction factor, η^* would be 9.26. This means that ^{232}Th will not always be triggered to fission or neutron capture but a large proportion produces $(n, xnpy)$ reactions hence the reproduction factor is very high. When spallation neutrons pass through this fuel, then the reproduced neutrons will have lesser energy and chances of $(n, xnpy)$ type reactions will be reduced and neutron capture will rise drastically to 391 mb when the neutron spectrum will be close to the fast spectrum and to 5350 mb when it further retards to the thermal spectrum. Obviously, toward the end of the ^{232}Th -fuel, chances of neutron capture, σ_a are enhanced. Although this will reduce the value of η toward the end of the fuel but the rate of conversion of ^{232}Th into ^{233}U will be enhanced through the following route,



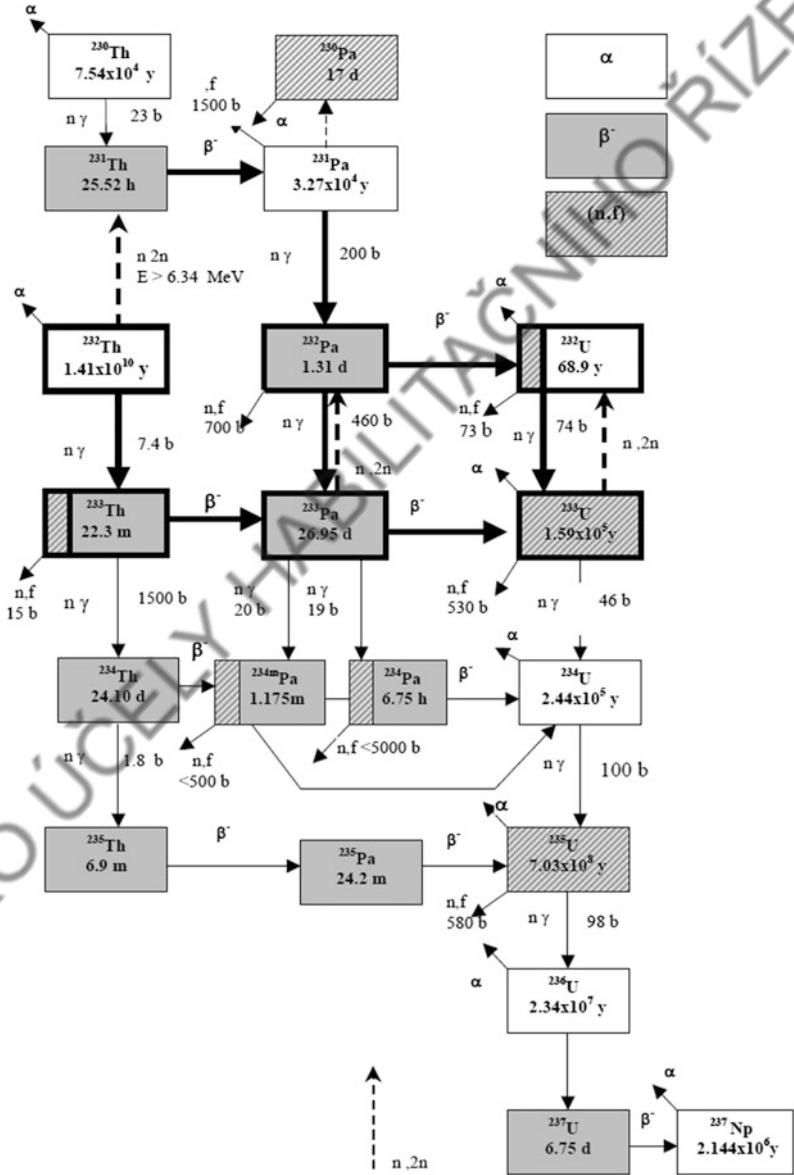
In case of fissile ^{233}U in the spallation neutron spectrum, $P = 0.981$, $P_f = 0.94$, $\nu = 2.49$, and $\langle n_{np} \rangle = 0.11$ only. For the given data $\sigma_f = 2209.7$ mb, $\sigma_c = 41.8$ mb, $\sigma_{np} = 66.01$ mb, then reproduction factor is calculated to be $\eta^* = 2.45$.

In case of a ^{232}Th – ^{233}U breeder, where ^{233}U will be highly produced due to high number of reproduction neutrons or the factor, η^* is high for the fertile ^{232}Th . The fissile ^{233}U will be consumed by way of the fission reaction and the reproduction factor in the fast spectrum reduces to $\eta = 2.41$ only. Resultantly, fissile ^{233}U will be produced at a faster rate than ^{234}U from the ^{233}U . One can easily calculate the breeding gain, $\text{BG} = \text{BR} - 1$ from the value of BR.

5.3 Extension of the Fuel Cycles

So far nuclear fuel cycle is meant for the complete cycle applications of a fuel for energy production, reprocessing, disposal, and refueling of a reactor after enrichment by fissile fuels. Normally, a part of the fertile and fissile fuels can be extracted from the unspent fuel as discussed in Chap. 1 in case of existing power reactors. In thermal and fast reactors there hold a ^{232}Th – ^{233}U fuel cycle, for example, as shown in Fig. 5.3, where it can be seen that the fuel cycle is limited in between $(n, 2n)$ and a few (n, γ) reactions besides a few β - and α -decays. In case of spallation neutron flux, a large number of nuclear reactions take place as shown in Table 3.4 of Chap. 3. Several other nuclear reactions of a produced nuclide from ^{232}Th and ^{233}U irradiation in the ADSS reactor will take place and they are not shown in Table 3.4. Bhatia and Kumar [15] have attempted to bring out a ^{232}Th fuel cycle of the ADSS neutron spectrum as Fig. 5.4. From this following is worth discussion

Fig. 5.3 The thorium chain, Th-U fuel cycle explored for thermal and fast reactors [16]



1. The fuel cycle in Fig. 5.4 is highly extended compared to the fuel cycle of a thermal and fast power reactor.
2. Neutron poisons of the thermal and fast reactors are no longer neutron poisons of an

ADSS where spallation neutron environment is dominant compared to neutron spectra of critical reactors. This is also discussed in Chap. 3 of this book with data displayed in its Table 3.5.

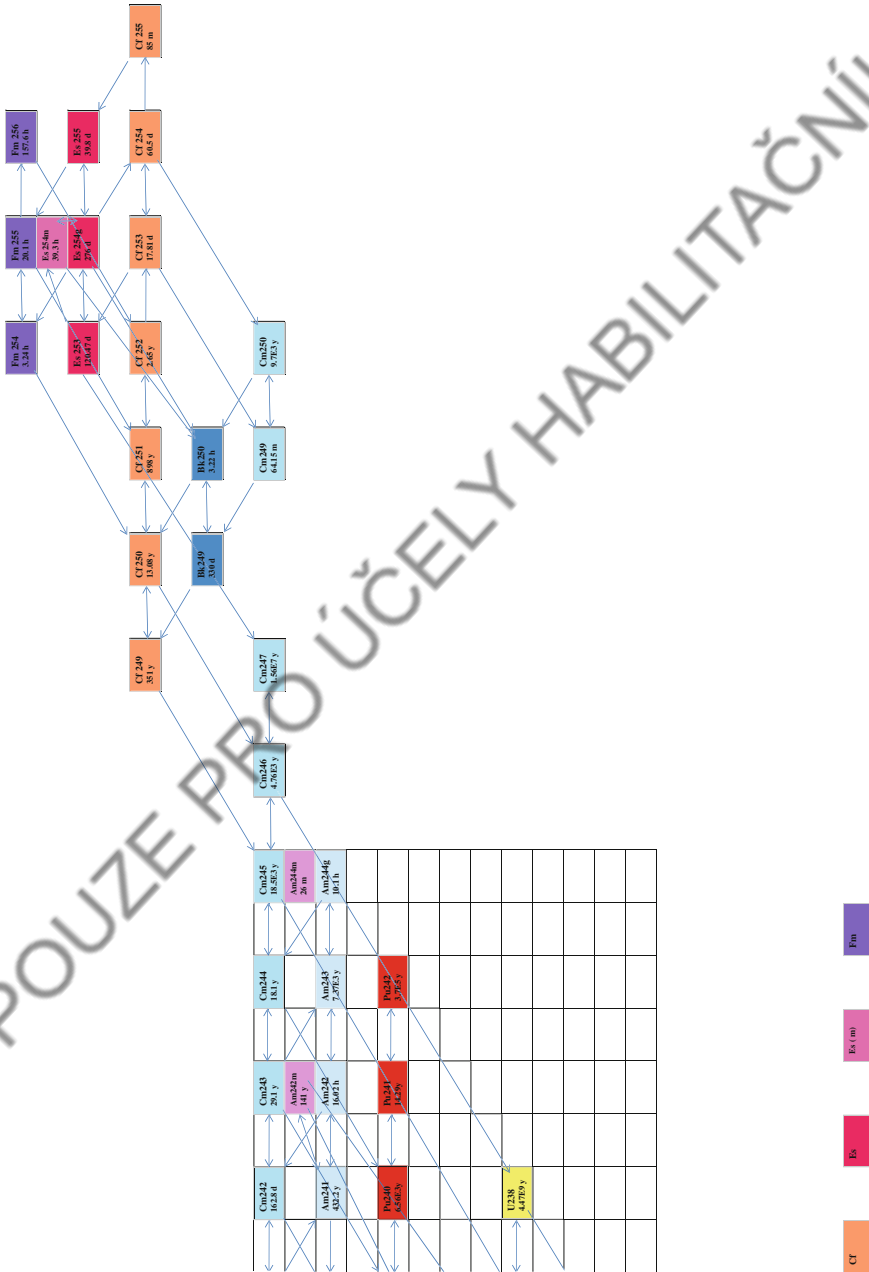


Fig. 5.4 Extended Th–U fuel cycle in the environment of high-energy spallation neutrons showing various possible reaction channels at high energy which are not feasible in a thermal or a fast spectrum [15]

References

1. Wallenius, J.: Transmutation of Nuclear Waste Reactor Physics. KTH, <http://www.neutron.kth.se/courses/Transmutation.shtml> and <http://www.acept.org/AIWOpdf/AIWO1-02-Wallenius.pdf>
2. Development of reprocessing technologies. https://www.iaea.org/About/Policy/GC/GC52/GC52InfDocuments/English/gc52inf-3-att4_en.pdf
3. Kumar V. et al.: Study of Spent Fuel Management by Transmutation in an Accelerator Driven Sub critical System, EPE 2014, Brno Czech Republic, p 681, published as 978-1-4799-3807-0/14/\$31.00 ©2014 IEEE
4. Kumar, V., Kumawat, H., Sharma, M.: Role of (n, xn) Reactions in ADS, IAEA-Benchmark and the Dubna CASCADE Code. *Pramana: J. Phys.* **68**, 315 (2007)
5. Junghans, A.R.: Transmutation of high-level radioactive waste: basics, methods, perspectives. In: Proceedings of Erinda-2 Colloquium, Dresden-Rossendorf, Germany (2013)
6. Kumar, V., et al.: A review of nuclear waste transmutation using accelerator beams up to several GeV: Talk delivered at 17th International Scientific Conference on EPE-2016, Praha (Czech Rep.) published as 978-1-5090-0908-4/16/IEEE (2016)
7. Sharma, M.: Ph.D. Thesis-Transmutation of Long-lived Isotopes of Conventional Reactors Using A.D. S. Concept. Ph.D. Thesis, University of Rajasthan, Jaipur, p. 177 (2010)
8. Adam, J. et al.: JINR Preprint P10-2000-28 (in Russian)
9. Adam, J., et al.: Transmutation of ^{129}I , ^{237}Np , ^{238}Pu , ^{239}Pu , and ^{241}Am using neutrons produced in target-blanket system 'Energy plus Transmutation' by relativistic protons. *Pramana-J. Phys.* **68**, 201 (2007)
10. Adam, J., et al.: A Study of reaction rates of (n, f), (n, γ) and (n, 2n) reactions in $^{\text{nat}}\text{U}$ and ^{232}Th by the neutron fluence produced in the graphite set-up (GAMMA-3) irradiated by 2.33 GeV deuteron beam. *Eur. Phys. J. A* **47**, 85 (2011)
11. Abanades, A., et al.: Results from the TARC Experiment: Spallation Neutron Phenomenology in Lead and Neutron-Driven Nuclear Transmutation by Adiabatic Resonance Crossing, *Nucl. Instr. Methods A* **478**, 577 (2002)
12. Van Atta, C.M., Lee, J.D., Heckrotte, W.: The electronuclear conversion of fertile to fissile material. UCRL 52144 (October 1976)
13. Turner, J.E.: *Atoms, Radiation and Radiation Protection*, 3rd edn. Wiley, New York (2007)
14. Bowman, C.D., et al.: Nuclear energy generation and waste transmutation using an accelerator-driven intense thermal neutron source. *Nucl. Instrum. Methods Phys. Res. Sect. A* **320**, 336–367 (1992)
15. Bhatia, C., Kumar, V.: Role of (n, xn) Reactions in Accelerator Driven Sub Critical Systems. LAP Lambert Academic Publishing (2011)
16. Thorium fuel cycle-Potential benefits & challenges. IAEA (May 2005), IAEA-TECDOC-1450, http://www-pub.iaea.org/MTCD/publications/PDF/TE_1450_web.pdf

Major Experimental Facilities for Development of Accelerator-Driven Subcritical System

Although the nuclear waste available in USA is in comparable amount that in Europe, yet, the EUROpean research program for the TRANsmutation of high-level nuclear waste in accelerator-driven systems (EUROTRANS) is initiated and funded heavily by the European Commission within its 6th Framework Program and it involves more than 40 partners which include research agencies, universities and nuclear industries. Initially, the program was planned for (i) advance design of a transmuter including its components including conceptual industrial design (ii) developing coupling of accelerator with the reactor (iii) studies related to advance fuels for transmuters (iv) studies and investigation of structure materials and heavy liquid metal technology and (v) collection of nuclear data with required precision.

In the following chapter, short description of all major experiments conducted world over in this direction, predated or postdated to EUROTRANS, is presented. To start with most of the experimental facilities and the setups have utilized existing experimental and calculated data from the models and codes and reached to an initial stage of realization. It is inferred that there is need of new data for several materials with better precisions and this is discussed in Chap. 4. There is a need of development of new materials for high energy radiation and for several strategically suitable situations as well.

In the following, several facilities emerged world over for pursuing experiments to fulfill requirement of the EUROTRANS are described.

6.1 FEAT and TARC Experiment

FEAT is short form of 'First experiment for testing energy gain in Energy Amplifier (EA) and Transmutation' as proposed by Nobel Laureate, Carlo Rubia in the year 1994 [1]. Later in this chapter, it will be seen that several experiments are conducted mainly for the reduction of average life of LLNW and hardly anyone for the study of energy production from the fertile component of the nuclear waste. Among several fission products which have long life and high radio-toxicity, ^{99}Tc and ^{129}I can be transmuted to reduce to either very low half-life or to become stable by way of neutron capture or other reactions. Looking at the properties of spallation neutrons on passing through lead (Pb), Rubia [2] proposed a new concept that neutrons in Adiabatic Resonance Crossing can be utilized for absorption in a long-lived fission product (LLFP) like ^{99}Tc ($t_{1/2} = 2.11 \times 10^5$ yr) for their Transmutation. It is abbreviated as TARC. Spallation neutrons after multiplication in a large lead block will have almost isotropic elastic scatterings and a 1 MeV neutron will suffer nearly 1,800 elastic collisions in its traversal length of about 60 m inside lead, and it attains kinetic energy

< 1 keV which lies in the resonance energy region. At 5.6 eV energy, it can be allowed to be absorbed in ^{99}Tc with a cross section ~ 4000 b compared to the cross section being 20 b in case of thermal and epithermal energy ≤ 1 eV. In fact, integral absorption cross section in the resonance region is ~ 310 b, again a very high cross section compared to the thermal, epithermal, and the high-energy regions. According to the concept of ‘transmutation by adiabatic resonance crossing’ (TARC), a neutron is contained in the large assembly for about 3 ms and finally it has high chance of absorption in ^{99}Tc to transmute it to become ^{100}Tc ($t_{1/2} = 15.8$ s) which finally decays to ^{100}Ru (stable).

The TARC setup is an assembly of rectangular lead (99.99% pure) blocks assembled finally in cylindrical manner with size $d \times l = 3.3 \times 3$ m², and its axis is aligned to the beam axis. Its weight is ~ 334 tones. Nearly 70% spallation neutrons produced by the proton beam on striking lead material inside a beam hole at the center of the assembly remain inside the assembly and in an area of radius 1 m, a region is produced which is least affected by the background neutrons reflected from the atmosphere. This is done by keeping the concrete shielding

far away from the setup. The setup is protected from the reflected neutrons from the ground also by introducing 44-cm-thick steel in between the setup and the ground and introducing 3-cm layer of B₄C-rich cement in between, for minimizing thermal neutrons. In Fig. 6.1, TARC setup is shown with mention of its dimensions [3]. For the FEAT experiment, 3.5 GeV/c proton beam extracted from the standard PS of CERN was used. It was a bunched beam having intensity $3 \times 10^7 - 2 \times 10^{10}$ particles per shot.

FLUKA code [4] is used to simulate the spallation neutron spectrum and transport of neutrons up to 19.6 MeV, and histories are recorded in a file. At higher than 19.6 MeV energies, transport is performed using the EA Monte Carlo simulation code specially written by the TARC group at CERN [5]. In fact, TARC experiment was conducted for the validation of the EA code like that CASCADE code was developed and validated by conducting experiments with GAMMA and $E + T$ setups at JINR, Dubna. They will be described later in this chapter.

Neutron database compilation [6] which carries several data files like ENDF VI-4, JENDL-3.2, JEF-2.2, EAF 4.2, CENDL-2.1, and

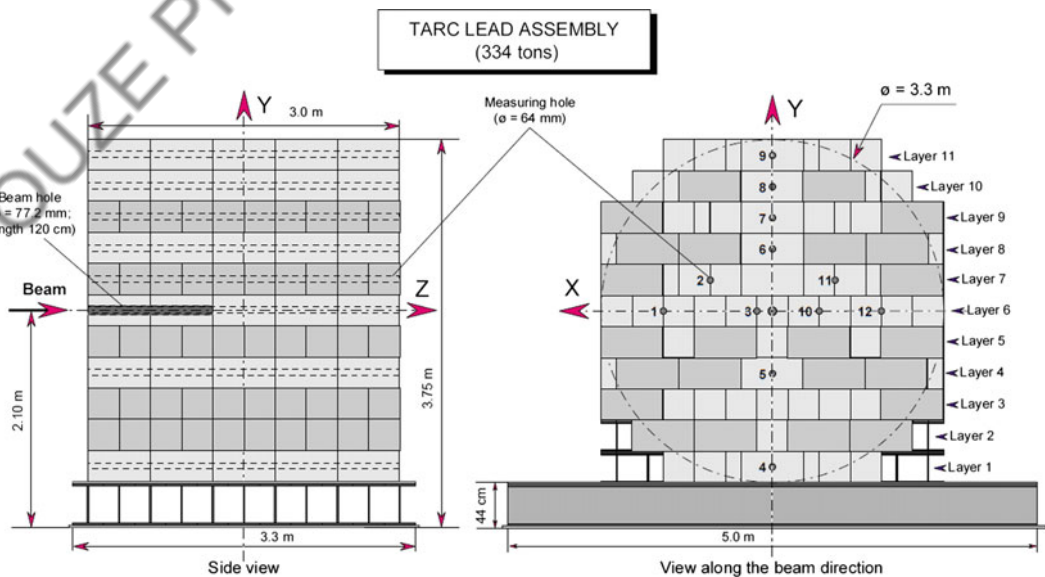


Fig. 6.1 TARC setup with mention of dimensions [3]

BROND-2 for different energy ranges and for specific materials has been utilized to prepare flat cross sections. It is a state-of-the-art procedure of utilization of data files after checking inconsistencies and after processing the raw data by the PREPRO code.

The TARC experiment takes care of the inaccuracies of the nuclear data and the material impurities whatsoever small, in the lead bulk. The setup has 12 holes for instrumentation and one big hole ($d \times l = 7.72 \times 120 \text{ cm}^2$) for the beam-related procedures. In Fig. 6.2, neutron fluence measured using the ^3He neutron detector in one of the hole positions is plotted with the simulated data of the dedicated EA code for the 2.5 GeV/c proton beam colliding the setup.

Transmutation rate of ^{99}Tc is deduced from the gamma from de-excitation of ^{100}Tc to ^{100}Ru . In Fig. 6.3, decay schemes of the three nuclei are given. By way of detection of ^{100}Ru by the gamma spectroscopy, rate of decay of ^{100}Tc is deduced and it can be verified from its built up rate from neutron activation of ^{99}Tc by the given neutron spectrum in the activation position.

Similarly, experiments of capture rates of long-lived fission products ^{129}I and ^{127}I are studied in the TARC setup. Also, production rates of ^{233}U from ^{232}Th and ^{239}Pu from ^{238}U are estimated in the setup. Some of its results of actinides will be discussed along with the results of GAMMA-3 and $E + T$ experiments later in the chapter.

6.2 n _ToF Experiments for Measurement of Cross Section

Abbreviation n _ToF is commonly used for 'neutron time of flight.' The time of flight concept is applicable for determination of kinetic energy, E of an object of mass, m . Thus, for a neutron of mass, m moving with non-relativistic speed, v , its kinetic energy, E_n (eV) can be measured in terms of time t (μs) taken in flight length, L (m) using the following relation after rationalization of units,

$$E_n = \frac{1}{2}mv^2 = \left(72.3 \times \frac{L}{t}\right)^2 \quad (6.1)$$

This leads to energy resolution, $(\Delta E/E)$,

$$(\Delta E/E) \sim 2 \times \Delta t/t \quad (6.2)$$

In case there can be uncertainty in measurement of length, L also then Eq. (6.2) is written as,

$$\Delta E/E = 2 \times \sqrt{[(\Delta t/t)^2 + (\Delta L/L)^2]} \quad (6.3)$$

In this case, position of start is defined by $L = 0$ and $t = 0$, and they are assumed to be measured precisely. If there is any difference in time of measurement and time of start of the projectile then corresponding correction will be required. As we know spallation neutron sources

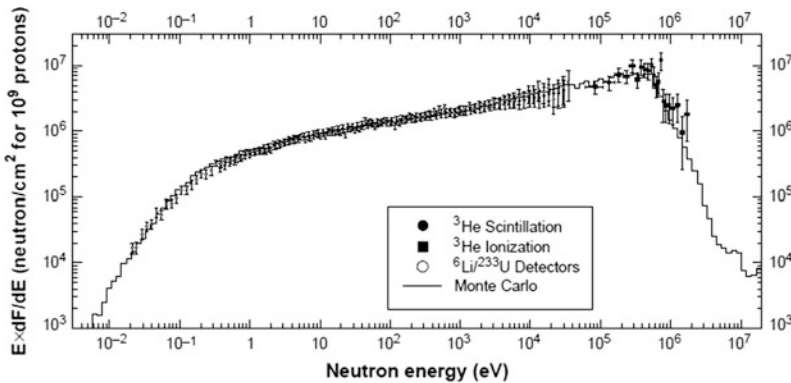
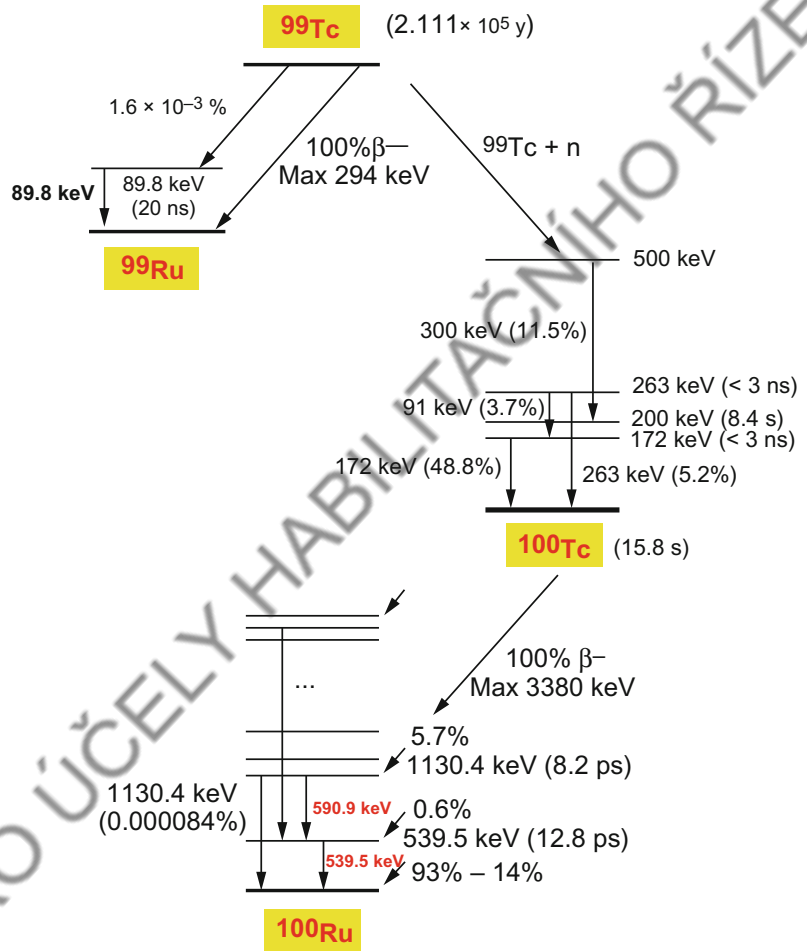


Fig. 6.2 Neutron fluence measured at $z = +7.5$, hole number '10' using the ^3He scintillator, ionization chamber, and $^6\text{Li}/^{233}\text{U}$ detectors (different for different

n -energy ranges) described in Ref. [3] and the calculated neutron fluence by using the MC code

Fig. 6.3 Decay schemes of ^{99}Tc , ^{100}Tc and ^{100}Ru



are driven by the accelerated particle beam, may be electron, proton, or deuteron, etc., therefore, pulse width will contribute toward Δt . For example, if there is a pulsed source of 100 ns width and a neutron time of flight is 11 m, then attainable energy resolution is $\sim 11.2\%$. Obviously, smaller pulse width and longer flight length, L , are most helpful for attaining better energy resolution which is required in resolving the highly narrow resonance peaks of cross sections in resonance region.

When a neutron is scattered by a nucleus on its way or it may have a nuclear reaction, then the scattered intensity I and incident intensity I_0 are related with the macroscopic cross section of scattering, $\Sigma = \sigma \times n$, by the following relation,

$$\frac{I}{I_0} = e^{-\Sigma x} \quad (6.4)$$

where n = number density and x = thickness in direction of the incident particle.

Thus, the total cross section σ can be written as

$$\sigma = 1/(nx) \times \ln\left(\frac{I_0}{I}\right) \quad (6.5)$$

Here, I_0/I is the inverse of the transmission coefficient, $1/T$ of the scattering material, and its measurement provides total cross section σ of the material. For having significant results of measurement of resonance cross section, it is essential that number of scatterings in the pure sample must be very large. This is possible with highly intense neutron beam and/or large thickness of the scattering material. Before starting an experiment, thickness of a sample needs to be optimized so that several secondary scatterings of incident particle do not take place in the given sample.

For a material composed of several isotopes, denoted by j , denominator of Eq. (6.5) can be substituted by $\sum_j N_j$ in place of $\sum_j n_j x$, and then the total cross section in the i th energy group can be written as,

$$\sigma(E_i) = \frac{1}{\sum_j N_j} \ln\left(\frac{1}{T_i}\right) \quad (6.6)$$

Wang et al. [7] have described the method of measurement of transmission coefficient using the Pohang Neutron facility (PNF) with details.

A major facility of cross-section measurement, the n _ToF facility at CERN, started in the year 2001 having 20 GeV/c pulsed proton beam (each pulse carries $3-7 \times 10^{12}$ protons) with pulse width of 7 ns is allowed to fall on massive Pb target to produce spallation neutrons. On an average, 300 n/p are produced for the given beam power [8]. Other charged particles produced in a collision are removed from the beam line by the 1.5 T sweeping magnet. According to Guerrero et al. [9], neutrons produced from the spallation target are moderated by borated water tank to give a desired neutron spectrum ranging from 0.025 eV to 1 GeV energy. Energy resolution is $\Delta E/E = 10^{-4}$. The neutrons are collimated two

times in an vacuum evacuated length of ~ 182 m and to converge into a beam spot of 2–8 cm diameter; then they are allowed to enter in the experimental hall of about 7.9 m length. In several experiments, liquid C_6D_6 scintillation detectors are employed in two modes of prompt gamma detection and the neutron detections. Its setup is shown in Fig. 6.4. One can refer to Tobias et al. [9] for the details of the detector. In several experiments at CERN n _ToF, capture reaction yield is determined using Eq. (6.7). Here, $Y(E_n)$ is a function of measured total (σ_T) and capture (σ_γ) cross sections that are determined by peak fitting to the transmitted intensity data of experiment.

Capture reaction yield is given by the following relation,

$$Y(E_n) = \mu(E_n) \left(1 - e^{-n\sigma_T(E_n) \frac{\sigma_\gamma}{\sigma_T}}\right) \quad (6.7)$$

Here, μ corresponds to multiple scattering correction, σ_γ and σ_T are the capture and total cross sections, and they are functions of E_n -energy and determined by R -matrix formalism.

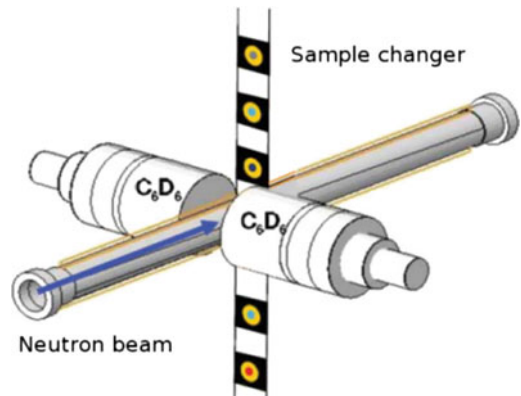


Fig. 6.4 Two C_6D_6 scintillation detectors ($d \times l = 12.7 \times 7.62$ cm²) placed across the neutron beam and above a sample changer. The samples are put on kapton (canning) foils spread on carbon sheet to avoid n -back scattering. Each detector carries about 1 L of liquid scintillator (see Tobias et al. [9])

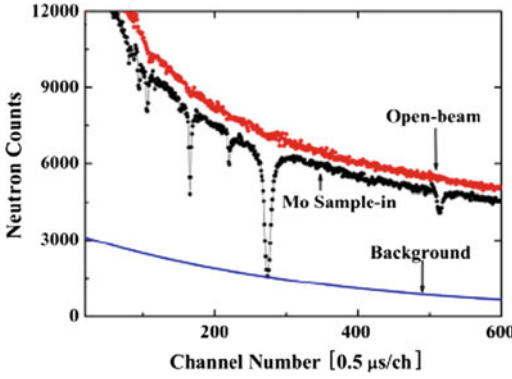


Fig. 6.5 Neutron counts versus the channel number in case sample in or open. Background spectrum is also projected [7]

In South Korea Pohang Neutron Facility, PNF [7] normally uses a large diameter ${}^6\text{Li-ZnS(Ag)}$ scintillator (BC702) for the neutron detection by way of ${}^6\text{Li}(n, \alpha){}^3\text{H}$ reaction where both α and ${}^3\text{H}$ charge particles contribute toward generation of signal on falling on the ZnS scintillator. The signals are converted to electric current by a PM tube. In the facility, two data-acquisition systems are used, e.g., NIM for $n\text{-}\gamma$ separation and CAMAC for the sample changer device and for the digitization of the ‘start’ and ‘stop’ signals. In Fig. 6.5, transmission spectrum of Mo sample taken at the PNF is shown along with the background counts. Reversed peaks correspond to the existence of resonances.

For the determination of resonance parameters, transmission spectrum is converted to cross-section versus neutron energy plot. Parameters are deduced from the SAMMY code [10] wherein multilevel R -matrix was used with Reich–Moore approximation [11] using the following relation,

$$\sigma_T = \frac{2\pi}{k^2} g \left\{ 1 - \cos 2\phi \left(1 - \frac{\Gamma_n \Gamma}{2d} \right) - \sin 2\phi \frac{\Gamma_n (E_\lambda - E)}{d} \right\}. \quad (6.8)$$

E is the neutron energy and E_λ is the resonance energy, g is the statistical factor, $g = \frac{2J+1}{2(2I+1)}$ and width, $d = \left[(E_\lambda - E)^2 + \left(\frac{\Gamma}{2}\right)^2 \right]$,

here, J is the spin of the resonance state and I is spin of the target nucleus, ϕ is potential scattering phase shift, and $\Gamma = \Gamma_\gamma + \Gamma_n$ is the sum of gamma and neutron widths expressed in eV. In practice, values of E_λ , g , J and Γ 's are accessed from the theoretical data given by Mughabghab [12] for a large number of nuclei and their isotopes. Full width at half maxima, Γ can be determined from the resonance peak and the peak height, σ_0 , related by the relation, $\sigma_0 = \frac{4\pi}{k^2} \frac{g\Gamma_n}{\Gamma}$ which allow determination of value of $g\Gamma_n$. In Table 6.1, data of measurements at CERN n _ToF and PNF are reported with references of several works shown in the table.

Derrien et al. [20] have presented results of transmission experiments conducted from the year 1972–1990 using ToF facility at Oak Ridge Electron Linear Accelerator (ORELA) including some more recent measurements. Most of the experiments have shown uncertainty more than >5% up to even 10%. In these measurements, Doppler and resolution-broadened capture cross sections were also calculated from the resonance parameters including self-shielding and multiple scattering effects. The n _ToF facility at CERN is world's highly placed facility of modern time and has longest path length ~ 185 m, and it has high capability of cross-section measurements with better accuracy. In particular, the facility has possibility of using very thin samples and precision is $\sim 6\%$ in case of averaged cross sections and $<3.5\%$ in case of resonance cross sections. Using the facility at CERN, González et al. have reported [22] preliminary results of a large number of resonance cross sections in the form of CS versus E_n plots in case of ${}^{151}\text{Sm}_2\text{O}_3$, ${}^{232}\text{Th}$, ${}^{209}\text{Bi}(n, \gamma)$, ${}^{204,206,207,208}\text{Pb}$ and the fission cross sections of ${}^{235}\text{U}$, ${}^{238}\text{U}$, and ${}^{209}\text{Bi}$ nuclei.

6.3 IREN—Facility at Dubna

A new Time of Flight (n _ToF) facility, Intense Resonance Neutron Source (IREN) is developed to conduct experiments using gammas and neutrons in the resonance energy region. It is located

Table 6.1 Resonances reported in various experiments. Sample details, energy range of measurement, reported number of resonances, finalized cross sections or the yield, and uncertainty are indicated

Target, mass, size	E_n -range	Number of resonances and energy	Cross-section or kernel value	Reference
^{58}Ni , 2.069 g, $d \times l = 19.91 \times 0.72 \text{ mm}^2$	0.027– 400 keV	51 resonances identified	11 peak CS measured at energies 5–100 keV with $\sim 6\%$ errors	[13] (CERN)
^{63}Ni (impurity of ^{59}Ni)	0.025– 200 keV	12 new + 1 ^{59}Ni	Absorption kernels measured	[14] (CERN)
^{151}Sm , 206.4 mg in Sm_2O_3	1 eV– 1 MeV	01 + several resonances at $E_n = 490\text{--}550 \text{ eV}$ identified	Maxwellian average, $3100 \pm 160 \text{ mb}$	[15] (CERN)
^{186}Os , 1.9999 g	1 eV– 1 MeV	Several resonance peaks in 100–200 eV range	A few barns to 100 barns	[16] (CERN)
^{209}Bi , $d \times l = 20 \times 6.1 \text{ mm}^2$	0.8– 23.15 keV	21 resonances identified, 05 cross-section values given at 5, 8, 20, 25 keV and 01 at E_{th}	Resonance parameters with $<3\%$ uncertainty and cross sections with $\sim 6\%$ uncertainty	[17] (CERN)
^{232}Th , 2.8037 g, 2 disks dia. = 1.5 cm	3.994– 991.452 keV	48, averaged over low and high energy range of corresponding peaks	0.958, 1.281, 1.097, 1.004, 0.912, 0.919, 0.848, 0.817, 0.800, 0.787, 0.761, 0.729, 0.685, 0.613, 0.641, 0.566, 0.545, 0.513, 0.497, 0.468, 0.456, 0.413, 0.365, 0.346, 0.318, 0.275, 0.248, 0.229, 0.220, 0.204, 0.192, 0.172, 0.179, 0.165, 0.158, 0.159, 0.156, 0.147, 0.144, 0.141, 0.140, 0.158, 0.154, 0.164, 0.178, 0.179, 0.156 and 0.135 (all in barns), $<3.5\%$ uncertainty	[18] (CERN)
^{238}U , 6.125(2) g, $53.90 \times 30.30 \text{ mm}^2$	22 eV– 25 keV	Several resonances	Only yield measurements with 2–3% accuracy are reported	[19] (CERN)
^{237}Np (n, f)	0.2– 1000 MeV	Fission cross-sectional curve	CS curve from ~ 0.1 to 2.4 b, CS are $\sim 6\%$ above the evaluated data. Few resonance peaks reported from 37 to 42 eV energy	[21] (CERN)
^{234}U (n, f)	500–590 eV	Several resonance peaks	Resonance peaks reported from 500 to 590 eV	[21] (CERN)
^{241}Am (32 mg)	0.025 eV– 1 MeV	Several resonances	CS not reported	[9] (CERN)
^{94}Mo in 94.025(1) g of $^{\text{nat}}\text{Mo}$	0.01–200 eV	$107.2 \pm 0.8 \text{ eV}$	CS not reported	[7] (PNF)

(continued)

Table 6.1 (continued)

Target, mass, size	E_n -range	Number of resonances and energy	Cross-section or kernel value	Reference
^{95}Mo in 94.025(1) g of $^{\text{nat}}\text{Mo}$	0.01–200 eV	44.75 ± 0.01 , 110.6 ± 1.0 , 118.5 ± 1.0 , 159.4 ± 0.3 eV	CS not reported	[7] (PNF)
^{96}Mo in 94.025(1) g of $^{\text{nat}}\text{Mo}$	0.01–200 eV	114.7 ± 0.4 , 131.4 ± 0.1 eV	CS not reported	[7] (PNF)
^{97}Mo in 94.025(1) g of $^{\text{nat}}\text{Mo}$	0.01–200 eV	71.2 ± 0.1 , 78.98 ± 0.59 , 109.09 ± 0.84 , 126.9 ± 1.1 eV	CS not reported	[7] (PNF)
^{98}Mo in 94.025(1) g of $^{\text{nat}}\text{Mo}$	0.01–200 eV	12.2 ± 0.1 eV	CS not reported	[7] (PNF)
^{100}Mo in 94.025(1) g of $^{\text{nat}}\text{Mo}$	0.01–200 eV	97.2 ± 0.7 eV	CS not reported	[7] (PNF)

at the Frank Laboratory for Neutron Physics at JINR from the year 1994 [23]. The facility is to provide pulsed gamma and neutrons with pulse duration of 400 ns and repetition rate to be 150 Hz [24]. The gamma and neutron sources can be used for the studies related to astrophysics, nuclear data, nuclear structure, symmetries and modifications of materials. According to Meshov et al. [25], IREN is a vertically developed facility at JINR Dubna planned for variety of experiments related to ADSS including cross-section measurements. The facility is planned to get an intense neutron source from an electron beam which falls on Tantalum like target and converted into gamma which hits the plutonium-enriched uranium core for conversion and multiplication of neutrons. In a way, neutron source is a subcritical reactor without collection of heat from nuclear energy. Its parameters are given in Table 6.2. Its first phase is already completed in the year 2010 attaining neutron intensity $\sim 10^{11} \text{ s}^{-1}$. However, on attaining higher neutron intensity $\sim 10^{15} \text{ s}^{-1}$, it will become world's number one facility. Its several characteristic parameters such as mean neutron rate and multiplication factor will be at least ten times of the GELINA facility. With the existing 60 m ToF, cross-section measurements have been made with high accuracy. Experiments such as radiation resistivity of GaAs and Si detectors, analysis of Boron content in Boron-containing ceramics, and analysis of rare elements Pd, Os, Ir, Pt, etc., content of gold-containing ore were

conducted among its first experiments. In Fig. 6.6, schematic view of neutron generation is shown without n -ToF.

The facility has planned following measurements of elements according to its priority list for the neutron cross-section measurements and covariance [27],

- 19 isotopes of actinides (cross-sectional covariance, nubar covariance) in priority order: $^{235,238}\text{U}$, ^{239}Pu , ^{237}Np , $^{240,241}\text{Pu}$, $^{241,242\text{m},243}\text{Am}$; ^{232}Th , $^{233,234,236}\text{U}$, $^{238,242}\text{Pu}$, $^{242,243,244,245}\text{Cm}$.
- 34 structural, moderator and coolant materials (cross-sectional covariance) in priority order: ^{16}O , ^{23}Na , ^{52}Cr , ^{58}Ni ; ^1H , ^{12}C , ^{28}Si , $^{90,91,92,94}\text{Zr}$, $^{206,207,208}\text{Pb}$, ^{209}Bi , ^4He , $^{6,7}\text{Li}$, ^9Be , ^{10}B , ^{15}N , ^{19}F , ^{27}Al , $^{56,57}\text{Fe}$, $^{155,156,157,158,160}\text{Gd}$, $^{166,167,168,170}\text{Er}$.

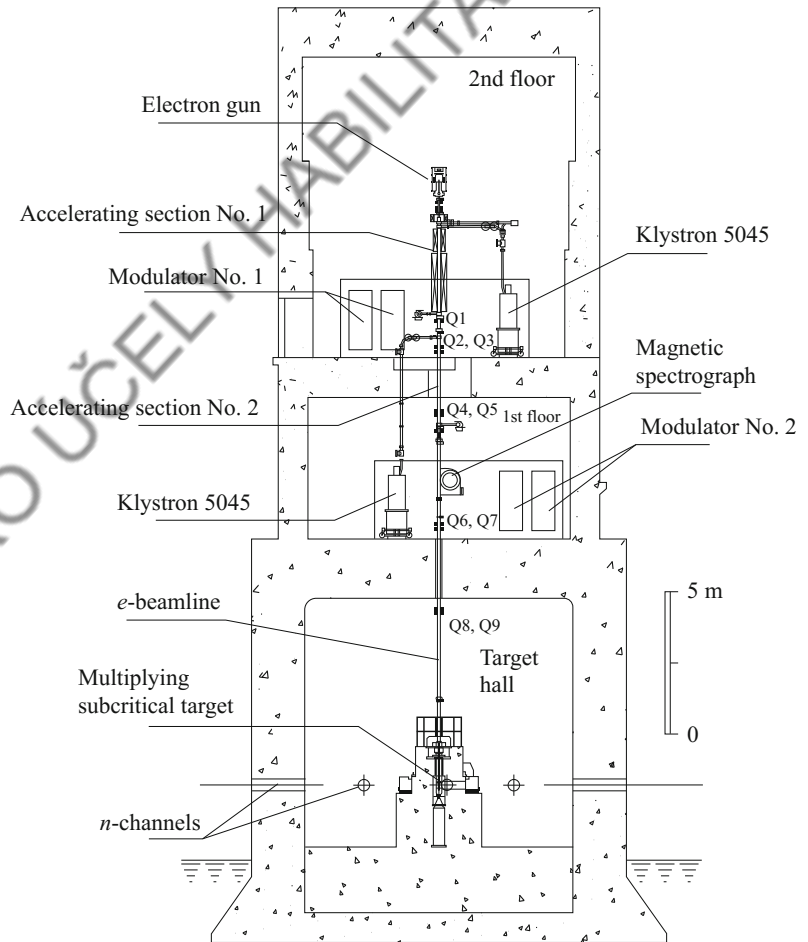
6.4 TRIGA

TRIGA stands for **T**rainig, **R**esearch, **I**sotopes, **G**eneral **A**tomics. Historically, General Atomics (GA) has been pioneer manufacture of fuel rods containing hydrogen in the 1950s. The GA metallurgists perfected making fuel rods of uranium–zirconium hydride (UZrH) as tough as stainless steel and corrosion-resistant fuels. Thus, its use was extended in the 1980s by designing and developing proliferation-resistant fuels

Table 6.2 Planned parameters of the IREN facility [25]

Parameters	Design	Stage 1 (year 2010)
Electron energy (MeV)	200	30
Peak current (A)	1.5	3.0
Beam pulse duration (ns)	200	100
Repetition frequency (Hz)	150	25 ÷ 50
Average beam power (kW)	9.0	0,225 ÷ 0,450
Multiplication target	Pt	W (no multiplication)
Average neutron flux (s ⁻¹)	1.16 × 10 ¹⁵	1 × 10 ¹¹

Fig. 6.6 IREN facility to have several neutron channels for experiments [26]



having low uranium content. In a way, TRIGA provides inherent safety than engineered safety by way of external design factors.

General Atomics has installed 66 reactors in universities, institutions, industries, and medical facilities in 24 countries. They have produced

low-power reactors ranging in between 0.1 and 16 MW. Some of them are pulsed reactors of high power also. TRIGA International is a joint venture company with CERCA of France which manufactures and sells TRIGA fuel [28] to research reactors. GA has pioneered its scope of

research in material production, defense, unmanned spacecrafts, and fusion education outreach, etc. In Fig. 6.7, fuel rods, special customized structures made with SiC materials with required geometries, and neutron reflectors like graphite and Zr_3Si_2 for better fast reactor efficiency are shown. GA has worked for several computational tools such as TRIGLAV [29] for burn-up calculations.

TRIGA performed several innovative experiments for the development of reactor fuels and validate the developed software packages. A 250 kW light water pool-type reactor TRIGA Mark II of Ljubljana has been developed by GA [30] using the TRIGLAV calculation package.

Pulsed TRIGA reactor at Mainz has been utilized to develop ultra-cold neutron (UCN) source. The thermal neutrons are cooled down to 6 °K. By putting the converter close to the reactor at $d \sim 39.5$ cm, UCN storage rate $\sim 178,000$ UCN per reactor pulse is achieved in the experiment. Maximum density achieved was 550,000 UCN per pulse [31]. As already known, a cold neutron may provide its better decay rate which is demanded in several cosmological studies and even in particle physics. The UCN itself is likely to provide a source for the new neutron spectroscopy in place of scalar optics, and it has high importance over the scalar optics as a neutron is highly penetrating in bulk of a

material. In this experiment, UCN density is also observed decreasing with time due to decay.

6.5 KEK Setup

Japan's special attention on research with spallation neutrons started taking shape in the year 1999 [32–34] when Japan Atomic Energy Research Institute (JAERI) and High Energy Accelerator Research Organization (KEK) planned for spallation source of 1 MW proton beam injection with 3 GeV of proton energy and 333 μ A of current with pulse duration of 25 Hz in which two 100 ns bunches are injected with 400 ns interval. Beam power ~ 220 kW is already achieved in February 2017. The spallation target is assumed to be Mercury (Hg). Monte Carlo simulation studies [35] are planned with combined NMTC/JAERI and MCNP. The design is unique from the point of crossing target and moderator system. In fact, it is termed as Target–Moderator–Reflector (TMR) system. Liquid hydrogen is used as the moderator flowing in reverse phase to the flowing Hg target and heavy water (D_2O) as the reflector [34]. Stainless steel SS316 is used as the container, and its related issues of radiation damage have been studied in case of other such facilities. The facility named as 'J-PARC 1 MW pulsed spallation neutron source JSNS' is

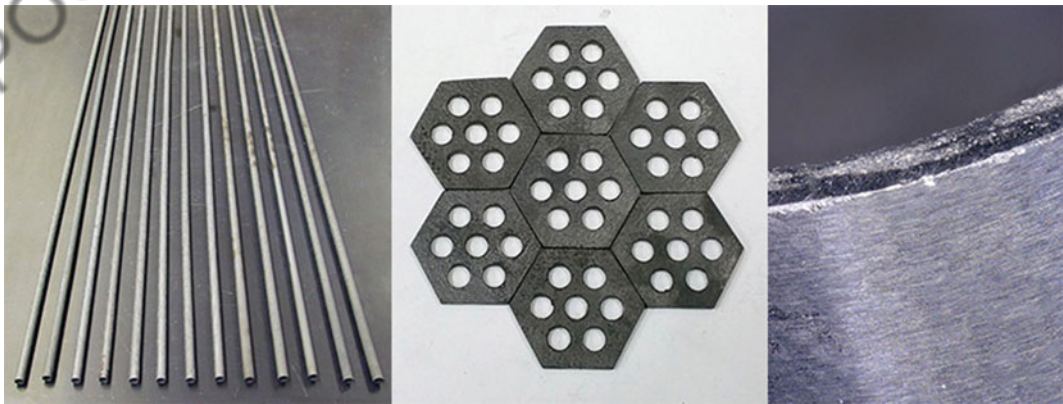


Fig. 6.7 Advance materials as fuel rods (left), structured geometries of special materials like SiC (middle), and neutron reflecting materials such as Zr_3Si_2 (right) [28]

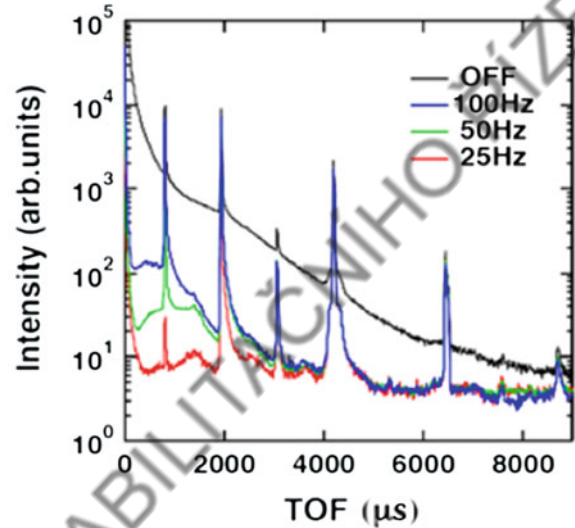
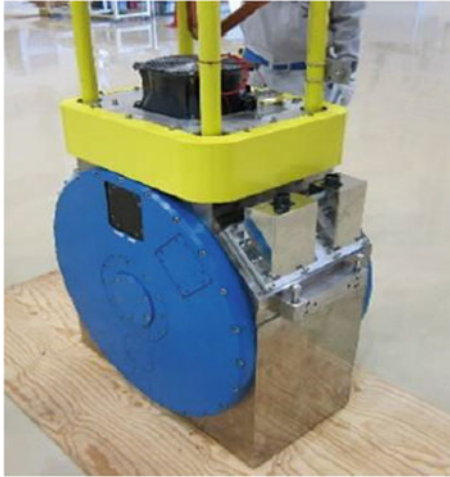


Fig. 6.8 (Left) T0 neutron chopper (right) ToF spectra for operation frequencies $f = 25, 50, 100$, and 'off' modes. Use of a chopper has an advantage of increasing

successfully launched in May 2008 [36, 37]. Besides, the center caters several developmental activities such as neutron detectors, supermirror devices, ^3He neutron spin filters, and choppers with high performance for material science research. With a neutron chopper, finer neutron bunches/burst can be obtained with the change of the chopper frequency as shown in Fig. 6.8.

At the JA-PARC, cold neutron facility is also developed by gradually thermalizing neutrons in heavy water having temperature gradient from 300 °K to less than 80 °K followed by cooling in He-II environment up to 10^{-3} °K [37]. At low temperatures, neutron momentum is transferred by way of phonons. At this stage, UCN are extracted in vacuum up to the cryogenic window placed in a superconducting magnet for the purpose of polarization. Various experiments are conducted with the UCN beam so attained.

In place of a reactor to be a neutron source, attempts are made for a spallation neutron source to be utilized for producing the UCN as shown in Fig. 6.9.

For the neutron scattering experiments, wherever focused neutron beams are required, achromatic focusing optics is important, hence,

the intensity of the pulse by shortening the path length and cutting down transport losses [36]

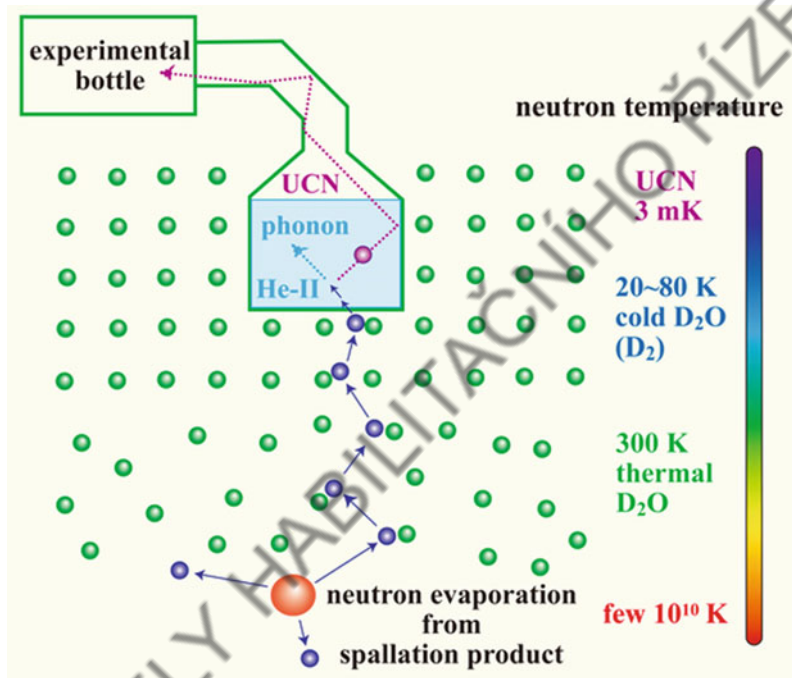
the 'focusing mirrors.' The purpose of the focusing mirror is to provide narrow area focus of a beam of wide energy range. This is achieved by depositing NiC/Ti on quartz glass. A wide-band neutron beam with wave length $\lambda = 3.64$ Å is focused within 0.25 mm in an attempt made in this direction.

6.6 BFS Setups

According to Russian language, BFS stands for 'Bol'shoy Fizicheskiy Stand' means 'Big Physical Facility' in English language. In the year 2009, Russian federation started a plan of development of Generation IV reactors. Thus, under the ROSTAM 2009, Russia Government decided the following plan to develop next generation nuclear energy technology on the basis of fast neutron reactors with a closed nuclear cycle [38]. Three critical assemblies, BFS-73-1, BFS-75-1, and BFS-76-1A, were created in BFS-1 and BFS-2 facilities along with BFS-109-2A created at IPPE, Obninsk recently in the year 2012.

The BFS-1 had become critical in the year 1961, and it was upgraded recently in the year

Fig. 6.9 Production of UCN by gradual moderation of the spallation neutrons [36, 37]



2016. It is likely to continue for one more decade. The facility was designed to study full-scale mock-ups of research and fast-power reactors (E_{therm} to 1,000 MW) with different types of fuels including the fertile fuel and coolant (Na, Pb, Pb–Bi, water, gas, and air) and various core and blanket layouts for conducting research for neutronic characteristics of critical assemblies. It is a vertical system with size being $d \times l = 2 \times 2.2 \text{ m}^2$ having an experimental opening of diameter $\sim 35 \text{ mm}$. Its critical parameters are given in Table 6.3.

Following experiments have been conducted at the facility,

1. Mock-up of IBR-2, BOR-60, and BN-350, MBIR, SVBR fast Russian reactors as well as foreign reactor mock-ups have been studied.
2. Studies to justify reactor safety of sodium- or lead-cooled fast reactors and VVER-type reactors are conducted.
3. Performed experiments for verification of techniques and specifications of neutron data as well as computer codes for the neutronic characteristics of fast and VVER-type reactors.

4. Experiments on safety justification of the fuel cycle and geological disposal are performed.

BFS-2 is a larger version of BFS-1 critical facility having size $d \times l = 5 \times 3.3 \text{ m}^2$, about 10,000 fuel tubes carrying fuel in the form of disks. Its power is 1 kW compared to 0.2 kW of BFS-1 facility. Its maximum neutron flux density is an order smaller than BFS-1 and reflector and coolant same as that of BFS-1. Fuel enrichment proportions are similar as that of BFS-1. Power of the reactor facilities has been 3,000 MW than 1,000 MW of the BFS-1.

The setup of BFS complex has been used for several experimental studies under commissioning agreements with the USA, China, Korea, France, Japan, India, and other countries.

6.7 MUSE and YALINA Setups

A comprehensive MUSE program (**M**ultiplication with an **E**xternal **S**ource) was started at the MASURCA facility in Cadarache, France [39], where a neutron generator consisting of a deuteron accelerator and a tritium target was coupled to a

Table 6.3 Key technical parameters of the BFS-1 facility

Characteristic	Parameter
Power	0.2 kW
Moderator for simulated light water reactors	Distillate, boric acid solution, polyethylene, graphite
Simulated coolant	Na, Pb, Pb–Bi, water, gas
Reflector	U, UO ₂ , Pb, Pb–Bi, steel, etc.
Fast neutron flux density, max.	$10^{10} \text{ cm}^{-2} \text{ s}^{-1}$
Core cooling	Natural convection or forced air cooling

subcritical core. Major part of the program was devoted to the investigation of methods for reactivity determination, pulsed neutron source methods, neutron noise methods, and the source jerk method. Some neutron statistics experiments such as fission rate distributions and spectral distributions have also been performed. In the beginning in year 1996, Cf neutron source was used for triggering. Later in the year 1998, generator GENEI 26 (**Generateur de Neutrons Intense**) was used. Its repeatability rate and wide pulses did not allow precise measurements. Thus, in the MUSE-4, GENEPI-1 (**GEnérateur de Neutrons Pulsé Intense**), deuteron sharp pulse (1 μs , 50 mA peak current) was used to produce 14 MeV neutron pulses with high repeatability rate. The facility was used for conducting several experiments during 2002–04 and finally dismantled in the year 2007.

Similarly, in the 6th EU framework, European research program for transmutation of high-level nuclear waste by way of an Accelerator-Driven System, IP-EUROTRANS was started. Under this activity, a zero-power subcritical facility, YALINA was installed. It is located at the Joint Institute of Power and Nuclear Research in Sosny outside Minsk, Belarus. Although YALINA does not fulfill the conceptual design of a future ADSS, yet, the neutronics of the subcritical core is an interesting feature as it can be applicable in both fast and thermal systems independent of the type of neutron source. The success of construction of the facility can be assumed as a necessary step toward a full-scale ADSS from the point of understanding the behavior of subcritical cores and the coupling between the main components, the accelerator, the target, and the core.

The facility is constructed to validate and test a possible online reactivity monitoring technique, and its booster is a subcritical fast and thermal core coupled to a neutron generator. As in MUSE-4, the generator in YALINA is an accelerated deuteron ion colliding with Ti target to produce 14 MeV neutrons. The deuteron ion can be in pulsed or continuous mode; hence, the neutron yield to be pulsed or continuous. As an example, in continuous mode, 1.5 mA current of the deuteron projectile can produce $\sim 10^{11}$ neutrons/s.

Both lead zone and the thermal polyethylene zones are shown in Fig. 6.10 with the Ti target in its center. The lead zone is termed as the booster of the primary neutrons produced by Ti target. In the innermost part of the lead booster, UO₂ with 36% enrichment or metallic uranium with 90% enrichment is acceptable as the alternative. Further, the inner fuel configuration is surrounded by 36% enriched UO₂. This is also known as the outer booster. Outside the rectangular configuration as shown in the sectional view, the thermal zone is loaded with UO₂ with 10% enrichment and the polyethylene (C₂H₄) assumingly a better moderator than heavy water. The two zones are separated by a thermal neutron filter or a valve zone of 108 pins of natural uranium and 116 pins of borated carbide, B₄C located in two outside rows of the fast zone. The thermal neutrons migrated from the thermal zone will be absorbed by the boron or ^{nat}U. Thus, the coupling of fast neutrons between the zones is maintained. The B₄C rods inserted in the thermal zone allow change of the reactivity of the system. Positions of extra control rods are also shown in Fig. 6.10. All the zones are enclosed inside the graphite

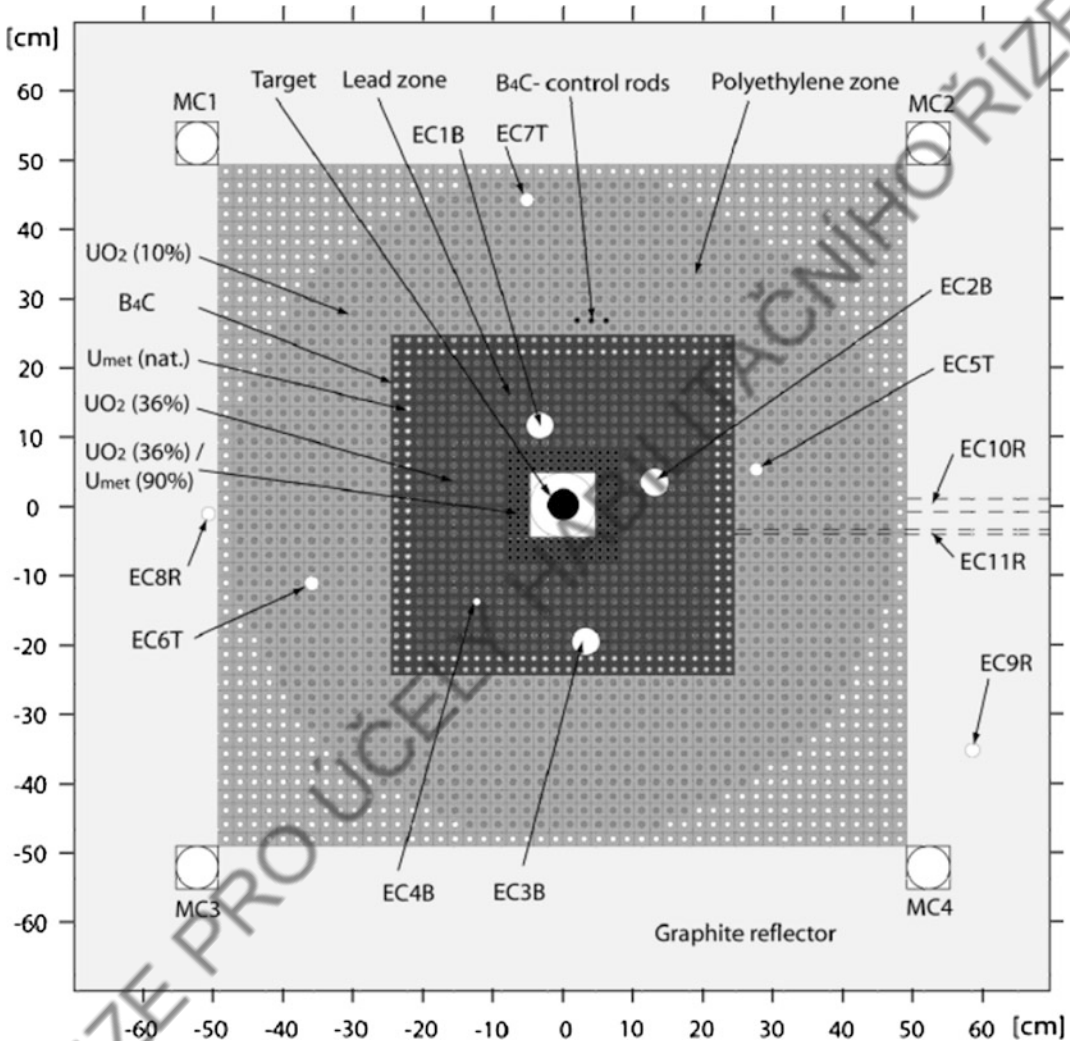


Fig. 6.10 A schematic view of YALINA booster reactor core with possibility of fast-thermal neutron flux zones [40]

reflector. The experimental channels are marked with EC or MC. For details, a reader is advised to follow Berglöf et al. [40].

In Table 6.4, data of criticality, k_{eff} estimated using MCNP code is shown for different loading configurations of the fast and thermal zones. It is understandable that high criticality and small criticality conditions can be achieved by changing configurations of the two zones. Effect of insertion of control rods is also studied. It may be pointed out that except the enrichment details of subcritical core, SC6 all other zones were studied by inserting controlled rods or without control rods.

We understand that changes in a reactor are quantified by the reactivity. A critical reactor has zero reactivity, a subcritical reactor has negative reactivity, and a supercritical has positive reactivity. Reactivity is measured in units as pro cent mille (pcm) and defined as, ρ

$$\rho = 1 - \frac{1}{k_{\text{eff}}} \quad (6.9)$$

Assessment of k_{eff} may be done from MCNP code using its KCODE option. Reactivity monitoring techniques have been described in Refs.

Table 6.4 Enrichment conditions of the booster zones of subcriticality and number of fuel pins, and expected criticality, k_{eff} [40]

Zone	Inner booster		Outer booster	Thermal zone	Expected k_{eff}
	90%	36%			
Enrichment level	90%	36%	36%	10%	
SC0	132	–	563	1141	0.977
SC3a	–	132	563	1077	0.950
SC3b	–	–	563	1090	0.950
SC6	–	132	563	726	0.850

[40–42] and according to the references, a neutron or a pulse of neutrons is introduced in the system which will give rise to prompt neutrons, say A_p and later delay neutrons are emitted and they may be called say A_d . An integral view of A_p and A_d measured with the help of detectors installed in the booster system can be used to measure the reactivity.

6.8 GUINEVERE and VENUS-F Setup

GUINEVERE stands for ‘Generator of Uninterrupted Intense Neutron at the lead Venus Reactor.’ It was launched in the year 2006 to operate with VENUS-F reactor at SCK_CEN site in Mol (Belgium). In this setup [43], a reactor is coupled vertically with GENEPI-3C neutron generator to operate in both pulsed and continuous modes. The GENEPI-3C machine is 250 kV deuteron accelerator with a copper target with titanium–tritium (TiT) or titanium–deuterium (TiD) deposits to provide 14 MeV or 2.5 MeV neutrons following $T(d, n)^4\text{He}$ or $D(d, n)^3\text{He}$ reactions, respectively. The machine is different to MUSE from the point of pulse size as well as being in continuous mode. In its DC mode, the beam can also be used in beam-trip mode. The beam spot size is 20–40 mm diameter, and intensity of produced neutrons would be $\sim 5 \times 10^{10}$ n/s. The VENUS-F core consists of fuel assembly (FA) arranged in a cylindrical geometry (~ 80 cm in diameter, 60 cm in height) has fuel $\sim 30\%$ ^{235}U -enriched metallic uranium. In the setup, the core neutrons will be moderated and reflected with solid lead (zero-power experiment) and all experimental details have been discussed by Baylac [44]. In a way, it is a prototype of MYRRHA innovative ADSS. Particularly,

GUINEVERE has a vertical coupling with a fast reactor cooled by lead.

Thus, as pointed out above, the GUINEVERE setup is designed to provide a unique experimental setup with continuous beam coupled to fast subcritical assembly for providing results for the following research themes,

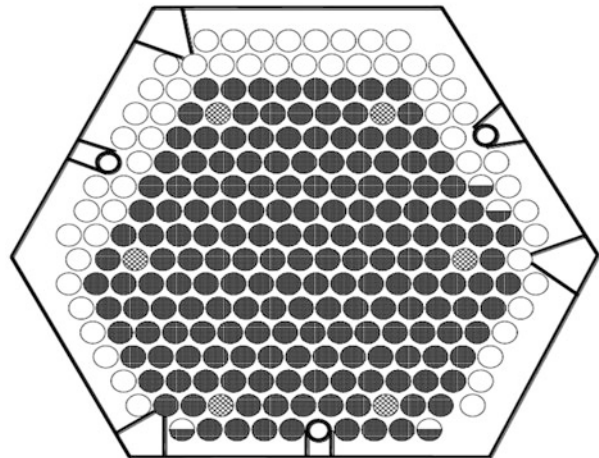
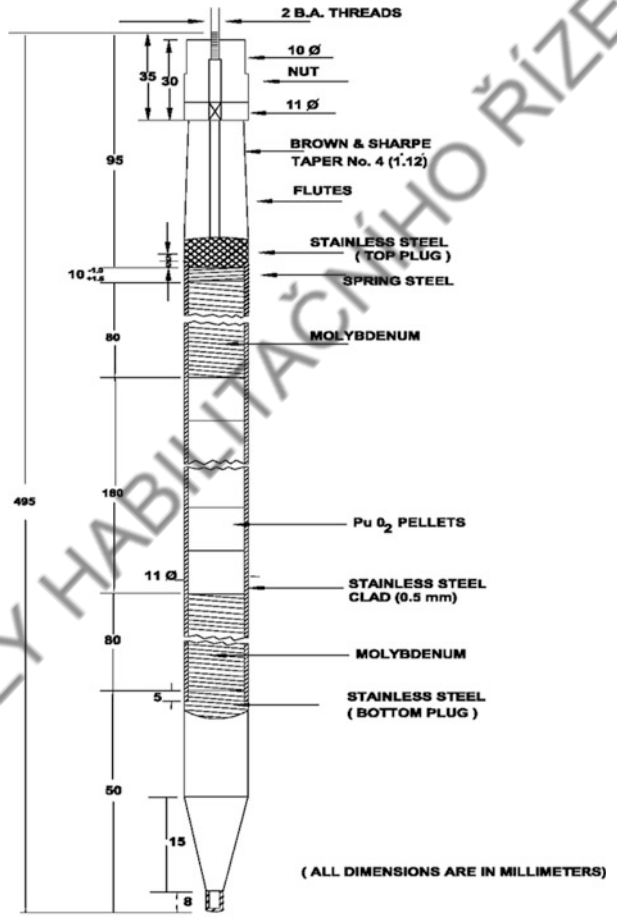
- (i) validation of the methodology of measuring the subcriticality level,
- (ii) investigation and validation of the operational procedures for a future ADSS,
- (iii) validation of neutronic codes, and
- (iv) safety and licensing issues related to a fast spectrum of an ADSS.

6.9 PURNIMA and KAMINI Experimental Reactors

PURNIMA is abbreviated for Plutonium Reactor for Neutronic Investigations in Multiplying Assemblies. PURNIMA-1 was built in 1970s [45] by BARC, Trombay, India, as India’s zero-power reactor fueled with plutonium oxide as its first experimental setup. Design of its fuel pin is shown in Fig. 6.11. The fuel pin carries PuO_2 pellets of 1 cm diameter tightly sandwiched between 8-cm-long molybdenum reflectors on both sides. Total length of fuel pin is 41 cm.

Isotopic composition of fuel by weight percentage is $^{239}\text{Pu}:$ $^{240}\text{Pu}:$ $^{241}\text{Pu}::95.75:4:0.25\%$. A detailed report of the setup is given by Basu et al. [46]. The setup was made critical at criticality = 1 at temperature 25 °C. With the given source intensity $\sim 1 \times 10^7$ n/s, fission rate is estimated to be 3.3×10^{10} /s producing

Fig. 6.11 (Up) Design of PuO₂ fuel pin and (below) core configuration of PURNIMA-1 with 175 full and 4 half fuel pin assemblies [45]. Assembly is triggered by Pu-Be neutron source. Hollow pins are dummy



- Full fuel pins
- Pu-Be Source pencils
- ◐ Half fuel pins
- SS tie rods

8.2×10^{10} n/s. Due to the fact that source neutrons are at the periphery of the setup and fission neutrons are in the core, then the criticality will be somewhat reduced for the reactor power of 1 W. At 25 °C, criticality is deduced to be 1.00039 ± 0.00441 .

PURNIMA-2, a thermal reactor, had reached criticality in May 1984. The reactor was fueled with uranyl nitrate solution (98.1862 weight percent of ^{233}U in $^{233}\text{UO}_2(\text{NO}_3)_2$) and beryllium oxide (BeO) as reflector. About 400 g of fissile ^{233}U produced in India was burnt in the reactor. This is purely an Indian reactor for the experimental activities like measurement of critical mass as a function of concentration of the solution, reactivity for various safety devices, and measurements of void and temperature coefficients of the reactivity. Details of the design, configuration, other experimental details and evaluations can be seen in Refs. [47–49]. Cross-sectional view through the center of the reactor is shown in Fig. 6.12 [49] with all its components and channels.

The uranium concentration used for the given configuration was 116.6 g/L for a critical mass of 457 g. The reactor was triggered by ^{252}Cf of strength $\sim 10^5$ n/s. Subsequently, the reactor was made critical with uranium concentrations of 103.8, 90.9, 81.5, 70.7, and 60.5 g/L also. It is also planned to be triggered by *d-t* neutron source [50]. Thus, the PURNIMA-2 reactor was decommissioned to produce PURNIMA-3 which became critical in November 1990, and subsequently, it paved way of design of KAMINI reactor.

KAMINI stands for **KAlpakkam MINI**, a zero-thermal-power reactor based on ^{233}U fuel (uranium–aluminum alloy) and moderated by light water and BeO being its neutron reflector. It is situated at IGCAR, Kalpakkam, an atomic power research center of Department of Atomic Energy, India. KAMINI became critical in October 1996. Figure 6.13 shows a schematic diagram of the reactor. The size of fuel assembly is $l \times b \times d = 275 \times 66 \times 66 \text{ mm}^3$ having fuel plates each of size $260 \times 62 \times 2 \text{ mm}^3$ and wrapped in aluminum frame.

6.10 BRAHMA Subcritical Facility at BARC

Sinha et al. [52] have reported progress of construction of a subcritical assembly developed at BARC, Trombay, with the objective of testing criticality of different fuels and dynamic and static features of neutronics of ADSS. The facility is driven by *d-t/d-d* neutron source; hence, coupling of an accelerator may be validated. So far preliminary results of flux and reactivity measurements using pulsed neutron source techniques have been obtained and they are presented in the article by Sinha et al. [52].

6.11 GAMMA Series of Experiments at JINR, Dubna

At JINR, Dubna, a large number of experiments are conducted by producing neutron spectra in collision of accelerated particle with a spallation target. Such neutron spectra are allowed to fall on a sample to produce a nuclear reaction. Several energy neutrons of the spectrum can produce a desired reaction, and the reaction rate is measured using the gamma spectroscopy. Cross section, σ of a reaction can be derived from the reaction rate, $R = \sigma \times \Phi$, where Φ is the incident particle flux expressed in units as n/cm²/s and σ in cm². In case of particle flux corresponds to a given energy spectrum in place of unique energy, cross section is known as an spectrum average cross section (sp. av. cs.) [53] and given by

$$\sigma_{\text{sp.av}} = \frac{\sum \sigma_i \phi_i}{\sum \phi_i} \quad (6.10)$$

and the flat cross section σ_i of the *i*th energy bin in between E and $E + dE$ is given by,

$$\sigma_i = \int \sigma(E) dE / \int dE \quad (6.11)$$

For the calculation of $\sigma_{\text{sp.av}}$ from Eq. (6.10), data of cross section, σ_i corresponding to neutron energy can be taken from the ENDF files if it is available at the given energy. For discretely available data, first flat cross sections are

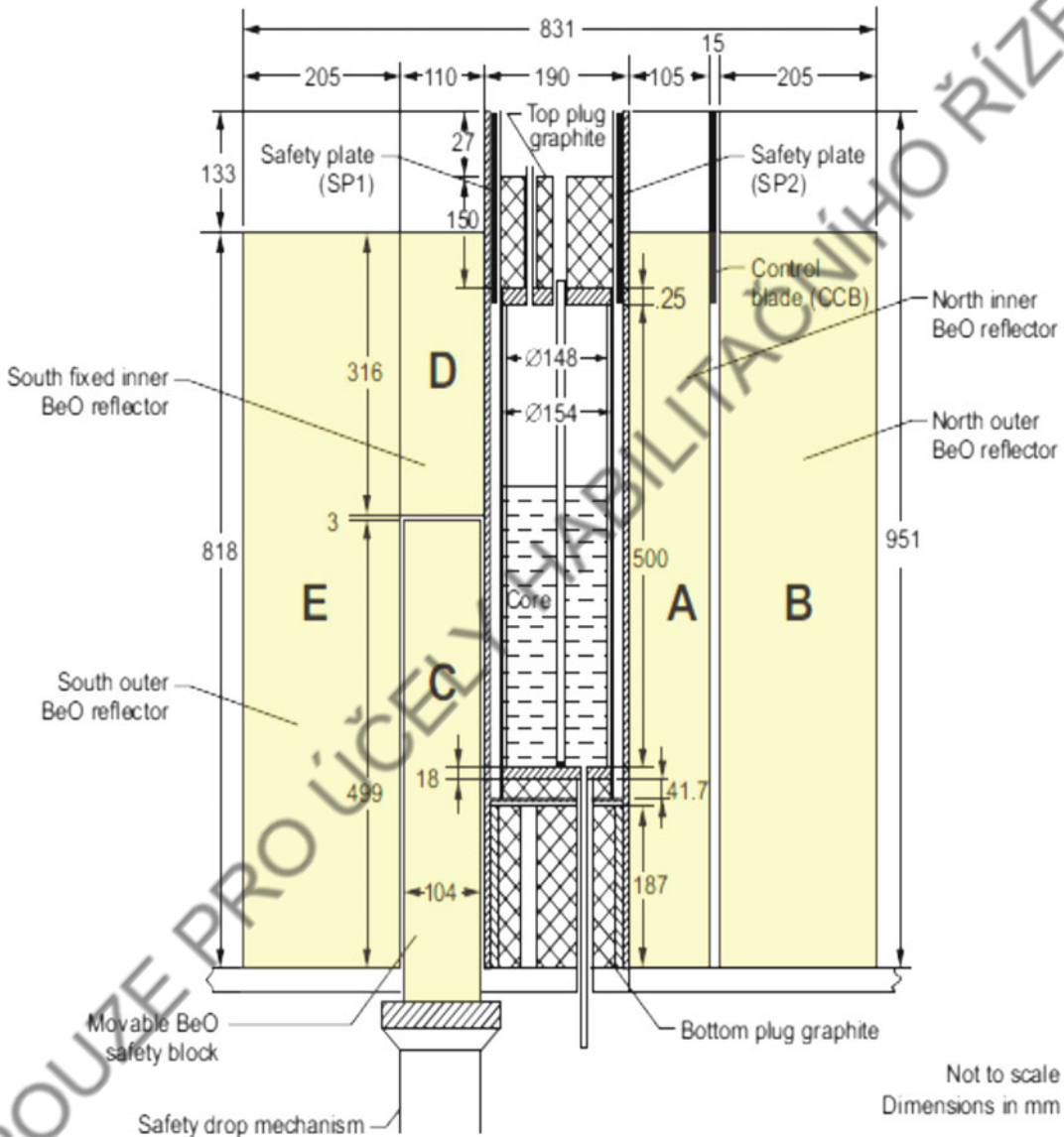


Fig. 6.12 A vertical cross-sectional view of the reactor through its center [49]. All dimensions are in mm

calculated by dividing the entire energy range into a number of groups as shown by Eq. (6.11).

As an example flat cross sections obtained from the evaluated data of ENDF/B VI.8 data file of Th (n, γ) reaction are plotted as function of neutron energy in Fig. 6.14. Thus, for a given neutron energy, 'spectrum average cross section,'

$\sigma_{sp,av}$ are calculated [55] from the flat cross sections obtained from standard PREPRO software. A series of GAMMA experiments have been performed using different neutron energy spectra by varying proton energy or by changing medium in between the spallation target and the sample which moderates the spallation neutron spectrum.

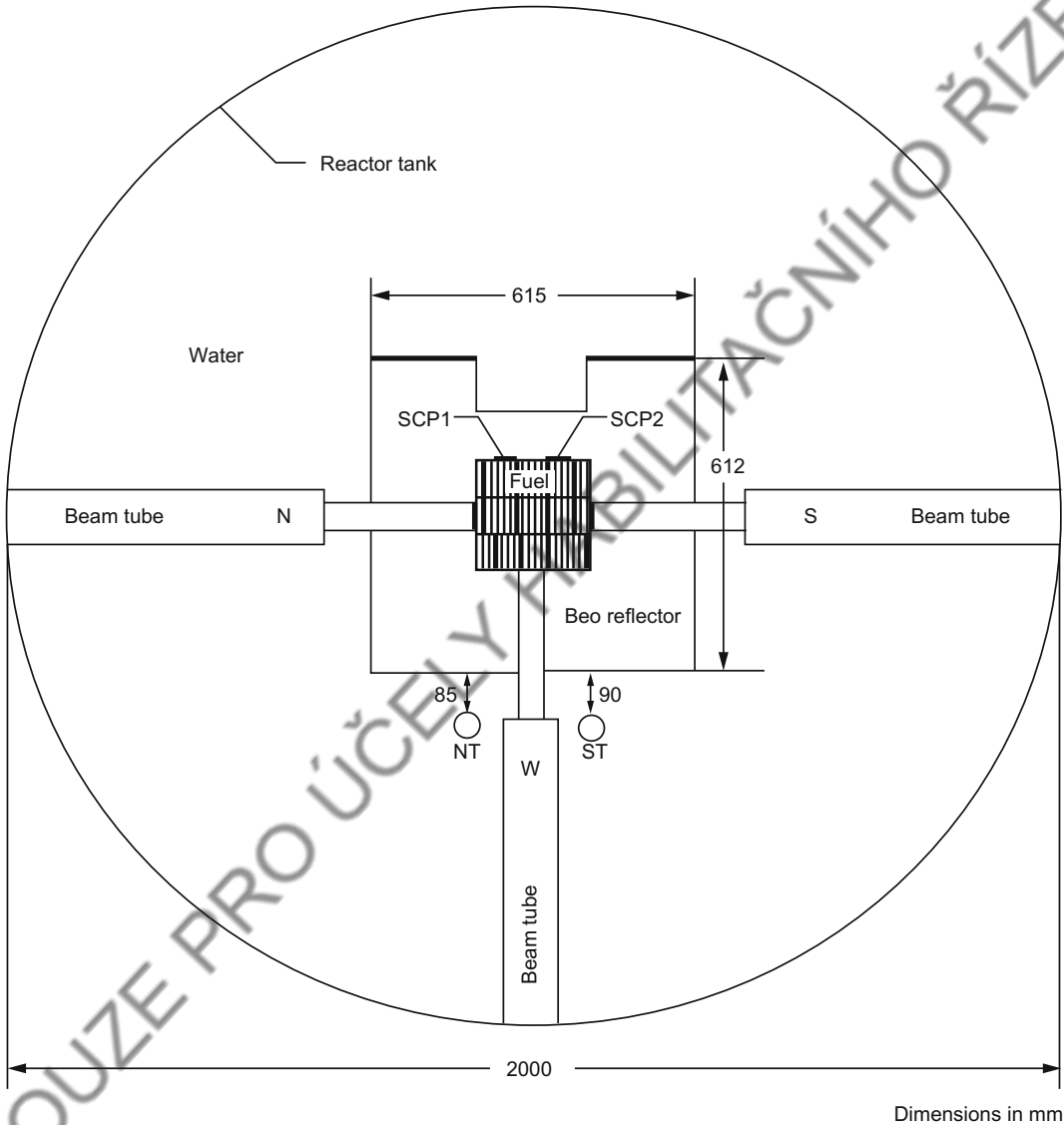


Fig. 6.13 KAMINI fuel and reflector assembly shown with three beam channels [51]

6.11.1 GAMMA-2

It is a setup where spallation neutron spectrum is produced from the impact of 1 GeV proton with

lead target of dimension, $2R \times L = 8 \times 20 \text{ cm}^2$. The lead target is covered with 6-cm-thick layer of paraffin $(\text{CH}_2)_n$ moderator. As calculated, 1 GeV proton will not lose its entire energy

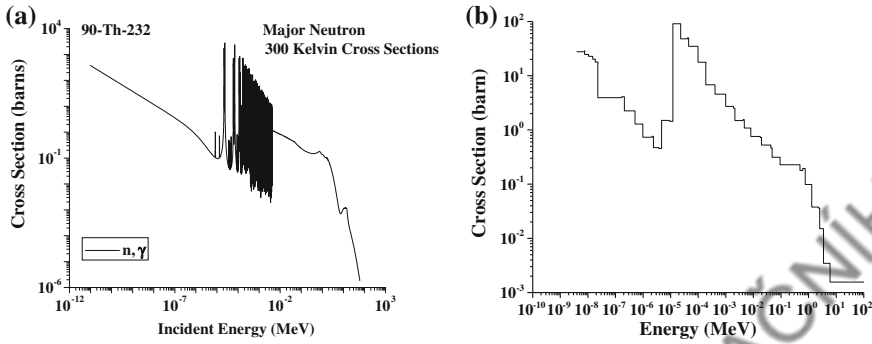


Fig. 6.14 (a) ENDF/B-VI.8 cross section data of ^{232}Th (n, γ) reaction (b) ‘flat’ cross section plot for the same reaction after processing by the PREPRO software

for the energy intervals considered in Dubna CASCADE code ver. 2004 [54].

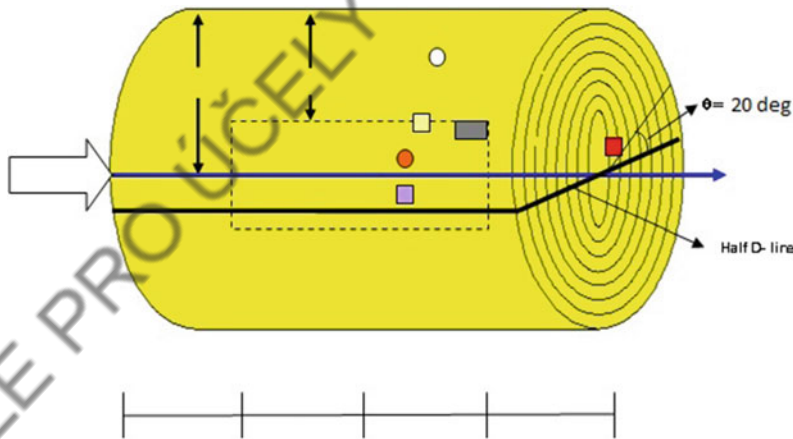


Fig. 6.15 GAMMA-2 setup showing lead spallation target inside the paraffin layer with proton beam impact on the left front. Activation sample of Th placed on lead and others on the paraffin surface is shown [55]

Positions of samples are shown in the following,

-  \rightarrow ^{232}Th -sample (size $3.2 \times 2.5 \times 0.00015 \text{ cm}^3$) placed at the interface of paraffin and Pb at $z = 25$,
-  \rightarrow ^{197}Au -sample placed at $z \sim 20 \text{ cm}$ on the outer surface of the paraffin,
-  \rightarrow ^{209}Bi -sample placed at $z \sim 20 \text{ cm}$ on the outer surface of the paraffin,

-  \rightarrow ^{115}In -sample placed at $z \sim 20 \text{ cm}$ on the outer surface of the paraffin,
-  \rightarrow ^{59}Co -sample placed at $z \sim 20 \text{ cm}$ on the outer surface of the paraffin,
-  \rightarrow ^{181}Ta -sample ($1.6 \times 1.65 \times 0.0431 \text{ cm}^3$) placed on the outer paraffin circular face of upper paraffin dee at $r = 4 \text{ cm}$, $z = 32 \text{ cm}$ and $\theta = 20^\circ$.

by way of ionization loss in passing through 20 cm length of lead including layer of paraffin in the situation that no nuclear collision takes place. In Fig. 6.15, lead + paraffin setup of the target is shown with proton beam striking at the left-side end of the lead target. In the lower part of the figure, a realistic experimental setup with the positions of different activation samples is shown.

The experiments are conducted to estimate neutron fluxes in different positions of the setup.

Incident proton beam distribution on the left end of the lead target at different radial distances is estimated from the Al-monitor detectors using the $^{27}\text{Al}(p, 3pn)^{24}\text{Na}$ reaction. The Al monitor is placed at -60 cm distance from the left end of the Pb target. Using γ -spectrometry of the activated Al foils, activity of the ^{24}Na yield is estimated to conclude intensity of beam which comes out to be $1.09E + 09$ protons/s for the irradiation time of 5.4836 h [53]. Using the CASCADE code ver.04 [54], neutron flux in (a) longitudinal position of ^{232}Th , (b) moderated neutrons in positions of four activation samples on cylindrical surface, and (c) moderated neutron on the forward face at the position of ^{181}Ta sample are simulated for the incident 1 GeV proton beam and given in Fig. 6.16a–c.

Using the cross-section data of (n, γ) , $(n, 2n)$, and $(n, 4n)$ reactions from the ENDF VI.8 data files, neutron flux is deduced from the measured reaction rates. Details of the experiment and reaction rates are given in Ref. [55], and some of the results are summarized in Table 6.5. It may be inferred that

- (i) Incident neutron flux on a sample in its given position is closely similar when estimated using the two reactions, e.g., (n, γ) and $(n, 2n)$ in case of ^{232}Th .
- (ii) Neutron flux is found to be in decreasing order when compared at axial position of four activation samples and at the forward face of the paraffin cylinder.

At the end face of the setup where ^{181}Ta sample is placed, several remnant beam protons

also produce reaction $^{181}\text{Ta}(p, pn)^{180}\text{Ta}$. Correction in the neutron flux corresponding to the (n, pn) reaction for producing ^{180}Ta is estimated [53]. Based on the neutron spectrum estimated as above, Adam et al. [55] have deduced ‘spectrum average cross sections’ for a large number of reactions including high-order (n, xn) reactions with $x = 3-9$ and several other reactions. They are given in Table 6.6.

6.11.2 GAMMA-3

The experimental setup GAMMA-3 provides a neutron flux produced by collision of 2.33 GeV deuteron beam with the lead target (size $d \times l = 8 \times 60$ cm²) which is subsequently moderated by the big block of graphite [56, 57]. The experiment was conducted at JINR Nuclotron for comparing with the results of TARC experiment [58] where n -flux was moderated by a large block of lead. The setup is different to the GAMMA-2 from the point of beam and the moderator.

GAMMA-3 experimental setup is shown in Fig. 6.17 where the graphite moderator of size $1.1 \times 1.1 \times 0.6$ m³ is made of 25 blocks of different sizes and the setup carries several experimental holes like ‘a’, ‘b,’ and ‘c’ particularly marked on the setup. In the middle, spallation target is placed and marked with letter, T . Sizes of holes ‘a’, ‘b,’ and ‘c’ are $d \times l = 14.6 \times 29.6$ cm², 8.8×36.3 cm², and 15.4×34.1 cm², respectively. In Fig. 6.17, cylindrical structure carrying experimental pockets for placing samples are shown and the similar cylinders are placed inside the holes ‘a’, ‘b,’ and ‘c’. Hole ‘a’ is closest to the target, T . Geometrical details of the setup can be seen in Ref. [56, 57]. Samples of ^{235}U were placed in two holes ‘a’ and ‘b’ only. Uranium and thorium samples were irradiated in the form of sandwiches of three very nearly identical foils as Th–Th–Th and U–U–U, and this arrangement has an advantage of accounting for the recoiled residual nuclei produced in the middle foil. Diameter of each foil is 15 mm, and mass of middle U and Th foils are 0.1723 and 0.0931 g,

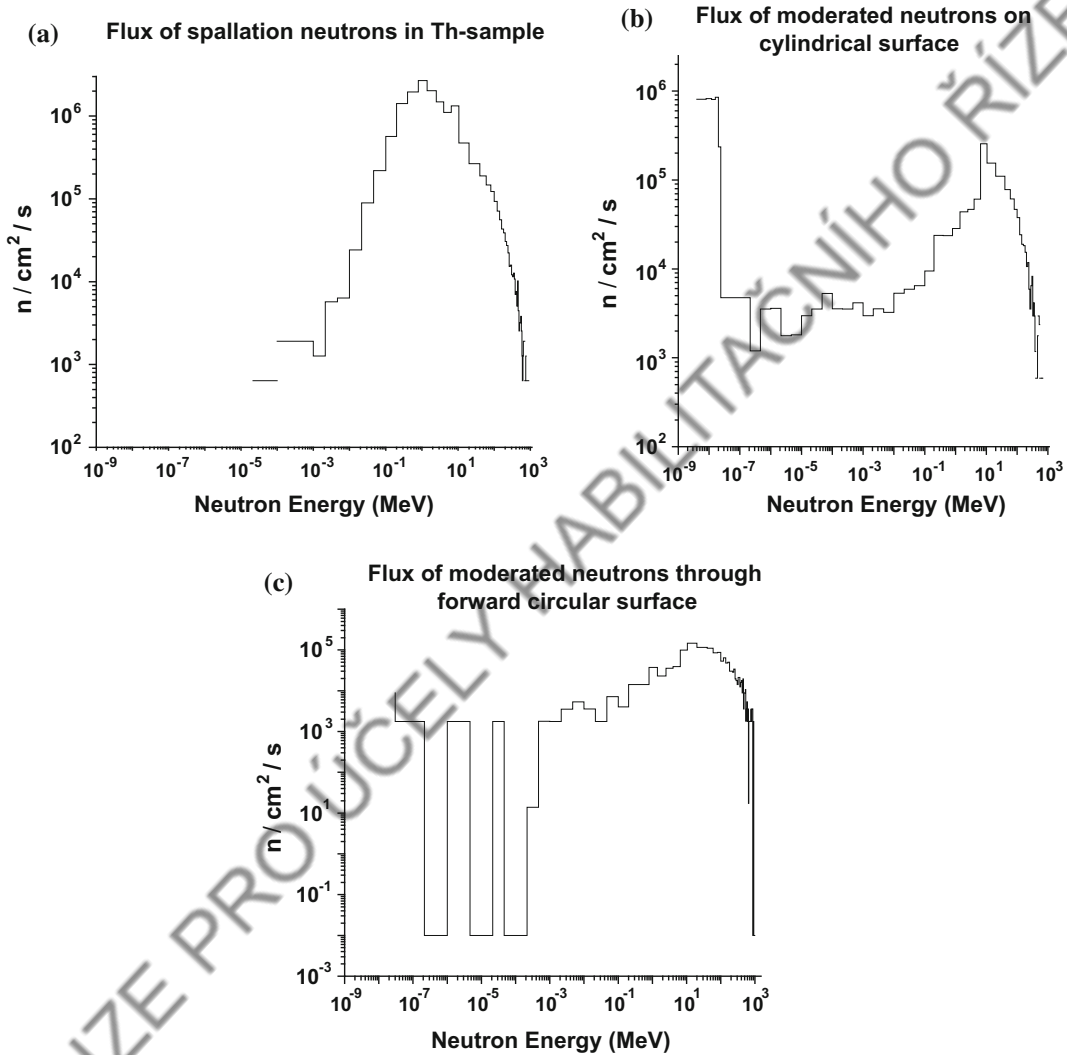


Fig. 6.16 Simulated flux of (a) spallation neutrons on ^{232}Th sample (b) moderated neutrons on paraffin surface at the ring position of four activation samples and

(c) moderated neutrons on the outgoing forward face at the position of ^{181}Ta sample [54]

respectively. The total masses of the sideward ^{232}Th and ^{235}U foils are 0.334 and 0.1763 g, respectively.

In the year 2007, spallation Pb target of the setup was irradiated with 2.33 GeV deuteron beam for 25 h 17 m and intensity of the beam was monitored by the reaction $^{27}\text{Al}(d, 3p2n)^{24}\text{Na}$ with the Al foils of thickness 6.95 mg/cm^2 and diameter 20 cm which was installed at a distance of 3.1 m from the center of

the lead spallation target in between the beam pipe and the spallation target. From the gamma spectrometry of Al foil, integral number of deuterons reaching the Pb target is estimated to be $N = (1.704 \pm 0.103) \times 10^{13}$.

Monte Carlo code MCNPX v 2.6.C was used [59] for simulation of (i) production of neutrons in collision of 2.33 GeV deuteron on the lead target and (ii) transport of neutrons through the graphite setup. As mentioned earlier that the

Table 6.5 Neutron flux deduced from the measured reaction rates [55] and average cross sections from the ENDF VI.8 compared with the values obtained from the CASCADE code [54]

S. No.	Surface, sample	Nuclear reaction	$\langle\sigma\rangle$	$\Phi = R/\sigma$ (n/cm ² /s)	CASCADE code (n/cm ² /s) [54]
1	Interface position, ²³² Th	²³² Th (<i>n</i> , γ) ²³³ Th	64.8 mb	$1.50 \pm 0.09 \times 10^7$	1.46×10^7
		²³² Th (<i>n</i> , 2 <i>n</i>) ²³¹ Th	0.253 b	$1.44 \pm 0.33 \times 10^7$	
2	Outer cylindrical surface of paraffin, ¹⁹⁷ Au	¹⁹⁷ Au (<i>n</i> , 2 <i>n</i>) ¹⁹⁶ Au	0.12 b	$0.746 \pm 0.023 \times 10^7$	0.64×10^7
		¹⁹⁷ Au (<i>n</i> , 4 <i>n</i>) ¹⁹⁴ Au	0.055 b	$0.577 \pm 0.022 \times 10^7$	
3	End circular face, ¹⁸¹ Ta	¹⁸¹ Ta (<i>n</i> , γ) ¹⁸² Ta	1.13 b	$1.24 \pm 0.29 \times 10^6$	1.43×10^6
		¹⁸¹ Ta (<i>n</i> , 2 <i>n</i>) ¹⁸⁰ Ta	0.612 b	$1.37 \pm .06 \times 10^6$	

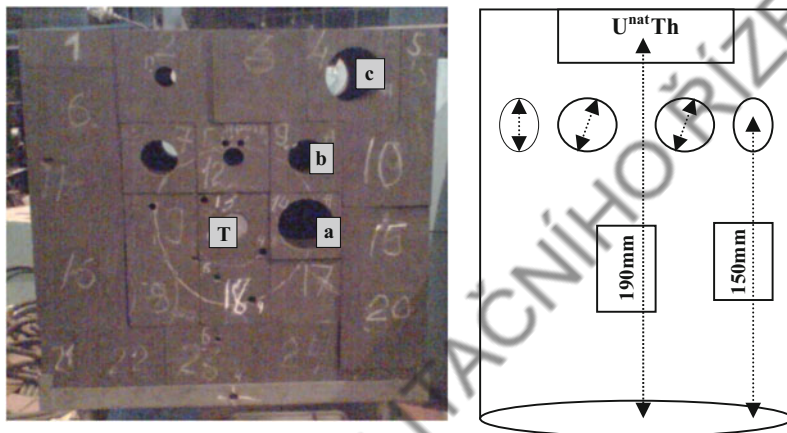
Table 6.6 Spectrum cross sections $\langle\sigma\rangle$ of different reactions deduced from the measurement of reaction rates, *R* [55]

Reaction	E_γ (keV)	E_{th} (MeV)	$\langle\sigma\rangle$
¹⁹⁷ Au (<i>n</i> , γ) ¹⁹⁸ Au	411.80	0.0	26.9 ± 0.67 b
¹⁹⁷ Au (<i>n</i> , α) ¹⁹⁴ Ir	328.40	~0.0	7.72 ± 0.05 mb
¹⁹⁷ Au (<i>n</i> , <i>p</i> + 6 <i>n</i>) ¹⁹¹ Pt	538.86	43.31	241 ± 3.7 mb
¹⁹⁷ Au (<i>n</i> , 6 <i>n</i>) ¹⁹² Au	316.50	38.92	33.67 ± 1.1 mb
¹⁹⁷ Au (<i>n</i> , 7 <i>n</i>) ¹⁹¹ Au	586.45	45.99	29.63 ± 2.0 mb
¹⁹⁷ Au (<i>n</i> , 8 <i>n</i>) ¹⁹⁰ Au	295.80	55.04	08.83 ± 0.14 mb
⁵⁹ Co (<i>n</i> , α) ⁵⁶ Mn	846.77	0.0	3.46 ± 0.16 mb
⁵⁹ Co (<i>n</i> , 2 <i>n</i>) ⁵⁸ Co	810.81	10.63	98.0 ± 2.69 mb
⁵⁹ Co (<i>n</i> , 4 <i>n</i>) ⁵⁶ Co	846.77	30.92	1.70 ± 0.12 mb
⁵⁹ Co (<i>n</i> , 5 <i>n</i>) ⁵⁵ Co	931.50	41.18	0.33 ± 0.06 mb
²⁰⁹ Bi (<i>n</i> , 6 <i>n</i>) ²⁰⁴ Bi	899.17	38.13	19.72 ± 0.36 mb
²⁰⁹ Bi (<i>n</i> , 7 <i>n</i>) ²⁰³ Bi	820.33	45.36	17.05 ± 0.31 mb
²⁰⁹ Bi (<i>n</i> , 8 <i>n</i>) ²⁰² Bi	960.66	54.29	11.82 ± 0.21 mb
²⁰⁹ Bi (<i>n</i> , 9 <i>n</i>) ²⁰¹ Bi	629.14	61.71	10.27 ± 0.21 mb
¹⁸¹ Ta (<i>n</i> , <i>pn</i>) ^{180m} Hf	332.28	5.98	0.53 ± 0.004 b
¹⁸¹ Ta (<i>n</i> , 4 <i>n</i>) ^{178m1} Ta	426.38	22.27	0.304 ± 0.013 b
¹⁸¹ Ta (<i>n</i> , 5 <i>n</i>) ¹⁷⁷ Ta	112.95	29.17	0.130 ± 0.006 b

²³²Th samples were irradiated in all the three holes, namely 'a', 'b,' and 'c' while the samples of ^{nat}U were irradiated in holes 'a' and 'b.' All the details of their positions as shown in Fig. 6.17 are included in the simulations. The results of simulated neutron flux falling on the two samples are given in Fig. 6.18. It can be seen

that there are humps of neutron fluxes at both low and high energies. Spectrum at low energy is pronounced because of the fact that a large number of neutrons are moderated in the graphite and fall in the thermal region. It may also be noted that at all energies, neutron fluence decreases from hole 'a' to hole 'c' because the

Fig. 6.17 (Up left) Graphite moderator block with spallation target at the middle and carrying several experimental holes (up right) packing cylinder having sample pockets and (below) positions of the samples on a cylinder fitted in a hole. ^{nat}U is placed at -9° and ^{232}Th at $+9^\circ$ from the center of the front face of the cylinder in the back of the circles [56]



distance of holes 'a' from the center of the Pb target is smaller than that of the hole 'c.'

In Table 6.7, results of reaction rate, R , both experimental and calculated [56], are given for the three experimental holes a , b , and c .

After a complete analysis of ^{nat}U sample irradiated in holes 'a' and 'b,' 11 fission products, namely $^{85\text{m}}\text{Kr}$, ^{93}Y , ^{99}Mo , ^{103}Ru , ^{105}Rh , ^{131}I , ^{132}Te , ^{133}I , ^{140}Ba , ^{141}Ce , and ^{143}Ce were observed. Also, ^{239}Np is observed as a product of $^{238}\text{U}(n, \gamma)$ reaction and ^{237}U as a product of $^{238}\text{U}(n, 2n)$ reaction occurred in the ^{nat}U sample. Similarly, in case of ^{232}Th sample irradiated in the hole 'a,' six fission products, namely $^{85\text{m}}\text{Kr}$, ^{99}Mo , ^{131}I , ^{133}Xe , ^{135}Xe , and ^{141}Ce are observed. Also, ^{233}Pa product corresponding to $^{232}\text{Th}(n, \gamma)$ reaction and ^{231}Th product corresponding to $^{232}\text{Th}(n, 2n)$ reaction are observed. In case of ^{232}Th in the hole 'b' only four fission products $^{85\text{m}}\text{Kr}$, ^{99}Mo , ^{131}I , and ^{141}Ce are observed along with ^{233}Pa and ^{231}Th . Lastly, in

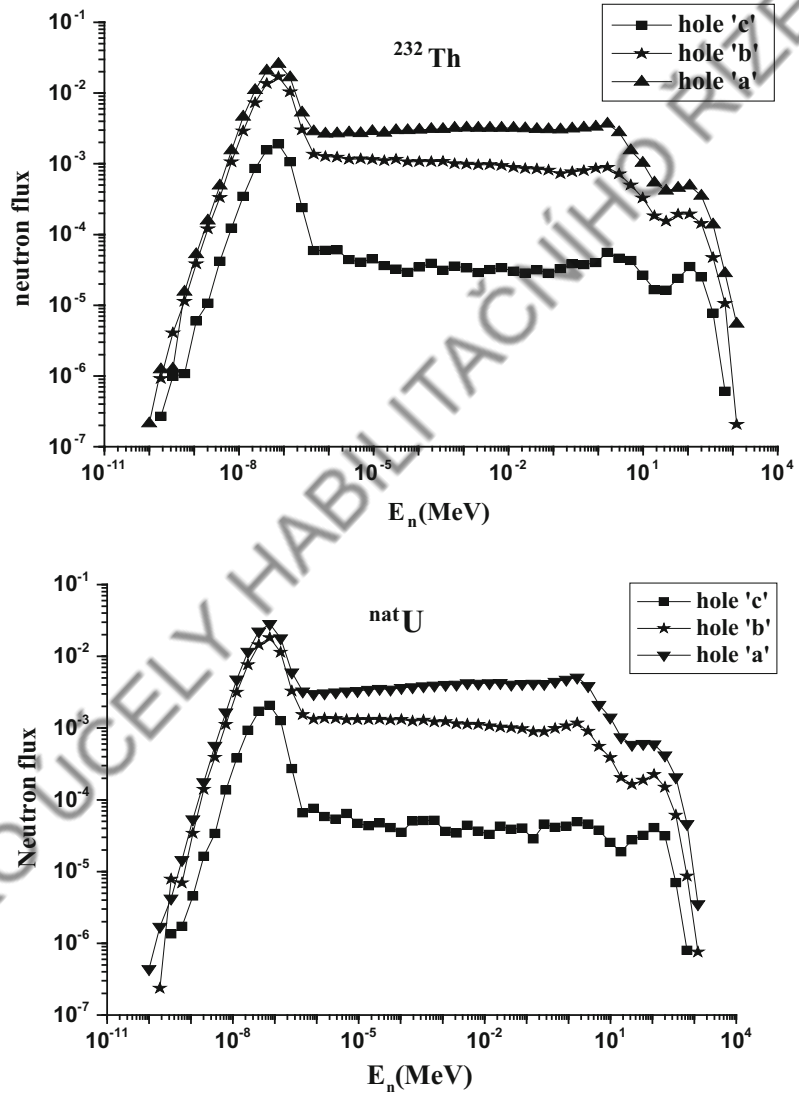
case of the hole 'c,' only ^{99}Mo is observed as a fission product and ^{233}Pa as a product of $^{232}\text{Th}(n, \gamma)$ reaction. This shows that as we go farther from the spallation source more and more, moderated neutrons have lesser probability of fission reaction to happen with ^{232}Th , partly due to lesser neutron energy and lesser available amount of neutron fluence. Similar inference was also drawn with the help of data of reaction rate, R given in Table 6.7.

Using the data of reaction rate, $R(A_r, Z_r)$ of (A_r, Z_r) product, transmutation power of a system as derived in Ref. [4] can be written as follows

$$P(A_r, Z_r) = R(A_r, Z_r) \cdot N_d \frac{A_r}{A_t} t_{\text{irr}} \quad (6.12)$$

Here, $N_d \cdot t_{\text{irr}} = N_D$ (an integral number of deuterons). On normalizing to 10^9 beam particles, one can write

Fig. 6.18 (Up) Simulated neutron flux ($n/cm^2/\text{deuteron}$) at the positions of ^{232}Th sample (on left) and $^{\text{nat}}\text{U}$ sample (below) in holes 'a', 'b,' and 'c' [56]



$$P_{\text{norm}}(A_r, Z_r) = 10^9 \frac{P(A_r, Z_r)}{N_D} \quad (6.13)$$

where N_d is the deuteron beam intensity, t_{irr} is the irradiation time and A_t is the target mass number. In Table 6.8, normalized transmutation power P_{norm} in GAMMA-3 experiment is compared for the two other experimental setups, viz. Transmutation by Adiabatic Resonance Crossing (TARC) [58] and $E + T$ [60].

Following observations can be made from the data of Table 6.8

1. Transmutation power in case of (n, γ) reaction for ^{232}Th and $^{\text{nat}}\text{U}$ is estimated independently for the two holes 'a' and 'b,' and it is found comparable. When we compare with the values obtained in case of different $E + T$ setups [60–62] and TARC assembly [58], then it may be inferred that P_{norm} is about an order of magnitude higher in graphite assembly than other $E + T$ and TARC assemblies.
2. On comparing $P_{\text{norm}}(n, 2n)$ for ^{232}Th in case of the graphite setup and the $E + T$ assembly, it may be pointed out that transmutation

Table 6.7 Calculated and experimental values of reaction rates of (n, γ) , (n, f) , and $(n, 2n)$ reactions for both ^{232}Th and $^{\text{nat}}\text{U}$ samples irradiated in the three positions a , b , and c inside the graphite moderator for the neutron fluencies in the three positions [56]. Values shown in the brackets correspond to the errors, e.g., $3.31(15) = 3.31 \pm .15$ and $0.49(1) = 0.49 \pm 0.01$

Hole position	Reaction	^{232}Th			$^{\text{nat}}\text{U}$		
		$^{232}\text{Th} (n, \gamma)$ ^{233}Pa	(n, f)	$^{232}\text{Th} (n, 2n)$ ^{231}Th	$^{238}\text{U} (n, \gamma)$ ^{239}Np	$^{\text{nat}}\text{U} (n, f)$	$^{238}\text{U} (n, 2n)$ ^{237}U
a	$R_{\text{expt.}} 'a'$	$3.31(15)E-25$	$1.06(21)E-26$	$8.9(11)E-27$	$3.38(11)E-25$	$2.42(33)E-25$	$2.83(19)E-27$
	$R_{\text{cal.}} 'a'$	$7.83E-25$	$5.09E-27$	$3.27E-27$	$1.63E-24$	$2.54E-25$	$2.73E-27$
	$R_{\text{expt.}}/R_{\text{cal.}}$	$0.423(19)$	$2.08(41)$	$2.72(34)$	$0.207(7)$	$0.95(13)$	$1.04(7)$
b	$R_{\text{expt.}} 'b'$	$1.96(5)E-25$	$2.55(69)E-27$	$1.06(22)E-27$	$2.31(8)E-25$	$1.57(24)E-25$	$7.47(83)E-28$
	$R_{\text{cal.}} 'b'$	$4.04E-25$	$1.78E-27$	$7.58E-28$	$6.07E-25$	$1.56E-25$	$7.63E-28$
	$R_{\text{expt.}}/R_{\text{cal.}}$	$0.49(1)$	$1.43(39)$	$1.39(29)$	$0.38(1)$	$1.01(15)$	$0.98(10)$
c	$R_{\text{expt.}} 'c'$	$3.38(16)E-26$	$3.16(88)E-28$	–	–	–	–
	$R_{\text{cal.}} 'c'$	$3.39E-26$	$2.13E-28$	$6.84E-29$	$3.73E-26$	$1.79E-26$	$6.61E-29$
	$R_{\text{expt.}}/R_{\text{cal.}}$	$0.997(5)$	$1.48(41)$	–	–	–	–

Table 6.8 Comparison of normalized transmutation power, P_{norm} of three assemblies, namely graphite-lead target of GAMMA-3, $E + T$ [60], and TARC [58]. Distances of the samples from the center of their respective assemblies are given as ' d '

Assembly	Graphite [56]			$E + T$ [60]	TARC [58]	
	Hole a	Hole b	Hole c			
Distance ' d ' (Th)	$d \sim 24$ cm	$d \sim 34$ cm	$d \sim 61$ cm	$d \sim 13$ cm	$Z = 22.5$ cm, $X = 122$ cm	$Z = 7.5$ cm, $X = 150$ cm
$^{232}\text{Th} (n, \gamma)$ ^{233}Pa	$3.32(15)E-16$	$1.97(5)E-16$	$3.39(16)E-17$	$3.09(13)E-17$	$3.8(3)E-17$	$1.0(2)E-17$
$^{232}\text{Th} (n, 2n)$ ^{231}Th	$8.9(11)E-18$	$1.06(22)E-18$	–	$1.59(16)E-18$	–	–
Distance ' d ' (U)	$d \sim 19$ cm	$d \sim 31$ cm	$d \sim 58$ cm	$d \sim 13$ cm	$d = 94$ cm, $Z = -22.5$ cm	$d = 107$ cm, $Z = -22.5$ cm
$^{238}\text{U} (n, \gamma)$ ^{239}Np	$3.39(11)E-16$	$2.32(8)E-16$	–	$2.87(9)E-17$	$7.7(2)E-17$ (hole 7)	$1.1(3)E-17$ (hole 6)
$^{238}\text{U} (n, 2n)$ ^{237}U	$2.82(19)E-18$	$7.44(83)E-19$	–	–	–	–

power is about seven times higher in the graphite setup than the $E + T$ assembly.

3. The above study is highly innovative, and it may have impact on the design of an ADSS for transmutation of LLNW.

6.12 Energy + Transmutation Experimental Setup

In the year 1999, JINR started ‘Energy + Transmutation’ program of research with the objective of ‘investigations of physical aspect of electronuclear energy generation and transmutation of radioactive waste of the reactors using the high energy beams of the Nuclotron, JINR (Dubna)’ [62–64]. Several experiments have been conducted using the proton beams of energies ranging from 0.7 to 3.7 GeV under the program. The experiments were focused on general aspects of energy generation, neutron multiplication, neutron spectra, neutron induced transmutation of long-lived minor actinides (specially ^{237}Np and ^{241}Am), fission product (^{129}I), and plutonium isotopes (^{238}Pu , ^{239}Pu). A review of the experiments has been published by Adam et al. [65] along with several other details of experiments. In the year 2005, the $E + T$ experimental setup was irradiated with 2.52 GeV deuteron beam to compare its results with earlier experiments with proton beams. Soon after it, in December 2006 the setup was irradiated with the 1.6 GeV deuteron beam [60]. In Fig. 6.19, basic structure of the $E + T$ setup is shown.

The whole assembly was covered with shielding of size having outer dimensions $\Delta X \times \Delta Y \times \Delta Z = 100 \times 106 \times 111 \text{ cm}^3$ as shown in Fig. 6.20.

Al foils are used as deuteron beam monitors and the beam is focused on the center of the lead target. Also, special efforts are made to detect centroid of the beam using the track detectors. In Fig. 6.21 (left), results of experimental beam distribution using Al foils and in Fig. 6.21 (right) results of track detectors are presented [60]. In

the experiment, integral number of beam hitting the spallation lead target $N_D \sim 1.93(25) \times 10^{13}$.

In simulations using the code MCNPX, the real coordinates of beam-hits, that were obtained from the track detectors, on the target were used. It is also important to mention that beam not only loses slight alignment with the beam axis but also may be asymmetric in time. Being asymmetric, it has definite effect on production and detection of nuclear products and beam correction become essential in calculations of reaction rates. In Fig. 6.22, beam profile of 1.6 GeV deuteron beam hitting the target of the experiment obtained from the accelerator scientists is given for an example.

Using the CASCADE code ver. 04, neutron flux in the position of the RA samples put on the top of the second section of $E + T$ assembly has been simulated [64] in the situation of total shielding as shown in Fig. 6.20. The input files of simulation by the CASCADE code and other details of the $E + T$ setup can be seen in Ref. [53]. In Fig. 6.23, simulated neutron flux of the setup irradiating the RA samples calculated from the CASCADE code and MCNPX are shown.

Looking at the details of the data in Fig. 6.23 in the neutron energy region 0.02–1000 MeV range, the two codes give comparable total flux and in the energy range smaller than 0.01 MeV, flux from the MCNPX is nearly an order of magnitude higher than CASCADE. According to MCNPX, total n -flux is $2.17 \times 10^7 \text{ n/cm}^2/\text{s}$ in good agreement with $2.31 \times 10^7 \text{ n/cm}^2/\text{s}$ obtained from the CASCADE code. It may be pointed out that the difference in distribution has been reduced in later version of the CASCADE code published as MONC [66].

In the $E + T$ setup, neutron irradiation of highly pure samples of ^{129}I , ^{127}I , and ^{237}Np was done also using the 2.52 GeV deuteron beam, putting samples on the top of the second section. Some of its results are shown in Table 6.9 in case of ^{237}Np [53].

A comparison of transmutation power for the (n, f) reactions of ^{237}Np and ^{239}Pu is compiled [67]

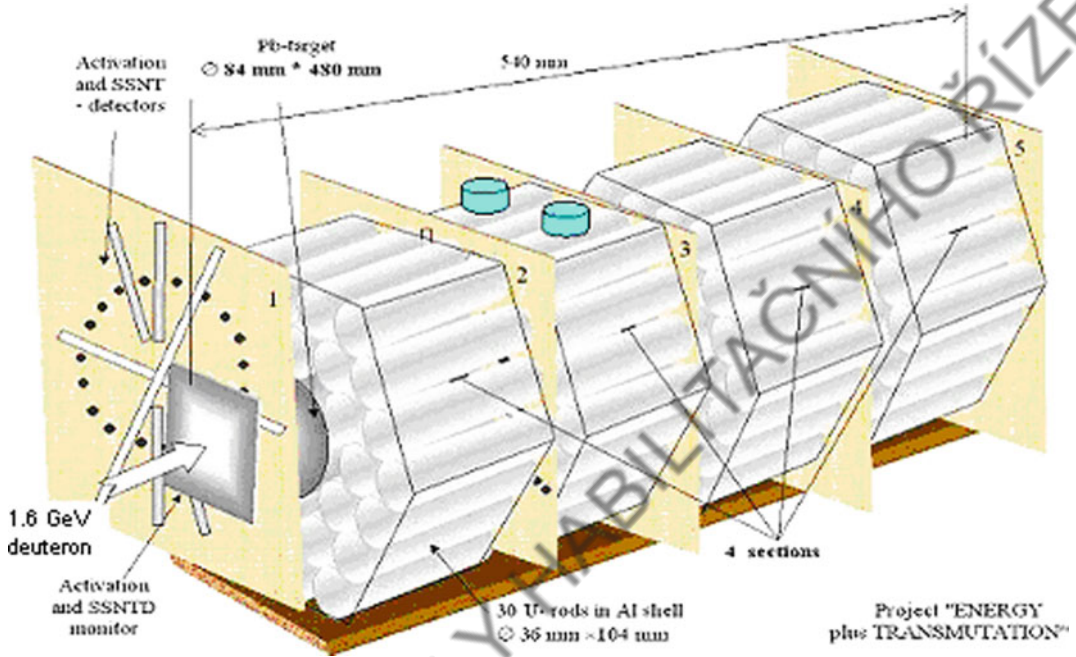


Fig. 6.19 Energy + transmutation setup is shown with massive lead spallation target in the middle of the four hexagonal sections of depleted ^{nat}U assemblies. Activation samples are placed on the top of the sections, and in

the middle of any two sections neutron flux monitor detectors are placed. Two radioactive samples like ¹²⁹I and ²³⁷Np are put on the top of the second uranium section [62, 64]

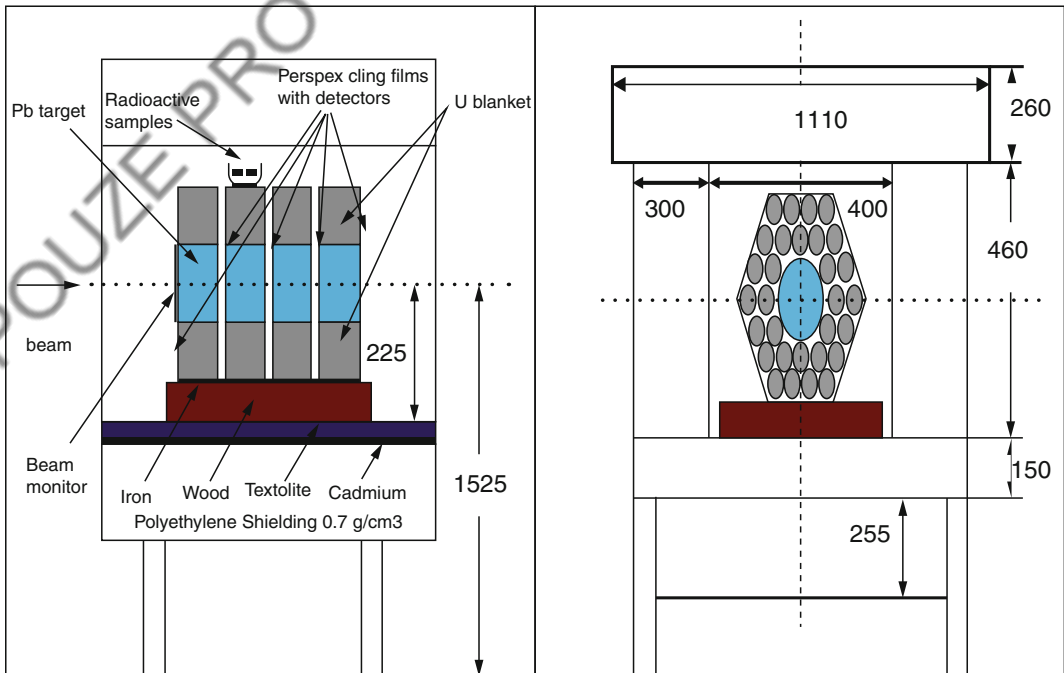


Fig. 6.20 (Left) Side view of energy + transmutation assembly with radiation shielding by polyethylene cover of dimensions $\Delta X \times \Delta Y \times \Delta Z = 100 \times 106 \times 111 \text{ cm}^3$, 0.1-cm-thick cadmium layer, textolite layer having thickness 3-cm, 9-cm-thick wood support, steel plate of

1 cm thickness, 0.1-cm-thick steel blanket cover, hexagonal uranium blanket around the central lead target. Thin beam monitor is shown in front of the lead target (right) front view of the setup with dimensions used in the simulations by the CASCADE code [62, 64]

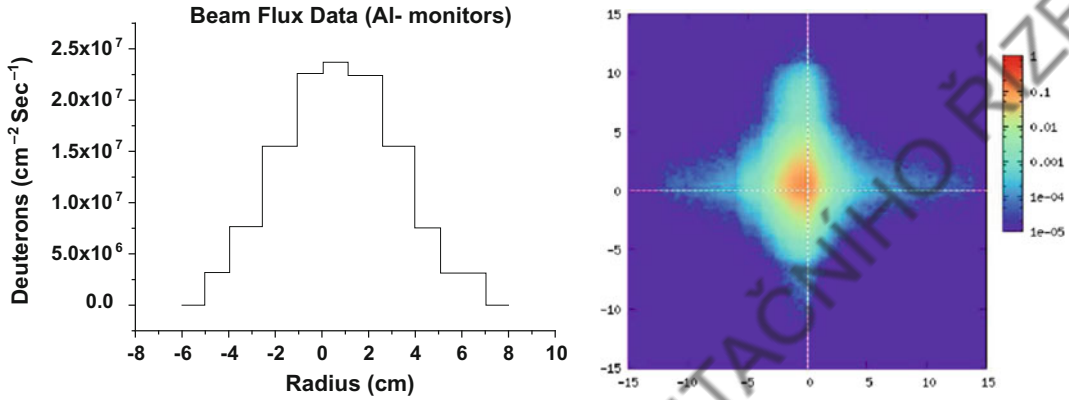
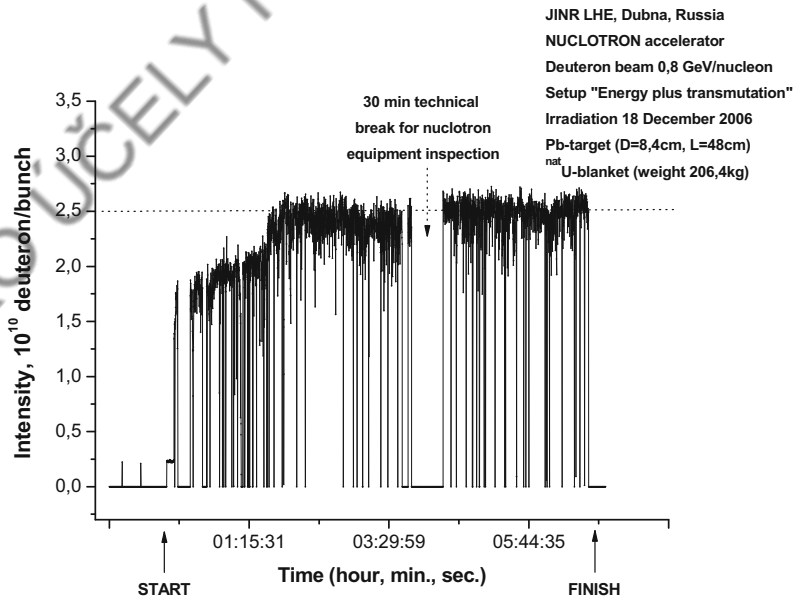


Fig. 6.21 (Left) Beam profile estimated ($n/\text{cm}^2/\text{s}$) using the Al foil monitors and (right) real beam profile detected using the track detectors [60]. Coordinates of centroid are

$x_c = -0.64(3)$ cm and $y_c = 0.39(8)$ cm with respect to the axis of the setup

Fig. 6.22 1.6 GeV deuteron beam profile used in the experiment [60]



for the $E + T$ setup using data of reaction rates given by Adam et al. [65] for the proton beams of energy ranging from 0.7 to 2 GeV. A detailed discussion of transmutation of RA samples using proton or deuteron beams of different energies has already been presented in Fig. 5.2 where it is inferred that transmutation in an experimental setup of ADSS by energy more than 1 GeV/n does not show much improvement compared to 1 GeV.

6.13 QUINTA—An Experimental Setup

During the Baldin seminars [68], Furman et al. [69] proposed to extend the $E + T$ -type setup by adding another uranium assembly and to create an entrance beam window. The new target assembly (TA) along with a mass of 500 kg of

natural uranium metal ($d \times l = 30 \times 65 \text{ cm}^2$) was identified as QUINTA which was irradiated by deuteron beams with energies ranging from 1 to 8 GeV. In the experiments, number of deuterons on the target ranged from 3 to 5×10^{13} for each energy. In Fig. 6.24, a schematic view of the setup as been projected. The setup is highly equipped with detector systems for the measurement of beam intensity and the activation samples placed at different positions inside the setup as well as on the top of the uranium assembly. In Fig. 6.25, uranium assembly shown

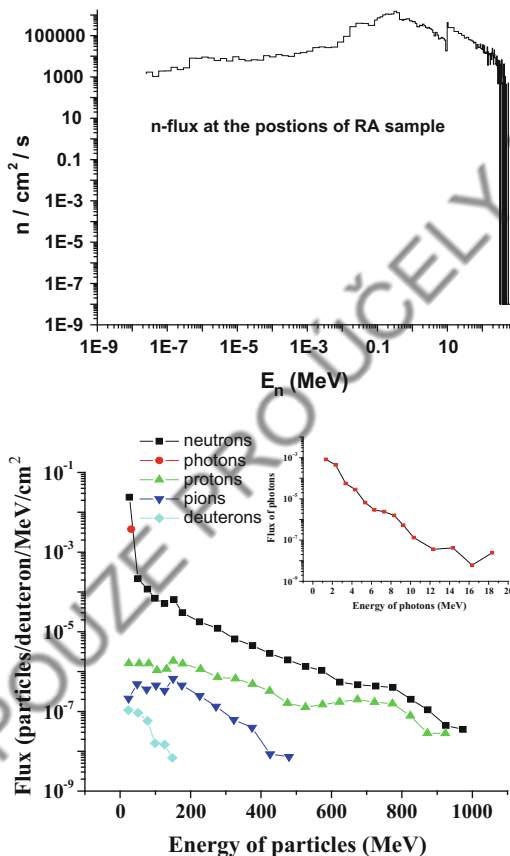


Fig. 6.23 (Up) Neutron flux, as simulated from the CASCADE code, passing through the ^{129}I and ^{237}Np radioactive (RA) samples placed on the top of the second section of U/Pb assembly. Nearly same n -distribution is obtained from the code for the U and Th samples [53]. (Below) Simulation of various produced particles hitting the target, carried out using MCNPX by using the real coordinates of beam [60]. Units of flux and energy scale in case of MCNPX simulations are different to that given in left-side figure

at the center of earlier Fig. 6.24 is shown separately along with entrance beam window placed before each uranium assembly.

Asquith et al. [70] have measured reaction rates of (n, γ) and (n, xn) reactions produced in activation samples ^{209}Bi and ^{197}Au placed inside the setup irradiated by the deuteron beams of 1 and 4 GeV energy in two experiments separately. Mean values of total beam particles of 1 and 4 GeV energy are estimated to be $(1.50 \pm 0.16) 10^{13}$ and $(1.94 \pm 0.20) 10^{13}$ respectively. The activation samples were prepared to be sandwiched in between two 100- μm -thick muscovite mica sheets as the SSNTDs for the detection of fission fragments escaping the activation samples. Experimental results of ^{209}Bi (n, xn) reactions with $x = 4-7$ and ^{197}Au (n, γ) as well as ^{197}Au (x, yn) reactions with $y = 2-7$ reactions are found to be in good agreement with the calculated results following the MCNPX 2.7 manual [71]. Adam et al. [72] have also presented results of neutron flux measurements in an experiment with QUINTA setup using 4 and 8 GeV deuteron beams and threshold detector reactions, ^{27}Al $(n, y_1) ^{24}\text{Na}$, ^{27}Al $(n, y_2) ^{22}\text{Na}$, and ^{27}Al $(n, y_3) ^7\text{Be}$ having effective threshold energies as 5, 27 and 119 MeV. Experimental results are found in good agreement with the calculated results at lower neutron energies, i.e., 5–27 and 27–119 MeV in case of 4 GeV deuteron beam.

6.14 MYRRHA and EFIT—A Road Map of ADSS

MYRRHA is abbreviated for **M**ulti-purpose **h**ybrid **R**esearch **R**eactor for **H**igh-tech **A**pplications. In fact, SCK.CEN (Mol, Belgium) had initiated the MYRRHA project in 1998 to pave a road toward construction of an **e**xperimental facility for demonstration of the technical feasibility of **T**ransmutation in **A**ccelerator-**D**riven **S**ystem as the XT-ADS concept [73]. Thus, XT-ADS will be an advance version of MYRRHA. It has assumed inherent security feature by way of subcriticality of the system and to provide extra neutron flux by way of spallation process. The spallation neutrons not only initiate production of prompt and delayed

Table 6.9 Experimental spectrum average reaction rates measured in case of $E + T$ setup using 1.6 GeV deuteron beam for the ^{237}Np , ^{238}U , and ^{232}Th samples. In the parenthesis {}, values of reaction rates for 2.52 GeV deuteron beam are shown for comparison [53]

Reaction and product	^{237}Np	^{238}U	^{232}Th
$(n, \gamma) ^{238}\text{Np}$	$1.82(6)E-25$ { $1.62(8)E-25$ }	$2.92(21)E-26$	$2.91(14)E-26$
$(n, 2n) ^{231}\text{Th}$	–	–	$1.98(14)E-27$
$(n, f) ^{143}\text{Ce}$	–	$2.8(6)E-28$	–
$(n, f) ^{132}\text{Te}$	$1.61(12)E-27$ { $2.2(3)E-27$ }	$5.20(26)E-28$	–
$(n, f) ^{133}\text{I}$	$2.40(22)E-27$ { $2.6(8)E-27$ }	$1.78(22)E-28$	–
$(n, f) ^{135}\text{I}$	$2.21(22)E-27$	–	–
$(n, f) ^{135}\text{Xe}$	–	$1.37(32)E-27$	–
$(n, f) ^{140}\text{Ba}$	$1.54(17)E-27$	$6.39(18)E-28$	–
$(n, f) ^{99}\text{Mo}$	–	$5.06(86)E-28$	$6.9(13)E-29$
$(n, f) ^{97}\text{Zr}$	$1.98(12)E-27$ { $1.88(29)E-27$ }	–	–

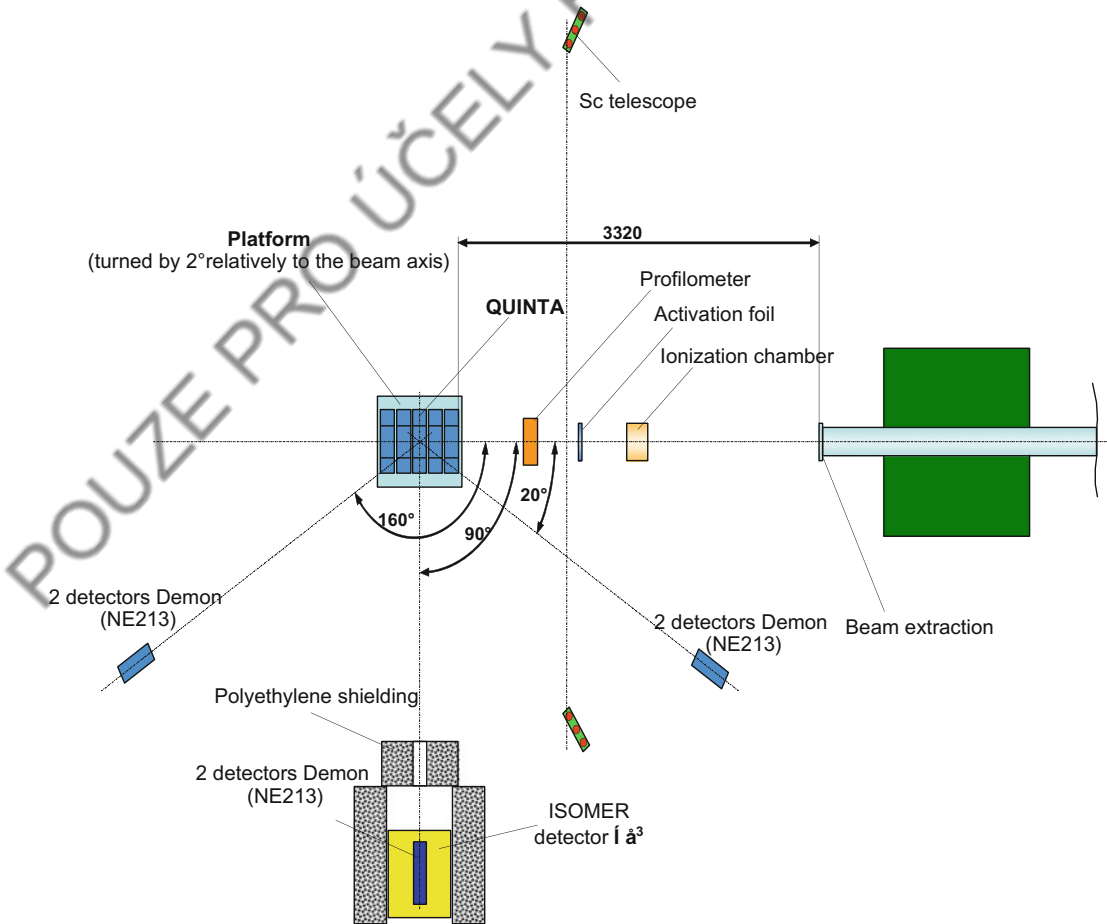


Fig. 6.24 Total schematic view of the QUINTA setup [69]

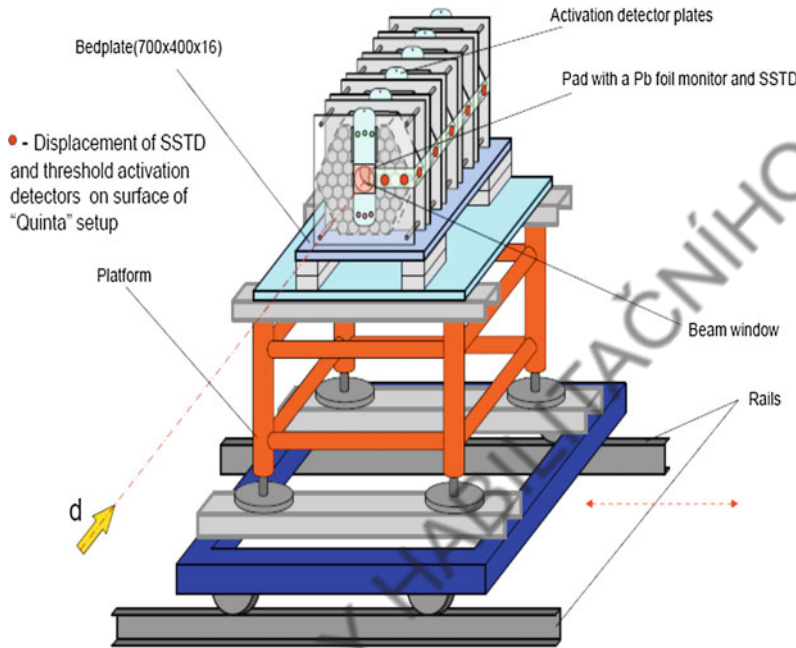


Fig. 6.25 A view of ^{235}U assembly of five sections with beam window before each section [69]

neutrons but multiply neutrons directly from the material of the reactor. Industrial design of extension of the demonstration design MYRRHA/XT-ADS is called as EFIT. According to Mueller [74], the main objective is to work towards a European Transmutation Demonstration in a step-wise manner, i.e., to provide (i) an advanced design of all the components of an XT-ADS system (ii) a generic conceptual design of a modular 'European Facility for Industrial Transmutation,' EFIT for the long-term objective of the program. Once the demonstration of EFIT starts working, it will need to be characterized with respect to (a) its transmutation efficiency, (b) easy in operation, and (c) its availability level. Comparative design parameters of MYRRHA, XT-ADS, and EFIT are shown in Table 6.10. The entire project is planned to be operational by the year 2020 with the help of several experimental test facilities like liquid heavy metal, Pb–Bi eutectic as target-cum-coolant and GUINEVERE described earlier. In Fig. 6.26, MYRRHA setup is shown with a table of its component assemblies.

6.15 Subcritical Assembly at Dubna (SAD)

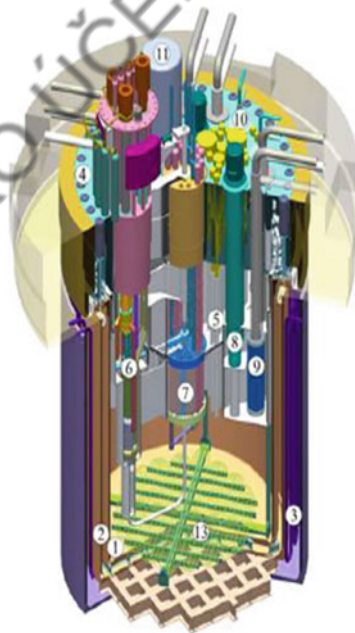
Planning of SAD was started with a view of utility of 660 MeV Phasotron accelerator and IBR-30 plutonium reactor at JINR, Dubna. Later, Polanski [75] suggested that MOX fuel ($\text{PuO}_2 + \text{UO}_2$) is a better fuel than metallic plutonium. In a series of simulations, various fuel combinations were tried [76, 77] for an electronuclear system and their results gave birth to the SAD proposal. Some of the basic parameters of the proposed facility are given in Table 6.11 [78]. In Fig. 6.27, proposed design of the reactor core is shown [79]. But the facility has not been realized up to level of its desired applications.

6.16 BURAN Setup

After a series of experiments such as GAMMA-2 and GAMMA-3, energy plus transmutation ($E + T$), and QUINTA as

Table 6.10 Comparison of design parameters of MYRRHA, XT-ADS, and EFIT setup

Parameters	MYRRHA (2005)	XT-ADS (2009)	EFIT
Goal	Concept demonstration	Prototype transmuter	Maximize the transmutation efficiency, easiness of operation and maintenance, high level of availability
Accelerator, E_p , I	LINAC, 350 MeV, 5 mA	LINAC, 600 MeV, 2.5 mA or as of MYRRHA	LINAC, 800 MeV, 20 mA
Beam entry into the reactor, interface	Top side, windowless	Top side, windowless	As of XT-ADS
Target and coolant	Pb–Bi	Pb–Bi	Pb
Core power	~ 50 MWth	~ 57 MWth	Several 100 MWth power
Fuel	MOX (except for a few MA fuel samples)	MOX (except for a few MA fuel assemblies)	Minor actinide fuel
Fuel power density	~ 1000 W/cm ³	700 W/cm ³	–
Criticality, k_{eff}	~ 0.95	~ 0.95	~ 0.97

Fig. 6.26 MYRRHA design with a table of components assemblies of the setup [73]

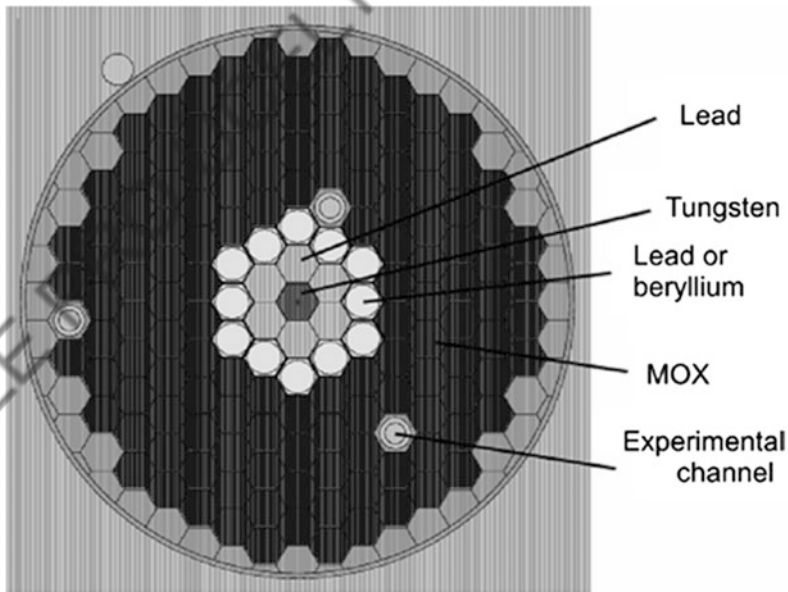
1. inner vessel
2. guard vessel
3. cooling tubes
4. cover
5. diaphragm
6. spallation loop
7. sub-critical core
8. primary pumps
9. primary heat exchangers
10. emergency heat exchangers
11. in-vessel fuel transfer machine
12. in-vessel fuel storage
13. coolant conditioning system

discussed earlier in the chapter, another series of possible experiments with a quasi-infinitely large depleted uranium assembly is being readied for neutron benchmark studies in the name

of BURAN at JINR, Dubna. BURAN stands for **big uranium** assembly. The schematic design of the BURAN setup is shown in Fig. 6.28 comprising of depleted 0.3% ²³⁵U + 99.7% ²³⁸U

Table 6.11 Proposed design parameters of SAD assembly [78]

Basic component	Basic parameters	Tentative value
Beam	Proton energy	660 MeV
	Beam power	1–2 kW depending on target assemblies
Spallation target	Concentric cylinders of W or Pb (center), solid Pb around followed by beryllium	Be will reduce neutron flux on the blanket
	n/p	12.95
	Heat generation	840 W
	Neutron intensity on blanket	1.143×10^{14} n/s
Fuel blanket	MOX	PuO_2 (0.297) + UO_2 (0.703)
	Shape and size	Pallets, 5.95 mm diameter
	No. of fuel units	132–141
	Power	30–114 kW depending on beam and target assembly



Target	Pb	W+Pb+Be	W+Pb
Fuel Elements	133-141	133	132
k_{eff}	0.952-0.972	0.974	0.974
E-gain	30 - 50	51	57
Beam power	1 kW	2 kW	2 kW
System power	30-50 kW	102 kW	114 kW

Fig. 6.27 Design of reactor core of SAD [79]

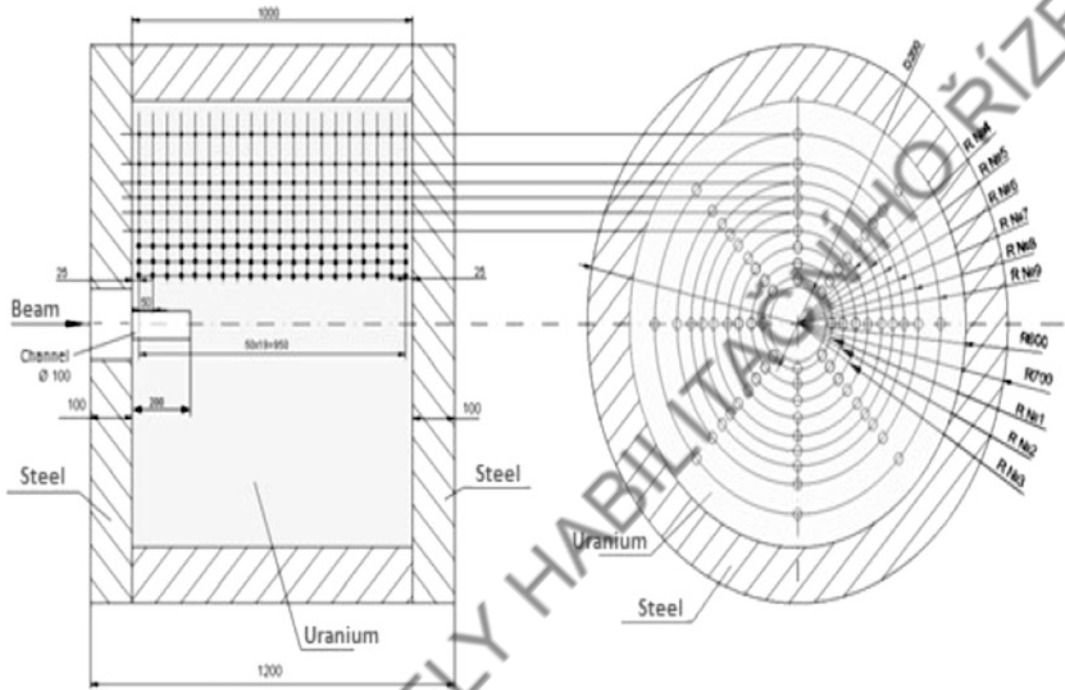


Fig. 6.28 Side view of cylindrical geometry of BURAN experimental setup at JINR, Dubna [80]

assembly of size $d \times l = 120 \times 100 \text{ cm}^2$ enclosed in 10-cm-thick steel covering. In the center of the cross section of the uranium block, there is a beam opening of 20 cm diameter and its depth is kept moveable at 0, 10, and 20 cm as per necessity.

Neutron spectra are simulated using MCNPX 2.7.0 in different positions of the setup for proton and deuteron beams and shown in Fig. 6.29 (left) and (right), respectively. Calculations show a marginally more peak value of neutron flux in case of deuteron than proton beam of same kinetic energy. Detailed results of MCNPX calculations for proton and deuteron are summarized in Table 6.12 [81], and they are helpful in design of experiments of benchmark related to fissions (n, f) and transmutations by (n, γ) reactions. In the last row of Table 6.12, calculated values of 'beam power gain, BPG' have been shown to be nearly same at all energies in case of the two projectiles [81].

6.17 GEM * STAR Setup

Green Energy Multiplier * Subcritical Technology for Alternative Reactor is a consortium aimed for (i) addressing world's energy issues, (ii) burn nuclear waste, natural uranium, depleted uranium, thorium and excess weapon-grade plutonium, (iii) to use a superconducting accelerator and Molten Salt fuel to achieve greatly improved safety issues and to address the issues of nuclear waste which are both economically and politically feasible, and (iv) GEM * STAR will even be cheaper than natural gas [82]. As a special feature of having Molten Salt fuel makes GEM * STAR very special as it reduces mechanical fatigues of solid reactor rods which normally occur because of frequent accelerator trips. Molten Salt may be a combination of variety of fuels, and its biggest advantage lies in

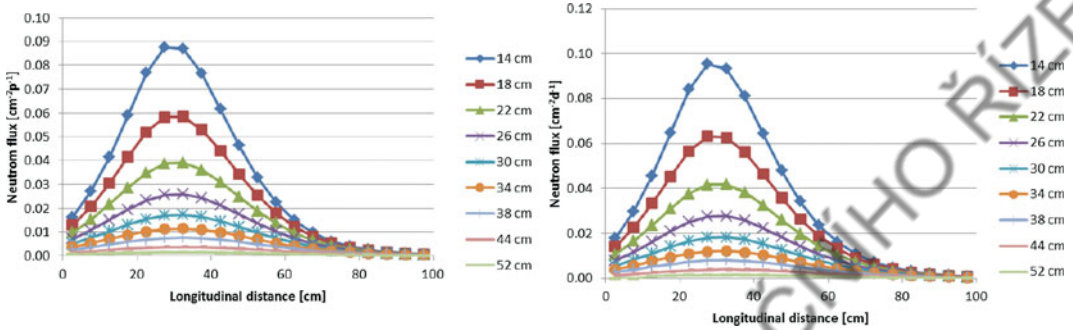


Fig. 6.29 (Left) Neutron flux per incident particle (cm^{-2}) plotted as function of axial distance for 1 GeV proton beam and (right) deuteron beam calculated using the

MCNPX [81]. Different curves correspond to the radial distances shown as legends along with the figures

Table 6.12 Average results of calculation of MCNPX for different beam energies [81]

	Protons			Deuterons		
$E_{p(d)}$ (GeV)	1	6	12	1	6	12
Total neutron multiplicity	126	770	1450	125	794	1455
Number $N(n, y)$	70	440	826	70	452	837
Number $N(n, f)$	16	100	183	15	100	183
$K_{BPG} = E_{tot}/E_{p(d)}$	3.82	3.75	3.5	3.82	3.85	3.55

safety against the corrosion issues. It also contains the fission products which can be separated in a cycle. Dynamically, it is highly stable.

6.18 Some More ADS Programs of Asian Countries

China has an ADS program named as C-ADS started from the year 2011 and to be completed in the year 2030. As per its first phase planning, ADS will run with accelerator of 15 MW power LINAC of 1.5 GeV beam with 10 mA current in continuous wave (CW) form. Accelerator will have superconducting cavities for avoiding beam noises which play important role in design of ADSS. The cavities are being developed at Institute of High Energy Physics, Beijing [83]. The project is advancing in convincing way as its couplers are already manufactured.

Japan has proposed its ADS plan for the reduction of burden of disposal of high-level waste by using ADS technology. An ADSS with the thermal power of 800 MW has been proposed, where 250 kg of minor actinide (MA) can be transmuted annually. A superconducting accelerator is being developed for coupling to Pb–Bi eutectic (LBE) spallation target. The corrosive activity of LBE is overcome by controlling oxygen concentration in LBE which forms an oxide layer on its surface. The J-PARC experimental facility and feasibility assessment are already discussed in Sect. 6.5. As the MAs act as fertile fuel, therefore, plutonium is added for the swing. The Japan ADSS is assumed to work at $k_{max} = 0.97$. Its basic design characteristics are given in Table 6.13 [84].

South Korea is using atomic power, and it has ambitious plan to have 40% energy consumption to be met by atomic power. More than 23

Table 6.13 Core physical parameters of 800 MW Japanese ADS [84]

Parameter	Value	Parameter	Value
Thermal power	800 MW	Initial MA inventory	2,500 kg
Active core diameter	236.6 cm	Effective (k_{eff})	Initial = 0.97, max. = 0.97, mini. = 0.94
Active core height	100.0 cm	Average power density	191 W/cm ³
Initial Pu (inner/outer)	30.0%/48.5%	Proton beam energy	1.5 GeV
Total heavy metal inventory	4,115 kg	Proton beam current	Max. = 17.9 mA, mini. = 8.1 mA

reactors are working on its land and it wants to add 11 more up to the end of 2024. South Korea is expected to produce 100,000 tons of nuclear waste by the end of the century and for that purpose it will need a safe disposal vault of 20 km² in rock caverns and about 500 m underground. According to South Korea's Atomic Energy Research Institute, KAERI, another point of view, pyro-processing technology could reduce waste by 95% compared to 20–50% from the existing reprocessing technology. Country's atomic energy plans are based on uranium fuel, and the country has hardly decided to start an ADSS plan. However, Korea's POSTECH institute has facility for cross-section measurements and KAERI at Seoul had started developing high-current pulsed proton beam accelerator of 100 MeV more than a decade back. According to Karel Samek, iTheC, presently, S. Korea's ADSS plans are getting to start at the university level and SKKU which is planning to produce a high-energy, high-current 5 MW cyclotron for the thorium-based ADSS reactor. The cyclotron will be developed for 1 GeV proton beam for a large number of studies related to ADS activity, and the ADSS may start in the year 2040.

At the same time, S. Korea has shown willingness to work with the USA for the pyro-processing, and according to a report [85] US has agreed to work on the technique jointly.

In Asia, India has been pioneer in initiating its atomic energy programs of peaceful applications of atomic energy in the year 1954. First experimental reactor Apsara, 1 MWt, was started soon

after. It has a long-term objective primarily for utilization of its major resource of thorium which is largely explored on its west and east sea shores. Basically, it has three-stage strategy of atomic energy sustenance. It has developed fast neutron spectrum experimental reactors for developing fast reactors and radiography of materials. It has upgraded its 14 MeV neutron source for higher current ion source also. Its Department of Atomic Energy is engaged in developing Advanced Heavy Water Reactor (AHWR) which aims at developing expertise for thorium utilization and demonstrating advanced safety concepts. Mixed thoria–urania and thoria–plutonia are the candidate fuels for the AHWR. A high-current (30 mA) proton beam LINAC is under development at BARC. Kapoor [86] has given road map of Indian ADS. During Jaipur workshop on Physics of ADSS [87], a spurt in ADS activity in India was noticed from the point of accelerator development and papers presented on developing a dynamics of Pb–Bi eutectic flow loop, developing CASCADE code for simulations and various other collaborative experiments in direction of planning of ADSS. In its stage III of atomic energy, India plans for enhancing breeding of ²³³U from thorium for utilization in fast reactors. PURNIMA reactor is redesigned to be run by (*d, t*) neutron source in subcritical mode, and the efforts will grow to develop understanding of coupling of an accelerator to a reactor and neutron utilization [88]. During this period, a road map of India's 'fast-thermal ADS' is also prepared for initiating the related activities at different places where expertise is being readied.

Explicitly, there is no dedicated ADSS plan presently working in India, but various programs are focused to gather working knowledge from its various academic and engineering projects in phase with several other nuclear countries have been doing for future. It may be inferred that ADS is an ambitious project from the point of availability of financial resources.

References

1. Andriamonje, S., et al.: Experimental determination of the energy generated in nuclear cascades by a high energy beam. *Phys. Lett. B* **348**, 697 (1995)
2. Rubbia, C.: Resonance enhanced neutron captures for element activation and waste transmutation. CERN Internal Report, CERN/LHC/97-04 (EET), June 1997
3. Abanades, A., et al.: CERN-SL-2001-033-EET Report (2001)
4. Ferrari, A., Sala, P.R.: The physics of high energy reactions' lectures at ICTP. In: Trieste Workshop, Apr 15–May 1996. Also, Fasso, A., Ferrai, A., et al.: A comparison of FLUKA simulations with measurements of fluence and dose in calorimeter structures. *Nucl. Instrum. Meth.* **A332**, 459 (1993)
5. European Commission, Community Research, Project Report, Nuclear Science and Technology, Neutron Driven Nuclear Transmutation by Adiabatic Resonance Crossing (TARC), EUR 19117 EN, European Commission, Luxemburg (1999)
6. OECD/NEA Data bank, Issy-les Moulineaux, France (1994)
7. Wang, T., et al.: Measurements of the total cross section and resonance parameters of molybdenum using pulsed neutrons generated by the electron linac. *Nucl. Instrum. Method. Phys. Res.* **B266**, 561 (2008)
8. Zucec, P., et al.: Experimental neutron capture data of ^{58}Ni from the CERN n_TOF facility. *Phys. Rev.* **C89**, 014605 (2014)
9. Guerrero, C., et al.: Performance of the neutron time-of-flight facility n_TOF at CERN. *Eur. Phys. J.* **49A**, 27 (2013) and Tobias J.W., et al.: High precision measurements of the ^{238}U (n, γ) cross sections at the n_TOF facility CERN. In: Proceedings of NEMEA-7/CIELO Workshop, Copy right OECD, pp. 149–157 (2014)
10. Larson, N.M.: RSICC Peripheral Shielding Routine Collection SAMMY-M2a: A Code System for Multilevel R-Matrix Fits to Neutron Data Using Bayes' Equations (PSR-158, SAMMY-M2a). Oak Ridge National Laboratory (1999)
11. Lane, A.M., Thomas, R.G.: R-matrix theory of nuclear reactions. *Rev. Mod. Phys.* **30**, 257 (1958)
12. Mughabghab, S.F.: Atlas of Neutron Resonances, 5th edn. National Data Center, BNL, Upton, USA
13. Zucec, P., et al.: Data available in article, [arXiv:1402.1032v1](https://arxiv.org/abs/1402.1032v1) [nucl-ex], 5 Feb 2014
14. Lederer, C., et al.: Neutron Capture Cross Section of Unstable ^{63}Ni : Implications for Stellar Nucleosynthesis (2013). [arXiv:1304.3310v1](https://arxiv.org/abs/1304.3310v1) [nucl-ex], 11 Apr 2013
15. Abbondanno, U., et al.: Neutron capture cross section measurement of ^{151}Sm at the CERN neutron time of flight facility (n_TOF). *Phys. Rev. Lett.* **93**, 161103 (2004)
16. Fujii, K., et al.: International Conference on Nuclear Data for Science and Technology (2007). <https://doi.org/10.1051/ndata:07519>, <http://nd2007.edpsciences.org> or <http://dx.doi.org/10.1051/ndata:07519>
17. Domingo-Pardo, C., et al.: New measurement of neutron capture resonances of ^{209}Bi . *Phys. Rev. C* **74**, 025807 (2006)
18. Aert, G., et al.: Neutron capture cross section of ^{232}Th measured at the n_TOF facility at CERN in the unresolved resonance region up to 1 MeV, *Phys. Rev. C* **73**, 054610 (2006), also, <http://hal.in2p3.fr/in2p3-00082118>
19. Tobias, J.W., et al.: High-precision measurement of the $^{238}\text{U}(n,\gamma)$ cross-section at the n_TOF facility, CERN, NEMEA-7/CIELO Workshop Proceedings, p. 149 (2014)
20. Derrien, H., et al.: Neutron Resonance Parameters of ^{238}U and the Calculated Cross sections from the Reich Moore Analysis of Experimental Data in the Neutron Energy Range from 0 keV to 20 keV, ORNL/TM-2005/241 (2005)
21. Paradela, C., et al.: Proceedings of the Final Scientific EFNUDAT Workshop. In: Chiaverri, E. (ed.) p. 33, 30 Aug–2 Sept 2010. CERN, Geneva (2010). Also, *Phys. Rev.* **C82**, 034601 (2010)
22. González, E.: On Behalf of the n_ToF Collaboration: Neutron Cross-Section for P&T and ADS at the n_ToF Facility at CERN (2010). https://indico.cern.ch/event/83067/attachments/1070068/1525949/Proceedings_EFNUDAT_August2010_REV_FINAL.pdf
23. IREN Project. Intense Resonance Neutron Source. Compiled by A.K. Krasnykh, V.L. Lomidze, A.V. Novokhatsky, Yu. P. Popov, W.I. Furman. Frank Laboratory of Neutron Physics, JINR, Dubna, 1994 and see V.L. Aksenov et al. *Acta Phys. Hung.* **75** (i-4), 341 (1994)
24. Antropov, V., Dolya, S., Kaminsky, A., Krasnykh, A., Laziev, E., Pjataev, V., Shvets, V., Sumbaev, A.: IREN Test Facility at JINR, LINAC 96, pp. 505–507. <https://accelconf.web.cern.ch/accelconf/196/PAPERS/TUP68.PDF>
25. Meshkov, I., Sisakian, A., Trubnikov, G.: IPAC 10, The First International Particle Accelerator Conference, Kyoto, Japan, 23–28 May 2010
26. Logatchev, P.V., et al.: Intense Resonance Neutron Source (IREN) A New Pulsed Source for Nuclear Physical and Applied Applications, <https://www.researchgate.net/publication/242182317>
27. Jeneva, N.B., et al.: Future Neutron Data Activity on the Neutron Source IREN (2011). <http://www.iaea.org>

- org/inis/collection/NCLCollectionStore/_Public/48/009/48009766.pdf
28. Advance Materials for Energy. <http://www.ga.com/advanced-materials>
 29. Persic, A.: TRIGLAV—A Program Package for Research Reactor Calculations. J. Stefan Report, US-DP-7862 (1998)
 30. Persic, A., Ravnik, M., Zagar, T.: European Nuclear Society, Berne (Switzerland), Belgian Nuclear Society (Belgium), International Atomic Energy Agency, Vienna (Austria), 217 p, pp. 187–191 (1999). https://inis.iaea.org/search/search.aspx?orig_q=RN:32034894
 31. Karch, J., et al.: Performance of the solid deuterium ultra-cold neutron source at the pulsed reactor TRIGA Mainz. Eur. Phys. J. **A50**, 78 (2014)
 32. Nagamiya, S.: JAER-KEK joint project on high intensity proton accelerators. In: Proceedings of International Conference on Radiation Shielding (ICRS-9), Tsukuba, 18–21 Oct 1999. J. Nucl. Sci. Technol. (Supplement 1) **40** (2000)
 33. JAERI-Tech 2000-003/KEK Report 99-5 (2000) (In Japanese). See also The Joint Project for High-Intensity Proton Accelerators, JAERI-Tech 056/KEK Report 99-4 (1999). Also see, <https://eventbooking.stfc.ac.uk/uploads/ioppab14/plostinar.pdf>
 34. Teshigawara, M., Watanabe, N., Kai, T., Nakashima, H., Nagao, T., Oyama, Y., Ikeda, Y., Kosako, K.: Neutronic Study on the JAERI 5 MW Spallation Neutron Source-Neutronic Performance of the Reference Target-Moderator-Reflector System and the Target Shape/Size Effects. JAERI-Research 99-020, Mar 1999
 35. Maekawa, F., et al.: First neutron production utilizing J-PARC pulsed spallation neutron source JSNS and neutronic performance demonstrated. Nucl. Instrum. Meth. Phys. Res. **620**, 159 (2010)
 36. Sakasai K., et al.: Materials and Life Science Experimental Facility at the Japan Proton Accelerator Research Complex III: Neutron Devices and Computational and Sample Environments. Quantum Beam Science **1**, 10 (2017) and see, UCN at KEK: Ultra Cold Neutron Source. <https://www.kek.jp/en/Facility/IPNS/UltraColdNeutronFacility/>
 37. Masatoshi F., et al.: 1-MW pulsed spallation neutron source (JSNS) at J-PARC. J. Neutron News **22**, 15 (2011) and <https://www.kek.jp/en/Facility/>
 38. Paranov, D.V., Paranova, E.D.: Generation IV Concepts USSR and Russia. <http://dx.doi.org/10.1016/B978-0-08-100149-300012-4>
 39. Soule, R., et al.: Neutronic studies in support of accelerator-driven systems: The MUSE experiments in the MASURCA facility. Nucl. Sci. Eng. **148**, 124 (2004)
 40. Berglöf, C., et al.: Pulsed Neutron Source Reference Measurements in the Subcritical Experiment YALINA-booster. ADS/ET-5. file:///G:/Book%20on%2014072017/Book%20on%20ADS27032017/Chapter%207KK/YELINA%20booster.pdf
 41. Persson, C.-M.: Reactivity Determination and Monte Carlo Simulation of the Subcritical Reactor Experiment—“Yalina”. KTH Engineering Science. ISBN 91-7178-015-7, Universitetservice US-AB, Stockholm (2005)
 42. Sjöstrand, N.G.: Measurement on a subcritical reactor using a pulsed neutron source. Arkiv för fysik **11**, 13 (1956)
 43. Billebaud, A., Baeten, P., Ait Abderrahim, H., Ban, G., Baylac, M., et al.: The GUINEVERE project for accelerator driven system physics. In: International Conference GLOBAL 2009. The Nuclear Fuel Cycle: Sustainable Options Industrial Perspectives, Sep 2009, Paris, France, pp. 1809–1815 (2009). Also, HAL Id: in2p3-00414431 <http://hal.in2p3.fr/in2p3-00414431>
 44. Baylac, M.: Some high lights of ADS programs in Europe. In: 1st International Workshop on Accelerator-Driven Sub-Critical Systems & Thorium Utilization, 27–29 Sept 2010, Virginia Tech. www1.phys.vt.edu/~kimballton/gem-star/workshop/presentations/baylac.pdf
 45. Iyengar, P.K., Srinivasan, M., Nargundkar, V.R., Chandramoleshwar, K., Subha Rao, K., Pasupathy, C.S., Das, S., Basu, T.K., Job, P.K.: PURNIMA fast critical facility, experiments and results. In: Proceedings of the Indo-Soviet Seminar on Fast Reactors, Kalpakkam, India, pp. 249–268 (1972)
 46. Basu, T.K., Radha, E., Reddy, C.P., Ganesan, S.: (evaluators) NEA/NSC/DOC/(95)03/I, vol. 1, PU-COMP-FAST-004, 30 Sept 2012
 47. Srinivasan, M., Chandramoleshwar, K., Job, P.K., Pasupathy, C.S., Subba Rao, K., Ray, A.K., Patil, R. K., Ramanujam, A.: Safety Analysis Report of Purnima-II: BeO Reflected U-233 Uranyl Nitrate Solution Reactor Experiment. BARC/I-790, Bhabha Atomic Research Centre (1984)
 48. Srinivasan, M., Chandramoleshwar, K., et al.: ^{233}U fueled homogeneous reactor PURNIMA-II: design features and experimental results. Paper Presented at the Seminar on Fast Reactor Fuel Cycle, IGCAR, Kalpakkam, 10–12 Feb 1986
 49. Basu, T.K., Radha, E., Reddy, C.P., Rasheed, K.K., Ganesan, S. (evaluators): PURNIMA-II: U-233 Uranyl Nitrate Solution Reactor with Beryllium Oxide Reflector, NEA/NSC/DOC/(95)03/V, vol. V, U233-SOL-THERM-007
 50. Kumar, R., Degweker, S.B., Patel, T., Bisnoi, S., Adhikari, P.S.: Reactor physics experiments in PURNIMA sub critical facility coupled with 14 MeV neutron source. In: Proceedings of the Second International Workshop on Accelerator-Driven Sub-critical Systems and Thorium Utilization (2011). Also see <https://inis.iaea.org/search/search.singlerecord.aspx?recordsFor=SingleRecord&RN=44027640>
 51. Radha, E., Reddy, C.P., Ganesan, S., Srinivasan, G., Ramalingam, P.V., Raj, B. (evaluators): Kalpakam Mini (KAMINI) Reactor: Beryllium-Oxide Reflected

- Water-Moderated ^{233}U -Fueled Reactor. NEA/NSC/DOC/(95)03/V, vol. V, U233-MET-THERM-001
52. Sinha, A., et al.: BRAHMMA: A compact experimental accelerator driven subcritical facility using D-T/D-D neutron source. *Ann. Nucl. Energy* **75**, 590 (2015)
 53. Sharma, M.: Transmutation of Long-Lived Isotopes of Conventional Reactors Using A.D.S. Concept. Ph. D. thesis, University of Rajasthan, Jaipur (2010)
 54. Barashenkov, V.S.: Monte Carlo Simulation of ionization and Nuclear Processes Initiated by Hadron an Ion Beams in Media. *Comput. Phys. Commun.* **126**, 28 (2000)
 55. Adam, J., et al.: Measurements of the neutron fluence on the spallation source at dubna. *KERNTECHNIK (J. Nucl. Eng. Energ. Syst. Radiat. Radiol. Prot.)* **70** 127 (2005)
 56. Adam, J., Bhatia, C., Katovsky, K., Kumar, V., Majerle, M., Pronskikh, V.S., Khilmanovich, A.M., Martsynkevich, B.A., Zhuk, I.V., Golovatiouk, V.M., Westmeier, W., Solnyshkin, A.A., Tsoupko-Sitnikov, V.M., Potapenko, A.S.: A study of reaction rates of (n,f), (n, γ) and (n,2n) reactions in ^{nat}U and ^{232}Th by the neutron fluence produced in the graphite set-up (GAMMA-3) irradiated by 2.33 GeV deuteron beam. *Eur. Phys. J. A* **47**, 85 (2011)
 57. Bhatia, C., Kumar, V.: Book: Role of (n, xn) Reactions in Accelerator Driven Sub-critical Systems. Lap-Lambert, Germany (2011). ISBN 978-3-8465-0684-4
 58. Abanades, A., Alexandre, J., Andriamonje, S., et al.: Results from the TARC experiment: Spallation neutron phenomenology in lead and neutron-driven nuclear transmutation by adiabatic resonance crossing. *Nucl. Inst. Meth. A* **478**, 577 (2002)
 59. Hendricks, J.S., et al.: MCNPX, Version 2.6.c, LA-UR-06-7991 (2006)
 60. Adam, J., et al.: A study of nuclear transmutation of Th and ^{nat}U with neutrons produced in a Pb target and U blanket irradiated by 1.6 GeV deuterons. *Eur. Phys. J. A* **43**, 159 (2010)
 61. Bhatia, C., Adam, J., Kumar, V., Katovsky, K., Majerle, M., Solnyshkin, A.A., Tsoupko-Sitnikov, V. M.: A Study of non-elastic reaction rates for the A.D. S. materials in the environment of spallation neutrons produced by 1.6 GeV d-beam. *Appl. Radiat. Isot.* **70**, 1254 (2012)
 62. Krivopustov, M.I., Chultem, D.: Experiments on electronuclear technology and transmutation of nuclear waste using synchrotron beams. *JINR News Dubna* **3**, 27 (1998)
 63. Krivopustov, M.I., Chultem, D., Tumendelger, T., et al.: Modeling of the electronuclear method of energy production and study of radioactive waste transmutation using a proton beam of the JINR synchrotron/nuclotron: research program of the laboratory of high energies. *JINR. In: Baldin, A.M. (ed.) JINR, 99–266. Dubna, pp. 135–139 (1999). Book of Abstracts of the 3rd International Conference on Accelerator Driven Transmutation Technologies and Applications*, (1999) Praha, Czech Republic, 7–11 June 1999, p. 55
 64. Barashenkov, V.S., Kumawat, H., Lobanova, V.A., Kumar, V.: Mathematical model of the electronuclear set-up on the beam of JINR Synchrotron. *Nucl. Instr. Meth. Phys. Res. B*, **217**, 352 (2004)
 65. Adam, J., et al.: Transmutation of ^{129}I , ^{237}Np , ^{238}Pu , ^{239}Pu , and ^{241}Am using neutrons produced in target-blanket system ‘Energy plus Transmutation’ by relativistic protons. *Pramana J. Phys.* **68**, 201 (2007)
 66. MONC.: Monte Carlo Nucleon Transport Code. http://bts.bare.gov.in/AuthStatic/auth_static.php/npd/monc/index.html, Accessed on 19 Dec 2016 (BARC internal access only)
 67. Kumar, V., Tundwal, A., Katovsky, K., Sharma, M.: A review of nuclear waste transmutation using accelerator beams up to several GeV. Talk Presented at 17th International Scientific Conference on EPE-2016, Praha, Czech Republic (2016). <http://ieeexplore.ieee.org/stamp/stamp.jsp?tp=&number=7521826&isnumber=7520888>
 68. Baldin, A.A., Belov, E.M., Galanin, M.V., et al.: Nuclear relativistic technologies (RNT) for energy production and utilization of spent nuclear fuel. Results of first experiments on physics justification of RNT. *Particles Nucl. Lett.* **6**, 1007 (2011) (in Russian). *JINR Preprint E1-2011-24*, Dubna (2011)
 69. Furman, W., et al.: Recent results of the study of ADS with 500 kg natural uranium target assembly QUINTA irradiated by deuterons with energies from 1 to 8 GeV at JINR NUCLOTRON. 2012 Proceedings of Science (Baldin ISHEPP XXI 086). http://pos.sissa.it/archive/conferences/173/086/Baldin%20ISHEPP%20XXI_086.pdf
 70. Asquith, N.L., et al.: Activation of ^{197}Au and ^{209}Bi in a fast spectrum sub-critical assembly composed of 500 kg natural uranium irradiated with 1 and 4 GeV deuterons. *Ann. Nucl. Energy* **63**, 742 (2014)
 71. Pelowitz, D.B.: MCNPX User’s Manual Version 2.7.0, LA-CP-11-00438 (2011)
 72. Adam, J., et al.: Measurement of the high energy neutron flux on the surface of the natural uranium target assembly QUINTA irradiated by deuterons of 4 and 8 GeV energy. *Phys. Procedia* **80**, 94 (2015)
 73. De Bruyn, D.: Engineering Design of the MYRRHA (Design Evolution from MYRRHA to XT-ADS) Part IX, School on Physics, Technology and Applications of Accelerator Driven Systems (ADS), 19–30 Nov 2007. ICTP, 1858-14 and Abderrahim, H.A., et al.: MyRRHA—A Multipurpose Fast Spectrum Research Reactor. *Energ. Convers. Manag.* **63**, 4 (2012)
 74. Mueller, A.C.: Transmutation of Nuclear Waste and the Future MYRRHA Demonstrator. <https://arxiv.org/pdf/1210.4297>

75. Polanski, A.: Monte Carlo modeling of electronuclear processes in experimental accelerator driven systems. *Acta Phys. Polonica*, **B11**(1), 95 (2000)
76. Barashenkov, V.S., Puzynin, I.V., Polanski, A.: Mathematical experiments with electronuclear systems. *J. Comput. Meth. Sci. Eng.* **2**(1–2), 5 (2002)
77. Barashenkov, V.S., Polanski, A., et al.: Fast sub-critical assembly with MOX fuel for research on nuclear waste transmutation. *Belarus NSA J. Phys. Tech.* **3**, 150–153 (2001)
78. Shvetsov, V.N., et al.: Sub critical assembly at Dubna (SAD): coupling all major components of accelerator driven subcritical system (ADS) for nuclear waste incineration. In: *International Symposium on Utilization of Accelerators*, Dubrovnik, Croatia, 5–9 June 2005. <http://www-naweb.iaea.org/napc/physics/meetings/dubrovnik2005/papers/82.pdf>
79. Polanski, A.: Simulations of accelerator driven systems (ADS). In: *Joint IAEA-ICTP Workshop on Nuclear Reaction Data for Advanced Reactor Technologies*. <https://www-nds.iaea.org/workshops/smr1944/Participants/28-May.../POLANSKI.ppt>
80. Tichý, P., Suchopár, M.: Future usage of quasi-infinite depleted uranium target (BURAN) for benchmark studies. In: *Proceedings of Science, XXII International Baldin Seminar on High Energy Physics Problems*, JINR, Dubna, Russia, 15–20 Sept 2014. <https://pos.sissa.it/225/065/pdf>
81. Furman, W.: Results of experiments 2012–2013 with massive uranium target setup QUINTA at nuclotron and plans for 2014–2016. In: *ISINN XXI*, Alushta, Ukraine, May 20–25 2013
82. Bowman, C., et al.: GEM*STAR* consortium staging and demonstration. In: *1st International Workshop on ADSS and Thorium Utilization*, Blacksburg, VA, 27–29 Sept 2010
83. Huang, T.M., et al.: High power input couplers for C-ADS. In: *Proceedings of SRF 2015*, Whistler, BC, Canada, THPB101, p. 1383 (2015). ISBN 978-3-95450-178-6
84. Tsujimoto, K., et al.: Neutronics design for lead-bismuth cooled accelerator-driven system for transmutation of minor actinide. *J. Nucl. Sci. Technol.* **41**, 21 (2004)
85. Nuclear Waste a Growing Headache for South Korea. <https://www.ndtv.com/world-news/nuclear-waste-a-growing-headache-for-south-korea-517345>
86. Kapoor, S.S.: Accelerator-driven sub-critical reactor system (ADS) for nuclear energy generation. *Pramana J. Phys.* **59**, 941 (2002)
87. Kumar, V. et al. (ed.): *Proceedings of Workshop on Physics of Accelerator Driven Subcritical System*. *Pramana J. Phys.* **68** (2007) (complete issue)
88. Banerjee, S.: Physics of ADS for energy and transmutation. In: *Inaugural Talk at the Workshop on Physics of ADS*, Jaipur, India, 23–25 Jan 2006

Radiation Damage and Development of a MC Software Tool

7

The chapter comprises innovative efforts taken in case of defining radiation damage. Older models and codes used for the estimation of radiation damage are considered as a matter of discussion elsewhere. In fact, simulation codes and models of calculation of data required for designing new energy systems, have more concern of comparison with the new experimental data which is being collected world over as described in earlier chapters. For computation of radiation damage up to several MeV energy, atomic collision cross section play much vital role than consideration of passage of the products of inelastic collision at these energies. In case of radiation damage by passage of gamma radiation estimation of single vacancies and interstitials is highly desired in design and modeling of several electronic devices. This requires attention to the subject of radiation damage too. Nevertheless, role of dynamical models including kinetic Monte Carlo have more vital role to play in future activities of applications of radiation in the field of medical science.

7.1 Radiation Damage—An Important Issue

In case of a power reactor issue of radiation damage is pertinently related to the structure material, core structure and shielding; whether the material remains intact or not without losing its functionality. Integrity of the fuel rods or fuel cells, coolant pipes, material used to contain the

inner or the outer cores is important under the severe irradiation by neutrons, gamma, charged particles, harsh temperature conditions, and the flow rate of the coolant, etc. This becomes a more important issue in case of fusion reactors and the ADSS where the inner wall of a fusion reactor and other structure materials in case of both face many times more intense neutron fluence. Neutrons not only activate the material but also multiply by way of $(n, xnyp)$ kind of reactions.

Radiation damage so far is measured in terms of displacements per atom (DPA) and according to one estimate [1] in case of thermal reactors the core sees a damage up to 20 DPA and it will rise up to ~ 120 in a fast reactor and even more in case of ADSS. In case of future generation IV reactors, it will be an order of magnitude higher particularly on the inner wall of a fusion reactor. Physical effects arising due to irradiation shown in Fig. 7.1 indicate that vacancies, dislocations, vacancy loops, voids, clustering, and microstructures, etc., become the cause of weakening of the materials. A material may become amorphous and swell crossing the designed boundaries. Embrittlement and corrosion of the metals are the physically visible effects. Formations of radicals in liquids causing many chemical reactions occur also due to soft radiation passage.

In Fig. 7.2, radiation damage of core structure materials of different nuclear reactors has been summarily shown.

Fig. 7.1 Physical effects of radiation damage in the bulk of matter [1]

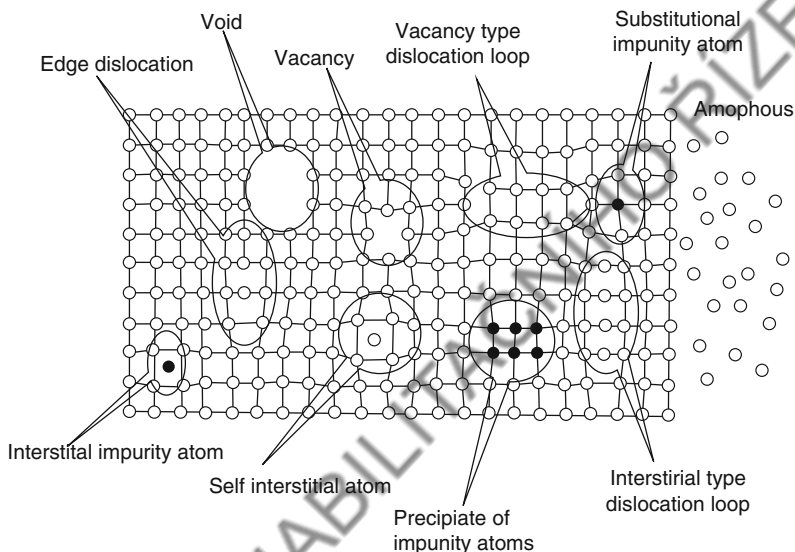
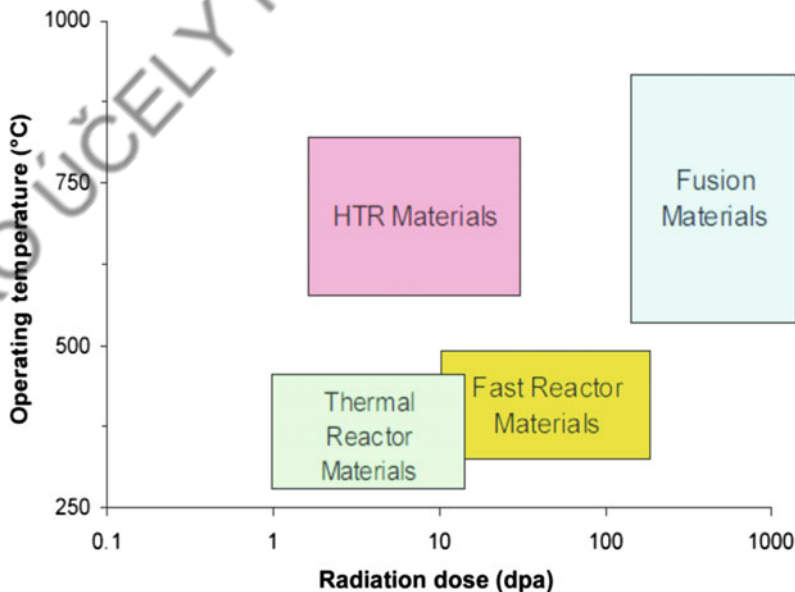


Fig. 7.2 Operating conditions of structure materials of different reactors [1]



Issues related to development of the subject of radiation damage and modern requirements of radiation resistant materials have been deliberated primarily in Ref. [2]. In fact, the subject of development of radiation resistant materials needs utmost attention of the initiatives of the new definitions and fundamental theoretical developments. In the chapter, such initiatives have been discussed which need further intensive research works.

7.1.1 Radiation Effects in Materials

Radiation damage has been an important issue of a power reactor and both its material and the structures are strongly built looking at the effects of radiation. Accelerator beam pipe and the materials in immediate surrounding are the second irradiated materials, and they are usually handled very carefully. Effects like ‘Channeling and sputtering’ became the subjects of high attraction in the area of

material studies in early 70s and 80s of last century. In the last two decades, material modification, synthesis, upgradation of materials have attracted attention heavily and at the same time they have made strong impact on economy also because of relatively easy access of variety of radiation sources, leave aside the matter of applications of radiation in medical treatments.

International Atomic Energy Agency (IAEA) has been regularly updating its maintenance activity of nuclear energy installations and those using radiation in different forms world over. In its several meetings such as SMORE-2008 [3] held at Kharkov (Ukraine) emphasis was laid on ‘Accelerator Simulations and Theoretical Modeling of Radiation Effects’ with cross sections, energy spectra, and other inputs on PKA codes being the key issues. Similarly, another meeting, TM-36842 [4] on the theme ‘Physics of materials under neutron and charged particle irradiations’ was called with the following objectives,

1. Expert review on radiation damage in stainless steels
2. Creation of databases within the existing and planned IAEA activities involving neutron and ion irradiations
3. Initiation of a CRP on examination of advanced materials subject to high-dose neutron irradiation
4. A focused workshop or activity on dpa and a more general workshop or activity on prospects and limitations of ion irradiation to simulate neutron damage

The main recommendation of this theme meeting, TM-36842, was made as under,

There is now a pressing need to upgrade/modify standards for materials irradiation and radiation damage produced by energetic particles and neutrons. The generally accepted reference method by which to compare irradiated test materials in different settings is DPA. In a simplistic model, dpa should be a means of normalizing experimental results independently of the irradiation source used be it either a research or power reactor, spallation source, or ion beam accelerator. Many experimental findings and numerical simulations over the

past decades have shown this is not satisfactory. No simple correlation exists between DPA and microstructural radiation damage.

In light of the recommendations of the two theme meetings of a prime organization, proper modeling of radiation damage is emphasized so that the quantities like DPA and similar other quantities can be replaced to provide better standard for the sake of easy normalization of irradiated materials to different intense radiation sources including ion beams. The issue has relevance with the strong neutron/radiation sources like that used in a fusion reactor and spallation neutron source of an accelerator-driven subcritical system of energy and transmutation.

On passage of radiation through matter in the form of solid, liquid, or gas following basic changes take place,

- (i) In solids, displacement of atoms is important. This generates Frenkel pairs, defects, clusters, voids, loops, and microstructures. Ionization is also an area of interest particularly in calculation of dose
- (ii) Displacements and clustering, ionization, radical formation, dipole excitation, and boiling effects are important in case of liquids. Liberation of gaseous molecules such as hydrogen and helium from heavy atoms has strong effects on liquid dynamics through bubbling, etc.
- (iii) Atomic excitation, ionization, and even plasma formation play more important role in gases than liquid and solids
- (iv) Neutron although a neutral particle, yet, displace atoms and additionally generate atomic cascades. A gamma ray interacts with orbital electrons and the ejected electron in turn displaces atoms. In a way, this is a novel method of displacing single atoms in depth with a little fraction of atomic cascades. In case of both neutron and gamma radiation, binary collision approach (BCA) is highly useful compared to irradiation by heavy ions where atom–atom potential is relatively more

important. Also, consideration of crystallographic structure of material is important for analyzing microstructures.

Crystallographic considerations have specific effects which can be summarized in the following. For this purpose, direction of irradiation of a specific material is worth consideration.

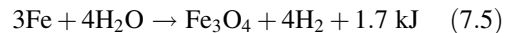
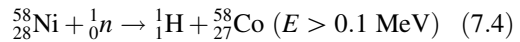
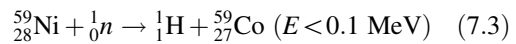
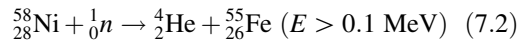
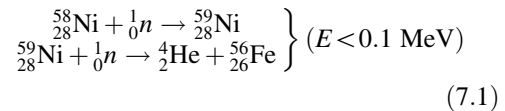
1. **Body-Centered Cubic (BCC):** Among the structure materials tungsten, iron, vanadium, and ferritic steels are BCC structures. Point defects in ferritic steels make it less plastic.
2. **Face-Centered Cubic (FCC):** Copper, austenitic steels, and nickel alloys are FCC structures. Swelling is more common in austenitic steel and nickel alloys because vacancies tend to create volume clusters. In Fig. 7.3, swelling of the stainless steel under strong neutron fluence has been shown.

Swelling arising in fuel pins of BN-660 reactor is found to be due to small variations in silicon content.

3. **Hexagonal Close Packed (HCP):** Zirconium and its alloys are HCP metals. SiC is poly-type hexagonal structure, e.g., 3C and 6H types. Radiation-induced growth is more prone in zirconium, graphite, and uranium and that can lead to dimensional changes in different directions. Although in the case of SiC for radiation resistance will be discussed later in the chapter in detail, and in Fig. 7.4 swelling and other features arising due to radiation damage are shown.

Some of the important issues of radiation damage are, for example, ‘irradiation creep’ which is a permanent deformation, and it depends mainly on the direction of the stress. On removal of the stress, the material does not come to the original shape and size. On irradiation, ‘phase transition’ can also be stimulated and that can also lead to negative radiation resistance. Influence of gamma and neutron radiation as the embrittlement of steel of a reactor pressure vessel

(RPV) in the ‘High Flux Isotope Reactor, (HFIR)’ [8–10] and corrosion of steel [11] have been observed. Helium embrittlement due to alpha emission in (n, α) reaction is also a well-known radiation effect. Similarly, hydrogen emission in (n, p) type reactions leads to bubble formation. Based on the physical behavior of gases, swelling rate of FCC austenitic steel is 1% per DPA while in case of ferritic steel [12] it is 0.2% per DPA. On one hand, Ni helps in stabilizing FCC base but on the other hand high Ni content of steels, such as PE16, becomes brittle. Obviously, reduction of Ni content of steel helps in corrosion of the steel. Conversion of Ni on impact of neutron can be studied following Eqs. (7.1)–(7.5). Alternatively, vanadium-based alloys are considered to be strong candidates for the first wall/blanket of a post-Next European Torus/International Thermonuclear Experimental Reactor, i.e., a fusion reactor, ITER [13].



7.1.2 Early Approaches of Assessment of Radiation Damage

All the old approaches of assessment of radiation damage are based on estimation of displacements per atom. It means that if DPA of an irradiated material is said to be equal to 1; then, all atoms of the irradiated material are on an average displaced one time. Here, displacement distance is an important issue as some of the displaced atoms very close to their vacated positions may recombine back to the original position because of change in some physical conditions, like

Fig. 7.3 (Up) Swelling of steel under strong irradiation [5], (Below) variation of pin length due to swelling in EI-847 fuel pins irradiated in BN-600 [6]

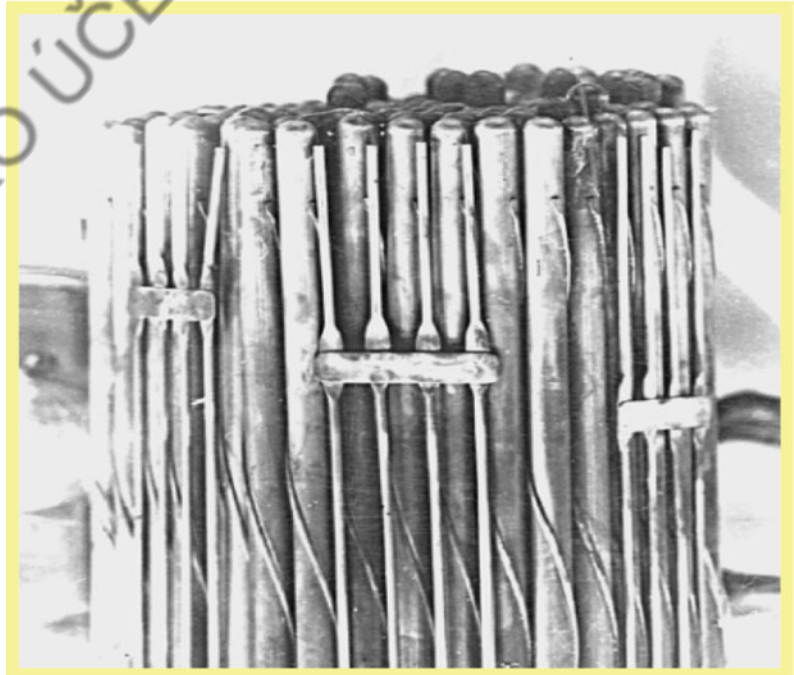
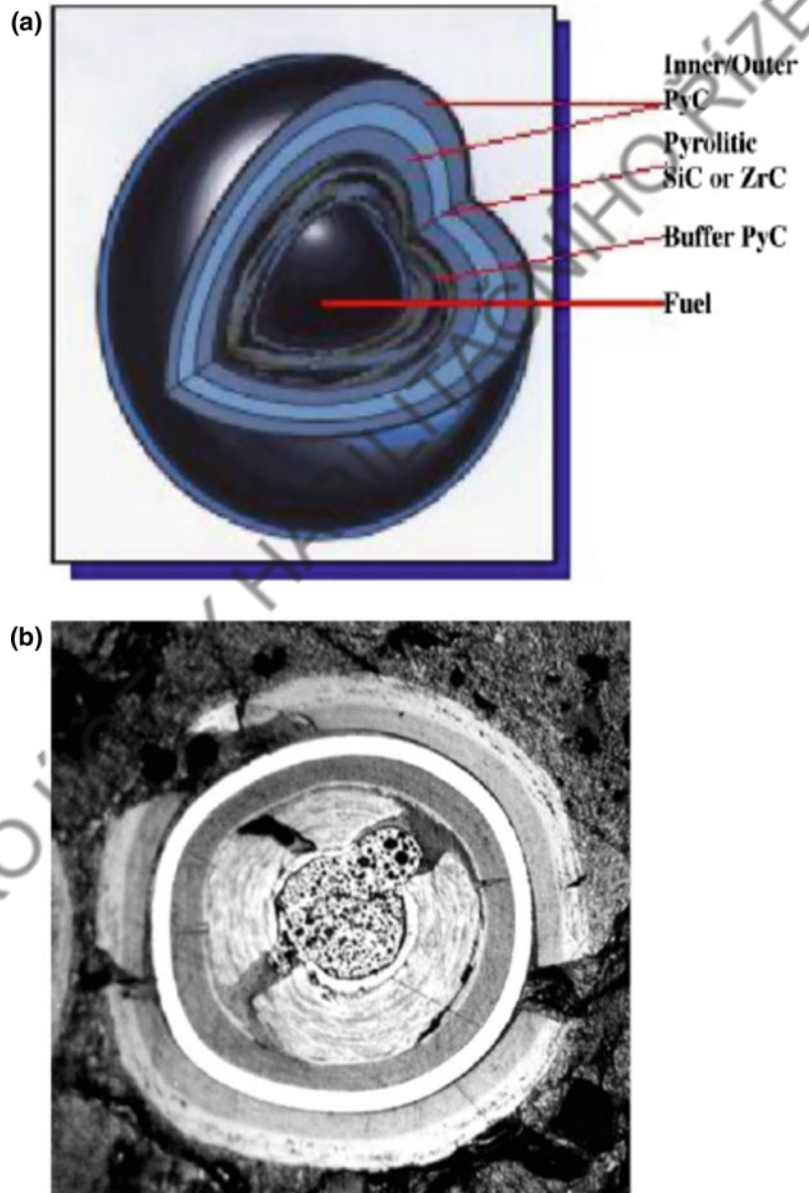


Fig. 7.4 (Up) A fuel cell for an advanced energy system before irradiation with SiC coating and (down) fuel cell after application in a reactor [7]



temperature. The calculation of DPA has been popular in case of structure and shielding materials of a reactor when exposed to neutron, gamma and fission products. The fission products lose energy very fast by the way of ionization. In case of fast reactors, fusion and ADSS kind of reactors displacements may also occur due to the following processes,

- (i) Energy transfer during an elastic or an inelastic scattering of a neutron,
- (ii) Recoil of a nucleus on emission of an energetic particle, usually subsequent to a capture reaction of a neutron or (n, α) , (n, p) , (n, d) , (n, γ) and other reactions,
- (iii) Energy transfer by another knocked off or recoil atom, or

- (iv) Energy transfer from a secondary (emitted) particle.

In fact, the produced particles generate another series of interactions and recoils. The produced particles may also stay inside at the position of its stopping in a vacant position or close to the atom of the material. All such processes contribute toward damage of material. Rate of radiation damage by a neutron of energy, E per unit time and per unit volume is given by,

$$D(E) = N\sigma_d E\varphi(E) \quad (7.6)$$

Where N is the atom density, φ is the neutron flux (no./cm²/s), and σ_d is the microscopic damage cross section (cm²). As mentioned above, there can be a number of ways of producing displaced atoms by elastic scattering or recoils produced in primary collisions like (n, α) , (n, p) , (n, d) , (n, γ) , or even secondary knocked-on atom (SKA) due to primary knocked-on atom (PKA). Total displacement cross section can be written as summation over all such processes,

$$\sigma_d(E) = \sum_n \sigma_{dn}(E) \quad (7.7)$$

Displacement cross section due to any primary type reaction can be calculated from

$$\sigma_{dn}(E) = \int_{E_d}^{E_T \max} \sigma_n(E) P_n(E, E_T) v(E_T) dE_T \quad (7.8)$$

Here, P_n is the probability of n^{th} type interaction with transferred energy E_T to a PKA out of the incident, E energy. The $v(E_T)$ is the effective number of displaced atoms due to transfer of E_T energy. Specifically, at low energy of neutrons elastic scattering is the dominant interaction.

7.1.2.1 Estimation of $v(E_T)$

Dienes and Vineyard [14] have systematically described how different models estimate $v(E_T)$

corresponding to transferred energy, E_T by a projectile to a PKA by calculating E_T from kinetics of a collision. For isolation of an atom from the bonding of other neighboring atoms of a lattice minimum threshold energy, E_d is needed to be transferred to the atom and this varies from material to material. In Table 4.3, values of E_d for a large number of elements have been given. According to one of the initial models, Kinchen and Peas [15],

$$v(E_T) = 0 \quad 0 < E_T < E_d \quad (7.9)$$

$$v(E_T) = 1 \quad E_d < E_T < 2E_d \quad (7.10)$$

$$v(E_T) = E_T / (2E_d) \quad 2E_d < E_T < E_{T1} \quad (7.11)$$

This shows that when the transferred energy, E_T rises beyond $2E_d$, then $v(E_T)$ rises linearly with E_T up to E_{T1} and beyond this it is saturated,

$$v(E_T) = E_{T1} / 2E_d \quad E_T > E_{T1} \quad (7.12)$$

As a matter of mechanism, hardcore scattering is assumed up to E_{T1} and all atoms receiving energy $< E_d$ return back to the original position. Later, Nelson model [16] corrects the formulation for the realistic scattering in place of hardcore approximation and the defect recombination. Torrens and Robinson [17] proposed a modified Kinchen-Peas model by applying electron excitation and redefined E_{T1} by $E_T - Q$ where Q is the energy lost in cascades. Also, they identified displacement efficiency factor to be $k \sim 0.8$. In the high E_T —region,

$$\begin{aligned} v(E_T) &= k(E_T - Q) / 2E_d; \\ E_T &= E_T - Q > 2E_d / k \end{aligned} \quad (7.13)$$

Later, the modified Kinchen-Peas model has been incorporated in NRT [18] model where energy invested in displacements is calculated according to the Lindhard et al. [19] approach for the whole range of energy. The NRT formula is widely adopted in calculations of radiation damage,

$$v(E_T) = kE_T' / 2E_d \quad (7.14)$$

with

$$\begin{aligned}
 E'_T &= E_T/[1 + k_L g(\varepsilon)], \\
 g(\varepsilon) &= 3.4008\varepsilon^{1/6} + 0.40244\varepsilon^{3/4} + \varepsilon, \\
 k_L &= 0.1337 Z_1^{1/6} (Z_1/A_1)^{1/2}, \\
 \varepsilon &= [A_2 E_T / (A_1 + A_2)] [a / Z_1 Z_2 e^2], \\
 a &= (9\pi^2 / 128)^{1/3} a_0 [Z_1^{2/3} + Z_2^{2/3}]^{-1/2} \quad \text{and}
 \end{aligned}$$

Here, a_0 is the Bohr's radius and suffix 1 and 2 are used for the projectile and target mass number (Z) and atomic mass (A) respectively and ε is a dimensionless energy. In a detailed discussion, Gopalakrishnan [20] has pointed out that (i) in the model E_d is taken to be 40 eV for all elements of the steel (ii) as the model depends mainly on the energy of PKA and in different interactions it will be different and for complicated inelastic interactions recoil energies will also involve angular anisotropy and (iii) the model assumes that all small displacements or the defects produced on irradiation will recombine back; therefore, their estimation is not considered in the model.

7.1.3 Monte Carlo Simulation Approach of JA-IPU Code

In the modern time with the availability of high computation power, it is imperative to develop a detailed code based on Monte Carlo simulations of the entire process of transport of radiation or particle like neutron, proton and heavy ion or even a photon through a complex material of several elements with the help of binary collision approximation involving all kinds of physical effects like ionization loss, excitations, displacement distances of recoils hence separation of displaced Frenkel pair (interstitial and vacancy) or the defects. This category of codes of radiation damage can accommodate the situations like escape out of an ejected ion or atom from the irradiated sample. In the following part of the chapter, details of the JA-IPU code with its two versions one for neutron [21] and other for gamma radiation [22] will be discussed. In the

code, chemical effects of irradiation like radical formation and combination are not considered. Several other codes involving dynamical behavior of colliding partners, time evolution of the event, velocity and temperature dependence of potentials, etc., have also been developed [23–25]. They are highly perspective as well as attractive from the point of exhausting observable physical and chemical aspects such as evolution of event on accommodating large number of variables and parameters. Such complications normally slow down the calculations. To discuss the dynamical modeling (DM) of radiation damage, a big volume of the text will be required hence it will be skipped. In the following discussion of JA-IPU code based on binary collision approach is presented in detail, and this also includes comparison of some of the results of the dynamical models.

7.1.3.1 Binary Collision Approach (BCA)

Binary collision of two particles is treated like collision of two billiard balls without involving any complicated field in between the two particles. Particularly, a neutron collision at low energy may safely be identified as a binary collision because elastic collision cross section is much higher than inelastic cross section including the absorption cross section. At high energies, neutron wavelength is shorter up to several tens of MeV energy, intra-particle approach will dominate and it may no longer be treated as a pure binary collision because of active involvement of many individuals for the sake of outcome of a collision. A collective behavior plays certain amount of role. Thus, at low energies most of the older models [17, 26] have adopted binary collision approach (BCA), for example, TRIM [27, 28] adopts BCA and it makes use of Monte Carlo techniques to describe the trajectory of the incident particle and the damage created in amorphous solids. Similarly, MARLOWE code [29, 30] also uses BCA and the code simulates the atomic collisions in crystalline targets. Incident projectiles can be an external beam or an internal source site from where a radiation is introduced in rest of the medium. The code

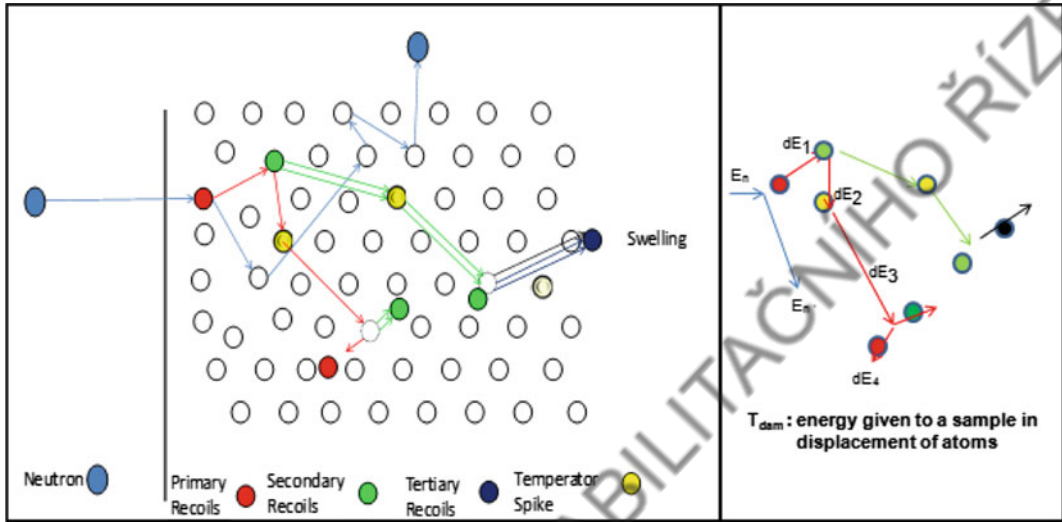


Fig. 7.5 Transport of a neutron in material and displacement of atoms. Both loss of KE and escape out are shown along with excited atom marked as spike

records tracks of a binary collision and the displaced atoms from their lattice sites until they either leave the medium or fall below the selected kinetic energy, i.e., displacement energy E_d . Calculations of damage of the medium have also been included in the code.

Development of the JA-IPU code is described at length in references [21, 22]. Accordingly, success of a code depends on procedure of random number generation and the number of generated histories of an event. Transport of a particle is assumed to be a straight line trajectory of length, l and on scattering from a target atom elastically it is diverted at polar angle, θ , and azimuthal angle, ϕ . Probability of path that a neutron for example, interacts in between the distance l and $l + \delta l$ is given by [31],

$$P(l)dl = \Sigma_T \delta l e^{-\Sigma_T l} \quad (7.15)$$

Here, Σ_T is the total macroscopic cross section which can be expressed as,

$$\Sigma_T = \Sigma_S + \Sigma_A = \Sigma_{EL} + \Sigma_{IN} + \Sigma_A \quad (7.16)$$

Here, Σ_S is scattering, Σ_A is absorption, Σ_{EL} is elastic, and Σ_{IN} is inelastic macroscopic cross sections related to the interaction. For the reason

that an interaction will be independent of the previous one, hence random, thus one can derive a relationship between random variable, R and interaction distance, l as the following,

$$l = -\frac{1}{\Sigma_T} \ln(R) \quad (7.17)$$

and the probability of interaction,

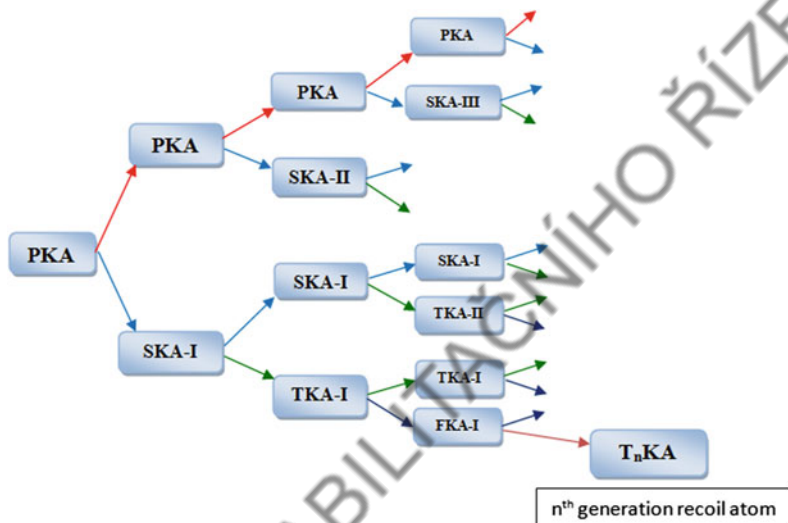
$$P(l) = 1 - e^{-\Sigma_T l} \quad (7.18)$$

After the interaction, when both the particle and recoil atom move then their new directions are decided by assigning new set of (θ, ϕ) coordinates with the help of another sets of two random numbers [31] independent to each other.

Using these simple geometrical aspects, one can assign directions to the recoils and the angular relationship between the incoming projectile and the recoiled atoms using kinetics of elastic collision.

Independent two cascading of primary projectile and the recoiled secondary atom are depicted in Fig. 7.5. The knocked-on atom by the projectile is designated as a PKA which later on generates its own cascade as shown in Fig. 7.6. The ongoing scattered projectile or the PKA may

Fig. 7.6 Atom-atom collision cascade generated by a primary knocked-on atom (PKA)



have another chance to produce next set of the atomic cascades. Thus, two kinds of cascades are generated, one due to projectile particle and other due to a PKA.

When a particle moves through a matter having either of the three, elastic, inelastic and absorption kind of interactions then they can be sorted out by applying following conditions,

- If $0 \leq R \leq \frac{\Sigma_{el}}{\Sigma_T}$, interaction is elastic.
 If $\frac{\Sigma_{el}}{\Sigma_T} \leq R \leq \frac{\Sigma_{in}}{\Sigma_T}$, interaction is inelastic.
 If $\frac{\Sigma_{in}}{\Sigma_T} \leq R \leq 1$, particle is absorbed.

In such simulation obviously, the material is supposed to be uniform density of single element. In case of composite target of more than one element, e.g., the case of SiC, selection of the target atom facing a collision is done through the sampling of random number, R , if $0 < R \leq \frac{\Sigma_{T,Si}}{\Sigma_T}$ for interaction to take place with Si atom and it will be interacting with C atom if $\frac{\Sigma_{T,C}}{\Sigma_T} < R \leq 1$. Here, $\Sigma_T = \Sigma_{T,Si} + \Sigma_{T,C}$. In this text, Monte Carlo simulation of neutron irradiation of three materials, e.g., Ni, Nb, and SiC are considered.

Monte Carlo Simulation of Neutron Irradiation

For the simulations of neutron cascade $n + A$, cross section data are taken from evaluated

ENDF/B-VII.0 library and plots for (a) $n + Ni$ (b) $n + Nb$ (c) $n + Si$ and (d) $n + C$ collisions are given in Fig. 7.7. It can be noted that at energies above the thermal energy up to a few MeV elastic collision cross sections in case of the four targets are much higher than inelastic cross sections barring a few energies around 10 eV in case of Ni and Nb. At such low energies, a target nucleus can only be excited and its recoil or explosion or evaporation will not take place being below E_d of the material. On the contrary, in case of fissile elements there will be a high possibility of nuclear fission.

Atom + Atom Collision Cross Section

When a neutron interacts with an atom, it transfers energy, T to the atom which may result in the displacement of atom from its original lattice site or it goes in excitation state. The recoiled atom is referred as PKA (Primary Knocked-on Atom). In fact, nucleus of the atom is assumed to be displaced along with its electron cloud. If the energy transferred to the atom is much more than the threshold energy E_d ($T > 2E_d$), the recoiled atom may further interact with another atom(s).

Mean free path, L of the displacement of atom is inversely proportional to the interaction cross section, $\sigma(E)$, i.e., higher the cross section, lesser is the m. f. p. length, where E is the PKA energy, for example.

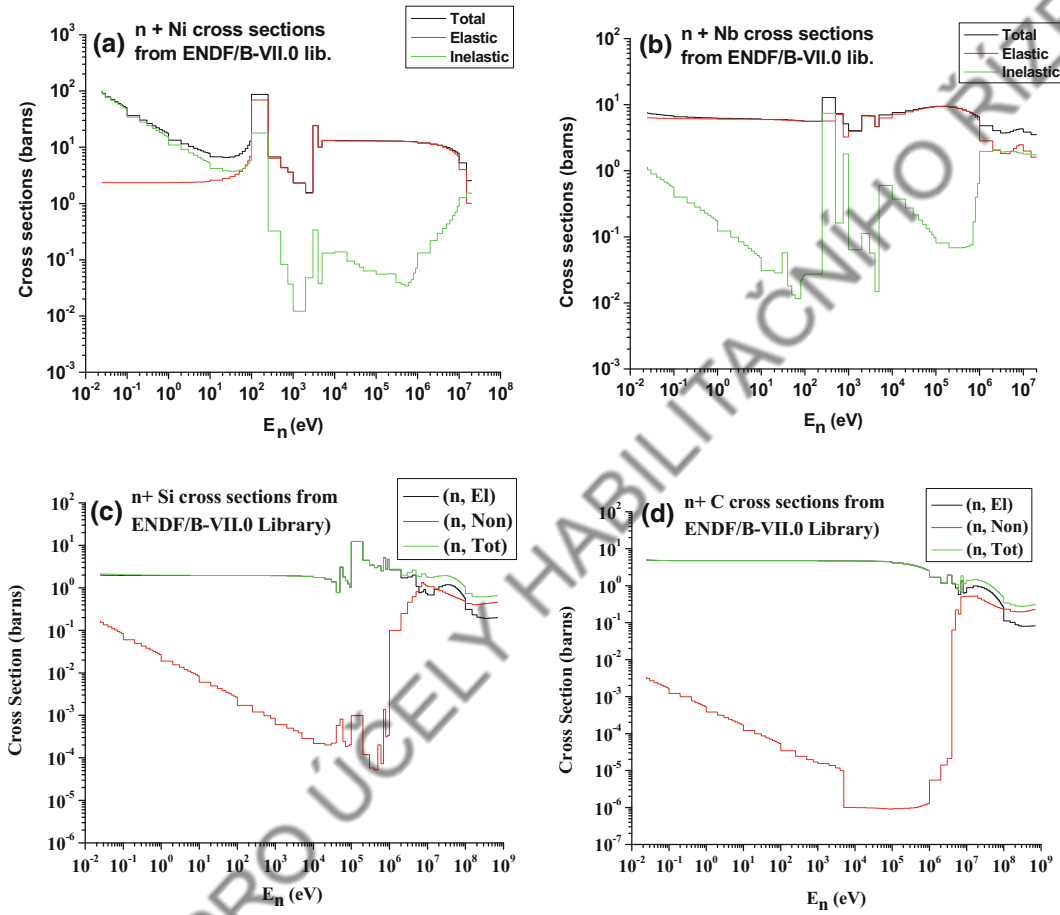


Fig. 7.7 Elastic, inelastic, and total evaluated neutron cross sections of **a** Ni, **b** Nb, **c** Si, and **d** C targets from the ENDF/B-VII.0 library

For the interaction cross section, σ_{int} at projectile energy, E to transfer energy, T to the target, the code uses the algorithm of IOTA code [32],

$$\begin{aligned}\sigma_{\text{int}}(E) &= \sum_{i=1}^N w_i \sigma_{\text{int}}^i(E) \\ &= \sum_{i=1}^N w_i \int_{E_d^i}^{T_{\text{max}}^i} d\sigma_i(E, T)\end{aligned}\quad (7.19)$$

Here,

- w_i Atomic fraction of the i th component of the target material
- E_d^i Effective threshold displacement energy of the i th component

T_{max}^i Maximal energy transferred from the incident ion to PKA

Differential cross section $d\sigma(E, T)$ is calculated as follows,

$$d\sigma_i(E, T) = \pi a^2 f(t^{1/2}) \frac{dt}{t^{3/2}} \quad (7.20)$$

where the function $f(t^{1/2})$ is calculated from the following equation,

$$f(t^{1/2}) = \lambda t^{1/2-m} [1 + (2\lambda t^{1-m})^q]^{-1/q} \quad (7.21)$$

In the JA-IPU code, values of λ , m and q parameters for $\text{IDS} = 0$ are taken from Table 1 of the IOTA manual Ref. [33]. Here, $\lambda = 1.309$, $m = 1/3$, $q = 2/3$ and

$$t = \frac{\varepsilon T}{\alpha^2 \varepsilon_0} \quad (7.23)$$

$$\varepsilon = \frac{E}{\varepsilon_0} = \frac{aA_2E}{Z_1Z_2e^2(A_1 + A_2)} \quad (7.24)$$

$$\alpha = \frac{4A_1A_2}{(A_1 + A_2)^2} \quad (7.25)$$

where Z_1 , A_1 , and Z_2 , A_2 are the atomic number and mass number of the projectile and the target material respectively. Threshold displacement energies are taken as [33]. Interaction cross sections of $^{63}\text{Ni} + ^{63}\text{Ni}$, $^{93}\text{Nb} + ^{93}\text{Nb}$, $^{12}\text{C} + ^{12}\text{C}$, $^{12}\text{C} + ^{28}\text{Si}$, $^{28}\text{Si} + ^{12}\text{C}$, and $^{28}\text{Si} + ^{28}\text{Si}$ have been calculated using the IOTA code and shown in Fig. 7.8a–f, respectively.

On irradiation when an atom is displaced from its position (in a crystal it is a lattice position) then a Frenkel pair is formed by the vacancy and the displaced atom. If displacement is small, i.e., $r_d < 0.75 \text{ \AA}$ [34], then it is assumed that there is a definite chance that the atom recombines back at the original position whenever getting suitable amount of kinetic energy. Primarily, because energy is invested in the small displacement so we count energy and call it as ‘defect’. Thus, ‘displacements’ and ‘defects’ are produced on irradiation along with the hot spikes which are the excited atoms. A frequent cascading of a particle may produce clusters and loops as well as a cluster of excited atoms called ‘spikes’.

Irradiation by Gamma

Damage of a medium by gamma rays takes place through electrons produced in Compton, photoelectric and pair production processes. Its Monte Carlo simulation is more cumbersome than by a neutron because of the additional orbital structure of atom and interaction of gamma with electron. For that purpose, in JA-IPU code, lattice structure of a material is generated. Point cross sections of the three processes are taken from the

ENDF/B-VII.0 library [35]. In the code, cross sections have been parameterized in different gamma energy regions before making use in the code for a faster computation. On interaction, the ejected electron loses energy by way of ionization, Bremsstrahlung, and finally on colliding with an atom. Elastic collision of electron with atom is considered as a billiard ball collision and collision cross sections are taken from a compilation by Mayol et al. [36]. For details, reader can refer to [22]. After an atom is displaced the atomic cascade is handled as in the case of neutron using the IOTA code. In Fig. 7.9, frequency of displacement distance of an atom from its lattice position shown as the simulated path lengths is plotted in case of a 50 keV vanadium (V) recoil colliding with vanadium in the medium. This generates cascades through the material and it can be seen that the total number of path lengths $< 0.75 \text{ \AA}$ which represent production of defects is comparable with the path lengths $> 0.75 \text{ \AA}$.

N_d Versus T_{dam} Regularity

Damage energy is defined as the energy that is invested in changing the pristine structure of the material. When an atom displaced from its original position getting energy more than E_d then it moves in the medium and loses its kinetic energy by ionization as well as displacing another atom of the medium. This can be a ‘displacement’ or a ‘defect’. It is also possible that the particle escapes out of the medium with certain nonzero energy, E_{esc} . Thus, $T_{\text{dam}} = \text{KE} - E_{\text{ioni}} - E_{\text{esc}}$. In case atom gets much larger energy than E_d , then it may further produce next generations of cascades. In Fig. 7.10, results of MC simulation of N_d and T_{dam} are plotted for the Ni and Nb materials for the spallation neutron spectra produced by a 660 MeV proton colliding with a thick Pb target [37]. The two quantities N_d and T_{dam} (eV) are calculated for each neutron per incident proton, (n/p). Similar plots have been worked out in the case of SiC irradiated by neutron spectra of AmBe and spallation neutrons [38] separately. In all cases of different materials, e.g., Nb, Ni, and SiC there is a linear behavior.

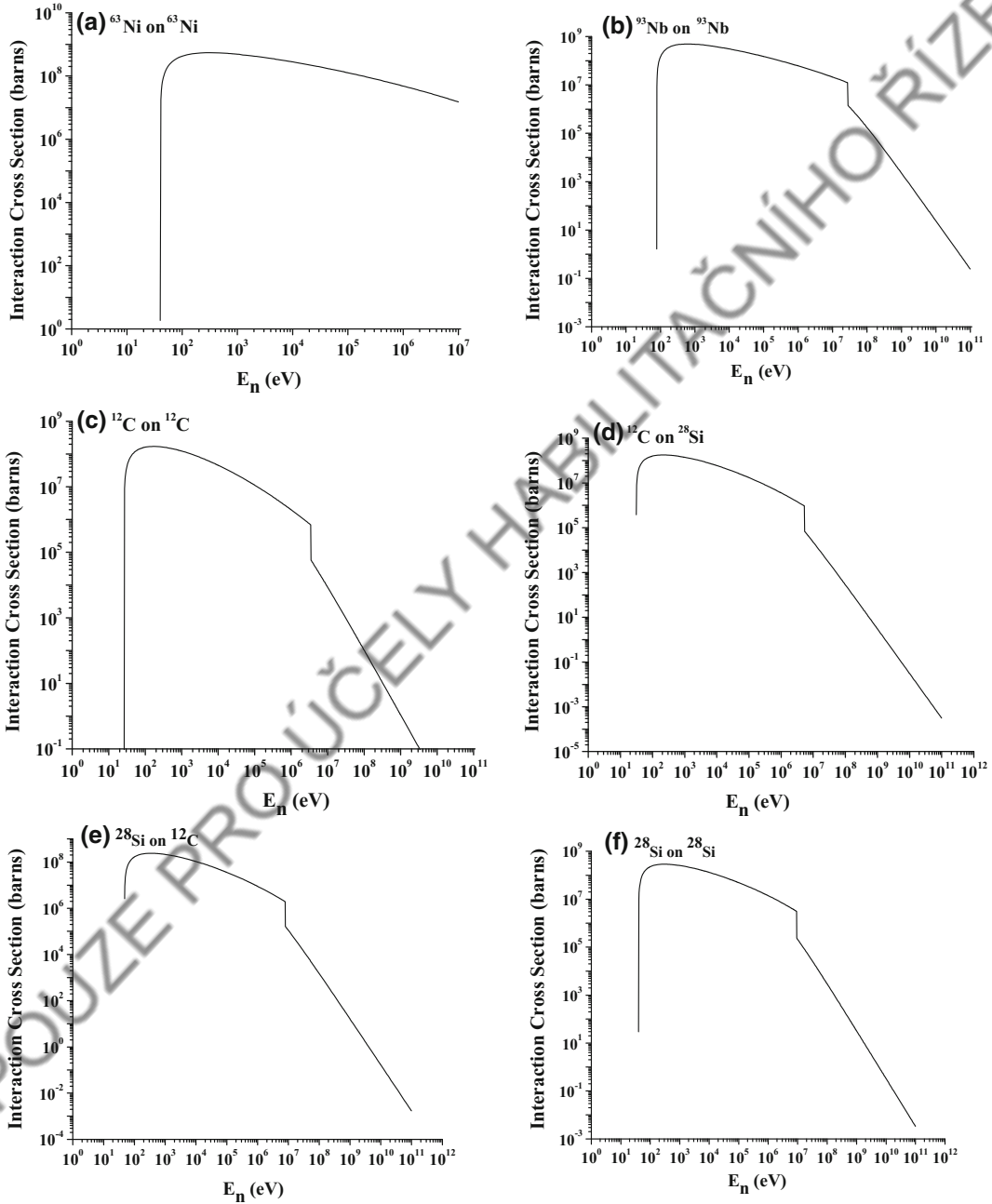
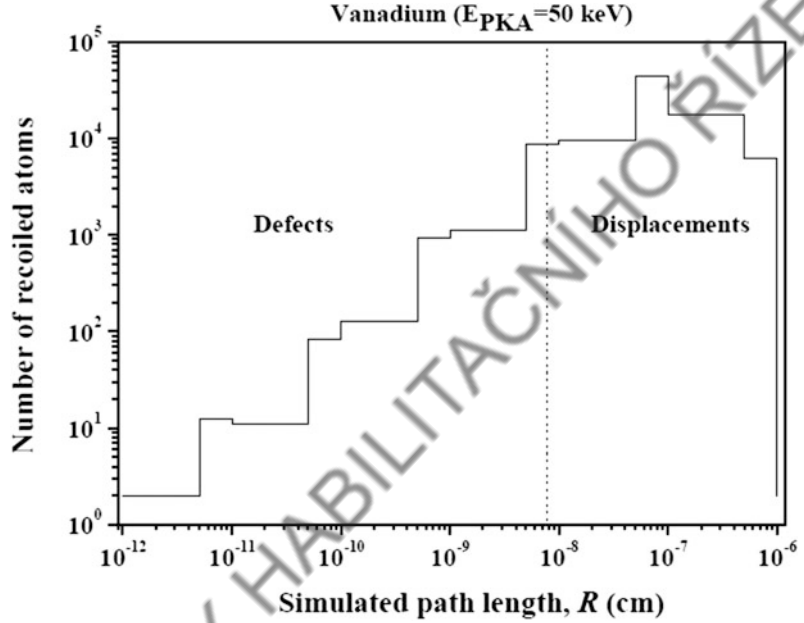


Fig. 7.8 Interaction cross sections of **a** $^{63}\text{Ni} + ^{63}\text{Ni}$, **b** $^{93}\text{Nb} + ^{93}\text{Nb}$, **c** $^{12}\text{C} + ^{12}\text{C}$, **d** $^{12}\text{C} + ^{28}\text{Si}$, **e** $^{28}\text{Si} + ^{12}\text{C}$, and **f** $^{28}\text{Si} + ^{28}\text{Si}$ calculated by the JA-IPU code

Fig. 7.9 Number of defects and displacements in transport of 50 keV vanadium ion through the vanadium medium



Similar linear behavior between N_d and T_{dam} is seen in case of incident beam of gamma on the Fe sample shown in Fig. 7.11 [38].

7.1.4 A Phenomenological Approach of Radiation Damage

Monte Carlo simulations of a large number of materials performed for irradiation by different neutron spectra and gamma, a common linear behavior between N_d and T_{dam} is noticed as shown in Figs. 7.10 and 7.11. In Table 7.1, values of slope k (eV^{-1}) are calculated from the basic plots given in the two figures between N_d and T_{dam} measured in units of eV/n in case of AmBe n -source and $\text{eV}/n/p$ in case of spallation neutrons.

In case of pure iron irradiated by gamma spectrum of Co^{60} source [39] value of slope, $k = 0.0234 \pm 0.0004 \text{ eV}^{-1}$ for the absorbed doses varying between 0.003 and 0.319 Gy. In irradiation of iron by the Co^{60} gamma spectrum, production of single displacements [39] has been observed which may not be possible in irradiation by neutron and heavy ion beams.

A phenomenological approach is developed by Kumar et al. [39] to correlate the displaced atoms of the irradiated material with the physical observables followed from the said regularity between N_d and T_{dam} ,

$$dN_d \propto dT_{\text{dam}} \quad (7.26)$$

$$dN_d = k dT_{\text{dam}}$$

with k being the proportionality constant and it is spectrum dependent. Defining damage volume, $V = (N_d/n_d)$ and $n_d = f(V, T_{\text{dam}})$,

It leads to [39] the following relation between change in N_d and change in volume, $\left(\frac{dV}{V}\right)$ arising due to dT_{dam} ,

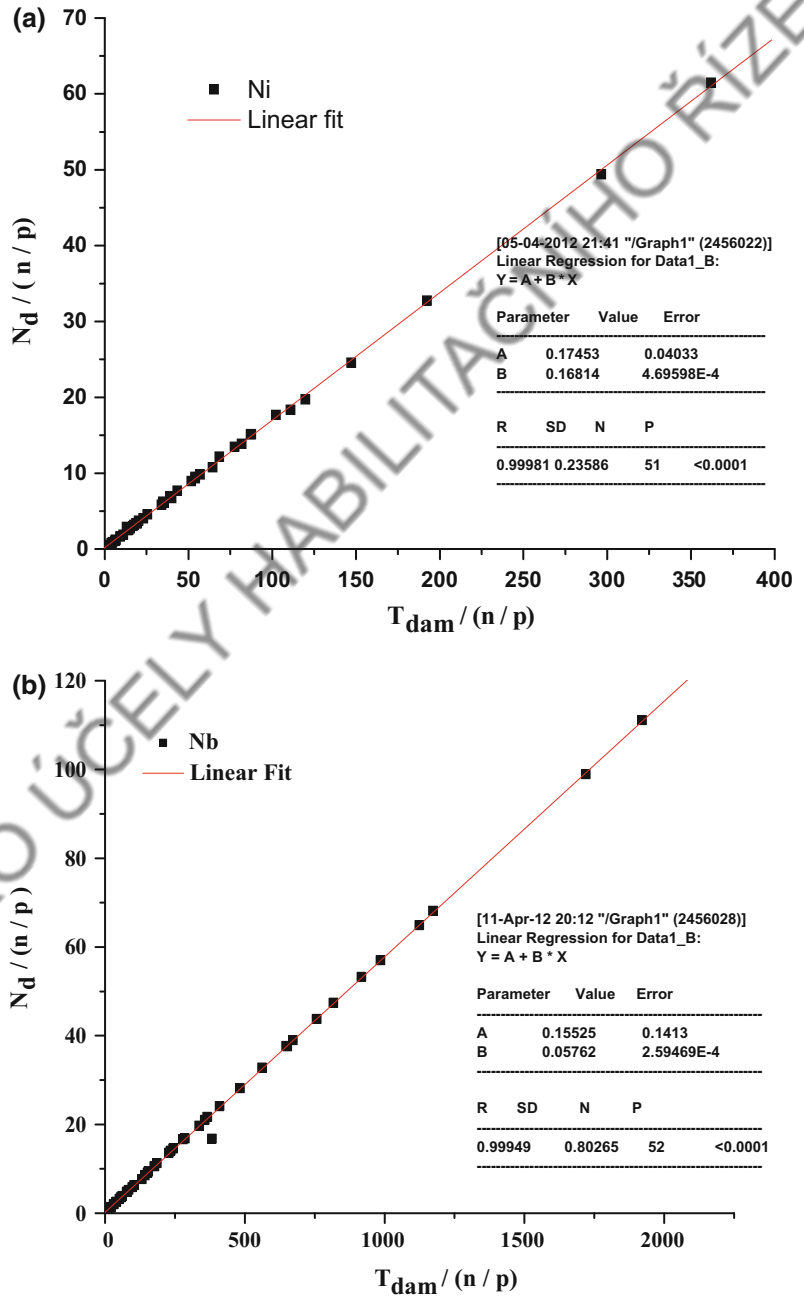
$$dN_d = \left(\frac{k}{V}\right) dT_{\text{dam}} - n_d \left(\frac{dV}{V}\right) \quad (7.27)$$

Following Brinkman [40],

$$\frac{\rho - \rho_0}{\rho_D - \rho_0} = \frac{dV}{V} \quad (7.28)$$

ρ_0 and ρ_D correspond to the resistivity of pristine and highly disordered state of a sample,

Fig. 7.10 MC simulation results of N_d (n/p) versus T_{dam} ($eV/n/p$) plotted for spallation neutron spectrum in case of (a) Ni and (b) Nb samples [37]



respectively. In the situation of non-availability of data of resistivity, ρ_D we assume that $\rho_D = x\rho_0$. Here, parameter $x > 0$ corresponds to a disordered state of irradiated material compared to pristine and it is also spectrum dependent

because different particle spectra may reach to a different disorder. For example, $dV = 0$ for no change in volume and this leads to $\rho = \rho_0$. Also, $dV = V$ corresponds to $\rho = \rho_D$ in case of relation (7.28). In that sense, much higher value of x than

Fig. 7.11 N_d (ph) versus T_{dam} (MeV/ph) plot for pure iron sample irradiated with different doses of Co^{60} beam [39]

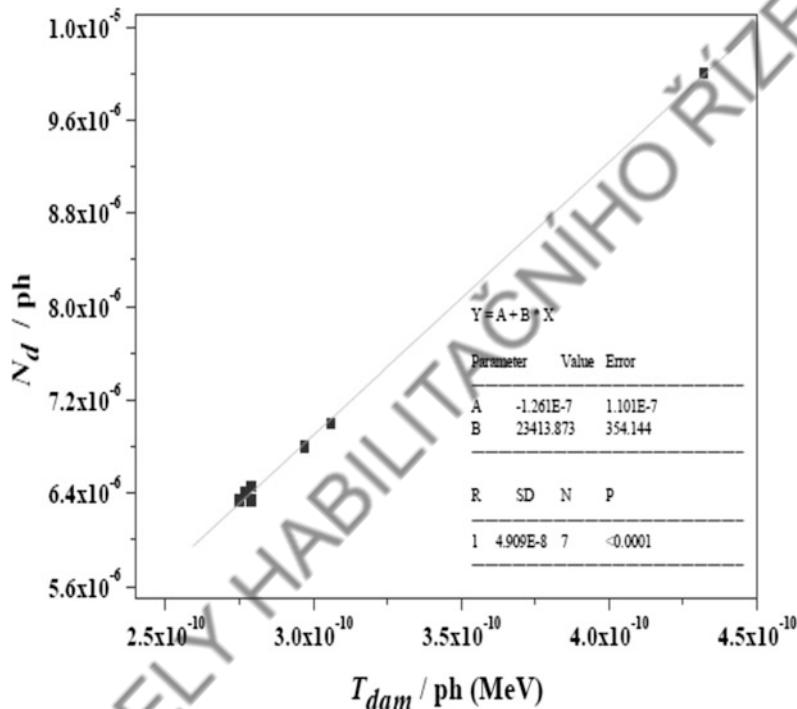


Table 7.1 Sizes of SiC, Nb, and Ni samples and slope, 'k' (eV^{-1}) deduced from the N_d and T_{dam} plots from the data of MC simulations

	Dimensions of the samples	Slope 'k' of T_{dam} versus N_d plot	
		AmBe n -spectrum	Spallation n -spectrum
SiC	$1 \times 1 \times 0.0314 \text{ cm}^3$	0.00062 ± 0.00003	0.05992 ± 0.00066
Nb	$2.4 \times 0.8 \times 0.024 \text{ cm}^3$	0.00138 ± 0.00001	0.05762 ± 0.00026
Ni	$2.5 \times 1.5 \times 0.002 \text{ cm}^3$	0.875	0.16814 ± 0.00045

zero may lead to more interesting results. Thus, relation (7.28) can be written as,

$$\frac{d\rho}{(x\rho_0 - \rho_0)} = \frac{dV}{V} \quad (7.29)$$

which leads to

$$d\rho = \rho_0(x-1) \left(\frac{k}{N_d} \right) dT_{dam} \quad (7.30)$$

where both 'k' and 'x' are spectrum dependent. It may be mentioned that small deformations lead to reduction of free volume between the atoms.

Taking $k = \frac{dN_d}{dT_{dam}}$, relation (7.30) can be written as,

$$(\rho - \rho_0) = \rho_0(x-1) \ln N_d \quad (7.31)$$

The relation (7.31) is applicable for irradiations where single displacements take place, for example, in case of incident gamma spectra, and it has been established using the positron annihilation spectroscopy [41]. Also, it shows rise of resistivity on increase of displaced atoms. The parameter x has prospects in designing of devices by ion beam irradiation.

7.1.5 Dynamic Model Approach and JA-IPU

As mentioned earlier, dynamic modeling of radiation damage is a much-involved process than simpler BCA approach. This has however capability of handling the natural processes, for example, dynamics of proteins and DNA on a timescale ranging from 10^{-9} to 10^{-6} s. To make statistically valid conclusions from the simulations, simulated time period should match the kinetics of the natural process. This is done through fine-tuning of speed of calculation and natural timings of a process. In real sense, it is ‘a state-of-the-art’ technique because of involvement of large number of variables and by bringing computation close to the speed of happening of an event. The technique is useful at level of small atomic energies. Using a dynamical model, (DM) events at the atomic scale say up to 10^{-11} s can be successfully simulated but not at lower timescales like femtosecond (10^{-15} s). Transmutation of the inner wall of the fusion reactor leads to fast degradation of the wall material at the timescale of dynamical modeling. Kinetic Monte Carlo (KMC) is a more effective technique, which simulates events

randomly with probabilities according to the corresponding event rates [42]. It provides [43] self-estimate of the time step as the simulation proceeds and is the most powerful approach available for making a dynamical prediction of mesoscale events. In case of radiation damage of a static medium, the two approaches are ineffective because of no consideration of movements of orbital electrons and vibrational and collective modes of oscillation of an atom.

Alonso et al. [25] have calculated the results by coupling DM with Kinetic Monte Carlo (KMC) simulations of damage production efficiency, η of a code in case of 20 keV vanadium as PKA traversing the vanadium medium. Damage production efficiency is defined as,

$$\eta = N_d/N'_{\text{NRT}} \quad (7.32)$$

$$\text{with } N_{\text{NRT}} = 0.8E_{\text{PKA}}/(2E_d) \quad (7.33)$$

Using the JA-IPU code damage production efficiency, η is calculated [44] for different energy of PKAs as shown in Fig. 7.12 considering electronic energy loss (EEL) and without considering EEL. It can be noted that DM approach gives $\eta \sim 26\%$ comparable with $\sim 28\%$ from the JA-IPU code.

Fig. 7.12 Damage production efficiency plotted for different energy PKAs for vanadium [44]

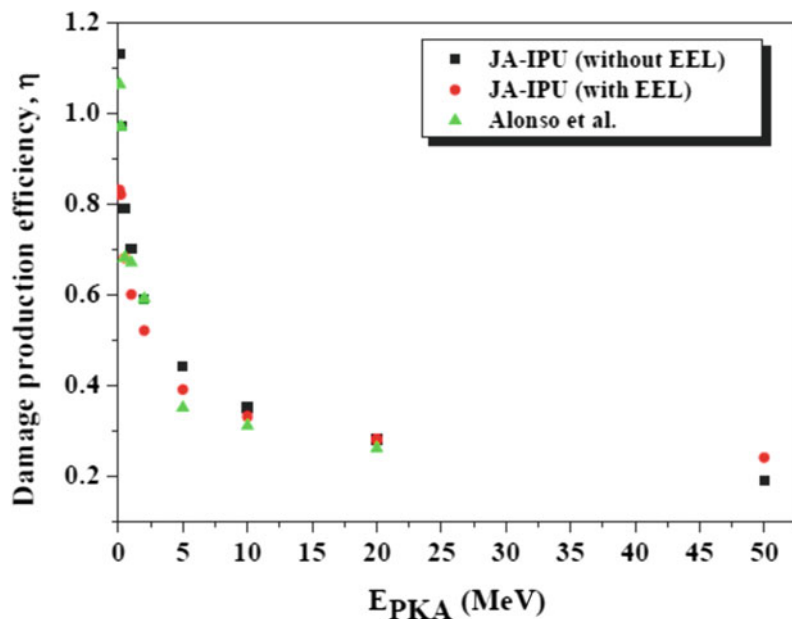


Fig. 7.13 DPA/year plotted with respect to E_{PKA} for the irradiation by the spallation neutron spectra [37]

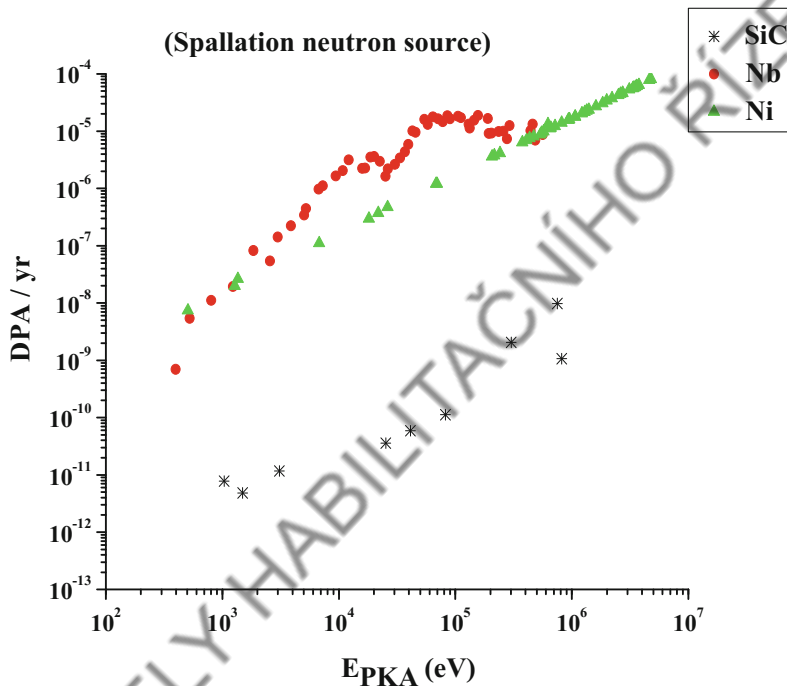


Table 7.2 Enhanced values of resistivity ($\rho - \rho_0$) and $\langle \sigma T_{dam} \rangle$ b keV values for SiC and Nb samples [45]

Sample	ρ_0 (Ω cm)	ρ (Ω cm)	$\rho - \rho_0$ (Ω cm)	$\langle \sigma T_{dam} \rangle$ (b keV)
SiC (spall)	2.45E-4	2.98E-4	0.53E-4	3.33E+10
Nb (AmBe)	4.40E-6	1.491E-4	1.447E-4	6.33E+12
Nb (spall)	4.40E-6	2.664E-4	2.62E-4	2.44E+15

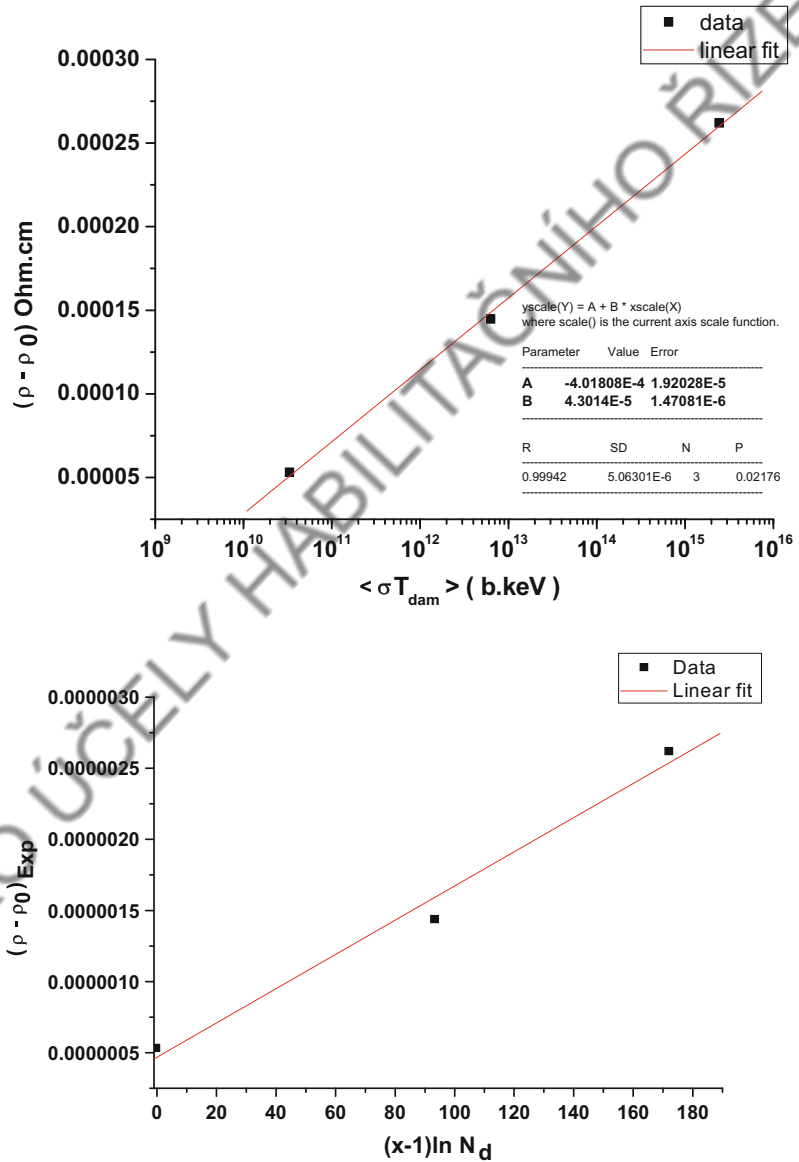
As noticed, the phenomenological approach developed as above opens ways for searching of suitable variables for answering the questions raised on the DPA and similar other quantities used to monitor the radiation damage. On calculating DPA using number of displaced atoms including defects, N_d from the JA-IPU code, and the E_{PKA} of an irradiation by the spallation neutron spectra in Fig. 7.13, DPA/year is plotted with E_{PKA} and it can be seen that the three materials, Ni, Nb, and SiC follow different variations. In case of the three materials average, DPA/year is $8.62E+1$ for Ni, $2.828E-2$ for Nb, and $6.75E-6$ in case of SiC, respectively. In case of a softer AmBe neutron spectrum, DPA/year is $1.521E-7$ and $1.03E-7$ for Ni and Nb, respectively, showing spectrum dependence of DPA/year.

In Table 7.2, data of change of resistivity ($\rho - \rho_0$) and ‘average damage energy cross

section’ $\langle \sigma T_{dam} \rangle$ is given for the SiC and Nb for the spallation neutron spectra additionally for Nb for the AmBe neutron spectra also. In Fig. 7.14 (a), $(\rho - \rho_0)$ versus $\langle \sigma T_{dam} \rangle$ plot is shown and it is qualitatively compared with $(\rho - \rho_0)$ versus $(x - 1) \ln N_d$ plot of Fig. 7.14b. Data of resistivity ρ is experimentally measured and given in the two plots and presented in Table 7.2. Values of N_d as well as $\langle \sigma T_{dam} \rangle$ are taken from the MC simulations using the JA-IPU code.

From the plots of Fig. 7.14, it may be inferred that the quantity like $\langle \sigma T_{dam} \rangle$ may be treated unique from the point of both target and different neutron spectra and it can probably replace earlier used quantity like DPA. More experiments may be planned with high energy gamma, ion beams to produce data of $\langle \sigma T_{dam} \rangle$ and measurable physical quantity like change in resistivity to validate the aforesaid observation.

Fig. 7.14 (U_p) $(\rho - \rho_0)$ versus $\langle \sigma T_{\text{dam}} \rangle$ plot and (below) $(\rho - \rho_0)$ versus $(x - 1) \ln N_d$ plot for the two spallation and AmBe neutron spectra as already discussed [37, 38]



In a study of radiation damage of HFIR, high rate of embrittlement of steel of high-pressure reactor by high energy flux of both gamma and neutrons was noticed [8, 46] and it was stressed that there is need of MC study of damage by gamma radiation because it can be understood that the neutron flux will be highly moderated at 30 cm passage than the gamma in the reactor. Using the JA-IPU code, radiation damage by gamma was estimated [47] and found it to be comparable with the observed results.

7.1.6 Radiation Resistant Materials

Emphasis is being laid on research and development of the radiation resistant materials (RR) both for the fuel cells, structure materials, shielding materials of gen. IV reactors including ADSS and fusion reactors. Heating and diffusion of radioactive material in cassettes and canisters used in reposition of the HLW is another serious concern and it demands development of RR materials with attention on the said problems. In case of

reposition, Ewing et al. [48, 49] have suggested that planning of development of the radiation resistant material needs to incorporate understanding of ion-matter interactions from the point of immobilization of high-level radioactive materials. Ceramics materials such as pyrochlore $A_2B_2O_7$, zirconolite $CaZrTi_2O_7$, zircon $ZrSiO_4$, monazite (La, Ce, Nd) PO_4 , and other complex oxides having high waste loading capacity, better thermal, mechanical, natural analogous and desired chemical properties are proposed as potential materials for the immobilization of high-level nuclear waste and waste form of ADSS. Among these ceramic materials, pyrochlore structure shows properties of inert fuel matrix for the radionuclides. In addition, some of the pyrochlores also have potential to be used as burnable neutron poisons in a nuclear reactor. In particular, isometric pyrochlores with the $A_2B_2O_7$ stoichiometry display capability to incorporate actinides (e.g., U, Np, Th, Pu, Am, and Cm) at the A-site, particularly Pu [50]. Compounds with strong ionic characteristics, such as zirconate ($A_2Zr_2O_7$), are generally considered to be more radiation resistant than covalent stannate ($A_2Sn_2O_7$). The in-situ TEM studies during ion irradiation showed that critical dose required for the amorphization of the $Gd_2Ti_2O_7$ is about 0.143 DPA [51]. The same group had also reported amorphization of the zirconate pyrochlore to be ~ 5.5 DPA at 300 °K, which is normally considered as radiation resistant. On annealing, recovery rate for radiation-induced defects in fully amorphized structure ($La_2Ti_2O_7$) is found to be higher than amorphous structure ($Gd_2Ti_2O_7$) due to critical role played by the topology of the amorphous materials [52]. This puts La-based composite in better condition than Gd composites. Also, it may be added that the ratio, $\sigma_{el}/\sigma_{inel}$ for neutrons with energy $E > 1$ MeV is several hundred times higher in case of La than Gd. This is because of lesser absorption cross section of neutrons in La than Gd.

Kulriya et al. [53] have investigated temperature-dependent structural stability of the bulk pyrochlore under swift heavy ion irradiation and observed improvement in the radiation resistant behavior on high temperatures. Also, stability of the bulk pyrochlore structure (space

group Fd-3 m) under ion bombardment has been shown to be governed by the ratio of the ionic radii of A and B cations (r_A/r_B). The materials like $La_2Zr_2O_7$ may further be explored for utilization as structure materials for the reposition and as a layer inside fuel cells.

Other materials that are proposed are SiC and ZrC and PyC in the form of layers in a fuel cell. Radiation resistant behavior of SiC in the spallation neutron spectrum has been found superior when compared with other metals like Ni and Nb. In Sect. 6.4, applications of several other RR materials like Zr_3Si_2 and SiC under the TRIGA setup by the General Atomics has already been discussed.

References

1. Development of Radiation Resistant Reactor Core Structural Materials. https://www.iaea.org/About/Policy/GC/GC51/GC51InfDocuments/English/gc51inf-3-att7_en.pdf
2. Inozemtsev, V., Zeman, A., Scandolo, S.: Development of Radiation Resistant Materials, pp. 20–24, ICTP (April, 2009). <http://indico.ictp.it/event/a08149/material/0/0.pdf>
3. TM-F1-34567.: Accelerator Simulations and Theoretical Modeling of Radiation Effects Report of the Technical Meeting (IAEA) Hosted by NSC-KIPT, Kharakov, pp. 9–13 (June, 2008). <http://www-naweb.iaea.org/naweb/physics/meetings/TM34567/login2.html>
4. TM-36842.: Physics of Materials Under Neutron and Charged Particle Irradiations, Report of the Technical Meeting Held in Vienna, pp. 16–19, Vienna (November, 2009)
5. Li, M.: Moving from Dpa to Changes in Materials Properties, Talk Delivered at Radiation Effects in Superconducting Magnet Materials (RESMM12), Fermilab, USA 14 Feb 2012. Also see, Frank Garner: Material Science and Technology. <https://doi.org/10.1002/9783527603978.mst0110>
6. Porollo, S.I.: Influence of silicon on swelling and microstructure in Russian austenitic stainless steel EI-847 irradiated to high neutron doses. J. Nucl. Mater. **378**(1), 17 (2008). http://www-pub.iaea.org/MTCD/Publications/PDF/Pub1548_web.pdf
7. Ryazanov, A.: Comparative physical behaviour of SiC materials under neutron and charged particle irradiations. In: Presented at IAEA Technical Meeting Entitled Physics of Materials Under Neutron and Charged Particle Irradiations, IAEA Head Quarters (November, 2009)
8. Alexander, D.E., Rehn, L.E.: Gamma-ray displacement damage in the pressure vessel of the advanced

- boiling water reactor. *J. Nucl. Mat.* **217**(1994), 213. Also: [http://dx.doi.org/10.1016/0022-3115\(94\)90325-5](http://dx.doi.org/10.1016/0022-3115(94)90325-5)
9. Cheverton, R.D., Merkle, J.G., Nanstad, R.K.: Oak Ridge National Laboratory Report, ORNL TM-10444 (1988)
 10. Cuba, V., Mucka, V., Pospisil, M.: Radiation Induced Corrosion of Nuclear Fuel and Materials. Available from: <http://cdn.intechweb.org/pdfs/28495.pdf> (Mansur, L.K., Farrell, K.: *J. Nucl. Mat.*, **170**, 236 (1990). [http://dx.doi.org/10.1016/0022-3115\(90\)90294-W](http://dx.doi.org/10.1016/0022-3115(90)90294-W))
 11. Kisilitsin, S.: Investigation of Shape Changes of Hexagonal Ducts of Spent Fuel Assemblies from the BN-350 Fast Neutron Nuclear Reactor TM-36842, Vienna, 16–19 Nov 2009. Reproduced by the International Atomic Energy Agency
 12. Wallenius, J.: Radiation Damage & GAS Production in Metals, Materials for Gen IV Nuclear Reactors, MATGEN-IV.2 from Iron to Steel. The Ice Hotel, Jukkasrvi, Sweden, 2–7 Feb 2009
 13. Chung, H.M., Loomis, B.A., Smith, D.L.: Development and testing of vanadium alloys for fusion applications. *J. Nucl. Mat.* **239**, 139 (1996)
 14. Dienes, G.J., Vineyard, G.H.: *Radiation Effects in Solids*. Interscience, New York (1957)
 15. Kinchin, G.H., Pease, R.S.: The displacement of atoms in solids by radiation. *Rep. Progr. Phys.* **18**, 1 (1955)
 16. Nelson, R.S.: AERE Report, R-6092 (1969)
 17. Robinson, M.T., Torrens, I.M.: Computer simulation of atomic-displacement cascades in solids in the binary-collision approximation. *Phys. Rev. B* **9**, 5008 (1974)
 18. Norgett, M.J., Robinson, M.T., Torrens, I.M.: A proposed method of calculating displacement dose rates. *Nucl. Eng. Des.* **33**, 50 (1975)
 19. Lindhard, J., et al.: Integral equations governing radiation effects. *Kgl. Dansk, Vid. Selsk, Mat. Fys. Medd.* **33**, 10 (1963), also, gymarkiv.sdu.dk/MFM/kdvs/mfm%2030-39/mfm-33-10.pdf
 20. Gopalakrishnan, V.: Nuclear Data Section, IGCAR, Kalpakkam, India, RPD/NDS/96 (2001)
 21. Kumar, V., Raghaw, N.S., Palsania, H.S.: A Monte Carlo Code for Radiation Damage by Neutrons. *Nucl. Sci. Eng.* **172**, 151 (2012)
 22. Tundwal, A., Kumar, V., Raghaw, N.S.: Monte Carlo Simulation of Radiation Damage by Gamma Rays, p. 749. *IEEE Xplore* (2014). <https://doi.org/10.1109/epe.2014.6839457> [and for details, Ambika Tundwal: Ph.D. thesis entitled: A Monte Carlo Code for Radiation Damage of Reactor Fuel cells, Steel and Polyethylene by High Energy Gamma and Electrons, April (2016), GGSIP University, New Delhi (India)]
 23. Phythian, W.J.: A comparison of displacement cascades in copper and iron by molecular dynamics and its application to microstructural evolution. *J. Nucl. Mat.* **223**(3), 245 (1995). [https://doi.org/10.1016/0022-3115\(95\)00022-4](https://doi.org/10.1016/0022-3115(95)00022-4)
 24. Stoller, R.F.: Point defect survival and clustering fractions obtained from molecular dynamics simulations of high energy cascades, *J. Nucl. Mater.* **1996**, 233–237, 999 (1996). [http://dx.doi.org/10.1016/S0022-3115\(96\)00261-9](http://dx.doi.org/10.1016/S0022-3115(96)00261-9)
 25. Alonso, E., Catrula, M.J., Diaz De La Rubia, T., Perlado, J.M.: Simulation of damage production and accumulation in vanadium. *J. Nucl. Mat.* **276**, 221 (2000). Accessed <http://dx.doi.org/>, [https://doi.org/10.1016/s0022-3115\(99\)00181-6](https://doi.org/10.1016/s0022-3115(99)00181-6)
 26. Robinson, M.T.: The binary collision approximation: Background and introduction. In: *Proceedings of the International Conference on Computer Simulations of Radiation Effects in Solid*, Hahn-Meitner Institute Berlin, Berlin, Germany, 23–28 Aug (1992)
 27. Ziegler, J.F., Biersack, J.P., Littmark, U.: *The Stopping and Range of Ions in Solids. The Stopping and Ranges of Ions in Matter*, Vol. 1. Pergamon Press, New York (1985)
 28. Ziegler, J.F., Biersack, J.P.: Updated Version of a Computer Code for Calculating Stopping and Ranges. *The Stopping and Ranges of Ions in Matter*, Vol. 1. Pergamon Press, New York (1985)
 29. Robinson, M.T.: Slowing-down time of energetic atoms in solids. *Phys. Rev. B* **40**, 10717 (1989)
 30. MARLOWE (Version 13): Available from the Radiation Shielding Information Center, Oak Ridge National Laboratory, Post Office Box 2008, Oak Ridge, Tennessee 37831-6362, U.S.A.
 31. Srinivasan, P.: Monte Carlo Simulation of Neutron Phenomena, Applications of Monte Carlo Methods in Nuclear Science and Engineering. ISBN: 978-81-8372-047-2 (April, 2009)
 32. Broeders, C.H.M., Yu, A., K. Konobeyev, Voukelatou, K.: IOTA—A Code to Study Ion Transport and Radiation Damage in Composite Materials. Forschungszentrum Karlsruhe GmbH, FZKA 6984, Karlsruhe, Germany, ISSN: 0947-8620 (2004)
 33. ASTM E521-96.: Standard Practice for Neutron Radiation Damage Simulation by Charged Particle Radiation, Annual Book of ASTM Standard, vol. 12.02. American Society of Testing and Material, Wes Conshohocken, PA (2009)
 34. Zarkadoula, E.: The nature of high-energy radiation damage in iron. *J. Phys. Condens. Matter.* **25**, 125402 (2013)
 35. International Atomic Energy Agency. Evaluated Nuclear Data File-ENDF B VII.0. <https://www-nds.iaea.org/public/download-endf/>. Accessed 18 Jan 2009
 36. Mayol, R., Salvat, F.: Atomic Data and Nuclear Data Tables, pp. 55–154 (1997). <http://dx.doi.org/10.1006/adnd.1997.0734> (Article No. DT970734, 65 1)
 37. Raghaw, N.S., et al.: A monte carlo simulation of radiation damage of SiC and Nb using JA-IPU code. *J. Energy Power Eng.* **9**, 967 (2015)
 38. Kumar, V., Raghaw, N.S., Tundwal, A., Korovin, Y., Adam, J.: A Study of Radiation Resistant Material using JA-IPU Code of Radiation Damage: A Talk Presented at the Annual Scientific session

- NRNU-MEPH-2015 held at INPE, Obninsk from 1–4 Feb 2015
39. Tundwal, A., Kumar, V., Datta, A.: Gamma radiation induced resistivity changes in iron. *Ind. J. Phys.* **91**, 293 (2017)
 40. Brinkman, J.A.: Production of atomic displacements by high energy particles. *Am. J. Phys.* **24**(4), 246 (1956). <http://dx.doi.org/10.1119/1.1934201>
 41. Kumar, V., Tundwal, A., Vijay, Y.K., Palsania, H.S.: Investigation of defect production in iron on gamma irradiation using the doppler broadening technique. *Ind. J. Pure App. Phys.* **54**, 51 (2016)
 42. Was, G.S.: *Fundamental of Radiation Material Science: Metal and Alloys*. Springer, Berlin, Heidelberg, New York. ISBN 978-3-540-49471-3 (2007)
 43. Voter, A.F.: Introduction to the Kinetic Monte Carlo Method. In: *Radiation Effects in Solids*. Springer (2005). Also see indico.ictp.it/event/a09140/session/28/contribution/19/material/0/0.pdf
 44. Tundwal, A., Kumar, V., Raghaw, N.S., Datta, A.: Monte carlo simulation of radiation damage produced in iron and vanadium by primary knock on atom 'PKA'. *Radiat. Eff. Defects Solids* **171**(7–8), 658 (2016)
 45. Raghaw, N.S.: Ph.D. Thesis Entitled: A Study of Radiation Damage of Materials Irradiated by High Energy Neutron and Charged Particles—A Simulation and Validation, (June 2016), University of Rajasthan, Jaipur, India
 46. Alexander, D.E., Rehn, L.E.: The contribution of high energy gamma rays to displacement damage in LWR pressure vessels. *J. Nucl. Mat.* **209**, 212 (1994)
 47. Tundwal, A., Kumar, V.: Estimation of radiation damage of iron by a reactor gamma spectrum. *Kerntechnik* **80**(5) (2015)
 48. Ewing, R.C., et al.: Nuclear waste form for the immobilization of plutonium and "Minor" actinides. *J. Appl. Phys.* **95**, 5949 (2004)
 49. Burns, P.C., et al.: Nuclear fuel in a reactor accident. *Science* **335**, 1184 (2012) and Ewing R.C. Long-term storage of spent nuclear fuel. *Nature Materials* **14**, 252 (2015)
 50. Lian, J., et al.: Radiation-induced effects in pyrochlores and nanoscale materials engineering. *Nucl. Instr. Methods Phys. Res. B* **250**, 128 (2006)
 51. Lian, J., et al.: Ion-beam implantation and cross-sectional TEM characterization of Gd₂Ti₂O₇ pyrochlore. *Nucl. Instr Methods Phys. Res B* **242**, 448 (2006)
 52. Park, S., et al.: Response of Gd₂Ti₂O₇ and La₂Ti₂O₇ to swift ion irradiation and annealing. *Acta Mater.* **93**, 1 (2015)
 53. Kulriya, P.K., et al.: In-situ high temperature irradiation setup for temperature dependent structural studies of materials under swift heavy ion irradiation. *Nucl. Instr. Methods in Phys. Res. B* **342**, 98 (2015)

Neutronic, Kinetic, and Thermal-Hydraulic Calculation of Accelerator Driven Target-blanket; Cross-section Libraries Testing

K. Katovsky, D. Kobyłka, J. Krepel

*Czech Technical University in Prague, Faculty of Nuclear Science and Physical Engineering,
Department of Nuclear Reactors*

V Holesovickach 2,180 00 Praha 8, Czech Republic, kjr@troja.fjfi.cvut.cz

Abstract

Calculation and computer modelling is very important for the search and evaluation of physical characteristics of every new reactor concept, such as accelerator driven system. Some neutronic calculation of ADS model blanket based on fluoride salts of actinides and fission products was performed (neutron flux parameters, multiplication factor dependencies etc.). Thermal-hydraulic analyses of the ADS reactor core with fluid fuel, and kinetic calculation of subcritical reactor with external neutron source and fluid fuel (which is one of the issues coupled with accelerator driven systems important for safety studies) was also proceeded. Nuclear data and various cross-section libraries influence to multiplication factor of ADS model blanket was separately studied.

Neutronic calculation was computed by general monte carlo transport code MCNP. To study nuclear data influence is necessary to convert libraries from ENDF format to ACE format for MCNP, code NJOY was used to do that. Main world-widely used cross-section libraries were tested, such as ENDF/B, JEF, JENDL, BROND, CENDL and also available high energy libraries. Effects of various code versions (MCNP and NJOY) were studied too.

For kinetics study of an ADS blanket with external neutron source and with fluid fuel based on fluorine salts were used point-kinetics equations modified by leakage of delay neutron precursor. For numerical solution of this equations was created code Bokin 2000 which was next applied to several selected transients of subcritical reactor system. From preliminary calculations can be seen that using molten fluoride salts acting as fuel and coolant simultaneously can cause a new type of transient effect during the fuel pump failure. The slowdown of the fuel flow decreases the leakage of delayed neutrons and thus β increases. However, the response of the system is mostly determined by the value of thermal feedback coefficient.

Preliminary calculations of a radial power density distribution in different modifications of blanket have been done up today. To calculate a solution to the Navier-Stokes equations for liquids, with volume changes as functions of the temperature and movable heat sources, modern computer techniques and fitting simulation codes, which are based on suitable numerical methods are needed. They are called the CFD computer programmes and two of them were used: PHOENICS 3.2.0 based on the finite volume method, and a module FlowPlus for the programme package COSMOS 2.5, which is based on the finite element method.

Introduction:

Department of Nuclear Reactors FNSPE CTU Prague deals with experimental works on training reactor VR-1 Sparrow which relate to ADS research, teaching students, testing materials and characteristics of these various systems etc. ([12], [13]). In order to have success with this experiments and well interpret theirs results, it is very important make amount of theoretical and

computation work. This poster shows an example of this research work made on DNR. Except neutron-physic, thermal-hydraulic, kinetic calculation there are also provided many other kind of computation and theoretical analysis. Modern computation codes are kept at one's disposal and some others are produced.

I. Nuclear data libraries influence on neutronic calculation of ADS blanket

During any new calculation of new reactor concept there are many factors, which can influence the results. One of them is various nuclear data, especially cross section libraries. Problems with nuclear data are excessive in new systems with specifics requirements such as Accelerator Driven Systems. That is because of special phenomena like high energy incident neutrons or protons, special materials of the core (fission products, higher actinides, fluorides, special construction materials etc.) and other exceptions such as molten fuel or high neutron fluxes. These are problems also studied In Dept. of Nuclear Reactors. In the field of neutronic calculations are used codes MCNP

(versions 4A, 4B, 4C), WIMS, DIFER (czech diffusion code [14]), OMEGA or ANISN, for data preparation is used code NJOY (version 97 or 99). For testing various libraries was used sensitivity analysis method of multiplication factor of ADS blanket described below. Multiplication factor (k_{eff}) was computed by code MCNP-4B or 4C (various results of versions was compared). As default value of k_{eff} was chosen value obtained as result of computation by MCNP-4B and with default data supplied together with this code using ZAID ending .60c. Tested data were from widely used libraries ENDF/B-6.5, JEF-2.2, JENDL-3.2 and rarely used CENDL-2.1 and BROND-2. Older libraries

ENDF/B-5 and 4 were also tested cause they are used in old version of often used codes (e.g. MCNP-4A). Data was prepared by code NJOY version 97.115 and difference between versions 99.24 (new and old data format switch in acer module) was also tested. With new data format for MCNP version 4C was also tested new high energy tapes from available libraries such as ENDF/B-6.6 processed by NJOY version 99.24. Effect of NJOY parameters was also tested.

The blanket was obtained from work [7] with some minor changes in geometry and of course fuel and salt changes. Blanket isotopes composition is hypothetical and was made only for testing purposes. There is for example uranium which will probably not be used in transmutation technologies, it's only for data testing here. In every calculations data for only one of isotopes changed while the others have retained default data. Variance of result reflects the data influence. In the tables there is also result of percentage negative reactivity ($\rho = \frac{k_{eff} - 1}{k_{eff}}$) which better show the differences. Computation was performed for temperature 293.15 K (graphite in MCNP 01t at 300K). Default k_{eff} is 0.97513

Hypothetic ADS blanket was created for this purpose. It is graphite blanket with channels containing fluoride salt of Li-Na, fission products (FP) and higher actinides (HA), uranium and plutonium. The idea was to have there main dangerous isotopes from spent fuel which will have to be used in accelerator driven technologies (see *Tab.1*).

Fluorides	%	Fuel	%
Base LiNaF (LiF:NaF=80:20)	97	⁹⁹ Tc	1
Fuel (FP, HA, U, Pu fluorides)	3	¹²⁹ I	1
		¹³⁷ Cs	1
		²³⁵ U	2
		²³⁸ U	90
		²³⁷ Np	1
		²³⁹ Pu	1
		²⁴¹ Am	1
		²⁴⁴ Cm	1
		²⁴⁹ Cf	1

Tab. 1: Material composition of blanket used for computation

st. dev. 0.00144 (reactivity -2.55%). MCNP-4C set value 0.97560 st. dev. 0.00129 ($\rho=2.50\%$). Main results of computations are in *Tab. 2*, many other results can be found in [11].

	ENDF/B-6.5			ENDF/B-5		
	k_{eff}	st. dev.	ρ	k_{eff}	st. dev.	ρ
⁹⁹ Tc	0.97455	0.00133	-2.61	0.97642	0.00117	-2.41
¹²⁹ I	0.97607	0.00133	-2.45	0.97607	0.00133	-2.45
¹³⁷ Cs	0.96716	0.00130	-3.40	0.96716	0.00130	-3.40
²³⁵ U	0.97231	0.00132	-2.85	0.97437	0.00116	-2.63
²³⁸ U	0.97903	0.00117	-2.14	0.97847	0.00126	-2.20
²³⁷ Np	0.97456	0.00128	-2.61	0.97459	0.00118	-2.61
²³⁹ Pu	0.97208	0.00131	-2.87	0.97601	0.00133	-2.46
²⁴¹ Am	0.97476	0.00120	-2.59	0.97635	0.00131	-2.42
²⁴⁴ Cm	0.97731	0.00122	-2.32	0.97338	0.00137	-2.73
²⁴⁹ Cf	1.47278	0.00131	32.10	-	-	-
	JENDL-3.2			JEF-2.2		
	k_{eff}	st. dev.	ρ	k_{eff}	st. dev.	ρ
⁹⁹ Tc	0.97611	0.00126	-2.45	0.97424	0.00139	-2.64
¹²⁹ I	0.96697	0.00128	-3.42	0.96657	0.00142	-3.46
¹³⁷ Cs	0.97309	0.00121	-2.77	0.97811	0.00128	-2.24
²³⁵ U	0.97714	0.00129	-2.34	0.97240	0.00124	-2.84
²³⁸ U	0.97998	0.00121	-2.04	0.97750	0.00140	-2.30
²³⁷ Np	0.97755	0.00125	-2.30	0.97403	0.00132	-2.67
²³⁹ Pu	0.97384	0.00125	-2.69	0.97491	0.00121	-2.57
²⁴¹ Am	0.97918	0.00129	-2.13	0.97052	0.00119	-3.04
²⁴⁴ Cm	0.97263	0.00116	-2.81	0.97541	0.00120	-2.52
²⁴⁹ Cf	0.97849	0.00126	-2.20	0.96685	0.00117	-3.43

Tab. 2: Main results of multiplication factor reflected data influence of main HA and FP in hypothetic ADS core

This computation shows that there are almost no problems with thermal data range in cross-sections

in most of used elements. It can be also seen when we have cross-section in graph. Minor problems are

with exceptional FP and HA. There are also some differences caused by error in data evaluation or processing in NJOY. This field requires further research and evaluation. Main problems are in high energy region where available data are scarce and

often in resonance area where cross sections vary a lot. Differences between versions of computation or procession codes are mostly only in the range of st. deviation [11].

II. Thermal-hydraulic analysis

The most important calculations, except the neutronic ones, are the thermal-hydraulic analysis of the reactor core. This fact is the same in the case of operating reactors and new designs of Accelerator-Driven Systems (ADS) blankets. Heat removal is a limiting factor of reactor power. It has one of the most significant impacts on reactor safety. It determines reactor design and in the case of ADS with molten fuel-coolant has a critical influence on reactor dynamics.

At the Department of Nuclear Reactors there are two computer codes for calculation of complex tasks in the field of fluid mechanics and heat transfer: PHOENICS 3.2.0 and program package COSMOS/M 2.6 with a module FlowPlus 4.1.

The first calculations were made after acquiring the thermophysical properties of the fuel-coolant and their implementation into both available programs. Fluoride molten salts are anticipated, but the exact mixture proportion is not available yet, because of its dependence on other requirements. Two groups of molten salts are noticed most frequently in primary circuit of ADS: mixtures of LiF-NaF-KF and LiF-BeF₂ with small amount of nuclear fuel

(Pu, U or Th) and transmutable isotopes. Because of lack of sources acquiring physical properties of these salts was a difficult task. Moreover, the most cited data in references were acquired from the only one source [1]. This fact can constantly cause errors in the calculations. The data of various sources vary significantly. There are few data available for individual properties of salts, namely dependence on temperature and dependence on molar ratios of single components of mixtures. Collection and analysis of data for various salts will continue.

Verification calculations of both used programs were made first. For this purpose the benchmark example of flow in a simple pipe was used - diameter 2m, height 2m, thermal power 300MW, inlet velocity 0.6366 m/s and temperature 888K, salt: 44.7%LiF - 11%NaF - 40.3%KF - 4%UF₄. Obtained results of velocity, temperature, and density calculations were compared. Basic shapes of all fields from both programs are similar. Some little differences could be interpreted as computing errors. *Fig. 1* shows an example of the temperature on the outlet cross-section.

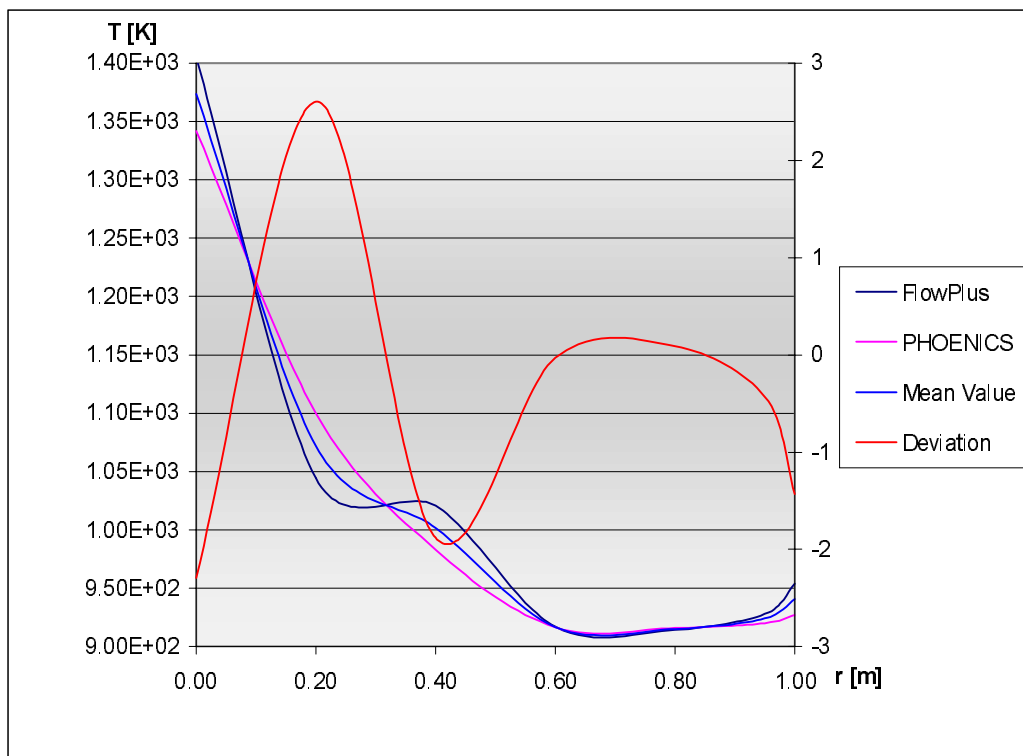


Fig. 1: Radial dependence of the outlet temperature (The second axis shows deviation of PHOENICS results to the mean values, expressed in percents)

Computations were made for 8 salts (Tab. 3) in PHOENICS 3.2.0 for these geometry and boundary conditions:

- 2D geometry, Y - axis symmetry, diameter 2m, height 2m
- 300 MW_t power, density distribution given in 100 (10x10) nodes; the power density distribution was computed from diffusion equation for subcritical systems
- inlet conditions velocity 0.6366 m/s, temperature 888K, zero velocity on the outer wall
- gravitation force in Y direction up stream
- K-epsilon turbulence model
- 17 240 cells (126 in radial direction, 140 in Z direction), 1100 sweeps

No.	LiF	BeF2	NaF	KF	UF4
1	46,5		11,5	42	0
2	44,5		10,9	43,5	1,1
3	45,3		11,2	41	2,5
4	44,7		11	40,3	4
5	50	50			0
6	69	31			0
7	67	30,5			2,5
8	71	16			13

Tab. 3: Salts used for computations

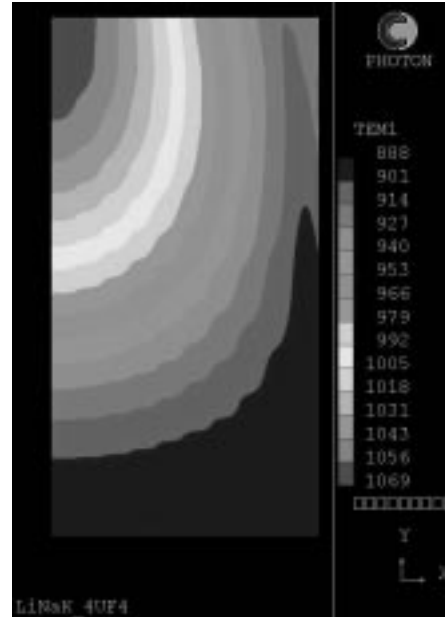


Fig. 2: An example of computation results with the salt mixture 44.7%LiF–11%NaF–40.5%KF–4%UF₄: The temperature field (The density and dynamic viscosity fields have a similar shape as the above temperature field)

The maximal values of both computed physical variables are in the core axis. This supposed result defines the critical place of the blanket. Salts comparison shows the great dependence of results on the used salts. The molten salts with higher fuel ratio give one of the most adverse values (high

temperature and high acceleration compared to zero velocity on the outer wall in the core axis). The velocity fields show that radial velocity, just as radial flow, is very small. It is the typical characteristic of all molten salts.

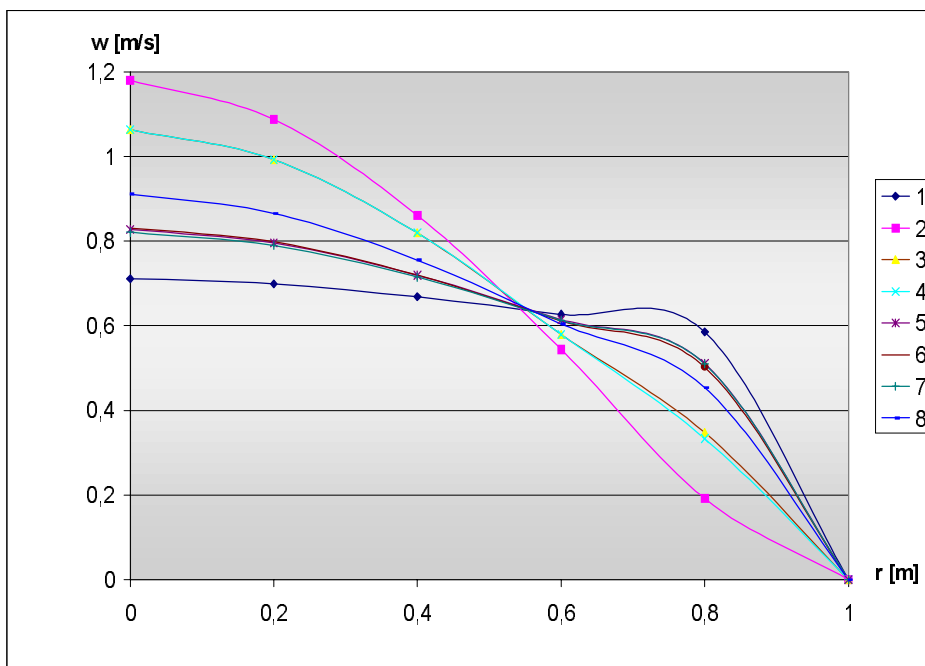


Fig. 3: An example of computation radial dependence of outlet velocity for salts in Tab. 3

III. Kinetics of subcritical reactor with external neutron source and with fluid fuel

Kinetics of the subcritical reactor with external neutron source and fluid fuel is one of the issues related to the research of accelerator-driven systems. The study of kinetics on the Department of

Nuclear Reactors is divided into two parts – experimental and theoretical. In next part some aspects of theoretical study are described.

Leakage of Delayed Neutrons

The fuel in the form molten salt flows through the primary circuit. The fissionable elements are homogeneously distributed in this fluoride salt, however the fission reaction runs only in the reactor core. In the pipeline and heat exchanger the fuel distribution is subcritical. The precursors of delayed neutrons originated from fission reaction are drifted by the fuel flow out of the core. Most of the decays of precursors produce delayed neutrons, which support the fission reaction.

However, there is a small part of precursors of delayed neutrons, which decay in other parts of the primary circuit. Neutrons thus produced are lost for the fission reaction. The resultant quantity of lost neutrons depends mainly on the ratio between fuel

volume in the core and in the whole primary circuit, fuel velocity being of great importance. The overall effect of this phenomenon is that the delayed neutron fraction β is smaller.

The leakage of the neutrons was evaluated in a stable state, when the velocity of the fuel flow is constant. Next it was supposed that the fuel flows through the core in each channel axially and is irradiated with homogenous neutron flux. The length of the channel in core is L_c , and the total length of primary circuit is L_T . Under this assumption and for each part of the primary circuit, the equations for concentration of precursor of each delayed neutron group C_i have the following form:

$$\frac{\partial}{\partial t} C_i(z, t) + v \frac{\partial}{\partial z} C_i(z, t) = \frac{k\beta_i}{l} N(z, t) - \lambda_i C_i(z, t) \quad \text{for } 0 \leq z \leq L_C \quad \text{and} \quad (1)$$

$$\frac{\partial}{\partial t} C_i(z, t) + v \frac{\partial}{\partial z} C_i(z, t) = -\lambda_i C_i(z, t) \quad \text{for } L_C \leq z \leq L_T, \quad (2)$$

where v is the velocity of the fuel, k effective reproduction factor, l prompt neutron lifetime, β_i delayed neutron fraction for a i -th group of precursors, and λ_i decay constant. To solve these equations the Laplace transformation and condition $C_i(z, 0) = 0$ were used. After the backward Laplace transformation the resulting functions

expanded to power series. Then, supposing that the neutron flux was independent of axial co-ordinate z and that for most cases $N(t) = N_0 e^{-\alpha t}$, where $\alpha = 1/T$ and T is a reactor period, the first terms of the power series expansion of the functions are expressed as:

$$C_i(z, t) = \frac{k\beta_i N_0 e^{\alpha t}}{l(\alpha + \lambda_i)(1 - e^{-(\alpha + \lambda_i)T_i})} \left\{ 1 - e^{-(\alpha + \lambda_i)(z/v)} + e^{-(\alpha + \lambda_i)(z/v + T_{Az})} - 1 \right\} \quad \text{for } 0 \leq z \leq L_C \quad \text{and} \quad (3)$$

$$C_i(z, t) = \frac{k\beta_i N_0 e^{\alpha t}}{l(\alpha + \lambda_i)(1 - e^{-(\alpha + \lambda_i)T_i})} \left\{ e^{-(\alpha + \lambda_i)T_{Az}} - 1 \right\} \quad \text{for } L_C \leq z \leq L_T, \quad (4)$$

where $T_C = L_C/v$ expresses the duration of fuel flow through core, and $T_T = L_T/v$ expresses the duration of fuel flow through the whole primary circuit. Finally, the leakage of neutrons can be evaluated by the relative quantity of neutron

precursors in the core in proportion to all precursors in the primary circuit and for each group of delayed neutrons. This ratio is designed $f_i(\alpha)$ and given by:

$$f_i(\alpha) = 1 - \frac{\int_0^{L_T} C_i(z,t) dz}{\int_0^{L_T} C_i(z,t) dz} \quad (5)$$

The fraction above can be reduced by the time dependent form $e^{\alpha t}$ and hence:

$$f_i(\alpha) = 1 - \frac{(1 - e^{-(\alpha + \lambda_i)T_C})(1 - e^{-(\alpha + \lambda_i)(T_T - T_C)})}{T_C(\alpha + \lambda_i)(1 - e^{-(\alpha + \lambda_i)T_T})} \quad (6)$$

When the power of the reactor is stable ($\alpha=0$), it results from equation (6) that the ratio is:

$$f_i(0) = 1 - \frac{(1 - e^{-\lambda_i T_C})(1 - e^{-\lambda_i(T_T - T_C)})}{T_C \lambda_i (1 - e^{-\lambda_i T_T})} \quad (7)$$

In case $T_C \ll T_T$, almost all delayed neutrons will be released outside the core; on the other hand, when $T_C \gg T_T$, the leakage from the core will be negligible. For each value of fraction $x = \frac{T_C}{T_T}$ between 0.1 and 0.9, the ratio $f_i(0)$ depends only on $\lambda_i T_C$.

Point Kinetic Equations

For all calculations described in this paper were used point kinetic equations with a correction to neutron leakage. This approach was sufficient for the purpose of a preliminary study. The correction was applied to β , which in the solid fuel reactor is given by $\beta = \sum_i \beta_i$.

The point kinetic equations used for this case are:

$$\frac{dN(t)}{dt} = \frac{\rho - \beta_f}{\Lambda} N(t) + \sum_i \lambda_i C_i + S(t) \quad \text{and} \quad \frac{dC_i(t)}{dt} = \frac{\beta_i f_i(0)}{\Lambda} N(t) - \lambda_i C_i, \quad (9)$$

where Λ is the average time of neutron origin, and ρ is reactivity. Next, the numerical Peano-Baker method was used to solve these equations. The program Bokin 2000, which was then applied to several selected issues

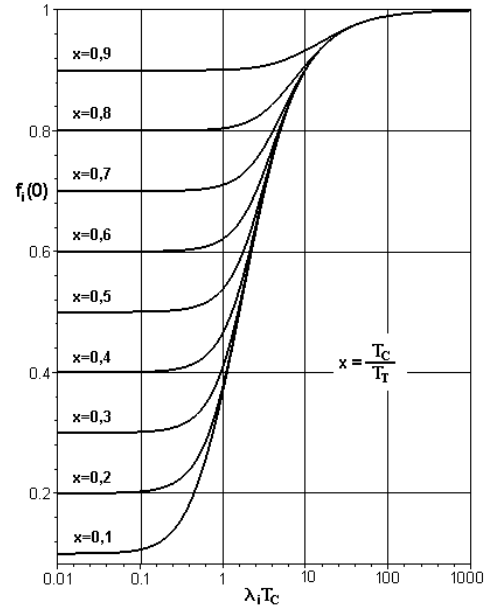


Fig.4.: Function $f_i(0)$ depending on $\lambda_i T_C$ for each x between 0.1 and 0.9.

However, in the reactor with flowing fuel:

$$\beta_f = \sum_i \beta_i f_i(0). \quad (8)$$

of subcritical reactor kinetics, was based on this method.

Fuel Pump Failure

The flowing fuel in the subcritical reactor enables not only continuous reprocessing and purifying the ADS fuel, but there is also a possibility to create a new type of transient effect in case of fuel pump failure. In such case the fuel stops flowing through the reactor, and the heat is not carried out of the core. The changes of fuel velocity also influence delayed neutron leakage; therefore β is increasing. On the other hand, the heat is not carried out of the core and the temperature of the

$$\Delta\rho_v = \sum_{i=1}^6 f_i(v)\beta_i = \sum_{i=1}^6 \left(1 - \frac{(1 - e^{-\lambda_i T_C(v)})(1 - e^{-\lambda_i(T_T(v) + T_C(v))})}{T_C(v)\lambda_i(1 - e^{-\lambda_i T_T(v)})} \right) \beta_i \quad (10)$$

where $T_C = T_{C,0}/v$, and $T_T = L_{T,0}/v$. $T_{C,0}$ and $T_{T,0}$ express the duration of fuel flow through the core and through whole primary circuit before fuel pump failure. Next, it was supposed that the influence of the increasing temperature on reactivity is linear and is given by:

$$\Delta\rho_T = Ac\Delta T \quad (11)$$

where Ac is the temperature coefficient and ΔT is the temperature difference caused by fuel. This result was also used in development of program Bokin 2000. An example of the system's behavior during the fuel pump failure was calculated for a plutonium reactor system with subcriticality -5β . The neutron source was not stopped during the transient effect, and the calculation was made for four values of the temperature coefficient Ac (0, -0.00001, -0.00005, and -0.0001). It was supposed that the values

fuel increases. The influence of the thermal effect on the reactor behavior depends mostly on the temperature coefficient Ac . Generally, there are two effects, and the resulting impact on the reactivity for every Ac can differ.

The first significant event is due to the influence of flowing fuel velocity on the reactivity. This influence can be expressed by using $f_i(v)$ in this form:

overheating. The final influence on the reactivity from both effects will be:

$$\Delta\rho(t) = \Delta\rho_v(t) + \Delta\rho_T(t) \quad (12)$$

of the other variables were $T_{C,0} = 5 \text{ s}$, $T_{T,0} = 20 \text{ s}$, and $v_0 = 1 \text{ m/s}$; the fuel stopped flowing after 30 second from the fuel pump failure. The response of the system was mostly dependent on the value of the temperature coefficient Ac . Next figure shows the progress of reactor power after the failure for each Ac .

Summary of the time-dependent behaviour

The biggest difference between a reactor with solid fuel and a reactor with fluid fuel is that in the fluid fuel system a small part of delayed neutron precursors is drifted out of the core. The resultant quantity of neutron loss depends mainly on the fuel velocity and on the ratio between fuel volume in the core and in the whole primary circuit. However, using fluid fuel brings great advantage in the possibility of continuous reprocessing and purifying its composition. The subcriticality of the system is also an advantage from the safety point of view. The response of the system to the sine change of reactivity or neutron

source frequency is also sinusoidal, and the power quickly follows the changes. Hence, the system can be controlled by neutron source intensity. The safety requirements may however demand regulation rods.

Using molten fluoride salts acting as fuel and coolant simultaneously can cause a new type of transient effect during fuel pump failure. The fuel flow slowdown decreases the leakage of delayed neutrons and thus β increases. However, the response of the system mostly depends on the value of temperature coefficient Ac .

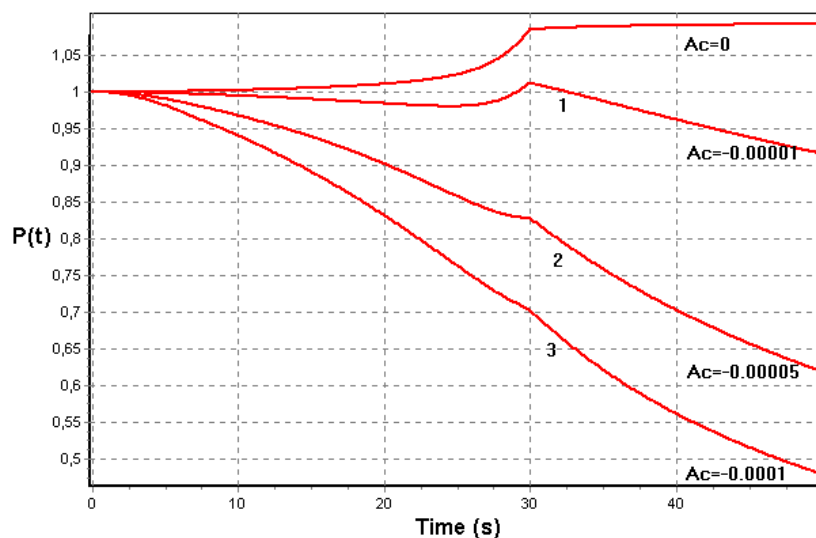


Fig. 5. Progress of the plutonium thermal reactor power after the fuel pump failure for each temperature coefficient A_c . The subcriticality was -5β ; fuel flow stopped 30 seconds after failure.

References

- [1] JANZ G. J.: Molten Salts Handbook, ACADEMIC PRESS - New York, 1967
- [2] JANZ G. J., TOMKINS R. P. T.: Physical Properties Data Compilations Relevant to Energy Storage. - IV. Molten Salts: Data on Additional Single and Multi-Component Salt Systems, U.S. Department of Commerce / National Bureau of Standards, 1981
- [3] SPALDING B., POLIS: PHOENICS On-Line Information System, 2000
- [4] FlowPlus – Solver User's Guide, Blue Ridge Numerics, Incorporated, 2000
- [5] MacFarlane R. E., Muir D. W.: The NJOY Nuclear Data Processing System, Version 91. Los Alamos National Laboratory, 1994
- [6] McLane V., Dunford C. L., Rose P. F.: ENDF-102 Data Formats and Procedures for Evaluated Nuclear Data Files ENDF-6. Brookhaven National Laboratory, 1997.
- [7] Mikisek M.: Transmutation systems based on subcritical nuclear reactors driven by external neutron source. Master Degree Project, CTU Prague, 1998.
- [8] Akcasu, Z. A., Lellouche, G. S., Shotkin, J. M.: Mathematical Methods in Nuclear Reactor Dynamics. Academic Press, New York, 1971.
- [9] Gudowski, W., Moller, E.: Neutron kinetics of advanced ATW-system. 7th International conference ICENES'93 Makuhari, Chiba, Japan 1993.
- [10] Hetrick, D. L.: Dynamics of Nuclear Reactors. University of Chicago – Press, 1971.
- [11] Katovsky K., Model ADS blanket computation with emphasis on nuclear data and cross section libraries. Master Degree Project, CTU Prague, 2001.
- [12] Matejka K., Rataj J., Uher J.: Experimental study of ADS on Faculty of Nuclear Sciences and Physical Engineering. ADDTA 2001, poster presentation, Reno, 2001.
- [13] Matejka K., Zeman J.: Preparation of Specialists for ADS on CTU Prague, FNSPE, Dept. of Nuclear Reactors. ADDTA 2001, poster presentation, Reno, 2001.
- [14] Ryvola J.: 3-Dimensional Computer Code Syndi. Research Study, CTU Prague, 1984.

Investigation of Cross-Sections for the Formation of Residual Nuclei in Reactions Induced by 660 MeV Protons Interacting with Natural Uranium Targets

J. Adam^{*,1,2}, K. Katovský^{**,3,2}, R. Michel⁴, A. Balabekyan^{2,5}, V.M. Tsoupko-Sitnikov², V.G. Kalinnikov², V.S. Pronskikh², A.A. Solnyshkin², V.I. Stegailov²

¹ Czech Academy of Science, Nuclear Physics Institute, Řež near Prague, Czech Republic

² Joint Institute for Nuclear Research, Dubna near Moscow, Russian Federation

³ Czech Technical University, Department of Nuclear Reactors, Prague, Czech Republic

⁴ Center for Radiation Protection and Radioecology, University Hanover, Germany

⁵ Yerevan State University, Armenia

Thin natural uranium targets were irradiated by a 660 MeV proton beam from the Phasotron accelerator in the Joint Institute for Nuclear Research in Dubna, Russia. Cross sections for the formation of residual nuclei ${}^{\text{nat}}\text{U}(p, \text{xpyn})_Z^{\text{A}}\text{Res}$ are determined by methods of gamma-spectroscopy. Until now 81 long-lived ($T_{1/2} > 100$ days), 121 intermediate-lived ($1 \text{ day} < T_{1/2} < 100$ days) and 224 short-lived ($T_{1/2} < 1$ day) isotopes (44 of them are in a meta-stable state) were observed, and a lot of unanalyzed lines yet remain left. Final results of 42 long-lived isotopes and upper cross-section limits for 25 isotopes are presented in this paper. Some background neutron yields are also presented. The numerical results for σ of intermediate- and shorter-lived isotopes are revealed now. These new data will be compared with theoretical simulations using intra-nuclear cascade and high-energy codes including those developed within the HINDAS project and calculations provided by LANL. All these final experimental and theoretical results will be presented at the Nuclear Data for Science and Technology (ND2004) conference.

I. INTRODUCTION

The Laboratory of Nuclear Problems of the Joint Institute for Nuclear Research in co-operation with academical institutions like the Czech Technical University in Prague, the University of Yerevan, the University of Hanover, and the Academy of Science of the Czech Republic is interested in high-energy proton and neutron reactions related with investigations for the transmutation of nuclear waste. Natural uranium targets, used in this experiment, were included in the research program of the HINDAS project [1], in which the University of Hanover has participated. All these institutions have been active in a research dedicated to the Accelerator-Driven Transmutation of nuclear waste as well as in the area of high-energy nuclear-data research. Results obtained during these studies, which are still in progress, can be used for a comparison with other data gained from the HINDAS project [2] and alternative research [3], and they are, of course, useful for benchmarking intra-nuclear cascade codes [4,5]. The results have been obtained by γ -spectroscopy method. This method, in comparison with the Inverse-Kinematics Method [6] has benefits in the possibility of measuring yields of the meta-stable states of residual nuclei and in the potentiality of using radioactive samples (targets) (like ${}^{129}\text{I}$, ${}^{241}\text{Am}$, ${}^{237}\text{Np}$ [8], ${}^{239}\text{Pu}$ etc.), which is also possible at the nTOF facility [7]. The precision of the cross-section measurement is also better. Disadvantages of this method are lower sensitivity of registration, and impossibility of measuring the yields of very long-lived and stable residual nuclei as well as very short-lived nuclei ($T_{1/2} < 1$ min). Capital costs and use of already existing accelerator facilities are conveniences for this method, but on the other side long time consumption for the yield measurements and data processing handicaps it.

Corresponding Authors: *Tel.: +7-09621-62175, Fax: +7-09621-66666, E-mail: jadam@nusun.jinr.ru

**Tel.: +420-284-681-075, Fax: +420-284-680-764, E-mail: k.katovsky@sh.cvut.cz

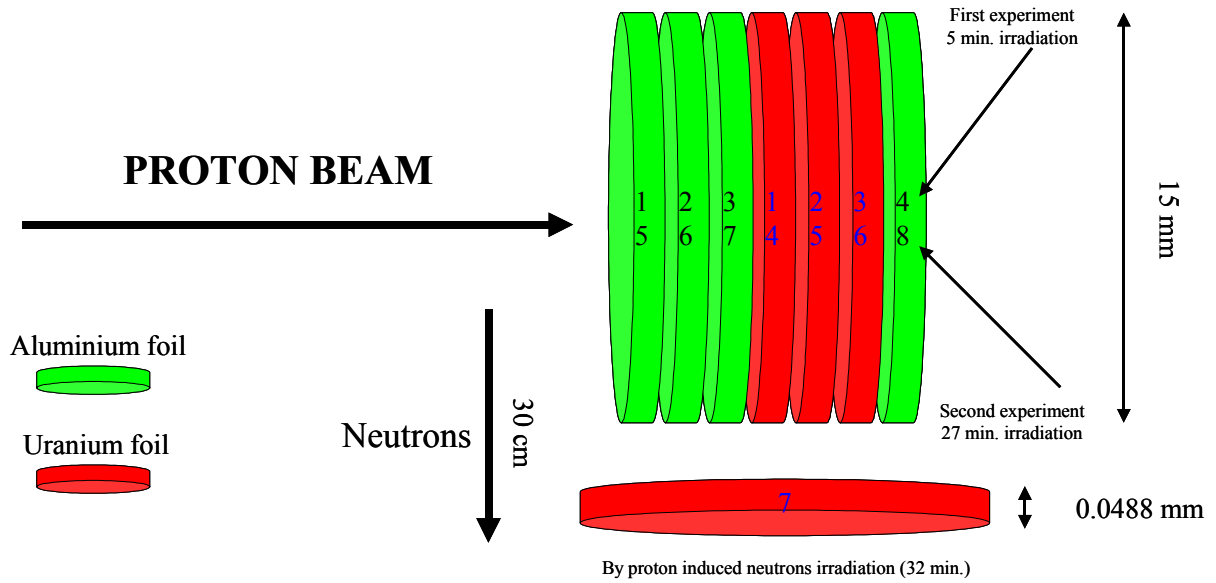


Figure 1: Set-up of the experiment

II. EXPERIMENTAL METHODS – IRRADIATION, GAMMA MEASUREMENT, AND DATA HANDLING

The experiment was carried out in the external beam of the JINR LNP Phasotron accelerator with a total beam current of $2.20 \mu\text{A}$ ($2.02 \mu\text{A}$ respectively); the beam current on the targets was $0.8 \mu\text{A}$. Proton irradiation was made in two steps – 5 min short irradiation with a total proton flux of $1.5 \cdot 10^{15}$ for the detection of short-lived isotopes and 27 min long irradiation with a total proton flux of $8.09 \cdot 10^{15}$ for the measurement of intermediate- and long-lived isotopes. There was also a third uranium-target sample (No.7 in Figure 1), which was placed 30 cm perpendicular to the beam on the plane of the targets No. 1-6 and which was irradiated by background neutrons produced in these targets. Targets made from natural uranium (consisting of three isotopes: ^{234}U - abundance 0.0054 % and $T_{1/2} = 2.455(6) \cdot 10^5 \text{ y}$, ^{235}U - 0.7204 %; $7.038(5) \cdot 10^8 \text{ y}$ and ^{238}U - 99.2742 %; $4.468(3) \cdot 10^9 \text{ y}$ [9]) metal foils were exposed to the proton beam with an energy of 660 MeV. The diameter of the irradiated target samples was 15 mm; the thickness was 0.0477 mm and their weights ca. 165 mg (Table 3). The experimental set-up is shown in Figure 1. The sample sets number one $^{\text{nat}}\text{U}_{(1)}$ (No. 1-3) and number two $^{\text{nat}}\text{U}_{(2)}$ (No. 4-6) were irradiated by the proton beam. A two-coordinate proportional chamber controlled the profile and the position of the beam during irradiation of the targets. The size of the beam in horizontal (x) and vertical (y) direction could be described by Gaussians with the $\text{FWHM}(x) = 19.2 \text{ mm}$ and $\text{FWHM}(y) = 16.2 \text{ mm}$. Aluminum foils were used in order to monitor the beam. For monitoring purposes, the reaction $^{27}\text{Al}(p,3p\text{n})^{24}\text{Na}$ was used. Good agreement gives also the reaction $^{27}\text{Al}(p,10p11\text{n})^7\text{Be}$, while $^{27}\text{Al}(p,3p3\text{n})^{22}\text{Na}$ gives ca. 30% smaller values for the proton current (Table 1). For the current calculations, the following reaction cross-sections were used: $\sigma(^{24}\text{Na}) = 10.8(7) \text{ mb}$, $\sigma(^{22}\text{Na}) = 15.0 \text{ mb}$, $\sigma(^7\text{Be}) = 5.0 \text{ mb}$ [10]. The third uranium-target sample $^{\text{nat}}\text{U}_{(3)}$ was placed 30 cm perpendicular to the beam on the plane formed by the targets $^{\text{nat}}\text{U}_{(1)}$ and $^{\text{nat}}\text{U}_{(2)}$, and was irradiated by background neutrons produced by $^{\text{nat}}\text{U}_{(1,2)}(p, \text{xpy}\text{n})^{\text{A}}_{\text{Z}}\text{Res}$ reactions. Final results for 11 neutron-induced reaction yields are shown in Table 6. In Table 5a, the final results for the 42 proton-induced reaction yields of long-lived residual nuclei are shown, while Table 5b displays upper limits for the yields of isotopes observed in the spectra but without final results determined. The final yields of intermediate- and short-lived isotopes produced in the proton-induced reactions will be presented at the ND2004 conference. Neutron results are presented as B-factor – number of residual nuclei $^{\text{A}}_{\text{Z}}\text{Res}$ per one incident proton and per one gram of the target.

Table 1: Results of the monitor reactions

^{24}Na		^{22}Na		^7Be	
Q	$I_p[\mu\text{A}]$	Q	$I_p[\mu\text{A}]$	Q	$I_p[\mu\text{A}]$
First irradiation - Al monitor (No.2), ^{235}U (No.1)					
$2.069(10)\cdot 10^7$	0.803	$2.70(7)\cdot 10^7$	0.755	$9.82(9)\cdot 10^6$	0.823
Second irradiation - Al monitor (No.6), ^{235}U (No.2)					
$2.004(9)\cdot 10^7$	0.804	$2.466(16)\cdot 10^7$	0.712	$9.13(8)\cdot 10^6$	0.807

Table 2: Characteristics of the targets

	$^{235}\text{U}_{(1)}$ -No.2	$^{235}\text{U}_{(2)}$ -No.5	$^{235}\text{U}_{(2)}$ -No.7
Weight [mg]	160.8	164.0	164.2
Thickness [mm]	0.0478	0.0487	0.0488
Activity [kBq]	1.442	1.472	1.473
Beam intensity	$0.8 \mu\text{A}$	$0.8 \mu\text{A}$	neutrons
Irradiation time [min]	5	27	32
Total proton flux	$1.5\cdot 10^{15}$	$8.09\cdot 10^{15}$	neutrons

Table 3: Weights of the samples

^{235}U		Al monitor	
Foil No.	Weight [mg]	Foil No.	Weight [mg]
1	161.0	1	29.9
2	160.8	2	30.3
3	152.4	3	30.4
4	171.9	4	29.6
5	164.0	5	29.9
6	166.3	6	29.3
7	164.2	7	30.3
		8	30.5
		9	30.3

Measurement of γ -rays

The basic properties of the HPGe detectors, which were used in our experiment, are given in Table 4. The measurement of the first $^{235}\text{U}_{(1)}$ sample was started 12 minutes after the irradiation, and the measurement of the second target $^{235}\text{U}_{(2)}$ was started after a cooling time of about 12 hours. The first sample was measured ca. 11 hours, and the last measurement of the second sample was made after a cooling time of 700 days.

Table 4: Characteristics of the γ -ray measurements

HPGe detector	CANBERRA GR-1819	ORTEC (old) GMX-23200	ORTEC (new) GMX-20190	ORTEC GeLP-36360/13
Relative efficiency	18.9 %	27.7 %	28.3 %	not indicated
Resolution [keV] ($E_\gamma=1332 \text{ keV}$)	1.78	1.86	1.84	At 5.9keV, 335eV At 122keV, 580eV
Amplifier	ORTEC 973	CANBERRA 2024	CANBERA 2026	CANBERA 2020
ADC	ORTEC 921 SPECTRUM MASTER	ORTEC 919 SPECTRUM MASTER	ORTEC 919 SPECTRUM MASTER	ORTEC 921 SPECTRUM MASTER
Filter	1 mm Pb +2 Cd + 2 Cu	2 mm Cd + 2 Cu	No	No
Sample	$^{235}\text{U}_{(1)}$, $^{235}\text{U}_{(2)}$	$^{235}\text{U}_{(3)}$	Al	$^{235}\text{U}_{(2)}$
Distance [cm]	116 – 17, 26 – 1	1	2.3, 5.0, 16.0	4.5, 2,5
Measurement time	1.2m – 72m, 85m – 18d	80m – 5d	160m – 467m	5d, 10d, 13d
Cooling time	12m – 10h 20m, 11h16m – 500d	1h20m – 11d	50m – 11d13h	403d, 545d, 700d
Number of meas.	36, 58	33	45	3

We have chosen such a distance between detector and radioactive samples ($^{235}\text{U}_{(1)}$, $^{235}\text{U}_{(2)}$) that the dead time was approximately 20%, and we measured in this geometry until the dead time decreased to app. 10%. We measured the efficiency of the HPGe detector in every position. The last 10 measurements of the second sample (meas. time about 14 days) were done without filter. Three long-time measurements were also made on the planar X-Ray detector for better detection of long-lived isotopes.

Table 5a,b : Final results and upper limits of residual nuclei production cross-sections in proton reactions with ^{nat}U

Residual Nuclei	Type of cross-sec. and decay	Half life	Cross-section [mbarn]	Residual Nuclei	Type of cross-sec. and decay	Half life	Cross-section limit [mbarn]
²² Na (G)	C(ϵ, β^+)	2.6019(4) y	0.020(5)	⁵⁵ Fe (G)	C(ϵ)	2.73(3) y	< 1.7 mb
⁴² Ar (G)	C(β^-)	32.9(11) y	0.47(10)	⁶⁸ Ge (G)	C(ϵ)	270.8(3) d	< 0.34 mb
⁵⁴ Mn (G)	I(ϵ)	312.3(4) d	0.257(15)	⁸⁵ Kr (G)	C(β^-)	10.756(18) y	< 4.8 mb
⁵⁷ Co (G)	C(ϵ)	271.79(9) d	0.0580(20)	⁹⁰ Sr (G)	C(β^-)	28.79(6) y	< 51 b
⁶⁰ Co (G)	"I"(β^-)	5.2714(5) y	0.814(40)	⁹³ Nb (M)	"I"(β^- , IT)	16.13(14) y	< 240 mb
⁶⁵ Zn (G)	C(ϵ, β^+)	244.26(26) d	0.267(15)	¹⁰⁹ Cd (G)	C(ϵ)	462.6(4) d	< 0.50 mb
⁷⁵ Se (G)	C(ϵ)	119.779(4) d	0.72(3)	¹¹³ Cd (M)	"I"(β^- , IT)	14.1(5) y	< 0.68 mb
⁸⁸ Y (G)	C(ϵ, β^+)	106.65(4) d	5.74(30)	¹²¹ Sn (M)	C(IT, β^-)	55(5) y	< 21 mb
¹⁰⁶ Ru (G)	C(β^-)	373.59(15) d	39.2(12)	¹²⁷ Te (M)	C(IT, β^-)	109(2) d	< 4.0 mb
¹⁰¹ Rh (G)	C(ϵ)	3.3(3) y	0.440(22)	¹⁴⁵ Pm (G)	C(ϵ, α)	17.7(4) y	< 2.5 mb
¹⁰² Rh (M)	I($\beta^-, \epsilon, \beta^+$)	3.742(10) y	2.22(10)	¹⁴⁷ Pm (G)	C(β^-)	2.6234(2) y	< 540 mb
¹¹⁰ Ag (M)	I(β^-, ϵ)	249.79(20) d	9.41(27)	¹⁵¹ Sm (G)	C(β^-)	90(8) y	< 2.8 b
¹⁰⁹ Cd (G)	C(ϵ)	462.6(4) d	3.60(24)	¹⁵⁷ Tb (G)	C(ϵ)	71(7) y	< 21 mb
¹¹³ Sn (G)	C(ϵ)	115.09(4) d	1.30(7)	¹⁵⁹ Dy (G)	C(ϵ)	144.4(2) d	< 0.76 mb
¹¹⁹ Sn (M)	C(β^-)	293.1(7) d	14.0(16)	¹⁷⁰ Tm (G)	I(β^-, ϵ)	128.6(3) d	< 7.0 mb
¹²³ Sn (G)	C(β^-)	129.2(4) d	13.6(9)	¹⁷¹ Tm (G)	C(β^-)	1.92(1) y	< 14 mb
¹²⁵ Sb (G)	C(β^-)	2.7582(11) y	18.1(6)	¹⁷⁴ Lu (M)	I(IT, ϵ)	142(2) d	< 3.1 mb
¹²¹ Te (M)	I(IT, ϵ)	154(7) d	5.1(3)	¹⁸² Ta (G)	C(β^-)	114.43(3) d	< 0.15 mb
¹²³ Te (M)	I(IT)	119.7(1) d	8.1(5)	¹⁸¹ W (G)	C(ϵ)	121.2(2) d	< 0.36 mb
¹³⁴ Cs (G)	"I"(β^-, ϵ)	2.0648(10) y	5.57(15)	¹⁸⁴ Re (M)	I(IT, ϵ)	169(8) d	< 0.10 mb
¹³⁷ Cs (G)	C(β^-)	30.07(3) y	15.6(8)	¹⁹⁵ Au (G)	C(ϵ)	186.09(4) d	< 1.2 mb
¹³³ Ba (G)	C(ϵ)	10.51(5) y	7.2(3)	²⁰⁸ Po (G)	C($\alpha, \epsilon + \beta^+$)	2.898(2) y	< 440 mb
¹³⁹ Ce (G)	C(ϵ)	137.640(23) d	6.0(4)	²¹⁰ Po (G)	C(α)	138.376(2)	< 3 b
¹⁴⁴ Ce (G)	C(β^-)	284.893(8) d	9.0(4)	²²⁸ Ra (G)	C(β^-)	5.75(3) y	< 390 mb
¹⁴³ Pm (G)	C(ϵ)	265(7) d	1.21(5)	²³⁵ Np (G)	C(ϵ, α)	396.1(12) d	< 100 b
¹⁴⁴ Pm (G)	I(ϵ)	363(14) d	1.02(5)				
¹⁴⁶ Pm (G)	I(β^-, ϵ)	5.53(5) y	1.02(6)				
¹⁴⁵ Sm (G)	C(ϵ)	340(3) d	1.74(12)				
¹⁵⁰ Eu (G)	I($\beta^-, \epsilon, \beta^+$)	36.9(9) y	0.67(5)				
¹⁵² Eu (G)	"I"($\beta^-, \epsilon, \beta^+$)	13.537(6) y	0.61(4)				
¹⁵⁴ Eu (G)	"I"(β^-, ϵ)	8.593(4) y	0.35(5)				
¹⁵⁵ Eu (G)	C(β^-)	4.7611(13) y	0.9(3)				
¹⁵¹ Gd (G)	C(ϵ)	124(1) d	0.96(16)				
¹⁵³ Gd (G)	C(ϵ)	240.4(10) d	1.50(6)				
¹⁷³ Lu (G)	C(ϵ)	1.37(1) y	0.260(17)				
¹⁷⁴ Lu (G)	"I"(ϵ, β^+)	3.31(5) y	0.63(5)				
¹⁷⁷ Lu (M)	I(IT, β^- , IT, β^-)	160.4(3) d	0.028(3)				
¹⁷² Hf (G)	C(ϵ, β^+)	1.87(3) y	0.223(8)				
¹⁹⁴ Os (G)	C(β^-)	6.0(2) y	3.03(30)				
²⁰⁷ Bi (G)	C(ϵ, β^+)	31.55(5) y	7.8(9)				
²²⁷ Ac (G)	C(β^-)	21.773(3) y	1.37(14)				
²²⁸ Th (G)	C(α)	1.9116(16) y	4.9(3)				

C cumulative

I independent

"I" almost independent (left and right saturated from very long-lived isotopes)

Half-lives and reaction properties were taken from [11].

Table 6: Reaction yields produced by background neutrons

Residual Nuclei	Type of decay	Half life	B-coefficient [nuclei per proton and per gram of target]
⁵⁸ Co	$\epsilon+\beta^+$	70.86(7) d	$(2.69\pm 0.076) \cdot 10^{-8}$
⁶⁰ Co	β^-	5.2714(5) y	$(4.68\pm 0.7) \cdot 10^{-7}$
⁷⁵ Se	ϵ	119.779(4) d	$(1.06\pm 0.046) \cdot 10^{-7}$
⁸³ Rb	ϵ	86.2(1) d	$(6.62\pm 0.204) \cdot 10^{-8}$
⁸⁵ Sr	ϵ	64.84(2) d	$(3.243\pm 0.07) \cdot 10^{-8}$
⁸⁸ Y	$\epsilon+\beta^+$	106.65(4) d	$(4.025\pm 0.4) \cdot 10^{-7}$
¹¹³ Sn	$\epsilon+\beta^+$	115.09(4) d	$(1.094\pm 0.03) \cdot 10^{-7}$
¹²⁶ Sb	β^-	12.46(3) d	$(1.54\pm 0.34) \cdot 10^{-9}$
¹³² Te	β^-	3.204(13) d	$(1.81\pm 0.097) \cdot 10^{-9}$
¹³¹ I	β^-	8.02070(11) d	$(2.12\pm 0.15) \cdot 10^{-9}$
²³⁹ Np	β^-	2.3565(4) d	$(5.96\pm 1.31) \cdot 10^{-7}$

Data handling

The analysis of the experimental results started with the calculation of the proton-beam intensity, by which the ^{nat}U targets were irradiated. The preliminary values of the number Q of nuclei formed per second in the Al monitors and the current I_p of protons, which irradiated the targets were determined from Al monitors (foils No.2, No.6 - Table 1). We did not make the coincidence summing corrections which are negligible for $d = 15$ cm, small

for $d = 5$ cm, but we performed them for $d = 2$ cm, where they are significant. Processing of the measured data was made by the Deimos code in interactive mode [12]; energy calibration, background subtraction, subtraction of single/double emission peaks, efficiency calibration, determination of experimental half-lives, corrections for coincidence summing etc. were made by a special code system developed [13,14] in the past and during this data processing. A total number of 97 spectra were analyzed, which corresponds to approximately 30000 gamma lines. The results for long-lived isotopes are almost final, for shorter-lived isotopes with a half-life less than 100 days preliminary results have already been obtained. Corrections for overlapping peaks, coincidence summing, and corrections for intensity suppression are in progress.

REFERENCES

- [1] KONING, A.; BEIJERS, H; BENLLIURE, J. ET ALL: *HINDAS - a European Nuclear Data Programme for Accelerator-driven Systems*. Seventh Information Exchange Meeting on Actinide and Fission Product Partitioning and Transmutation, Jeju, Republic of Korea, 2002.
- [2] BERNAS, M.; ARMBRUSTER, P.; BENLLIURE, J. ET AL.: *238U (1 A GeV) + p: Nuclide Cross-Sections and their Kinematics Properties*. TRAMU Workshop, GSI Darmstadt, Germany, September 2003.
- [3] TITARENKO, YU.E.; BATYAEV, V.F.; MASHNIK, S.G.; PRAEL, R.E. ET AL.: *Nuclide Production in ¹⁹⁷Au, ²⁰⁸Pb, and ^{nat}U Irradiated with 0.8-1 GeV Protons: Comparison with other Experiments and with Theoretical Predictions*. TRAMU Workshop, GSI Darmstadt, Germany, September 2003.
- [4] MASHNIK, S.G.; PRAEL, R.E.; SIERK, A.J. ET AL.: *Benchmarking Ten Codes against the Recent GSI Measurement of the Nuclide Yields from 208Pb, 197Au, and 238U +p Reactions at 1 GeV/nucleon*. Journal of NUCLEAR SCIENCE and TECHNOLOGY, Sup.2, p.785-788, Proc. of ND2001, Tsukuba, Japan, August 2002.
- [5] MASHNIK, S.G.; SIERK, A.J.: *Recent Developments of the Cascade-Excitation Model of Nuclear Reactions*. Journal of NUCLEAR SCIENCE and TECHNOLOGY, Sup.2, p.720-725, Proc. of ND2001, Tsukuba, Japan, August 2002.
- [6] TAIEB, J.; SCHMIDT, K.-H.; TISSAN-GOT, L. ET AL.: *Evaporation Residues Produced in the Spallation Reaction 238U+p at 1 A GeV*. Nuclear Physics A724, 413, 2003.
- [7] GONZALEZ-ROMERO, E.; ABBONDANNO, U.; AERTS, G.; ALVAREZ, F.; ET AL.: *Measurement of the Neutron Capture Cross-Sections of ²³³U, ²³⁷Np, ^{240,242}Pu, ^{241,243}Am and ²⁴⁵Cm with a Total Absorption Calorimeter at n_TOF*. CERN INTC-2003-036, INTC-P-182, CERN 2003.
- [8] ADAM, J. ET AL.: *Investigation of the Formation of Residual Nuclei in Reactions Induced by 660 MeV Protons Interacting with Radioactive ²³⁷Np, ²⁴¹Am and ¹²⁹I Targets*. Journal of NUCLEAR SCIENCE and TECHNOLOGY, Sup.2, p.272-275, Proc. of ND2001, Tsukuba, Japan, August 2002.

- [9] ROSMAN, K. J. R.; TAYLOR, P. D. P. (COMMISSION ON ATOMIC WEIGHTS AND ISOTOPIC ABUNDANCES): *Isotopic Compositions of the Elements 1997*. Pure and Applied Chemistry, vol. 70, p. 217, 1998.
- [10] CUMMING, J. B.: *Monitor Reactions for High-Energy Proton Beams*. Ann. Rev. Nucl. Sci., 13, 261-86, 1963.
- [11] CHU, S.Y.F.; EKSTROM, L.P.; FIRESTONE, R.B.: *The Lund/LBNL Nuclear Data Search*. Version 2.0, February 1999.
- [12] FRANA, J.: *The Deimos code*. Acta Polytechnica-Nukleonika, vol. 38, p. 127, 1998.
- [13] ADAM, J. ET AL.: *Program Package and Supplements to Activation Analysis for Calculations of Nuclear Reactions Cross-Sections*. JINR P10-2000-28, Dubna, 2000.
- [14] ADAM, J. ET AL.: *Determination of Nuclear Reactions Cross-Sections in Complex Nuclear Decay Chain*. JINR P15-2001-3, Dubna, 2001.

Investigation of Formation of Residual Nuclei from ^{nat}U by Reactions with 660 MeV Protons

J. Adam^{*,1,2}, K. Katovský^{**1,3}, R. Michel⁴, A. Balabekyan^{1,5},
V. M. Tsoupko-Sitnikov¹, V. G. Kalinnikov¹, V. S. Pronskikh^{1,6},
A. A. Solnyshkin¹, V. I. Stegailov¹, S. G. Mashnik⁷, R. E. Prael⁷, K. K. Gudima^{7,8}

¹Joint Institute for Nuclear Research, Dubna near Moscow, Russian Federation

²Czech Academy of Sciences, Nuclear Physics Institute, Rez near Prague, Czech Republic
Tel.: +7-09621-62175, Fax: +7-09621-66666, E-mail: jadam@nusun.jinr.ru

³Czech Technical University, Department of Nuclear Reactors, Prague, Czech Republic
Tel.: +420-284-681-075, Fax: +420-284-680-764, E-mail: k.katovsky@sh.cvut.cz

⁴Center for Radiation Protection and Radioecology, University Hanover, Germany
⁵Yerevan State University, Armenia

⁶St. Petersburg State Institute of Technology, St. Petersburg, Russian Federation

⁷Los Alamos National Laboratory, Los Alamos, New Mexico, U.S.A.

⁸Institute of Applied Physics, Academy of Science of Moldova, Chisinau, Moldova

Abstract. Thin natural uranium targets were irradiated by a 660 MeV proton beam from the Phasotron accelerator at the Joint Institute for Nuclear Research in Dubna, Russia. Cross-sections of the formation of residual nuclei $^{nat}\text{U}(p, xpyn)_Z^A\text{Res}$ are determined by methods of gamma spectroscopy. Until now, 43 long-lived ($T_{1/2} > 100$ days) isotopes were observed and their cross-sections determined. More than 350 intermediate-lived ($1 \text{ day} < T_{1/2} < 100$ days) and short-lived ($T_{1/2} < 1$ day) isotopes have been identified in the γ -spectra and many unanalyzed lines yet remain. Final results for 43 long-lived isotopes and upper cross-section limits for 27 long-lived isotopes are presented in this paper and compared with results by five different models.

INTRODUCTION

Results obtained during this study, which is still in progress, can be used for a comparison with other data measured in the framework of the HINDAS project [1,2] and they are useful for benchmarking intranuclear cascade codes [3,4]. The results have been obtained by the γ -spectroscopy method. This method, in comparison with the inverse-kinematics method [5], has the advantage of measuring yields of residual nuclei in meta-stable (M) states and the possibility of using radioactive samples as targets (like ^{129}I , ^{241}Am , ^{237}Np [6], ^{239}Pu etc.). The precision of the cross-section measurement is usually better. Disadvantages of this method are a lower sensitivity of registration and impossibility of measuring very long-lived and stable residual nuclei yields. Capital costs and use of already existing accelerator facilities are the conveniences of this method, but, on the other hand, long time consumption for the yield measurements and data processing handicaps it.

EXPERIMENT

Two experiments were carried out in the external beam of the Phasotron accelerator with 660 MeV protons and a total beam current of 2.20 μA (2.02 μA respectively); the beam current on the targets was 0.8 μA in both irradiations (determined by activation beam monitors). Proton irradiation was done in two experiments – 5 min for short irradiation with a total proton flux of $1.5 \cdot 10^{15}$ for the detection of short-lived isotopes and 27 min for long irradiation with a total proton flux of $8.09 \cdot 10^{15}$ for the measurement of intermediate- and long-lived isotopes. Two targets made from natural uranium metal foils were exposed to the proton beam with energy of 660 MeV. The diameter of the irradiated target samples was 15 mm; the thickness was 0.0477 mm, and their weight ca. 165 mg. Aluminum foils were used in order to monitor the intensity of the beam. For calibration, the following reaction cross section was used: $\sigma(^{24}\text{Na}) = 10.8(7)$ mb [7]. The gamma spectra of activated uranium targets were measured with coaxial and planar HPGe detectors.

RESULTS

Processing and analyzing of the measured data were made using the DEIMOS code [8] by a special code system [9,10]. Cross-sections of formation of product nuclei from the present work are given in Table 2. Part of our data are compared (Fig.1) with cross-sections of 800-MeV protons measured by Y. E. Titarenko et al. [12] and with the 1-GeV data by J. Taieb et al. [5] and M. Bernas et al. [13]. The last data have been measured using the inverse-kinematics method, where 1 A GeV ^{238}U projectiles irradiated a hydrogen target. These data present only independent cross-sections, while the present work and [12] contain also cumulative cross-sections. For our comparison, we calculated cumulative cross-sections from [5,13]. Although, the energies of projectiles differ substantially, the values of cross-sections do not change so much. For $Z < 28$ and $64 < Z < 74$, there are no data in [5,13] and we can not compare our results. Note that in some cases our results are more precise than the data from [5,12,13] and we have also obtained more complete results than Y. E. Titarenko et al. [12].

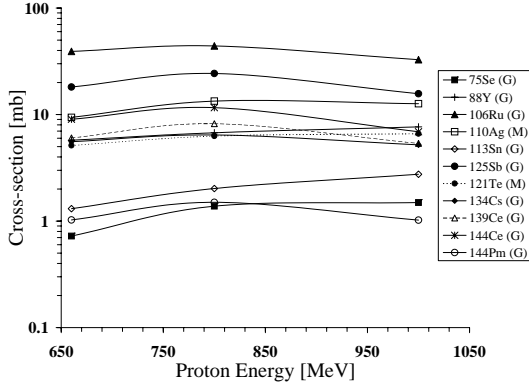


FIGURE 1. Various experimental results of residual nuclei yields from the reaction $p + ^{238}\text{(nat)U}$: the present data are at 660 MeV, the data by Y. E. Titarenko et al. [12], at 800 MeV, and by J. Taieb et al. [5] and M. Bernas et al. [13], at 1 GeV.

We analyzed all the data measured in the present work using five models incorporated in the following codes: the Liege IntraNuclear-Cascade model (INCL) [14,15] coupled with the ABLA evaporation/fission model [16]; the improved Cascade-Exciton Model (CEM) code CEM2k [17] coupled with the Generalized Evaporation/fission Model code GEM2 [18]; the Los Alamos version of the Quark-Gluon String Model LAQGSM [19] coupled with GEM2 [18] (see details in [21]); and CEM2k and LAQGSM both coupled with the sequential-binary-decay model

GEMINI [20]. Our qualitative comparison is presented in Figure 2.

For a quantitative comparison of experimental data with the calculations, we use the average deviation factor $\langle F \rangle$ with its standard deviation $S(\langle F \rangle)$.

$$\langle F \rangle = 10 \sqrt{\left\langle \left(\log \left[\frac{\sigma^{\text{cal}}}{\sigma^{\text{exp}}} \right] \right)^2 \right\rangle}$$

$$S(\langle F \rangle) = 10 \sqrt{\left\langle \left(\left| \log \left(\frac{\sigma^{\text{cal}}}{\sigma^{\text{exp}}} \right) - \log(\langle F \rangle) \right| \right)^2 \right\rangle}$$

For such a comparison, only 33 from the total 43 measured cross sections were selected. For instance, if only an isomer or only a ground state of a nuclide was measured, such nuclides were excluded from the quantitative comparison. The Tab. 1 shows values of $\langle F \rangle$ and $S(\langle F \rangle)$ for all compared products, where N is the total number of comparisons, $N_{30\%}$ is the number of comparisons in which the calculated and measured values differ by not more than 30 %, while $N_{2,0}$ shows the number of comparisons where the difference was not more than a factor of two.

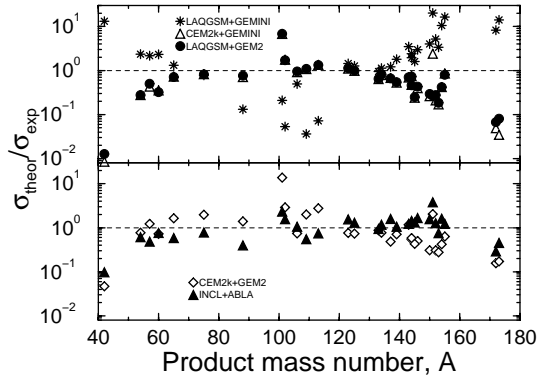


FIGURE 2. Ratios of calculated to experimental cross sections for the reaction 660-MeV protons on ^{nat}U .

TABLE 1. Quantitative comparison of experimental and calculated results for the 33 selected isotopes.

Model	All 33 selected isotopes		
	$N/N_{30\%}/N_{2,0}$	$\langle F \rangle$	$S(\langle F \rangle)$
CEM2k+GEM2	31/4/17	2.90	2.08
CEM2k+GEMINI	31/7/16	4.22	3.18
LAQGSM+GEM2	31/7/17	3.70	2.75
LAQGSM+GEMINI	33/5/10	5.42	2.78
INCL+ABLA	32/9/24	2.07	1.68

TABLE 2. Final results and upper limits of residual nuclei production cross-sections in reaction: $p+^{238(\text{nat})}\text{U}$. Comparison is made with the results by Y. E. Titarenko et al. [12], J. Taieb et al. [5], and M. Bernas et al. [13].

Residual Nuclei	Type of cross-sec. and decay	Half life	Cross-section [mb]	Cross-section [12],[mb]	I-Cross-section [5,13],[mb]	C-Cross-section [5,13],[mb]
²² Na (G)	C(ϵ, β^+)	2.6019(4) y	0.020(5)			
⁴² Ar (G)	C(β^-)	32.9(11) y	0.47(10)			
⁵⁴ Mn (G)	I(ϵ)	312.3(4) d	0.257(15)			
⁵⁵ Fe(G)	C(ϵ)	2.73(3)y	< 1.7			
⁵⁷ Co (G)	C(ϵ)	271.79(9) d	0.058(20)			
⁶⁰ Co (G)	“I”(β^-)	5.2714(5) y	0.814(40)			
⁶⁵ Zn (G)	C(ϵ, β^+)	244.26(26) d	0.267(15)		0.46(7)	0.46(7)
⁶⁸ Ge(G)	C(ϵ)	270.8(3)d	< 0.34			
⁷⁵ Se (G)	C(ϵ)	119.779(4) d	0.72(3)	1.38(17)	1.30(21)	1.49(32)
⁸² Kr(G)	C(β^-)	10.756(18) y	< 4.8		10.5(9)	19.6(20)
⁹⁰ Sr(G)	C(β^-)	28.79(6) y	< 51 000		11.9(7)	26.0(12)
⁸⁸ Y (G)	C(ϵ, β^+)	106.65(4) d	5.74(30)	6.74(52)	6.51(52)	7.66(69)
⁹³ Nb(M)	“I”(IT)	16.13(14)y	< 240			7.56(38)
¹⁰⁶ Ru (G)	C(β^-)	373.59(15) d	39.2(12)	44.0(61)	16.6(13)	32.7(26)
¹⁰¹ Rh (G)	C(ϵ)	3.3(3) y	0.440(22)		3.00(15)	3.54(18)
¹⁰² Rh (M)	I($\beta^-, \epsilon, \beta^+$)	3.742(10) y	2.22(10)			5.28(37)
¹¹⁰ Ag (M)	I(β^-, ϵ)	249.79(20) d	9.41(27)	13.3(8)		12.6(5)
¹⁰⁹ Cd (G)	C(ϵ)	462.6(4) d	3.60(24)		4.41(44)	5.18(52)
¹¹³ Cd(M)	“I”(β^-, IT)	14.1(5)y	< 0.68			12.5(5)
¹¹³ Sn (G)	C(ϵ)	115.09(4) d	1.30(7)	2.02(18)	2.39(24)	2.75(33)
¹¹⁹ Sn (M)	C(β^-)	293.1(7) d	14.0(16)			11.0(4)
¹²¹ Sn(M)	C(IT, β^-)	55(5) y	< 21			11.6(5)
¹²³ Sn (G)	C(β^-)	129.2(4) d	13.6(9)		9.28(37)	14.29(64)
¹²⁵ Sb (G)	C(β^-)	2.7582(11) y	18.1(6)	24.3(21)	9.3(5)	15.68(82)
¹²¹ Te (M)	I(IT, ϵ)	154(7) d	5.1(3)	6.28(44)		6.61(53)
¹²³ Te (M)	I(IT)	119.7(1) d	8.1(5)			8.02(48)
¹²⁷ Te(M)	C(IT, β^-)	109(2)d	< 4.0			8.18(33)
¹³⁴ Cs (G)	“I”(β^-, ϵ)	2.0648(10) y	5.57(15)	6.43(52)	5.19(15)	
¹³⁷ Cs (G)	C(β^-)	30.07(3) y	15.6(8)		3.89(27)	10.58(72)
¹³³ Ba (G)	C(ϵ)	10.51(5) y	7.2(3)		3.86(34)	7.76(68)
¹³⁹ Ce (G)	C(ϵ)	137.640(23) d	6.0(4)	8.20(54)	2.28(11)	5.36(34)
¹⁴⁴ Ce (G)	C(β^-)	284.893(8) d	9.0(4)	11.6(10)	1.52(9)	6.89(52)
¹⁴³ Pm (G)	C(ϵ)	265(7) d	1.21(5)		1.01(12)	1.58(12)
¹⁴⁴ Pm (G)	I(ϵ)	363(14) d	1.02(5)	1.50(14)	1.02(15)	
¹⁴⁵ Pm(G)	C(ϵ, α)	17.7(4)y	< 2.5		0.88(5)	1.98(17)
¹⁴⁶ Pm (G)	I(β^-, ϵ)	5.53(5) y	1.02(6)		0.84(4)	
¹⁴⁷ Pm(G)	C(β^-)	2.6234(2)y	< 540		0.75(5)	5.20(50)
¹⁴⁵ Sm (G)	C(ϵ)	340(3) d	1.74(12)		0.70(7)	1.10(12)
¹⁵¹ Sm(G)	C(β^-)	90(8) y	< 2800		0.436(22)	2.02(39)
¹⁵⁰ Eu (G)	I($\beta^-, \epsilon, \beta^+$)	36.9(9) y	0.67(5)		0.558(33)	
¹⁵² Eu (G)	“I”($\beta^-, \epsilon, \beta^+$)	13.537(6) y	0.61(4)		0.491(24)	
¹⁵⁴ Eu (G)	“I”(β^-, ϵ)	8.593(4) y	0.35(5)		0.315(16)	
¹⁵⁵ Eu (G)	C(β^-)	4.7611(13) y	0.9(3)		0.221(15)	0.51(5)
¹⁵¹ Gd (G)	C(ϵ)	124(1) d	0.96(16)		0.47(12)	
¹⁵³ Gd (G)	C(ϵ)	240.4(10) d	1.50(6)		0.45(5)	
¹⁵⁷ Tb (G)	C(ϵ)	71(7) y	< 21			
¹⁵⁹ Dy (G)	C(ϵ)	144.4(2) d	< 0.76			
¹⁷⁰ Tm(G)	I(β^-, ϵ)	128.6(3) d	< 7.0			
¹⁷¹ Tm (G)	C(β^-)	1.92(1) y	< 14			
¹⁷³ Lu (G)	C(ϵ)	1.37(1) y	0.260(17)			
¹⁷⁴ Lu (G)	“I”(ϵ, β^+)	3.31(5) y	0.63(5)			
¹⁷⁴ Lu (M)	I(IT, ϵ)	142(2) d	< 3.1			
¹⁷⁷ Lu (M)	I(IT, β^-)	160.4(3) d	0.028(3)			
¹⁷² Hf (G)	C(ϵ, β^+)	1.87(3) y	0.223(8)			

¹⁷⁸ Hf (M)	I(IT)	31(1) y	0.28(10)		
¹⁸² Ta (G)	C(β^-)	114.43(3) d	< 0.15		
¹⁸¹ W (G)	C(ϵ)	121.2(2) d	< 3.6	0.0120(18)	1.97(25)
¹⁸⁴ Re (M)	I(IT, ϵ)	169(8) d	< 0.10	0.0110(11)	
¹⁹⁴ Os (G)	C(β^-)	6.0(2) y	3.03(30)		
¹⁹⁴ Ir (M)	I(β^-)	171(11) d	< 0.045		
¹⁹⁵ Au (G)	C(ϵ)	186.09(4) d	< 1.2		
²¹⁰ Pb (G)	C(α)	22.3(3) y	< 4.2	0.068(7)	
²⁰⁷ Bi (G)	C(ϵ, β^+)	31.55(5) y	7.8(9)	0.045(5)	8.4(21)+[0.5]
²⁰⁸ Po (G)	C($\alpha, \epsilon + \beta^+$)	2.898(2) y	< 440	0.270(32)	
²¹⁰ Po (G)	C(α)	138.376(2)	< 3000	[0.088]	
²²⁸ Ra (G)	C(β^-)	5.75(3) y	< 390		
²²⁷ Ac (G)	C(β^-)	21.773(3) y	1.37(14)	1.31(20)	1.31(20)
²²⁸ Th (G)	C(α)	1.9116(16) y	4.9(3)	2.74(41)	4.48(68)
²³² U (G)	C(α)	68.9(4) y	< 140	1.01(15)	7.14(107)
²³⁵ Np (G)	C(ϵ, α)	396.1(12) d	< 1900		

C - cumulative; I - independent; "I" - almost independent (left or/and right saturated from very long-lived isotopes); Half-lives and reaction properties were taken from [11]. The values given in brackets [] in work [5], see the last two columns, are apparent production cross-sections, influenced by the radioactive decay inside the fragment separator.

CONCLUSION

Values (and upper limit) of cross sections for 43 (and 27) residual nuclei with $100 \text{ d} < T_{1/2} < 100 \text{ y}$ were measured for the reaction of 660 MeV protons on ^{nat}U. We compare our results with similar experimental data at 800 MeV [12] and with inverse-kinematics measurements at 1 GeV on ²³⁸U [5,13]. Our data are compared also with the calculations by five different models. The best agreement (but not perfect enough) was achieved with the INCL+ABLA and CEM2k+GEM2 results. None of the models tested here reproduce all the experimental data well enough and all of them should be improved further.

This work was supported in part by the US DOE, the CRDF Project MP2-3025, and by the NASA ATP01 Grant NRA-01-01-ATP-066.

REFERENCES

- Koning, A., Beijers, H, Benlliure, J. et al., *HINDAS – a European Nuclear Data Programme for Accelerator-driven Systems*. Seventh Information Exchange Meeting on Actinide and Fission Product Partitioning and Transmutation, Jeju, Republic of Korea, 2002.
- Bernas, M., Armbruster, P., Benlliure, J. et al., *TRAMU Workshop*, GSI Darmstadt, Germany, September 2003.
- Mashnik, S.G., Prael, R.E., Sierk, A.J. et al, *Journal of Nuclear Science and Technology*, Sup.2, p.785-788, Proc. of ND2001, Tsukuba, Japan, August 2002.
- Mashnik, S.G., Sierk, A.J., *Journal of Nuclear Science and Technology*, Sup.2, p.720-725, Proc. of ND2001, Tsukuba, Japan, August 2002.
- Taieb, J., Schmidt, K.-H., Tassan-Got, L. et al., *Nuclear Physics A724*, 413, 2003.
- Adam, J. et al., *Journal of Nuclear Science and Technology*, Sup.2, p.272-275, Proc. of ND2001, Tsukuba, Japan, August 2002.
- Cumming, J. B., *Ann. Rev. Nucl. Sci.*, 13, 261-86, 1963.
- Frana, J., *J.Radioanal.Nucl.Chem*, 257, 583-589 (2003).
- Adam, J. et al., *Preprint JINR*, P10-2000-28, Dubna, 2000.
- Adam, J. et al., *Preprint JINR*, P15-2001-3, Dubna, 2001.
- Chu, S.Y.F.; Ekstrom, L.P., Firestone, R.B.: *The Lund/LBNL Nuclear Data Search*. Version 2.0, February 1999.
- Titarenko, Y.E.; Batyaev, V.F., Karpikhin, E.I. et al., *Final Project Technical Report of ISTC 839B-99*. http://www-nds.iaea.org/indc_sel.html.
- Bernas, M., Armbruster, P., Benlliure, J. et al., *Nucl.Phys. A725*, 213-253 (2003).
- A. Boudard, J. Cugnon, S. Leray, and C. Volant, *Phys. Rev.*, C66, 044615, (2002), No. 4, pp: 044615-1 -- 044615-28.
- J. Cugnon, C. Volant, and S. Vuillier, *Nucl. Phys.*, A620, 475-509 (1997).
- J.-J. Gaimard and K.-H. Schmidt, *Nucl. Phys.*, A531, pp. 709-745 (1991).
- S. G. Mashnik and A. J. Sierk, *Proc. AccApp2000* (Washington DC, USA, 2000), La Grange Park, IL, USA, 2001, pp. 328-341; E-print: nucl-th/0011064.
- S. Furihata, *Nucl. Instr. Meth.*, B171, pp. 252-258 (2000).
- K. K. Gudima, S. G. Mashnik, and A. J. Sierk, LANL Report LA-UR-01-6804, Los Alamos (2001).
- R.J. Charity et al., *Nucl. Phys.*, A483, pp.371-405 (1988).
- S.G. Mashnik et al. *Advances in Space Research 34*, pp.1288–1296 (2004).

Transmutation Studies of Radioactive Nuclides

J. Adam^{1,3}, **K. Katovsky**², **M. Majerle**³, **A. Balabekyan**⁴,
M.I. Krivopustov¹, **A.A. Solnyshkin**¹, **V.I. Stegailov**¹,
S.G. Stetsenko¹, **V.M. Tsoupko-Sitnikov**¹, **W. Westmeier**⁵

¹JINR – Joint Institute for Nuclear Research, Joliot-Curie 2, 141 980 Dubna, Moscow Region, Russia

²CTU – Czech Technical University in Prague, Department of Nuclear Reactors, V Holesovickach 2, 180 00 Prague, Czech Republic

³CAS – Czech Academy of Science, Nuclear Physics Institute, Husinec-Rez, 250 68 Rez near Prague, Czech Republic

⁴YSU – Yerevan State University, Alex Manoogian 1, Yerevan, Armenia

⁵PUM – Philipps-Universität in Marburg, Fachbereich Chemie, Biegenstrasse 10, 35037 Marburg, Germany

Abstract. The Target-blanket facility “Energy+Transmutation” was irradiated by a proton beam extracted from the “Nuclotron” Accelerator in the Laboratory of High Energies of Joint Institute for Nuclear Research in Dubna, Russia. Neutrons generated by the spallation reactions of 0.7, 1.0, 1.5, and 2 GeV protons on the lead target and interact with the sub-critical uranium blanket. In the neutron field outside the blanket, radioactive neptunium, plutonium, and americium samples were irradiated and transmutation reaction yields (residual nuclei production yields) were determined using methods of γ -spectrometry. The results of transmutation studies of ^{237}Np , ^{238}Pu , ^{239}Pu , and ^{241}Am are presented.

1 Introduction

Accelerator Driven Systems are recent projects which give new ideas to the end of fuel cycle; such systems can be used to incinerate long-lived fission products and minor actinides produced by conventional fission reactors. They could also prove to be useful to burn out a large amount of plutonium from nuclear weapons. Inside the system within thick heavy metal target, spallation reactions generate high neutron fluxes and transmutation of selected isotopes takes place in the sub-critical blanket.

2 Experimental Setup Specification

“Energy plus Transmutation” (“E+T”) is a lead-uranium target blanket system (Figure 1, [1]). The total length of the lead target inside four sections is 480 mm; the total Pb-thickness is 456 mm. The diameter of lead is 84 mm and the total mass is 28.7 kg. The blanket contains four sections (Figure 2). Each section is fuelled by 30 uranium rods in aluminum shell with a diameter of 36 mm, a length of 104 mm and a mass of 1.720 kg. The total mass of each section is 51.6 kg of natural uranium, so the whole blanket mass is 206.4 kg. The slits, which experimental instruments and detectors are inserted into, were based between each two sections. The entering side of the beam is covered with the aluminum beam monitor and other activation or solid-state nuclear track detectors (SSNTD). The other detectors are lying on the top of the blanket.

On the top of the second section a set of radioactive samples (^{238}Pu , ^{239}Pu , ^{237}Np , and ^{241}Am) were placed (Figure 3). Sample properties are listed in Table 1 and their placement are indicated in Table 2. The place numeration follows from up to down regarding the Figure 3. The other isotopes purity are practically



Figure 1. Photography of the “Energy+Transmutation” Pb/^{nat}U assembly outside the shielding before fixing of the detectors

Transmutation Studies of Radioactive Nuclides

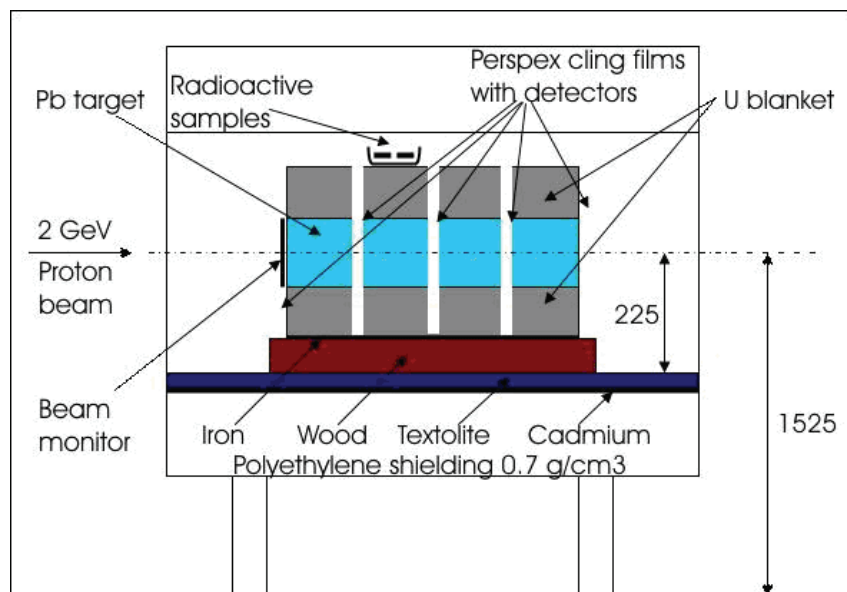


Figure 2. Simplified design of the “Energy+Transmutation” assembly inside its shielding as used in the experiment (sideways view)

Table 1. Radioactive samples properties

Nuclei	0.7 GeV		1 GeV		1.5 GeV		2 GeV	
	m [mg]	A [mCi]	m [mg]	A [mCi]	m [mg]	A [mCi]	m [mg]	A [mCi]
²³⁷ Np	1015	0.78	987	0.690	1011	0.745	1011	0.745
²³⁸ Pu	51.7	879	51.7	879	–	–	51.6	877
²³⁹ Pu	511	31.68	511	31.68	466	27.6	446	27.65
²⁴¹ Am	–	–	–	–	–	–	186	638

Table 2. Radioactive samples placing

Nuclei	0.7 GeV Cell No	1 GeV Cell No	1.5 GeV Cell No	2 GeV Cell No
²³⁷ Np	4	4	1+2	3
²³⁸ Pu	2	2	-	2
²³⁹ Pu	3	3	2+3	2+3
²⁴¹ Am	–	–	–	1

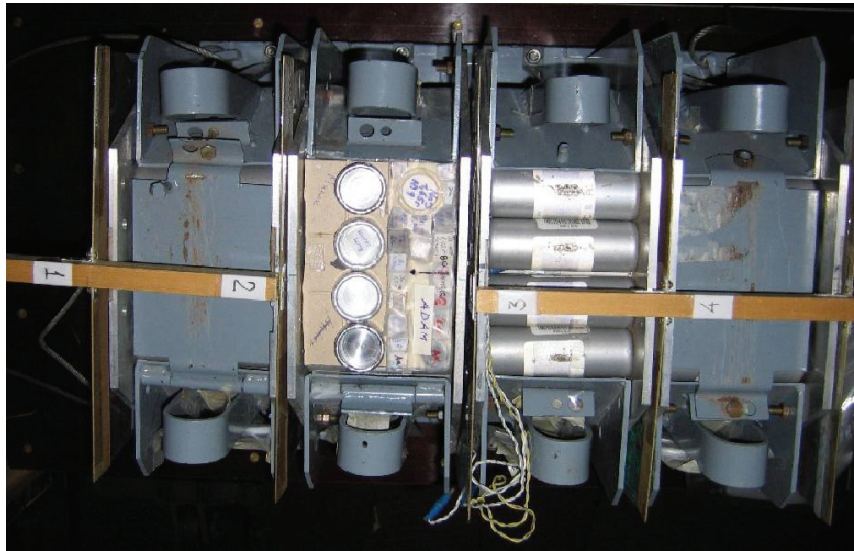


Figure 3. Top view of “E+T” setup with radioactive samples (RA-samples) on it. Beam goes from the left.

100% for ^{237}Np , ^{239}Pu , and ^{241}Am . The $^{238}\text{PuO}_2$ targets contain 72.92(16)% of ^{238}Pu , 16.75(14)% of ^{239}Pu and rest small mixture of $^{240,241,242}\text{Pu}$ (2.87(6)%, 0.35(4)%, 0.11(1)%). The target samples were hermetically packed in duralumin capsules (Figure 4) with the weight 17.51 g (in 0.7, 1.0, and 2.0 GeV experiments) or 78.8 g (in 1.5 GeV experiment).

Measurements of γ -rays were performed on the High-Purity Germanium detectors (properties are given in Table 3). Specific feature of experiments with radioactive targets is that the self-radiation of the targets produces high background that makes it difficult to measure the yield of the product nuclei, com-

Table 3. Characteristics of HPGe detectors used for γ -rays measurements

HPGe detector	CANBERRA GR1819	ORTEC GMX-23200	ORTEC GMX-20190-P
Relative efficiency	18.9%	27.7%	28.3%
Resolution ($E_\gamma = 1332 \text{ keV}$)	1.78 keV	1.86 keV	1.80 keV
Amplifier	ORTEC 973	CANBERRA 2024	CANBERRA 2026
ADC	ORTEC MASTER 921	ORTEC MASTER 919	ORTEC MASTER 919

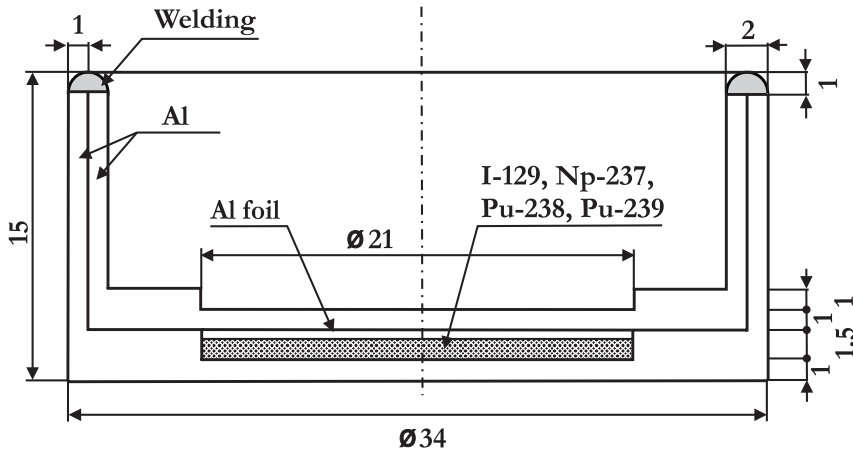


Figure 4. Radioactive sample description

parison of γ -spectra of ^{238}Pu , ^{239}Pu which were measured before irradiation and background γ -spectrum see on Figure 5. Spectra were measured for 10 000 s and the spectrum of ^{239}Pu was normalized to the same number of atoms as ^{238}Pu .

The intensity of the γ -radiation I_γ of ^{241}Am is distributed in energy E_γ this way

$$\begin{aligned} \sum_\gamma I_\gamma(E_\gamma \leq 103 \text{ keV}) : \sum_\gamma I_\gamma(103 \text{ keV} < E_\gamma \leq 400 \text{ keV}) : \\ : \sum_\gamma I_\gamma(E_\gamma > 400 \text{ keV}) = 0.392 : 0.831 \times 10^{-4} : 0.912 \times 10^{-5}. \end{aligned}$$

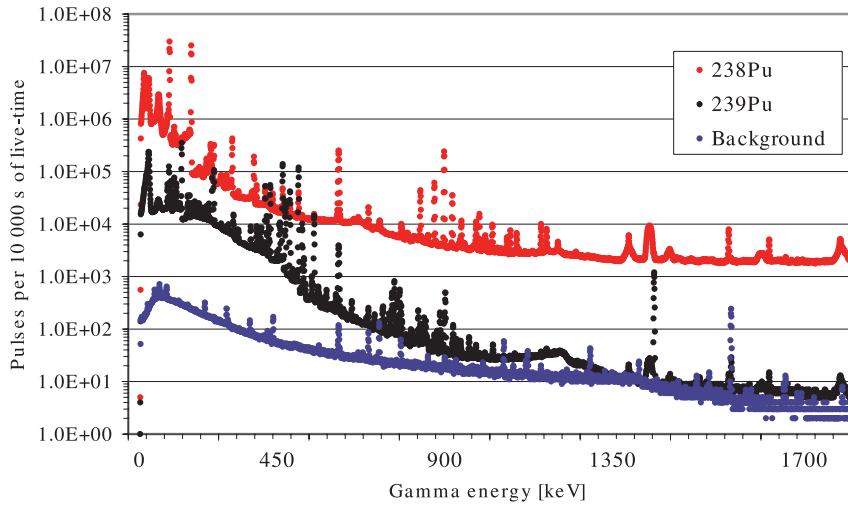


Figure 5. Comparison of γ -spectra for two isotopes of Plutonium and background measured with CANBERRA HPGe detector

The intensities I_γ are given for the decay probability and the remaining 60% occur through the electron conversion channel. When we used 10 mm Pb + 2 mm Cd + 2 mm Cu filter, then we are able to increase for measurement of ^{241}Am the solid angle by a factor of ~ 700 .

For ^{237}Np the I_γ is distributed in E_γ this way

$$\begin{aligned} \sum_\gamma I_\gamma(E_\gamma \leq 103 \text{ keV}) : \sum_\gamma I_\gamma(103 \text{ keV} < E_\gamma \leq 400 \text{ keV}) : \\ : \sum_\gamma I_\gamma(E_\gamma > 400 \text{ keV}) = 0.167 : 0.548 : 0.0168. \end{aligned}$$

But we used the same filter for the ^{237}Np target to optimize the counting rate and measurement geometry. We increased the counting rate of HpGe detector approximately 4 times using a fast spectroscopy amplifier and a high-rate multichannel buffer MASTER 921 instead of 4-input multichannel buffer MASTER 919. Then ^{237}Np and ^{241}Am were measured on distance 134 mm and 250 mm from CANBERRA GR1819 detector, correspondingly. When measurements of ^{238}Pu and ^{239}Pu were performed with the same electronic devices and with 1 mm Pb + 2 mm Cd + 2 mm Cu filter the distance of these RA samples from detector was 12 mm. The first measurement of the sample started 2–6 hours after the end of irradiation. The measurement times varied from 0.5 to 48 hours; all measurements were usually performed within 12 days. The identification possibility of residual nuclei is within the range of half an hour to one month in their half-lives.

Processing of the measured data was performed by an interactive mode of the Deimos code [2]; energy calibration, background γ -ray lines subtracting, single and double escape peaks subtracting, efficiency calibration, experimental half-lives determination, *etc.*, were made by a system of codes [3,4]. Hundreds of γ -ray lines were analyzed. Identification was made according to energy, half-life, and agreement of intensity of the peaks and a special attention to multiplex peaks was emphasized.

From every i -spectrum we analyzed all the observed γ -rays peak with energy $E_\gamma(j)$ and with area $S(i, j)$ measured with absolute efficiency $\varepsilon_\gamma^{\text{abs}}(j)$. The intensity per decay of γ -ray is $I_\gamma(j)$. If $Q(A_r, Z_r, i, j)$ is a rate of residual radioactive nuclei with mass number A_r and atomic number Z_r and the decay constant λ , we could determine this value by means of the relation (1).

$$Q(A_r, Z_r, j, i) = \frac{S(j, i) \cdot \eta_A(A_t, Z_t, j) \cdot \eta_B(\lambda) \cdot \eta_C(j) \cdot \eta_D \cdot \lambda \cdot e^{\lambda t_2(i)} \cdot \frac{t_{\text{real}}(i)}{t_{\text{live}}(i)}}{\varepsilon_\gamma^{\text{abs}}(j) \cdot I_\gamma(j) \cdot (1 - e^{-\lambda t_1}) \cdot (1 - e^{-\lambda t_{\text{real}}(i)}})} \quad (1)$$

where t_1 , $t_2(i)$, $t_{\text{real}}(i)$, and $t_{\text{live}}(i)$ are irradiation, cooling, real measuring time, and live measuring time (after deduction of dead time). The self-absorption correction $\eta_A(A_t, Z_t, E(j))$ for the γ -radiation with energy $E_\gamma(j)$ in the target with mass number A_t and atomic number Z_t was calculated with the density and

dimensions of the targets by the formula (2)

$$\eta_A(A_t, Z_t, E(j)) = \frac{\mu(A_t, Z_t) \cdot d}{1 - e^{-\mu(A_t, Z_t) \cdot d}} \quad (2)$$

where $\mu(A_t, Z_t)$ is the total attenuation coefficient for a given γ -ray with energy $E_\gamma(j)$ in the source material and d is the thickness of the target. This correction for the γ -rays of energy higher than 300 keV turned out to be less than 1.5% in the target ^{241}Am and less than 5% in the ^{237}Np target. A correction for non-constant beam intensity $\eta_B(\lambda)$ was also made, see formula (3).

$$\eta_B(\lambda) = \frac{1 - e^{-\lambda \cdot t_1}}{t_{\text{irr}} \cdot \sum_i^N \left\{ \frac{1}{t_p(i)} \cdot W(i) \cdot e^{-\lambda \cdot t_e(i)} \cdot (1 - e^{-\lambda \cdot t_p(i)}) \right\}} \quad (3)$$

where t_{irr} is irradiation time, $t_e(i)$ is the end of irradiation time, starting from pulse (i) minus pulse time $t_p(i)$. $W(i)$ is number of protons in a single pulse divided by total number of protons, N is total number of recorded pulses. This correction was done for all the residual nuclei. $\eta_C(j)$ is a coincidence summing correction and η_D is a correction for non-point geometry of the measured sample. The average value $Q(A_r, Z_r, i)$ from one spectrum was calculated as the weighted mean value of the single-line values $Q(A_r, Z_r, i, j)$, and the final $Q(A_r, Z_r)$ value was received in the same way from all i -measured spectra. As results the number of incident protons N_p , the “B-value” and the reaction rate R were calculated (Eq. (1)-(6)).

$$N_p = \frac{Q(A_r, Z_r)}{\sigma(A_r, Z_r) \cdot N_S} \quad (4)$$

Where N_p is number of incident protons per second [s^{-1}], $\sigma(A_r, Z_r)$ is cross-section of reaction [cm^2] and N_S is number of atoms on the surface of target [atom/cm^2] given by formula

$$N_S = \frac{N_A \cdot m}{A \cdot S} \quad (5)$$

Where N_A is Avogadro constant ($6.0221415 \cdot 10^{23}$ [mol^{-1}]), m mass of target [g], A amount mass of target in 1 mol [g], and S square of target [cm^2]. The reaction rate R per number of incident protons and per number of atoms in the target ($N_t = S \cdot N_S$) becomes:

$$R(A_r, Z_r) = \frac{\text{Number of produced nuclei with}(A_r, Z_r)}{(1 \text{ target isotope atom}) \cdot (1 \text{ incident proton})} = \frac{Q(A_r, Z_r)}{N_t \cdot N_p} \quad (6)$$

On the other hand the reaction rate R [$\text{proton}^{-1} \cdot \text{atom}^{-1}$] is related to the neutron fluency as follows

$$R(A_r, Z_r) = \int_{E_{\text{thr}}(A_r, Z_r)}^{\infty} \sigma_{A_r, Z_r}(E_n) \cdot \Phi(E_n) dE_n \quad (7)$$

Here, $\Phi(E_n)$ is neutron fluency [$\text{neutron}/(\text{cm}^2 \cdot \text{MeV} \cdot \text{proton})$] passing through the sample, E_{thr} is the threshold neutron energy for the given reaction in the particular nuclei of the sample.

Facility the “E+T” was irradiated by the Nuclotron accelerator’s proton beam with different energies. The total number of protons captured by the target is obtained from aluminum monitors and processed by standard methods of γ -spectrometry. The Al-monitor contains a stack of three thin aluminium foils where center foils were used. The stack of Al-foils was mounted approximately 60 cm before the Pb target in order to avoid activation from backscattered particles [5]. For such monitoring purposes the reaction $^{27}\text{Al}(p,3\text{pn})^{24}\text{Na}$ was used. The values of cross-sections for ^{24}Na production [6] 11.08(20) mb, 10.51(17) mb, 9.93(17) mb, and 9.58(17) mb were used for calculation of the integral number of protons with energies 0.7, 1.0, 1.5, and 2.0 GeV, respectively. The Al-foil was cut into 3 concentric rings with external diameters of 80, 120, and 160 mm and a central circle with diameter of 21 mm. We measured these rings and circle in order to determine their activities and respective beam profiles see Tables 4–7 and Figure 6. The parameters of the beams should be added to experimentally determined beam profiles and displacement obtained by other monitors and track detectors, see Table 8 and [7]. We can see that for protons with energy 0.7 and 2.0 GeV the beams were broad and a part of protons missed the lead target.

Table 4. Proton beam properties, part a – 0.7 GeV

I-number of foils	D(i)-D(i-1)[cm]	A(i)[Bq]	$\frac{N_p(i)}{S(i)}$ [protons/cm ²]
1	2.1–0.0	28(1)	308(14)E+09
2	8.0–2.1	199(5)	164(4)E+09
3	12.0–8.0	83(3)	51(2)E+09
4	16.0–12.0	21(1)	9.1(4)E+09
$\frac{(3+4)}{\text{sum}}$ [%]			31(6)
Time of irradiation [min]			530.60
Integral number of protons on Pb target			0.88(4)E+13

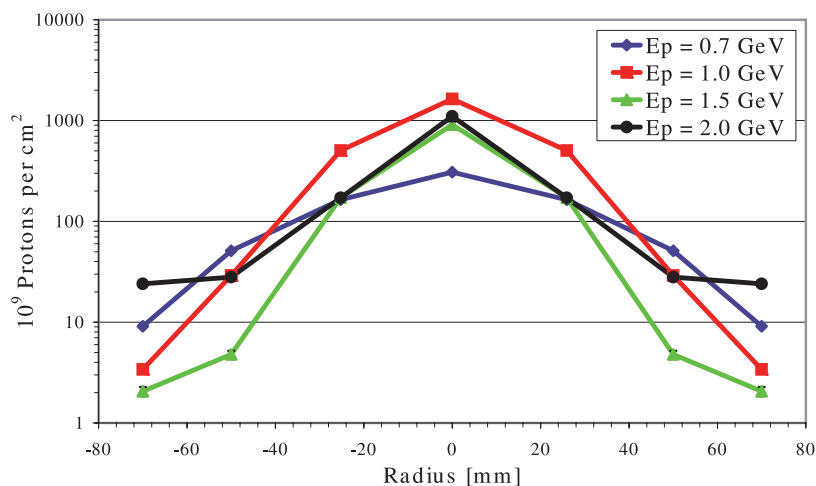


Figure 6. Beam profile measurement results

Table 5. Proton beam properties, part b – 1.0 GeV

I-number of foils	D(i)-D(i-1)[cm]	A(i)[Bq]	$\frac{N_p(i)}{S(i)}$ [protons/cm ²]
1	2.1–0.0	145(2)	1639(16)E+09
2	8.0–2.1	603(7)	504(6)E+09
3	12.0–8.0	46(1)	29(1)E+09
4	16.0–12.0	7.6(4)	3.4(2)E+09
$\frac{(3+4)}{\text{sum}}$ [%]			7(4)
Time of irradiation [min]			423.40
Integral number of protons on Pb target			2.93(13)E+13

Table 6. Proton beam properties, part c – 1.5 GeV

I-number of foils	D(i)-D(i-1)[cm]	A(i)[Bq]	$\frac{N_p(i)}{S(i)}$ [protons/cm ²]
1	2.1–0.0	53.6(33)	912(57)E+09
2	8.0–2.1	149(9)	172(11)E+09
3	12.0–8.0	5.6(5)	4.79(40)E+09
4	16.0–12.0	3.3(4)	2.06(21)E+09
$\frac{(3+4)}{\text{sum}}$ [%]			4.2(5)
Time of irradiation [min]			722.92
Integral number of protons on Pb target			1.10(5)E+13

Table 7. Proton beam properties, part d – 2.0 GeV

I-number of foils	D(i)-D(i-1)[cm]	A(i)[Bq]	$\frac{N_p(i)}{S(i)}$ [protons/cm ²]
1	2.1–0.0	275(7)	1104(28)E+09
2	8.0–2.1	575(15)	171(4)E+09
3	12.0–8.0	128(4)	28(1)E+09
4	16.0–12.0	155(4)	24(1)E+09
$\frac{(3+4)}{\text{sum}}$ [%]			25(4)
Time of irradiation [min]			463.13
Integral number of protons on Pb target			1.18(15)E+13

Table 8. Results and approximation of beam profiles [7]

Experiment (Proton energy) [GeV]	0.7	1.0	1.5	2.0
Beam integral [1E13]	1.47(5)	3.40(15)	1.14(6)	1.25(6)
Beam integral on lead target [1E13]	0.88(4)	2.93(13)	1.10(5)	1.18(15)
FWHM (vertical) [cm]	5.91(21)	4.1(3)	3.7(5)	5.4(3)
FWHM (horizontal) [cm]	5.91(21)	2.5(3)	2.4(5)	3.8(3)
Fraction of beam outside Pb target [%]	< 27	< 6	< 6	< 20
Position (vertical) [cm]	-0.4(9)	0.2(2)	0.1(2)	0.3(2)
Position (horizontal) [cm]	0.2(2)	0.0(2)	0.3(2)	-1.4(2)

3 Results

Detail results of measurements of γ -ray from ^{237}Np target after irradiation by secondary neutrons generating on Pb target and uranium blanket during experiment with proton energy 2.0 GeV are given in Tables 9 and 10. Fission products and ^{238}Np were found in this experiment. We can see from Table 10 that ^{129}Sb was recognized by means of only one γ -ray line and only in one experiment. Gamma-rays with energy less than 500 keV were not observed. Residual nucleus ^{24}Na was induced in (n, α) reaction on Al-capsule. The reaction rate for fission can be established by means of cumulative yields of fission products. These are known in literature for three energies of neutrons: thermal ($E_n = 0.025$ eV), fast $E_n = 500$ keV, and high-energy $E_n = 14$ MeV. In first approximation we summed experimental values $R(A_r, Z_r)$ for all observed fission products. For example when we used protons with energy of 0.7 GeV we received $\sum_R R(A_r, Z_r) = 5.91 \times 10^{-27}$. Sum of cumulative yields of fission products in reaction with thermal neutrons calculated from corresponding residual nuclei, using data from JEFF 3.1 library, is equal to 27.2(45)% if sum of independent yields is 200%. Then full experimental yields including unobserved fission products is $R_{\text{total yields}} = 43(8) \times 10^{-27}$ and $R_{\text{fission}} = 21.5(40) \times 10^{-27}$. We calculated R values for fission (TNoF) with different assumptions about the

Table 9. Residual nuclei produced and observed in ^{237}Np sample (R factor results); fission and (n,γ) reactions results

Residual nuclei	R 0.7 GeV [E27]	R 1 GeV [E27]	R 1.5 GeV [E27]	R 2 GeV [E27]
Sr-92	2.2(3)	–	1.50(19)	0.86(18)
Zr-97	0.80(24)	2.10(9)	2.12(7)	1.59(8)
Ru-105	–	–	1.97(28)	–
Sb-129	–	–	1.65(31)	1.11(32)
Te-132	0.56(12)	1.79(18)	1.77(28)	1.47(11)
I-133	0.83(40)	2.14(21)	2.01(24)	1.82(28)
I-135	1.52(22)	1.35(26)	2.36(28)	1.96(18)
TNoF a)	21.2(42)	31.1(72)	42.4(67)	30.4(53)
TNoF b)	20.8(40)	30.8(66)	40.2(58)	29.2(47)
TNoF c)	27.0(54)	41.2(90)	46.9(56)	35.3(56)
TNoF d)	21.9(43)	32.5(75)	41.6(62)	30.4(53)
Np-238	56.1(24)	151(5)	140(3)	133(3)
(n,γ) /fiss. a)	2.65(49)	4.86(94)	3.30(49)	4.55(71)
(n,γ) /fiss. b)	2.70(46)	4.90(88)	3.48(46)	4.39(66)
(n,γ) /fiss. c)	2.08(24)	3.67(31)	2.98(23)	3.77(30)
(n,γ) /fiss. d)	2.56(47)	4.65(90)	3.37(48)	4.37(65)

a) TNoF (Total Number of Fission per one target nucleus) is calculated using cumulating yields for $E_n = 0.025$ eV

b) for $E_n = 500$ keV (400 keV for Pu-238)

c) for $E_n = 14$ MeV

d) for weighted value of cumulated yields (data from library JEFF 3.1) for $E_n = 0.025$ eV, $E_n = 500$ keV, and $E_n = 14$ MeV

energy of neutrons. It's evident (Table 12) that TNoF does not differ more than by 20–30%. The ratio of reaction rates for $(n,\gamma)/(n,f)$ changes with the energy of protons from value 2.0 to 3.8 for the ^{237}Np target. We tried to establish the effective energy of neutrons for fission of ^{237}Np by the another way. $R_{\text{fission}}(i, E_n(j))$ was established from every $R(i)$ value separately and from each energy of neutrons $E_n(1) = 0.025$ eV, $E_n(2) = 500$ keV, and $E_n(3) = 14$ MeV. If we would had only neutrons with energy 14 MeV, then all $R_f(i, E_n(3))$ will be the same in framework of errors and the χ^2 will be closed to 1 when we calculated the weight mean value. The calculation of weight mean value of R_f for each our experiment was done for different suggestion about $E_n(j)$, $j = 1, 2, 3$. Minimum χ^2 in all four experiments were found for ^{237}Np for $E_n = 14$ MeV but for ^{239}Pu for $E_n = 0.025$ eV, see Table 13. For ^{237}Np we observed just seven (experiment with $E_p = 1.5$ GeV) or less fission products, which are lying on or nearby on expected maxima of an A -distribution, and from that we can just suggest that the effective energy of neutrons is between 500 keV and 14 MeV.

Table 10. Results of analyze of γ -ray spectra ^{237}Np after irradiation with secondary neutrons. Experiment with $E_p = 2.0$ GeV

Isotope or γ -Energy [keV]	I_g [%]	$T_{1/2}$ Theory or Experiment	R [E27]	Number of spectra
Na-24		14.959(1)h	0.087(4)	\Leftarrow
1368.63	100	15.09(21)h	0.087(4)	9
2754.03	99.9	14.9 (3) h		9
Sr-92		2.71(1) h	0.86(18)	\Leftarrow
1383.89	90.00	2.6 h	0.86(18)	2
Zr-97		16.91(5) h	1.59(8)	\Leftarrow
658.08	98	18.7(16)h	1.56(12)	7
743.35	92.9	15.9(14) h	1.61(10)	7
Sb-129		4.40(1) h	1.11(32)	\Leftarrow
812.80	42.30		1.11(32)	1
Te-132		3.204(2) d	1.47(11)	\Leftarrow
667.72	101.7	3.4(15) d	1.34(15)	7
772.61	77.9	2.8(6) d	1.66(18)	6
954.58	18.10		1.7(7)	1
I-133		20.8(1) h	1.82(28)	\Leftarrow
529.87	86.3	26(43) h	1.82(28)	6
I-135		6.57(2)h	1.96(18)	\Leftarrow
1131.51	22.5	9(6) h	1.79(29)	3
1260.41	28.6	6.5(16)h	1.99(25)	3
1678.06	9.52		2.3(7)	1
Np-238		2.11(2)d	133(3)	\Leftarrow
882.63	0.87	1.95(15)d	139(10)	9
918.69	0.59	1.77(22)d	129(11)	10
923.98	2.86	2.01(6) d	136(7)	10
936.61	0.40	2.3(10) d	129(22)	3
941.38	0.54	2.0(4) d	129(22)	5
962.77	0.70	2.2(4) d	148(12)	8
984.45	27.8	2.07(4) d	131(6)	11
1025.87	9.6	2.07(4) d	131(7)	11
1028.54	20.3	2.08(3) d	133(7)	11

Unfortunately, only 5 fission products of ^{238}Pu were observed due to high activity of this target before irradiation, small sample mass, different cross-section, see Figure 5 and Tables ??, and also the γ -ray spectra shape. Higher number of fission products was observed in the ^{239}Pu sample. The same procedure as in ^{237}Np case was used to determine the average/total number of fissions per one target for both plutonium isotopes and for americium as well. We did not observe any fission product when ^{241}Am sample was measured after irradiation

Transmutation Studies of Radioactive Nuclides

Table 11. Relative yields of fission products, reaction $^{237}\text{Np}(n,f)$

Fission product	Energy of neutrons			Energy of protons [GeV]			
	0.0252 eV	500 keV	14 MeV	0.7	1.0	1.5	2.0
	Library cumulative yield			Weighted cumulative yield			
	Library sum of independent yield			Weighted sum of independ. yield			
Sr-92	4.17(46)	4.37(18)	4.01(92)	4.29		4.28	4.29
	4.13(94)	4.33(113)	3.97(104)	4.25		4.24	4.25
Zr-97	5.84(134)	6.11(17)	5.35(59)	5.94	5.00	5.93	5.93
	5.85(180)	6.11(180)	5.35(153)	5.94	5.94	5.93	5.93
Ru-105	2.65(61)	3.10(19)	3.45(55)			3.17	
	2.66(69)	3.12(75)	3.46(73)			3.19	
Sb-129	0.97(16)	1.76(41)	3.10(50)			2.05	2.06
	0.97(46)	1.76(75)	3.10(66)			2.05	2.06
Te-132	4.53(50)	4.75(19)	3.98(64)	4.58	4.58	4.57	4.57
	4.52(82)	4.75(76)	3.98(102)	4.58	4.58	4.57	4.57
I-133	6.47(414)	6.46(413)	4.45(285)	6.03	6.02	6.01	6.00
	10.2(272)	6.28(92)	4.44(104)	5.94	5.92	5.91	5.91
I-135	6.90(76)	6.71(19)	4.16(96)	6.17	6.15	6.14	6.13
	6.92(129)	6.72(105)	4.15(102)	6.18	6.18	6.15	6.13
Sum	31.5(45)	33.3(46)	28.5(45)	27.0	22.7	32.2	29.0
Sum	35.3(38)	33.1(29)	28.5(28)	26.9	22.6	32.0	28.8

Table 12. ^{237}Np – Total number of fission per one proton per second calculated from each produced isotope (fission product)

Nuclide	0.7 GeV	1 GeV	1.5 GeV	2 GeV
	$R_{\text{fission}}[1 \times 10^{27}]$			
92Sr	51.3(81)	–	35.0(53)	20.1(45)
97Zr	13.5(41)	35.4(23)	35.7(21)	26.8(19)
105Ru	–	–	62.1(103)	–
129Sb	–	–	80.7(23)	54.0(194)
132Te	12.2(27)	39.1(47)	38.7(66)	32.1(33)
133I	13.8(110)	35.6(230)	33.5(218)	30.3(202)
135I	25.1(40)	21.9(45)	38.4(54)	32.0(38)
Average	17.53	33.67	37.10	28.03
inter. err.	1.89	1.87	1.73	1.42
exter. err.	4.80	3.18	2.27	1.18

of secondary neutrons. We were able to estimate just upper limit for several of them. In Table 17 the limits and limited ratios $R(^{241}\text{Am})/R(^{239}\text{Pu})$ are given. For ^{238}Pu and ^{239}Pu , these ratios are approximately equal for different residual nuclei. If we suppose that ratios $R(^{241}\text{Am})/R(^{239}\text{Pu})$ are also approximately

Table 13. Value of χ^2 received in analysis of average $R_{fission}$

Proton Energy	0.7 GeV	1.0 GeV	1.5 GeV	2.0 GeV
Neutron Energy	$^{237}\text{Np} - \chi^2$			
0.025 eV	7.6	2.8	2.3	1.7
500 keV	7.5	4.2	2.2	1.8
14 MeV	3.2	0.81	0.64	1.3
$\langle \text{weighted} \rangle$	6.5	2.9	1.7	1.6
	$^{239}\text{Pu} - \chi^2$			
0.025 eV	2.4	2.5	3.0	20
500 keV	3.1	3.3	5.1	27
14 MeV	5.6	3.5	7.9	40

Table 14. Fission cross-section for important isotopes

E_n [eV]	Fission XS [barn]			
	^{238}Pu	^{239}Pu	^{237}Np	^{241}Am
2.46E-02	18.17	756.92	0.02	3.19
5.00E+05	1.40	1.61	0.46	0.10
1.40E+07	2.72	2.42	2.16	2.67

Table 15. Residual nuclei produced and observed in ^{238}Pu sample, R factor results

Residual nuclei	R 0.7 GeV [E27]	R 1 GeV [E27]	R 1.5 GeV [E27]	R 2 GeV [E27]
Zr-97	–	3.2(3)	–	17.7(22)
Ru-105	–	–	–	23.6(59)
Sb-129	–	0.66(34)	–	–
I-132	–	3.24(39)	–	7.5(31)
I-133	–	2.28(54)	–	6.5(24)
Xe-135	–	2.58(52)	–	15.0(13)
TNoF a)	–	20(7)	–	86(16)
TNoF b)	–	23(8)	–	94(19)

equivalent for different residual nuclei, then we can assume that

$$\sigma(^{241}\text{Am}(n, f)) < 2.2 \cdot \sigma(^{239}\text{Pu}(n, f)).$$

More precise estimation of the TNoF can be done if we will know the distribution of secondary neutrons in space where radioactive targets were placed. As we didn't know the experimental neutron spectra well, we performed calculation of neutron spectra. The latest release of MCNPX (version 2.5.0) was used to simulate the experimental results. Nuclear reactions of incident protons with material, the transport, and further reactions of secondary particles are imple-

Transmutation Studies of Radioactive Nuclides

Table 16. Residual nuclei produced and observed in ^{239}Pu sample, R factor results

Residual nuclei	R 0.7 GeV [E27]	R 1 GeV [E27]	R 1.5 GeV [E27]	R 2 GeV [E27]
Sr-91	1.96(8)	2.14(8)	4.52(18)	5.57(64)
Sr-92	1.19(19)	2.2(3)	4.11(64)	4.14(59)
Y-92	2.39(24)	5.91(58)	7.52(76)	12.12(12)
Zr-97	5.52(51)	3.24(30)	8.82(80)	11.35(10)
Mo-99	5.37(22)	5.38(22)	9.73(39)	13.71(18)
Ru-103	11.03(52)	5.26(25)	10.54(50)	19.57(37)
Ru-105	3.22(13)	4.9(2)	9.08(37)	13.76(25)
Sb-128	0.106(11)	0.129(16)	0.213(27)	0.37(6)
Sb-129	0.66(7)	1.19(12)	2.08(21)	3.2(9)
Te-132	4.18(17)	3.45(14)	4.59(19)	13.81(40)
I-131	-	2.8(1)	-	12.8(8)
I-132	-	2.67(63)	-	9.5(16)
I-133	6.23(21)	6.08(21)	11.04(38)	16.94(15)
I-135	3.90(10)	4.86(12)	8.78(22)	12.2(4)
Xe-135	5.48(62)	7.67(89)	11.5(13)	38.99(48)
Ce-143	3.29(13)	3.23(13)	7.47(30)	11.4(13)
Ba-140	0.52(16)	4.2(13)	7.4(22)	12.2(18)
La-140	-	0.588(70)	-	1.3(2)
TNoF a)	52(8)	46(3)	52(2)	68(5)
TNoF b)	55(7)	48(5)	54(3)	71(5)
TNoF c)	62(8)	52(4)	60(3)	78(7)

Table 17. Upper limits computed for residual nuclei expected as most probably produced in ^{241}Am sample, R factor estimation for 2 GeV experiment

Residual nuclei	$T_{1/2}$	2 GeV R upper limit [E27]	$R(^{241}\text{Am})$ $R(^{239}\text{Pu})$
Sr-91	9.630 h	< 35.5	< 6.4
Sr-92	2.710 h	< 17.0	< 4.1
Zr-97	16.900 h	< 24.3	< 2.2
Mo-99	2.748 d	< 338	< 25
Ru-103	39.260 d	< 547	< 28
Ru-105	4.440 h	< 43.3	< 3.1
Sb-129	4.400 h	< 37.0	< 12
Te-132	3.204 d	< 49.8	< 3.6
I-133	20.800 h	< 56.5	< 3.3
I-135	6.570 h	< 36.9	< 3.0
Ce-143	33.040 h	< 543	< 48

mented in the code. The geometrical description of the setup assembly used in the simulation is seen in Figure 2. In the description are included precise di-

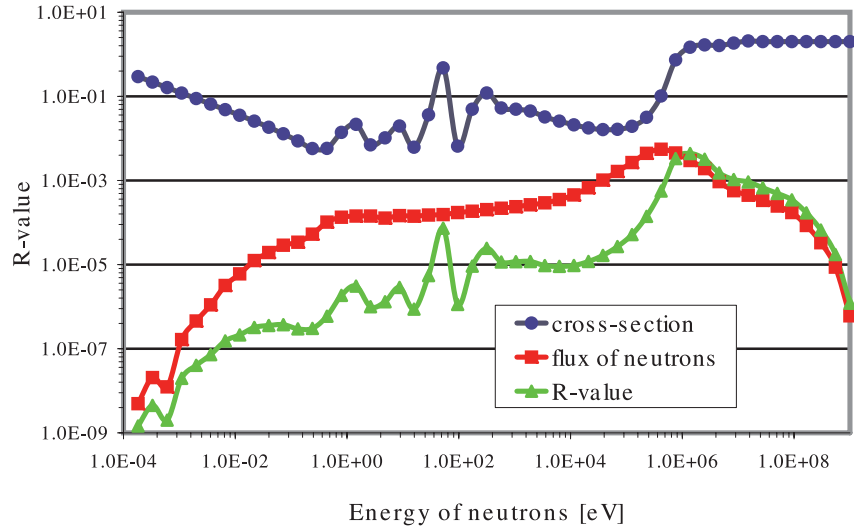


Figure 7. Flux of neutrons ($E_p = 2.0$ GeV), cross-section of reaction $^{237}\text{Np}(n,f)$, reaction rate of fission

mensions and physical properties of used materials (lead target, uranium rods in hexagonal lattice, polyethylene box with cadmium shielding, metal and aluminum holders of the target/blanket, wooden plates on which target/blanket is mounted). Smaller details (screws, small holders) and iron construction outside the polyethylene box were not taken in the account, after it was found by the simulations that their influence on the results is negligible.

In the experiment the radioactive samples are located on the top of the second section of the blanket. For the simulations, the mention place was divided to four cells with dimensions $36 \text{ mm} \times 36 \text{ mm} \times 1.5 \text{ mm}$ and the flux of neutrons (or protons) averaged over a cell. The flux [$\text{particles}/\text{MeV}\cdot\text{cm}^2$] was calculated for each cell. The Gaussian shape of real sizes and positions (displacement from an axis of Pb target, see Table 8) of the proton beam for all 4 energies of protons was used. The number of incident protons was 3.2×10^7 for each calculation. In order to speed up the simulations, a small cluster of computers and MCNPX compiled with the support for MPI were used. The models and libraries used in simulations were: CEM2k INC model with the LA150N and LA150H libraries implemented in MCNPX.

Neutron spectra were divided into 52 energy groups from 1×10^{-5} eV to 2 GeV (up to each proton energy). We compared calculated neutron fluxes for different proton energies among each other, see Figure 8 and 9. Maximum of the flux is in energy group with upper energy limit of a 0.759 MeV for all four proton

Transmutation Studies of Radioactive Nuclides

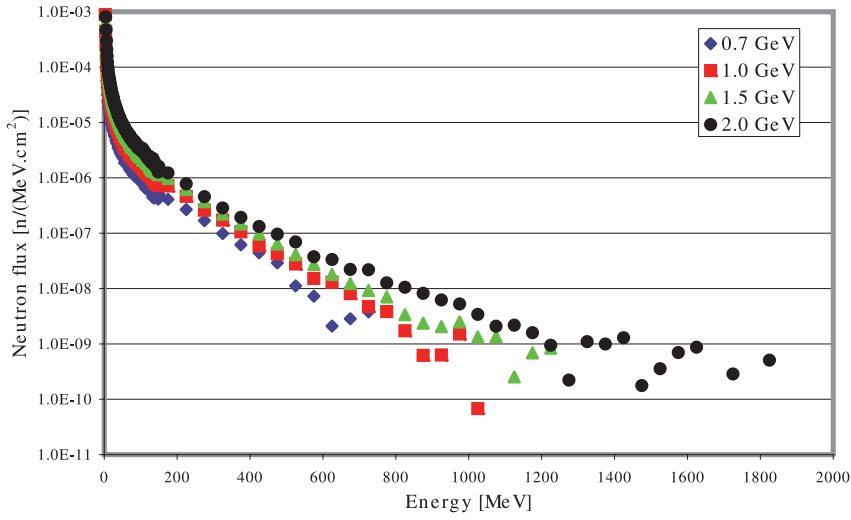


Figure 8. Calculated estimation of secondary neutron spectra (detailed high energy region)

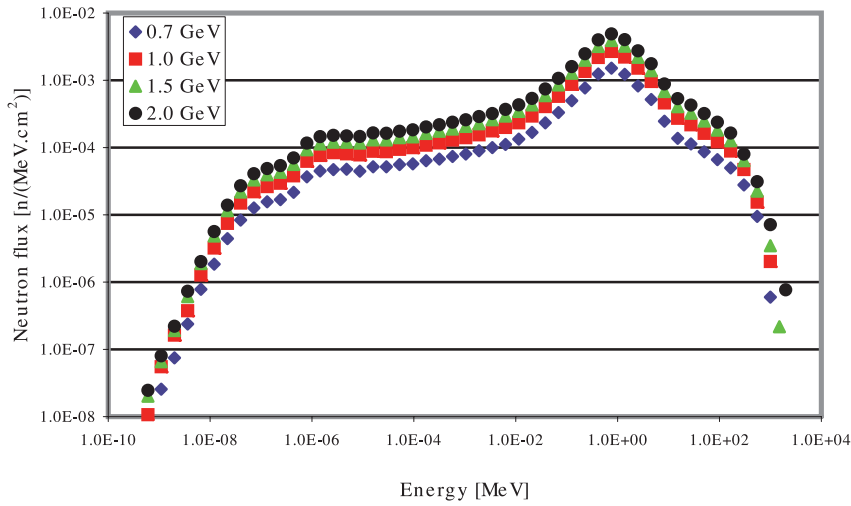


Figure 9. Calculated estimation of secondary neutron spectra (detailed low energy region)

energies. Ratio of integral calculated fluxes are

$$\Phi_{\Sigma}(E_p = 0.7 \text{ GeV}) : \Phi_{\Sigma}(E_p = 1.0 \text{ GeV}) : \Phi_{\Sigma}(E_p = 1.5 \text{ GeV}) : \Phi_{\Sigma}(E_p = 2.0 \text{ GeV}) = 1 : 1.728 : 2.613 : 3.287.$$

The shape of calculated neutron spectra is practically identical in broad energy

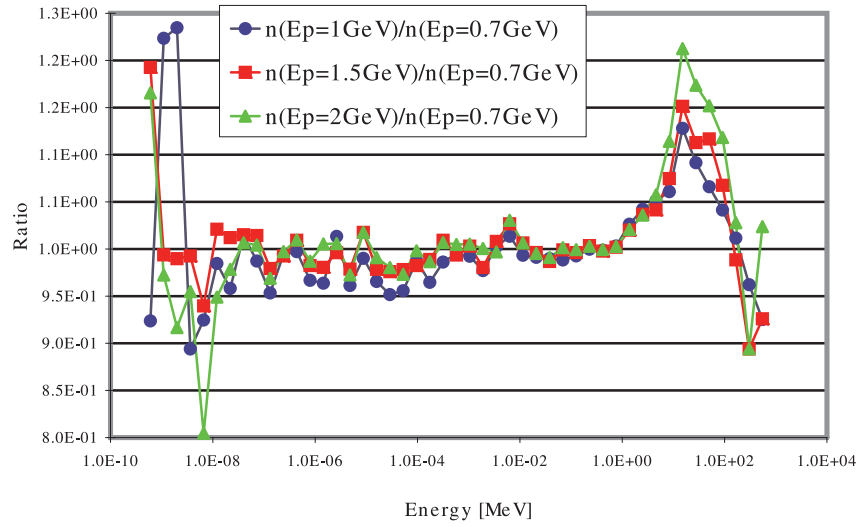


Figure 10. Neutron fluxes comparison (calculated spectra renormalized to 0.7 GeV values and to their maximum values at $E_n = 0.759$ MeV)

interval until few MeV, some differences we can see in the high-energy region of 8–150 MeV. These differences are within the range of 20% [Figure 10]. Discrepancies in the beginning of the spectra ($E_n < 1 \times 10^{-8}$ MeV) and in its end ($E_n > 150$ MeV) are caused by statistics.

In Tables 18–22 are given fluxes of secondary neutrons and protons in different boxes for all incident proton energy. We can see that neutron flux in box 1 and 4 are almost equivalent for every proton energy and the same is true for box 2 and 3. There is not correlation between the shift of center of proton beams, see Table 8, and ratios of neutron flux from different boxes. The statistical errors for proton fluxes are about 20% and in framework of these errors we do not observed any correlation between the shift of center of proton beam and ratios of proton fluxes in our boxes. The ratios of neutron spectra for different boxes

Table 18. Flux ratio 1

Box	0.7 GeV	Neutron flux [n/MeV · cm ²]		
		1.0 GeV	1.5 GeV	2.0 GeV
1	0.00794	0.0142	0.0212	0.0266
2	0.0097	0.0173	0.0255	0.0322
3	0.00981	0.0175	0.0253	0.032
4	0.00819	0.0145	0.0208	0.0263
sum	3.56E-02	6.35E-02	9.28E-02	1.17E-01

Table 19. Flux ratio 2

Box	Proton flux [p/MeV·cm ²]			
	2.0 GeV	1.5 GeV	1.0 GeV	0.7 GeV
1	2.76E-05	1.97E-05	1.53E-05	9.92E-06
2	4.17E-05	5.20E-05	3.26E-05	2.20E-05
3	4.06E-05	4.26E-05	4.11E-05	2.37E-05
4	2.67E-05	1.81E-05	1.68E-05	1.27E-05
sum	1.37E-04	1.32E-04	1.06E-04	6.83E-05
sum p/ sum n	6.83E-02	6.62E-02	5.29E-02	3.42E-02

Table 20. Flux ratio 3

Box	p/n			
	2.0 GeV	1.5 GeV	1.0 GeV	0.7 GeV
1	1.04E-03	9.29E-04	1.08E-03	1.25E-03
2	1.30E-03	2.04E-03	1.88E-03	2.27E-03
3	1.27E-03	1.68E-03	2.35E-03	2.42E-03
4	1.02E-03	8.70E-04	1.16E-03	1.55E-03

Table 21. Flux ratio 4

E_p [GeV]	n	500-p
0.7	0.0356	0.03416
1.0	0.0635	0.0529
1.5	0.0928	0.0662
2.0	0.1171	0.0683

Table 22. Flux ratio 5

E_p [GeV]	$\max(E_p)/\max(0.7)$	$\text{Int}(E_p)/\text{Int}(0.7)$
0.7	1	1
1.0	1.763	1.728
1.5	2.572	2.613
2.0	3.086	3.283

for 2 GeV incident proton energy are given on Figure 11, the same picture can be seen for the others energy of protons. The shape of neutron spectrum in box 1 is almost equivalent with the shape of neutron spectrum in box 4 and also $\Phi(E_n(\text{box } 2)) \sim \Phi(E_n(\text{box } 3))$. Ratio $\Phi(E_n(\text{box } 2))/\Phi(E_n(\text{box } 4))$ has wide maximum about 1.3 at $E_n \sim 0.2$ MeV.

In the same energy group division as calculated, we produced group-wise library cross-sections of sample materials. We used code NJOY 99.112 and library JEFF 3.1 [8]. We made another imagination and condense neutrons into

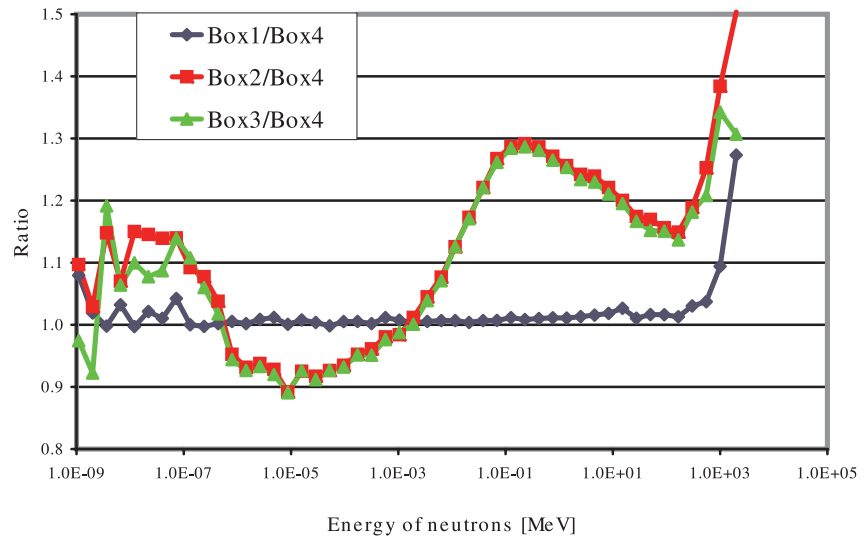


Figure 11. Ratio of neutron fluxes

3 major energy groups (linear division), Figure 12. That was motivated by the reason that in the literature one can find detail mass distribution of the fission

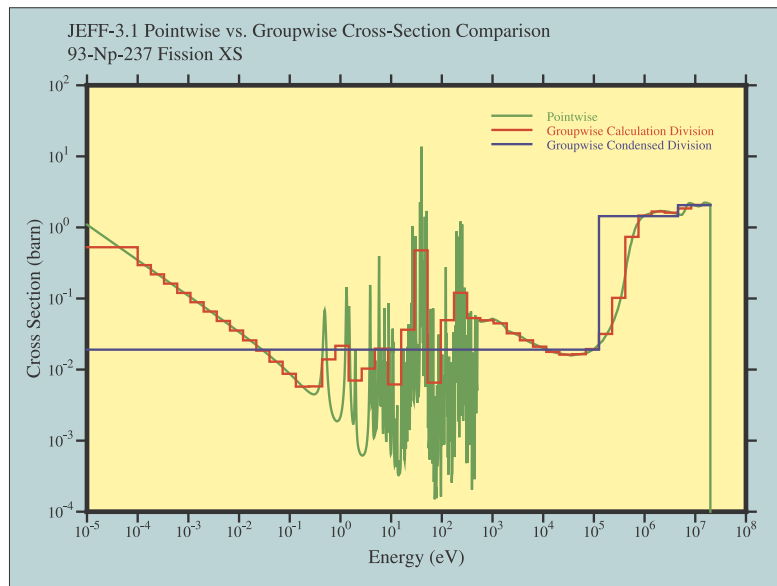


Figure 12. Group-wise structure used to TNOF estimation

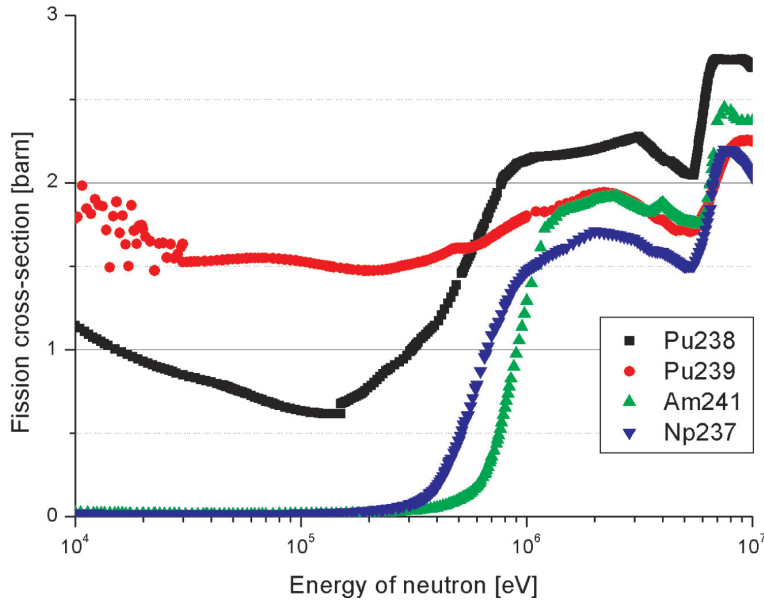


Figure 13. Neutron fission cross-section comparison for high-energy region (1e4 to 2e7 eV, from JEFF-3.1 library)

products from fission of Pu, Np isotopes with neutrons of three various energies – thermal (0.025 eV), unresolved-resonance-energy fast neutrons (500 keV) and high-energy fast neutrons (14 MeV). So that’s why we divided neutrons into three major energy regions:

- ‘thermal’, ‘epithermal’, and ‘resonance’ groups ($a(1) = 1 \times 10^{-5}$ eV to $a(2) = 1.26 \times 10^5$ eV)
- ‘resolved’, ‘unresolved’ resonance, and ‘fast’ groups ($a(2) = 1.26 \times 10^5$ eV to $a(3) = 4.57 \times 10^6$ eV)
- ‘fast’, ‘high-energy’, and ‘spallation’ groups ($a(3) = 4.57 \times 10^6$ to $a(4) =$ high limit $\sim \max 2 \times 10^9$ eV).

The weight factor of fission by neutron $W_j(t)$ with energy in region j is introduced using relation (8).

$$w_j(t) = \frac{\int_{a(j)}^{a(j+1)} \sigma_f(t, E_n) \Phi(E_n) dE_n}{\int_1^4 \sigma_f(t, E_n) \Phi(E_n) dE_n} \quad (8)$$

Where $j \in \hat{3}$ and $t \in \{^{237}\text{Np}, ^{238}\text{Pu}, ^{239}\text{Pu}, ^{241}\text{Am}\}$.

We performed manual integration of cross-section and calculated neutron fluxes in each of 3 groups (product of cross-section and flux of each 52 groups and

sum-condensation into 3 groups), so we obtained fission yields for these three energy intervals, Figure 12. Then we calculated group-weights (relative number of fissions produced by neutrons with energies within the energy intervals), Table 23. We can see from this table that the weights ($w_j(t)$) for given RA target nuclei (t) change with energy of incident proton smoothly and very little, not more then on 10% from $E_p = 0.7$ GeV to $E_p = 2.0$ GeV. For ^{237}Np the weight ($w_1(^{237}\text{Np})$) is very small, about 1%, for epithermal region of neutrons and highest weight for resonance region of neutrons in all four experiments. For ^{239}Pu there is high weight of first epithermal group.

Using these weights and library fission yields (JEFF 3.1 camelbacks) we calculated mean weight yields ($\langle Y_{\text{cum}}(t,r) \rangle$) of fission products (r) for our experimental conditions, see formula (9).

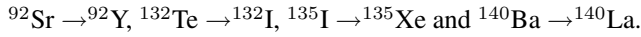
$$\langle Y_{\text{cum}}(t,r) \rangle = w_1(t) \cdot Y_{\text{cum}}(t,r,1) + w_2(t) \cdot Y_{\text{cum}}(t,r,2) + w_3(t) \cdot Y_{\text{cum}}(t,r,3) \quad (9)$$

In such approximation we can assume that ratio between $R_{\text{exp}}(t,r)$ value for each observed fission product (r) and relative production yield ($\langle Y_{\text{cum}}(t,r) \rangle$) obtained by commented way for the same residual nuclei are constant for given RA-sample (t= ^{237}Np , ^{238}Pu , ^{239}Pu) and each proton energy. If we calculate mean weighted value of ratios $\frac{R_{\text{exp}}(t,r)}{\langle Y_{\text{cum}}(t,r) \rangle}$ for all observed residual nuclei we can hope to receive minimum $\chi^2_{<}$ value comparing with $\chi^2_{>}$ – values in Table 13. But performed

Table 23. Group-weighted factors for total number of fission calculation (in energy column is fission rate value)

Energy of Secondary Neutrons	0.7 GeV	Energy of protons		
		1.0 GeV	1.5 GeV	2.0 GeV
Weight for ^{239}Pu				
Epithermal	9.03E-01	9.00E-01	9.01E-01	9.00E-01
Resonance	8.45E-02	8.67E-02	8.56E-02	8.59E-02
Fast	1.27E-02	1.37E-02	1.37E-02	1.44E-02
Weight for ^{238}Pu				
Epithermal	2.91E-01	2.82E-01	2.85E-01	2.82E-01
Resonance	6.05E-01	6.08E-01	6.04E-01	6.02E-01
Fast	1.04E-01	1.10E-01	1.11E-01	1.15E-01
Weight for ^{237}Np				
Epithermal	1.28E-02	1.20E-02	1.22E-02	1.21E-02
Resonance	7.75E-01	7.69E-01	7.65E-01	7.59E-01
Fast	2.12E-01	2.19E-01	2.22E-01	2.29E-01
Weight for ^{241}Am				
Epithermal	1.89E-01	1.79E-01	1.82E-01	1.81E-01
Resonance	6.04E-01	6.06E-01	6.00E-01	5.95E-01
Fast	2.07E-01	2.14E-01	2.18E-01	2.24E-01

such calculation we obtained little bit higher $\chi^2_{<}$ than χ^2 for $j = 3$ energy neutron region. All observed residual nuclei from ^{237}Np fission have different mass number A , it means that all decay chains of nuclei followed to observed residual nuclei r do not partly cover. Then we can pass from cumulative yield $Y_{\text{cum}}(t,r)$ to corresponding sum of independent yield $\sum_r Y_{\text{ind}}(t,r)$, see Table 11, and from sum of observed independent yields one find the total reaction rate for all residual nuclei and from them the reaction rate of fission. There is know that the sum of independent yields is not identical with corresponding cumulative yield and the relation between them depend on half-live of nuclei in decay chain [4]. The differences between cumulative and sum of independent yields for observed residual nuclei of ^{237}Np are negligible except for $r=^{133}\text{I}$, see Table 11. For ^{239}Pu were identified several residual nuclei with the same mass number A :



In these cases when we pass from cumulative to sum of independent yields, several independent yields appear two times, but we must accept only one value, of course. The total number of fission per one proton per one target nuclei is now obtained by more sophisticated way, see Table 12. However, values are very close each other.

Reaction rates of $^{237}\text{Np}(n,\gamma)$ and $^{237}\text{Np}(n,f)$ were calculated by means of neutron flux estimated in corresponding boxes see Table 2 and cross-section value given in library JEFF3.1 [8], see Table 24. It is necessary underline that library data are finished at $E_n = 20$ MeV and when cross-section is high at upper energy we can received sensitive uncertainty in calculation result. From Table 24 and also from Figures 14, 15, and 16 more or less good agreement is placed between experimental and calculation R value for $^{237}\text{Np}(n,\gamma)$ reaction for all

Table 24. Comparison of experimental and calculation reaction rates, $r = R_{\text{calc}}/R_{\text{exp}}$

Reaction	E_p [GeV]	0.7	1.0	1.5	2.0
^{237}Np	$R(\text{cal})$	6.74E-26	1.13E-25	1.66E-25	2.04E-25
	$R(\text{exp})$	5.61(24)E-26	1.51(5)E-25	1.40(3)E-25	1.33(3)E-25
	r	1.20	0.75	1.19	1.53
^{237}Np	$R(\text{cal})$	4.24E-27	7.75E-27	1.25E-26	1.71E-26
	$R(\text{exp})$	2.2(4)E-26	3.2(8)E-26	4.2(6)E-26	3.0(5)E-26
	r	0.19	0.24	0.30	0.56
^{239}Pu	$R(\text{cal})$	1.21E-25	2.11E-25	3.12E-25	3.90E-25
	$R(\text{exp})$	5.5(7)E-26	4.8(5)E-26	5.4(3)E-26	7.1(5)E-26
	r	2.20	4.40	5.78	5.50
^{241}Am	$R(\text{cal})$	5.90E-27	1.08E-26	1.60E-26	2.03E-26
	$R(\text{exp})$				< 1.4E-25
	r				> 0.15

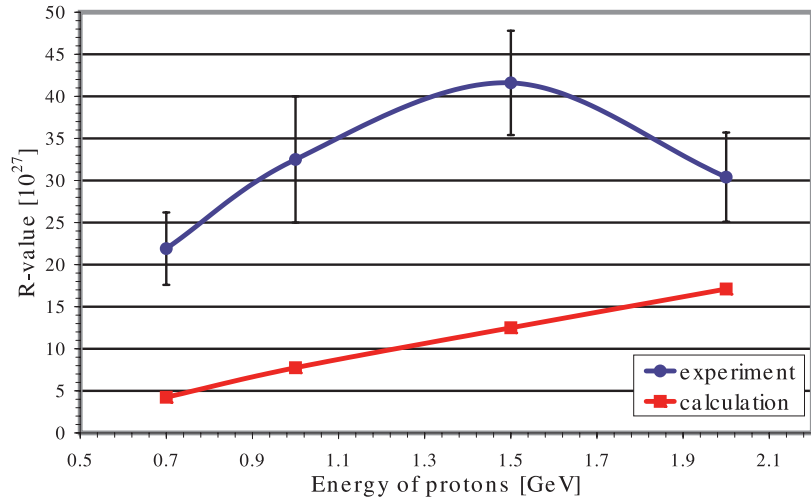


Figure 14. Reaction rate of $^{237}\text{Np}(n,f)$

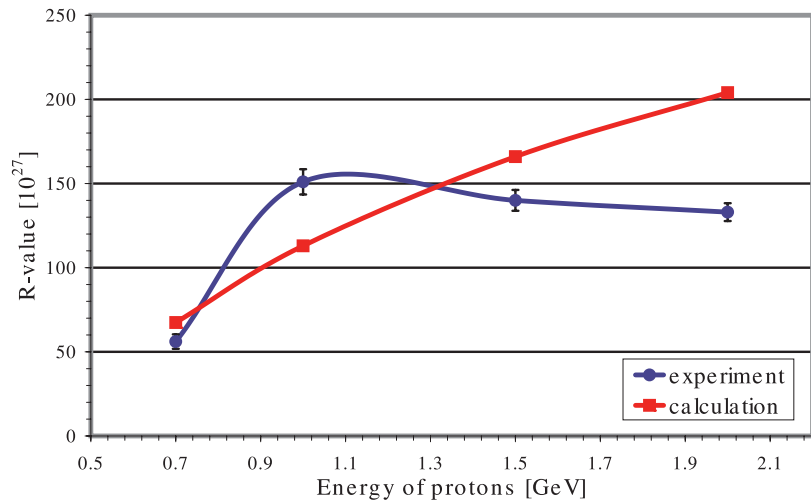


Figure 15. Reaction rate of $^{237}\text{Np}(n,\gamma)$

incident proton energy. But the dependence of these reaction rates on incident proton energy is not linear. Experimental values R_{fission} for ^{237}Np are 5 to 2 times higher than calculated for $E_p = 0.7$ GeV to $E_p = 2.0$ GeV. The average ratio $\left(\frac{R_\gamma}{R_f}\right)_{\text{exp}}$ is 3.39(44) for our four experiments, but these calculation ones change monotonically from 15.9 to 11.9 with increasing energy of bombardment protons.

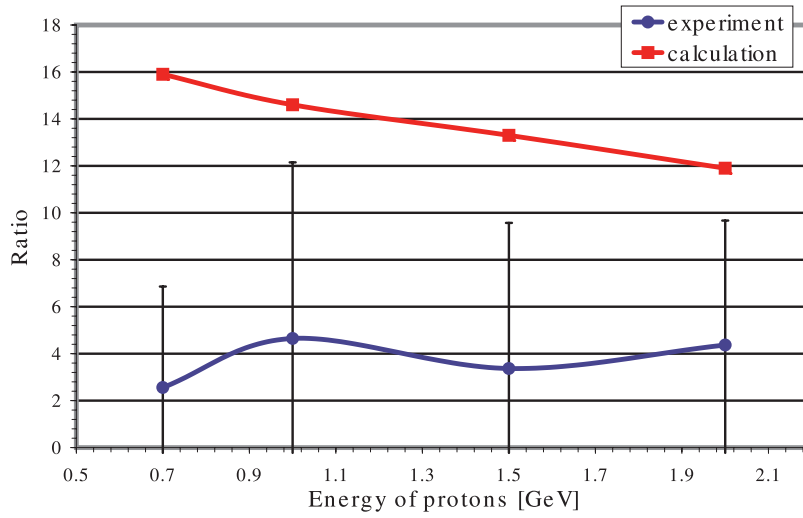


Figure 16. Ratio of reaction rates $R(n,\gamma)/R(n,f)$

4 Conclusion

A large number of absolute nuclide production yields (termed as R -values) from stable as well as highly radioactive samples were measured on the “E+T” setup for primary proton kinetic energies in the range $0.7 \text{ GeV} < E_p < 2 \text{ GeV}$. The data may serve as a viable database for the adjustment of theoretical model computer codes and to compare calculated results for experimental findings. “Energy + Transmutation” is a unique facility and its potential should be used to do as much experimental work as possible. Using the obtained data, we calculated transmutation of the radioactive samples, see Table 25, in which we took 10 mA current of the accelerator and irradiation of 30 days. The experimental results presented are the first results of plutonium transmutation at “Energy+Transmutation” target-blanket system. Comparable experimental results with deuterons and “E+T” are soon expected.

Table 25. Incineration of radioactive nuclei [%] with secondary neutrons produced in “E+T” setup using protons with various energies and hypothetical current 10 mA

Radioactive Isotope	0.7 GeV	1.0 GeV	1.5 GeV	2.0 GeV
Incineration in 30 days [%]				
^{237}Np	1.64	3.53	3.66	3.18
^{238}Pu	–	0.34	–	1.42
^{239}Pu	0.91	0.79	0.90	1.17
^{241}Am	–	–	–	< 2.6

Acknowledgement

The authors are grateful to the operating crew of the “Nuclotron” accelerator of LHE, JINR Dubna for irradiation and good beam parameters, and the Dr. Vera Bradnova for the experiment’s minutes managing and photographic support. Part of this work has been supported by the International Science and Technical Center grant No.1372, the other parts by other grants and variable funding.

References

- [1] Krivopustov, M.I., Chultem, D., Adam, J. *et al.* (2003) *Kerntechnik* **68** 48–55.
- [2] Frana, J. (2003) *J. Radioanal. Nucl. Chem* **257** 583–589.
- [3] Adam, J., Pronskikh, V.S., Balabekyan, A.R. *et al.* (2000) *Preprint JINR P10-2000-28*, Dubna.
- [4] Adam, J., Balabekyan, A.R., Pronskikh, V.S. *et al.* (2002) *Applied Radiation and Isotopes* **56** 607–613.
- [5] Wan, J.S., Ochs, M., Vater, P. *et al.* (1999) *NIM* **B155** 110–115.
- [6] Westmeier, W., Brandt, R., Langrock, E.-J. *et al.* (2005) *Radiochem. Acta* **93** 65–73.
- [7] Wagner, V (2006) Unpublished talk from Jaipur conf.
- [8] Experimental Nuclear Reaction Data (EXFOR) IAEA-NDS;
[http://www-nds.iaea.org\(exfor\)](http://www-nds.iaea.org(exfor)).

A study of nuclear transmutation of Th and ^{nat}U with neutrons produced in a Pb target and U blanket irradiated by 1.6 GeV deuterons

J. Adam^{1,2,a}, K. Katovsky^{1,3}, M. Majerle², M.I. Krivopustov¹, V. Kumar⁴, Chitra Bhatia⁴, Manish Sharma⁴, A.A. Solnyshkin¹, and V.M. Tsoupko-Sitnikov¹

¹ Joint Institute for Nuclear Research, Dubna near Moscow, 141 980, Russian Federation

² Czech Academy of Science, Nuclear Physics Institute, Řež near Prague, 250 68, Czech Republic

³ Department of Nuclear Reactors, Czech Technical University in Prague, Czech Republic

⁴ HENP Laboratory (ADS Program), Physics Department, University of Rajasthan, Jaipur, India

Received: 16 June 2009 / Revised: 23 November 2009

Published online: 16 January 2010 – © Società Italiana di Fisica / Springer-Verlag 2010

Communicated by R. Krücken

Abstract. The spallation lead target in the “Energy plus Transmutation” set-up, covered with uranium blanket, was irradiated by the 1.6 GeV deuteron beam from the Nuclotron accelerator at the Joint Institute for Nuclear Research in Dubna. The neutrons generated in the subcritical uranium blanket are used to activate the radioactive uranium and thorium samples outside the blanket. Rates of the (n, γ) , (n, f) and $(n, 2n)$ reactions are determined for some residual nuclei. The ratio of the reaction rates $R(n, 2n)/R(n, f)$ is estimated to be 27(9)%. Contributions of the neutrons with energy $E_n > 20$ MeV to the (n, f) reaction rate is $\sim 57\%$ for ^{232}Th and $\sim 37\%$ for ^{nat}U , respectively. To compare with the experimental results, the reaction rates are simulated by generating the neutron fluxes employing two different models, the beam shapes by the MCNPX 2.6.c code and making use of the appropriate libraries of cross-sections. The transmutation power of the set-up is estimated using the average (n, γ) and $(n, 2n)$ reaction rates and compared with some of the results of the TARC experiment.

1 Introduction

The availability of high-energy spallation neutrons broadens the scope of possible investigations related to modification of the fuel cycles, transmutation, multi-fragmentation of the fuel elements, simulation of radiation damage and development of radiation resistant materials, in particular in a context of the design and development of Accelerator Driven Subcritical Systems (ADS) for the transmutation of long-lived nuclear waste (LLNW) from conventional reactors and nuclear weapons [1–3]. It is important that in the ADS a very high neutron flux is available both for the transmutation and for the energy production [4]. Recall that in the mixed environment of low- and high-energy neutrons in the ADS, the role of (n, xn) reactions in i) neutron multiplication, ii) energy production, and iii) incineration of the radioactive nuclides, like ^{239}Pu from ^{nat}U and ^{233}U from ^{232}Th , is enhanced. Thus, the neutron economy is expected to be different in the ADS compared to a conventional critical reactor. Thus, there is a renewed interest in measurements of the cross-sections and the reaction rates of (n, γ) , (n, f) and (n, xn) reactions [5], motivated

also by a need of better understanding (n, xn) reactions with $x > 2$ and cross-sections for the design of ADS and the medical applications. This inspired the PDS-XADC [6] program in Europe and some nuclear countries like USA, Russia, France, Japan and India have also laid down their road maps [7] for the development of the ADS. Many other countries have also initiated their experimental and theoretical activities in this direction.

These days the high-energy beams of neutrons are available at CERN [8] for measurements of point cross-sections with high precision. The n-TOF facility at CERN has been in operation for the last 8 years. This facility makes possible a systematic and very precise study of neutron-induced reactions in the energy range from 1 eV to 250 MeV and has provided measurements of cross-sections of the capture and fission reactions on a large number of samples including ^{232}Th , $^{233,234,235,236,238}\text{U}$, ^{237}Np , $^{241,243}\text{Am}$ and ^{245}Cm (the data analysis of these measurements is in progress). Useful information about the design parameters, such as the transmutation power of the ADS, can be derived from the measured reaction rates. Using such data, methods of estimating the transmutation power of ADS-like systems can be developed and employed to understand their potential to transmute the

^a e-mail: iadam@jinr.ru

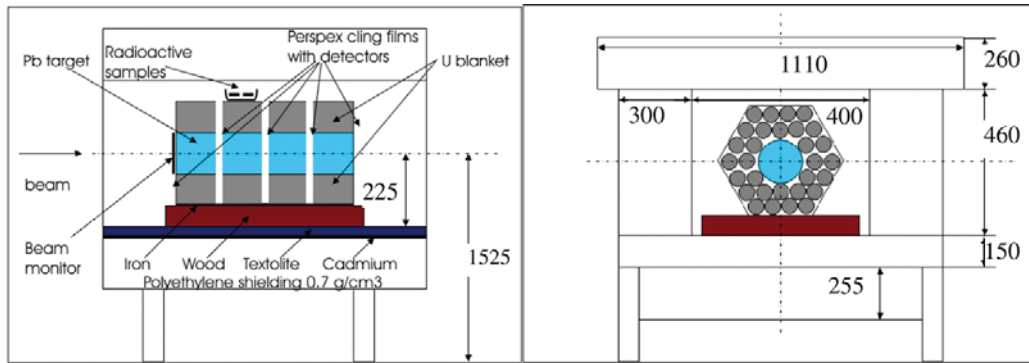


Fig. 1. Simplified front and side views of the “Energy plus Transmutation” set-up inside its shielding as used in our experiment. Under the uranium assembly layers of 1 cm thick iron, 9 cm thick wood and 3 cm textolite are used for strong base. On four sides of the assembly a layer of 1 mm thick cadmium is used for stopping thermal neutrons. This is followed by a thick layer of the polyethylene grains.

LLNW and to utilize the fertile fuel for the energy production. For the physics studies of the ADS, the experiment of Transmutation by Adiabatic Resonance Crossing (TARC) [9] has been conducted, in which the spallation neutrons were moderated in the resonance region by a huge lead assembly to achieve a high transmutation rate. Similarly, in another experiment known as “Energy plus Transmutation”, ($E+T$) [10] at JINR, Dubna, both moderation and amplification of the spallation neutrons takes place inside the uranium blanket around the spallation target. In the experiments with $E+T$ assembly, a deuteron beam is used which has an advantage of getting more secondary neutrons, even with an energy comparable to the beam energy.

In the present paper, the method of estimating the transmutation power of a system from the measured reaction rates of the residual radioactive nuclides of the (n, γ) , (n, f) and (n, xn) reactions is described. The experimental results of transmutation power of ^{232}Th and $^{\text{nat}}\text{U}$ in the “ $E+T$ ” set-up have been obtained and compared with some of the results of the TARC experiment. Recall that the basic differences in the two experiments are the deuteron beam and the uranium blanket in the “ $E+T$ ” set-up compared to the proton beam and a huge lead moderator in the TARC experiment. Experimental results of the average reaction rates are also compared with the results of simulations employing the MCNPX Monte Carlo code.

In sect. 2 a description of the experimental “ $E+T$ ” set-up and the deuteron beam profile are given in brief. Section 3 presents the procedure of measurements and method of analysis and sect. 4 summarizes our experimental results. Simulations by Monte Carlo codes and discussions of the results and conclusions are in sects. 5 and 6, respectively.

2 Experimental set-up and beam intensity

The “Energy plus Transmutation” set-up (figs. 1, 2) is a system of the lead target and the uranium blanket [10]. The total length of its four sections is 480 mm, the length



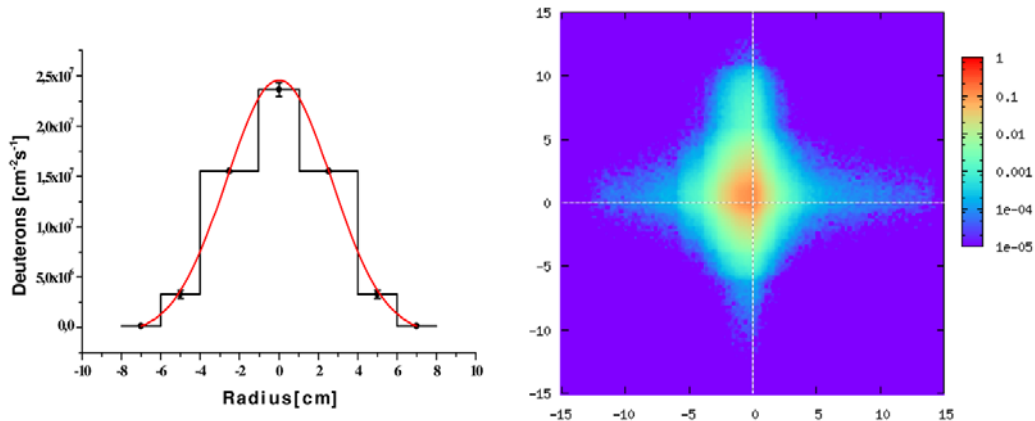
Fig. 2. Top view of the “Energy plus Transmutation” set-up with radioactive samples placed on top of it. Beam enters from the left side. The samples shown in this figure are assumed to occupy a volume of $36 \times 36 \times 1.5 \text{ cm}^3$ for the sake of simulation by MCNPX.

of the lead target is 456 mm. The diameter of the lead is 84 mm and its total mass is 28.7 kg. The blanket contains four sections (see fig. 1). Each section contains 30 uranium rods and each rod is enclosed in an Al shell. The total mass of each section is 51.6 kg of natural uranium, so the whole blanket mass is 206.4 kg. Between each two sections there are gaps of 8 mm, into which experimental instruments and detectors may be inserted. Details of the design of the set-up are discussed at length by Barashenkov *et al.* [11].

On the top of the second section of the blanket our $^{\text{nat}}\text{U}$ and ^{232}Th samples, a set of other radioactive samples (^{129}I , ^{238}Pu , ^{239}Pu and ^{237}Np) and threshold detectors have been placed. The distance d of the ^{232}Th sample from the center of our set-up is 13.1 cm. Our irradiated uranium and thorium samples were in the form of sandwiches of three identical foils (Th-Th-Th and U-U-U). This arrangement has an advantage of accounting for the recoiling residual nuclei produced in the middle foil. The diameter of these foils is 15 mm and the weight of middle U and Th foils is 172 mg and 93.2 mg, respectively. The “Energy plus Transmutation” set-up was irradiated by the deuteron beam with an energy of 1.6 GeV at the

Table 1. Deuteron beam ($E_d = 1.6$ GeV) profile determined using three concentric rings and a central disc of Al monitor.

i -th Al foil	$D(i)$ [cm]	Weight [mg]	$Q(^{24}\text{Na})$ [s^{-1}]	Activity [Bq]	N_d [s^{-1}]	N_d/S [cm^{-2}]	Flux [$N_d \text{ cm}^{-2} \text{ s}^{-1}$]
1	2.1	24	196(6)	60.41	8.18E+07	5.66E+11	2.36E+7
2	8.0	318	1735(42)	534.6	7.24E+08	3.70E+11	1.55E+7
3	12.0	428	496(13)	152.5	2.07E+08	7.89E+10	0.33E+7
4	16.0	598	28(2)	8.6	1.17E+07	3.18E+9	1.33E+5

**Fig. 3.** Results of the beam profile measurements. On the left-hand side, the average flux density is given in deuterons/ cm^2/s (see last column of table 1). On the right-hand side the “real” beam profile received from one track detector is shown.

Nuclotron accelerator in Dubna. The irradiation was performed in December 2006 and lasted roughly 400 minutes.

The total number of deuterons hitting the lead target is obtained from thin aluminum monitors, which are processed by the standard gamma spectrometry method. The Al monitor contains a stack of three thin aluminum foils of thickness $6.6975 \text{ mg} \cdot \text{cm}^{-2}$ each. The central foil was used to register the recoiling product nuclei. The stack of Al foils was mounted approximately 60 cm before the Pb target in order to avoid activation from backscattered particles and neutrons [12]. For monitoring purpose the reaction $^{27}\text{Al}(d, 3p2n)^{24}\text{Na}$ was used. The value of production cross-sections for ^{24}Na at high energies are available for 2.33 GeV [13], 6 GeV and 7.30 GeV deuteron energies [14] and they are $15.25 \pm 1.5 \text{ mb}$, $14.1 \pm 1.3 \text{ mb}$ and $14.7 \pm 1.2 \text{ mb}$, respectively. At relativistic energies two nucleons in deuteron behave approximately as two separate entities [15]. Thus, the ratio of experimental values of $\sigma(^{27}\text{Al}(1.165 \text{ GeV/A } d, 3p2n)^{24}\text{Na})/\sigma(^{27}\text{Al}(1.165 \text{ GeV } p, 3pn)^{24}\text{Na})$ is 1.495. In the same way, for the deuteron energy 0.8 GeV/A we got $\sigma(^{27}\text{Al}(0.8 \text{ GeV/A } d, 3p2n)^{24}\text{Na})$ to be 16.03 mb, taking the measured value for the proton cross-section to be $\sigma(^{27}\text{Al}(0.81 \text{ GeV } p, 3pn)^{24}\text{Na}) = 10.07(20) \text{ mb}$ [16]. The Al foil was cut into 3 concentric rings with external diameters of 80, 120, and 160 mm and a central disc with a diameter of 21 mm. We measured these rings and the central disc in order to determine their activities for deducing the corresponding beam intensity and beam profile (see table 1 and fig. 3).

The values of the rate production $Q(^{24}\text{Na})$ given in table 1 were corrected for fluctuations in the beam inten-

sity ($\eta_B = 0.9865$) and for coincidence summing correction to be $\eta_C = 1.017$ for $E_\gamma = 1368 \text{ keV}$ and $\eta_C = 1.053$ for $E_\gamma = 2754 \text{ keV}$. The error in deuteron fluency corresponds only to statistical error in the calculation of the $Q(^{24}\text{Na})$ value. This error would increase when the systematic error for the extrapolated values of cross-sections at lower energies is included, which we have not done here since only a few experimental data are available in the literature. In the absence of data for the 0.8 GeV/A deuteron energy we assumed that the error does not exceed 10%. The final values of the integral beam intensity are given in table 2, the integral beam intensity N_D hitting the Pb target is $1.93(25) \cdot 10^{13}$.

The set of our Al monitor give us limited and rather rough information about the shape of the beam. The average flux densities of deuterons, see table 1, were fitted to the Gaussian profile with $\sigma(\text{FWMH}) = 5.16(16) \text{ cm}$, see the left side of fig. 3. A more precise analytical description of the beam shape was obtained from I.V. Zhuk. The 37 ^{nat}Pb foils ($0.7 \times 0.7 \times 0.03 \text{ cm}$) covered by fission-track detectors were irradiated by the deuteron beam in front of the lead target. The width parameters of the beam spot were determined from the data on a track density *versus* space coordinates of the centroid. The coordinates of the beam centroid are obtained as $x_c = -0.64(3) \text{ cm}$ and $y_c = 0.39(8) \text{ cm}$ with respect to the axis of the set-up with $x(\text{FWMH}) = 2.87(6) \text{ cm}$ and $y(\text{FWMH}) = 1.92(19) \text{ cm}$. The details of this method are given in [17]. These data are treated as the parameters of the “gauss” beam spot in the simulation of the flux by MCNPX. The shape of the beam shown on the right side of fig. 3 was used and call the “real” beam in simulations.

Table 2. Final values of deuteron beam intensity (N_d) and the integral number of deuterons (N_D).

i -th foils	N_d [1/s]	err. (N_d) [1/s]	N_D [integral]	err. (N_D) [integral]	Fraction of the sum
1 + 2	8.06E+08	2.00E+07	1.93E+13	4.80E+11	78.7(2)%
3 + 4	2.18E+08	5.74E+07	5.23E+12	1.37E+11	21.3(6)%
Sum	10.24E+08	7.74E+07	2.45E+13	6.17E+11	100%

We performed [18] simulations of the reaction rates for Au, Al, Bi thin metallic foils placed on top of the blanket. We found that the shape of the beam does not have significant effect, as long as it is parallel and symmetric around the target axis and the beam centre coincides with the target centre. However, calculations showed that a 2 mm inaccuracy in the beam centre can result in up to 15% inaccuracy in the $R(A_r, Z_r)$ values of the activation.

3 Measurement procedure and method of analysis

Neutrons produced in bombardment of the lead target by the 1.6 GeV deuteron beam are multiplied and moderated in the U blanket. The escaping secondary neutrons activate the samples of ^{nat}U and ^{232}Th and the reaction products are identified by using the gamma spectrometry. The gamma-ray measurements have been performed using the HPGe detectors. We have used the coaxial detector with a relative efficiency of 18.9% and a resolution of 1.78 keV at 1332 keV and a planar detector with diameter 36 mm, thickness 13 mm with resolution 335 eV at 5.9 keV and 580 keV at 122 keV. All measurements have been carried out without any filters. First measurements of the samples were started 2.4 hours after the irradiation had stopped. The measurement times varied from 0.5 to 24 hours. All measurements have been performed within 29 days. Under these conditions, only those residual nuclei can be studied which have half-life in the range of half an hour to one month. A coaxial detector is used to provide information of peaks ranging from 20 keV to 3 MeV and a planar detector is used for ~ 5 keV to 700 keV.

The processing of the measured data of gamma rays was performed in the interactive mode of the DEIMOS code [19]. Energy calibration, subtraction of background gamma-ray lines and single and double escape peaks, efficiency calibration and determination of experimental half-lives were made by the analysis codes described in [20,21]. Hundreds of gamma-ray lines were analyzed. The identification of nuclei was made when the energy, half-life and intensity of peaks agreed with the corresponding values in the data library [22].

The possibility of the identification of residual nuclei with mass and atomic number A_r and Z_r from measurements of the gamma rays depends on the activity of the residual nuclei and on the gamma-ray intensity per decay $I_\gamma(j)$. The indices j denote the different gamma rays emitted by given nuclei with A_r , Z_r . Since different reactions result in the production of residual nuclei with different

decay constants $\lambda(A_r, Z_r)$, we measured each irradiated sample several times, and these gamma spectra are labeled by indices i ($i = 1, 2, 3, \dots$). In the case of the Al monitor and the ^{nat}U and ^{232}Th samples the production rate $Q(A_r, Z_r, i, j)$ for a given j -gamma-ray following the beta decay of the respective radioactive nucleus A_r , Z_r and for the measured i spectrum, can be determined from the following relation:

$$Q(A_r, Z_r, j, i) = \frac{S(j, i)\eta_A(Z_t, j)\eta_B(\lambda)\eta_C(j)\eta_D e^{\lambda t_2(i)} t_{\text{real}}(i)}{\varepsilon_\gamma^{\text{abs}}(j)I_\gamma(j)(1 - e^{-\lambda t_1(i)})(1 - e^{-\lambda t_{\text{real}}(i)}) t_{\text{live}}(i)}, \quad (1)$$

where t_1 , $t_2(i)$, $t_{\text{real}}(i)$ and $t_{\text{live}}(i)$ are the irradiation, cooling, real, and live measurement times. The time $t_{\text{live}}(i)$ is defined from the relation $t_{\text{live}}(i) = t_{\text{real}}(i) - \text{dead time}(i)$, where the dead time (i) is that part of the real time (i) in which the gamma-spectrometer counted no gamma rays registered by the HPGe detector. The coefficient $\eta_A(Z_t, j)$ accounts for the self-absorption of gamma ray in the sample with Z_t . The $\eta_B(\lambda)$ is the correction for the fluctuation of the beam intensity and it is determined for each residual product nucleus. The coefficient $\eta_C(j)$ is the coincidence summing correction and the η_D is the correction for non-point geometry of the measured sample. More detailed explanation of all of these corrections is given in the appendix.

The average value $Q(A_r, Z_r, i)$ for the i -th spectrum is calculated as the weighted mean value of $Q(A_r, Z_r, i, j)$ for different gamma transitions j . The final $Q(A_r, Z_r)$ value is obtained in the same way from all the i spectra. This procedure is applied both to Al monitor and the samples of ^{nat}U and ^{232}Th .

From the Al monitors, the numbers of incident deuterons per second N_d [s^{-1}] is obtained from the following relation:

$$N_d = \frac{Q(A_r, Z_r)}{\sigma(A_r, Z_r)N_S}. \quad (2)$$

Here, $\sigma(A_r, Z_r)$ is the reaction cross-section [cm^2], N_S is the number of atoms on the surface of the target [atoms/cm^2]. It is assumed that all atoms N_t along the thickness are subjected to an interaction with a projectile. $N_t = S \cdot N_S$, where S is the surface area [cm^2].

The absolute rates $R(A_r, Z_r)$ of the independent and cumulative reactions in different ^{nat}U and ^{232}Th samples were determined as the ratio of the number of produced residual nuclei A_r , Z_r per seconds, per the number of atoms of the sample N_t and per the number of incident

Table 3. Results of the analysis of the gamma-ray spectra of ²³²Th after irradiation by secondary neutrons from $E_d = 1.60$ GeV. All corrections are included. (+) denotes mixing due to other nuclides.

Isotope Energy [keV]	Activity [Bq] I_γ [%]	$T_{1/2}$ (Library) $T_{1/2}$ (exp.)	Full corr. $= \eta_A \eta_B \eta_C$	$\langle R \rangle$ $R(A_r, Z_r \cdot j)$	Number of spectra
Th-231	56.3(56)	25.520(10) h		1.60(16)E-27	
25.646	14.50	27 h	3.1786	1.53(20)E-27	2-X
81.227	0.89		1.1444	7.1(17)E-27	1-X (+)
84.216	6.60	29 h	1.0660	1.72(25)E-27	2-X
89.944	0.94	13(4) d	1.0905	1.21(25)E-26	3-X (+)
Pa-233	42.1(14)	26.967(2) d		3.03(10)E-26	
75.354	1.39		1.1385	2.09(46)E-25	1-X (+)
86.814	1.97		1.1117	2.9(13)E-26	1-X
103.941	0.87	23(10) d	1.0851	3.83(32)E-26	5-X
300.110	6.62	19(9) d	1.0175	2.69(25)E-26	5-X
300.110	6.62	23(3) d	1.0151	2.83(18)E-26	5-C
311.890	38.6	33.5(27) d	1.0228	3.35(15)E-26	6-X
311.890	38.6	28.2(8) d	1.0171	3.14(15)E-26	5-C
340.710	4.47	23(8) d	1.0121	2.89(25)E-26	5-X
340.710	4.47	25(4) d	1.0110	2.70(17)E-26	5-C
375.450	0.679	20(8) d	0.9792	5.1(16)E-26	2-C
398.620	1.390	16(3) d	0.9228	4.47(46)E-26	5-C (+)
415.760	1.745	17(3) d	0.9680	2.84(27)E-26	5-C
Mo-99	1.04(12)	2.7475(4) d		7.63(89)E-29	
140.681	89.43	2.9(26) d	1.0760	8.4(13)E-29	3-X
140.681	89.43	2.6(17) d	1.0770	6.9(13)E-29	3-C

deuterons N_d . For the theoretical calculation of the reaction rate we have used the relation

$$R(A_r, Z_r) = \int_{E_{\text{thr}}(A_r, Z_r)}^{\infty} \sigma(A_r, Z_r, E_n) \cdot \Phi(E_n) dE_n. \quad (3)$$

Here, $\Phi(E_n)$ is the neutron flux passing through the sample and expressed as neutrons/cm²/MeV/deuteron, E_{thr} is the threshold neutron energy of the given reaction.

The transmutation power $P(A_r, Z_r)$ may be defined as the quantity of produced masses $m(A_r, Z_r)$ per unit mass of the target $m(A_t, Z_t)$. In ref. [9] it is called the transmutation rate and is expressed in terms of the normalized activity $a(A_r, Z_r)$ (without accounting for the decay of (A_r, Z_r) nuclei during the irradiation) as follows:

$$P(A_r, Z_r) = \frac{A_r \cdot a(A_r, Z_r)}{\lambda(A_r, Z_r) m(A_t, Z_t) N_{\text{avo}}}, \quad (4)$$

where N_{avo} is the Avogadro constant. Alternatively, we can deduce from relation (4) a relation for $P(A_r, Z_r)$ in terms of the reaction rate

$$P(A_r, Z_r) = R(A_r, Z_r) \cdot N_d \frac{A_r}{A_t} \cdot t_{\text{irr}}. \quad (5)$$

The normalized transmutation power for 10^9 beam particles can be expressed as $P_{\text{norm}}(A_r, Z_r) = 10^9 P(A_r, Z_r) / N_D$. Here N_D is the integral number of deuterons ($N_D = N_d \cdot t_{\text{irr}}$).

4 Experimental results

Detailed results of gamma-ray measurements from activated ²³²Th and ^{nat}U are given in tables 3 and 4. The data in bold correspond to the upper variable of the heading which is also shown in bold. In the last column, numbers correspond to the spectra from which the gamma ray was observed, the letter X denotes the planar detector and the letter C the coaxial detector. The plus sign in brackets (+) indicates that the given gamma line is a doublet, *i.e.*, its intensity is a sum of two gamma rays following the beta decay of different isotopes.

The following observations concern the results given in tables 3 and 4:

- i) The total correction $\eta = \eta_A \eta_B \eta_C$ is higher than unity for low E_γ , *e.g.*, it is 3.17 for $E_\gamma = 25.65$ keV for ²³¹Th. The major factor responsible for the large value of η is the self-absorption correction (η_A), which is equal to 3.03. For high-energy gammas, η_A drops, *e.g.*, for $E_\gamma \sim 300$ keV it is $\eta_A \sim 1.01$ for ²³²Th and $\eta_A = 1.02$ for ^{nat}U.

The summing correction η_C depends on the decay scheme of the product. For example, its highest value is 1.269 for $E_\gamma = 954.55$ keV in the decay of ¹³²Te.

The beam correction η_B is close to 1 in the case of the residual nucleus with higher half-life, *e.g.*, for ¹³⁵I

Table 4. Results of the analysis of the gamma-ray spectra of ^{nat}U after irradiation with secondary neutrons from $E_d = 1.60$ GeV. All corrections are included. (+) denotes mixing due to other nuclides.

Isotope Energy [keV]	Activity [Bq] I_γ [%]	$T_{1/2}$ (Library) $T_{1/2}$ (exp.)	Full corr. $= \eta_A \eta_B \eta_C$	$\langle R \rangle$ $R(A_r, Z_r \cdot j)$	Number of spectra
Np-239	849(40)	2.3565(4) d		2.97(14)E-26	
106.125	27.2	2.388(15) d	1.121	2.67(12)E-26	6-X
106.125	27.2	2.39(6) d	1.110	2.64(16)E-26	3-C
209.753	3.42	2.36(5) d	1.130	3.77(17)E-26	5-X
209.753	3.42	2.44(10) d	1.092	3.56(21)E-26	3-C
228.183	10.76	2.45(6) d	1.140	3.50(15)E-26	6-X
228.183	10.76	2.49(4) d	1.050	3.36(21)E-26	3-C
277.599	14.38	2.35(3) d	1.099	2.91(13)E-26	5-X
277.599	14.38	2.45(9) d	1.064	2.96(21)E-26	3-C
315.879	1.60	1.8(3) d	0.933	3.04(25)E-26	4-X
315.879	1.60	2.30(12) d	0.938	2.81(25)E-26	2-C
334.309	2.07	2.04(14) d	0.837	2.47(21)E-26	5-X
334.309	2.07	3.2 d	0.843	2.03(20)E-26	2-C
Mo-99	14.1(16)	2.7475(4) d		5.74(65)E-28	
140.681	89.43	2.72(9) d	1.151	6.05(32)E-28	5-X
140.681	89.43	3.00(15) d	1.152	4.78(36)E-28	4-C
181.063	5.99	0.8 d	1.106	1.61(28)E-27	2-X
181.063	5.99		1.148	1.05(19)E-27	1-C
739.500	12.13	1.6 d	1.117	7.7(11)E-28	2-C
Te-132	11.5(10)	3.204(2) d		5.46(46)E-28	
49.720	15.0	4.7(11) d	1.793	8.3(8)E-28	6-X
49.720	15.0		1.739	2.3(7)E-27	1-C
228.160	88.0	2.45(6) d	1.068	3.11(15)E-27	6-X (+)
228.160	88.0	2.49(4) d	1.059	1.26(9)E-27	4-C (+)
522.650	16.6	8(4) d	1.286	5.7(9)E-28	3-C
630.190	13.3		1.157	3.9(11)E-28	1-C
667.72	101.7	2.47(29) d	1.123	5.5(4)E-28	3-C
772.61	77.9	3.4(5) d	1.096	4.9(4)E-28	3-C
954.55	18.7	4.0(21) d	1.229	5.2(7)E-28	3-C
I-133	35(18)	20.8(1) h		3.2(16)E-28	
529.87	86.3	14.4 h	0.998	5.1(7)E-28	2-X
529.87	86.3	20 h	0.998	1.78(22)E-28	2-C
I-135	175(14)	6.57(2) h		7.13(57)E-28	
546.557	7.20		1.039	8.0(19)E-28	1-C
1131.511	22.74		1.029	7.2(12)E-28	1-C
1260.409	28.90		0.986	7.0(11)E-28	1-C
1457.560	8.73		0.973	5.3(15)E-28	1-C
1678.027	9.62		0.940	8.5(17)E-28	1-C
1791.196	7.77		0.973	7.5(15)E-28	1-C
Xe-135	152(58)	9.14(2) h		8.6(38)E-28	
249.760	89.9	16.6(33) h	1.010	5.8(23)E-28	3-X
249.760	89.9	10.7(10) h	1.010	1.37(32)E-27	2-C
Ba-140	3.38(10)	12.752(3) d		6.40(19)E-28	
29.964	14.1		3.978	1.4(5)E-27	1-X
328.762	20.3	30(40) d	1.210	9.9(55)E-28	3-C

Table 4. Continued.

Isotope Energy [keV]	Activity [Bq] I_γ [%]	$T_{1/2}$ (Library) $T_{1/2}$ (exp.)	Full corr. $= \eta_A \eta_B \eta_C$	$\langle R \rangle$ $R(A_r, Z_r \cdot j)$	Number of spectra
487.021	45.5	18(11) d	1.108	6.20(59)E-28	3-C
537.261	24.39	17(5) d	1.021	8.9(55)E-28	4-C
1596.210	95.4	11.5(20) d	1.131	6.41(20)E-28	5-C
Ce-143	24.5(54)	33.039(6) h		5.0(11)E-28	
57.356	11.7	32.4 h	1.448	8.7(10)E-28	2-X
57.356	11.7		1.450	6.3(19)E-28	1-C
293.266	42.8	33.6 h	1.049	6.0(8)E-28	2-X
293.266	42.8	103(36) h	1.039	2.8(6)E-28	4-C
664.571	5.69	60 h	1.000	6.9(25)E-28	2-C

($T_{1/2} = 6.57$ h) $\eta_B = 0.97$ and for ^{132}Te ($T_{1/2} = 3.2$ d) $\eta_B = 0.997$.

- ii) Results of the reaction rate R are fairly consistent and complementary for all gamma energies for the given radioactive nuclide. Similarly, results obtained for coaxial or planar detectors are also in close agreement with each other and this enhances confidence in the analysis of the product. Experimental values of half-lives of decay nuclides with errors are in reasonable agreement with the values available in the literature and this justifies our identification of residual nuclides.
- iii) We have observed seven fission products for ^{nat}U and only one fission product for ^{232}Th . To explain this, first notice that the calculated and experimental ratios of $R(\text{n, fission}; ^{nat}\text{U})/R(\text{n, fission}; ^{232}\text{Th}) \sim 4$, see table 6. Second, the ratio of the mass of ^{nat}U and of the ^{232}Th sample is about 2. Altogether, there may be a difference of one order of magnitude in the observation of the fission products from ^{nat}U and ^{232}Th .

5 Simulations by Monte Carlo codes and discussion of results

In this section simulations of the neutron fluxes and of the reaction rates of the produced nuclides are performed with utmost care of the models available with the codes and the beam characteristics. The Monte Carlo code MCNPX v2.6.c [23] is used to simulate the production and transport of secondary particles in the set-up. The particle production is handled by several spallation models, which describe the reaction in two steps, *i.e.*, an intra-nuclear cascade with a pre-equilibrium stage (INC) and with an evaporation stage (EVAP). Two combinations of newer models (out of several included in MCNPX) are used in the simulation, *i.e.*, i) CEM03, INC with CEM03 EVAP [24] and ii) INCL4, INC [25] with ABLA EVAP models [26, 27].

The “ $E + T$ ” set-up was implemented in the code with the parameters given in fig. 1 and the beam parameters (displacement and profile) determined from a set of SSNTD [17] and one track detector. The data from these detectors were fitted by the Gaussian profile with σ_x (FWMH) = 2.87 cm and σ_y (FWMH) = 1.92 cm with beam centroid at $x_c = -0.64$ cm and $y_c = 0.39$ cm in the

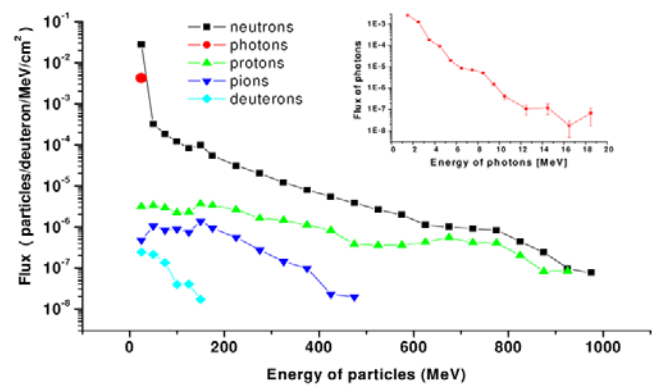


Fig. 4. The simulated neutron, photon, proton, pion and deuteron spectra on top of the second section of our set-up using the INCL model and real beam. The insert is a spectrum of photons with energies from 0 to 20 MeV.

simulations and referred to as “gauss”. Similarly, where the track density from the SSNTD detector is used in the definition of the beam profile then it is referred to as “real”, see fig. 3 (right side).

For the purpose of simulations, the area above the second section containing the samples was divided into four boxes (labeled by 1, 2, 3, 4) along the central line with dimensions of $36 \times 36 \times 1.5 \text{ mm}^3$, see fig. 2, and the fluxes of neutrons, photons, deuterons, pions and protons are calculated for each cell in units of particles/MeV/cm². An example of the simulated spectra is shown in fig. 4, in which the total flux of neutrons is $2.86\text{E-}2$ neutrons/cm²/deuteron. The proton flux is 1000 times lower and the fluxes of pions, deuteron and photon are $2\text{E}+4$, $5\text{E}+5$ and 5 times lower than the neutron flux, respectively. In fig. 5 the ratio of the neutron flux in box 3 to the box 4 for the two cases of simulation —a) INCL + real beam and b) CEM + real beam, is displayed. Although the difference between these ratios lies within the statistical uncertainties, we can see that the ratio $\Phi(E_n(\text{box } 3))/\Phi(E_n(\text{box } 4))$ has a wide maximum of ~ 1.3 in the energy range $E_n > 0.2$ MeV. In the thermal energy region the high peak corresponding to the INCL + real beam compared to the values of the CEM + real beam has no meaning; it is due to very large

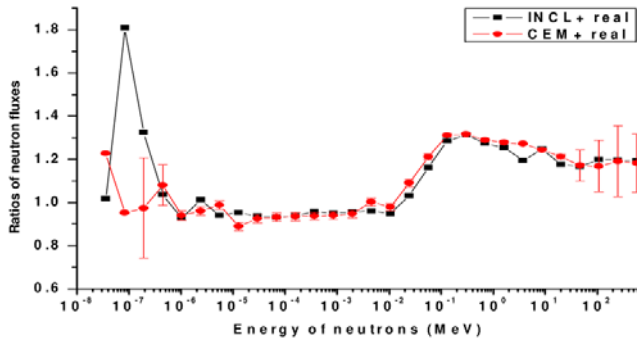


Fig. 5. Ratio of neutron fluxes in box 3 normalized to box 4 for two variants of simulations: INCL + real beam and CEM + real beam.

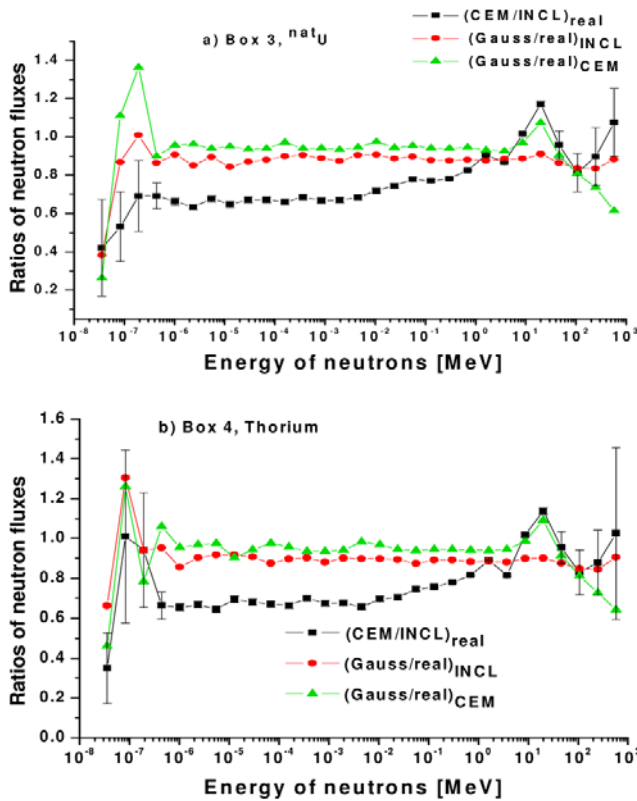


Fig. 6. Ratio of neutron flux simulated in box 3 (upper part of figure) and box 4 (lower part of figure) with different combinations of models and beam shapes. $(\text{CEM}/\text{INCL})_{\text{real}}$ marks the ratio $\Phi(\text{CEM} + \text{real})/\Phi(\text{INCL} + \text{real})$, $(\text{gauss}/\text{real})_{\text{INCL}}$ marks the ratio $\Phi(\text{INCL} + \text{gauss})/\Phi(\text{INCL} + \text{real})$ and $(\text{gauss}/\text{real})_{\text{CEM}}$ marks the ratio $\Phi(\text{CEM} + \text{gauss})/\Phi(\text{CEM} + \text{real})$. The statistical uncertainty is shown only for one ratio, $(\text{CEM}/\text{INCL})_{\text{real}}$, since for the other two ratios it is almost the same.

statistical errors in both simulations. These errors are not shown in the figure to avoid complexity.

The neutron flux ratios were calculated taking different combinations of intra-nuclear models and beam shapes, *e.g.*, i) INCL + real, ii) INCL + gauss, iii) CEM + real, and iv) CEM + gauss for the box 3 (where U is placed) and box 4 (where Th is placed) and are displayed in fig. 6. The simulation by the INCL model gives more neutrons

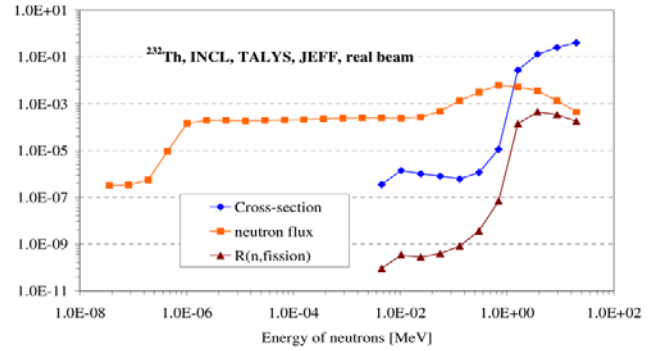


Fig. 7. Fission cross-section [barn], neutron flux [$n \cdot \text{cm}^{-2} / \text{deuteron}$] and reaction rate [$\times 10^{-24} \cdot \text{fission}/\text{deuteron}$] of $^{232}\text{Th}(n, f)$.

with energy from 1 eV to 1 MeV (from about 20% to 30%) than the simulation using the CEM model. Considering the “real” shape of the beam profile the simulation gives 10% and 5% more neutrons with $E_n < 1$ MeV for the INC and the CEM models, respectively, than the “Gaussian” shape of the beam profile.

The reaction rates $R(A_r, Z_r)$ are calculated by the convolution of the simulated spectra of produced particles with the appropriate cross-sections (F4+FM card in MCNPX). In the MCNP code cross-section data up to 20 MeV are taken from the ENDF/B-VI library and the missing data of the cross-section of (n, γ) and (n, f) reactions are taken from the JEFF-3.1 library [28]. Above 20 MeV neutron energy, 1 MeV bins are made for the spectra of produced particles and for spectra above 150 MeV, 50 MeV bins are used. In these cases the numbers of particles in the bins are multiplied by the appropriate cross-sections calculated from the TALYS-1.0 code [29, 30] up to 200 MeV and from the CEM03 model [24] above 200 MeV. Thus, reaction rates of reactions $^{232}\text{Th}(n, f)$, $^{232}\text{Th}(n, \gamma)$, $^{232}\text{Th}(n, 2n)$ for the box 3 and $^{\text{nat}}\text{U}(n, f)$ and $^{\text{nat}}\text{U}(n, \gamma)$ reactions in box 4 are estimated. The dependence of the neutron flux, cross-sections and reaction rates on the neutron energy are estimated for all reactions given above, but to save space only results of (n, f) and (n, γ) reactions in ^{232}Th are given in figs. 7 and 8, respectively.

To evaluate the experimental values of fission rates for values available in the data base we have made another distribution by condensing neutrons into two major groups for the fertile ^{238}U and ^{232}Th and three groups for the fissile ^{235}U , since mass distributions of the fission products are available only for three energies of neutrons, *i.e.*, for the thermal energy of 0.0252 eV (only for ^{235}U), for the unresolved resonance energy at 400 keV and for the high energy at 14 MeV. From the paper of Batenkov *et al.* [31] it follows that fission mass yields in the range 90 to 140 may be predicted within 30% for the proton energy above 20 MeV up to 96 MeV. It is also well known [32] that if the same compound nucleus is produced in neutron- ($E_n > 20$ MeV) and proton- ($E_p > 20$ MeV) induced reactions, then one expects the characteristic of fission to be identical. Since data for the yield of fission products at

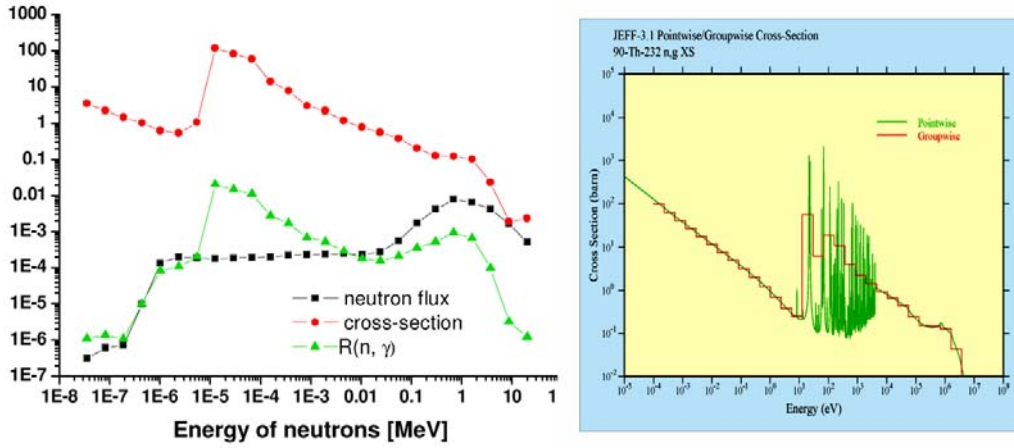


Fig. 8. On the left, cross-section [barn], neutron flux [$\text{n} \cdot \text{cm}^2/\text{deuteron}$] and reaction rate [$\times 10^{-24} \cdot \text{nuclei}/\text{deuteron}$] of ^{232}Th (n, γ) using the INCL + real beam. In the right panel, pointwise cross-sections from the JEFF-3.1 library are compared with the groupwise cross-sections from the code NJOY 99.122.

Table 5. Group weight factors for calculations of the total number of fissions.

Energy of neutrons	^{232}Th	^{235}U	^{238}U	^{nat}U
Epithermal	$6.72 \cdot 10^{-7}$	0.636	$7.12 \cdot 10^{-5}$	$4.65 \cdot 10^{-3}$
Resonance	0.663	0.318	0.715	0.712
Fast	0.337	0.046	0.285	0.283

very high energies is not available, we can use the following three broad energy categories:

- thermal, epithermal and resonance —from $a(1) = \text{E-5 eV}$ to $a(2) = 1.26\text{E}+5 \text{ eV}$,
- unresolved resonance and fast neutrons —from $a(2) = 1.26\text{E}+5 \text{ eV}$ to $a(3) = 4.57\text{E}+6 \text{ eV}$,
- fast and high-energy neutrons —from $a(3) = 4.57\text{E}+6 \text{ eV}$ up to $a(4) =$ the total deuteron kinetic energy (1600 MeV),

and calculate the weight factors $w_j(t)$ for the energy regions, $j = 1, 2, 3$ etc. from the following:

$$w_j(t) = \frac{\int_{a(j)}^{a(j+1)} \sigma_j(t, E_n) \Phi(E_n) dE_n}{\int_{a(1)}^{a(4)} \sigma_j(t, E_n) \Phi(E_n) dE_n}, \quad (6)$$

where $j = 1, 2, 3$ for ^{235}U and $j = 2, 3$ for ^{238}U and ^{232}Th and t stands for different nuclei in the sample, for example ^{235}U , ^{238}U and ^{232}Th in our case. We performed integration of products of the cross-section and of the neutron flux in each region to obtain the weight factors (see table 5). With the help of these weights $w_j(t)$ and the JEFF-3.1 library of fission yields, $Y_{\text{cum}}(t, r, j)$ we estimate mean weight yields, $Y_{\text{cum}}(t, r)$, where r stands for the observed fission product. For our experimental obser-

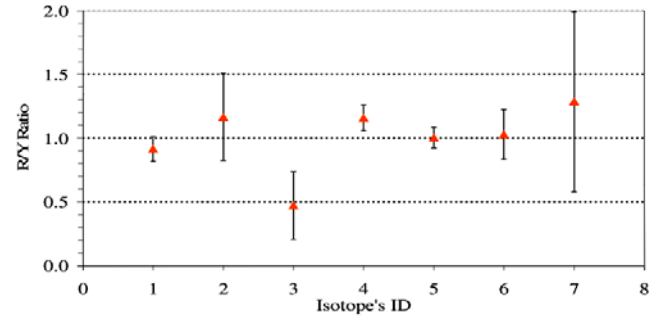


Fig. 9. The relative ratio of $R_{\text{exp}}(^{nat}\text{U}, r) / (Y_{\text{cum}}(^{nat}\text{U}, r))$. Here on the X-axis 1 = ^{99}Mo , 2 = ^{132}Te , 3 = ^{133}I , 4 = ^{135}I , 5 = ^{135}Xe , 6 = ^{140}Ba , and 7 = ^{143}Ce nuclides.

variations of fission products we have calculated

$$Y_{\text{cum}}(\text{Th}, ^{99}\text{Mo}) = w_2(\text{Th}) \cdot Y_{\text{cum}}(\text{Th}, ^{99}\text{Mo}, 2) + w_3(\text{Th}) \cdot Y_{\text{cum}}(\text{Th}, ^{99}\text{Mo}, 3), \quad (7)$$

$$Y_{\text{cum}}(\text{U}_{\text{nat}}, r) = [0.007204(w_1(^{235}\text{U}) \cdot Y_{\text{cum}}(^{235}\text{U}, r, 1) + w_2(^{235}\text{U}) \cdot Y_{\text{cum}}(^{235}\text{U}, r, 2) + w_3(^{235}\text{U}) \cdot Y_{\text{cum}}(^{235}\text{U}, r, 3))] + [0.992742(w_2(^{238}\text{U}) \cdot Y_{\text{cum}}(^{238}\text{U}, r, 2) + w_3(^{238}\text{U}) \cdot Y_{\text{cum}}(^{238}\text{U}, r, 3))], \quad (8)$$

where $r = ^{99}\text{Mo}$, ^{132}Te , ^{133}I , ^{135}I , ^{135}Xe , ^{140}Ba , and ^{143}Ce for ^{nat}U . It is found from the data of independent yields in the JEFF-3.1 library that $Y_{\text{cum}}(t, r, e)$ for an observed fission product in the case of ^{nat}U varies only by 13% in the energy range from $E_n = 400 \text{ keV}$ to 14 MeV. Therefore, with such approximation we can assume that the ratio between $R_{\text{exp}}(t, r)$ for each observed fission product (r) and relative production yield $Y_{\text{cum}}(t, r)$ are constant for the same residual nucleus and for the given sample ^{nat}U or ^{232}Th and that comes true as seen through the data in fig. 9. If all residual nuclei having different mass numbers A_r are observed, it means that all decay chains of nuclei

Table 6. Comparison of the results of the experiment and of the calculation: INCL —intra-nuclear cascade; CEM —Cascade Exciton Model; real —the measured shape using the SSNTDs and gauss (Gaussian) —the assumed shape of the beam with parameters given in sect. 4. Remarks: C-g, sign for CEM-gauss; C-r, for CEM-real; I-g, for INCL-gauss; I-r, for INCL-real.

Reaction	^{232}Th			$^{\text{nat}}\text{U}$	
	(n, γ)	(n, f)	(n, 2n)	(n, γ)	(n, f)
Reaction rate, exp.	3.03(10)E-26	5.89(60)E-27	1.60(16)E-27	2.97(14)E-26	2.24(10)E-26
$R(\text{CEM-gauss})$ all E_n	1.46E-26	1.53E-27	1.18E-27	3.13E-26	6.32E-27
$E_n > 20$ MeV [%]	0.004	52.4	25.9	0.006	32.9
$R(\text{CEM-real})$ all E_n	1.62E-26	1.76E-27	1.10E-27	3.26E-26	6.96E-27
$E_n > 20$ MeV [%]		57.4			37.0
$R(\text{INCL-gauss})$ all E_n	2.17E-26	1.71E-27	9.05E-28	4.49E-26	6.64E-27
$E_n > 20$ MeV [%]		58.0			37.5
$R(\text{INCL-real})$ all E_n	2.49E-26	1.94E-27	9.98E-28	4.67E-26	7.59E-27
$E_n > 20$ MeV [%]		58.2			38.4
$R(\text{C-g})/R(\text{C-r})$	0.90	0.87	1.07	0.96	0.91
$R(\text{C-g})/R(\text{I-g})$	0.67	0.89	1.30	0.70	0.95
$R(\text{C-r})/R(\text{I-r})$	0.65	0.91	1.10	0.70	0.92
$R(\text{I-g})/R(\text{I-r})$	0.87	0.88	0.91	0.96	0.87
$R(\text{exp})/R(\text{I-r, calc.})$	1.22(4)	3.04(30)	1.60(15)	0.64(3)	2.95(13)
$R(\text{exp})/R(\text{C-r, calc.})$	1.40(5)	3.35(33)	1.45(14)	0.91(4)	3.22(14)

followed up to the observed residual nucleus. Then we can pass from the cumulative yield to the corresponding sum of independent yields $\Sigma_r Y_{\text{ind}}(t, r)$ and from this one can find total reaction rate for all residual nuclei. This gives the reaction rate of the fission. It may be understood more clearly in the following way: a produced nuclide (A_r, Z_p) in a reaction may have a sequence of β -decays and finally to decay to (A_r, Z_r), which is registered in the experiment. For all such products (A_r, Z_r) from a given target we find out the experimental fission rates by equating $R_{\text{exp}}\{t(\text{n, f}), r\} = 2R_{\text{exp}}(A_r, Z_r)/\Sigma_p Y_{\text{ind}}(t, A_r, Z_{p \rightarrow r})$. From these partial fission rates we estimate the weighted fission rate, $R_{\text{exp}}\{t(\text{n, f})\}$. In case we are able to identify several residual nuclides with same A_r and different Z_r and Z_q , the two sums $\Sigma_p Y_{\text{ind}}(t, A_r, Z_{p \rightarrow r})$ and $\Sigma_p Y_{\text{ind}}(t, A_r, Z_{p \rightarrow q})$ are expected to be strongly correlated and in this situation we should accept only one of them (that with smaller error). As an example, we observed ^{135}I and ^{135}Xe from the $^{\text{nat}}\text{U}$ and we know that ^{135}I is accumulated from the decay chain $^{135}\text{Sn} \rightarrow ^{135}\text{Sb} \rightarrow ^{135}\text{Te} \rightarrow ^{135}\text{I}$ and similarly, ^{135}Xe is cumulated from $^{135}\text{Sn} \rightarrow ^{135}\text{Sb} \rightarrow ^{135}\text{Te} \rightarrow ^{135}\text{I} \rightarrow ^{135}\text{Xe}$. In this situation, we accept the sum of the independent yield for ^{135}Xe and not ^{135}I . The experimental values $R_{\text{exp}}(\text{n, f})$ for ^{232}Th and $^{\text{nat}}\text{U}$ targets calculated as above are given in table 6.

In table 6 calculated reaction rates are established summing the partial ones $R(A_r, Z_r, E_n)$ from the lowest-up to the highest-energy bins of the neutrons. There are several different combinations of models and beam shapes and all of them cannot be shown in this paper. As an example, we present the results for $^{232}\text{Th}(\text{n, f})$ and $^{232}\text{Th}(\text{n, } \gamma)$ in figs. 7 and 8, respectively, but similar plots for $^{\text{nat}}\text{U}$ are not shown here. Finally, only the conclusive results inferred from such plots are given in table 6. Some

columns of the table do not contain numerical values, since they were very small. Secondly, as the collision of proton may also lead to fission, we have estimated $R(\text{p, fission})$ for protons to be $3.57\text{E-}29$ and $5.18\text{E-}29$ for the ^{232}Th and $^{\text{nat}}\text{U}$, respectively (making use of the INCL model and the real beam). These values are only 1.84% and 0.68% of the full amount of $R(\text{n, fission}) + R(\text{p, fission})$. Similarly, for the (n, 2n) reactions, $R(\text{p, pn})$ for the ^{232}Th is evaluated by means of the same version of simulation and its value is found to be $1.55\text{E-}30$, that is 0.155% of the full value of $R(\text{n, 2n}) + R(\text{p, pn})$. It is also important to point out that the evaluation of experimental fission rates from the reaction rates of different fission products can have systematic errors, since we have found few fission products in the case of uranium and only one in the case of the thorium sample. On the other hand, for the sake of comparison, the yield of fission products is known with good accuracy only for three energies of neutrons from the JEFF-3.1 data library. The systematic errors in the experimental values $R_{\text{exp}}(\text{n, f})$ for ^{232}Th and $^{\text{nat}}\text{U}$ samples are estimated as follows: we calculate the sum of independent yields, $\Sigma_r Y_{\text{ind}}(t, r, e)$ for $t = ^{235}\text{U}$, ^{238}U and ^{232}Th for the two cases of energy ranges defined as $e = 1, 2$ and 3 for ^{235}U and 2 and 3 for ^{238}U and ^{232}Th . For every case of the target this sum is normalized to 2, since there are two fragments in the fission. The sum of the errors in such yields, $\Sigma_r \sigma\{Y_{\text{ind}}(t, r, e)\}$ lies between 0.364 and 0.462 and the ratio $\Sigma_r \sigma\{Y_{\text{ind}}(t, r, e)\}/\Sigma_r Y_{\text{ind}}(t, r, e)$ is the systematic error and is found to be $\sim 10\%$.

The transmutation of ^{232}Th to ^{233}U proceeds mainly in the low-energy neutron flux through the neutron capture reactions,

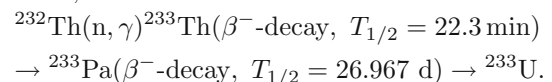


Table 7. Comparison of some experimental conditions in TARC [9] irradiated with protons of momentum 3.5 (identified as particle 1) and 2.75 GeV/c (identified as particle 2) and the present experiment with a deuteron beam of energy 1.6 GeV.

	²³² Th foils			^{nat} U foils	
	Present	TARC		Present	TARC
	(n, γ), (n, 2n)	(n, γ)	(n, 2n)	(n, γ)	(n, γ)
Weight (no.1) (mg)	93.2	132	158	172	290
Weight (no.2) (mg)			678		
Diameter (no.1) (mm)	15	12.7	12.5	15	12.7
Square (no.2) (mm ²)			870		
Radial distance (no.1) (mm)	131	1220	~ 40	138	1070
Radial distance (no.2) (mm)		1500	~ 85		940
Beam particle	deuteron	proton	proton	deuteron	proton
Beam energy	1.6 GeV	3.5 GeV/c	2.5 GeV/c	1.6 GeV	3.5 GeV/c
Sum of particle	$1.93 \cdot 10^{13}$	$2.14 \cdot 10^{13}$		$1.93 \cdot 10^{13}$	$2.14 \cdot 10^{13}$
Sum of particle (no.1)			$4.80 \cdot 10^{12}$		
Sum of particle (no.2)			$9.01 \cdot 10^{12}$		
Irradiation time (h)	6.65	8.5		6.65	8.5

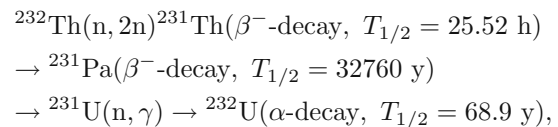
The determination of the production rate of ²³³Th is difficult due to its small half-life and its decay scheme. There are only two gamma rays having intensity more than 1% per decay, *i.e.*, 29.374 keV ($I_\gamma = 2.5\%$) and 86.477 keV ($I_\gamma = 2.7\%$). We have found nine gamma rays corresponding to the beta decay of ²³³Pa and this allowed us to establish the reaction rate R with statistical error 3.3%.

It is important that on the lower-energy side of the neutron spectrum one can assume that there is uncertainty in estimation of the flux calculated by a code. We know that in our case (flux simulated by MCNPX at $E_n = 0.87$ eV) the flux is small ($\sim 1\%$ of the peak value). Assuming that such flux exists down up to thermal energy (0.025 eV) the calculated reaction rates of ²³²Th(n, γ), ^{nat}U(n, γ) will be enhanced by 82% and 18.6%, respectively. On the other hand, if this flux was zero in this region then these reaction rates would decrease by 0.5% and 0.12%, respectively. Another valid reason for these differences is the fact that the neutron fluxes are estimated from the Monte Carlo code (see fig. 6) which may not be fully validated. These shortcomings may only be overcome in future. In the analysis of data of this experiment all other corrections are implemented in the best possible way.

We estimate the normalized transmutation power of ²³²Th using eq. (5) to be $P_{\text{norm}}(^{233}\text{Pa}) = 3.09(13)\text{E-}17$ [g/g] for our set-up. This can be compared with the TARC data [9] obtained by the irradiation of a Pb target by protons. In the TARC experiment secondary spallation neutrons were moderated in Pb assembly weighing ~ 334 tons having cross-sectional diameter $d \sim 3.3$ m and length being 3 m. The comparison of some of the conditions of the two experiments with ²³²Th and ^{nat}U samples is given in table 7. In the TARC experiment $P_{\text{norm}}(^{233}\text{Pa}) = 3.8(3)\text{E-}17$ [g/g] in hole “8” at position $z = 22.5$ cm and $x = 122$ cm

and $P_{\text{norm}}(^{233}\text{Pa}) = 1.0(2)\text{E-}17$ [g \cdot g⁻¹] in hole “9” at $z = 7.5$ cm and $x = 150$ cm (see fig. 111 of [9]).

For the proposed ²³²Th fuel the neutron multiplication from the (n, xn) non-fission reactions is not negligible as their cross-section is comparable with the fission cross-section [33]. In our ²³²Th sample we have observed gamma peaks corresponding to the (n, 2n) reactions. Furthermore, the following chain of the reactions leads to the production of ²³²U:



which is responsible for the large part of the short-term radiotoxicity, while ²³¹Pa is responsible for the long-term radiotoxicity.

The data obtained from the planar HPGe detector are used for the study of ²³¹Th. The most intensive gamma-rays with energy 25.646 keV ($I_\gamma = 14.5\%$) and the 84.216 keV ($I_\gamma = 6.6\%$) were seen without any ambiguity. The average reaction rate as given in table 3 is $1.60(16)\text{E-}27$. In the case of irradiation of the Th sample we are able to identify only one fission product (⁹⁹Mo). Nevertheless, for this we have evaluated the reaction rate of fission of ²³²Th and it comes out to be $R_{\text{fission}}(^{232}\text{Th}) = 5.89(70)\text{E-}27$. From eq. (7) the weight yield of ⁹⁹Mo comes out to be $2.593(83)\text{E-}2$ per fission. The ratio of reaction rates in our sample $R(n, 2n)/R(n, f)$ is $0.27(9)$ carrying 0.04 as the statistical error and ~ 0.08 as the systematic error due to the non-availability of data of fission yield at high energy, $E_n > 14$ MeV. Thus, it may be assumed that the contribution of the (n, 2n) reactions is significant for the neutron multiplication.

Abanades *et al.* [9] have measured the Th(n, 2n) reaction and placed Th samples on different distances from

the center of TARC set-up. Experimental conditions in the present experiment and the TARC are given in table 7. According to the TARC experiment, for sample 1 placed at $d \sim 4$ cm, $B(^{231}\text{Th}) = 0.635(63)\text{E-6}$ and $1.32(13)\text{E-6}$ for the two gammas, $E_\gamma = 25.646$ keV and 84.216 keV, respectively. Similarly, for sample 2 placed at $d \sim 8.5$ cm $B(^{231}\text{Th}) = 1.05(16)\text{E-6}$ and $2.11(32)\text{E-6}$, for $E_\gamma = 25.646$ keV and 84.216 keV, respectively. It can be seen that TARC results for the two gamma energies are different by about 100%. In our experiment $R(^{231}\text{Th}) = 1.53(20)\text{E-27}$ for $E_\gamma = 25.646$ keV and $R(^{231}\text{Th}) = 1.72(25)\text{E-27}$ for 84.216 keV, respectively, for the distance $d = 13.1$ cm from the centre of the “Energy plus Transmutation” set-up. In our case the two values are comparable (see column 5 of table 3).

The measured transmutation power estimated from the $^{238}\text{U} (n, \gamma)^{239}\text{U}$ reaction in our experiment is $P_{\text{norm}}(^{239}\text{U}) = 2.87(9)\text{E-17}$ [g/g] to be compared with TARC data $P_{\text{norm}}(^{239}\text{U}) = 1.1(3)\text{E-17}$ [g/g] and $7.7(2)\text{E-17}$ [g/g] for $z = -22.5$ cm and for the hole 6 and hole 7 located at $d = 107$ cm and 94 cm, respectively, from the centre of the set-up (see also fig. 112, of ref. [9]).

6 Conclusions

Some of the most important conclusions of this study can be summarized as follows:

- i) In this study 32 spectra of activated Th and $^{\text{nat}}\text{U}$ samples including the spectra of Al monitors were taken using the planar and coaxial gamma detectors. 157 peaks were observed and analyzed and their energy, intensity, and the half-lives of corresponding nuclides were established. By means of these values the residual nuclei were identified. Experimental reaction rates of residual nuclei ^{233}Pa , ^{231}Th and ^{99}Mo for the ^{232}Th sample and ^{239}Np , ^{99}Mo , ^{132}Te , ^{133}I , ^{135}I , ^{135}Xe , ^{140}Ba , and ^{143}Ce for the $^{\text{nat}}\text{U}$ sample were estimated. Comparing the reaction rates and relative yields of the fission products the experimental fission reaction rates of ^{232}Th and $^{\text{nat}}\text{U}$ were determined for the neutron environment of the set-up, which is different from the neutron environment of the thermal and fast reactors. From the data of (n, f) reactions given in the last two rows of the table 6 the ratio, $R(\text{exp})/R(\text{I-r, calc.})$ for the ^{232}Th and $^{\text{nat}}\text{U}$ samples is $3.04(30)$ and $2.95(13)$, respectively, for the INCL model + “real” beam shape. Similarly, the ratio $R(\text{exp})/R(\text{C-r, calc.})$ is equal to $3.35(33)$ and $3.22(14)$ for the ^{232}Th and $^{\text{nat}}\text{U}$ samples, respectively, for the combination of CEM model + “real” beam shape. From these observations it may be inferred that there is almost no difference in the predictions of fission cross-sections, hence the reaction rates by the two models, *i.e.*, the INCL with ABLA and the CEM with EVAP. Secondly, the ratio being close to 3 shows that the library of fission cross-sections calls for upgrade.
- ii) Similarly, on comparing the results given in table 6 for the (n, γ) reactions in ^{232}Th and $^{\text{nat}}\text{U}$ it may be pointed out that deviations of theoretical values from the experimental values do not exceed 40%. For the

(n, 2n) reactions the experimental values are higher by about 45% and 60% compared to the calculated values using the INCL with ABLA EVAP and the CEM with EVAP models, respectively. The calculations using the “real” or “gauss” shapes of the deuteron beam introduce differences from 4% to 13% only in both models. Ratios of the calculated reaction rates assuming the CEM with EVAP and the INCL with ABLA EVAP models along with the “real” shape of the beam vary from 0.65 to 1.10.

- iii) $R(n, 2n)/R(n, f)$ for the ^{232}Th sample being $\sim 27\%$ suggests that the contribution of the (n, 2n) reactions is significant from the point of view of neutron multiplication. If it was possible to detect reactions corresponding to the other (n, xn) reactions in our sample then this study might provide more useful information about the total neutron contribution of these reactions and also about the competition between the (n, f) and (n, xn) reactions as pointed out by Kumar *et al.* [33]. This suggests the need of more elaborate experiments where higher order (n, xn) reactions and (n, f) reactions can be studied simultaneously.
- iv) It may also be inferred that there is a very little amount of data on neutron cross-sections of (n, γ), (n, f) or (n, 2n) reaction at energy $E > 20$ MeV and in this situation one has to take data from the well-validated deterministic codes.
- v) The normalized transmutation power of (n, γ) and (n, 2n) reactions on ^{232}Th and the (n, γ) reaction on $^{\text{nat}}\text{U}$ are evaluated and compared with the data from the TARC experiment in table 7. For (n, γ) reactions our values of P_{norm} for the samples placed at 13.1 cm from the center of “Energy plus Transmutation” set-up are comparable with the TARC samples placed ~ 100 cm from the center of the TARC set-up. This difference of distance can be understood from the difference in the neutron spectra, *i.e.*, much more low-energy neutrons are there in the TARC than in our set-up and also from the fact that $\sim 70\%$ of the created neutrons do not escape the massive Pb target of TARC. Secondly, the initial proton energy in TARC experiment is more than two times higher than the deuteron energy in the “Energy plus Transmutation” set-up and this results in larger number of neutrons in the TARC. The normalized transmutation power of the (n, 2n) reaction in ^{232}Th is almost the same in our case and the TARC, which are placed at 4 cm and 8.5 cm from the center of the TARC set-up.
- vi) The results of the reaction rates estimated from different gamma-ray energies from the decay of nuclide show consistency in the present experiment and this generates confidence in our observations.

Appendix A.

Appendix A.1. Self-absorption correction

The coefficient $\eta_A(A_t, Z_t, E(j))$, used in relation (1) accounts for the self-absorption of gamma ray in the sample

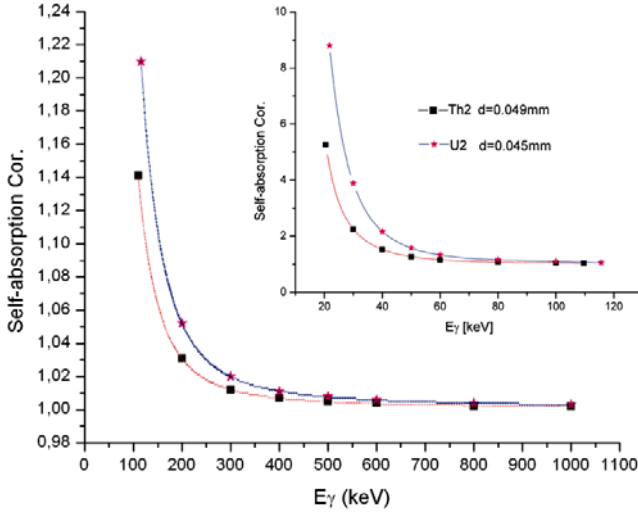


Fig. 10. Self-absorption correction, η_A , for Th and U samples as a function of E_γ .

(A_t, Z_t) of thickness d , has been calculated as follows:

$$\eta_A(Z_t, E(j)) = \frac{\mu(Z_t, E(j)) \cdot d}{1 - e^{-\mu(Z_t, E(j)) \cdot d}}, \quad (\text{A.1})$$

where $\mu(Z_t, E(j))$ is the total attenuation coefficient for a given gamma ray with energy $E_\gamma(j)$ in the source material of the target. The values of attenuation coefficients for the two elements and different gamma energies are taken from refs. [34–36] where the precision of calculation is $\sim 2\%$. The corresponding η_A are shown as thick points in fig. 10. The thin curves corresponds to $\eta_A = \{\exp(a_0 + a_1(\ln E) + a_2(\ln E)^2 \dots)\}^{-1}$ and this provides interpolation between the thick points for the required energy of the peak. This correction for the gamma ray of energy higher than 300 keV turned out to be less than 1.2% in the Th target and less than 2.2% in the U target. The dependence of $\eta_A(A_t, Z_t, E(j))$ on the energy of gamma ray for the ²³²Th and ^{nat}U target is given in fig. 10.

Appendix A.2. Correction for beam fluctuation

Similarly, the correction for fluctuation of beam intensity $\eta_B(\lambda)$ has been performed for each residual product with decay constant, λ , using the following relation:

$$\eta_B(\lambda) = \frac{1 - e^{-\lambda \cdot t_{\text{irr}}}}{t_{\text{irr}} \cdot \sum_i^N \{(1/t_p(i)) \cdot W(i) \cdot e^{-\lambda t_e(i)} \cdot (1 - e^{-\lambda \cdot t_p(i)})\}}, \quad (\text{A.2})$$

where t_{irr} is the total irradiation time and $t_p(i)$ is the start and $t_e(i)$ is the end time of the i -th pulse. The fraction $W(i)$ is the number of deuterons in a single i -th pulse divided by the total number of deuterons. N is the total number of recorded pulses. All values t_{irr} , $t_p(i)$, $t_e(i)$ and $W(i)$, which we need for the calculation of the correction

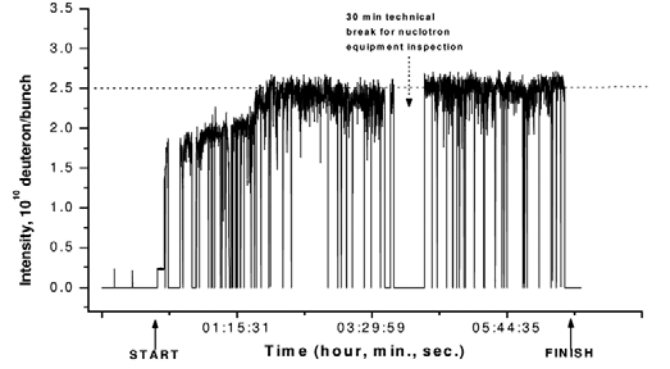


Fig. 11. Intensity profile of the 1.6 GeV deuteron beam (as received from the Nuclotron staff) used for irradiation of the Pb target.

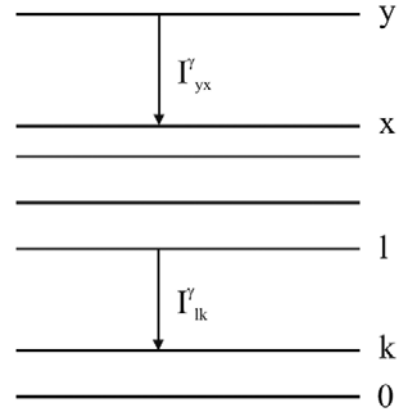


Fig. 12. Coincidence scheme.

due the intensity beam fluctuations, are received from the protocol about irradiation conditions in our experiment, see fig. 11.

Appendix A.3. Coincidence summing correction

Coincidence summing correction $\eta_C(j)$ has been calculated using the “coicorr” program [37]. The code is based on the expression of the coincidence intensity losses and summations via matrix evolution method [38]. If we study the influence of the $y \rightarrow x$ transition to $l \rightarrow k$ (fig. 12) we have to know absolute efficiencies of the full energy peak of gamma rays equivalent to the transitions ε_{lk}^f and the total absolute efficiencies of gamma rays equivalent to the transitions ε_{lk}^t . We know the intensities —the full absolute intensity of the transition I_{lk} and the absolute intensity of the accompanying gamma ray I_{lk}^γ , where $I_{lk} = I_{lk}^\gamma(1 + \alpha_{lk})$. In the case of coincidences of $y \rightarrow x$ and $l \rightarrow k$ gamma rays the summing gamma peak occurs in the gamma spectrum and real peaks corresponding to the $y \rightarrow x$ transition and $l \rightarrow k$ transition seem to have lower intensity. The total number of levels is m .

If we neglect angle correlations, then the coincidence correction of the gamma-peak intensity of the $l \rightarrow k$ tran-

sition $\eta_C(j)_{lk}$ can be derived as

$$[\eta_C(j)_{lk}]^{-1} = \left[M_{lk}^f \left(1 - \sum_{y>x}^m \sum_{x=l}^{m-1} M_{yx}^t C_{xl} - \sum_{j>i}^k \sum_{i=0}^{k-1} C_{kj} M_{ji}^t \right) + \sum_{v=k+1}^{l-1} M_{lv}^f C_{vv} M_{vk}^f \right]. \quad (\text{A.3})$$

The used symbols are defined as follows:

$$M_{lk}^f = \varepsilon_{lk}^f I_{lk}^\gamma \quad \text{and} \quad M_{lk}^t = \varepsilon_{lk}^t I_{lk}^\gamma,$$

$$C_{xl} = \left(\delta_{xl} + \sum_{z=1}^{x-1} [(\hat{d})^z]_{xl} \right) \frac{d_{lk}}{I_{lk}},$$

where δ_{ij} is Kronecker's delta and the matrix \hat{d} is defined as

$$\hat{d} = \begin{pmatrix} 0 & 0 & 0 & \dots & 0 \\ d_{10} & 0 & 0 & \dots & 0 \\ d_{20} & d_{21} & 0 & \dots & 0 \\ \vdots & \vdots & \vdots & \dots & 0 \\ d_{m0} & d_{m1} & d_{m2} & \dots & 0 \end{pmatrix} \wedge d_{10} = 1 \wedge d_{lk} = \frac{I_{lk}}{\sum_{w=0}^{l-1} I_{lw}}.$$

The expression (A.3) is applicable only for binary coincidences of two gamma rays, however, it was extended to multiple coincidences and can include also coincidences with X-rays and annihilation gamma rays [39,40]. The program reads data from the LUND database [22] and calculates the matrix of $\eta_C(j)$ corrections, which are applied to the results of the R value.

Authors are grateful to the operation crew of the Nuclotron accelerator of LHE, JINR Dubna for irradiation and good beam parameters, and Dr. Vera Bradnova for managing, photographic support and preparing minutes of the experiment. Authors are also grateful to META Centrum (Czech Republic) for offering computers for the calculations. The experiments were supported by the Czech Committee for the collaboration with JINR Dubna. Part of this work has been supported by grant of BRNS (DAE-India).

References

1. C.D. Bowman *et al.*, Nucl. Instrum. Methods A **320**, 336 (1992).
2. Carlo Rubbia, J.A. Rubio *et al.*, *Conceptual design of a fast neutron operated high power energy amplifier*, CERN/AT/95-44 (ET) 1995.
3. C. Rubbia, *A high gain energy amplifier operated with fast neutrons*, in *Proceedings of the International Conference on Accelerator-Driven Transmutation Technologies and Applications, Las Vegas (NV), US, 1994*, AIP Conf. Proc. **346**, 44 (1995).
4. A.J. Janssen, *Transmutation of fission products in reactors and accelerator-driven systems*, ECN-R-94-001 (January 2004).
5. A.J. Koning *et al.*, Nucl. Instrum. Methods: Phys. Res. A **414**, 49 (1998).
6. V.P. Bhatnagar, S. Casalta, M. Hugon, *Nuclear waste partitioning and transmutation in the EURATOM fifth and sixth framework*, talk presented at *Seventh Information Exchange Meeting on Actinides and Fission Product Partitioning and Transmutation, 14-16 Oct. 2002, Jeju, Korea*.
7. H. Nifenecker, O. Meplan, S. David, *Accelerator Driven Sub-critical Reactors* (Institute of Physics Publishing, Bristol and Philadelphia, 2003).
8. U. Abbondanno *et al.*, in *Proceedings of the International Conference on Nuclear Data for Science and Technology, Santa Fe, New Mexico (USA), 26 September - 1 October 2004*, AIP Conf. Proc. **769**, 724 (2005).
9. A. Abanades, J. Aleixandre, S. Andriamonje *et al.*, Nucl. Instrum. Methods: Phys. Res. A **478**, 577 (2002).
10. M.I. Krivopustov, D. Chultem, J. Adam *et al.*, Kerntechnik **68**, 48 (2003).
11. V.S. Barashenkov, H. Kumawat, V.A. Lobanova, V. Kumar, Nucl. Instrum. Methods: Phys. Res. B **217**, 352 (2004).
12. J.-S. Wan, M. Ochs, P. Vater *et al.*, Nucl. Instrum. Methods: Phys. Res. B **155**, 110 (1999).
13. J. Banaigs, J. Berger, J. Dulfo, L. Goldzahl *et al.*, Nucl. Instrum. Methods **95**, 307 (1971).
14. P. Kozma, V.V. Yanovsky, Czech. J. Phys. **40**, 393 (1990).
15. J. Blocki, J. Randrup, W.J. Swiatecki, C.F. Tsang, Ann. Phys. (N.Y.) **105**, 427 (1977).
16. G.L. Morgan, K.R. Alrick, A. Saunders, F.C. Cverna *et al.*, Nucl. Instrum. Methods: Phys. Res. B **211**, 297 (2003).
17. S.R. Hashemi-Nezhad, Igor Zhuk, M. Kievets *et al.*, Nucl. Instrum. Methods: Phys. Res. A **591**, 517 (2008).
18. Mitja Majerle, V. Wagner, A. Krasa, J. Adam *et al.*, Nucl. Instrum. Methods: Phys. Res. A **580**, 110 (2007).
19. J. Frana, J. Radioanal. Nucl. Chem. **257**, 583 (2003).
20. J. Adam, V.S. Pronskikh, A. Balabekyan *et al.*, Preprint JINR, P10-2000-28, Dubna.
21. J. Adam, A. Balabekyan, V.S. Pronskikh *et al.*, Appl. Radiat. Isotopes **56**, 607 (2002).
22. S.Y.F. Chu, L.P. Ekstrom, R.B. Firestone, <http://nucldata.nuclear.lu.se>.
23. J.S. Hendricks *et al.*, MCNPX, version 2.6.c, LA-UR-06-7991 (2006).
24. S.G. Mashnik *et al.*, J. Phys. Conf. Ser. **41**, 340 (2006).
25. A. Boudard, J. Cugnon, S. Leray, C. Volant, Phys. Rev. C **66**, 044615 (2002).
26. A.R. Junghans, M. de Jong, H.G. Clerc, A.V. Ignatyuk, G.A. Kudyayev, K.H. Schmidt, Nucl. Phys. A **629**, 635 (1998).
27. J. Benlliure, A. Grewe, M. de Jong, K.H. Schmidt, S. Zhdanov, Nucl. Phys. A **628**, 458 (1998).
28. Experimental Nuclear Reaction Data (EXFOR) IAEA-NDS 2008.
29. A.J. Koning *et al.*, in *Proceedings of the International Conference on Nuclear Data for Science and Technology, Santa Fe, New Mexico, USA, 26 September - 1 October 2004*, AIP Conf. Proc. **769**, 1154 (2005).
30. A. Koning, S. Hilaire, M. Duijvestijn, www.talys.eu.
31. O.I. Batenkov *et al.*, *Comparison of measured and calculated mass distributions of fission fragments in proton-induced fission of ^{232}Th , ^{235}U , ^{238}U and ^{237}Np at intermediate energies*, in *Proceedings of the International Conference on Nuclear Data for Science and Technology, Santa*

- Fe, New Mexico, USA, 26 September - 1 October 2004*, AIP Conf. Proc. **769**, 625 (2005).
32. T. Ohtsuki *et al.*, Phys. Rev. C **44**, 1405 (1991).
33. V. Kumar, H. Kumawat, Chitra Bhatia, *A study of ADS materials using the CASCADE code, IAEA Technical Meeting TM34567 on the Accelerator Simulation and Theoretical Modeling of Radiation Effects (SMoRE), Kharkov, Ukraine, June 9-13, 2008*, <http://www-naweb.iaea.org/napc/physics/meetings/TM34567/login2.html>.
34. E. Storm, H. Izrael, Nucl. Data Tables A **7**, 563 (1970).
35. W.J. Veigele, At. Data Tables **5**, 51 (1973).
36. J.H. Hubbell, Int. J. Appl. Radiat. Isotopes **33**, 1269 (1982).
37. K. Katovsky, PhD Thesis, CTU Prague, 2008.
38. Y. Yoshizawa *et al.*, Nucl. Instrum. Methods **174**, 109 (1980).
39. K. Debertin, U. Schotzig, Nucl. Instrum. Methods **158**, 471 (1979).
40. U. Schotzig, K. Debertin, K.F. Walz, Int. J. Appl. Radiat. Isotopes **28**, 503 (1977).

NUCLEI
Experiment

Symmetric and Asymmetric Fission Modes in Proton-Induced Fission at 660 MeV of $^{238}\text{U}^*$

A. R. Balabekyan^{1)**}, G. S. Karapetyan¹⁾, N. A. Demekhina^{2),3)}, J. Adam²⁾, and K. Katovsky⁴⁾

Received February 8, 2010

Abstract—Fission product cross sections of intermediate-energy fission of ^{238}U were used in order to construct the charge and mass yield distributions. Enriched target of ^{238}U was irradiated by proton beam with energy 660 MeV for several hours at the LNP Phasotron, Joint Institute for Nuclear Research (JINR), Dubna, Russia. The charge distribution of the fission fragments was analyzed for calculation of isobaric cross sections. The mass yield curves were expanded into symmetric and asymmetric components according multimodal fission approach. The fissility values of actinides were calculated at given proton energy. The obtained results have been compared to the same data for targets ^{237}Np and ^{241}Am .

DOI: 10.1134/S1063778810110025

INTRODUCTION

Fission product cross sections of ^{241}Am , ^{238}U , and ^{237}Np actinides are the subject of interest, because they are essential data in management of radioactive waste from nuclear power plants. Fission cross section in the intermediate energy range has an important role as well as the emitted neutron number per fission reaction and fission neutron spectrum. On the other hand, experimental studies of fission cross section are recently available. However, the experimental data are not enough for actinide nuclei, especially for minor actinides.

The excitation energy of the fissioning system plays an important role in the dynamics of the fission process. Asymmetric fission, which is dominant at low energies, is characterized by a clear-cut manifestation of shell effects [1–6], whereas symmetric division is consistent with a classical liquid-drop picture of the fissioning nucleus [7, 8]. Among various information associated with nuclear fission phenomenon the problem of mass division has evoked interest. Particularly, this question is related to the intermediate energy region between the low and high energies, where the transition between the different fission modes (from asymmetric to symmetric) is supposed. The growth of the actinide fissility at this

energy range, in spite of the wide-spread assumption about the fission saturation, causes interest to this question.

According to theoretical presentation, the correlation of different fission channels depends on the configuration and position of the saddle and scission points on energy surface [9, 10]. The application of the hypothesis of the multicomponent fission have allowed to extract different components on the base of the decomposition of the mass yield curve [11, 12].

In the present paper the multimodal analysis of fission has been performed at the research energies at first. The experimental fragment cross sections are used to extract the characteristics of the charge and mass distributions of the fission fragments. The obtained fission cross section has allowed to estimate the fissility of actinides at low and intermediate energy ranges.

EXPERIMENTAL

Bombardment of the ^{238}U target by protons with energy 660 MeV was performed at LNP Phasotron, Joint Institute for Nuclear Research (JINR), Dubna, Russia. Fission fragment cross sections were measured by γ -ray spectrometry using high-purity Ge detector. The identification of the fission products was conducted by means of the definition of the half-lives, of the energies and intensities of the nuclear γ transitions of the radioactive fragments [13]. In the absence of radioactive precursors the cross section of fission fragments was determined by using the following form:

$$\sigma = \frac{\Delta N \lambda}{N_p N_n k \varepsilon \eta (1 - e^{-\lambda t_1}) e^{-\lambda t_2} (1 - e^{-\lambda t_3})}, \quad (1)$$

*The text was submitted by the authors in English.

¹⁾Yerevan State University, Armenia.

²⁾JINR, Dubna, Russia.

³⁾Yerevan Physics Institute, Armenia.

⁴⁾Department of Nuclear Reactors, Czech Technical University in Prague, Czech Republic.

**E-mail: balabekyan@ysu.am

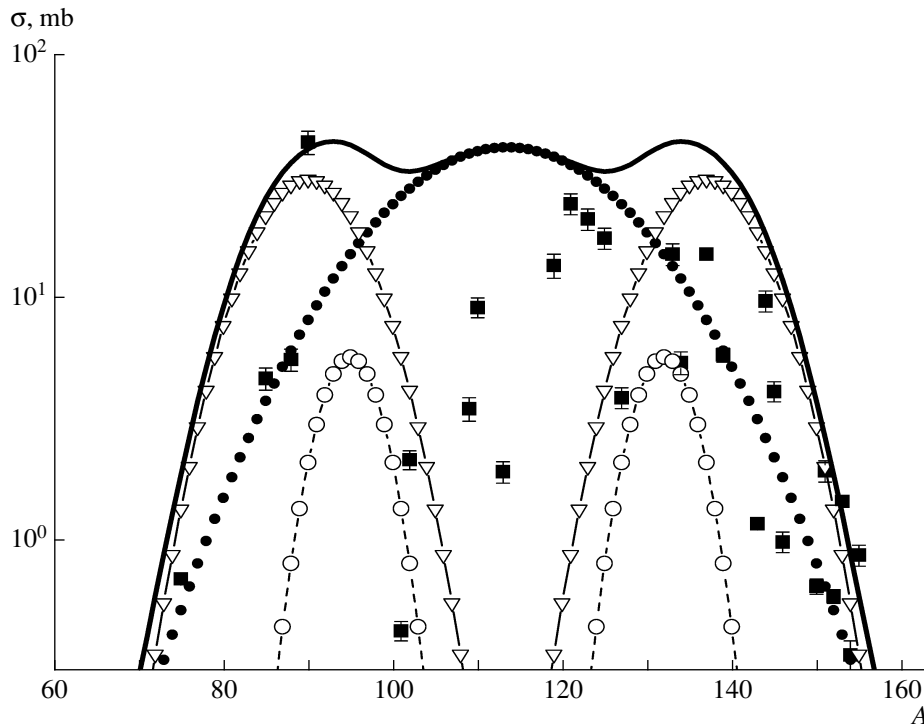


Fig. 1. Mass-yield curves for proton-induced fission of ^{238}U at $E_p = 660$ MeV. (■) Experimental points; solid curve is total fission yield σ_f ; (●) Superlong I mode; (○) Standard I mode; (▽) Standard II mode.

where σ is the cross section of the reaction product; ΔN is the area under the photopeak; N_p —the intensity of proton beam (part./s); N_n —the number of target nuclei on unit surface ($1/\text{cm}^2$); t_1 —the irradiation time; t_2 —the time of exposure between the end of irradiation and the beginning of measurements; t_3 —the time of measurement; λ —the decay constant (s^{-1}); η —the intensity of nuclear γ transitions; k —the total coefficient of the γ -ray absorption in the target and detector materials; ε —the detection efficiency. In this way the isotope formation in the nuclear reaction is determined as an independent (I) cross section directly.

To deduce the independent cross section from the measured radioactivity it is necessary to correct the contribution from precursors, if the precursor has a half-life period of the same order or more than daughter nucleus. Knowing the precursor cross section the independent cross section of the daughter can be calculated by the relation from [14]

$$\sigma_B = \frac{\lambda_B}{(1 - e^{-\lambda_B t_1})e^{-\lambda_B t_2}(1 - e^{-\lambda_B t_3})} \times \left[\frac{\Delta N}{N_p N_n k \varepsilon \eta} - \sigma_A f_{AB} \frac{\lambda_A \lambda_B}{\lambda_B - \lambda_A} \right] \times \left(\frac{(1 - e^{-\lambda_A t_1})e^{-\lambda_A t_2}(1 - e^{-\lambda_A t_3})}{\lambda_A^2} \right) \quad (2)$$

$$- \left. \frac{(1 - e^{-\lambda_B t_1})e^{-\lambda_B t_2}(1 - e^{-\lambda_B t_3})}{\lambda_B^2} \right],$$

where symbols A and B refer to, respectively, the parent and the daughter isotopes; f_{AB} designates the fraction of decay from nuclide A to B ; ΔN determines the area under the photopeak.

RESULTS AND DISCUSSION

The unmeasurable product cross sections were estimated in the present paper by means of the fragment charge distribution. Empirically, the charge distribution of fission products has been well represented by a Gaussian function, therefore, in the present work the analysis of the charge distribution is performed by the following function in the fitting procedure [15]:

$$\sigma_{A,Z} = \frac{\sigma(A)}{(C\pi)^{1/2}} \exp \left[-\frac{(Z - Z_p)^2}{C} \right], \quad (3)$$

where $\sigma_{A,Z}$ is the independent experimental cross section of the nuclide (Z, A); $\sigma(A)$ —the total isobar cross section for mass number A ; Z_p —the most probable charge for isobars, and C —the width parameter. The isobaric cross sections for different mass numbers are used for construction of the fission mass yield. The total mass yield $\sigma_f = \sum_A \sigma(A)/2$ was evaluated by summing all isobaric cross sections and

Table 1. Symmetric, asymmetric, total fission cross sections and the average number of pre-scission neutrons

Target	Energy, MeV	σ_f , mb	σ_S , mb	σ_{AS} , mb	σ_S/σ_{AS}
^{241}Am	660	1763.7 ± 265.0 [18]	1487.7 ± 223.0	276.0 ± 41.0	5.4 ± 1.0
^{238}U	660	1226.5 ± 183.9 1110 ± 300 [19] 1040 ± 75 [20]	698.3 ± 104.7	528.2 ± 79.2	1.32 ± 0.2
^{237}Np	660	1600.0 ± 240.0 1520 ± 160 [21] 1647 ± 100 [22] 1674 ± 102 [22]	1298.0 ± 195.0	302.0 ± 45.0	4.3 ± 1.0

Table 2. Contribution of symmetric fission mode and pre-scission neutron multiplicity

Target	Energy, MeV	σ_S/σ_f , %	ν_{pre}
^{241}Am	660	84.4 ± 17.0	15.0 ± 2.0
^{238}U	660	57.0 ± 10.0	12.0 ± 1.7
^{237}Np	660	81.1 ± 16.0	14.6 ± 2.0

multiplying by factor 0.5, because in the sum give the contribution both fragments formed in each fission event.

The application of the hypothesis of the multicomponent fission allowed to extract the different components on the base of the decomposition of the mass yield curve. According to this model [12], the mass-yield curve can be decomposed into three distinct fission components: one symmetric “Superlong I” and two asymmetric “Standard I”, “Standard II”. “Superlong” mode fragments are strongly elongated with masses around $A_f/2$. “Standard I” mode is characterized by influence of spherical neutron shell $N_H \sim 82$ and proton shell $Z_H \sim 50$ in the heavy fragments with masses $M_H \sim 132\text{--}134$. “Standard II” mode is characterized by influence of the deformed neutron shell closure $N_H = 86\text{--}88$ and proton shell $Z_H \sim 52$ in the heavy fragments with masses $M_H \sim 138\text{--}140$.

The Gaussians were used for presentation of the different fission modes with parameters depending on nuclear characteristics of fission fragment [12, 16]. The mass-yield distribution of the fission fragments is usually described by five-Gaussian fit of the form [17] (Fig. 1):

$$\sigma = \frac{K_{1AS}}{\sigma_{1AS}\sqrt{2\pi}} \exp\left[-\frac{(A - \bar{A}_S - D_{1AS})^2}{2\sigma_{1AS}^2}\right] + \frac{K'_{1AS}}{\sigma'_{1AS}\sqrt{2\pi}} \exp\left[-\frac{(A - \bar{A}_S + D_{1AS})^2}{2\sigma'_{1AS}{}^2}\right] \quad (4)$$

$$+ \frac{K_{2AS}}{\sigma_{2AS}\sqrt{2\pi}} \exp\left[-\frac{(A - \bar{A}_S - D_{2AS})^2}{2\sigma_{2AS}^2}\right] + \frac{K'_{2AS}}{\sigma'_{2AS}\sqrt{2\pi}} \exp\left[-\frac{(A - \bar{A}_S + D_{2AS})^2}{2\sigma'_{2AS}{}^2}\right] + \frac{K_S}{\sigma_S\sqrt{2\pi}} \exp\left[-\frac{(A - \bar{A}_S)^2}{2\sigma_S^2}\right],$$

where \bar{A}_S is the mean mass number, the asymmetric components are characterized by the positions of the peaks ($\bar{A}_S \pm D_{iAS}$), each components are characterized by the dispersions $\sigma_{iAS,S}(\sigma'_{iAS,S})$ and the normalization factors $K_{iAS,S}(K'_{iAS,S})$. The indexes AS , S designate the asymmetric and symmetric components.

The results of the fit allow to determine the total fission cross section and the cross sections of different fission components. These data are represented in Table 1 as well as for ^{241}Am and ^{237}Np from our recent work [18], where the total fission cross sections are compared with the data from [19–22]. The good agreement in the overlap energy region is found. The relative contributions of symmetric fission mode as well as the average number of neutrons prior to the fission for investigated nuclei are shown in Table 2. One can see from Table 2, the symmetric fission gives the appreciable contribution to the total fission cross section. With increasing excitation energy of fissioning nucleus, the symmetric fission component grows too, and attributes its to increasing neutron evaporation opening new fission channels, there exists a set of various fissioning nuclides. Therefore, the symmetric component is linked with the more neutron-deficient fissioning systems.

In Fig. 2 the ratio of symmetric to asymmetric fission (or the valley-to-peak ratio, V/P) depending on excitation energy (E^*) of fissioning nuclei is presented in the charge range $96 \geq Z_f \geq 90$, including the present experimental results and data from [17,

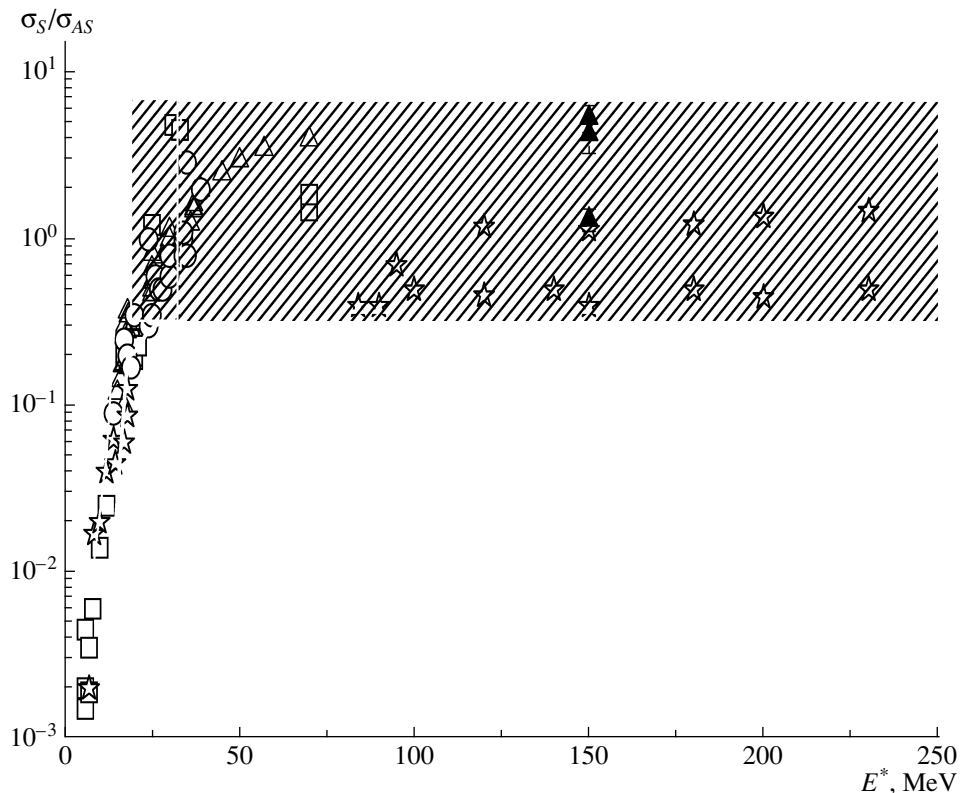


Fig. 2. Symmetric-to-Asymmetric fission ratio as a function of E^* for fission with different probe: (\blacktriangle) present work; (\square) (n, f) [17, 23, 24]; (\triangle) (p, f) [23, 25–28]; (\circ) (α, f) [23]; (\star) (γ, f) [29–31].

23–31]. Dash range indicates the variation of V/P above energy $E^* \approx 25$ MeV. The dependence of the σ_S/σ_{AS} ratio upon the excitation energy can show the evolution of the fission process. This picture is similar to reactions induced by different projectiles (protons, neutrons, photons): at small E^* the asymmetric fission dominates, with growth of E^* the probability of a symmetric mode quickly increases.

Earlier it was shown [27, 28] that the systematization of the fission cross sections on an extensive scale of the mass numbers permits to obtain the simple expression for the estimation of the different fission components:

$$(Z^2/A)_{\text{cr}} = 35.5 + 0.4(Z_f - 90), \quad (5)$$

where $(Z^2/A)_{\text{cr}}$ is the “critical” fissility parameter; Z_f is the charge of fissioning nucleus. It was predicted for the nuclei with $Z^2/A > (Z^2/A)_{\text{cr}}$ the predominance of the symmetric fission and the asymmetric one in the cases of $Z^2/A < (Z^2/A)_{\text{cr}}$. The $(Z^2/A)_{\text{cr}}$ for ^{241}Am , ^{238}U , and ^{237}Np are equal to 37.5, 36.3, and 36.7, respectively. The mean masses of these fissioning nuclei at given proton energy were obtained in our measurements $A \sim 227$, $Z \sim 95$ ($Z^2/A \sim 39.76$ for ^{241}Am); $A \sim 227$, $Z \sim 92$ ($Z^2/A \sim 37.29$ for ^{238}U);

$A \sim 223.4$, $Z \sim 93$ ($Z^2/A \sim 38.72$ for ^{237}Np), so the symmetric fission component should increase. It is necessary to notice that the difference between Z^2/A and $(Z^2/A)_{\text{cr}}$ is more for Am and Np nuclei, therefore symmetric fission in these nuclides is expressed more strongly. However, the possibility of the asymmetric fission for all fissioning nuclei remains at intermediate energy also because of broad mass and excitation energy distributions.

Our investigation produces the possibility to estimate the fissility for proton-induced fission. To calculate the fissility, the fission cross sections were divided by their respective total inelastic cross sections σ_{in} .

For proton-induced fission, we deduced the σ_{in} value from cascade-evaporation model [32]. The dependences of fissility for nuclei ^{241}Am , ^{238}U , and ^{237}Np on excitation energy of fissioning nucleus are shown on Fig. 3 together with data from different probes and calculations from [33]. One can see that the fission probabilities are about the same, independently of the tool used to excite the nuclear matter, and the fissility of the heavier element is getting larger. The fissility of ^{241}Am , ^{238}U , and ^{237}Np fissioning nuclei was less than unity at intermediate energies and

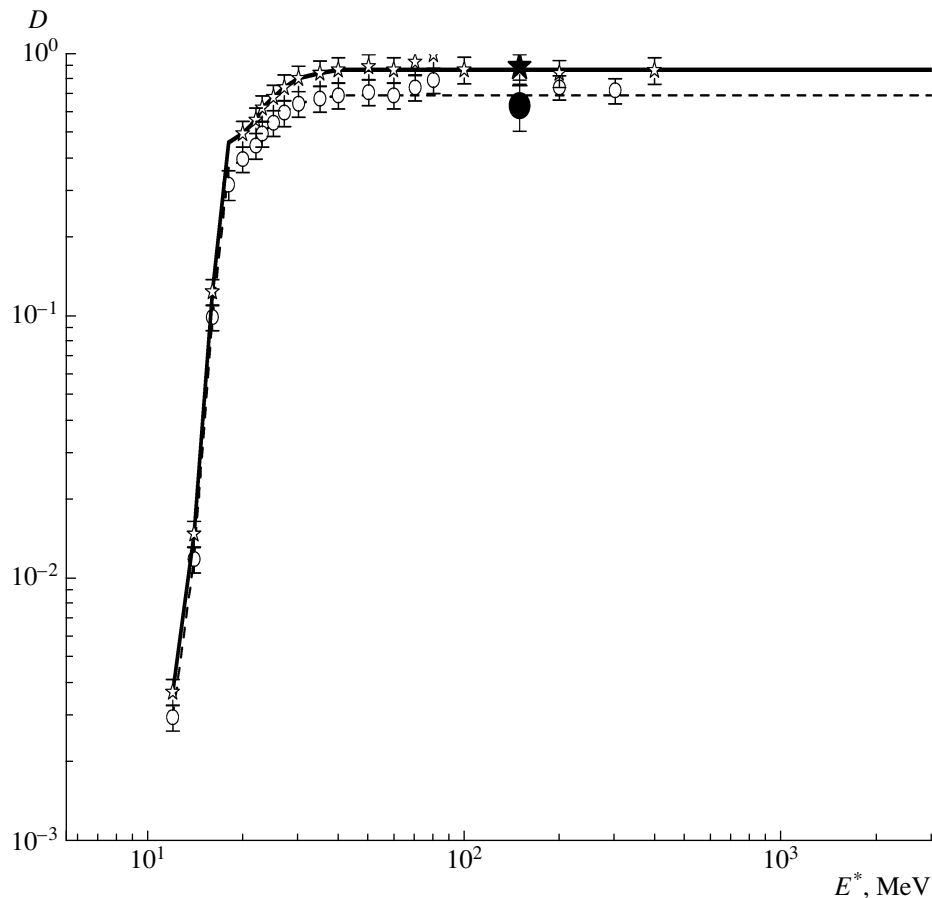


Fig. 3. Dependences of fissility for nuclei ^{241}Am , ^{238}U , and ^{237}Np on excitation energy of fissioning nucleus. Calculations from [33]: solid curve is ^{241}Am and ^{237}Np , dashed curve is ^{238}U . Experimental points: (●) present work for ^{238}U and (★) from [18] for ^{241}Am and ^{237}Np ; open symbols ((☆) ^{241}Am and ^{237}Np , (○) ^{238}U) are the systematics of experimental data from different probes [29, 33].

equals of 0.91 ± 0.14 , 0.64 ± 0.13 , and 0.85 ± 0.13 , respectively.

CONCLUSION

The charge and mass distributions of fragments for proton fission of ^{238}U at proton beam energy 660 MeV have been investigated. The charge and mass distribution analysis was made. The multimode fission model has allowed to decompose the total fission cross section into symmetric and asymmetric components. The photofission evolution from asymmetric to symmetric channel was considered.

The strong increasing of the symmetric component at high energy of protons is observed. The quantitative estimates of the various fission modes are obtained for the first time. Fissility of ^{241}Am , ^{238}U , and ^{237}Np in interaction at intermediate energies is obtained. The formation of a thermalized highly-excited nucleus in deep inelastic interaction of intermediate-energy particles, which decays independently of the

method of formation, allows to speak about universality of the nuclear fission mechanism.

REFERENCES

1. M. Goeppet-Mayer, *Phys. Rev.* **74**, 235 (1948).
2. P. Moller and S. G. Nilson, *Phys. Lett. B* **31**, 283 (1970).
3. P. Moller, S. G. Nilson, and J. R. Nix, *Nucl. Phys. A* **229**, 292 (1974).
4. V. M. Strutinsky, *Nucl. Phys. A* **122**, 1 (1968).
5. T. Ledergerber and H. C. Pauli, *Nucl. Phys. A* **207**, 1 (1973).
6. B. D. Wilkins, E. P. Steinberg, and R. R. Chasman, *Phys. Rev. C* **14**, 1832 (1976).
7. W. D. Myers and W. J. Swiatecki, *Nucl. Phys.* **81**, 1 (1966).
8. W. D. Myers and W. J. Swiatecki, *Ark. Fys.* **36**, 343 (1967).
9. V. V. Pashkevich, in *Proc. of the Intern. Conf. on the 50th Anniversary of Nuclear Fission, Leningrad, Russia, 16–20 Oct. 1989*, p. 241.

10. P. Frobrich and I. I. Gontchar, in *Proc. of the 2nd Intern. Conf. on Dynamical Aspects of Nuclear Fission, Smolenice, Slovakia, 14–18 Jun. 1994*, p. 182.
11. A. Turkevich and J. R. Niday, *Phys. Rev. C* **84**, 52 (1951).
12. U. Brosa, S. Grossman, and A. Muller, *Z. Naturforsch. A* **41**, 1341 (1986).
13. R. B. Firestone, *Tables of Isotopes*, 8th ed. [1998 Update (with CD ROM)], Ed. by S. Y. Frank Chu (CD-ROM editor) and C. M. Baglin (Wiley Intersci., New York, 1996).
14. H. Baba, J. Sanada, H. Araki, and A. Yokoyama, *Nucl. Instrum. Methods Phys. Res. A* **416**, 301 (1998).
15. H. Kudo, M. Maruyama, M. Tanikawa, et al., *Phys. Rev. C* **57**, 178 (1998).
16. T. Ohtsuki, Y. Hamajima, K. Sueki, et al., *Phys. Rev. C* **40**, 2144 (1989).
17. W. Younes, J. A. Becker, L. A. Bernstein, et al., *AIP Conf. Proc.* **610**, 673 (2002).
18. G. S. Karapetyan, A. R. Balabekyan, N. A. Demekhina, and J. Adam, *Yad. Fiz.* **72**, 955 (2009) [*Phys. At. Nucl.* **72**, 911 (2009)].
19. N. S. Ivanova, *Z. Empirische Textforsch.* **31**, 413 (1956).
20. V. A. Konshin et al., *Yad. Fiz.* **2**, 682 (1965) [*Sov. J. Nucl. Phys.* **2**, 489 (1965)].
21. V. A. Konshin et al., *Yad. Fiz.* **4**, 97 (1966) [*Sov. J. Nucl. Phys.* **4**, 69 (1966)].
22. A. Kotov et al., *Phys. Rev. C* **74**, 034605 (2006).
23. G. D. Adeev et al., Preprint INR-816/93 (Moscow, 1993).
24. V. M. Maslov, *Nucl. Phys. A* **717**, 3 (2003).
25. H. Kudo, H. Muramatsu, H. Nakahara, et al., *Phys. Rev. C* **25**, 3011 (1982).
26. M. Berezova, A. A. Bogatchev, O. Dorvaux, et al., *AIP Conf. Proc.* **912**, 362 (2007).
27. Chien Chung and J. J. Hogan, *Phys. Rev. C* **24**, 180 (1981).
28. Chien Chung and J. J. Hogan, *Phys. Rev. C* **25**, 899 (1982).
29. N. A. Demekhina and G. S. Karapetyan, *Phys. At. Nucl.* **71**, 27 (2008).
30. B. Schroder, G. Nydahl, and B. Forkman, *Nucl. Phys. A* **143**, 449 (1970).
31. S. A. Karamian, J. Adam, A. G. Belov, et al., *Phys. Rev. C* **62**, 024601 (2000).
32. V. S. Barashenkov, F. G. Gereghi, A. S. Iljinov, et al., *Nucl. Phys. A* **231**, 462 (1974).
33. T. Fukahori, O. Iwamoto, and S. Chiba, in *Proc. of the 7th Intern. Conf. on Nuclear Criticality Safety, ICNC 2003, Tokai-mura, Japan, 2003*, p. 144.

A study of reaction rates of (n, f) , (n, γ) and $(n, 2n)$ reactions in ^{nat}U and ^{232}Th by the neutron fluence produced in the graphite set-up (GAMMA-3) irradiated by 2.33 GeV deuteron beam

J. Adam^{1,2}, Chitra Bhatia³, K. Katovsky¹, V. Kumar^{3,7,a}, M. Majerle², V.S. Pronskikh¹, A.M. Khilmanovich⁴, B.A. Martynkevich⁴, I.V. Zhuk⁵, V.M. Golovatiouk¹, W. Westmeier⁵, A.A. Solnyshkin¹, V.M. Tsoupko-Sitnikov¹, and A.S. Potapenko⁶

¹ Joint Institute for Nuclear Research, Dubna (Moscow Region), 141980 Russian Federation

² Czech Academy of Science, Nuclear Physics Institute, Řež, Prague, 250 68 Czech Republic

³ HENP Laboratory (ADS Program), Physics Department, University of Rajasthan, Jaipur, India

⁴ Institute of Physics of National Academy of Sciences, Minsk, Belarus

⁵ Kernchemie Institute, Philips-Universität, Marburg, Germany

⁶ Joint Institute of Power and Nuclear Research, Sosny, Minsk, Belarus

⁷ University School of Basic and Applied Sciences, GGS IPU University, New Delhi

Received: 30 November 2010 / Revised: 8 June 2011

Published online: 22 July 2011 – © Società Italiana di Fisica / Springer-Verlag 2011

Communicated by R. Krücken

Abstract. Spallation neutrons produced in the collision of a 2.33 GeV deuteron beam with a large lead target are moderated by a thick graphite block surrounding the target and used to activate the radioactive samples of ^{nat}U and Th put at three different positions, identified as holes “a”, “b” and “c” in the graphite block. Rates of the (n, f) , (n, γ) and $(n, 2n)$ reactions in the two samples are determined using the gamma spectrometry. The ratios of the experimental reaction rates, $R(n, 2n)/R(n, f)$, for ^{232}Th and ^{nat}U are estimated in order to understand the role of the (n, xn) kind of reactions in Accelerator-Driven Sub-critical Systems. For the Th -sample, the ratio is $\sim 54(10)\%$ in the case of hole “a” and $\sim 95(57)\%$ in the case of hole “b” compared to $1.73(20)\%$ for hole “a” and $0.710(9)\%$ for hole “b” in the case of the ^{nat}U sample. Also the ratio of fission rates in uranium to thorium, $^{nat}\text{U}(n, f)/^{232}\text{Th}(n, f)$, is $\sim 11.2(17)$ in the case of hole “a” and $26.8(85)$ in hole “b”. Similarly, the ratio $^{238}\text{U}(n, 2n)/^{232}\text{Th}(n, 2n)$ is $0.36(4)$ for hole “a” and $0.20(10)$ for hole “b” showing that ^{232}Th is more prone to the (n, xn) reaction than ^{238}U . All the experimental reaction rates are compared with the simulated ones by generating neutron fluxes at the three holes from MCNPX 2.6c and making use of the LA150 library of cross-sections. The experimental and calculated reaction rates of all the three reactions are in reasonably good agreement. The transmutation power, P_{norm} as well as $P_{\text{norm}}/P_{\text{beam}}$ of the set-up is estimated using the reaction rates of the (n, γ) and $(n, 2n)$ reactions for both the samples in the three holes and compared with some of the results of the “Energy plus Transmutation” set-up and TARC experiment.

1 Introduction

Accelerator-Driven Sub-critical System (ADS) may be identified as a device for i) transmutation of nuclear waste [1,2] and ii) production of nuclear energy from a fertile fuel like thorium [3,4] besides the safety issues being better than a conventional critical reactor. These two aspects gave birth to the requirement of new nuclear data beyond the reactor neutron energies, developing Monte Carlo simulation codes for the design and modeling and developing experiments for the realization of the concept of ADS. It may be recalled that in the existing

databases like ENDF, JEFF, JENDL etc., only few data are available beyond 20 MeV neutron energy. Recently, simulated data up to ~ 200 MeV [5] from the already existing Monte Carlo codes like MCNPX [6], FLUKA [7] and CASCADE [8], deterministic codes like ALICE [9] and TALYS [10] and the parameterization methods after proper evaluation [11] have been added in the databases. In this direction for getting data of cross-sections with better precision in the energy range $E_n < 20$ MeV and similarly in the energy range of spallation neutrons, a large number of experimental facilities, namely PNF in Pohang [12], n-ToF at CERN [13] and IREN in Dubna [14], MYRRHA in Belgium [15], SAD [16] and DSAD [17],

^a e-mail: vkv1951@gmail.com

which later on will be identified as the “Energy + Transmutation” set-up at JINR etc., were planned and some of them are also operational. Similarly, SINQ at PSI [18], KEK in Japan [19], n-ToF at CERN [13] and a cluster of other research programs are being developed at LANL [20] for obtaining data, characterization and developing new materials. We know that from such facilities at neutron energies beyond 14 MeV, cross-sections of few candidate materials of ADS have also been reported [21] albeit with large errors and much better results are expected to come from the 200 m n-ToF facility at CERN in the near future. In the meantime, for the expeditious realization of the transmutation capability of a system based on the spallation neutrons, a few experiments of transmutation of long-lived fission products like ^{129}I and ^{99}Tc by the TARC experiment [22] at CERN and ^{129}I by the “Energy + Transmutation” (E+T) experiment [23] at JINR (Dubna) are conducted, and the spectrum averaged transmutation rates are measured. Also, methods of estimation of the transmutation power of a system are developed using the data of fission rates of ^{232}Th and $^{\text{nat}}\text{U}$, and the transmutation rates using the (n, γ) and $(n, 2n)$ reactions in the neutron field with energy ranging from thermal to the beam energy are obtained. For obtaining the spectrum average reaction rate theoretically, the neutron spectrum may be generated from a Monte Carlo simulation code like MCNPX and CASCADE and point cross-sections may be obtained partly from the databases and partly from deterministic codes like TALYS and ALICE. The so-estimated reaction rates are compared with the experimental data. This method proved to be very useful both for the validation of the Monte Carlo simulation codes [24–29] and to obtain the spectrum average cross-section of a reaction [30].

In the present GAMMA-3 experiment, a huge block of graphite is used to provide a number of positions of moderated spallation neutrons generated by the 2.33 GeV deuteron beam colliding with the lead target where the transmutation power of the set-up can also be measured using the data of radio-activity corresponding to various gamma peaks of the activated samples almost similarly as in the TARC and E+T experiments. The deuteron beam is used mainly for technical reasons. This experiment differs from the TARC and E+T experiments not only with respect to the beam particle but also because it has a different moderator. In the TARC experiment a thick lead target, in the E+T a natural uranium blanket and in the GAMMA-3 a thick graphite block, are used. The three experiments provide a first data set of the reaction rates of (n, γ) , $(n, 2n)$ and (n, f) reactions at different positions of the set-up as well as a comparative study for settling down some of the questions regarding the effectiveness of the neutron fluxes at different positions for a given transmutation reaction.

2 Experimental details

In the graphite set-up shown in fig. 1, the lead target of dimensions $d(\text{dia.}) \times l(\text{length}) = 8 \times 60 \text{ cm}^2$ is placed at the centre of the graphite block of dimensions

$l \times w \times b = 1.1 \times 1.1 \times 0.6 \text{ m}^3$. The graphite assembly is comprised of 25 blocks of different dimensions having several experimental holes for placing the activation samples and detectors. ^{232}Th sample is placed in three holes marked as “a”, “b” and “c” in the block number 14, 9 and 4, respectively as shown in fig. 1. The dimensions of the holes “a”, “b” and “c” are $d \times l = 14.6 \times 29.6 \text{ cm}^2$, $8.8 \times 36.3 \text{ cm}^2$, $15.4 \times 34.1 \text{ cm}^2$, respectively. Samples of $^{\text{nat}}\text{U}$ are placed in two holes, “a” and “b” while samples of ^{232}Th are placed in all the three holes. Block number 3, 4 and 5 and several other blocks visible in fig. 1 are used for other transmutation samples accompanied with threshold activation detectors. Uranium and thorium samples were irradiated in the form of sandwiches of three nearly identical foils (Th-Th-Th and U-U-U). This arrangement has the little advantage, compared to a single foil, that some of the nuclides produced in the sideward foils may be registered in the adjoining foil. We used the single (middle) foil and the double (sideward) foils for separate measurements because of the difference in self-absorption of the low-energy gamma rays being much higher compared to that of high-energy gammas (see fig. 3). The use of a single layer is preferred for the analysis of low-energy gammas and, for high-energy gammas, double-layered foils are used. This also provides improved statistics.

The diameter of these foils is 15 mm and the mass of the middle U foil is 172.3 mg, that of the middle ^{232}Th foil is 93.1 mg, while the total mass of the sideward foils is 334 mg for U and 176.3 mg for ^{232}Th .

The set-up was irradiated by a deuteron beam of 2.33 GeV energy at the Nuclotron accelerator in Dubna in March 2007. The irradiation started at 13 h 44 m 25 s on the 17th March, 2007 and ended at 15 h 01 m 20 s on the 18th March, 2007, *i.e.* it lasted about 25 hours and 17 minutes (=1517 minutes). The recorded intensity profile of the beam *versus* time is shown in fig. 2a. From the given time dependence of the beam, a correction, $\eta_b(T_{1/2})$ is calculated for each residual reaction product with half-life, $T_{1/2}$ and displayed in fig. 2b. Activation detectors, solid-state nuclear-track detectors and transmutation samples are used to measure the spectral fluences of the neutron field.

An aluminium foil (with thickness 6.7 mg/cm^2 and diameter 20 cm each) was installed at a distance of 3.1 m from the centre of the lead target in order to determine the beam profile and the number of deuterons hitting the lead target. The deuterons have been monitored using the reaction $^{27}\text{Al}(d, 3p 2n)^{24}\text{Na}$ [31] through the gamma spectrometry of the product nuclide ^{24}Na . After irradiation, the monitor foil was cut into four concentric rings with the inner ring having a circle of 2.1 cm diameter, the three following rings having outer diameters as 8.0, 12.0, and 16.0 cm, respectively. The number of deuterons measured on the two inner rings up to 8 cm diameter was 92(4)% of the total beam, and the integer number of deuterons hitting the Pb target is deduced to be $N_D = 1.7(1) \times 10^{13}$. From the track detectors the beam shape (see ref. [23]) is established to be a Gaussian with parameters, $X(\text{FWHM}) = 1.5 \pm 0.1 \text{ cm}$, $Y(\text{FWHM}) = 2.4 \pm 0.1 \text{ cm}$ with the beam center being

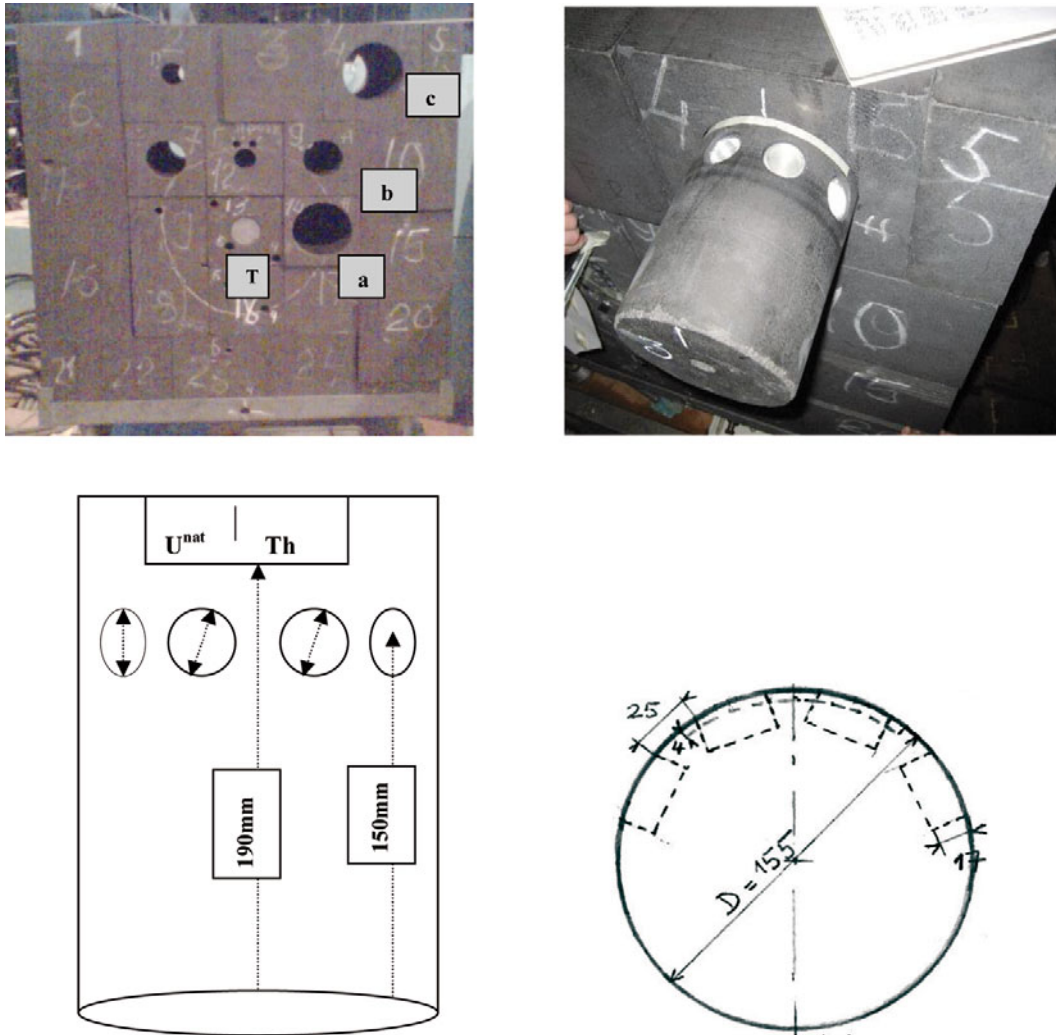


Fig. 1. Graphite assembly (upper left) of dimensions $1.1 \times 1.1 \times 0.6 \text{ m}^3$ with the lead target, T, of diameter 8 cm at the centre and the three experimental holes shown as “a”, “b” and “c” for the irradiation of different samples. A photograph of the cylinder (upper right) fitted in a hole is shown for clarity. The sample positions inside a hole are shown in the lower left figure as well as in the photograph. The positions of the samples on the cylinder fitted in a hole are shown in the lower right figure. ^{nat}U and ^{232}Th are placed at -9° and $+9^\circ$ in hole “a”, at -14° and $+14^\circ$ in hole “b” and at -9° and $+9^\circ$ in hole “c”, respectively, from the centre of the front face of the respective cylinder to the back of the circles. The four circles shown on the cylindrical surface are for the other samples placed in the experiment.

at $X_c = 0.7 \pm 0.1 \text{ cm}$, $Y_c = 0.2 \pm 0.1 \text{ cm}$. From the track detectors the integer number of deuterons turns out to be $\sim 1.85 \times 10^{13}$ and the percentage of beam hitting the lead 92.2% which agrees with the data obtained from the Al monitor.

3 Measurement procedure and method of analysis

We have used a coaxial detector with relative efficiency 18.9% and resolution of 1.78 keV at 1332 keV and a planar detector with diameter 36 mm, thickness 13 mm and resolution 335 eV at 5.9 keV and 580 eV at 122 keV. The coaxial detector is used to provide information on the peaks ranging from 20 keV to 3 MeV and the planar detector is used for the range $\sim 5 \text{ keV}$ to 700 keV.

All measurements have been done without any filters. Various measurement spectra are recorded up to a period of about one month for time intervals varying between 0.4 to 24 hours.

The measured gamma spectra are analyzed by the interactive mode of the DEIMOS code [32]. A detailed cascade of codes has been used for energy calibration, subtraction of background gamma-ray lines and single and double escape peaks, efficiency calibration and determination of experimental half-lives for the identification of several hundreds of gamma-ray lines. Various isotopes and fission fragments are assigned only when energy, half-life and intensity of peaks match with the values available in the literature [33]. For the details of the method of analysis of gamma peaks the reader is advised to refer to ref. [23].

After the identification and assignment of the element to a gamma peak the reaction rates have been calculated

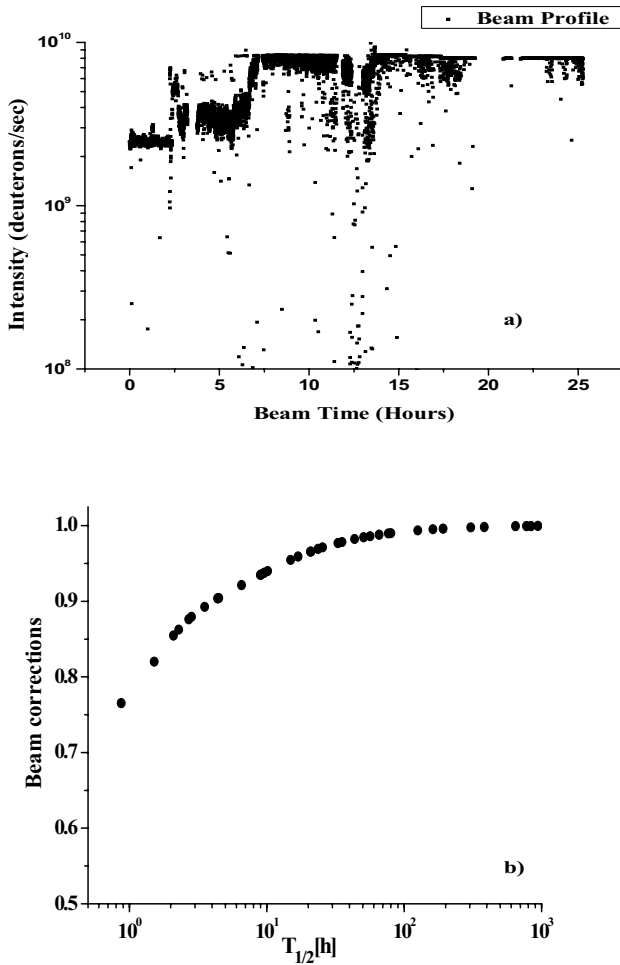


Fig. 2. a) Time dependence of the 2.33 GeV deuteron beam intensity, as received from the staff of the Nuclotron accelerator for the whole run. b) Beam corrections for residual nuclei in increasing order of η_b of elements: ^{134}I , ^{133}Te , ^{142}La , ^{127}Sn , ^{132}I , ^{92}Sr , ^{88}Kr , ^{92}Y , ^{129}Sb , ^{105}Ru , ^{135}Xe , ^{128}Sb , ^{140}Ba , ^{93}Y , ^{91}Sr , ^{24}Na , ^{97}Zr , ^{133}I , ^{112}Pd , ^{187}W , ^{143}Ce , ^{105}Ru , ^{48}Sc , ^{238}Np , ^{99}Mo , ^{132}Te , ^{47}Sc , ^{131}I , ^{48}Sc , ^{95}Nb and ^{103}Ru nuclides.

for every identified element with all the relevant correction factors of self-absorption η_a , beam intensity fluctuations η_b , and coincidence summing η_c (see the appendix in ref. [23]). Values of η_a , η_b , η_c have been estimated for the gamma peaks separately for the two samples of ^{232}Th and $^{\text{nat}}\text{U}$. The self-absorption corrections, η_a , for the two sideward double layers and the middle single layers of the ^{232}Th and $^{\text{nat}}\text{U}$ samples are plotted in figs. 3(a) and (b) for the low- and high-energy gammas, respectively, and from both figures it can be clearly seen that, for low-energy gammas η_a is very high, while for high-energy gammas it is close to unity. At energies beyond 1000 keV the correction is less than 1% and monotonously decreases to zero with increasing energy.

The coincidence summing correction, η_c , is calculated using the software COICOR and the Lund database [33], and this correction depends also on total efficiency of the registration of gamma rays including the Compton scat-

tering tail. The total correction factor, $\eta = \eta_a\eta_b\eta_c$, is given for each observed peak in tables 1 and 2.

The reaction rate, $R(A_r, Z_r)$ is defined as the number of produced residual nuclei, $Q(A_r, Z_r)$ per atom (N_t) of the sample per incident deuteron per second (N_d) as follows:

$$R(A_r, Z_r) = \frac{Q(A_r, Z_r)}{N_t N_d}. \quad (1)$$

The transmutation power, $P(A_r, Z_r)$ is defined as the quantity of produced mass $m(A_r, Z_r)$ per unit mass of the target $m(A_t, Z_t)$ [23] and, on normalization to 10^9 beam particles, we can write

$$P_{\text{norm}}(A_r, Z_r) = 10^9 \frac{P(A_r, Z_r)}{N_D}, \quad (2)$$

where N_D is the integer number of beam particles used in the irradiation time, t_{irr} .

4 Experimental results of reaction rates

After following all the detailed procedure related to the gamma spectrometry technique [23], the results in term of reaction rate, R , of the measurement of γ -rays from both the samples of ^{232}Th in the three irradiation holes “a”, “b” and “c” are given in table 1. Table 2 corresponds to the results of $^{\text{nat}}\text{U}$ of holes “a” and “b”. All the observed fission fragments and residual nuclides are listed in the aforesaid tables. In these tables, the results in boldface correspond to the upper variable of the heading which, itself, is shown in boldface. In the two tables, for example, the average value of all the observed peaks is given in boldface and the later values corresponding to individual peak are given in lightface.

From the data displayed in tables 1 and 2 the following observations can be made. The total number of spectra of the ^{232}Th and $^{\text{nat}}\text{U}$ samples analyzed to obtain the above results are 33 and 22, respectively, for all the three holes “a”, “b”, “c” and several hundreds of gamma-ray peaks belonging to these spectra are analyzed. After the complete analysis for $^{\text{nat}}\text{U}$ in hole “a” and “b”, 11 fission products, namely $^{85\text{m}}\text{Kr}$, ^{93}Y , ^{99}Mo , ^{103}Ru , ^{105}Rh , ^{131}I , ^{132}Te , ^{133}I , ^{140}Ba , ^{141}Ce and ^{143}Ce are observed along with ^{239}Np as a result of the (n, γ) reaction and ^{237}U as a result of the $(n, 2n)$ one. In the previous experiment using the E+T assembly [23], ^{237}U was not observed. For ^{232}Th in hole “a”, a total of 6 fission products, $^{85\text{m}}\text{Kr}$, ^{99}Mo , ^{131}I , ^{133}Xe , ^{135}Xe and ^{141}Ce are observed along with ^{233}Pa , *i.e.* the daughter elements produced upon decay of ^{233}Th as a result of the $^{232}\text{Th}(n, \gamma)$ reaction and of ^{231}Th as a result of $^{232}\text{Th}(n, 2n)$ are also observed. For ^{232}Th in hole “b”, all the above-mentioned fission products (except for ^{99}Mo , ^{133}Xe , ^{135}Xe) along with ^{233}Pa and ^{231}Th are observed. Lastly, in case of hole “c”, only ^{99}Mo is observed as a fission product and ^{233}Pa as a (n, γ) product. One important observation is that there is consistency in the reaction rates corresponding to the different gamma peaks of the same decaying nuclide. Comparison and discussions of these observations with the results of other experiments is being postponed to sect. 6.

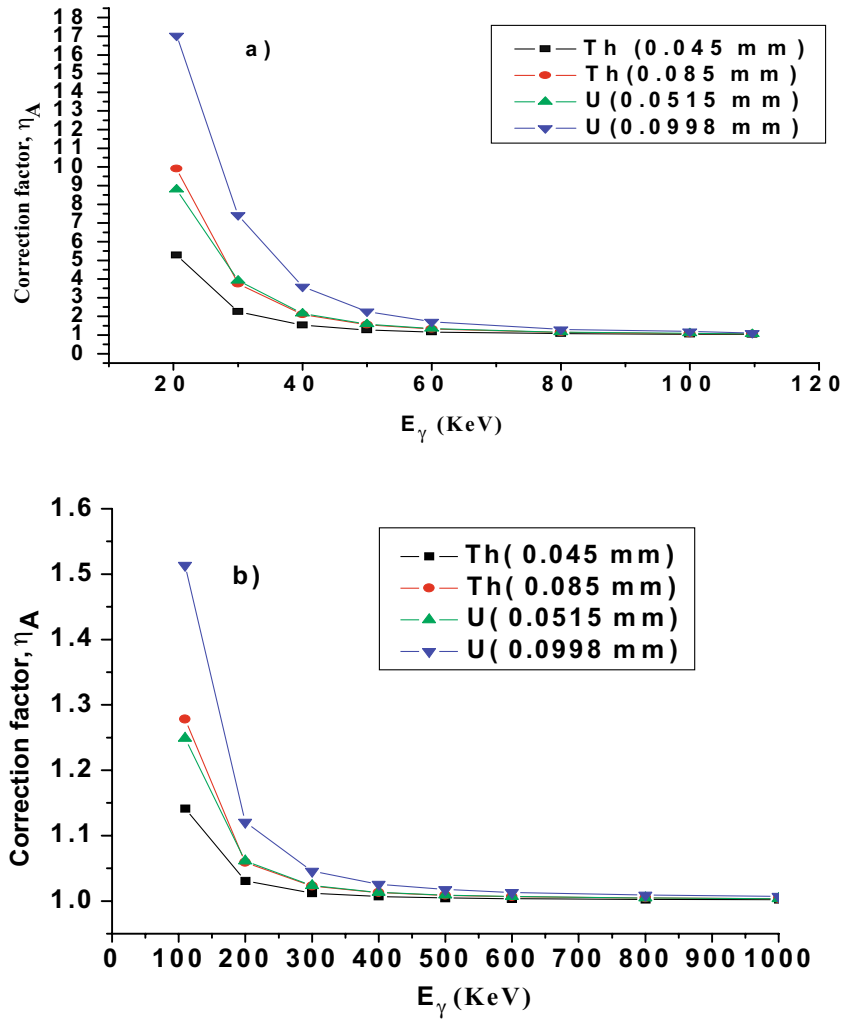


Fig. 3. Self-absorption correction factor, η_a , for single and double thicknesses of the ^{232}Th and ^{238}U samples for a) low gamma energy range (for Th from 20.47 to 109.65 keV and for U from 21.76 to 115.61 keV) and b) high gamma energy range (for Th from 109.65 to 1000 keV and for U from 115.61 to 1000 keV).

5 Monte Carlo simulations

5.1 Simulation of neutron flux at sample positions

Monte Carlo code MCNPX v2.6.C package of cascade model INCL4/ABLA and LA150 library is used [6] for the simulation of the production of neutrons in the collision of a 2.33 GeV deuteron beam with the lead target and their transport in the graphite set-up. As mentioned earlier the ^{232}Th samples were irradiated in all the three holes, namely “a”, “b” and “c” while the samples of ^{238}U were irradiated in holes “a” and “b” at the positions as shown in fig. 1. The results of the simulated neutron flux ($E d\phi/dE$) per incident deuteron falling on the samples of ^{232}Th and ^{238}U for the given positions in holes “a”, “b” and “c” are given in fig. 4. It can be clearly seen from the figures that there are low- and high-energy humps in the fluxes and the low-energy hump being pronounced shows that graphite is a good moderator. It may also be noted that at all energies, the neutron flux decreases from hole “a” to “c” because the distance of the holes from the centre of the Pb target increases gradually.

5.2 Calculation of the reaction rates using the neutron flux

After simulation of the neutron flux at the positions of the samples, spectrum average cross-sections for the (n, γ), (n, 2n) and (n, f) reactions are estimated using the pre-processing code NJOY 99.112 and the JEFF-3.1 nuclear data library [34] for the cross-sections of the (n, γ) and (n, f) reactions. Cross-sections of the (n, 2n) reaction are taken from the MCNPX code itself. The total-reaction rate is calculated by summing the partial reaction rates $R(A_r, Z_r, E_n)$ for all the energies from the thermal to the highest energy corresponding to the beam energy.

6 Analysis of the results and conclusions

6.1 Determination of group weight factors for calculation of the total number of fissions

Samples of ^{238}U and ^{232}Th are placed at different positions in the three holes, therefore, the fission takes place

Table 1. Results of activity [Bq], half-life $T_{1/2}$, average reaction rate $\langle R \rangle$ for ^{232}Th after irradiation by secondary neutrons in the holes “a”, “b” and “c”. All corrections are included in η . * denotes mixing due to another nuclide. Letter “M” corresponds to the number of γ -ray spectra, “X” to planar and “C” to coaxial detectors and “s” and “d” to the single and double layers of the sample, respectively.

Isotope E_γ [keV]	Activity [Bq] I_γ [%]	η -XsM η -CdM	a-hole		b-hole		c-hole					
			$T_{1/2}$ (Lib.) $T_{1/2}$ (Exp.)	$\langle R \rangle$ R	$T_{1/2}$ (Lib.) $T_{1/2}$ (Exp.)	$\langle R \rangle$ R	$T_{1/2}$ (Lib.) $T_{1/2}$ (Exp.)	$\langle R \rangle$ R	XsM CdM			
Th-231	371(37)		25.52(10)h	$\langle 7.61(83)E-27 \rangle$	25.52(10)h	$\langle 3.6(18)E-27 \rangle$						
25.646	14.50	3.900-Xs5	23.4(26)h	1.49(91)E-26	7.47h	3.41(97)E-27	Xs2					
25.646	14.50	5.337-Xd4	25.44(14)h	1.43(93)E-26								
81.227	0.89	1.107-Xs5	5.0(9)d	8.9(18)E-27	13(4)d	3.6(18)E-27	Xs7					
81.227	0.89	1.192-Xd5	6.5(18)d	8.6(26)E-27								
84.216	6.60	1.037-Xs7	12(3)d	6.5(11)E-27	–	4.9(21)E-27	Xs7					
84.216	6.60	1.105-Xd6	18(9)d	8.9(25)E-27								
89.944	0.94	1.070-Xs7	–	1.63(25)E-25*								
89.944	0.94	1.121-Xd6	87(25)d	2.04(6)E-25*								
Pa-233	419(11)		26.967(2)d	$\langle 3.20(8)E-25 \rangle$	26.967(2)d	$\langle 1.92(5)E-25 \rangle$		26.97(2)d	$\langle 3.38(16)E-26 \rangle$			
75.354	1.39	1.189-Xs7	160(80)d	3.7(20)E-25	–	2.39(26)E-25	Xs7	–	1.31(21)E-25*	Xs3		
75.354	1.39	1.222-Xd6	–	5.5(16)E-25	100(40)d	2.49(32)E-25	Xd6	–	1.19(9)E-25*	Xd6		
86.814	1.97	1.096-Xs7	33(19)d	6.0(33)E-25	67(17)d	4.6(17)E-25*	Xs7	18(11)d	2.81(12)E-25*	Xs7		
86.814	1.97	1.172-Xd6	58(9)d	7.2(27)E-25	49(7)d	4.7(19)E-25*	Xd6	–	3.48(15)E-25*	Xd6		
103.941	0.87	1.108-Xs6	42(11)d	3.46(77)E-25	20(4)d	1.94(8)E-25	Xs7	–	4.70(58)E-25*	Xs4		
103.941	0.87	1.122-Xd6	31(3)d	3.9(12)E-25	26(3)d	2.25(8)E-25	Xd6	27(11)d	5.8(12)E-25*	Xd6		
103.941	0.87	1.124-Cd2	–	3.81(77)E-25								
300.110	6.62	1.016-Xs7	42(4)d	4.1(12)E-25	49(8)d	2.86(9)E-25*	Xs7	20.60(6)d	1.36(5)E-25*	Xs7		
300.110	6.62	1.027-Xd6	41.8(28)d	5.1(12)E-25	54(10)d	3.13(21)E-25*	Xd6	–	1.59(12)E-25*	Xd2		
300.110	6.62	1.025-Cd3	38.8(12)d	5.4(24)E-25	39(11)d	3.28(13)E-25*	Cd4	153(20)d	1.70(15)E-25*	Cd4		
311.890	38.6	1.021-Xs7	29.2(2)d	2.78(7)E-25	30(4)d	1.69(4)E-25	Xs7	31(6)d	3.04(9)E-26	Xs7		
311.890	38.6	1.031-Xd6	28.9(9)d	3.48(9)E-25	29(3)d	1.83(9)E-25	Xd6	29.6(2.9)d	3.46(23)E-26	Xd6		
311.890	38.6	1.026-Cd3	25.9(6)d	3.66(14)E-25	20.6(18)d	1.99(7)E-25	Cd4	26.3(8)d	3.79(13)E-26	Cd4		
340.710	4.47	1.012-Xs7	36(9)d	2.95(8)E-25	19(9)d	1.83(7)E-25	Xs7	31(21)d	4.7(27)E-26	Xs6		
340.710	4.47	1.020-Xd6	21.9(18)d	3.78(11)E-25	36(11)d	2.05(15)E-25	Xd6	44(11)d	5.7(24)E-26	Xd6		
340.710	4.47	1.019-Cd3	31(4)d	3.87(20)E-25	25(3)d	2.16(9)E-25	Cd4	47(9)d	5.8(35)E-26	Cd3		

Table 1. Continued.

Isotope E_γ [keV]	Activiy [Bq] I_γ [%]	η -XsM η -CdM	a-hole		b-hole			c-hole		
			$T_{1/2}$ (Lib.) $T_{1/2}$ (Exp.)	$\langle R \rangle$ R	$T_{1/2}$ (Lib.) $T_{1/2}$ (Exp.)	$\langle R \rangle$ R	XsM CdM	$T_{1/2}$ (Lib.) $T_{1/2}$ (Exp.)	$\langle R \rangle$ R	XsM CdM
375.450	0.679	0.981-Xs3	23(14)d	3.01(20)E-25	13(7)d	2.16(20)E-25	Xs3			
375.450	0.679	0.986-Xd6	33(9)d	3.8(19)E-25	17(5)d	2.23(24)E-25	Xd5			
375.450	0.679	0.984-Cd3	27(4)d	4.3(16)E-25	29(12)d	2.75(17)E-25	Cd3			
398.620	1.390	0.929-Xs6	24(8)d	3.1(13)E-25	-	1.87(15)E-25	Xs4			
398.620	1.390	0.932-Xd6	37(10)d	3.8(14)E-25	17(5)d	2.22(12)E-25	Xd3			
398.620	1.390	0.927-Cd3	25.3(11)d	3.9(14)E-25	37(4)d	2.02(7)E-25	Cd4			
415.760	1.745	0.970-Xs6	26(8)d	2.8(11)E-25	18(4)d	1.85(8)E-25	Xs5	6.93(0.07)d	6.3(12)E-26	Xs2
415.760	1.745	0.975-Xd6	27(5)d	3.5(12)E-25	-	1.94(8)E-25	Xd4	11.3(0.01)d	5.29(74)E-26	Xd2
415.760	1.745	0.973-Cd3	28.4(2)d	3.9(16)E-25	20.6(2.8)d	2.13(7)E-25	Cd4	-	5.21(62)E-26	Cd2
Kr-85m	5.57(6)		4.48(8)h	(3.15(4)E-29)	4.48(8)h	(7.25(85)E-30)				
151.159	75	1.017-Xs4	1.7(9)d	3.16(6)E-29	-	7.4(12)E-30	Xs1			
151.159	75	1.130-Xd2	9.57(1)h	3.15(5)E-29						
Mo-99	2.37(19)		2.748(4)d	(1.99(19)E-28)	2.748(4)d	(5.55(88)E-29)			(5.5(19)E-30)	
140.681	89.43	1.023-Xs7	4.6(4)d	2.13(13)E-28	-	5.55(88)E-29	Xs3	-	5.5(19)E-30	Xs1
140.681	89.43	1.137-Xd4	11(4)d	1.75(12)E-28						
140.681	89.43	1.135-Cd2		2.56(26)E-28						
I-131	0.70(24)		8.021d	(1.69(59)E-28)	8.021d	(1.39(54)E-28)				
364.489	81.7	1.047-Xs1	-	1.66(81)E-28	-					
364.489	81.7	1.027-Xd1		1.73(85)E-28		1.39(54)E-28	Xd1			
Xe-133	1.89(12)		5.243(1)d	(3.00(20)E-28)						
80.997	38	1.062-Xs3	1.5(6)d	3.32(13)E-28						
80.997	38	1.263-Xd4	3.5(17)d	2.88(8)E-28						
Xe-135	12.6(13)		9.14(02)h	(1.06(14)E-28)						
249.770	90	0.969-Xs4	16.1(25)h	1.02(13)E-28						
249.770	90	1.000-Xd3	12.1(11)h	1.52(43)E-28						
Ce-141	0.26(2)		32.50(5)d	(2.52(74)E-28)	32.501(5)d	(6.6(29)E-29)				
145.441	48.2	1.136-Xs1		2.8(12)E-28	-	6.6(29)E-29	Xs1			
145.441	48.2	1.275-Xd2	7.74(8)d	2.35(95)E-28						

Note: Averaging is done without including the data marked with the sign *. The activities are calculated for the Th sample having mass 0.0932 g and assuming the start of measurement time to be the end of irradiation.

Table 2. Results of activity [Bq], half life $T_{1/2}$, average reaction rate $\langle R \rangle$ for ^{nat}U after irradiation by secondary neutrons in the holes “a” and “b”. All corrections are included in η . * denotes mixing due to another nuclide. Letter “M” corresponds to the number of γ -ray spectra, “X” to planar and “C” to coaxial detectors and “s” and “d” to the single and double layers of the sample, respectively.

Isotope E_γ [keV]	Activiy [Bq] I_γ [%]	η -XsM η -CdM	a-hole		b-hole		
			$T_{1/2}$ (Lib.) $T_{1/2}$ (Exp.)	$\langle R \rangle$ R	$T_{1/2}$ (Lib.) $T_{1/2}$ (Exp.)	$\langle R \rangle$ R	XsM CdM
U-237	22.8(8)		6.75 (1)d	$\langle 2.72(9)E-27 \rangle$	6.75 (1)d	$\langle 7.21(20)E-28 \rangle$	
26.345	2.43	11.67-Xd2	18.27d	7.3(13)E-26*			
26.345	2.43	6.374-Xs2	16d	1.89(50)E-26*			
59.541	34.5	1.821-Xd6	7.5(3)d	2.70(10)E-27	–	7.37(10)E-28	Xd2
59.541	34.5	1.413-Xs7	8.3(5)d	2.85(15)E-27	16.6h	6.95(13)E-28	Xs2
208.00	21.2	1.199-Xd6	6.7(4)d	2.52(10)E-27			
208.00	21.2	1.139-Xs7	7.1(5)d	2.97(12)E-27			
208.00	21.2	1.560-Cd3	5.7(5)d	1.64(75)E-27			
Np-239	7200(240)		2.3565(4)d	$\langle 3.11(10)E-25 \rangle$	2.3565(4)d	$\langle 2.08(20)E-25 \rangle$	
44.665	0.13	3.130-Xd4	2.6(3)d	3.66(27)E-25	1.91(21)d	2.70(56)E-25	Xd6
44.665	0.13	2.023-Xs4	3.0(4)d	2.65(22)E-25	1.3(6)d	3.74(75)E-25	Xs3
49.415	0.13	2.674-Xd7	5.0(6)d	8.7(22)E-25*	7.5(12)d	6.08(55)E-25*	Xd6
49.415	0.13	1.968-Xs7	4.21(29)d	7.1(15)E-25*	5.0(4)d	7.9(34)E-25*	Xs7
57.276	0.13	2.184-Xd6	1.65(5)d	7.6(16)E-25*	1.49(10)d	6.2(23)E-25*	Xd6
57.276	0.13	1.651-Xs7	1.78(8)d	8.3(11)E-25*	1.6(1)d	4.8(25)E-25*	Xs5
61.461	1.29	1.690-Xd6	2.28(5)d	3.61(12)E-25	2.44(2)d	1.90(63)E-25	Xd6
61.461	1.29	1.350-Xs7	2.47(3)d	2.95(10)E-25	2.36(5)d	2.67(75)E-25	Xs6
61.461	1.29	1.764-Cd3	2.26(6)d	2.77(21)E-25			
67.846	0.092	1.809-Xd6	2.29(11)d	5.9(7) E-25	3.21(1)d	2.71(47)E-25	Xd6
67.846	0.092	1.433-Xs7	2.39(18)d	3.89(40)E-25	2.7(5)d	3.24(63)E-25	Xs3
106.125	27.2	1.117-Xs7	2.40(11)d	2.94(7)E-25	2.368(27)d	1.86(5)E-25	Xs6
106.125	27.2	1.184-Xd6	2.35(6)d	3.75(10)E-25	2.41(03)d	2.02(6)E-25	Xd6
106.125	27.2	1.172-Cd3	2.34(2)d	3.04(14)E-25	3.71(15)d	1.99(3)E-25	Cd3
181.711	0.081	1.181-Xd4	1.81(20)d	3.33(31)E-25			
181.711	0.081	1.085-Xs5	2.5(3)d	2.74(23)E-25			
209.753	3.42	1.092-Xs7	2.39(12)d	3.97(9)E-25	2.38(4)d	3.18(6)E-25	Xs6
209.753	3.42	1.174-Xd6	2.32(4)d	4.91(12)E-25	2.41(19)d	3.59(12)E-25	Xd6
209.753	3.42	1.135-Cd4	2.43(3)d	4.69(28)E-25	2.20(5)d	2.88(19)E-25	Cd4
226.378	0.28	1.113-Xd6	2.25(12)d	3.53(19)E-25	2.11(19)d	5.06(83)E-25	Xs5
226.378	0.28	1.069-Xs7	2.40(9)d	2.99(16)E-25	3.1(4)d	2.12(47)E-25	Xd6
228.183	10.76	1.087-Xs7	2.48(9)d	3.62(9)E-25*	–	2.14(5)E-25*	Xs2
228.183	10.76	1.152-Xd6	2.41(4)d	4.53(15)E-25*	2.53(18)d	3.01(8)E-25*	Xd6
228.183	10.76	1.082-Cd4	2.46(6)d	4.14(12)E-25*	2.10(3)d	2.69(32)E-25*	Cd4
254.418	0.11	1.072-Xd5	1.98(19)d	3.63(37)E-25	–	1.92(35)E-25	Xd6
254.418	0.11	1.039-Xs5	1.35(13)d	3.21(50)E-25	1.6d	2.26(59)E-25	Cd2
254.418	0.11	1.085-Cd1		2.56(4)E-25			
277.599	14.38	1.075-Xs7	2.38(15)d	3.16(7)E-25	2.32(23)d	1.88(35)E-25	Xs6
277.599	14.38	1.115-Xd6	2.35(30)d	3.98(10)E-25	2.39(4)d	1.84(28)E-25	Xd6
277.599	14.38	1.079-Cd4	2.34(19)d	3.38(13)E-25	2.5(6)d	2.15(29)E-25	Cd4

Table 2. Continued.

Isotope E_γ [keV]	Activiy [Bq] I_γ [%]	η -XsM η -CdM	a-hole		b-hole		
			$T_{1/2}$ (Lib.)	$\langle R \rangle$	$T_{1/2}$ (Lib.)	$\langle R \rangle$	XsM
			$T_{1/2}$ (Exp.)	R	$T_{1/2}$ (Exp.)	R	CdM
285.460	0.79	1.107-Xd5	2.26(6)d	2.48(22)E-25	2.42(8)d	1.81(34)E-25	Xd6
285.460	0.79	1.080-Xs7	2.44(6)d	2.78(9)E-25	1.53d	1.66(21)E-25	Xs2
285.460	0.79	1.135-Cd1		3.61(16)E-25	3.0(17)d	2.53(79)E-25	Cd3
315.879	1.60	0.923-Xs7	2.34 (3)d	2.95(9)E-25	2.35(8)d	1.89(15)E-25	Xs6
315.879	1.60	0.941-Xd6	2.32(4)d	3.73(22)E-25	2.34(4)d	1.72(6)E-25	Xd5
315.879	1.60	0.946-Cd3	2.34(16)d	234(16)E-25	2.34(16)d	2.07(4)E-25	Cd3
334.309	2.07	0.828-Xs7	2.47(4)d	2.99(10)E-25	2.37(08)d	1.98(13)E-25	Xs7
334.309	2.07	0.842-Xd6	2.32(5)d	3.65(22)E-25	2.47(7)d	1.67(6)E-25	Xd5
334.309	2.07	0.848-Cd4	2.34(3)d	3.29(13)E-25	3.1(2)d	2.13(5)E-25	Cd3
Kr-85m	126(5)		4.480(8)h	$\langle 1.58(6)E-27 \rangle$	4.480(8)h	$\langle 9.05(18)E-29 \rangle$	
151.159	75	1.130-Xd2	4.4h	1.63(8)E-27	4.49h	1.14(8)E-28	Xd2
151.159	75	1.017-Xs4	4.65(13)h	1.52(7)E-27	3.9(5)h	9.04(55)E-29	Xs3
304.870	75	0.923-Xs3	3.8(19)h	2.09(37)E-27			
Y-93	374(18)		10.18(8)h	$\langle 5.60(27)E-27 \rangle$			
266.90	7.3	1.011-Xd3	11.0(9)h	5.82(43)E-27			
266.90	7.3	1.002-Xs4	10.5(9)h	5.47(33)E-27			
Zr-97	638(149)		16.74(11)h	$\langle 7.5(17)E-27 \rangle$	16.744(11)h	$\langle 4.69(33)E-27 \rangle$	
743.36	93	0.964-Cd3	18(10)h	7.5(17)E-27	12(8)d	4.69(33)E-27	Cd3
Mo-99	129(3)		2.7475(4)d	$\langle 6.76(18)E-27 \rangle$	2.7475(4)d	$\langle 3.53(46)E-27 \rangle$	
140.681	89.43	1.081-Xs7	2.845(24)d	6.47(40)E-27	2.94(12)d	3.21(91)E-27	Xs7
140.681	89.43	1.291-Xd6	2.80(8)d	6.90(26)E-27	2.98(5)d	5.2(15)E-27	Xd5
140.681	89.43	1.292-Cd4	3.06(09)d	8.2(21)E-27	2.90(6)d	6.1(24)E-27	Cd4
181.063	5.99	1.092-Xs6	4.0(12)d	7.0(6)E-27	2.1(5)d	2.87(20)E-27	Xs4
181.063	5.99	Xd5	3.23(21)d	6.74(44)E-27			
739.500	12.13	1.108-Cd4	3.1(7)d	5.52(99)E-27	3.3(2)d	4.77(28)E-27	Cd4
Ru-103	5.0(3)		39.26(20)d	$\langle 3.41(12)E-27 \rangle$	39.26(2)d	$\langle 2.60(37)E-27 \rangle$	
497.080	90.9	1.017-Xd3	27(20)d	3.40(33)E-27	–	3.21(75)E-27	Xd1
497.080	90.9	1.016-Xs3	80(70)d	3.49(27)E-27	28(20)d	2.40(43)E-27	Cd4
497.080	90.9	1.017-Cd3	39(4)d	3.39(14)E-27			
Rh-105	106(9)		35.36(60)h	$\langle 1.40(9)E-27 \rangle$	35.36 (6)h	$\langle 8.2(9)E-28 \rangle$	
319.14	19	1.031-Xd4	65(10)h	1.35(13) E-27	–	9.2(17)E-28	Xd1
319.14	19	1.022-Xs4	34.6(55)h	1.45(13)E-27	–	7.8(11)E-28	Cd1
I-131	21.2(5)		8.021(11)d	$\langle 3.02(6)E-27 \rangle$	8.021(11)d	$\langle 2.26(31)E-27 \rangle$	
284.305	6.14	1.046-Xd2	9.3 d	3.9(6)E-27	2.42(8)d	2.29(67)E-27	Xd5
284.305	6.14	1.022-Xs1		3.8(10)E-27			
364.489	81.7	1.047-Xd6	8.6(3)d	2.97(9)E-27	9.2(6)d	1.95(52)E-27	Xd6
364.489	81.7	1.031-Xs6	7.8(7)d	2.99(13)E-27	10.0(14)d	3.08(83)E-27	Xs5
364.489	81.7	1.047-Cd4	8.14(13)d	3.07(11)E-27	6.4(17)d	2.24(59)E-27	Cd4
Te-132	71(20)		3.204(2)d	$\langle 3.42(19)E-27 \rangle$	3.204(2)d	$\langle 3.45(12)E-27 \rangle$	
49.720	15.0	2.486-Xd6	5.0(6)d	1.01(47)E-26*	–	1.27(7)E-26*	Xd6
49.720	15.0	-Xs7	4.21(29)d	7.59(77)E-27*			

Table 2. Continued.

Isotope E_γ [keV]	Activiy [Bq] I_γ [%]	η -XsM η -CdM	a-hole		b-hole		
			$T_{1/2}$ (Lib.) $T_{1/2}$ (Exp.)	$\langle R \rangle$ R	$T_{1/2}$ (Lib.) $T_{1/2}$ (Exp.)	$\langle R \rangle$ R	XsM CdM
228.160	88.0	1.041-Xs7	2.49(9)d	3.41(47)E-26*			
228.160	88.0	1.094-Xd6	2.49(4)d	3.2(6)E-26*	2.53(18)d	3.00(9)E-26*	Xd6
228.160	88.0	1.085-Cd4	2.46(6)d	3.9(14)E-26*	2.10(3)d	2.53(6)E-26*	Cd4
522.650	16.6	1.154-Xs3	5.1(28)d	5.09(43)E-27	–		
522.650	16.6	1.167-Xd4	3.4(9)d	4.27(33)E-27	–	3.32(5)E-27	Xd6
522.650	16.6	1.286-Cd2	2.91(29)d	4.19(28)E-27		3.52(22)E-27	Cd2
630.190	13.3	1.096-Xd6	4.9(2)d	2.94(8)E-27	–		
630.190	13.3	1.154-Cd3	4.9(2)d	2.99(11)E-27		3.87(8)E-27	Cd2
667.72	101.7	1.084-Xs7	3.11(14)d	4.21(15)E-27			
667.72	101.7	1.089-Xd5	3.42(15)d	4.22(16)E-27			
667.72	101.7	1.159-Cd3	3.07(5)d	3.49(15)E-27	3.3(1)d	2.69(38)E-27	Cd3
772.61	77.9	0.994-Cd3	3.05(8)d	3.55(16)E-27	3.7(2)d	2.80(37)E-27	Cd3
954.55	18.7	0.993-Cd3	5.0(11)d	3.91(26)E-27	3.8(1)d	3.09(27)E-27	Cd3
I-133	302(7)		20.8(1)h	$\langle 6.40(27)E-27 \rangle$	20.8(1)h	$\langle 3.35(15)E-27 \rangle$	
529.87	86.3	0.969-Xs5	20.8(7)h	6.35(22)E-27	–	3.28(5)E-27	Xs2
529.87	86.3	0.980-Xd4	21.0(7)h	6.69(22)E-27	21.7 h	3.10(13)E-27	Xd4
529.87	86.3	0.980-Cd4	22.68 h	5.31(48)E-27	30.96 h	3.84(11)E-27	Cd3
Xe-133	141(21)		5.243(1)d	$\langle 1.25(18)E-26^* \rangle$	5.243(1)d	$\langle 3.9(7)E-27 \rangle$	
80.997	38	1.620-Xd6	7.8(5)d	1.33(9)E-26*	–	3.6(10)E-27	Xd6
80.997	38	1.301-Xs7	13.3(24)d	8.7(19)E-27*	7.4(12)d	4.1(10)E-27	Xs7
160.613	0.066	0.994-Xd2		1.16(36)E-25*			
160.613	0.066	0.912-Xs6	4.0(12)d	1.33(18)E-25*			
Xe-135	649(198)		9.14(2)h	$\langle 4.1(12)E-27 \rangle$			
249.770	90	1.000-Xd3	12.9(4)h	5.1(21)E-27			
249.770	90	0.969-Xs5	15.1(20)h	3.6(15)E-27			
Ba-140	28(2)		12.752(3)d	$\langle 5.59(19)E-27 \rangle$	12.752(3)d	$\langle 3.73(32)E-27 \rangle$	
29.964	14.1	7.696-Xd6	6.4(16)d	8.7(16)E-27			
162.660	6.22	1.266-Xd4	6.2(14)d	6.97(44)E-27			
162.660	6.22	1.223-Cd4	12.0(8)d	7.3(17)E-27			
304.9	4.29	1.132-Cd2	10.70 d	5.16(47)E-27			
328.762	20.3	1.103-Xd4	20(8)d	5.4(8)E-27			
328.762	20.3	1.241-Cd3	16.1(2)d	6.59(47)E-27			
423.75	3.15	1.025-Cd4	8.5(2)d	5.96(59)E-27	10.3(2)d	4.67(93)E-27	Cd4
487.021	45.5	1.064-Xd4	21(9)	5.4(7)E-27			
487.021	45.5	1.116-Cd4	16.1(2)d	5.06(20)E-27	11(4)d	5.58(53)E-27	Cd4
537.261	24.39	1.016-Xd4	11.4(21)d	5.72(41)E-27			
537.261	24.39	1.040-Cd4	13.4(1)d	5.93(32)E-27	11(3)d	4.08(63)E-27	Cd4
815.7	23.28	0.993-Cd4	17(4)d	5.55(79)E-27	11.02(4)d	4.67(63)E-27	Cd4
867.8	5.50	1.047-Cd2	-	5.90(83)E-27	3.37d	3.53(10)E-27	Cd2
1596.210	95.4	1.125-Cd4	17(3)d	4.58(55)E-27	13(4)d	7.75(67)E-27	Cd4
Ce-141	10.0(3)		32.501(5)d	$\langle 5.65(13)E-27 \rangle$	32.501(5)d	$\langle 3.88(44)E-27 \rangle$	

Table 2. Continued.

Isotope E_γ [keV]	Activiy [Bq] I_γ [%]	η - XsM η - CdM	a-hole		b-hole		
			$T_{1/2}$ (Lib.) $T_{1/2}$ (Exp.)	$\langle R \rangle$ R	$T_{1/2}$ (Lib.) $T_{1/2}$ (Exp.)	$\langle R \rangle$ R	XsM CdM
145.441	48.2	1.275-Xd6	44(7)d	5.53(16)E-27	–	4.31(16)E-27	Xd5
145.441	48.2	1.136-Xs7	65(18)d	5.65(40)E-27	39(10)d	3.26(13)E-27	Xs7
145.441	48.2	1.275-Cd3	30.7(25)d	5.93(24)E-27	20(10)d	4.70(20)E-27	Cd4
Ce-143	222(5)		33.039(6)h	$\langle 6.49(10)E-27 \rangle$	33.039(6)h	$\langle 3.44(18)E-27 \rangle$	
57.356	11.7	1.456-Xs6	42.7(19)h	1.18(4)E-26*	38.4(6)h	1.41(6)E-26*	Xs5
57.356	11.7	1.900-Xd5	39.6(12)h	1.34(11)E-26*	38.4(6)h	1.12(4)E-26*	Xd5
293.266	42.8	1.021-Xs6	32.4(10)h	6.54(19)E-27	31.2(05)h	2.80(9)E-27	Xs3
293.266	42.8	1.054-Xd2	32.2(6)h	6.63(19)E-27	35.04(4)h	3.39(12)E-27	Xd4
293.266	42.8	1.044-Cd4	37.2(4)h	6.6(14)E-27	40.2(4)h	3.45(6)E-27	Cd3
350.98	3.23	0.828-Xs3	41(12)h	7.3(9)E-27			
350.98	3.23	0.850-Xd3	89(19)h	7.4(7)E-27			
664.571	5.69	1.026-Xd1		6.11(17)E-27			
664.571	5.69	0.986-Cd4	16.16(17)h	6.27(79)E-27			
721.86	5.39	0.970-Cd2	70.56h	5.3(17)E-27	–	3.74(6)E-27	Cd2

Note: Averaging is done without including the data marked with the sign *. The activities are calculated for the U sample with mass 0.1723 g and assuming the start of measurement time to be the end of irradiation.

differently since i) the neutron flux is different in these positions, ii) the rate of fission of ²³⁵U is different than that of ²³⁸U, and iii) all the fission products may not be observed in the experiment. In this situation, the measured production rate of a fission product needs to be converted into the total fission rate. As an approximation, we may know the weight factors of fission as functions of neutron energy and the position in a set-up. The fission reaction rate $R(t, r, E_n)$ of a neutron having energy E_n , ranging from the thermal to the maximum projectile energy, interacting with a target “t” and producing a fission product “r”, corresponds to the cumulative yield $Y(t, r, E_n)$ of the said product. Thus the measured rate $R_{exp}(t, r) = \sum_{E_n} R(t, r, E_n)$ corresponds to the mean cumulative yield $Y_{cum}(t, r)$. In case of ²³⁵U data both the independent yield and the cumulative yields are available at 0.025 eV, 400 keV and 14 MeV. However, for ²³⁸U and ²³²Th the data are available for 400 keV and 14 MeV. Thus, the full range of the neutron energy is divided into the following three ranges and it is assumed that Y_{cum} stays roughly constant in these ranges.

- Thermal, epithermal and resonance from 1×10^{-5} eV to 1.26×10^5 eV.
- Unresolved resonance and fast neutrons from 1.26×10^5 eV to 4.57×10^6 eV.
- Fast and high-energy neutrons from 4.57×10^6 eV to the beam energy, *i.e.* 2.33 GeV.

$Y_{cum}(t, r)$ for ²³²Th may be calculated using the following relation:

$$Y_{cum}(^{232}\text{Th}, r_1) = w_2(\text{Th}) \cdot Y_{cum}(^{232}\text{Th}, r_1, 2) + w_3(\text{Th}) \cdot Y_{cum}(^{232}\text{Th}, r_1, 3), \quad (3)$$

where, $r_1 = ^{85m}\text{Kr}, ^{99}\text{Mo}, ^{131}\text{I}, ^{133}\text{Xe}, ^{135}\text{Xe}$ and ¹⁴¹Ce for ²³²Th.

The weight factor, w_j is defined as the fraction of a fission reaction rate in the j -th energy range. This is calculated using the JEFF-3.1 data library of fission cross-sections and the neutron flux in different positions of say ²³²Th in the three holes. For the composite targets like ^{nat}U to account for the abundance of isotopes the following relation is used:

$$Y_{cum}(t, r) = \sum_{i,j} a_i w_{ij} Y_{cum}(i, j, r).$$

The weight factors w_j for ²³²Th and reduced group factors, $a_i w_{ij}$ for ²³⁵U ($i = 1$) and ²³⁸U ($i = 2$) are given in table 3. The sum of group weight factors $\sum w_j$ and $\sum_{i,j} a_i w_{ij}$ are equivalent to one. In case of ^{nat}U, $a_1 = 0.0072$ and then w_{1j} needs to be calculated for ²³⁵U and $a_2 = 0.9928$ for ²³⁸U and w_{2j} needs to be calculated as in the case of ²³²Th with $r = ^{85m}\text{Kr}, ^{93}\text{Y}, ^{99}\text{Mo}, ^{103}\text{Ru}, ^{105}\text{Rh}, ^{131}\text{I}, ^{132}\text{Te}, ^{133}\text{I}, ^{140}\text{Ba}, ^{141}\text{Ce}$ and ¹⁴³Ce for ^{nat}U.

Thus, the ratio R/Y is estimated using values of the experimental reaction rate, $R_{expt}(t, r)$ for the r -fission

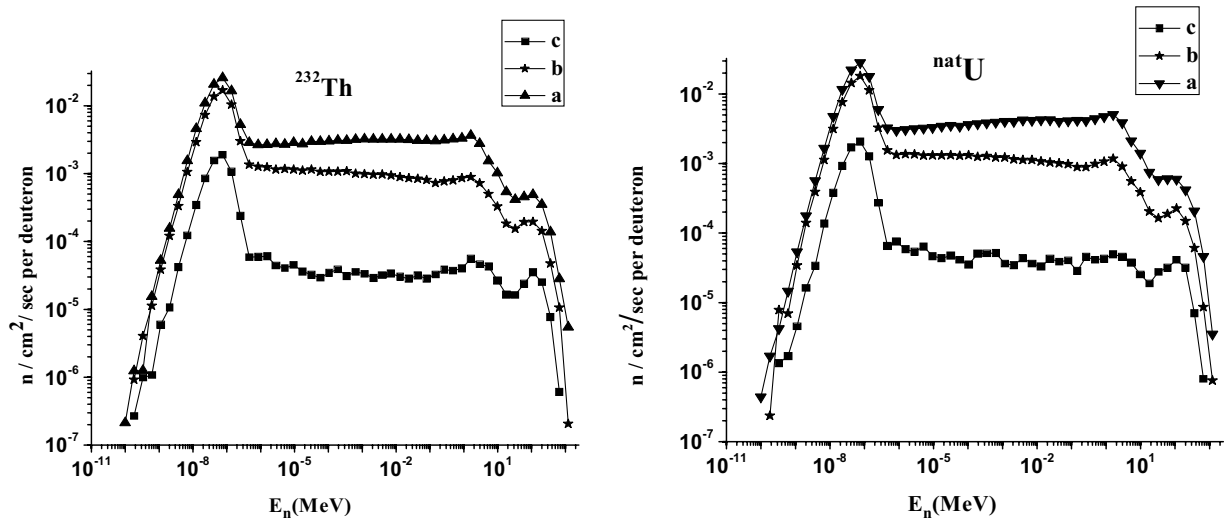


Fig. 4. $E_d\phi/dE$ per incident deuteron versus neutron energy, E_n at the position of the ^{232}Th sample (left) and the $^{\text{nat}}\text{U}$ sample (right) in holes “a”, “b” and “c” simulated using the Monte Carlo MCNPX Code without the presence of the sample in a hole.

Table 3. Group weight factors w_j for the calculations of total number of fissions.

Range of neutron Energy, j	^{232}Th	^{235}U	^{238}U	$^{\text{nat}}\text{U}$
(Hole a)				
Epithermal	4.24E-06	0.9377	3.301E-05	0.9377
Resonance	0.285	9.063E-04	2.087E-02	2.178E-02
Fast	0.715	3.972E-04	3.992E-02	4.032E-02
(Hole b)				
Epithermal	3.38E-06	0.9721	2.696E-06	0.9721
Resonance	0.225	3.296E-04	7.874E-03	8.204E-03
Fast	0.775	1.902E-04	1.953E-02	1.955E-02
(Hole c)				
Epithermal	1.01E-06	0.9737	1.090E-05	0.9737
Resonance	0.133	1.231E-04	3.123E-03	3.246E-03
Fast	0.869	2.055E-04	2.285E-02	2.289E-02

fragments and the mean cumulative production yield, $Y_{\text{cum}}(t, r)$ as determined above. The normalization ratio R/Y is plotted for $^{\text{nat}}\text{U}$ and ^{232}Th in case of the holes “a” and “b” in fig. 5. From these plots it is observed that for a given sample, say $^{\text{nat}}\text{U}$, the fission fragment ratio R/Y stays roughly independent of the product “r”.

This in turn gives the reaction rate of fission. It is a well-known fact that the sum of independent yields is not equal to corresponding cumulative yield and the relation between them depends on the half-lives of the nuclei present in the decay chain [35]. A particular fission product (A_r, Z_r) may be produced in a fission reaction directly and the same (A'_r, Z'_r) may also appear on the decay of another product. Also, it may happen that some of them are not observed in the gamma-spectrometry because of their half-life, which may be very short or very long. Thus, we can use the sum of the independent yields $\sum_r Y_{\text{ind}}(t, r)$ instead of the cumulative yield if the decay corrections for

the previous nuclide could be neglected and we calculate the total reaction rate for the fission from all residual nuclei as follows:

$$R_{\text{exp}}(\text{fission}, t, r) = \frac{200R_{\text{exp}}(t, r)}{\sum_{r'=1}^r Y_{\text{ind}}(t, r')} = \frac{200R_{\text{exp}}(t, r)}{Y_{\text{cum}}(t, r)}.$$

The experimental values of $R_{\text{exp}}(\text{fission})$ for ^{232}Th in holes “a”, “b” and “c” and $^{\text{nat}}\text{U}$ in holes “a” and “b” are calculated. Averaging the value $R_{\text{exp}}(\text{fission}, t, r)$ of the individual fission product we calculate the total fission rate $R_{\text{exp}}(t, \text{fission})$ and it is given in table 4 for $^{\text{nat}}\text{U}$ and ^{232}Th samples in their respective holes. The theoretical reaction rate are also calculated for all the observed reactions, *i.e.* (n, γ) , $(n, 2n)$ and $(n, \text{fission})$ for both ^{232}Th and $^{\text{nat}}\text{U}$ samples in the holes “a”, “b” and “c” using the Monte Carlo MCNPX, JEFF-3.1 and NJOY 99.112 codes, and displayed along with the experimental values in table 4. Their discussion is postponed for the next section.

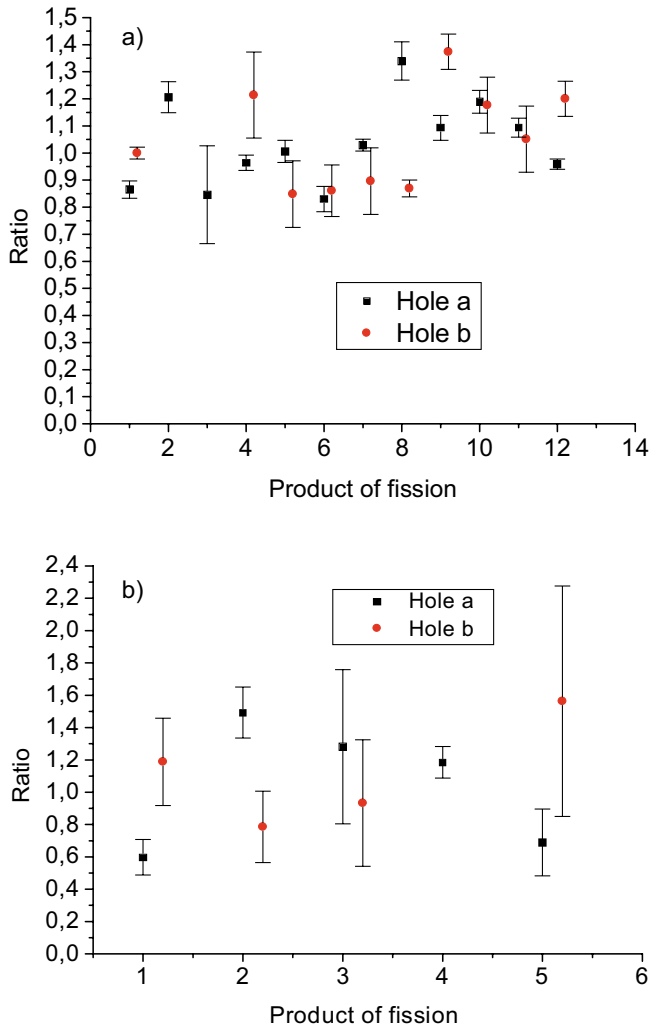
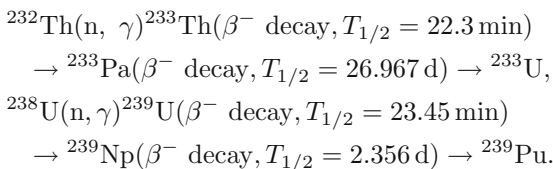


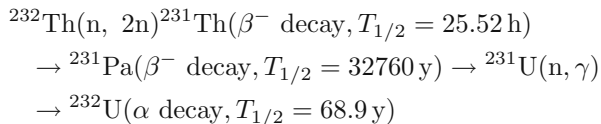
Fig. 5. a) The ratio $(R_{\text{exp}}(^{\text{nat}}\text{U}, r))/(Y_{\text{cum}}(^{\text{nat}}\text{U}, r))$ for the 11 fission products and b) the ratio $(R_{\text{exp}}(\text{Th}, r))/(Y_{\text{cum}}(\text{Th}, r))$ for the 5 fission products normalized over the average of the ratio taken over “r” are compared for corresponding fission fragments in holes “a” and “b”.

6.2 Calculation of transmutation power

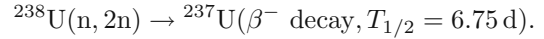
The transmutation of ^{232}Th to ^{233}U and ^{238}U to ^{239}Pu by (n, γ) reactions can be written as the following decay chains:



Similarly for the (n, 2n) reactions in the case of ^{232}Th and ^{238}U ,



and, for uranium,



In the experiment, the product nuclides ^{233}Pa , ^{231}Th , ^{239}Np and ^{237}U have been observed and P_{norm} has been estimated using eq. (2) of sect. 3 corresponding to the (n, γ) and (n, 2n) reactions of ^{232}Th and ^{nat}U samples for the holes “a”, “b” and “c” using the values of R_{exp} of table 4. The P_{norm} results of this experiment are displayed in table 5 along with the results of other experiments, *viz.* E+T [23] and the TARC [22] for the sake of comparison.

The following observations can be made from the experimental and theoretical results:

- i) The experimental values of the reaction rates $R_{\text{expt.}}$ for all the three reactions, *i.e.* (n, γ), (n, 2n) and (n, fission) for both ^{nat}U and ^{232}Th samples decrease as we go from hole “a” which is closer to the target than the hole “b” and hole “c”. This is due to the fact that the neutron flux gets moderated and its magnitude also decreases with the distance from the target.
- ii) In the case of both ^{232}Th and ^{nat}U samples, the value of the ratio E/C of the (n, γ) reaction is much smaller than unity in the two holes “a” and “b”. In the case of ^{232}Th in hole “c”, E/C is close to unity, probably because of the fact that neutrons are highly moderated and the cross-sections at low energies are well determined. The reason of inconsistency, in the case of holes “a” and “b”, may be either due to the cross-sections or to the simulated neutron flux. Obviously, in the two holes the flux is nearly similar up to ~ 0.1 eV.

In the case of ^{nat}U , the value of E/C of (n, fission) is about 40% less than unity in both holes “a” and “b”. The situation is rather the opposite in the case of ^{232}Th , where the ratio $E/C \sim 2$. From the data in table 3, we understand that the flux in the three holes in the case of ^{nat}U is dominated by the epithermal flux and, if we assume that it is overestimated by a certain amount and that this may be fixed up in later works, then this argument solves the problems of both (n, γ) and (n, fission) reactions because the ratios of the two reactions will move towards unity. In this circumstance, a part of the epithermal flux needs to be cut down and to be added in the thermal region. However, by this argument of overestimation of epithermal flux the problem of the E/C ratio of the Th (n, 2n) reaction cannot be solved. Probably, the reason of this problem is related to the availability of the cross-sections of (n, 2n) reactions with less precision at an energy higher than 15 MeV. The value of $E/C \sim 1$ in the case of ^{238}U (n, 2n) may be a matter of chance. This overemphasizes the fact that the neutron flux needs to be simulated with much higher accuracy and certainly there is the need for experimental determination of the flux for such experiments.

- iii) For ^{232}Th in hole “a”, the ratio of $R_{\text{exp}}(\text{n, 2n})/R_{\text{exp}}(\text{n, f})$ is 54(10)% compared to $R_{\text{theo}}(\text{n, 2n})/R_{\text{theo}}(\text{n, f}) = 64.24\%$. For the hole “b” the ratio $R_{\text{exp}}(\text{n, 2n})/R_{\text{exp}}$

Table 4. Comparison of experimentally measured (E) and calculated (C) reaction rates in the three holes. For the calculations the JEFF 3.1 library is used.

Hole a						
	^{232}Th			$^{\text{nat}}\text{U}$		
Reaction	(n, γ)	(n, f)	(n, 2n)	$^{238}\text{U}(\text{n}, \gamma)$	$^{\text{nat}}\text{U}(\text{n}, \text{f})$	$^{238}\text{U}(\text{n}, 2\text{n})$
$R_{\text{expt}}(E)$	3.20(8)E-25	1.40(19)E-26 1.70(29)E-26*	7.6(8)E-27	3.11(10)E-25	1.57(21)E-25	2.72(9)E-27
$R_{\text{cal}}(C)$	7.83E-25	5.09E-27	3.27E-27	1.63E-24	2.54E-25	2.73E-27
E/C	0.409(10)	2.75(37)	2.33(25)	0.191(6)	0.618(83)	0.945(26)
Hole b						
	^{232}Th			$^{\text{nat}}\text{U}$		
Reaction	(n, γ)	(n, f)	(n, 2n)	$^{238}\text{U}(\text{n}, \gamma)$	$^{\text{nat}}\text{U}(\text{n}, \text{f})$	$^{238}\text{U}(\text{n}, 2\text{n})$
$R_{\text{expt}}(E)$	1.92(5)E-25	3.8(13)E-27 4.4(13)E-27*	3.6(18)E-27	2.08(20)E-25	1.02(12)E-25	7.21(20)E-28
$R_{\text{cal}}(C)$	4.04E-25	1.78E-27	7.58E-28	6.07E-25	1.56E-25	7.63E-28
E/C	0.475(12)	2.1(7)	4.7(24)	0.343(33)	0.654(77)	0.945(26)
Hole c						
	^{232}Th			$^{\text{nat}}\text{U}$		
Reaction	(n, γ)	(n, f)	(n, 2n)	$^{238}\text{U}(\text{n}, \gamma)$	$^{\text{nat}}\text{U}(\text{n}, \text{f})$	$^{238}\text{U}(\text{n}, 2\text{n})$
$R_{\text{expt}}(E)$	3.38(16)E-26	5.0(18)E-28 5.1(18)E-28*	–	–	–	–
$R_{\text{cal}}(C)$	3.39E-26	2.13E-28	6.84E-29	3.73E-26	1.79E-26	6.61E-29
E/C	0.997(47)	2.4(9)	–	–	–	–

* They correspond to the values obtained on inclusion of data from TALYS code at higher than 14 MeV energy and the method of calculation is explained in appendix A. In the discussions these values are not included as they are with large uncertainties and they are not purely from the experiment.

Table 5. Comparison of the normalized transmutation power $P_{\text{norm}}/P_{\text{beam}}$ of three assemblies, namely graphite-lead target ($P_{\text{beam}} = 0.06979\text{ W}$), Energy plus Transmutation (Pb target and U blanket) ($P_{\text{beam}} = 0.2064\text{ W}$) and TARC ($P_{\text{beam}} = 0.3083\text{ W}$). The distances of the samples from the centre of their respective assemblies are given as d . The values with the sign * correspond to P_{norm} .

Assembly	Graphite			E+T	TARC	
	Hole a	Hole b	Hole c			
Distance $d(\text{Th})$	$d \sim 24\text{ cm}$	$d \sim 34\text{ cm}$	$d \sim 61\text{ cm}$	$d \sim 13\text{ cm}$	$Z = 22.5\text{ cm},$ $X = 122\text{ cm}$	$Z = 7.5\text{ cm},$ $X = 150\text{ cm}$
$^{232}\text{Th}(\text{n}, \gamma) \rightarrow ^{233}\text{Pa}$	4.60(11)E-15 *3.21(8)E-16	2.77(7)E-15 *1.93(5)E-16	4.86(23)E-16 *3.39(16)E-17	1.50(7)E-16 *3.09(13)E-17	1.23(10)E-16 *3.8(3)E-17	3.2 (6)E-17 *1.0(2)E-17
$^{232}\text{Th}(\text{n}, 2\text{n})^{231}\text{Th}$	1.09(11)E-16 *7.6(8)E-18	5.2(26)E-17 *3.6(18)E-18	–	7.7(8)E-18 *1.59(16)E-18	–	–
Distance “ d ” (U)	$d \sim 19\text{ cm}$	$d \sim 31\text{ cm}$	$d \sim 58\text{ cm}$	$d \sim 13\text{ cm}$	$Z = -22.5\text{ cm},$ $d = 107\text{ cm}$	$Z = -22.5\text{ cm},$ $d = 94\text{ cm}$
$^{238}\text{U}(\text{n}, \gamma) \rightarrow ^{239}\text{Np}$	4.48(14)E-15 *3.12(10)E-16	3.00(29)E-15 *2.09(20)E-16	–	1.39(5)E-16 *2.87(9)E-17	3.6(10)E-17 *1.1(3)E-17 Hole 6	2.50(6)E-16 *7.7(2)E-17 Hole 7
$^{238}\text{U}(\text{n}, 2\text{n})^{237}\text{U}$	3.89(13)E-17 *2.71(9)E-18	1.03(3)E-17 *7.18(20)E-19	–	–	–	–

(n,f) is 95(57)% compared to $R_{\text{theo}}(n,2n)/R_{\text{theo}}(n,f) = 42.84\%$. This shows that agreement is reasonably good in both cases.

- iv) In the case of ^{nat}U , the ratio $R_{\text{exp}}(n, 2n)/R_{\text{exp}}(n, f)$ is 1.73(20)% and $R_{\text{cal}}(n, 2n)/R_{\text{cal}}(n, f)$ is 1.07% in hole “a” and for hole “b” the ratio $R_{\text{exp}}(n, 2n)/R_{\text{exp}}(n, f)$ is 0.710(9)% and $R_{\text{cal}}(n, 2n)/R_{\text{cal}}(n, f)$ is 0.49%. It is evident that the ratio is very small in the case of hole “b” compared to hole “a” and the reason may be the presence of the fissile component ^{235}U in ^{nat}U . This may be due to the fact that the fission cross-section is higher at lower neutron energies that are dominant in hole “b” compared to hole “a”. This is made clear in next point v).
- v) From the ratio of the experimental reaction rates, $^{nat}\text{U}(n, f)/^{232}\text{Th}(n, f)$, being 11.2(17) for hole “a” and 26.8(85) for hole “b” it is clear that there is a higher flux of moderated neutrons in hole “b” than in hole “a” which enhances the fission rate of ^{235}U . Or, in other words, $^{nat}\text{U}(n, f)_b/^{nat}\text{U}(n, f)_a \sim 0.65(12)$ and $\text{Th}(n, f)_b/\text{Th}(n, f)_a \sim 0.27(10)$ also support the afore-said view that there is a bigger component of slowed-down neutrons in hole “b” than in hole “a”.
- vi) Similarly, the ratio of the experimental reaction rates $^{238}\text{U}(n, 2n)/^{232}\text{Th}(n, 2n) = 0.36(4)$ for hole “a” and 0.20(10) for hole “b” shows that ^{232}Th is more prone to the (n, xn) reaction than ^{238}U .

The following observations can be made about the normalized transmutation power, P_{norm} (see table 5 for the data) for both ^{nat}U and ^{232}Th in the three holes “a”, “b” and “c”.

- i) P_{norm} for both ^{232}Th and ^{238}U samples deduced using the reaction rates of (n, γ) and (n, 2n) reactions decreases as we go from the hole “a” to “c”, *i.e.* on increasing the distance d from the centre of the spallation neutron source. This is due to the fact that both the flux and the energy decrease with the distance. It seems that the flux probably decreases much faster than the energy because the rate of the (n, γ) reaction should not increase if only the average energy decreased.
- ii) The transmutation power in the case of the (n, γ) reaction for ^{232}Th and ^{238}U independently for holes “a” and “b” is found comparable and when we compare it with the E+T and TARC assemblies it is found to be about an order of magnitude higher than both the E+T and TARC assemblies results.
- iii) The value of P_{norm} in the case of ^{232}Th (n, 2n) reaction is ~ 2.1 (11) times higher in hole “a” than in hole “b” and in the case of $^{238}\text{U}(n, 2n)$ it is about 3.78(11) times higher in hole “a” than in hole “b”. The difference in the ratio of transmutation powers of hole “a” to hole “b” in the case of (n, γ) reactions of ^{232}Th and ^{238}U is comparable but in the case of (n, 2n) reactions the ratio is 2.1(11) for Th and 3.78(16) for ^{238}U . These values may be considered approximately the same when the experimental errors are taken into account. The data of the cross-sections of (n, 2n) reactions given in

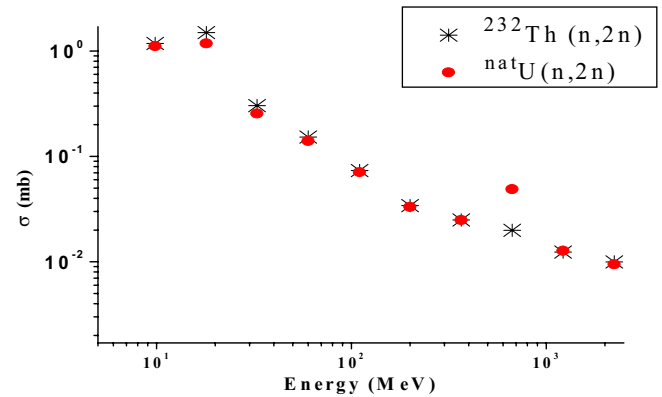


Fig. 6. Comparison of the cross-sections of ^{232}Th (n, 2n) and ^{238}U (n, 2n) reactions from the TALYS code.

fig. 6 also show that they are comparable and confirm the above-mentioned conclusion.

- iv) On comparing P_{norm} (n, 2n) for ^{232}Th in the case of graphite with E+T assemblies, it may be pointed out that the transmutation power is about 5 times higher in the graphite assembly than the E+T assembly.

The neutron flux in the graphite assembly in the irradiation positions of the ^{232}Th and ^{nat}U samples ranging from thermal energy to ~ 1000 MeV shows that it is equivalent to neither the thermal nor the fast reactor flux. In this range of energy, three kinds of reactions (n, γ), (n, f) and (n, 2n) have been observed in both ^{232}Th and ^{nat}U samples. Because of the small neutron flux and the small amounts of the two samples we could not observe the higher-order (n, xn) reactions. In this experiment graphite has been used as a moderator while in the TARC experiment lead acts as a moderator as well as a neutron multiplier by means of the (n, xn) kind of reactions. Thus, simulation of the neutron flux by a code is expected to be cleaner in the case of graphite than in that of lead, due to the fact that lesser uncertainty is involved from the viewpoint of the cross-sections of high-order (n, xn) reactions.

Another important point about our experiment is that reaction rates deduced from different gamma peaks show consistency and we have taken the averages of the reaction rates with the help of only the singular gamma peaks without any interference of other elements.

Transmutation powers of the set-up are obtained using the two transmutation reactions, namely (n, γ) and (n, 2n), and compared with the results of the E+T set-up and the TARC set-up considering reactions rates at the closest possible distances in the three experiments.

From the data of the reaction rates of (n, 2n) and (n, f) reactions in the three holes it may be inferred that the two reactions seems to be complementary, *i.e.* in certain neutron environments if the reaction rate of (n, f) increases, then the reaction rate of (n, 2n) decreases and, at the same time the reaction rate of the ^{232}Th (n, 2n) reaction is higher than that of the $^{238}\text{U}(n, 2n)$ reaction. The effect was first pointed out in the simulation data of the CASCADE code in the case of fertile and fissile materials [36].

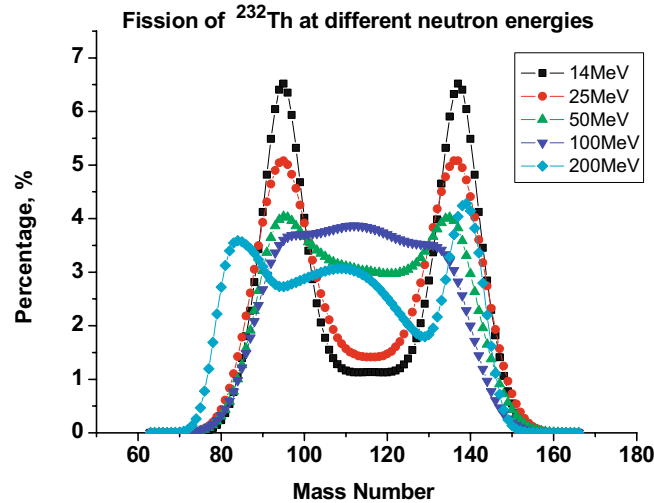


Fig. 7. Mass distribution of the fission products of ^{232}Th at five neutron energies calculated using the TALYS code.

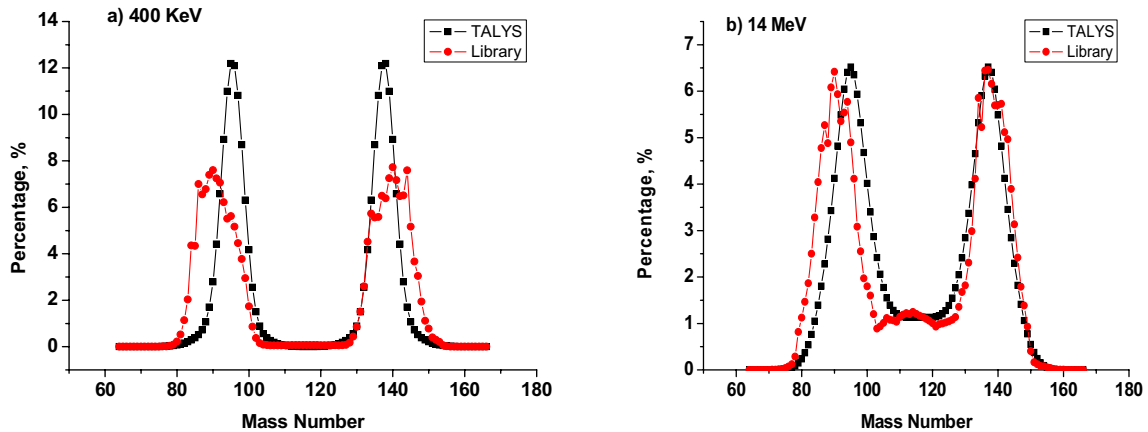


Fig. 8. Comparison of the mass distribution of fission products from the TALYS code and the Library in the case of a) 400 keV, and b) 14 MeV energies.

The authors are grateful to the operation crew of the Nuclotron accelerator of LHE, JINR, Dubna, for performing the irradiation and for the good beam parameters, and Dr. V. Bradnova for managing the support and preparing the minutes of the experiment. The authors are also grateful to META Centrum (Czech Republic) for offering the computers for the calculations. The experiments were supported by the Czech Committee for the collaboration with JINR, Dubna. Part of this work has been supported by the grant of BRNS (DAE-India) and the Indo-Russian ILTP and RFFI 09-02-92670 project grants.

Appendix A.

From the data of the weight factors given in table 3, it may be noted that the group weight factor for ^{232}Th is dominant in the case of fast-neutron energy for all three holes. We also understand that the cross-sections for the ^{232}Th (n, f) reaction are higher in this neutron energy interval. Since, there is no precise and systematic experimental data available for the independent and cumulative yields of fission products in the case of high-energy neu-

trons; $E_n > 14$ MeV, so, we have used TALYS for calculating the cross-section and the independent yields of fission products for the energies $E_n = 0.001, 0.01, 0.1, 0.4, 1.5, 10, 14, 20, 25, 35, 50, 75, 100, 150, 200$ MeV in the case of ^{232}Th and other actinides.

In fig. 7 the mass distribution of fission products in the ^{232}Th (n, f) reaction is given at few energies of neutrons and, in fig. 8, a comparative study of the mass distribution of fission products calculated using the cross-sections from the TALLYS code and the experimental (Library) is shown at two energies, *i.e.* $E_n = 400$ keV and 14 MeV. It is clear, from fig. 8, that at 400 keV, a large discrepancy is observed between the calculated and the experimental values, however, at 14 MeV the agreement is much better. We can assume that such a situation may also exist in the comparison of the experimental and calculated values of sums of independent yields in the corresponding chain products at the two energies.

In this way, we calculated the group weight factors at energies > 14 MeV and listed them in table 6. Summing over all the independent yields of nuclides preceding the

Table 6. Group weight factors w_j calculated for the range of energy given in column 1 and in column 2 those neutron energies for which the yield is calculated using data from the TALYS code are given for the ^{232}Th . In columns 3, 4 and 5, the calculated weight factors are given for the three holes.

$E_i - E_n$ [MeV]	E_j [MeV]	Hole a	Hole b	Hole c
1.00E-10–0.157	2.52E-08	1.95E-06	5.62E-06	6.02E-06
0.157–5.28	0.400	0.162	0.267	0.338
5.28–32.8	14	0.322	0.419	0.377
32.8–60	35,50	0.076	0.058	0.069
60–125	75,100	0.123	0.083	0.076
125–2.33E03	150,200	0.316	0.172	0.140
Sum		1.000	1.000	1.000

Table 7. Sum of independent yields up to the fission product, r of ^{232}Th taken at different energies of neutrons. In the case of TALYS data the average corresponding to the given set of energies is displayed.

r	0.4 MeV (Library)	14 MeV (Library)	35, 50 MeV (TALYS)	75, 100 MeV (TALYS)	150, 200 MeV (TALYS)	Normalization factor at 14 MeV TALYS/Library
^{99}Mo	2.919	1.953	1.614	1.543	1.395	2.391(120)
^{131}I	1.513	2.306	2.520	2.075	1.582	1.470(87)
^{133}Xe	4.532	4.115	3.574	3.256	2.269	1.133(57)
^{141}Ce	7.106	5.722	3.567	2.339	3.079	0.844(57)

Table 8. Deduced reaction rate of the fission of ^{232}Th using the experimental data of yields from the library at 400 keV and 14 MeV.

Fission product	Hole a $R_{\text{exp}} \times \text{E-28}$	Hole b $R_{\text{exp}} \times \text{E-28}$	Hole c $R_{\text{exp}} \times \text{E-28}$
^{99}Mo	190(42)	50(13)	5.0(18)
^{131}I	155(63)	132(58)	–
^{133}Xe	144(30)	–	–
^{141}Ce	97(34)	25(12)	–
Average	140(19)	38(21)	5.0(18)

Table 9. Deduced reaction rate of the fission ^{232}Th using the experimental data of yields from the library for the two neutron energies, 400 keV and 14 MeV and the data of the calculated yields for 35, 50, 75, 100, 150 and 200 MeV.

Fission product	Hole a $R_{\text{exp}} \times \text{E-28}$	Hole b $R_{\text{exp}} \times \text{E-28}$	Hole c $R_{\text{exp}} \times \text{E-28}$
^{99}Mo	236(32)	53(9)	5.1(18)
^{131}I	198(74)	142(56)	
^{133}Xe	194(42)		
^{141}Ce	118(52)	25(12)	
Average	170(29)	44(13)	5.1(18)

decay chain of the measured fission product, the equivalence $Y_{\text{cum}}(^{232}\text{Th}, r) = \sum_{r'=1}^r Y_{\text{indep}}(^{232}\text{Th}, r')$ also holds true. Since it is not possible to know the yield for the isomeric state from the TALYS code, we have not included the contribution of $^{85\text{m}}\text{Kr}$ -like nuclides in the present calculation and also the contribution from ^{135}Xe is not presently included because the cumulative yield is not equivalent to the sum of the corresponding independent yields due to large uncertainties in the decay of nuclides in the chain.

From the data in table 6 it is clear that w_j are significantly high at higher energies and the division of range of neutron energy may enhance the accuracy in our calculations compared to when we consider a very wide range of energies.

In table 7, the sum of independent yields is given for the five sets of energy values of the four observed fission

products. In the last column, the ratio of the value at 14 MeV, obtained from the TALYS code, to the value available in the data library is given to show the differences in the two values. The values given in columns 3, 4 and 5 are normalized with respect to the ratio given in the last column.

In table 8, the data of reaction rates deduced using the method given in sect. 6.1 and the data of the independent yield at the two energies 400 keV and 14 MeV is presented for the fission of ^{232}Th placed in the holes “a”, “b” and “c”. In table 9, similar results are given on including the data of the yields calculated from the TALYS code. It is important to point out that, with the inclusion of the calculated data at energies higher than 14 MeV, the reaction rates are enhanced by $\sim 21\%$ for example in case of hole “a”.

In conclusion it may be stressed that there is a need for more systematic experimental data at neutron energies higher than 14 MeV for better calculations in the case of the application of spallation neutrons in ADS-like systems.

References

1. C.D. Bowman *et al.*, Nucl. Instrum. Methods A **320**, 336 (1992).
2. A.J. Janssen, *Transmutation of Fission Products in Reactors and Accelerator-Driven Systems*, ECN-R-94-001 (1994).
3. C. Rubbia, J.A. Rubio *et al.*, *Conceptual design of a fast neutron operated high power energy amplifier*, CERN/AT/95-44 (ET), (1995). See also C. Rubbia, *A high gain energy amplifier operated with fast neutrons*, *Proceedings of the International Conference on Accelerator-Driven Transmutation Technologies and Applications, Las Vegas (NV) 1994*, AIP Conf. Proc., vol. **346** (AIP Publishing, 1994).
4. F. Sokolov, K. Fukuda, H.P. Nawada, *Thorium fuel cycle - Potential benefits and challenges*, IAEA-TECDOC-1450 (2005).
5. Experimental Nuclear Reaction Data, <http://www-nds.iaea.org/various1.htm>, www-nds.iaea.org/, www.nndc.bnl.gov/.
6. J.S. Hendricks *et al.*, MCNPX, version 2.6.c, LA-UR-06-7991 (2006).
7. A. Fasso, A. Ferrari, J. Ranft, P.R. Sala, *FLUKA: present status and future developments*, in *Proceedings of the IV International Conference on Calorimetry in High Energy Physics, La Biodola (Italy) 21-26 September (1993)*, edited by A. Menzione, A. Scribano (World Scientific, 1994) pp. 493-502.
8. V.S. Barashenkov, Comput. Phys. Commun. **126**, 28 (2000).
9. C.H.M. Broeders *et al.*, FZK 7183 (2006); <http://bibliothek.fzk.de/zb/berichte/FZKA7183.pdf>.
10. A.J. Koning *et al.*, in *Proceedings of the International Conference on Nuclear Data for Science and Technology, Santa Fe, USA, Sept. 26 - Oct. 1 (2004)* and www.talys.eu.
11. Y.A. Korovin *et al.*, Nucl. Instrum. Methods A **562**, 721 (2006); Yu.N. Shubin *et al.*, INDC (CCP) 385 (1995) Vienna.
12. G.N. Kim *et al.*, Nucl. Instrum. Methods A **485**, 458 (2002).
13. G. Tagliente, n-TOF Collaboration, Braz. J. Phys. **34**, 1033 (2004); also see S. Andriamonje *et al.*, CERN/INTC/2000-040 CERN (2000).
14. A.K. Krasnykh, V.L. Lomidze, A.V. Novokhatsky, Yu.P. Popov, W.I. Furman (Editors), *IREN Project. Intense Resonance Neutron Source*, Frank Laboratory of Neutron Physics, JINR, Dubna (1994).
15. H.A. Abderrahim, P. Baeten *et al.*, Nucl. Phys. News **20**, 24 (2010); <http://www.sckcen.be/myrrha/>.
16. V. Shvetsov *et al.*, Nucl. Instrum. Methods Phys. Res. A **562**, 886 (2006).
17. V.S. Barashenkov, H. Kumawat, V.A. Lobanova, V. Kumar, Nucl. Instrum. Methods Phys. Res. B **217**, 352 (2004).
18. B. Blau *et al.*, Neutron News **20**, 5 (2009); <http://sinq.web.psi.ch/>.
19. Shinichi Sakamoto *et al.*, Nucl. Instrum. Methods Phys. Res. A **562**, 638 (2006).
20. T. Ino *et al.*, Nucl. Instrum. Methods A **525**, 496 (2004).
21. E. Kim *et al.*, Nucl. Sci. Eng. **129**, 209 (1998).
22. A. Abanades *et al.*, Nucl. Instrum. Methods A **478**, 577 (2002).
23. J. Adam *et al.*, Eur. Phys. J. A **43**, 159 (2010).
24. J. Adam, V.S. Barashenkov, H. Kumawat, V. Kumar *et al.*, Kerntechnik **70**, 127 (2005).
25. J. Adam, V.S. Barashenkov, H. Kumawat, V. Kumar *et al.*, Euro. Phys. J. A **23**, 61 (2005).
26. Yu.E. Titarenko *et al.*, Phys. Rev. C **65**, 064610 (2002).
27. Yu.E. Titarenko *et al.*, Phys. Rev. C **78**, 034615 (2008).
28. V. Kumar, Chitra Bhatia, H. Kumawat, *CASCADE data for the A.D.S materials for its Benchmarking*, in *PSI Proceedings 09-01*, **30** (2009).
29. V. Kumar, Chitra Bhatia, H. Kumawat, J. Adam, Eur. Phys. J. A **40**, 231 (2009).
30. Manish Sharma, V. Kumar *et al.*, Pramana J. Phys. **68**, 307 (2007); with entries 33004001-20.
31. J. Banaigs, J. Berger, J. Dulfo, L. Goldzahl *et al.*, Nucl. Instrum. Methods **95**, 307 (1971).
32. J. Frana, J. Radioanal. Nucl. Chem. **257**, 583 (2003).
33. S.Y.F. Chu, L.P. Ekstrom, R.B. Firestone, <http://nucleardata.nuclear.lu.se>.
34. *The JEFF-3.1 Nuclear Data Library*, JEFF report 21, edited by A. Koning *et al.*, Organisation for Economic Co-operation and Development, Nuclear Energy Agency, Paris, 2006.
35. J. Adam, A. Balabekyan, V.S. Pronskikh *et al.*, Appl. Rad. Isotopes **56**, 607 (2002).
36. V. Kumar, H. Kumawat, Chitra Bhatia, Probl. At. Sci. Technol. **4**, 80 (2009).

Supersymmetric fission of heavy nuclei induced by intermediate-energy protonsA. Deppman,^{*} E. Andrade-II,[†] V. Guimarães,[‡] and G. S. Karapetyan[§]*Instituto de Física, Universidade de São Paulo, P. O. Box 66318, 05315-970 São Paulo, SP, Brazil*O. A. P. Tavares^{||}*Centro Brasileiro de Pesquisas Físicas-CBPF/MCTI Rua Dr. Xavier Sigaud, 150, 22290-180 Rio de Janeiro - RJ, Brazil*A. R. Balabekyan[¶]*Yerevan State University, Faculty of Physics, Alex Manoogian I, Yerevan 0025, Armenia*N. A. Demekhina^{**}*Yerevan Physics Institute, Alikhanyan Brothers 2, Yerevan 0036, Armenia and Joint Institute for Nuclear Research (JINR), Flerov Laboratory of Nuclear Reactions (LNR), Joliot-Curie 6, Dubna 141980, Moscow, Russia*J. Adam^{††}*Joint Institute for Nuclear Research (JINR), Flerov Laboratory of Nuclear Reactions (LNR), Joliot-Curie 6, Dubna 141980, Moscow, Russia*F. Garcia^{‡‡}*Departamento de Ciências Exatas e Tecnológicas-DCET Centro de Pesquisas em Ciência e Tecnologias das Radiações - CPqCTR Universidade Estadual de Santa Cruz - UESC, Rodovia Jorge Amado km 16, Ilhéus - BA, Brazil*K. Katovsky^{§§}*Czech Technical University, Department of Nuclear Reactors, Prague, Czech Republic*

(Received 5 September 2013; published 13 December 2013)

In this work we present the results for the investigation of intermediate-mass fragment (IMF) production with the proton-induced reaction at 660 MeV on ^{238}U and ^{237}Np target. The data were obtained with the LNR Phasotron U-400M Cyclotron at Joint Institute for Nuclear Research (JINR), Dubna, Russia. A total of 93 isotopes, in the mass range of $30 < A < 200$, were unambiguously identified with high precision. The fragment production cross sections were obtained by means of the induced-activation method in an off-line analysis. Mass-yield distributions were derived from the data and compared with the results of the simulation code CRISP for multimodal fission. A discussion of the supersymmetric fragment production mechanism is also given.

DOI: [10.1103/PhysRevC.88.064609](https://doi.org/10.1103/PhysRevC.88.064609)

PACS number(s): 24.75.+i, 25.85.-w, 25.40.-h, 25.70.-z

I. INTRODUCTION

Nuclear dynamics is a complex problem where puzzling aspects of quantum mechanics and the natural difficulties of many-body systems are interconnected. Besides these factors, the strong interaction, which is not completely understood at present time, adds new challenges for calculations in the nonperturbative regime. Collective nuclear phenomena, such as fission, particle or cluster evaporation, and nuclear fragmentation, offer the possibility to study those complex

features of nuclear dynamics. Aside from the interest in fundamental nuclear physics, there are many applications where the knowledge of fragment formation dynamics in nuclear reactions would be helpful. For instance, information on intermediate mass fragment (IMF) cross section is relevant for the design of accelerator-driven systems (ADS) and radioactive ion-beam (RIB) facilities, as well as in the study of resistance of materials to radiation.

Fragments in high energy nuclear collisions can be produced by spallation, fission, and/or multifragmentation processes. Hufner [1], using the mass number of the fragments A and their multiplicity M as classification parameters, defined these processes in the following way:

- (1) spallation is the process in which only one heavy fragment with a mass close to the target mass, A_T , is formed (a special case of spallation is the so-called deep spallation where $M = 1$ but $A \sim \frac{2}{3}A_T$);
- (2) fission is the process in which $M = 2$ and A is around $A_T/2$;
- (3) multifragmentation is the process where $M > 2$ and $A < 50$.

^{*}adeppman@gmail.com[†]esegundo@if.usp.br[‡]valdir@dfn.if.usp.br[§]ayvgay@ysu.am^{||}oaptavares@cbpf.br[¶]balabekyan@ysu.am^{**}demekhina@nrmil.jinr.ru^{††}iadam@jinr.ru^{‡‡}fermingv@gmail.com^{§§}k.katovsky@sh.cvut.cz

Emission of light particles, with atomic number $Z \leq 2$, usually dominates the yield of reaction products for light target nuclei, while for heavy targets spallation and fission residues also give significant contribution. Thus, by adopting the definition that IMF are particles with $A > 4$ but lighter than fission fragments ($A < 100$), they can be formed through the following processes: i) Fission of nuclei mass number in the range of 120–130 [2]; ii) Spallation, including the emission of IMF, the so-called associated spallation [3]; iii) Multifragmentation of heavy nuclei [4].

For heavy targets, multifragmentation would be the only mechanism for the formation of IMF. Indeed, in Ref. [4], it was found that in the inverse-kinematics reaction of $3.65A$ MeV ^{208}Pb on ^1H , the formation of ^{12}C nucleus presents the characteristics of multifragmentation, with a possible small contribution of binary process. The formation of IMF was also observed in measurements at lower energies, see Refs. [5–7], but in these cases, the dynamics of the process indicates a binary decay with no evidence for multifragmentation. Hence, the study of the production of IMF by reactions with heavy target nuclei at intermediate energies can give new information on the nuclear dynamics. In the present work, our objective is to present new data on the measured cross sections for residual nuclei in the IMF region, obtained from reactions induced by 660 MeV protons on heavy target nuclei, and the corresponding analysis performed with Monte Carlo calculations using the CRISP code [8,9], as described below.

II. THEORETICAL ASPECTS OF IMF FORMATION

It is generally assumed that, at intermediate energies, the nuclear reaction proceeds in two stages. The first stage would correspond to an incoming fast projectile colliding with a single nucleon or with several nucleons, transferring momentum and energy to the nucleus, and leaving the residual nucleus accompanied by several light particles. The second stage would correspond to the decay of the residual nucleus, which is already in statistical equilibrium, by the emission of nucleons or clusters of nucleons. At high energies, where the excitation energy per nucleon of the residual nucleus is $E_x/A \geq 3.5$ MeV/nucleon, multifragmentation of the nucleus can take place. This reaction mechanism differs from evaporation since it describes a sudden breakup of the nucleus instead of a successive emission of particles.

In the framework described above, the formation of IMF from heavy targets at intermediate energies could only be attributed to a process in which fission takes place at some point in a long evaporation chain (both pre- and postfission), which is very unlikely. In fact, the fission probability for heavy nuclei drops very fast as the mass number decreases [10–12], and thus, a long evaporation chain would lead to lower fissility nuclei. Another possibility for the formation of IMF would be a very long evaporation chain leading to light spallation products. This mechanism is limited by the maximum excitation energy allowed for the nucleus before multifragmentation becomes dominant, since evaporation would cool the nucleus before the IMF region is reached. Increasing the excitation

energy above the 3.5 MeV/nucleon threshold would only increase the contribution from multifragmentation and, in this way, the IMF formed in reactions with heavy targets should be dominated by fragmentation products. Hence, for excitation energies below the multifragmentation threshold, the formation of IMF from heavy nuclei would be very unlikely.

The formation of IMF was observed in the inverse-kinematics reaction of ^{238}U on proton at 1A GeV [5], where the cross sections for 254 light nuclides in the element range of $7 \leq Z \leq 37$ was measured. Based on a detailed study of the experimental kinematic information, the authors identified such nuclides as binary decay products of a fully equilibrated compound nucleus, whereas clear indications for fast breakup processes were absent. Although these results are corroborated by those from Refs. [6,7], they are in contradiction with the scenario described in Ref. [1]. One possible explanation for the binary production of IMF from reactions induced on heavy targets would be by considering highly asymmetric fission fragments which can still undergo evaporation to form, at the end, a nuclide in the region of IMF. This process would correspond to a modification in the classification given by Hufner [1] by using a less restrictive definition for fission, since in this case, the fragment would have mass number quite different from $A_T/2$. This superasymmetric mechanism would corroborate the conjecture that evaporation and fission are manifestation of a single mechanism, called binary decay [13,14]. A complete investigation of this possibility involves the description of the entire process from the primary interaction of the incident proton up to the evaporation of nucleons from the fission fragments. Such a task can only be performed through the Monte Carlo method.

Here we used the CRISP code to calculate all of the features of the nuclear dynamics during the reaction. CRISP is a Monte Carlo code for simulating nuclear reactions [15] where it is assumed that nuclear reactions can be separated in the two stages already mentioned above: the intranuclear cascade and the evaporation/fission process. This code has been developed during the last 25 years, and it has been successfully used to describe many different reactions. The main characteristic of the intranuclear cascade calculation with CRISP is the multicollisional approach [16,17], where the full nuclear dynamics is considered in each step of the cascade. In this process the nucleus is modeled by an infinite square-potential which determines the level structure for protons and neutrons. The effects of the nuclear potential are present in the transmission of the particles through the nuclear surface or through an effective mass according to the Walecka mean field approximation [18]. The multicollisional calculation is accomplished by constantly updating all of the kinematic variables of all particles inside the nucleus, which opens the possibility for treating more realistically many nuclear phenomena. For instance, the anti-symmetrization criteria, which stipulates a strict observation of the Pauli Principle, allows the separation of the intranuclear cascade from the thermalization process [19]. The effectiveness of such an approach can be verified in the processes which are predominantly dependent on the intranuclear cascade step, such as kaon production and hypernuclei decay. Such

processes have been studied with the CRISP code with results compatible with experiments [20,21]. Also, fission of several nuclei has been studied in the quasi-deuteron region [19], where the Pauli blocking mechanism is very important in the determination of the residual nucleus.

The evaporation/fission competition was first studied with the CRISP code in Refs. [22–24], giving for the first time an explanation for the saturation below the unity for the fissility of heavy nuclei observed in photofission experiments at intermediate energies [25,26]. After, the code was extended to simulate reactions at energies up to 3.5 GeV [27], showing also good agreement with experimental data. After nuclear thermalization, the competition between fission and evaporation processes, which includes neutrons, protons and α particles, is determined by the ratios between their respective widths according to the Weisskopf model for evaporation and to the Bohr-Wheeler model for fission. These ratios are given by

$$\frac{\Gamma_p}{\Gamma_n} = \frac{E_p}{E_n} \exp\{2[(a_p E_p)^{1/2} - (a_n E_n)^{1/2}]\}, \quad (1)$$

and

$$\frac{\Gamma_\alpha}{\Gamma_n} = \frac{2E_\alpha}{E_n} \exp\{2[(a_\alpha E_\alpha)^{1/2} - (a_n E_n)^{1/2}]\}. \quad (2)$$

for evaporation and by

$$\frac{\Gamma_f}{\Gamma_n} = K_f \exp\{2[(a_f E_f)^{1/2} - (a_n E_n)^{1/2}]\}, \quad (3)$$

where

$$K_f = K_0 a_n \frac{[2(a_f E_f)^{1/2} - 1]}{(4A^{2/3} a_f E_n)}, \quad (4)$$

for fission. The parameters a_i stand for the density levels calculated by Dostrovsky's parametrization [28] and E_i is given by

$$\begin{aligned} E_n &= E - B_n, & E_p &= E - B_p - V_p, \\ E_\alpha &= E - B_\alpha - V_\alpha & E_f &= E - B_f, \end{aligned} \quad (5)$$

where B_n , B_p , and B_α are the separation energies for neutrons, protons, and α 's, respectively, and B_f is the fission barrier. V_i stands for the Coulomb potential.

At each n th step of the evaporation, the excitation energy of the compound nucleus is modified by

$$E^n = E^{n-1} - B - V - \varepsilon, \quad (6)$$

where ε is the kinetic energy of the emitted particle.

If the nucleus undergoes fission, the production of fragments is determined according to the multimodal-random neck rupture model (MM-NRM) [29], which takes into account the collective effects of nuclear deformation during fission by the liquid-drop model and single-particle effects by microscopic shell-model corrections. The microscopic corrections create valleys in the space of elongation and mass number, where each valley corresponds to a different fission mode [29].

According to the MM-NRM, the fragment mass distributions are determined by the uncorrelated sum of the different fission modes. In principle, it is supposed that there are three

distinct fission modes for heavy nuclei: symmetric Superlong (S) mode and two asymmetric modes standards I ($S1$) and II ($S2$). In the superlong mode, the fissioning system with mass A_f presents itself at the saddle-point in an extremely deformed shape with a long neck connecting the two forming fragments, which will have masses around $A_f/2$. The standard I mode is characterized by the influence of the spherical neutron shell $N_H \sim 82$ and of the proton shell $Z_H \sim 50$ in the heavy fragments with masses $M_H \sim 132$ – 134 . The standard II mode is characterized by the influence of the deformed neutron shell closure $N = 86$ – 88 and proton shell $Z_H \sim 52$ in the heavy fragments with masses $M_H \sim 138$ – 140 .

The fission cross section as a function of mass number is then obtained by the sum of three Gaussian functions, corresponding to the three modes mentioned above [30]:

$$\begin{aligned} \sigma(A) = & \frac{1}{\sqrt{2\pi}} \left[\frac{K_{1AS}}{\sigma_{1AS}} \exp\left(-\frac{(A - A_S - D_{1AS})^2}{2\sigma_{1AS}^2}\right) \right. \\ & + \frac{K_{1AS}}{\sigma_{1AS}} \exp\left(-\frac{(A - A_S + D_{1AS})^2}{2\sigma_{1AS}^2}\right) \\ & + \frac{K_{2AS}}{\sigma_{2AS}} \exp\left(-\frac{(A - A_S - D_{2AS})^2}{2\sigma_{2AS}^2}\right) \\ & + \frac{K_{2AS}}{\sigma_{2AS}} \exp\left(-\frac{(A - A_S + D_{2AS})^2}{2\sigma_{2AS}^2}\right) \\ & \left. + \frac{K_S}{\sigma_S} \exp\left(-\frac{(A - A_S)^2}{2\sigma_S^2}\right) \right], \quad (7) \end{aligned}$$

where A_S is the mean mass number determining the center of Gaussian functions; and K_i , σ_i , and D_i are the intensity, dispersion, and position parameters of the i th Gaussian functions. The indexes AS , S designate the asymmetric and symmetric components.

The CRISP code works on an event-by-event basis, and therefore, the parameter A_S in Eq. (1) is completely determined by the mass of the fissioning nucleus A_f , that is, $A_S = A_f/2$. The positions of the heavy and light peaks of the asymmetric components in the mass scale are given by the quantities $A_S + D_{iAS} = A_H$ and $A_S - D_{iAS} = A_L$, where A_H and A_L are the masses of the heavy and light fragment, respectively. The values of $A_H + A_L = 2A_S$ are treated as the mass of the undergoing fission nuclei in the respective channel.

One important observable in the fission process is the charge distribution of a given isobaric chain with mass number A . It is assumed that this charge distribution is well described by a Gaussian function characterized by the most probable charge Z_p of an isobaric chain with mass A (centroid of the Gaussian function) and the associate width parameter Γ_z of the distribution as follows [31,32]:

$$\sigma_{A,Z} = \frac{\sigma_A}{\Gamma_z \pi^{1/2}} \exp\left(-\frac{(Z - Z_p)^2}{\Gamma_z^2}\right), \quad (8)$$

where $\sigma_{A,Z}$ is the independent cross section of the nuclide with charge Z and mass A .

The values for Z_p and Γ_z can be represented as linear functions of the mass number of the fission fragments,

$$Z_p = \mu_1 + \mu_2 A, \quad (9)$$

and

$$\Gamma_z = \gamma_1 + \gamma_2 A. \quad (10)$$

Here μ_i and γ_i were determined by considering a systematic analysis of atomic number distributions of fission fragments. The values obtained for all parameters used in the present work are reported in Table II.

It is important to emphasize that the CRISP code has been used to simulate nuclear reactions of several kinds, such as those induced by protons [33–35], photons [19,27,36–38], electrons [39,40], or hypernuclei [21,41,42], with energies from 50 MeV up to 3.5 GeV, and on nuclei with masses going from $A = 12$ up to $A = 240$ and with several observables: spallation products, strange particles, fission products, hyperon-decay particles, fragment mass, and atomic number distributions. The code has been applied in the study for development of nuclear reactors [43–45]. Thus, the CRISP code is a reliable tool to investigate properties of nuclear reactions.

III. EXPERIMENTAL PROCEDURE

In the following we describe how the data present in this work have been obtained. A natural uranium target of 0.164 g and 0.0487 mm thick and a neptunium target of 0.742 g and 0.193 mm thick were exposed to an accelerated proton beam of 660 MeV in energy from the LNR Phasotron, Joint Institute for Nuclear Research (JINR), Dubna, Russia [46]. The proton flux was determined by the use of an aluminum monitor with known cross section [47]. The monitor, the same size as the target, was irradiated together with the target. The irradiation time was 27 min and the proton beam intensity was about 3×10^{14} protons per min. The induced activity of the targets was measured by two detectors, an HPGe detector with efficiency of 20% and energy resolution of 1.8 keV (1332 keV ^{60}Co) for the ^{238}U target and a Ge(Li) detector with efficiency of 4.8% and energy resolution of 2.6 keV (1332 keV ^{60}Co) for the ^{237}Np target. The identification of the reaction products and the determination of their production cross section were performed considering the half-lives, energies, and intensities of γ transitions of the radioactive fragments.

In the absence of a parent isotope, the cross section of fragment production for each fragment is determined by using the following equation:

$$\sigma = \frac{\Delta N \lambda}{N_p N_n k \epsilon \eta (1 - \exp(-\lambda t_1)) \exp(-\lambda t_2) (1 - \exp(-\lambda t_3))}, \quad (11)$$

where σ denotes the cross section of the reaction fragment production (mb); ΔN is the yield under the photopeak; N_p is the projectile beam intensity (min^{-1}); N_n is the number of target nuclei (in $1/\text{cm}^2$ units); t_1 is the irradiation time; t_2 is the time of exposure between the end of the irradiation and the beginning of the measurement; t_3 is the time measurement; λ is the decay constant (min^{-1}); η is the intensity of γ transitions; k is the total coefficient of γ -ray absorption in target and detector materials; and ϵ is the γ -ray-detection efficiency.

When the isotope production in the reaction under investigation is direct and independent (I) of the parent nuclei decay, the cross section is determined by Eq. (11). If the yield of a given isotope receives a contribution from the β^\pm decay of neighboring unstable isobar, the cross section calculation becomes more complicated [48]. If the formation probability of the parent isotope is known from experimental data or if it can be estimated on the basis of other sources, then the independent cross sections of daughter nuclei can be calculated by the relation:

$$\sigma_B = \frac{\lambda_B}{(1 - \exp(-\lambda_B t_1)) \exp(-\lambda_B t_2) (1 - \exp(-\lambda_B t_3))} \times \left[\frac{\Delta N}{N_p N_n k \epsilon \eta} - \sigma_A f_{AB} \frac{\lambda_A \lambda_B}{\lambda_B - \lambda_A} \left(\frac{(1 - \exp(-\lambda_A t_1)) \exp(-\lambda_A t_2) (1 - \exp(-\lambda_A t_3))}{\lambda_A^2} - \frac{(1 - \exp(-\lambda_B t_1)) \exp(-\lambda_B t_2) (1 - \exp(-\lambda_B t_3))}{\lambda_B^2} \right) \right], \quad (12)$$

where the subscripts A and B in the variables refer to the parent and daughter nucleus, respectively; the coefficient f_{AB} specifies the fraction of nuclei A decaying to nuclei B (this coefficient gives the information on how much the β decay affects our data; and $f_{AB} = 1$ when the contribution from the β decay corresponds to 100%); and ΔN is the total photopeak yield associated with the decays of the daughter and parent isotopes. The effect of the forerunner can be negligible in some limit cases, for example, in the case where the half-life of the parent nucleus is very long, or in the case where the fraction

of its contribution is very small. In the case when parent and daughter isotopes could not be separated experimentally, the calculated cross sections are classified as cumulative ones (C).

IV. RESULTS AND DISCUSSION

The mass distribution, as cross sections as a function of mass number A , for the fragment produced by 660 MeV proton induced reactions on uranium and neptunium targets are shown in Figs. 1 and 2. In both distributions a prominent

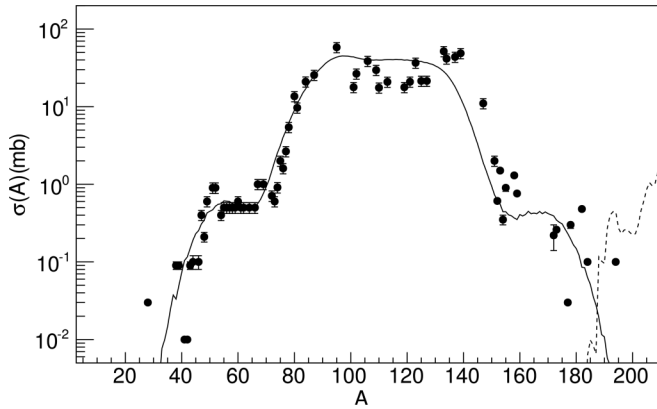


FIG. 1. Mass distribution of binary-decay products from the proton induced reaction at 660 MeV on ^{238}U target. Circles represent the measured isobaric cross sections from the present work and from the data taken from Refs. [46,49,50]. The solid line corresponds to the fission process and the dashed line represents the results of deep-spallation, both calculated with the CRISP code.

peak is observed around the symmetric fragment mass, which is indeed composed of fragments from the symmetric fission mode. The distributions, however, present also a contribution from two asymmetric modes [8,9]. Here we used the code CRISP to interpret these experimental distributions.

Some previous analysis for the mass distributions of the $p+^{237}\text{Np}$ and $p+^{238}\text{U}$ systems have been performed for the mass range of $70 < A < 150$ [9]. In this work, we have added new data in the region of intermediate mass fragment (IMF) corresponding to $30 < A < 70$ and data in the region of $150 < A < 200$ from Ref. [46]. The measured cross sections for the fragments in the mass range of $30 < A < 70$ are listed in Table I, where the quoted errors include contributions from those associated with the statistical significance of experimental results (2–3%), those in measuring the target thickness (3%), and those in determining the detector efficiency (10%).

Usually, studies on the production of fission fragments do not extend to light nuclei and the inclusion of this region in our analysis can bring up interesting features of the dynamics for fission fragment production. In fact, theoretical calculations, based on the mass asymmetry parameter and fission barrier

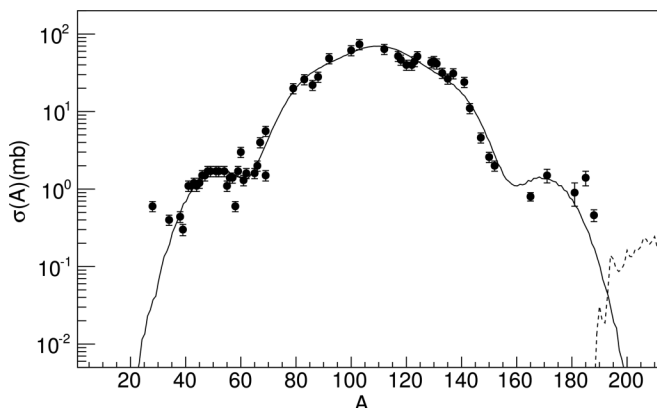


FIG. 2. Idem for the ^{237}Np target.

height [5], have shown that, for heavy targets and for reactions at intermediate or low energies, the cross sections for IMF are very small. As a consequence most of the experimental observations for fission available in the literature seem to die out for atomic numbers below $Z = 28$.

In Figs. 1 and 2 we can observe a shoulder formed in the mass region of $30 < A < 70$ for both ^{238}U and ^{237}Np target distributions. The presence of IMF in reactions at energy as low as the one of the present study can hardly be attributed to multifragmentation. The observation of another shoulder in the region of $170 < A < 200$, for both distributions, reinforces the idea of a binary process as the origin of the IMF. These observations, therefore, are in agreement with the results obtained by Ricciard *et al.* [5]. In this work, we present the results of a study performed with the simulation code CRISP, where the new experimental data set in the light mass region is described as a possible product of a fission or spallation process. To this end, as described in the next section, we have included an extra superasymmetric fission mode to the code.

V. SUPERASYMMETRIC FISSION MODE

To take into account the possibility of a superasymmetric fission, we included another mode, S_3 , to the CRISP code, which can be described by the usual Gaussian shape from MM-NRM,

$$\sigma(A)_{3AS} = \frac{1}{\sqrt{2\pi}} \left[\frac{K_{3AS}}{\sigma_{3AS}} \exp\left(-\frac{(A - A_S - D_{3AS})^2}{2\sigma_{3AS}^2}\right) + \frac{K_{3AS}}{\sigma_{3AS}} \exp\left(-\frac{(A - A_S + D_{3AS})^2}{2\sigma_{3AS}^2}\right) \right]. \quad (13)$$

As in the case of the three modes previously analyzed in Ref. [9], K_{3AS} , σ_{3AS} , and D_{3AS} , are fitting parameters which allow us to describe the experimental data for fragments produced through the fission channel. In addition to the fission, we calculated the mass distributions for fragments produced by the deep-spallation process. The results are also shown in Figs. 1 and 2, where we observe, that with the inclusion of the superasymmetric mode, the experimental data are well described by the fission mechanism according to the CRISP calculations. The deep-spallation mechanism gives only a very small contribution in the region of heavy fragments, showing that, in fact, the superasymmetric fission is the relevant mechanism for the production of fragments in the region of $160 < A < 200$.

The best-fit values for the parameters used in the MM-NRM approach are shown in Table II. The parameters for the S , S_1 , and S_2 modes were already discussed in Ref. [9]. Therefore, we focus here on the parameters for S_3 . The superasymmetric mode contributes with 0.6% and 1.2% of the total fission cross section for the ^{238}U and for ^{237}Np targets, respectively. The total fission cross sections are 1140 mb for ^{238}U and 1360 mb for ^{237}Np . The width for the S_3 distribution is somewhat larger than those for S_1 and S_2 , but smaller than that for S mode. The most striking feature of the superasymmetric mode is the mass number gap around 60 a.m.u. with respect

TABLE I. Cross section for the measured IMFs products from reaction induced by 660 MeV protons on ^{238}U and ^{237}Np targets.

Element	Type	Cross section, mb		Element	Type	Cross section, mb	
		^{238}U	^{237}Np			^{238}U	^{237}Np
^{28}Mg	C	$0.0043 \pm 4.3 \times 10^{-4}$	0.186 ± 0.020	^{52}Fe	I	$6.5 \times 10^{-4} \pm 5.5 \times 10^{-5}$	0.01 ± 0.01
$^{34}\text{Cl}^m$	C	$7.7 \times 10^{-4} \pm 1.5 \times 10^{-5}$	0.08 ± 0.02	^{54}Mn	I	0.11 ± 0.01	0.28 ± 0.03
^{38}S	I	$0.007 \pm 1.4 \times 10^{-4}$	≤ 0.08	^{55}Co	C	0.02 ± 0.002	≤ 0.036
^{38}Cl	I	0.04 ± 0.008	≤ 0.28	^{56}Mn	C	0.15 ± 0.02	0.69 ± 0.07
^{39}Cl	C	0.053 ± 0.005	0.023 ± 0.003	^{56}Co	I	0.07 ± 0.01	0.03 ± 0.006
^{41}Ar	C	$0.0037 \pm 7.4 \times 10^{-4}$	0.73 ± 0.07	^{56}Ni	I	≤ 0.002	≤ 0.007
^{42}K	C	$0.007 \pm 7.0 \times 10^{-4}$	≤ 0.40	^{57}Co	I	0.059 ± 0.006	0.20 ± 0.02
^{43}K	C	0.023 ± 0.002	0.45 ± 0.06	^{57}Ni	C	$0.0011 \pm 1.1 \times 10^{-4}$	≤ 0.01
^{43}Sc	C	0.012 ± 0.001	0.23 ± 0.02	$^{58}\text{Co}^{m+g}$	I	0.17 ± 0.02	0.13 ± 0.02
^{44}Ar	C	$\leq 2.5 \times 10^{-4}$	0.089 ± 0.02	^{59}Fe	C	0.27 ± 0.03	1.21 ± 0.12
^{44}K	I	$0.031 \pm 5.0 \times 10^{-5}$	0.22 ± 0.04	$^{60}\text{Co}^{m+g}$	C	0.33 ± 0.03	1.70 ± 0.20
$^{44}\text{Sc}^g$	I	≤ 0.0025	≤ 0.15	^{60}Cu	C	≤ 0.006	≤ 0.053
$^{44}\text{Sc}^m$	I	0.065 ± 0.007	0.12 ± 0.01	^{61}Cu	C	0.04 ± 0.004	≤ 0.057
^{45}K	C	–	0.24 ± 0.05	^{65}Ni	C	$0.0017 \pm 1.7 \times 10^{-4}$	≤ 0.04
$^{46}\text{Sc}^{m+g}$	I	0.036 ± 0.004	0.94 ± 0.09	^{65}Zn	I	0.10 ± 0.01	0.87 ± 0.17
^{47}Ca	C	0.024 ± 0.002	≤ 0.067	^{65}Ga	C	≤ 0.02	≤ 0.043
^{47}Sc	I	0.17 ± 0.02	0.63 ± 0.06	^{66}Ni	C	0.015 ± 0.002	0.20 ± 0.05
^{48}Sc	I	0.044 ± 0.004	0.42 ± 0.04	^{66}Ga	I	0.051 ± 0.005	≤ 0.084
^{48}V	I	0.022 ± 0.002	0.48 ± 0.05	^{66}Ge	C	≤ 0.003	≤ 0.13
^{48}Cr	I	≤ 0.0014	0.01 ± 0.001	^{67}Cu	C	0.55 ± 0.06	2.10 ± 0.21
^{49}Cr	C	0.025 ± 0.005	0.073 ± 0.015	^{67}Ga	C	0.06 ± 0.006	0.20 ± 0.02
^{51}Cr	C	0.41 ± 0.04	0.20 ± 0.02	$^{69}\text{Zn}^m$	C	0.041 ± 0.004	0.80 ± 0.16
$^{52}\text{Mn}^g$	I	$0.0015 \pm 1.5 \times 10^{-4}$	0.077 ± 0.008	^{69}Ge	C	0.03 ± 0.003	0.051 ± 0.012
$^{52}\text{Mn}^m$	I	$0.0085 \pm 8.5 \times 10^{-4}$	0.205 ± 0.03				

to the symmetric fragment for both cases studied here. Our results confirm that IMF at intermediate energies are formed predominantly through a binary process, and that it is described by a superasymmetric fission mode.

As shown in the present work, a good description of the fragment production for the full range of mass of $30 < A < 200$ was obtained by considering the fission mechanism. This

might indicate that this is, in fact, the actual predominant mechanism. However, we can not totally exclude the possibility that a description of the experimental data would also be achieved by considering some other sort of mechanism, such as evaporation with the inclusion of the associated spallation and with emission of fragments heavier than the α particle.

TABLE II. Parameters for the mass distribution calculations.

Parameter	^{238}U	^{237}Np
K_{1AS}	$(2.0 \pm 5.0)\%$	$(1 \pm 1)\%$
σ_{1AS}	3.5 ± 0.8	4.5 ± 0.4
D_{1AS}	18.5 ± 0.4	21.3 ± 0.4
K_{2AS}	$(19 \pm 5)\%$	$(7.7 \pm 0.8)\%$
σ_{2AS}	6.0 ± 0.5	6.5 ± 0.6
D_{2AS}	18.0 ± 0.4	28.3 ± 0.5
K_{3AS}	$(0.5 \pm 0.5)\%$	$(1.2 \pm 0.3)\%$
σ_{3AS}	7.0 ± 0.5	8.0 ± 0.7
D_{3AS}	57.0 ± 0.4	62.0 ± 0.3
K_S	$(56 \pm 5)\%$	$(79.0 \pm 7.0)\%$
σ_S	13.0 ± 0.5	13.7 ± 1.0
μ_1	4.1 ± 0.6	5.0 ± 0.8
μ_2	0.38 ± 0.01	0.37 ± 0.01
γ_1	0.92 ± 0.08	0.59 ± 0.02
γ_2	0.003 ± 0.001	0.005 ± 0.0002

VI. CONCLUSION

The cross sections for fragments produced by the proton-induced fission on ^{238}U and ^{237}Np at 660 MeV were measured at the LNR Phasatron (JINR). The fragment mass distributions covering the region of $20 < A < 200$, allowed the investigation of the production mechanism for the intermediate mass fragments (IMF) in the mass range of $20 < A < 70$. It was found that, for each of the IMF observed in the low mass region, there was a heavier counterpart in the region of $170 < A < 200$, indicating that they are actually produced by a binary process. This hypothesis was tested with the use of the CRISP code by including an additional superasymmetric fission mode described according to the MM-NRM approach. The results show, indeed, that it is possible to give an accurate description of the fragment production in the entire mass region of $20 < A < 200$ by considering the evaporation/fission mechanism in the CRISP code with the usual

fission modes, namely, one symmetric and two asymmetric, and including a fourth superasymmetric mode. This last mode produces fragments that are around 60 a.m.u., far from the symmetric fragment mass, and contributes with 0.6% and 1.2% to the total fission cross section for ^{238}U and ^{237}Np , respectively. Our results are in agreement with previous results obtained by Ricciardi *et al.* [5] evidencing the binary production mechanism for the IMF at intermediate energy nuclear reaction.

ACKNOWLEDGMENTS

G.K. is grateful to the Fundação de Amparo à Pesquisa do Estado de São Paulo (FAPESP) 2011/00314-0 and 2013/01754-9, and also to the International Centre for Theoretical Physics (ICTP) under the Associate Grant Scheme. A.D. acknowledges the partial support from CNPq under grant no. 305639/2010-2 and FAPESP under Grant No. 2010/16641-7. E.A. acknowledges the support from FAPESP under Grant No. 2012/13337-0. We thank Prof. Wayne Seale for reviewing the text.

-
- [1] J. Hufner, *Phys. Rep.* **125**, 129 (1985).
- [2] W. Loveland, C. Luo, P. L. McGaughey, D. J. Morrissey, and G. T. Seaborg, *Phys. Rev. C* **24**, 464 (1981).
- [3] Y. Yariv and Z. Fraenkel, *Phys. Rev. C* **20**, 2227 (1979).
- [4] B. Grabez, *Phys. Rev. C* **48**, R2144 (1993).
- [5] M. V. Ricciardi, P. Armbruster, J. Benlliure *et al.*, *Phys. Rev. C* **73**, 014607 (2006).
- [6] A. A. Kotov, L. N. Andronenko, M. N. Andronenko *et al.*, *Nucl. Phys. A* **583**, 575 (1995).
- [7] H. W. Barz, J. P. Bondorf, H. Schulz *et al.*, *Nucl. Phys. A* **460**, 714 (1986).
- [8] A. Deppman, E. Andrade-II, V. Guimarães, G. S. Karapetyan, and N. A. Demekhina, *Phys. Rev. C* **87**, 054604 (2013).
- [9] A. Deppman, E. Andrade-II, V. Guimarães, G. S. Karapetyan, A. R. Balabekyan, and N. A. Demekhina, *Phys. Rev. C* **88**, 024608 (2013).
- [10] D. A. de Lima, J. B. Martins, and O. A. P. Tavares, *Il Nuovo Cim. A* **103**, 701 (1990).
- [11] M. L. Terranova and O. A. P. Tavares, *Phys. Scr.* **49**, 267 (1994).
- [12] T. Fukahori, O. Iwamoto, and S. Chiba, in *Proceedings of the 7th International Conference on Nuclear Criticality Safety, ICNC 2003*, JAERI-conf, 2003-019, edited by Nihon Genshiryoku Kenkyuujo and Nihon Genshiryoku Gakkai (Japan Atomic Energy Research Institute, Tokai-mura, Japan, 2003), Parts 1–2, p. 144.
- [13] L. G. Moretto, *Nucl. Phys. A* **247**, 211 (1975).
- [14] S. B. Duarte, O. A. P. Tavares, F. Guzman *et al.*, *Atom. Data and Nucl. Data Tables* **80**, 235 (2002).
- [15] A. Deppman, S. B. Duarte, G. Silva *et al.*, *J. Phys. G: Nucl. Part. Phys.* **30**, 1991 (2004).
- [16] T. Kodama, S. B. Duarte, K. C. Chung, and R. A. M. S. Nazareth *Phys. Rev. Lett.* **49**, 536 (1982).
- [17] M. Goncalves, S. de Pina, D. A. Lima *et al.*, *Phys. Lett. B* **406**, 1 (1997).
- [18] B. D. Serot and J. D. Walecka, in *Advances in Nuclear Physics* edited by J. W. Negele and E. Vogt, Vol. 16 (Plenum Press, New York, USA, 1986), p. 1.
- [19] A. Deppman *et al.*, *J. Phys. G: Nucl. Part. Phys.* **30**, 1991 (2004).
- [20] S. de Pina *et al.*, *Phys. Lett. B* **434**, 1 (1998).
- [21] I. Gonzalez *et al.*, *J. Phys. G: Nucl. Part. Phys.* **38**, 115105 (2011).
- [22] A. Deppman *et al.*, *Phys. Rev. Lett.* **87**, 182701 (2001).
- [23] A. Deppman *et al.*, *Nucl. Instrum. Methods Phys. Res. B* **211**, 15 (2003).
- [24] A. Deppman *et al.*, *Comp. Phys. Comm.* **145**, 385 (2002).
- [25] N. Bianchi *et al.*, *Phys. Lett. B* **299**, 219 (1993).
- [26] J. C. Sanabria *et al.*, *Phys. Rev. C* **61**, 034604 (2000).
- [27] A. Deppman, G. Silva, S. Anefalos, S. B. Duarte, F. García, F. H. Hisamoto, and O. A. P. Tavares, *Phys. Rev. C* **73**, 064607 (2006).
- [28] I. Dostrovsky, P. Rabinowitz, and R. Bivins, *Phys. Rev.* **111**, 1659 (1958).
- [29] U. Brosa, S. Grossman, and A. Muller, *Z. Naturforschung* **41**, 1341 (1986).
- [30] W. Younes, J. A. Becker, L. A. Bernstein *et al.*, *Nuclear Physics in the 21st Century: International Nuclear Physics Conference (INPC 2001)* (AIP, New York, 2001) [*AIP Conf. Proc.* **610**, 673 (2001)].
- [31] H. Kudo, M. Maruyama, M. Tanikawa, T. Shinozuka, and M. Fujioka, *Phys. Rev. C* **57**, 178 (1998).
- [32] M. C. Duijvestijn, A. J. Koning, J. P. M. Beijers, A. Ferrari, M. Gastal, J. van Klinken, and R. W. Ostendorf, *Phys. Rev. C* **59**, 776 (1999).
- [33] S. A. Pereira *et al.*, *Nucl. Sci. Eng.* **159**, 102 (2008).
- [34] E. Andrade-II *et al.*, *J. Phys. G: Nucl. Part. Phys.* **38**, 085104 (2011).
- [35] E. Andrade-II, J. C. M. Menezes, S. B. Duarte *et al.*, *EPJ Web Conf.* **21**, 10001 (2012).
- [36] A. Deppman, O. A. P. Tavares, S. B. Duarte, J. D. T. Arruda-Neto, M. Gonçalves, V. P. Likhachev, and E. C. de Oliveira, *Phys. Rev. C* **66**, 067601 (2002).
- [37] E. Andrade-II, E. Freitas, O. A. P. Tavares *et al.*, *XXXI Workshop on Nuclear Physics in Brazil* (AIP, New York, 2009) [*AIP Conf. Proc.* **1139**, 64 (2009)].
- [38] A. Deppman, G. Silva, S. Anefalos, S. B. Duarte, F. García, F. H. Hisamoto, and O. A. P. Tavares, *Phys. Rev. C* **73**, 064607 (2006).
- [39] V. P. Likhachev *et al.*, *Nucl. Phys.* **713**, 24 (2003).
- [40] V. P. Likhachev *et al.*, *Phys. Rev. C* **68**, 014615 (2003).
- [41] I. Gonzales *et al.*, *J. Phys. Conf. Series* **312**, 022017 (2011).
- [42] F. Krmpotic *et al.*, *Nuclear Structure and Dynamics 2012* (AIP, New York, 2012) [*AIP Conf. Proc.* **1491**, 117 (2012)].
- [43] S. Anefalos *et al.*, *International Conference on Nuclear Data for Science and Technology 2004* (AIP, New York, 2004) [*AIP Conf. Proc.* **769**, 1299 (2005)].
- [44] S. Anefalos *et al.*, *Nucl. Sci. Eng.* **151**, 82 (2005).
- [45] A. Deppman *et al.*, *Sci. Tech. Nucl. Inst.* **2012**, 480343 (2012).
- [46] J. Adam, K. Katovsky, R. Michel, and A. Balabekyan, *International Conference on Nuclear Data for Science and Technology 2004* (AIP, New York, 2004) [*AIP Conf. Proc.* **769**, 1043 (2005)].
- [47] J. B. Cumming, *Ann. Rev. Nucl. Sci.* **13**, 261 (1963).
- [48] H. Baba, J. Sanada, H. Araki *et al.*, *Nucl. Instrum. Methods Phys. Res. A* **416**, 301 (1998).
- [49] G. S. Karapetyan, A. R. Balabekyan, N. A. Demekhina, and J. Adam, *Phys. At. Nucl.* **72**, 911 (2009).
- [50] A. R. Balabekyan, G. S. Karapetyan, N. A. Demekhina *et al.*, *Phys. At. Nucl.* **73**, 1814 (2010).

Neutron Spectrum Determination of the p(35 MeV)-Be Source Reaction by the Dosimetry Foils Method

M. Štefánik,^{1,2,*} P. Bém,¹ M. Götz,¹ K. Katovský,³ M. Majerle,¹ J. Novák,¹ and E. Šimečková¹

¹*Nuclear Physics Institute of the Academy of Sciences of the Czech Republic, Řež 130, 250 68, Czech Republic*

²*Czech Technical University in Prague, Faculty of Nuclear Sciences and Physical Engineering, Břehová 7, Prague, 115 19, Czech Republic*

³*Brno University of Technology, Faculty of Electrical Engineering and Communication, Technická 10, Brno, 616 00, Czech Republic*

The thick target neutron field of source reaction $p + \text{Be}$ was investigated for a proton energy of 35 MeV. The spectral neutron flux at 0° for two target-to-sample distances was determined by using the dosimetry foils activation method. The present p(35)-Be white neutron spectra provide the suitable basis for irradiation experiments and integral tests of nuclear data.

I. INTRODUCTION

The cyclotron based fast neutron generators of the white- and quasi-monoenergetic spectra are operated at the Department of Nuclear Reactions of the Nuclear Physics Institute utilizing the variable-energy proton beam (up to 37 MeV) and the D_2O (flow), Be (thick), and $^7\text{Li}(\text{C})$ target stations [1]. The intensity and energy range of produced neutron fields are suitable for the integral and differential validation of the neutron cross-sections within the ADTT (Accelerator-Driven Transmutation Technology) and fusion-relevant (IFMIF – International Fusion Materials Irradiation Facility) research programs.

In neutron activation experiments, the irradiated samples are usually fixed in the vicinity of the source target, and the dimensions of the target and samples are comparable with the target-to-sample distance. Due to a lack of differential yield data at requested energy and angular range, the MCNPX calculations need to be validated against the independent experiments. Recently, the dosimetry-foils activation method was successfully used for the validation of an MCNPX prediction of spectral flux characteristics for the p- D_2O (thick) reaction [2, 3]. In the present work, this method was employed to determine the spectra of the Be(p,xn) source reaction at the positions of irradiated samples.

A. Neutron Activation Method, Reaction Rate

To determine the spectral flux at the position of irradiated samples, the standard multi-foil activation method is utilized. It makes possible the reconstruction of the neutron spectrum by using the γ -activities of radionuclides produced by the activation reactions in a set of activation foils irradiated in this field. The result of activation measurements is the *reaction rate* per one target nuclei (s^{-1}), and is defined as

$$P_R = \frac{S_\gamma \lambda \frac{t_{\text{real}}}{t_{\text{live}}} e^{\lambda t_{\text{cool}}}}{N_0 \varepsilon_\gamma I_\gamma (1 - e^{-\lambda t_{\text{irr}}})(1 - e^{-\lambda t_{\text{real}}}) \eta_B}, \quad (1)$$

where λ is the decay constant, S_γ the area under the full energy peak, N_0 the number of target nuclei, ε_γ the detection efficiency, I_γ the intensity per decay, t_{irr} and t_{cool} the irradiation and cooling time, t_{real} and t_{live} the real and live time of the spectroscopic measurement, and η_B a correction for beam fluctuation. The reaction rate is proportional to neutron flux ϕ ($\text{cm}^{-2}\text{s}^{-1}\text{MeV}^{-1}$) since

$$P_R = \int_{E_{\text{thresh}}}^{E_{\text{max}}} \sigma(E_n) \phi(E_n) dE_n, \quad (2)$$

where the σ is the microscopic activation cross-section.

II. MATERIALS AND METHODS

A. Beryllium Target Station NG-2

Powerful fast neutron sources usually provide intense neutron beams from proton or deuteron bombardment

* Corresponding author: milan.stefanik@jfifi.cvut.cz

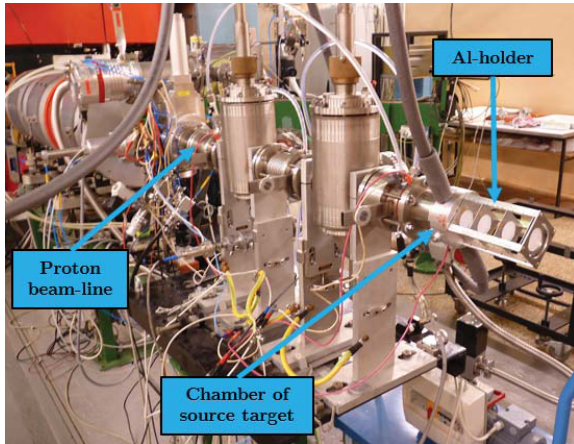


FIG. 1. Beryllium target station of the NG-2 neutron generator at the NPI with aluminum holder of activation foils.

of a thick beryllium target. In standard operation, the beryllium target station at NPI (Fig. 1) produces a white spectrum with spectral yield of 1.2×10^{11} n sr⁻¹ in the forward direction for proton energies up to 20 MeV. During operation, the beryllium target, with thickness of 8 mm, is cooled by ethanol to a temperature of 5 °C. However, the high energy and high intensity p(35)-Be white neutron field for activation experiments has been developed recently, and the neutron spectra are presented in this work.

B. The p-Be Neutron Source Reaction

During bombardment of the beryllium target by protons at energy $E_p=35$ MeV, the high energy neutron spectrum component is mostly produced in the ${}^9\text{Be}(p,n){}^9\text{B}$ reaction to the ground state ($Q = -1.85$ MeV) and partially to highly excited states (2.3 MeV, 1.4 MeV), while the low energy spectrum component is produced in three body break-up processes. The structure of the low energy spectrum is mainly formed by the reactions of ${}^9\text{Be}(p,np){}^8\text{Be}$ ($Q = -1.67$ MeV), ${}^9\text{Be}(p,\alpha){}^5\text{Li}$ ($Q = -3.54$ MeV), and ${}^9\text{Be}(p,\alpha){}^5\text{He}$ ($Q = -2.67$ MeV) with subsequent ${}^5\text{He}$ break-up to neutron and α -particle ($Q = 0.89$ MeV).

Figure 2 shows the MCNPX calculated neutron spectra and its dependence on various thicknesses of beryllium. The neutron spectrum of thin targets (0.25 mm and 0.5 mm) is produced almost entirely by monoenergetic protons and consists of well distinguishable peaks of neutrons from the ${}^9\text{Be}(p,n){}^9\text{B}$ reaction to ground and excited states. By increasing the target thickness, the proton beam energy degrades by ionizing effects in the target and induces the neutron production reactions at lower energies. Due to this effect, the spectrum changes in shape from semi-monoenergetic peaks to a broad continuous spectrum.

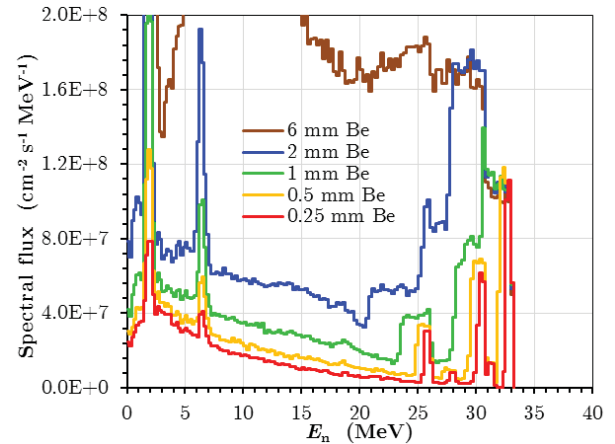


FIG. 2. The MCNPX calculated p(35)-Be neutron spectra for various thicknesses of bare beryllium target without backing.

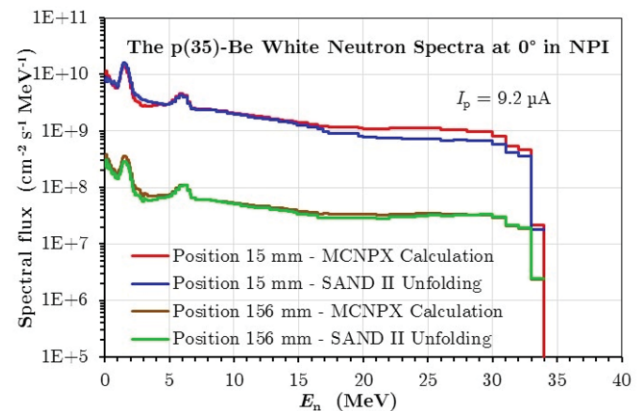


FIG. 3. Neutron fields of NG-2 generator at two irradiation positions measured by multi-foil activation technique at NPI.

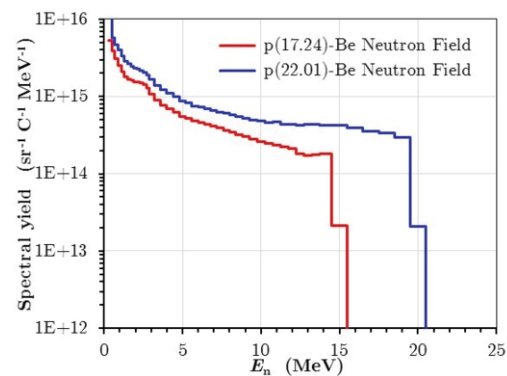


FIG. 4. Spectral neutron yield on the beryllium target measured by the NE213 scintillation detector in Braunschweig [8].

C. Neutron Field Measurement

The current research program at the NPI requires the usage of a high energy neutron field above 20 MeV, and

TABLE I. The C/E ratios for adjusted neutron spectra.

Reaction	C/E Position 15 mm	C/E Position 156 mm	E_{thresh} (MeV)
$^{27}\text{Al}(n,\alpha)^{24}\text{Na}$	0.91	0.94	3.25
$^{93}\text{Nb}(n,2n)^{92\text{m}}\text{Nb}$	0.99	1.02	9.06
$^{93}\text{Nb}(n,4n)^{90}\text{Nb}$	–	0.90	29.08
$^{93}\text{Nb}(n,\alpha)^{90\text{m}}\text{Y}$	0.86	–	0.00
$^{197}\text{Au}(n,2n)^{196}\text{Au}$	–	1.12	8.11
$^{197}\text{Au}(n,3n)^{195}\text{Au}$	1.12	1.11	14.79
$^{197}\text{Au}(n,4n)^{194}\text{Au}$	1.02	0.93	23.21
$^{197}\text{Au}(n,\gamma)^{198}\text{Au}$	1.04	1.02	0.00
$^{89}\text{Y}(n,2n)^{88}\text{Y}$	0.80	0.87	11.61
$^{89}\text{Y}(n,\gamma)^{90\text{m}}\text{Y}$	0.88	0.99	0.00
$^{59}\text{Co}(n,2n)^{58}\text{Co}$	0.97	0.98	10.63
$^{59}\text{Co}(n,3n)^{57}\text{Co}$	0.96	0.94	19.35
$^{59}\text{Co}(n,p)^{59}\text{Fe}$	1.13	1.03	1.57
$^{59}\text{Co}(n,\alpha)^{56}\text{Mn}$	1.07	0.96	0.00
$^{59}\text{Co}(n,\gamma)^{60}\text{Co}$	1.01	1.01	0.00
$^{115}\text{In}(n,n')^{115\text{m}}\text{In}$	–	1.05	0.34
$^{\text{nat}}\text{Lu}(n,x)^{173}\text{Lu}$	0.97	1.10	14.51
$^{\text{nat}}\text{Lu}(n,x)^{176\text{m}}\text{Lu}$	0.97	0.96	0.00
$^{176}\text{Lu}(n,\gamma)^{177}\text{Lu}$	1.01	1.00	0.00
$^{\text{nat}}\text{Ti}(n,x)^{46}\text{Sc}$	0.98	0.83	1.62
$^{\text{nat}}\text{Ti}(n,x)^{47}\text{Sc}$	1.16	1.14	0.00
$^{\text{nat}}\text{Ti}(n,x)^{48}\text{Sc}$	1.10	1.06	3.28
$^{\text{nat}}\text{Ni}(n,x)^{57}\text{Co}$	1.16	1.14	6.05
$^{\text{nat}}\text{Ni}(n,x)^{60}\text{Co}$	1.18	–	2.12
$^{\text{nat}}\text{Ni}(n,x)^{57}\text{Ni}$	1.13	1.21	12.43
$^{\text{nat}}\text{Fe}(n,x)^{56}\text{Mn}$	0.93	1.03	2.97
$^{\text{nat}}\text{Fe}(n,x)^{54}\text{Mn}$	0.92	0.96	12.14
$^{\text{nat}}\text{Fe}(n,x)^{51}\text{Cr}$	0.84	1.02	0.00
$^{209}\text{Bi}(n,3n)^{207}\text{Bi}$	0.98	0.77	14.42

therefore the operation of a Be-target station (with 8 mm Be-target) was successfully tested at a proton energy of 35 MeV (beam current of 9.2 μA), which is nearly the maximum energy provided by the U-120M cyclotron. The

novel p(35)-Be neutron field was developed by utilization of the multi-foil activation method.

For the neutron spectrum determination at two irradiation positions (15 and 156 mm), eleven activation foils (Al, Nb, Y, MnNi, Co, In, Lu, Au, Ti, Fe, Bi) were used. The induced γ -ray activities of irradiated foils were investigated by the nuclear γ -spectrometry technique, and subsequently the reaction rates were calculated. To unfold the neutron spectrum, a modified version of the SAND-II [4] code with support for nuclear data from the EAF-2007 library [5] up to 55 MeV was used. For the unfolding iterative procedure, the initial guess neutron spectrum calculated by the MCNPX code [6] using the ENDF/B-VII proton library [7] was employed.

The unfolded spectra and MCNPX predictions are shown in Fig. 3; the corresponding C/E ratios are summarized in Table I and assess the uncertainties of the adjusted spectra. Unfolded spectrum at the 156 mm position corresponds well with the MCNPX calculation; however, at the 15 mm position, the space integration effect of neutron yield becomes evident. The shape of spectra is in good agreement with measurements in Braunschweig [8] (see Fig. 4).

III. CONCLUSIONS

The high intensity p-Be white neutron field was developed at a proton energy of 35 MeV, the neutron spectra were determined by activation method for two irradiation positions. The novel p(35)-Be spectra have a flat shape; the neutrons from the three body break-up process contribute to the low energy spectrum component. The spectral shape is in good agreement with time-of-flight measurement of other authors at lower proton energies.

The p(35)-Be neutron spectra are convenient for cross-section data validation in the energy range relevant to the IFMIF, for testing the radiation hardness of electronics, and for the ADTT research program.

- [1] P. Bem, PROC. ND2007, Nice, France, 555 (2007).
 [2] S.P. Simakov *et al.*, FUS. ENG. DESIGN **82**, 2510 (2007).
 [3] M. Stefanik *et al.*, TRANSACT. OF ANS **106**, 894 (2012).
 [4] SAND-II-SNL, PSR-345, UKAEA FUS (1996).
 [5] R.A. Forrest *et al.*, EAF-2007 **48**, UKAEA FUS (2007).
 [6] L.S. Waters *et al.*, MCNPX USER'S MANUAL V. 2.1.5.

- [7] M.B. Chadwick *et al.*, NUCL. DATA SHEETS **112**, 2887 (2011).
 [8] H.J. Brede *et al.*, NUCL. INST. METHODS **A274**, 332 (1989).



Conference on the Application of Accelerators in Research and Industry, CAARI 2016,
30 October – 4 November 2016, Ft. Worth, TX, USA

Determination of the Secondary Neutron Flux at the Massive Natural Uranium Spallation Target

M. Zeman^{a,b*}, J. Adam^{b,c}, A.A. Baldin^{b,d}, W.I. Furman^b, S.A. Gustov^b, K. Katovsky^a,
J. Khushvaktov^b, I.I. Mar`in^b, F. Novotny^a, A.A. Solnyshkin^b, P. Tichy^{b,c,e},
V.M. Tsoupko-Sitnikov^b, S. I. Tyutyunnikov^b, R. Vespalec^{b,e}, J. Vrzalova^{b,c,e},
V. Wagner^{c,e}, L. Zavorka^{b,e}

^a Brno University of Technology, Brno 616 00, Czech Republic

^b Joint Institute for Nuclear Research, Dubna 141 980, Russia Federation

^c Nuclear Physics Institute of the ASCR, Rez near Prague 250 68 Czech Republic

^d Institute for Advanced Studies "OMEGA", Dubna 141 980, Moscow region, Russian Federation

^e Czech Technical University in Prague, Prague 166 36, Czech Republic

Abstract

The flux of secondary neutrons generated in collisions of the 660 MeV proton beam with the massive natural uranium spallation target was investigated using a set of monoisotopic threshold activation detectors. Sandwiches made of thin high-purity Al, Co, Au, and Bi metal foils were installed in different positions across the whole spallation target. The gamma-ray activity of products of (n,xn) and other studied reactions was measured offline with germanium semiconductor detectors. Reaction yields of radionuclides with half-life exceeding 100 min and with effective neutron energy thresholds between 3.6 MeV and 186 MeV provided us with information about the spectrum of spallation neutrons in this energy region and beyond. The experimental neutron flux was determined using the measured reaction yields and cross-sections calculated with the TALYS 1.8 nuclear reaction program and INCL4-ABLA event generator of MCNP6. Neutron spectra in the region of activation sandwiches were also modeled with the radiation transport code MCNPX 2.7. Neutron flux based on excitation functions from TALYS provides a reasonable description of the neutron spectrum inside the spallation target and is in good agreement with Monte-Carlo predictions. The experimental flux that uses INCL4 cross-sections rather underestimates the modeled spectrum in the whole region of interest, but the agreement within few standard deviations was reached as well. The paper summarizes basic principles of the method for determining the spectrum of high-energy neutrons without employing the spectral adjustment routines and points out to the need for model improvements and precise cross-section measurements.

* Corresponding author.

E-mail address: Miroslav.Zeman@vutbr.cz

© 2017 Published by Elsevier B.V. This is an open access article under the CC BY-NC-ND license (<http://creativecommons.org/licenses/by-nc-nd/4.0/>).

Peer-review under responsibility of the Scientific Committee of the Conference on the Application of Accelerators in Research and Industry

Keywords: ADS; spallation target; neutron flux; threshold activation detectors

1. Introduction

The Accelerator Driven Systems (ADS) is one of the ways to transmute spent nuclear fuel (SNF) from nuclear power plants and high level radioactive material, originally planned to be used for military purposes. Such a system consists of the external particle source, accelerator, spallation target made of a heavy metal, and a blanket consisting of SNF or other nuclear material. The principle of ADS has been described in details, e.g. (Grand et al. 1985) and (Bowman et al. 1992). Projects focused on ADS research are realized around the world. For example, in Europe the MYRRHA project is being built, see more details elsewhere (Abderrahim et al. 2010). The project will be based on nuclear reactor with ability to operate in both subcritical and critical modes driven by a proton accelerator. Other projects are planned around the world, for example TEF in Japan - (Sasa 2015) and C-ADS in China (Huang et al. 2015).

An important parameter for transmuted SNF and high-level radioactive material is the neutron spectrum of a spallation source. Both the spectrum and intensity of the secondary neutron field vary with the position inside the target. The detection of the secondary neutron field in spallation targets can be done with helium detectors, track detectors, or threshold activation detectors. Recently, several activation experiments were performed at the Joint Institute for Nuclear Research (JINR) within the international collaboration E&T-RAW, see e.g. (Zavorcka et al. 2015), (Khushvaktov et al. 2016) and (Adam et al. 2015).

This paper provides a description of two such experiments carried out with the spallation target made of natural uranium. In these experiments, monoisotopic threshold activation detectors in the form of sandwiches were used for characterization of neutron field generated in the spallation target. The target was irradiated with a 660 MeV proton beam. The detectors were placed inside of the spallation target in different positions. The main focus of the measurement were the (n,xn) reactions leading to the production of radioisotopes with $T_{1/2}$ higher than 100 minutes in the interval of the threshold energies from 3 MeV up to 186 MeV. The energy spectrum of secondary neutron field was determined across the whole volume of the spallation target.

2. Experimental methods

The experiments were carried out at JINR, at the Dzhelapov Laboratory of Nuclear Problems. The *QUINTA* target was composed of five natural uranium cylinders. The cylinders were 36 mm in diameter and 104 mm in length. Uranium cylinders were clad in 1 mm thick aluminum. The cylinders were fixed in hexagonal aluminum sections with wall thickness of 5 mm. Sections were separated by 17 mm wide air gaps. The first section had a beam window, 80 mm in diameter, four other sections had no windows. The total weight of the target was 540 kg, where the mass of metallic uranium was 512 kg. *QUINTA* is shown in Figure 1. The set-up was surrounded by the 100 mm thick lead shielding.

2.1. Target irradiation

The irradiation was performed using a synchrocyclotron particle accelerator, called Phasotron. The Phasotron accelerates protons up to 660 MeV. The protons impinge into the *QUINTA* target and generate the secondary neutron field. Two experiments were performed using high purity monoisotopic sandwiches. The samples positions are shown in Figure 1 b). All samples were fixed on the aluminum plates. The samples of ^{27}Al , ^{59}Co and ^{197}Au were packed like a sandwich. The ^{209}Bi samples were fixed on the right side of the sandwiches at aluminum plates. Figure 2 represents the sandwich of samples with bismuth. The masses of the samples were about 1.3 g for aluminum, 6 g for the bismuth samples, 5.5 g for the cobalt samples and 1g for the gold samples. In the first experiment five activation sandwiches

were irradiated, shown as red dots in Figure 1. b). Other five sandwiches were irradiated in the second experiment, shown as blue dots in Figure 1 b). The locations of the sandwiches inside spallation target are presented in Table 1. The number of the protons was calculated from three aluminum monitors in parameters $100 \times 100 \text{ mm}^2$. The $^{27}\text{Al}(p,x)^{24}\text{Na}$ reaction was followed and the cross-section corresponding to the proton energy 660 MeV was $(10.8 \pm 0.3) \text{ mb}$. The cross-section was calculated as the weighted average from experimental values available in literature (Aleksandrov et al. 1996, Friedlander et.al 1955, Michel et al. 1986, Morgan et al. 2003 and Taddeucci et al. 1997). For the first experiment the number of protons was $8.57(28) \times 10^{14}$ and the time of irradiation was 4 hours and 54 minutes. In the second experiment *QUINTA* target was irradiated for 5 hours and the number of protons was $2.53(5) \times 10^{15}$.

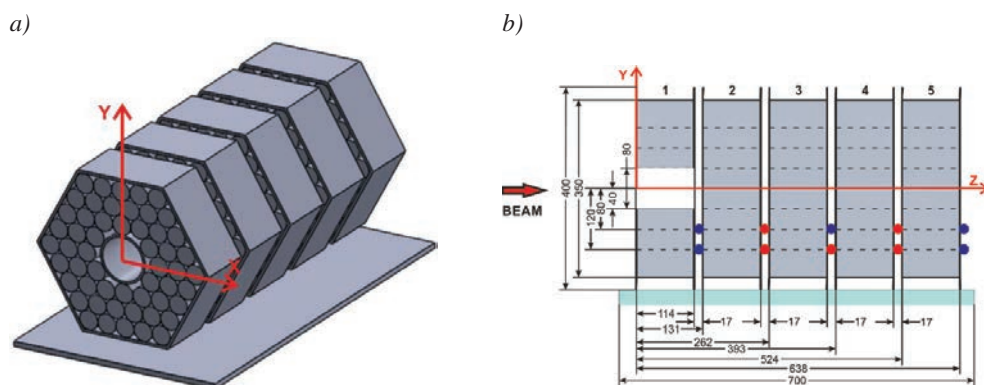


Fig. 1. Spallation target QUINTA (a) general and (b) side views (red dots - first experiment, blue dots – second experiment).

Table 1. Positions of samples with coordinates.

1 st experiment Sample	Sample location			2 nd experiment Sample	Sample location		
	X (mm)	Y (mm)	Z (mm)		X (mm)	Y (mm)	Z (mm)
No. 1	0	-80	254	No. 6	0	-80	123
No. 2	0	-120	254	No. 7	0	-120	123
No. 3	0	-120	385	No. 8	0	-80	385
No. 4	0	-80	516	No. 9	0	-80	647
No. 5	0	-120	516	No. 10	0	-120	647

2.2. Samples measurements

After irradiation, the samples were transported to the gamma-ray spectroscopy laboratory YaSNAPP-2. There the samples were unpacked and their gamma-spectra were obtained with high purity germanium detectors. Table 2 shows list the reactions and isotopes of interest with their threshold energies, half-lives, gamma-lines and intensity of gamma-lines. The full-energy peaks of reaction products were measured for a sufficiently long period to minimize statistical uncertainties. The time of measurement ranged from 10's of minutes to several days. Each sample was measured at least six times and the value of the dead time was always held below 10%.

3. Data processing

The main part of the data analysis was performed with the gamma-spectroscopic program DEIMOS32, which was developed at the Czech Academy of Sciences (Frana 2003). The main principle of the program is based on searching the gamma-ray energies in the measured spectra and integrating the areas of full-energy peaks. The peak areas are fitted by the Gaussian function. The experimental reaction rates of the produced residual nuclei are then calculated

from the measured activity at the end of irradiation. The experimental reaction rate is defined as the number of produced residual nuclei per one atom in the sample and one incident particle. The experimental reaction rate R_{Exp} is calculated as shown in equation (1).

$$R_{Exp} = \frac{S(E_\gamma)C_{abs}(E_\gamma)B_a}{I_\gamma \varepsilon_p(E_\gamma)} \frac{t_{real}}{t_{live}} \frac{1}{N_A} \frac{1}{N_P} \frac{e^{(\lambda t_0)}}{1 - e^{(-\lambda t_{real})}} \frac{\lambda t_{irr}}{1 - e^{(-\lambda t_{irr})}} C_{coisum} \quad (1)$$

where $S(E_\gamma)$ is the peak area, $C_{abs}(E)$ is the self-absorption correction, B_a is the beam intensity correction, I_γ is the gamma-line intensity per decay, $\varepsilon_p(E)$ is the full-energy peak efficiency, t_{real} is the real measurement time, t_{live} is the live time of the measurement, N_A is the number of atoms in the sample, N_P is the number of incident particles during irradiation, t_0 is the time between end of irradiation and start of the measurement, λ is the decay constant, t_{irr} is the time of irradiation, and C_{coisum} is the correction for true coincidence summing, as described elsewhere (Sudár 2002).

The next step was to determine the experimental neutron flux according to equation (2). This equation represents a general recipe for the reaction rate calculation - an integral of the product of the neutron flux $\varphi(E_n)$ and the cross-section $\sigma(E_n)$. The experimental neutron flux was calculated using (n,xn) reactions, which are shown in Table 2. The experimental values of the neutron flux were compared with the simulation. More information on simulation of the whole experiment and cross-sections is provided in the next section.

$$R = \int_{E_{th}}^{\infty} \sigma(E_n) \varphi(E_n) dE_n \quad (2)$$

Table 2. Residual nuclei with their threshold energies, half-lives, γ -lines and intensities.

Reaction	TALYS 1.8 E_{th} (MeV)	INCL 4.2 E_{th} (MeV)	Half-life	γ -ray energies (keV)	γ -ray intensities (%)
$^{59}\text{Co}(n,p)^{59}\text{Fe}$	3.6	5.9	44.5 days	1099.3; 1291.6	56.5; 43.2
$^{27}\text{Al}(n,\alpha)^{24}\text{Na}$	6.6	8.6	15 hours	1368.6; 2754	100; 99.9
$^{197}\text{Au}(n,2n)^{196}\text{Au}$	8.4	8.5	6.18 days	355.7; 332.9	87; 22.9
$^{59}\text{Co}(n,2n)^{58}\text{Co}$	10.8	12.3	70.9 days	810.8	99
$^{59}\text{Co}(n,3n)^{57}\text{Co}$	21	25.1	271.8 days	122.06; 136.5	85.6; 10.7
$^{27}\text{Al}(n,2n\alpha)^{22}\text{Na}$	34.8	32.9	2.6 years	1274.5	99.9
$^{209}\text{Bi}(n,6n)^{204}\text{Bi}$	40.9	38.5	11.22 hours	899.15; 374.7	98.8; 82
$^{209}\text{Bi}(n,7n)^{203}\text{Bi}$	49.1	48	11.8 hours	820.3; 825.2	30; 14.6
$^{209}\text{Bi}(n,9n)^{201}\text{Bi}$	64.6	68.7	108 minutes	629.1; 936.2	24; 11.3
$^{27}\text{Al}(n,x)^7\text{Be}$	186	427.3	53.12 days	477.6	10.5

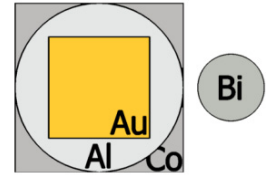


Fig. 2. Placement of samples in the sandwiches.

Two main steps of the determination of the mean neutron flux are shown in equations (3)-(6). A reaction with the maximum threshold energy, i.e., $^{27}\text{Al}(n,x)^7\text{Be}$, serves as the initial input parameter. Equation (3) shows the first step of the calculation, in which the threshold energy is that of the $^{27}\text{Al}(n,x)^7\text{Be}$ reaction (186 MeV) and the E_{max} is the maximum energy of neutron spectrum, i.e., 660 MeV. In this interval, the reaction rate is calculated by multiplying the mean value of neutron flux by the integral of reaction cross-section. Finally, as follows from equation (4), knowing the experimental reaction rate and reaction cross-section allows determining the mean value of the neutron flux in the given interval of neutron energies.

$$R_n = \varphi_n \int_{E_{th} (^{27}\text{Al}(n,x)^7\text{Be})}^{E_{max}} \sigma_n(E) \cdot dE \quad (3)$$

$$\varphi_n = \frac{R_n}{\int_{E_{th} (^{27}\text{Al}(n,x)^7\text{Be})}^{E_{max}} \sigma_n(E) \cdot dE} \quad (4)$$

The φ_{n-1} neutron energy range is calculated from the $^{209}\text{Bi}(n,9n)^{201}\text{Bi}$ reaction rate. The range of neutron flux is taken from the threshold energy of $^{209}\text{Bi}(n,9n)^{201}\text{Bi}$ (64.6 MeV) to the threshold energy for reaction $^{27}\text{Al}(n,x)^7\text{Be}$ (186 MeV). The determination of the threshold energies is explained below. Further calculation of neutron flux is described in equations (5) and (6). Calculations were repeated for all the measured reaction rates until the lowest threshold reaction - $^{59}\text{Co}(n,p)^{59}\text{Fe}$ in most cases - was reached. More details are provided elsewhere (Adam et al. 2015).

$$R_{n-1} = \varphi_{n-1} \int_{E_{th} (^{209}\text{Bi}(n,9n)^{201}\text{Bi})}^{E_{th} (^{27}\text{Al}(n,x)^7\text{Be})} \sigma_{n-1}(E) \cdot dE + \varphi_n \int_{E_{th} (^{27}\text{Al}(n,x)^7\text{Be})}^{E_{max}} \sigma_n(E) \cdot dE \quad (5)$$

$$\varphi_{n-1} = \frac{R_{n-1} - \varphi_n \int_{E_{th} (^{27}\text{Al}(n,x)^7\text{Be})}^{E_{max}} \sigma_n(E) \cdot dE}{\int_{E_{th} (^{209}\text{Bi}(n,9n)^{201}\text{Bi})}^{E_{th} (^{27}\text{Al}(n,x)^7\text{Be})} \sigma_{n-1}(E) \cdot dE} \quad (6)$$

4. Simulation of the experiments

4.1. Cross-section calculation

With regard to equations (3-6), the accuracy of the neutron flux determination depends strongly on the quality of i) measured reaction rates and ii) predictions of excitation functions for neutron induced reactions. At neutron energies above 20 MeV it is almost inevitable to use physics models for calculation of reaction cross-sections since no experimental data covers the whole region of interest, i.e., up to 660 MeV. For many years, TALYS and MCNP event generators have been powerful tools for cross-section prediction with many improvements implemented in the updated versions released consecutively.

In this work, the latest version of the TALYS-1.8 code (Koning et al. 2015), was used for predicting the cross-sections employing the Constant temperature and Fermi gas phenomenological level density model. A combination of the intranuclear cascade model INCL 4.2 (Boudard et al. 2002) and the GSI-KHS_V3p version of the fission-evaporation model ABLA (Junghans et al. 1998), was selected to calculate the reaction cross-sections using the GENXS option (Prael 2004) and (Mashnik et al. 2013) of MCNP6 (Pelowitz 2013).

The cross-section calculations were performed in steps of increasing neutron energy. In the case of TALYS, 1 MeV bins were used from 1 to 100 MeV, and 10 MeV bins were used from 100 to 660 MeV. In the case of MCNP6, 1 MeV bins were used from 1 to 20 MeV, 2.5 MeV bins were used from 20 to 100 MeV, and 20 MeV bins were used from 100 to 660 MeV. This provided a sufficient amount of information for a smooth interpolation of cross-section data. The relative uncertainty of the MCNP6 prediction was kept below 3% for all reactions above the effective threshold energy.

The performance of both models was compared to the experimental data from EXFOR in Figure 3 and Figure 4, which show the excitation functions of the $^{197}\text{Au}(n,2n)^{196}\text{Au}$ and $^{59}\text{Co}(n,3n)^{57}\text{Co}$ reactions, respectively. In general, a mutual discrepancy of nuclear models becomes more obvious as the number of neutrons in the output reaction channel increases. Considering the majority of studied reactions, a relatively close agreement between EXFOR data and TALYS predictions was observed. Conversely, an obvious disagreement between available experimental data and the results of INCL4-ABLA simulations is characteristic for some reactions, which reflects the fact that the intranuclear models are not suitable for calculation of cross-sections below ~ 150 MeV, as already mentioned (Engle et al. 2014).

The excitation functions for (n,x) reactions were also used for calculating the effective threshold energy, which is defined as the energy at which the cross-section has approximately its average value (Turner 2007). The effective threshold energies are presented in Table 2. Note that the majority of threshold energies calculated by TALYS has in

general lower values. The list of threshold energies determines not only the boundaries of intervals in which the experimental neutron flux is calculated, but also tally energy bin structure of the neutron flux simulation, as described in the next subsection.

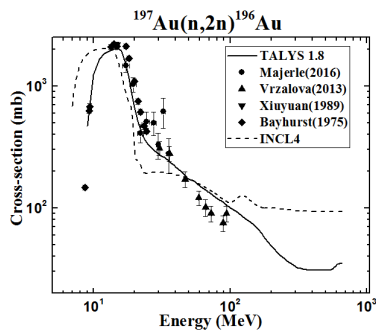


Fig. 3. Experimental and calculated cross-section of ^{196}Au .

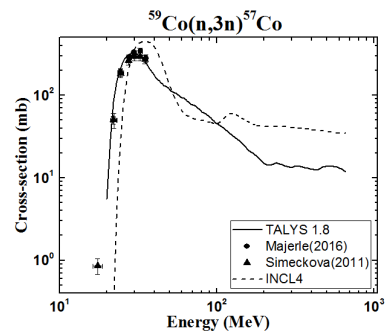


Fig. 4. Experimental and calculated cross-section of ^{57}Co .

4.2. Neutron flux simulations

It is important to note that the neutron flux resulting from Monte Carlo simulations does not serve as a guess flux for spectral adjustment routines. In this work, the neutron energy distribution was calculated in order to draw comparison between experimental results and code predictions. The use of spectral adjustment methods for the determination of the spallation neutron flux up to 100 MeV can be found elsewhere (Mosby et al. 2016).

The MCNPX 2.7 radiation transport code (Pelowitz 2011) was used for simulation of the neutron flux in exact positions of the activation foils. F4 tally was chosen for scoring the flux averaged over a cell. The same set of event generators as for cross-section predictions, i.e. INCL4-ABLA, was selected for the simulation of the neutron spectrum. Thus, the experimental neutron flux can be used for direct validation of the above mentioned physics models.

A comparison between the experimentally determined neutron flux and MCNPX predictions is discussed in the following section.

5. Experimental results and comparison

The results of the experimental neutron flux calculated from reaction rates in aluminum, bismuth, cobalt and gold, as well as Monte-Carlo simulations are shown in ten figures below (Figure 5 - Figure 14). Each figure describes comparison between experimental and simulated neutron flux for specific position in the spallation target *QUINTA*. The experimental values of the neutron flux are shown as blue points (centers of the individual energy intervals), and the simulations are shown as red line. The steps of the red line represent threshold energy values of different reactions used to calculate mean neutron flux. The experimental results were obtained using cross-section predicted by TALYS 1.8 and physics model INCL 4.2. In the figures, the TALYS-based data were chosen for better agreement between experiment and calculation for these experimental data (see information below).

Both the experimental uncertainty of reaction rates and the uncertainty in cross-section prediction contribute to the total uncertainty of the experimental neutron flux. The experimental uncertainty is composed of the uncertainty of beam integral, statistical uncertainty in determination of the full-energy peak area (usually below 5%) and the systematic uncertainties of sample weight (0.01%) and detector efficiency (3%).

The highest experimental value of the neutron flux was found to be on the front of the section number three ($Z=254$ mm) at position $Y=-80$ mm from the beam center - see Figure 7. The neutron flux at this position was calculated in the interval of threshold energies from 3.6 MeV up to 6.7 MeV, for reaction $^{59}\text{Co}(n,p)^{59}\text{Fe}$, reaching the

value $1.84(48) \times 10^{-4}$ ($1/(\text{cm}^2 \cdot \text{MeV} \cdot \text{proton})$). The second lowest flux was detected at the back of the section five ($Z=647$ mm) at position -120 mm from the beam center. The neutron flux was calculated for the same interval of the threshold energies as in previous case and the value of the neutron flux was $1.57(41) \times 10^{-5}$ ($1/(\text{cm}^2 \cdot \text{MeV} \cdot \text{proton})$). More information about how the neutron flux changes inside the target is provided in Table 3 and Table 4 which contain ratios of the flux in the individual threshold sandwiches compared to the maximal neutron flux measured behind section number two at radial position $Y=-80$ mm and $Y=-120$ mm, respectively. Evidently, the experimental neutron flux decreases with increasing both longitudinal and radial distance. This is mainly due to neutron scattering, leakage and absorption of neutrons in nuclear reactions.

Table 5 shows the experimental neutron flux at position $Z=123$ mm and $Y=-80$ mm (in front of the second target section). There is some disagreement between the experimental neutron flux based on INCL4-ABLA cross-sections and flux modeled using the INCL 4.2 event generator (the experiment is rather underestimated). On the other hand, as already mentioned in Section 4.1, the experimental cross-section did not agree well with the cross-section prediction for some reactions. For this reason, the TALYS-based data were selected to make a comparison between the experiment and simulation in the following illustrations.

A decent agreement between the experimental flux (TALYS cross-section) and the results of simulation was reached within a few standard deviations across the whole target, which proves the practicality and usefulness of the presented method of neutron spectrum determination. Obviously, any future improvements in cross-section predictions would significantly increase the accuracy of our method.

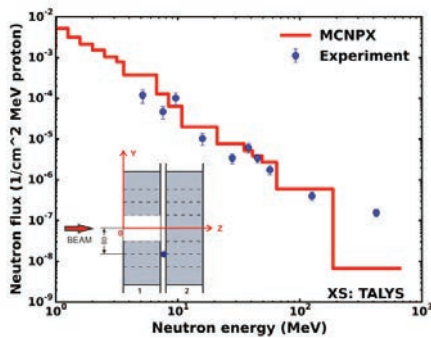


Fig. 5. Experimental calculation and simulation of the neutron flux in spallation target *QUINTA*, $Z=123$ mm and $Y=-80$ mm.

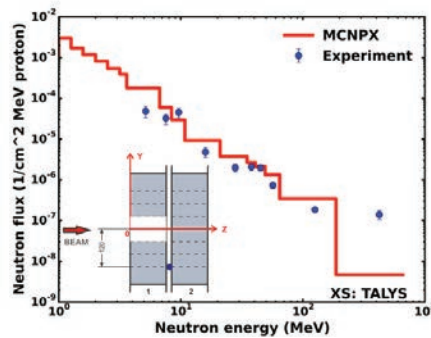


Fig. 6. Experimental calculation and simulation of the neutron flux in spallation target *QUINTA*, $Z=123$ mm and $Y=-120$ mm.

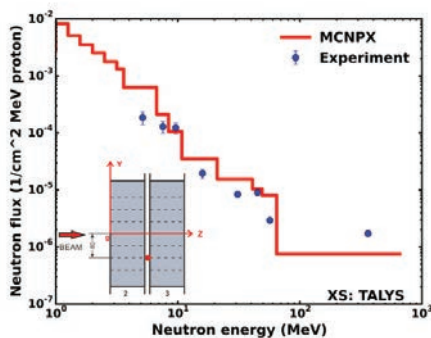


Fig. 7. Experimental calculation and simulation of the neutron flux in spallation target *QUINTA*, $Z=254$ mm and $Y=-80$ mm.

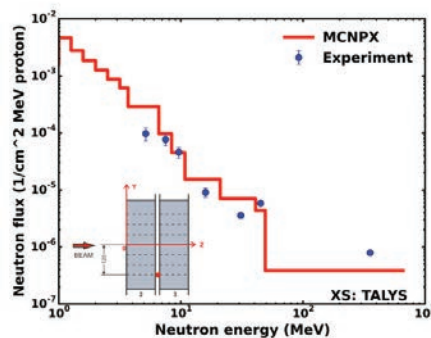


Fig. 8. Experimental calculation and simulation of the neutron flux in spallation target *QUINTA*, $Z=254$ mm and $Y=-120$ mm.

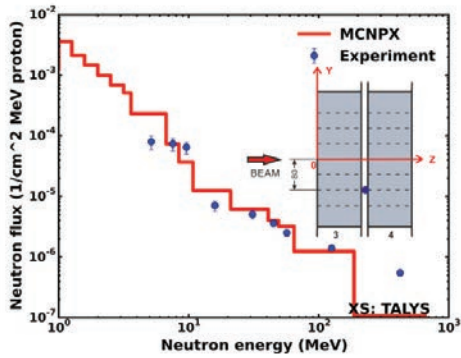


Fig. 9. Experimental calculation and simulation of the neutron flux in spallation target *QUINTA*, $Z=385$ mm and $Y=-80$ mm.

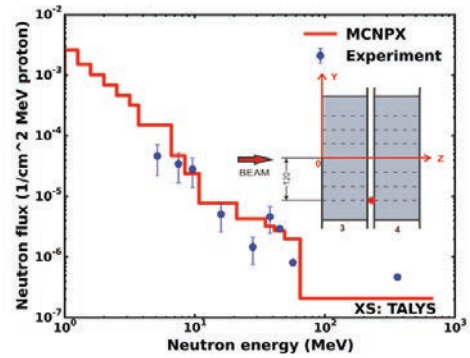


Fig. 10. Experimental calculation and simulation of the neutron flux in spallation target *QUINTA*, $Z=385$ mm and $Y=-120$ mm.

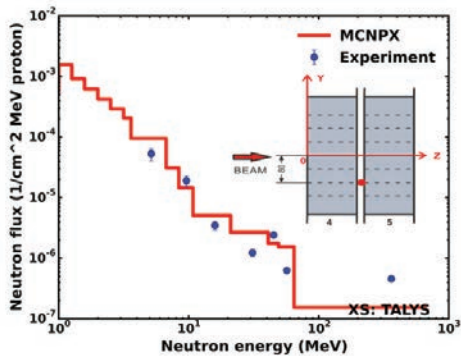


Fig. 11. Experimental calculation and simulation of the neutron flux in spallation target *QUINTA*, $Z=516$ mm and $Y=-80$ mm.

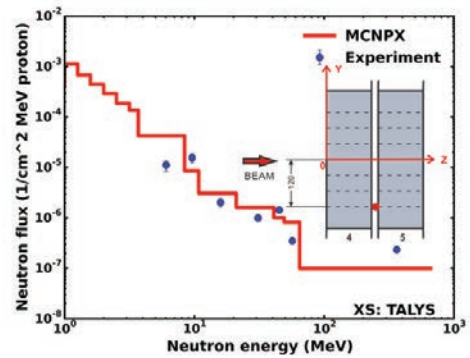


Fig. 12. Experimental calculation and simulation of the neutron flux in spallation target *QUINTA*, $Z=516$ mm and $Y=-120$ mm.

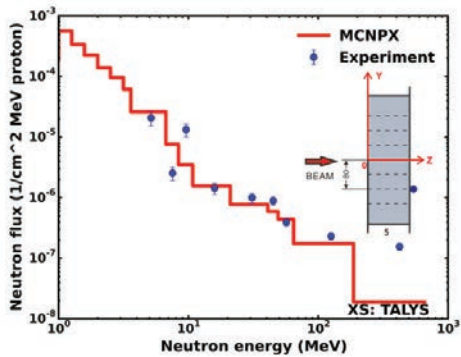


Fig. 13. Experimental calculation and simulation of the neutron flux in spallation target *QUINTA*, $Z=647$ mm and $Y=-80$ mm.

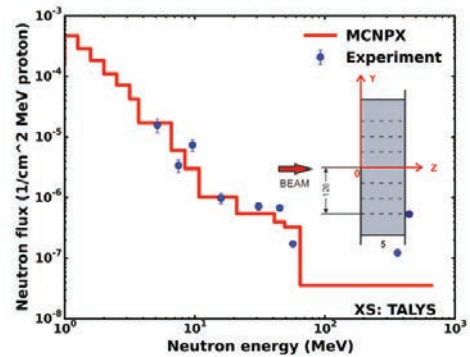


Fig. 14. Experimental calculation and simulation of the neutron flux in spallation target *QUINTA*, $Z=647$ mm and $Y=-120$ mm.

Table 3. Ratios of the neutron flux at position Y=-80 mm compared to the highest neutron flux at the 2nd section (Z=254 mm).

Energy interval		Ratio of the neutron flux (-)			
En _{Min} (MeV)	En _{Max} (MeV)	Z(mm) 123	Z(mm) 385	Z(mm) 516	Z(mm) 647
3.6	6.7	0.6(3)	0.4(2)	0.28(10)	0.11(4)
6.7	8.4	0.4(2)	0.6(2)	-	0.02(1)
8.4	10.8	0.8(3)	0.5(2)	0.16(5)	0.11(3)
10.8	21	0.5(2)	0.4(1)	0.18(5)	0.07(2)
21	40.9	-	0.6(1)	0.15(3)	0.12(3)
40.9	49.1	0.4(1)	0.4(1)	0.27(2)	0.10(1)
49.1	64.6	0.6(1)	0.9(1)	0.21(1)	0.13(2)
64.6	660	-	-	0.27(1)	

Table 4. Ratios of the neutron flux at position Y=-120 mm compared to the highest neutron flux at the 2nd section (Z=254 mm).

Energy interval		Ratio of the neutron flux (-)			
En _{Min} (MeV)	En _{Max} (MeV)	Z(mm) 123	Z(mm) 385	Z(mm) 516	Z(mm) 647
3.6	6.7	0.5(2)	0.5(3)	-	0.16(6)
6.7	8.4	0.4(2)	0.5(3)	-	0.04(1)
8.4	10.8	1.00(34)	0.6(3)	0.3(1)	0.16(5)
10.8	21	0.5(2)	0.6(3)	0.22(6)	0.11(3)
21	40.9	-	-	0.28(5)	0.20(3)
40.9	49.1	0.3(1)	0.5(1)	0.25(2)	0.12(1)

Table 5. Experimental neutron flux – cross-section calculated by TALYS 1.8 and physics model INCL 4.2.

TALYS 1.8				INCL 4.2			
En _{Min} (MeV)	En _{Max} (MeV)	Neutron flux (1/(cm ² ·MeV·proton)).	Cal/Exp (-)	En _{Min} (MeV)	En _{Max} (MeV)	Neutron flux (1/(cm ² ·MeV·proton)).	Cal/Exp (-)
3.6	6.7	1.19(44)E-04	3.16(116)	8.5	12.3	4.26(120)E-05	1.25(35)
6.7	8.4	4.7(16)E-05	2.7(10)	12.3	21.1	1.21(32)E-05	1.4(37)
8.4	10.8	1.02(36)E-04	0.6(2)	21.1	29.6	5.25(114)E-06	1.6(4)
10.8	21	1.03(33)E-05	1.9(6)	29.6	38.5	3.8(8)E-06	1.6(4)
21	34.9	3.4(10)E-06	2.23(64)	38.5	50.8	2.16(47)E-06	1.9(4)
34.9	40.9	6.19(159)E-06	0.9(2)	50.8	68.7	1.07(23)E-06	2.4(5)
40.9	49.1	3.4(8)E-06	1.14(28)	68.7	660	1.8(3)E-07	0.6(1)
49.1	64.6	1.8(4)E-06	1.5(4)				
64.6	187	4.01(96)E-07	1.5(4)				
187	660	1.6(3)E-07	0.043(9)				

6. Conclusion

A set of experiments were performed in order to determine the neutron flux in the spallation target called *QUINTA*, which was irradiated by the 660 MeV proton beam at the Joint Institute for Nuclear Research. The secondary neutron field was monitored by a set of threshold activation detectors in various positions in the target *QUINTA*. The experimental values of the neutron flux were found from the specific reactions in monoisotopic materials (aluminum, bismuth, cobalt and gold) and were compared to the neutron flux simulations carried out in MCNPX 2.7 using the intranuclear cascade model INCL 4.2. The cross-sections used for calculation of the experimental neutron flux were calculated with TALYS 1.8 and with MCNP6 using INCL 4.2. The cross-sections calculated with TALYS 1.8 showed better agreement between experimental values and simulations than the physics model INCL 4.2.

The neutron flux was calculated between threshold energies of specific (n,xn) reactions. The highest neutron flux was detected at the back of second target section (Z=254 mm), at the position 80 mm from the beam center (Y=-80 mm). The intensity of the secondary neutron field decreased as both the vertical and horizontal distances from the beam axis increased.

The discrepancies between the experimental and simulated flux were found to be within a few standard deviations and could be caused by inaccurate predictions of reaction cross-sections. The results indicate that further improvements in nuclear models should be implemented, especially at higher energies. The results also demonstrate that those models are in urgent need of new experimental data for their validation, which is particularly important for research focused on ADS and other applications of spallation neutrons.

Acknowledgement

This work was performed on the behalf of Energy and Transmutation collaboration at the JINR. Our group also wants to express thanks to Phasotron accelerator staff for their technical support. This work was financially supported by Ministry of Youth and Education and Ministry of Finances of the Czech Republic. The project was also supported from the LO1210, FEKT-S-14-2520 projects at the BUT. The author is the Brno Ph.D. Talent Scholarship Holder - Funded by the Brno City Municipality.

References

- Abderrahim, H.A., Beaten, P., de Bruyn, D., Heyse, J., Schuurmans P., Wagemans, J., 2010. MYRRHA, a Multipurpose hYbrid Research Reactor for High-end Applications. *Nuclear Physics News*. 20(1), 24-28.
- Adam, J., Baldin, A.A., Chilap, V., et al. 2015. Measurement of the High Energy Neutron Flux on the Surface of the Natural Uranium Target Assembly QUINTA Irradiated by Deuterons of 4 and 8 GeV Energy. *Physics Procedia*. 80, 94-97.
- Aleksandrov, Yu. V. et al.. 1996. (p,x) Reactions Cross Sections on Aluminum at Intermediate Energy of Protons.
- Boudard, A., Cugnon, J., Leray, S., Volant, C., 2002. Intranuclear cascade model for a comprehensive description of spallation reaction data. *Physical Review C*. 66-044615, p. 1-28.
- Bowman, C.D., Arthur, E.D., Lisowski, P.W., et al. 1992. Nuclear energy generation and waste transmutation using an accelerator-driven intense thermal neutron source. *Nuclear Instruments and Methods in Physics Research Section A: Accelerators, Spectrometers, Detectors and Associated Equipment* 320(1-2), 336-367
- Engle, J.W., James, M.R., Mashnik S.G., et al. 2014. MCNPX characterization of the secondary neutron flux at the Los Alamos Isotope Production Facility. *Nuclear Instruments and Methods in Physics Research Section A: Accelerators, Spectrometers, Detectors and Associated Equipment*. 754, 71-82.
- Franca, J., 2003. Program DEIMOS32 for gamma-ray spectra evaluation: A computer program for the analysis of gamma-ray spectra. *Journal of Radio-analytical and Nuclear Chemistry*, vol. 257, issue 3, p. 583-587.
- Friedlander, G., Hudis, J., Wolfgang, R.L., 1955. Disintegration of Aluminum by Protons in the Energy Range 0.4 to 3.0 GeV. *Physical Review* Vol.99, p.263
- Grand, P., Takahashi H. 1985. Breeding nuclear fuels with accelerators — replacement for breeder reactors. *Nuclear Instruments and Methods in Physics Research Section B: Beam Interactions with Materials and Atoms* 10, 454-459.
- Huang, S., Jia, H., Niu, H., et al. 2015. Design and RF test of MEBT buncher cavities for C-ADS Injector II at IMP. *Nuclear Instruments and Methods in Physics Research Section A: Accelerators, Spectrometers, Detectors and Associated Equipment*. 799, 44-49.
- Junghans, A.R., de Jong, M., Clerc, H.-G., Ignatyuk, A.V., Kudyayev, G.A., Schidt, K.-H., 1998. Projectile-fragment yields as a probe for the collective enhancement in the nuclear level density. *Nuclear Physics A*. 629(3-4), 635-655.
- Khushvaktov, J., Adam J., Baldin, A.A., et al. 2016. Interactions of secondary particles with thorium samples in the setup QUINTA irradiated with 6GeV deuterons. *Nuclear Instruments and Methods in Physics Research Section B: Beam Interactions with Materials and Atoms*. 381, 84-89.
- Koning, A., Hilaire, S., and Goriely, S., 2015. TALYS-1.8, A nuclear reaction program, User manual.
- Mashnik, S.G., 2013. MCNP6 Study of Spallation Products from 500 MeV p + ¹³⁶Xe, LA-UR-13-23189, Los Alamos National Laboratory.
- Miche, I R., Dragovitsch, P., Englert, P., et al. 1986. On the depth dependence of spallation reactions in a spherical thick diorite target homogeneously irradiated by 600 MeV protons: Simulation of production of cosmogenic nuclides in small meteorites. *Nuclear Instruments and Methods in Physics Research Section B: Beam Interactions with Materials and Atoms*. 16, 61-82.
- Morgan, G. L., Alrick, K. R., Saunders, A., et al. 2003. Total cross sections for the production of ²²Na and ²⁴Na in proton-induced reactions on ²⁷Al from 0.40 to 22.4 GeV. *Nuclear Instruments and Methods in Physics Research Section B Beam Interactions with Materials and Atoms*. 211, 297-304.
- Mosby, M.A., Engle, J.W., Jackman, K.R., Nortier, F.M., Birnbaum, E.R., 2016. Determination of spallation neutron flux through spectral adjustment techniques. *Nuclear Instruments and Methods in Physics Research Section B: Beam Interactions with Materials and Atoms*. 381, 29-33.
- Pelowitz, D.B. (Ed). 2013. MCNP6TM User's Manual Version 1.0, LA-CP-13-00634.
- Pelowitz, D.B. (Ed). 2011. MCNPX User's Manual Version 2.7.0, LA-CP-11-00438.
- Prael, R.E., 2004. Tally Edits for the MCNP6 GENXS Option, LA-UR-11-02144, Los Alamos National Laboratory.
- Sasa, T., 2015. Design of J-PARC Transmutation Experimental Facility. *Progress in Nuclear Energy*. 82, 64-68.
- Sudár, S., 2002. "TRUECOINC", a software utility for calculation of the true coincidence correction, IAEA-TECDOC-1275, p. 37-48.
- Taddeucci, T. N., Ullmann, J., Rybarczyk L. J., et al. 1997. Total cross sections for production of ⁷Be, ²²Na, and ²⁴Na in p+⁷Li and p+²⁷Al reactions at 495 and 795 MeV. *Physical Review C*, 55, 1551-1554.
- Turner, J.E., c2007. Atoms, radiation, and radiation protection. 3rd completely rev. and enl. ed. Weinheim, Federal Republic of Germany.
- Zavorka, L., Adam, J., Baldin, A.A., et al. 2015. Neutron-induced transmutation reactions in ²³⁷Np, ²³⁸Pu, and ²³⁹Pu at the massive natural uranium spallation target. *Nuclear Instruments and Methods in Physics Research Section B: Beam Interactions with Materials and Atoms*. 349, 31-38.

Measurements of the cross sections of the $^{186}\text{W}(n,\gamma)^{187}\text{W}$, $^{182}\text{W}(n,p)^{182}\text{Ta}$, $^{154}\text{Gd}(n,2n)^{153}\text{Gd}$, and $^{160}\text{Gd}(n,2n)^{159}\text{Gd}$ reactions at neutron energies of 5 to 17 MeV

Rajnikant Makwana,¹ S. Mukherjee,^{1,*} P. Mishra,¹ H. Naik,² N. L. Singh,¹ M. Mehta,³ K. Katovsky,⁴ S. V. Suryanarayana,⁵ V. Vansola,¹ Y. Santhi Sheela,⁶ M. Karkera,⁶ R. Acharya,² and S. Khirwadkar³

¹Physics Department, Faculty of Science, The Maharaja Sayajirao University of Baroda, Vadodara 390002, India

²Radiochemistry Division, Bhabha Atomic Research Centre, Mumbai 400 085, India

³Divertor Division, Institute for Plasma Research, Gandhinagar 382 428, India

⁴Department of Electrical Power Engineering, Brno University of Technology, Brno, Czech Republic

⁵Nuclear Physics Division, Bhabha Atomic Research Centre, Mumbai 400 085, India

⁶Department of Statistics, Manipal University, Manipal 576 104, India

(Received 8 March 2017; revised manuscript received 8 May 2017; published 9 August 2017)

The cross sections of the $^{186}\text{W}(n,\gamma)^{187}\text{W}$, $^{183}\text{W}(n,p)^{183}\text{Ta}$ and $^{154}\text{Gd}(n,2n)^{153}\text{Gd}$, $^{160}\text{Gd}(n,2n)^{159}\text{Gd}$ reactions were measured at the neutron energies 5.08 ± 0.165 , 8.96 ± 0.77 , 12.47 ± 0.825 , and 16.63 ± 0.95 MeV. Standard neutron activation analysis technique and off-line γ ray spectrometry were used for the measurement and analysis of the data. Measurements were done in the energy range where few or no measured data are available. The results from the present work are compared with the literature data based on the EXFOR compilation. The experimental results are supported by theoretical predictions using nuclear modular codes TALYS 1.8 and EMPIRE 3.2.2. The predictability of different one-dimensional models available in TALYS 1.8 and Levdn models in EMPIRE 3.2.2 were tested. A detailed comparison of experimental results with theoretical model calculations is made.

DOI: [10.1103/PhysRevC.96.024608](https://doi.org/10.1103/PhysRevC.96.024608)

I. INTRODUCTION

Nuclear reaction cross section data are of prime importance for reactor technology. When the reactor is in operation, it produces neutrons that penetrate through several materials, such as fuel, structural, controlling, and shielding materials, etc. It is important to have nuclear reaction cross section data for all these materials, at all possible neutron energies [1], for the development of the reactor technology. There are numerous measured nuclear data available in the EXchange FORmat (EXFOR) library [2]. However, it is important to have more experimental nuclear data, measured with high accuracy in the energy range between thermal and 20 MeV for a number of reactor materials [2]. Tungsten (W) and gadolinium (Gd) are two such materials. W is selected as a divertor material for the upcoming fusion device—International Thermonuclear Experimental Reactor (ITER) [3]. In ITER the DT reaction generates 14.6 MeV neutrons, which are scattered from the surrounding materials, thus neutrons will have energies from thermal to 14.6 MeV [4–9]. These neutrons interact with the divertor material of the reactor and can open different nuclear reaction channels. In accelerator driven subcritical system (ADSs), W is used in different parts, hence it can face neutrons with higher energies [10]. Further, Gd is an important rare earth element, which is used in control rods. Its nitrate form is useful for reactor control through moderator as liquid poison, as well as a secondary shutdown device in PHWR reactors [11]. Gadolinium nitrate is more advantageous due to its properties, such as high thermal neutron capture cross section, quick burnout, greater solubility, and a more efficient removal by ion exchange systems compared with

boron [12]. Hence it is important to have accurate cross section data for all the tungsten and gadolinium isotopes in the energy range from thermal to 20 MeV. Accurate experimental data are also needed to validate the various theoretical nuclear models [13]. In view of this, in the present work, cross sections for the $^{186}\text{W}(n,\gamma)^{187}\text{W}$, $^{183}\text{W}(n,p)^{183}\text{Ta}$, $^{154}\text{Gd}(n,2n)^{153}\text{Gd}$, and $^{160}\text{Gd}(n,2n)^{159}\text{Gd}$ reactions at the neutron energies of 5.08 ± 0.165 , 8.96 ± 0.77 , 12.47 ± 0.825 , and 16.63 ± 0.95 MeV were measured by neutron activation analysis (NAA) and the off-line γ ray spectrometry technique. The above mentioned reaction cross sections were also calculated by using the computer codes TALYS 1.8 and EMPIRE 3.2.2. Different LD models available in TALYS 1.8 and Levdn models in EMPIRE 3.2.2 were used to validate the present experimental results.

In this paper, the experimental details are discussed in Sec. II. Section III describes the data analysis. The neutron flux and average neutron energy calculations used to obtain reaction cross sections, with suitable corrections incorporated to obtain accurate cross section results, are also discussed in this section. Section IV presents the theoretical calculations, followed by results and discussions in Sec. V. A summary and conclusions are given in Sec. VI.

II. EXPERIMENTAL DETAILS

The experiment was carried out by using the BARC-TIFR Pelletron facility in Mumbai, India. The neutrons were produced using the $^7\text{Li}(p,n)^7\text{Be}$ reaction. A proton beam was targeted on natural lithium foil of thickness 8.0 mg/cm^2 . The Li foil was wrapped with 3.7 mg/cm^2 tantalum in front and 4.12 mg/cm^2 on the back. The energies of the proton beam were selected to be 7.0, 11.0, 15.0, and 18.8 MeV. The samples were kept at a distance of 2.1 cm from the Li target in the

*Corresponding author: sk.mukherjee-phy@msubaroda.ac.in

TABLE I. Details of the irradiation in the present experiment.

	Irradiation 1	Irradiation 2	Irradiation 3	Irradiation 4
Proton energy (MeV)	18.8	7.0	15.0	11.0
Total irradiation time (h:min)	5:00	11:15	7:00	16:05
Beam current (nA)	150	110	150	120

forward direction. The targets were irradiated for different irradiation times. The irradiation details are given in Table I. A schematic view of the irradiation setup is shown in Fig. 1. In the present measurements, the natural samples of W (99.97%) in the form of 1.0 mm thick and about a quarter of a circle with radius of 1 to 3 cm were used. Gd samples were made in the form of a pellet with radius of 0.65 cm and of thickness from 0.5 to 1.0 mm using Gd₂O₃ (99.9%) powder. The weight of the samples was measured using a digital microbalance weighing machine. The mass of W samples in different sets of irradiations were 3.6689 g (irradiation 1), 0.7826 g (irradiation 2), 0.8344 g (irradiation 3), and 0.504 g (irradiation 4). The samples of Gd were with mass of 0.4071 g (irradiation 1) and 0.9102 g (irradiation 3). In each irradiation, indium (In) and thorium (Th) foils were used as flux monitors. After a suitable cooling time, the irradiated samples were mounted on different Perspex plates and kept in front of the precalibrated high purity germanium (HPGe) detector. A Baltic company HPGe detector with 4-K channels MCA and MAESTRO spectroscopic software was used to measure the γ ray spectra from the irradiated sample. The HPGe detector system was calibrated using a standard ¹⁵²Eu multi- γ -ray source. The efficiency of the detector was also determined at different γ energies using the same source. The γ ray activities of the irradiated samples were measured for different counting times. The prominent γ ray energies emitted from the irradiated samples and other spectroscopic data are given in Table II. Isotopic abundances are taken from the literature [14]. The threshold energies of the reactions are calculated using the Q value calculator provided online by National Nuclear Data Centre (NNDC) [15]. The daughter nuclide half-life and details of the emitted prominent γ rays are taken from the literature [16]. Typical γ ray spectra obtained from the irradiated W and Gd samples are shown in Figs. 2(a)–2(b).

III. DATA ANALYSIS

A. Neutron activation analysis

The experimental data were analyzed by using the standard neutron activation analysis (NAA) technique. In this technique,

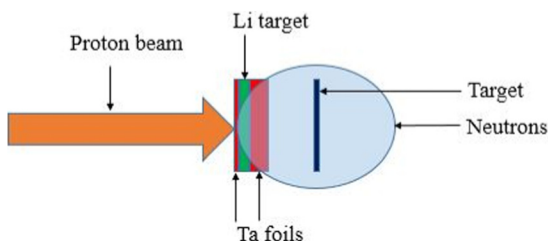


FIG. 1. Experimental arrangement showing neutron production using Li(p,n) reaction.

the nuclear reaction rate or the rate of production of daughter isotopes depends on the number of target nuclei available and the neutron flux incident on it. This activation method is generally followed to measure reaction cross section by irradiating the target isotope with neutrons, when the products emit characteristic γ rays having sufficiently long half-life and γ branching abundances. The cross section of the selected reactions can be determined using the following equation [17]:

$$\sigma = \frac{A_{\gamma} \lambda (t_c / t_r)}{N \phi I_{\gamma} \varepsilon (1 - e^{-\lambda t_i}) (1 - e^{-\lambda t_c}) e^{-\lambda t_w}}, \quad (1)$$

where

- A_{γ} = number of detected γ ray counts;
- λ = decay constant of product nucleus (s^{-1});
- t_i = irradiation time (s);
- t_w = cooling time (s);
- t_c = counting time (s);
- t_r = real time (clock time) (s);
- ϕ = incident neutron flux ($n \text{ cm}^{-2} \text{ s}^{-1}$);
- I_{γ} = branching intensity of γ ray;
- ε = efficiency of detector for the chosen γ ray;
- N = number of target atoms.

In the above equation, the activity (A_{γ}) is measured using an HPGe detector for different γ rays emitted from the daughter isotopes. Because of the half-lives of the isotopes of interest, several rounds of γ ray counting were done. The dead time of the detector system was kept below 0.6% during the entire counting process. The numbers of target nuclei were calculated from the weight of the sample and isotopic abundances. The calculation of the neutron flux was done using the γ ray spectra of irradiated In and Th foils. Other standard parameters of the reactions were taken from the literature [14–16].

B. Neutron flux and average neutron energy

The neutrons were generated by ⁷Li(p,n)⁷Be reactions. Below 2.4 MeV, this reaction produces monoenergetic neutrons [18]. Above 2.4 MeV, the first excited state of ⁷Be at 0.43 MeV is populated and produces a second group of neutrons [18,19]. Above 6 MeV, the three body interaction and other excited states also contribute in the neutron production along with the main neutron group [18,19]. Although there are lower energy subgroups of neutrons, the primary (main) group of neutrons can be used to measure the reaction cross section as it has higher neutron flux and higher neutron energy (forming a peak). The reaction cross section measured at this

TABLE II. Selected nuclear reactions, target isotopic abundance, threshold energy of reaction, product nucleus with half-life, and energies of prominent γ rays with branching intensities.

Reaction	Isotopic abundance (%) [14]	Threshold energy (MeV) [15]	Product nucleus	Half-life [16]	Prominent γ -ray energy (keV); (branching intensity %) [16]
$^{186}\text{W}(n,\gamma)^{187}\text{W}$	28.43		^{187}W	24.0 h	479.5(26.6); 685.7(33.2)
$^{182}\text{W}(n,p)^{182}\text{Ta}$	26.50	1.037	^{182}Ta	114.74 d	1121.3(35.24)
$^{154}\text{Gd}(n,2n)^{153}\text{Gd}$	2.18	8.953	^{153}Gd	240.4 d	103.1(21.1)
$^{160}\text{Gd}(n,2n)^{159}\text{Gd}$	21.86	7.498	^{159}Gd	18.479 h	363.5(11.78)

averaged peak energy. The spectrum averaged neutron energy can be given as [20]

$$E_{\text{mean}} = \frac{\int_{E_{\text{ps}}}^{E_{\text{max}}} E_i \phi_i dE}{\int_{E_{\text{ps}}}^{E_{\text{max}}} \phi_i dE}, \quad (2)$$

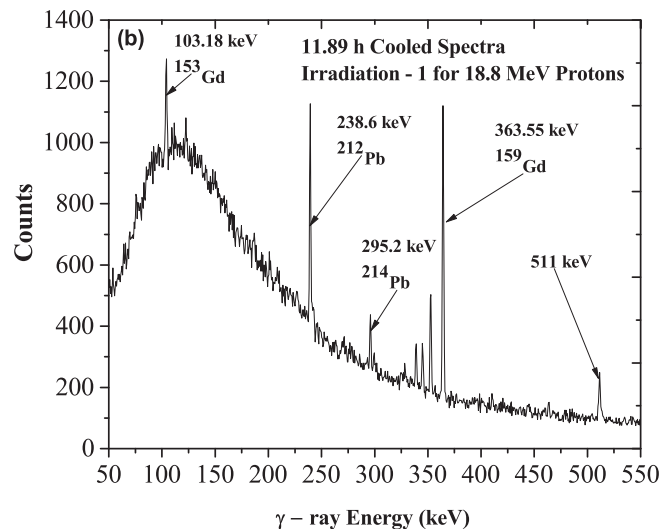
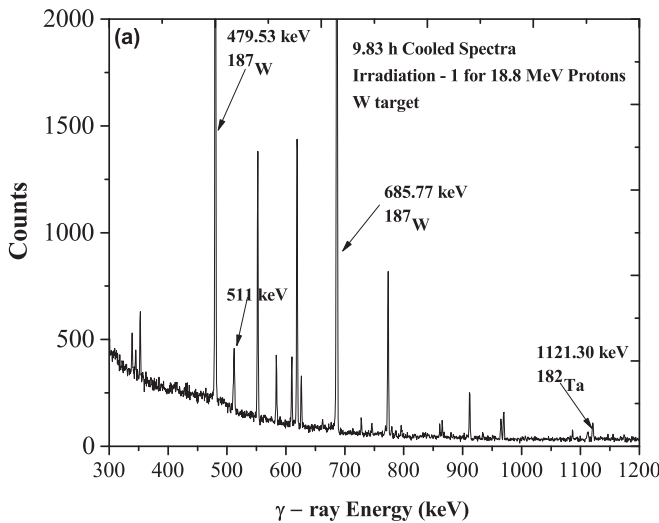


FIG. 2. (a) Typical γ ray spectra for W target obtained by using HPGe detector. (b) Typical γ ray spectra for Gd target obtained by using HPGe detector.

where

E_{ps} = peak forming start neutron energy;

E_{max} = maximum neutron energy;

E_i = energy bin;

ϕ_i = neutron flux of energy bin E_i ;

E_{mean} = effective mean energy.

The neutron spectra for 7.0, 11.0, 15.0, and 18.8 MeV were derived by taking data from various available publications [18–22]. The neutron spectra corresponding to all the four incident proton energies are shown in Figs. 3(a)–3(d). The average peak energies obtained by using Eq. (2) are given in Table III.

In order to analyze the data, it is necessary to accurately calculate the neutron flux incident on the target. In the present experiment, $^{115}\text{In}(n,n')^{115\text{m}}\text{In}$ and $^{232}\text{Th}(n,f)^{97}\text{Zr}$ monitor reactions were used for the neutron flux measurement. The reaction products $^{115\text{m}}\text{In}$ and ^{97}Zr have a half-life of 4.486 and 16.749 h respectively [16]. The emitted characteristic γ lines are given in Table IV. Typical γ ray spectra obtained from both the monitors are shown in Fig. 4.

The calculations of the neutron flux incident on the target were done by using the spectrum averaged neutron cross section for the monitor reactions by using the relatively recent data available from the EXFOR data library for $^{115}\text{In}(n,n')$ [23–26] and for $^{232}\text{Th}(n,f)$ [27–30]. The spectrum averaged cross section was calculated using the following equation:

$$\sigma_{\text{av}} = \frac{\int_{E_{\text{th}}}^{E_{\text{max}}} \sigma_i \phi_i dE}{\int_{E_{\text{th}}}^{E_{\text{max}}} \phi_i dE}, \quad (3)$$

where

E_{th} = threshold energy of the monitor reaction;

E_{max} = maximum neutron energy;

σ_i = cross section at energy E_i for monitor reaction from EXFOR [23–30];

ϕ_i = neutron flux of energy bin E_i from the Figs. 5(a)–5(d);

σ_{av} = spectrum averaged cross section.

The calculated spectrum averaged cross sections for both the monitor reactions are given in Table III. The neutron flux incident on targets for all the four irradiations were calculated

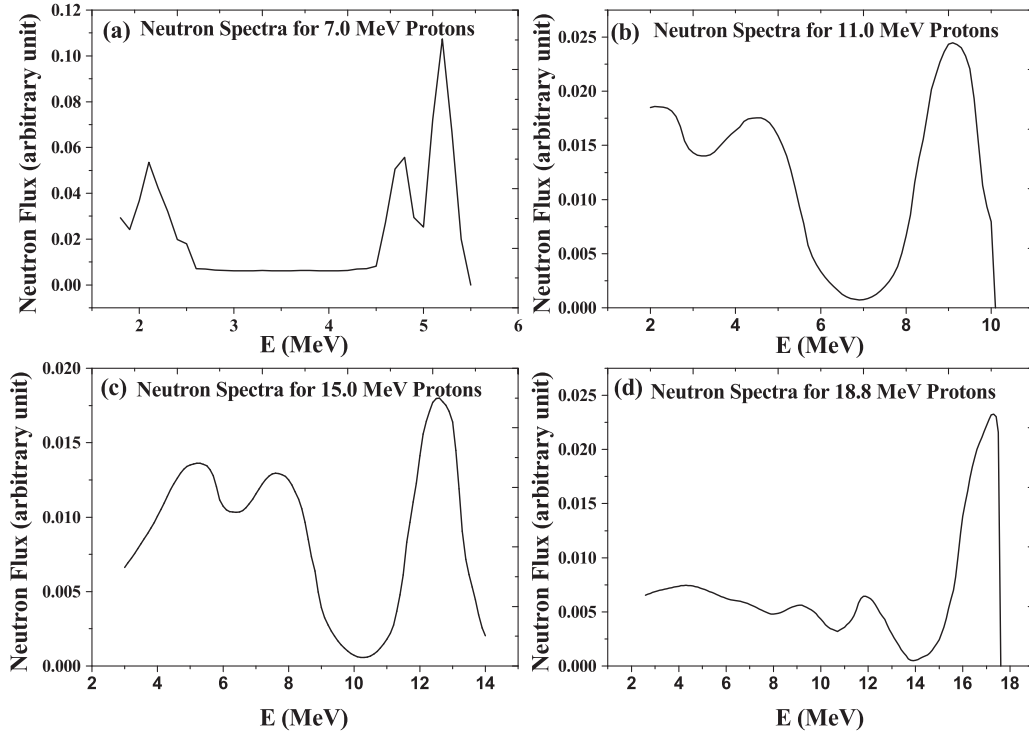


FIG. 3. (a)–(d) ${}^7\text{Li}(p,n){}^7\text{Be}$ neutron spectra for the 7.0 (a), 11.0 (b), 15.0 (c), and 18.8 (d) MeV proton energies.

using the following activation equation:

$$\phi = \frac{A_\gamma \lambda (t_c / t_r)}{N \sigma_{\text{av}} I_\gamma \varepsilon (1 - e^{-\lambda t_i})(1 - e^{-\lambda t_c}) e^{-\lambda t_w}}. \quad (4)$$

All the parameters are same as in Eq. (1).

In the case of a fission reaction monitor, the fission yield term (Y) will come in the denominator on the right side of the above Eq. (4). In the cross section calculations, the measured values of the average neutron flux from both the monitors were taken, as both these values are in agreement with each other within the limits of the experimental errors as discussed later in Sec. V.

C. Cross section correction for lower energy neutrons

In order to measure the cross section for neutrons of main peak, it is necessary to make corrections due to the contributions from lower energy neutrons. This correction is not required when the neutron source is purely monoenergetic, which is not the present case. As mentioned earlier, in addition to a primary neutron group, there exist secondary neutron groups arising due to an excited state of ${}^7\text{Be}$ and three-body reactions above 2.4 and 6 MeV respectively [18]. These secondary groups produce neutrons at lower energies and in addition to the primary group neutrons [18,19]. As the primary neutron exhibits a distinct broad peak always at much higher energy with a high neutron flux, it can be considered as a quasimonoenergetic source. It is possible to remove the contributions to the reaction cross sections due to

TABLE III. The spectrum averaged neutron energies and respective neutron flux from two different monitor reactions.

	Irradiation 1	Irradiation 2	Irradiation 3	Irradiation 4
Proton energy (MeV)	18.8	7.0	15.0	11.0
Neutron energy from Eq. (2) (MeV)	16.63 ± 0.95	5.08 ± 0.165	12.47 ± 0.825	8.96 ± 0.77
Spectrum averaged cross section for In monitor (mb)	188.94	223.88	253.79	302.85
Calculated neutron flux from ${}^{115}\text{In}(n,n'){}^{115\text{m}}\text{In}$ ($n \text{ cm}^{-2} \text{ s}^{-1}$)	6.2891×10^7	4.6304×10^6	1.8054×10^7	1.6009×10^6
Spectrum averaged cross section for Th monitor (mb)	341.67	99.04	269.58	220.01
Calculated neutron flux from ${}^{232}\text{Th}(n,f){}^{97}\text{Zr}$ ($n \text{ cm}^{-2} \text{ s}^{-1}$)	6.2885×10^7	4.5709×10^6	1.7090×10^7	1.5850×10^6

TABLE IV. The monitor reaction with the product nucleus and prominent γ lines.

Monitor reaction	Product nucleus (half-life) [16]	Prominent γ line (branching intensity %) [16]
$^{115}\text{In}(n,n')^{115\text{m}}\text{In}$	$^{115\text{m}}\text{In}$ (4.486 h)	336.24 (45.8)
$^{232}\text{Th}(n,f)^{97}\text{Zr}$	^{97}Zr (16.749 h)	743.36 (93.0)

low energy neutrons from the primary neutron group by the process of making a tailing correction. In the present work, the tailing correction has been done using the method given in the literature [20].

The cross sections have been calculated using the NAA Eq. (1) and the neutron flux from monitor reactions. For a capture reaction, one has to use total neutron flux, but for the reactions having threshold energy, the neutron flux must be corrected. To do this, one has to remove the neutron flux from minimum to threshold energy neutrons, by taking the area under the neutron spectra. For instance, the $^{154}\text{Gd}(n,2n)^{153}\text{Gd}$ reaction has a threshold energy of 8.953 MeV. Hence, the flux for this reaction must be the area under the curve shown from “A” (threshold energy) to “B” (maximum neutron energy) (Fig. 5). This will correct the actual neutron flux used to produce the desired daughter isotopes. Using this neutron flux, a set of cross sections of all reactions has been calculated. In order to remove the effective spectrum average cross section from the threshold to the minimum energy of the peak of interest (E_{ps}), theoretical calculations using modular code TALYS 1.8 have been carried out to obtain the reaction cross sections versus neutron energy. These calculated cross sections at different energies are convoluted with the neutron flux as shown in Fig. 3(a). The spectrum average cross section for each reaction was calculated from threshold to minimum energy (E_{ps}), and it is subtracted from the previous cross section dataset. Thus the final value obtained gives the cross section for the reaction at the spectrum average neutron peak energy.

Using the above method, the cross sections for the $^{182}\text{W}(n,p)^{182}\text{Ta}$, $^{186}\text{W}(n,\gamma)^{187}\text{W}$, $^{154}\text{Gd}(n,2n)^{153}\text{Gd}$, and $^{160}\text{Gd}(n,2n)^{159}\text{Gd}$ reactions were measured at the neutron

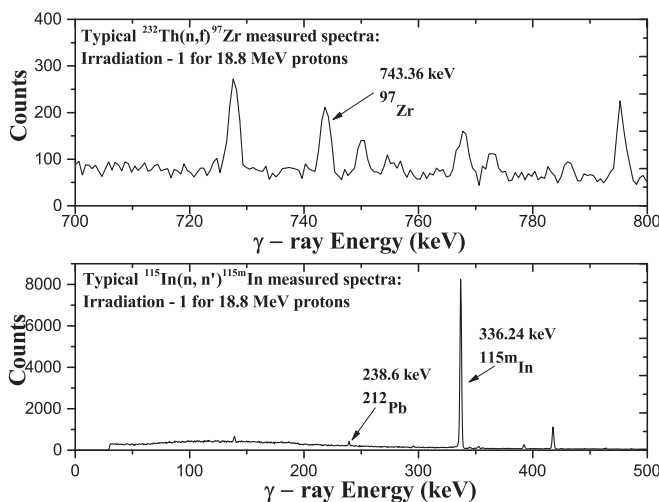


FIG. 4. Typical monitor reaction γ ray spectra using HPGe detector.

energies of 5.08, 8.96, 12.47, and 16.63 MeV. In the $^{160}\text{Gd}(n,2n)^{159}\text{Gd}$ and $^{158}\text{Gd}(n,\gamma)^{159}\text{Gd}$ reactions, a common γ ray of 363.54 keV ($I_{\gamma} = 11.78\%$) is emitted. Therefore, it is necessary to remove this part of the cross section from this capture reaction. At higher energies, the (n,γ) reaction has a very small contribution compared to the lower energy neutrons. Since the lower energy neutron part has been already corrected using the above method, the cross section obtained is purely due to the $(n,2n)$ reaction. In the same way, the tailing corrections have been applied for all the reactions studied in the present work.

IV. THEORETICAL CALCULATIONS

In order to theoretically understand the measured cross section results, two well-known nuclear reaction modular codes, TALYS 1.8 and EMPIRE 3.2.2, were used [13]. Both codes are being used worldwide for nuclear data prediction for the emission of γ , neutron, proton, deuteron, triton, and other particles. Both codes used the reaction parameters from the RIPL database [31]. These codes consider the effect of level density parameters, compound, pre-equilibrium, and direct reaction mechanisms as a function of incident particle energy. The optical model parameters were obtained by using a global potential, proposed by Koning and Delaroche [32]. The compound reaction mechanism was incorporated using the Hauser-Feshbach model [33]. The pre-equilibrium contribution was accounted for by an exciton model that was developed by Kalbach [34]. In the present work, the

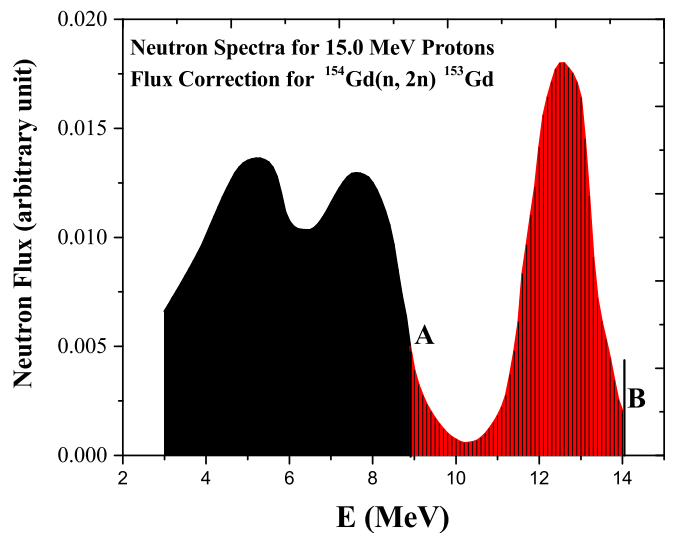


FIG. 5. Neutron flux correction for the threshold energy reactions, shown for $^{154}\text{Gd}(n,2n)^{153}\text{Gd}$ reaction with threshold energy of 8.953 MeV labeled by A and maximum neutron energy labeled by B.

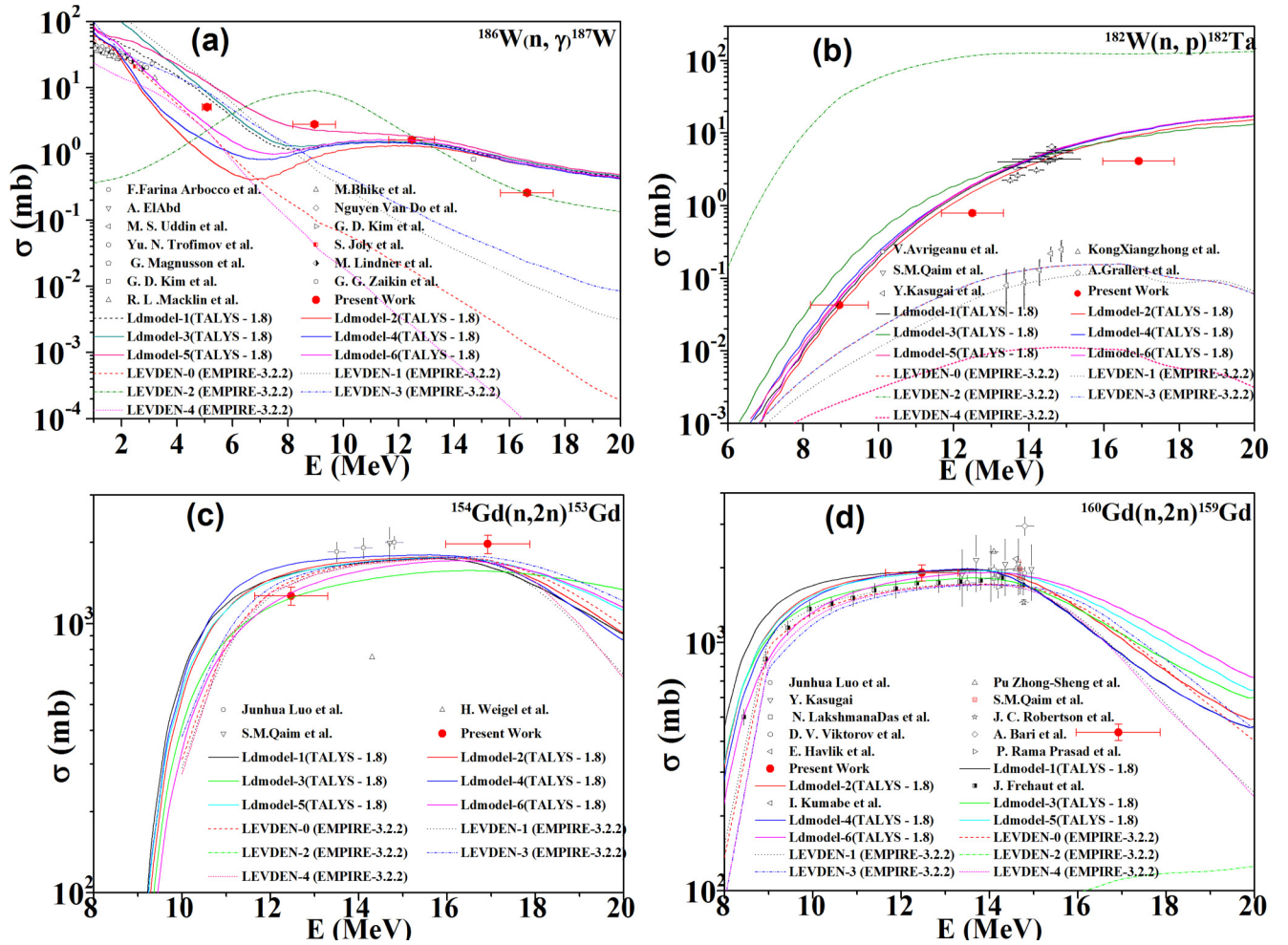


FIG. 6. (a)–(d) Present measured cross section for $^{186}\text{W}(n, \gamma)^{187}\text{W}$ and $^{182}\text{W}(n, p)^{182}\text{Ta}$, $^{154}\text{Gd}(n, 2n)^{153}\text{Gd}$ and $^{160}\text{Gd}(n, 2n)^{159}\text{Gd}$ reactions compared with EXFOR and predicted cross section data using different theoretical nuclear models of TALYS 1.8 and EMPIRE 3.2.2; The LEVDEN-2 model of EMPIRE 3.2.2 predicts very low values (below 100 mb) of cross sections comparing to other models hence it cannot be seen in plot of $^{154}\text{Gd}(n, 2n)^{153}\text{Gd}$.

calculations have been done with all the default parameters except changing the LD model and level density parameters. The present results along with EXFOR data were compared with these predicted data as shown in Figs. 6(a) and 6(b).

V. RESULTS AND DISCUSSION

The main objective of the present study was to provide a set of reaction cross section data in the energy range where there are very few or no measurements available in the literature. These cross sections are important for the accurate reactor design and also to improve the existing nuclear database. Hence the present experimental data for W and Gd isotopes become more important. Further, in this energy region, the standard nuclear models play an important role to validate the present measured experimental data. The major uncertainties in the present reaction cross sections are given in Table V.

The measured data were supported by the theoretical predictions using EMPIRE 3.2.2 and TALYS 1.8. There are different options of level density given in EMPIRE 3.2.2. The level density parameter values Levden = 0, 1, 2, 3, 4 uses

various well known models described in various publications [31,35–39]. By varying these parameters, the cross section for the selected reactions from threshold to 20 MeV were calculated. The predicted and experimental results are shown in Figs. 6(a)–6(d). In TALYS 1.8, the different LD model options were varied from LD model 1 to LD model 6 for the selected nuclear reactions and the experimental cross sections

TABLE V. Major uncertainties incorporated in the present cross section results.

Parameter	Limit (%)
Counting rate	$\leq 4-5$
Efficiency calibration	≤ 3
Self-absorption	≤ 0.2
Mass	≤ 0.001
Neutron flux	≤ 6
I_γ	≤ 3

TABLE VI. Comparison of present experimental data different model predictions using TALYS 1.8 and EMPIRE 3.2.2.

Energy (MeV)	$^{186}\text{W}(n,\gamma)^{187}\text{W}$ reaction cross section (mb)												
	Measured	TALYS 1.8						EMPIRE 3.2.2					
		LD model 1	LD model 2	LD model 3	LD model 4	LD model 5	LD model 6	Levden 0	Levden 1	Levden 2	Levden 3	Levden 4	
5.08 ± 0.165	5.079 ± 0.39	7.23	0.885	8.37	1.53	12.1	2.80	2.24	12.8	2.24	8.83	2.2903	
8.96 ± 0.77	2.767 ± 0.19	1.22	0.871	1.31	1.17	2.26	1.26	0.108	0.618	9.01	0.827	0.0453	
12.47 ± 0.825	1.620 ± 0.11	1.46	1.30	1.48	1.43	1.81	1.58	0.0181	0.0794	1.86	0.146	0.0027	
16.63 ± 0.95	0.257 ± 0.02	0.726	0.676	0.753	0.683	0.799	0.716	0.00129	0.0107	0.249	0.0226	8.41E-5	
Energy (MeV)	$^{182}\text{W}(n,p)^{182}\text{Ta}$ reaction cross section (mb)												
	Measured	TALYS 1.8						EMPIRE 3.2.2					
		LD model 1	LD model 2	LD model 3	LD model 4	LD model 5	LD model 6	Levden 0	Levden 1	Levden 2	Levden 3	Levden 4	
8.96 ± 0.77	0.043 ± 0.003	0.04813	0.04141	0.12659	0.06359	0.05509	0.05307	0.00964	0.00544	31.0747	0.00964	0.00194	
12.47 ± 0.825	0.793 ± 0.06	1.789	1.52	2.33301	1.87	1.86	1.92	0.0842	0.0495	118	0.0842	0.00803	
16.63 ± 0.95	4.092 ± 0.28	10.2	8.89	8.4404	10.2	10.4	10.5	0.163	0.147	124	0.163	0.0107	
Energy (MeV)	$^{154}\text{Gd}(n,2n)^{153}\text{Gd}$ cross section (mb)												
	Measured	TALYS 1.8						EMPIRE 3.2.2					
		LD model 1	LD model 2	LD model 3	LD model 4	LD model 5	LD model 6	Levden 0	Levden 1	Levden 2	Levden 3	Levden 4	
12.47 ± 0.825	1265 ± 98	1534	1556	1248	1659	1520	1298	1444	1412	22.2	1479	1397	
16.63 ± 0.95	1973 ± 153	1683	1725	1571	1737	1735	1703	1748	1744	65.3	1774	1744	
Energy (MeV)	$^{160}\text{Gd}(n,2n)^{159}\text{Gd}$ cross section (mb)												
	Measured	TALYS 1.8						EMPIRE 3.2.2					
		LD model 1	LD model 2	LD model 3	LD model 4	LD model 5	LD model 6	Levden 0	Levden 1	Levden 2	Levden 3	Levden 4	
12.47 ± 0.825	1913 ± 143	1938	1919	1765	1935	1901	1828	1669	1679	52.9	1642	1660	
16.63 ± 0.95	435 ± 33	1009	1155	1183	1005	1364	1465	1213	1027	106	1282	999	

were compared. The details of these parameters are given in the TALYS 1.8 manual [39,40].

As shown in Fig. 6(a) for the $^{186}\text{W}(n,\gamma)^{187}\text{W}$ reaction, the Levden = 2 of EMPIRE 3.2.2 gives a relatively better agreement compared to other Levden values. But at lower energy the Levden = 2 does not give satisfactory predictions. Moreover, all other level density models of EMPIRE 3.2.2 show discrepancies with each other and predicts a lower cross section as compared to the present experimental results. In the case of TALYS 1.8 analyses, results of all the LD model options are in good agreement with the data of present measurements. For the $^{182}\text{W}(n,p)^{182}\text{Ta}$ reaction, all TALYS 1.8 LD model are in good agreement. The EMPIRE Levden models show a discrepancy with most of EXFOR and the present data. For the $^{154}\text{Gd}(n,2n)^{153}\text{Gd}$ and $^{160}\text{Gd}(n,2n)^{159}\text{Gd}$ reactions, the experimental results are in good agreement with both the TALYS 1.8 and EMPIRE 3.2.2 predictions, except Levden = 2, being listed as a future option in the EMPIRE input file. Only the measurement at 16.63 MeV neutron energy of $^{160}\text{Gd}(n,2n)^{159}\text{Gd}$ is under estimated then the predicted values. Overall the theoretical predictions support the present results. The measured cross section values and the different model predicted values are compared at the same energies in Table VI. In general, TALYS 1.8, for all the selected models, gives better agreement compared to EMPIRE 3.2.2 in predicting the present experimental results.

VI. SUMMARY AND CONCLUSIONS

Cross sections for the $^{182}\text{W}(n,p)^{182}\text{Ta}$, $^{186}\text{W}(n,\gamma)^{187}\text{W}$, $^{154}\text{Gd}(n,2n)^{153}\text{Gd}$, and $^{160}\text{Gd}(n,2n)^{159}\text{Gd}$ reactions were measured at the neutron energies 5.08 ± 0.165 , 8.96 ± 0.77 , 12.47 ± 0.825 , and 16.63 ± 0.95 MeV by using the neutron activation analysis technique and incorporating standard tailing corrections [18]. The cross sections have been measured in an energy range where very few or no measurements are available. The different correction terms are discussed in order to

achieve accurate cross section results. The spectrum averaged neutron energy and accurate flux measurements have also been duly incorporated. The neutron flux at different energies has been calculated by using two monitor reactions and the values thus obtained were found to be in good agreement. The average flux values from the two monitor reactions were taken for cross sections calculation. The cross sections for the $^{186}\text{W}(n,\gamma)^{187}\text{W}$ reaction have been measured at four different energies. In the case of $^{182}\text{W}(n,p)^{182}\text{Ta}$ the cross sections are reported at 8.96 ± 0.77 , 12.47 ± 0.825 , and 16.63 ± 0.95 MeV. For the $^{154}\text{Gd}(n,2n)^{153}\text{Gd}$ and $^{160}\text{Gd}(n,2n)^{159}\text{Gd}$ reactions, the cross sections are reported at 12.47 ± 0.825 , and 16.63 ± 0.95 MeV neutron energies. All the measurements have been compared with the theoretical modular codes TALYS 1.8 and EMPIRE 3.2.2. It may be concluded that TALYS 1.8 gives an overall satisfactory agreement with the present experimental and EXFOR results for most of the selected LD model as compared to EMPIRE 3.2.2 predictions. However, in the case of (n,γ) reaction, Levden = 2 of EMPIRE gives somewhat better predictions as compared to other Levden models in the energy region above 12 MeV. The cross section data presented in this work are important for the future fission/fusion reactor technology.

ACKNOWLEDGMENTS

One of the authors (S.M.) thanks the DAE-BRNS for the sanction of a major research project (Sanction No. 36(6)/14/22/2016-BRNS). The authors are grateful to Dr. S. C. Sharma (Scientific Officer, BARC – TIFR Pelletron Accelerator Facility) for preparing the Li target and for his help in the experimental setup. The authors acknowledge gratefully the help of Prof. J. F. Sharpey Schafer, Retired Professor, Liverpool University, and former Director, iThemba LABS, South Africa, for his valuable suggestions and corrections in the manuscript. Thanks are also due to N. Barot, N. Agrawal, P. K. Mehta, and K. Chaudhari for their help in the target preparation.

-
- [1] A. J. Koning and J. Blomgren, Nuclear data for sustainable nuclear energy, JRC Scientific and Technical Report No. EUR23977EN-2009, 2009, retrieved from https://cordis.europa.eu/pub/fp6-euratom/docs/candidate-final-report_en.pdf.
- [2] Cross Section Information Storage and Retrieval System (EXFOR), IAEA, Vienna, Austria, <http://www.nds.iaea.or.at/exfor/> (online).
- [3] M. Lehnen *et al.*, *J. Nucl. Mater.* **463**, 39 (2015).
- [4] J. Qing, Y. Wu, M. Regis, and J. W. Kwan, *IEEE Trans. Nucl. Sci.* **56**, 1312 (2009).
- [5] J. Reijonen, F. Gicquel, S. K. Hahto, M. King, T. P. Lou, and K. N. Leung, *Appl. Radiat. Isotopes* **63**, 757 (2005).
- [6] Y. Wu, J. P. Hurley, Q. Ji, J. Kwan, and K. N. Leung, *IEEE Trans. Nucl. Sci.* **56**, 1306 (2009).
- [7] V. Voitsenya *et al.*, *Rev. Sci. Instrum.* **72**, 475 (2001).
- [8] G. De Temmerman, R. A. Pitts, V. S. Voitsenya, L. Marot, G. Veres, M. Maurer, and P. Oelhafen, *J. Nucl. Mater.* **363-365**, 259 (2007).
- [9] K. H. Behringer, *J. Nucl. Mater.* **145**, 145 (1987).
- [10] Y. Gohar, I. Bolshinsky, and I. Karnaukhov, NEA/NSC/DOC(2015)7, 254(2015), retrieved from [http://www.oecd.org/officialdocuments/publicdisplaydocumentpdf/?cote=NEA/NSC/DOC\(2015\)7&docLanguage=En](http://www.oecd.org/officialdocuments/publicdisplaydocumentpdf/?cote=NEA/NSC/DOC(2015)7&docLanguage=En).
- [11] R. Vijayalakshmi, D. K. Singh, M. K. Kotekar, and H. Singh, *J. Radioanal. Nucl. Chem.* **300**, 129 (2014).
- [12] S. Dutta, P. Suryanarayanan, A. R. Kandalgaonkar, R. S. Sharma, H. Bose, and V. K. P. Unny, *BARC News Lett.* **271**, 2 (2006).
- [13] N. Dzysiuik, I. Kadenko, A. J. Koning, and R. Yermolenko, *Phys. Rev. C* **81**, 014610 (2010).
- [14] K. J. R. Rosman and P. D. P. Taylor, *Pure Appl. Chem.* **70**, 217 (1998).
- [15] <http://www.nndc.bnl.gov/qcalc/index.jsp>, retrieved on 11 November 2016.
- [16] http://www.nndc.bnl.gov/nudat2/indx_dec.jsp, retrieved on 21 March 2017.
- [17] V. Vansola *et al.*, *Radiochim. Acta* **103**, 817 (2015).

- [18] C. H. Poppe, J. D. Anderson, J. C. Davis, S. M. Grimes, and C. Wong, *Phys. Rev. C* **14**, 438 (1976).
- [19] J. D. Anderson, C. Wong, and V. A. Madsen, *Phys. Rev. Lett.* **24**, 1074 (1970).
- [20] D. L. Smith *et al.*, Corrections for Low Energy Neutrons by Spectral Indexing, retrieved from <https://www.oecdnea.org/science/docs/2005/nsc-wpec-doc2005-357.pdf>.
- [21] P. M. Prajapati *et al.*, *Eur. Phys. J. A* **48**, 1 (2012).
- [22] M. W. Mcnaughton, N. S. P. King, F. P. Brady, J. L. Romero, and T. S. Subramanian, *Nucl. Instrum. Methods* **130**, 555 (1975).
- [23] A. A. Lapenas, *Neutron* (ZINATNE, Riga, USSR, 1975), p. 80.
- [24] G. Loevestam, M. Hult, A. Fessler, T. Gamboni, J. Gasparro, R. Jaime, P. Lindahl, S. Oberstedt, and H. Tagziria, *Nucl. Instrum. Methods Phys. Res., Sect. A* **580**, 1400 (2007).
- [25] Y. Agus, I. Celenk, and A. Ozmen, *Radiochim. Acta* **92**, 63 (2004).
- [26] M. S. Uddin, S. Sudar, S. M. Hossain, R. Khan, M. A. Zulquarnain, and S. M. Qaim, *Radiochim. Acta* **101**, 613 (2013).
- [27] O. A. Shcherbakov, A. Yu. Donets, A. V. Evdokimov *et al.*, in *International Seminar on Interactions of Neutrons with Nuclei, Dubna, Russia, 2001* (2001), Vol. 9, p. 257.
- [28] R. K. Jain, *Pramana* **49**, 515 (1997).
- [29] I. Garlea, Chr. Miron-Garlea, H.N. Rosu, G. Fodor, and V. Raducu, *Rev. Roum. Phys.* **37**, 19 (1992).
- [30] F. Manabe, K. Kanda, T. Iwasaki, H. Terayama, Y. Karino, M. Baba, and N. Hirakawa, Fac. of Engineering, Tohoku Univ. Tech. Report 52(Issue 2) (1988) 97.
- [31] R. Capote *et al.*, *Nucl. Data Sheets* **110**, 3107 (2009).
- [32] A. J. Koning and J. P. Declaroche, *Nucl. Phys. A* **713**, 231 (2003).
- [33] W. Hauser and H. Feshbach, *Phys. Rev.* **87**, 366 (1952).
- [34] C. Kalbach, *Phys. Rev. C* **33**, 818 (1986).
- [35] <https://www-nds.iaea.org/RIPL-3/densities/>, retrieved on 28 February 2017.
- [36] A. V. Ignatyuk, K. K. Istekov, and G. N. Smirenkin, *Sov. J. Nucl. Phys.* **29**, 450 (1979).
- [37] A. V. Ignatyuk, J. L. Weil, S. Raman, and S. Kahane, *Phys. Rev. C* **47**, 1504 (1993).
- [38] A. Gilbert and A. G. W. Cameron, *Can. J. Phys.* **43**, 1446 (1965).
- [39] S. Hilaire, M. Girod, S. Goriely, and A. J. Koning, *Phys. Rev. C* **86**, 064317 (2012).
- [40] A. Koning, S. Hilaire, and S. Goriely, *TALYS-1.6 - A Nuclear Reaction Program*, User Manual, 1st ed. (NRG, Westerduinweg, 2013).

Cross sections of nuclear isomers from the interaction of protons with the thin thorium target

R.R. Holomb^{1,2,*}, S.A. Tari², K. Katovsky¹, I. Haysak², J. Adam^{3,4}, V.B. Brudanin³, R. Vespalec⁴, J. Vrzalova^{3,4}, L. Zavorka³, M. Zeman^{1,3}, D.V. Karaivanov^{3,5}, A.A. Solnyshkin³, D.V. Philosophov³, J. Khushvaktov³, and V.M. Tsupko-Sitnikov³

¹Technological University of Brno, Brno, Czech Republic

²Uzhgorod National University, Uzhgorod, Ukraine

³Joint Institute for Nuclear Research, Dubna, Russia

⁴Institute of Nuclear Physics, Czech Academy of Sciences, Rez, Czech Republic

⁵Institute for Nuclear Research and Nuclear Energy, Sofia, Bulgaria

Abstract. The paper shows the results of experimental gamma spectra obtained with a thorium ^{232}Th target and an aluminum collector irradiated at the JINR Synchrocyclotron with the internal beam of energies of 100 and 600 MeV. For ^{232}Th there were identified 258 and 222 gamma lines that belong to 45 and 55 nuclides, respectively. For Al - 238, 330 lines and 81, 119 nuclides, respectively. The cross sections of fragmentation of the ^{232}Th and Al nuclei under the interaction with protons 100 and 600 MeV was determined. A comparison of the obtained cross sections of the reaction with theoretical calculations was performed.

1 Introduction

The interest of the world scientific community in the research of this kind is primarily associated with the problem of transmutation of the long-lived radioactive waste and the creation of subcritical nuclear power plants with the uranium-thorium cycle controlled by Accelerator Driven Subcritical Systems (ADS). These installations may also partially take on the function of the radioactive waste disposal. Also of great interest is the ability to use ^{238}U and ^{232}Th as nuclear fuel since these isotopes are more common in nature than ^{235}U .

The purpose is to study the process of separation of ^{232}Th protons.

The task is processing the experimental γ -spectrum experiment performed on the Synchrocyclotron (Phasotron) at JINR, Dubna.

The object of the study is the ^{232}Th nucleus.

The subject of the research is the reaction of fission and fragmentation of the ^{232}Th nucleus under the interaction with protons.

The research methods are the γ -spectroscopy of the irradiated target and the collector of the fragments. For theoretical calculations a Monte Carlo method using the MCNP 6 1.0 program with the CEM model was used.

*e-mail: xholom05@stud.feec.vutbr.cz

1.1 JINR

In Russia, a number of studies on the irradiation of small targets on direct proton beams have been performed in ITEP. These works studied the transmutation of the long-lived waste, primarily ^{129}I and younger actinides ^{237}Kr , ^{238}U , ^{239}Pu , ^{241}Am , have been conducted within the framework of a broad international collaborative work on the subcritical installation "Energy plus transmutation", "QUINTA" and "BURAN" on the Phasotron beam LFBE [1,2].

1.2 MYRRHA

A multipurpose hybrid research reactor for application in the field of high technology is the setup using fast neutrons with the lead-bismuth coolant and heat capacity of 50-100 MW. It is designed as a system using an accelerator to operate in subcritical and critical modes. The reactor is scheduled to be commissioned in 2023 [3].

1.3 Installation of neutron generation in KIPT

The US government supports the development, construction and operation of an ADS system (neutron source research facility, KHPTI) at the Kharkiv Institute of Physics and Technology (KPI) of Ukraine under the Russian Research Reactor Fuel Return (RRRFR) program of the United States Department of Energy.

This device consists of a sub-critical accelerator system that uses the low-enriched uranium oxide with a cooling fluid (water) and the beryllium-carbon reflector. An electron accelerator is used to create a neutron source used by a subcritical device to function. The target of this installation is in the middle of the tungsten plate or the natural uranium used to create neutrons that cool water. Tungsten or uranium is the target material for generating neutrons. Water, like the coolant and the aluminum alloy structure, are used as a target. The target configuration is designed to place a beam square profile and hexagonal fuel geometry. The power of the accelerator beam is 100 kW from 100 MeV electrons [4].

2 Experiment

The experiment was performed on the Phasotron in DLNP, JINR (Fig. 1). The maximum energy of accelerated protons at Phasotron is 660 MeV.

The main parameters of the Phasotron are:

1. Energy of accelerated protons – $T_p = (659 \pm 6)$ MeV.
2. Energy dispersion – $T_e = (3.1 \pm 0.8)$ MeV.
3. Frequency of proton acceleration cycles (modulation frequency) – 250 Hz.

Emittance at the boundary of the scattered magnetic field of the Phasotron:

1. Horizontal $e_x = (5,1 \pm 2,3)$ cm*mrad.
2. Vertical $e_y = (3.4 \pm 1.4)$ cm*mrad.
3. Intensity of the extracted proton beam mode "fast" output (pulse duration 30 mks) (2-2,5) mA.
4. Intensity of the extracted proton beam in the "slow" output mode (beam extended in time for 85% of the modulation period (~ 4 mc)) (1.6-2.0) mA.
5. Extracted proton beam has a microstructure — bunches of particles with a duration of about 10 ns follow with an interval of about 70 ns.

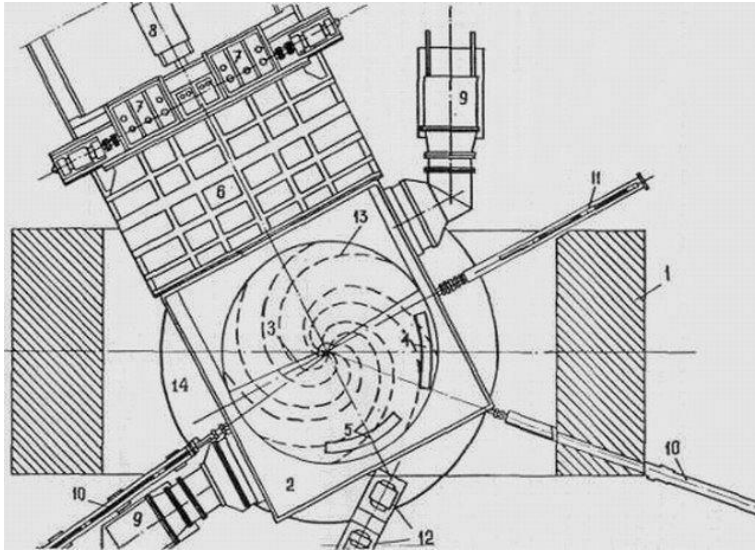


Figure 1: Schema of the Phasotron in DLNP, JINR

1 – magnet housing; 2 – vacuum chamber; 3 – duant; 4 – output channel; 5 – SI-electrode for beam stretching; 6 – intermediate chamber; 7 – variator; 8 – HF generator; 9 – vacuum pumps; 10 – samplers; 11 – ion source rod; 12 – the first magnetic elements of the proton path; 13 – spiral shimmy for the spatial variation of the magnetic field; 14 – magnet excitation winding

The samples, using a special device, were placed in the accelerator chamber at a radius corresponding to the energy of protons 100 and 600 MeV at the current of $0.3 \mu\text{A}$. The position of the 100 and 600 MeV beams was determined by placing an aluminum foil inside the accelerator and perpendicular to the proton beam and evaluating the activity of the foil. For the target, foils of ^{232}Th were used with a thickness of 100 microns and a weight of 149.5 mg placed between two Al foils with thickness of 50 μm . The foil area was 1.5 cm^2 . The target was placed in such way that the proton beam was hitting the edge of the target as it shows on Fig. 2. The dimensions of the beam in the cross section were $\Delta X = 2.5 \text{ cm}$ and $\Delta Y = 2.6 \text{ cm}$. To determine the integral flow of protons falling on the ^{232}Th samples, an activation method of ^{27}Al with ^{24}Na was used. For this purpose, two sides of the ^{232}Th were placed close to the ^{27}Al foil (50 μm). As a result, for each of the irradiations, an integral proton flow on samples was determined, which was $7.64 \cdot 10^{12}$.

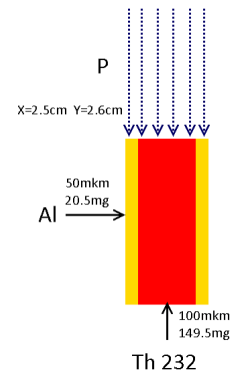


Figure 2: ^{232}Th target

After irradiation, the samples were removed from the chamber of the Phasotron and moved to the spectroscopic complex YSNAPP-2, which separately measured the spectra of γ radiation of the ^{232}Th and ^{27}Al foils using the HPGe-detector of the CANBERRA company with an efficiency of 18% and a resolution of 1.9 keV in the line 1332 keV ^{60}Co . The measurement time was 1 m, 2 m, 4 m, 8 m, 16 m, 30 m, 1h, 2 h, 4 h, 6 h, 12 h, 1d, 2d [5].

3 Processing of gamma spectra

The processing of the gamma spectra was carried out using the DEIMOS32 program to find positions of peaks, their areas and other parameters. The identification of the nuclei formed in ^{232}Th samples as a result of nuclear reactions with protons was carried out using a set of scripts based on the Ruby programming language (AttCor, EffCor, MidLit5, NonLin64, PureGam, SepDepe, SigmaJ7, TimeConst, TrueConic, TransCs9). After that, the cross sections of the obtained isotopes were compared with data from the Los Alamos National Laboratory under the program MCNP6 1.0 (the database of theoretically calculated cross sections of isotopes CEM100.asc) [6], [7].

4 Results

4.1 ^{232}Th

For 100 MeV, 45 nuclides were identified. The identified nuclides have a mass number in the range of 71–224 with spaces in the range of values 100–110 and 150–223. Fig. 1 shows the dependence of the cross section of the fragmentation of nuclei on the mass number A. The intervals of the mass number of nuclides correspond to the intervals of the atomic number Z 44, 45 (Fig. 3a) and 61–88 (Fig. 3b).

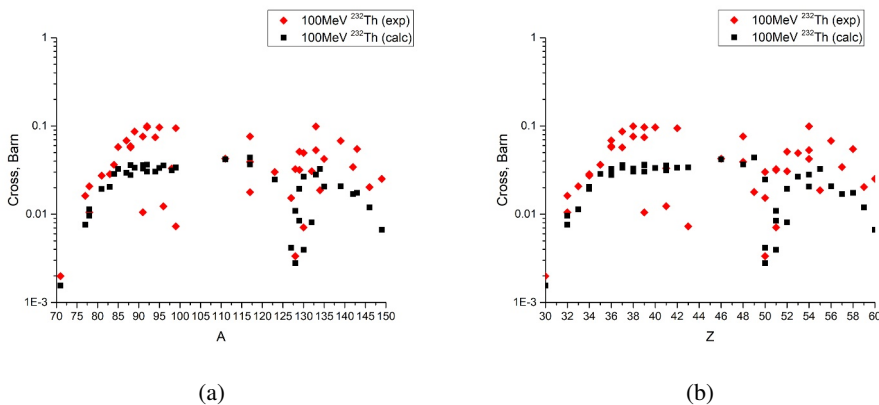


Figure 3: Graph of the cross sections for thorium irradiated by 100 MeV protons

As a result of processing of gamma spectra measured for the irradiated thorium target, 222 gamma lines were identified. The comparison of the obtained data with published results allowed identification of 55 nuclides by energy and half-life. The identified nuclides have a mass number in the 68–211 range with spaces in the range of values 134–142 and 143–186. The spacing of the mass number of nuclides corresponds to spaces of the serial number Z of 54–57 (Fig. 4a) and 58–77 (Fig. 4b). The sections of fragmentation of the ^{232}Th nucleus under the action of 600 MeV of protons were determined, respectively.

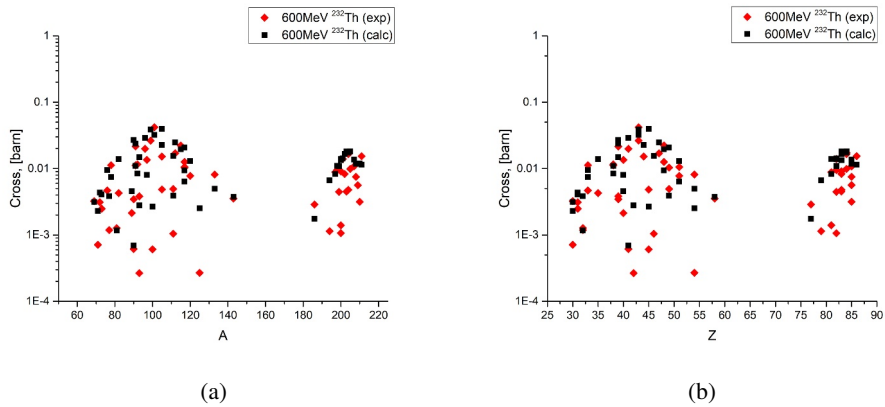


Figure 4: Graph of the cross sections for thorium irradiated by 600 MeV protons

4.2 Al

The 81 nuclides were identified. The identified nuclides have a mass number in the range of 24–233 with spaces in the range of values Z and A 63–71 (Fig. 5a) and 150–171 (Fig. 5b), respectively. Fig. 5 shows the dependence of the fragmentation cross section of nuclei on the mass number A. Fig. 6 shows the dependence of the fragmentation cross section of nuclei on the serial number Z.

The 119 nuclides were identified. The identified nuclides have a mass number in the range of 7–237 with spaces in the range of values Z and A 58–69 and 143–167, respectively. Fig. 6a shows the dependence of the fragmentation cross section of nuclei on the mass number A. Fig. 6b shows the dependence of the fragmentation cross section of nuclei on the serial number Z.

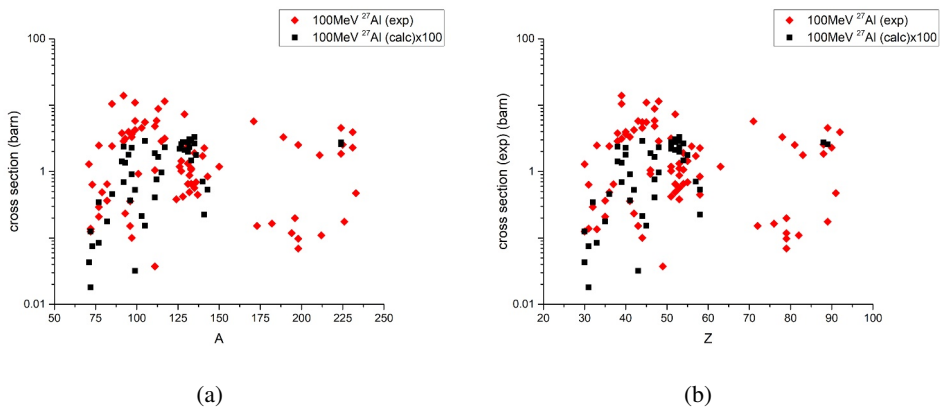


Figure 5: Graph of the cross sections for aluminum irradiated by 100 MeV protons

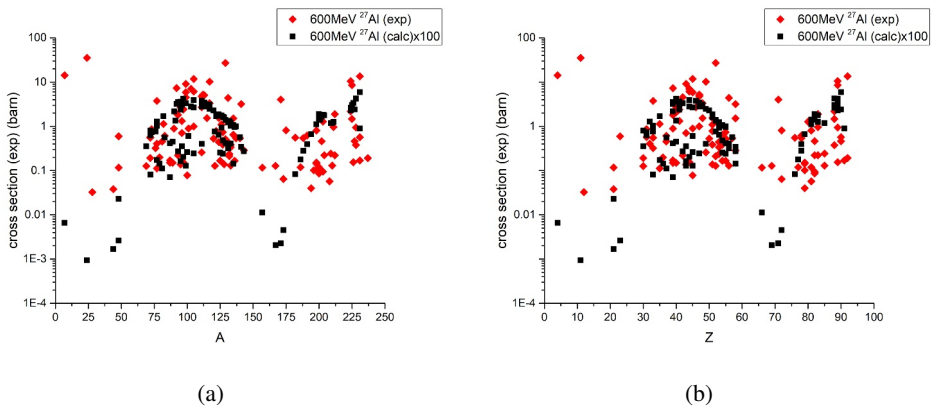


Figure 6: Graph of the cross sections for aluminum irradiated by 600 MeV protons

5 Conclusion

The experimental data on the fragmentation of the ^{232}Th nucleus under the influence of protons in the energy of 100 and 600 MeV have been processed. The experiment is performed at the Phasotron in JINR, Dubna. The sections of fragmentation of the ^{232}Th nucleus have been obtained depending on the charge and mass number of the reaction fragments. For the 100 MeV ^{232}Th targets the 258 gamma lines that belong to 45 nuclides and 222 belong to 55 nuclides in case of 600 MeV have been identified. For the Al collector, the 238 gamma lines belonging to 81 nuclides in case of 100 MeV and 330 lines for 119 nuclides in case of 600 MeV, respectively, have been identified. The incommensurability of the number of lines for the target and the collector can be explained by the different distribution of fragments by kinetic energy. For the mass and charge spectra, the separation and fragmentation reactions are clearly divided.

References

- [1] J.H. Khushvaktov, J. Adam, A.A. Baldin, W.I. Furman, S.A. Gustov, Yu.V. Kish, A.A. Solnyshkin, V.I. Stegailov, J. Svoboda, P. Tichy, V.M. Tsoupko-Sitnikov, S.I. Tyutyunnikov, R. Vespalec, J. Vrzalova, V. Wagner, B.S. Yuldashev, L. Zavoroka, M. Zeman, *Applied Radiation and Isotopes* **137**, 102-107 (2018)
- [2] I. Adam, V. Wagner, I. Vrzalova, L. Zavoroka, M. G. Kadykov, V.S. Pronsky, A.A. Solnyshkin, V.I. Steigailov, M. Suhopar, S.I. Tyutyunnikov, V.I. Furman, Zh. Khushvaktov, V.M. Tsupko-Sitnikov, V.V. Chilap, *Applied Radiation and Isotopes* **107**, 225-233 (2015)
- [3] <http://www.atomic-energy.ru/news/2012/01/16/30122>
- [4] M.I. Ayzatskiy, B.V. Borts, A.N. Vodin, P.A. Demchenko, A.Yu. Zelinskiy, I.M. Karnaukhov, V.A. Kushnir, V.V. Mitrochenko, A.O. Mytsykov, I.M. Neklyudov, S.N. Oleynik, F.A. Peev, G.D. Pugachev, S.A. Soldatov, I.V. Ushakov, Y. Gohar, I. Bolshinsky, Ya.L. Chi, S.L. Pei, S.H. Wang, W.B. Liu, *Problems of atomic science and technology* **79**, 3-9 (2012)
- [5] R. Holomb, K. Katovský, I Adam, M. Zeman, I. Haysak, A. Solnyshkin, J. Khushvaktov, R. Vespalets, in *Proceedings of the 2018 19th International Scientific Conference on Electric Power Engineering (EPE)* (Brno: VUT, 2018) 527-531
- [6] S.G. Mashnik and A.J. Sierk, LANL Report LA-R-12-01364 (2012)
- [7] F.B. Brown, LANL Report LA-UR-13-23040 (2013)